



Theses and Dissertations

2023-06-26

Acoustic Directivity: Advances in Acoustic Center Localization, Measurement Optimization, Directional Modeling, and Sound Power Spectral Estimation

Samuel David Bellows
Brigham Young University

Follow this and additional works at: <https://scholarsarchive.byu.edu/etd>



Part of the [Physical Sciences and Mathematics Commons](#)

BYU ScholarsArchive Citation

Bellows, Samuel David, "Acoustic Directivity: Advances in Acoustic Center Localization, Measurement Optimization, Directional Modeling, and Sound Power Spectral Estimation" (2023). *Theses and Dissertations*. 10021.

<https://scholarsarchive.byu.edu/etd/10021>

This Dissertation is brought to you for free and open access by BYU ScholarsArchive. It has been accepted for inclusion in Theses and Dissertations by an authorized administrator of BYU ScholarsArchive. For more information, please contact ellen_amatangelo@byu.edu.

Acoustic Directivity: Advances in Acoustic Center Localization, Measurement
Optimization, Directional Modeling, and Sound Power Spectral Estimation

Samuel David Bellows

A dissertation submitted to the faculty of
Brigham Young University
in partial fulfillment of the requirements for the degree of
Doctor of Philosophy

Timothy W. Leishman, Advisor
Brian E. Anderson
Tracianne B. Neilsen
Brian D. Jeffs
Kent L. Gee

Department of Physics and Astronomy
Brigham Young University

Copyright © 2023 Samuel David Bellows

All Rights Reserved

ABSTRACT

Acoustic Directivity: Advances in Acoustic Center Localization, Measurement Optimization, Directional Modeling, and Sound Power Spectral Estimation

Samuel David Bellows
Department of Physics and Astronomy, BYU
Doctor of Philosophy

Sound radiation from an acoustic source typically exhibits directional behavior, as is the case for the human voice, musical instruments, and loudspeakers, to name just a few. The necessity of directional data for many applications, such as sound source modeling, microphone placement, room acoustical design, and auralization, motivates directivity measurements. However, these measurements require careful understanding and implementation to produce the most meaningful results. Accordingly, this dissertation addresses several topics relevant to directivity theory, measurement, processing, and application. It first expands and amends previously published concepts of an acoustic source center and demonstrates the close relationship between the center and a source's far-field directional response. This relationship subsequently leads to an acoustic centering method that improves source placements within directivity measurement arrays. The dissertation then addresses several measurement considerations, including the required numbers of sampling positions for directivity measurements, quadrature rules applicable to standardized dual-equiangular sampling schemes, and a source's far-field response from arbitrarily shaped microphone arrays. Selected directivity results for the human voice and musical instruments illustrate applications of the developed measurement theories for procuring high-resolution results over a sphere. Compiled voice and musical instrument directivities now appear in an open-source database for use in room acoustical modeling, microphone placements, and other applications. To better elucidate and help predict sound source radiation, this work proposes several theoretical models, including equivalent point-source models, low-frequency radiation from a radially vibrating cap set on a rigid spherical shell with a circular aperture, and radiation from a vibrating cap on a rigid sphere with imposed mode shapes. Finally, this dissertation presents two microphone placement methods for audio and other applications. The first method approximates the measurement of a source's sound power spectrum through a single-channel measurement; the second considers microphone placement for maximum perceived loudness. The work's various developments, results, and conclusions will assist researchers and practitioners in better evaluating, predicting, and applying sound source directivities for many uses.

Keywords: directivity, sound radiation, musical instruments, speech, modeling

ACKNOWLEDGMENTS

This work would not have been possible without the generous donations made by Dr. William Strong and others in establishing the William James and Charlene Fuhriman Strong Family Musical Acoustics Endowed Fellowship Fund. Dr. Strong's decades-long efforts in furthering musical acoustics research at the university culminated in this fund which financially supported this work.

I am deeply grateful for my advisor, Dr. Timothy Leishman, who provided me with the intellectual freedom to explore the wide variety of topics addressed in this work. His mentoring, support, and encouragement have been invaluable to me during my graduate studies.

Many thanks to the numerous students who assisted with measurements and analysis, including Joseph Avila, Jayden Smith, Dallin Harwood, Rachel Edelman, Dallin Haslim, Kevin Hatch, Kennen Brooks, and Ian Bacon. Without them, many of the results of this work would not have been possible.

Special thanks to Jeremy Peterson for assistance with the construction of the measurement arc, artificial blowers, and other contraptions used in this work.

Lastly, I am grateful for the encouragement from family and friends, especially from my wife Elise who patiently supported me during my studies.

Contents

Table of Contents	iv
List of Figures	xii
List of Tables	xxxii
Preface	1
I The Acoustic Center	5
1 Low-Frequency Acoustic Center	6
1.1 Introduction	6
1.2 Theory of the Low-Frequency Acoustic Center	10
1.3 Application to Spherical Source Configurations	13
1.4 Examples of Spherical Source Configurations	17
1.4.1 Radially Oscillating Sphere	17
1.4.2 One Point Source on a Rigid Sphere	17
1.4.3 Radially Oscillating Cap on a Rigid Sphere	21
1.4.4 Axially Oscillating Cap on a Rigid Sphere	21
1.4.5 Two Point Sources on a Rigid Sphere	25
1.4.6 Multiple Point Sources on a Rigid Sphere and Related Extensions	27
1.5 Generalization to Nonspherical Source configurations	29
1.5.1 General Formulation	30
1.5.2 Point Source Distribution	31
1.6 Experimental Example	34
1.6.1 Centering Results	34
1.6.2 Directivity Correction	37
1.7 Discussion	39
1.8 Conclusions	42
2 Acoustic Centering Using Acoustical Holography	44
2.1 Introduction	44

2.2	Theory	49
2.2.1	Far-field Nature of Radiating Sources	49
2.2.2	Effect of Source Translation on Far-field Directivity	51
2.2.3	Effect of Small Translations	60
2.3	Acoustic Center Revisited	64
2.4	Acoustic Centering Algorithm	65
2.5	Theoretical Results	68
2.5.1	Multipoles	68
2.5.2	Point Source Distribution	69
2.5.3	Point Source on a Sphere	74
2.6	Discussion	76
2.7	Conclusions	77
3	Phase Algorithm for Acoustic Centering	79
3.1	Introduction	79
3.2	Algorithm	80
3.2.1	Far-field Phase Relationship	80
3.2.2	Phase-based Centering Algorithm	82
3.3	Theoretical Results	86
3.4	Experimental Results	87
3.5	Conclusions	91
4	Comparison of Pressure Field Translation Methods	92
4.1	Introduction	92
4.2	Expansion Coefficients of Pressure Field	93
4.3	Direct Method	95
4.4	Results	97
4.5	Analysis	100
4.6	Conclusions	100
II	Measurement Theory	101
5	Spatial Aliasing and Source Order	102
5.1	Introduction	102
5.2	Source Order	104
5.2.1	Far-Field Propagation as a Filter	104
5.2.2	Effect of Source Translation	108
5.2.3	Effect of Body Diffraction	108
5.3	Methods for Estimating the Effective Source Dimension from Data	109
5.3.1	Spectral Energy Method	111
5.3.2	Directivity Deviation Method	111

5.4	Results	112
5.4.1	Musical Instruments	112
5.4.2	Speech	112
5.5	Discussion and Conclusions	116
6	Quadrature for Dual-Equiangular Sampling	117
6.1	Introduction	117
6.2	Numerical Integration For Equiangular Sampling Schemes	120
6.2.1	Azimuthal Sampling	120
6.2.2	Polar Sampling	121
6.2.3	Chebyshev Quadrature	122
6.2.4	Chebyshev-Lobatto Quadrature	127
6.2.5	Chebyshev-Radau Quadrature	128
6.2.6	Hemispherical Quadrature Rules	129
6.3	Spherical Harmonic Expansions	130
6.4	Pressure-Field Expansions	136
6.4.1	Spatial Aliasing	137
6.4.2	Effect of Azimuthal Sampling Density	141
6.4.3	Far-field Projection	142
6.4.4	Hemispherical Directivities	146
6.5	Conclusions	148
7	Spherical Directivities from Arbitrarily Shaped Arrays	149
7.1	Introduction	149
7.2	Formulation	151
7.2.1	HELS Method	151
7.2.2	Far-Field Directivity Pattern	153
7.3	Numerical Results	153
7.3.1	Array Sampling Schemes	153
7.3.2	BEM Results	154
7.3.3	Numerical Experimental Errors	156
7.4	Experimental Results	160
7.4.1	Princeton Reverb	161
7.4.2	Twin Reverb	163
7.5	Discussion	164
7.6	Conclusions	165
III	Directivity Measurement Results	167
8	Gamelan Gong Directivity	168
8.1	Introduction	168

8.2	Methods	171
8.2.1	Measurements	171
8.2.2	Signal Processing	174
8.2.3	Spherical Harmonics and Directivity Functions	175
8.3	Results	179
8.3.1	Directivity Results	179
8.4	Analysis	184
8.4.1	Modal Frequencies	184
8.4.2	Directivity Index	187
8.4.3	Impact of Side Walls on Median Plane Symmetry	192
8.5	Discussion	192
8.6	Conclusions	194
9	Influence of Musician Diffraction on Clarinet Directivity	195
9.1	Introduction	195
9.2	Musician Diffraction and Absorption	198
9.3	Modeling Absorption and Diffraction with Array Shading	200
9.4	Directivity Measurements	203
9.5	Results	205
9.5.1	Diffraction Effects	205
9.5.2	Shading Results	206
9.6	Conclusions	208
10	Effect of Head Orientation on Speech Directivity	209
10.1	Introduction	209
10.2	Methods	210
10.2.1	Measurements	210
10.2.2	Processing	212
10.2.3	Directivity Functions	212
10.3	Results	213
10.3.1	Head and Torso Diffraction	213
10.3.2	Head Orientations	214
10.4	Analysis	217
10.4.1	Neglecting Head Orientation	217
10.4.2	Neglecting Torso Diffraction	217
10.4.3	Neglecting Effect of Head Orientation on Torso Diffraction	218
10.5	Conclusions	219
11	Trumpet Directivities Derived from a Multiple-Capture Method	221
11.1	Introduction	221
11.2	Methods	224
11.2.1	Measurement Procedure	224

11.2.2	Data processing and analysis	226
11.3	Results	232
11.3.1	Narrowband Frequency Response Functions	232
11.3.2	Spherical Harmonic Expansions	235
11.3.3	Spatial Aliasing	236
11.3.4	Spatial Filtering	240
11.3.5	Far-field Propagation	240
11.3.6	Directivity Index	241
11.4	Analysis	243
11.4.1	Zenith Variance	243
11.4.2	Comparison with Artificial Directivity	246
11.4.3	Symmetry	247
11.4.4	Comparison of Results from Previous Work	248
11.5	Discussion	249
11.6	Conclusions	251
12	Development of a Musical Instrument Directivity Database	253
12.1	Introduction	253
12.2	Methods	259
12.2.1	Measurement system	259
12.2.2	Measurement procedure	261
12.2.3	Data processing	262
12.3	Validation Experiments	271
12.3.1	Coherence Balloons	272
12.3.2	Single-Capture System	273
12.3.3	Perturbation Tests	273
12.4	Selected Results	274
12.4.1	Narrowband	274
12.4.2	Far-field Propagation	277
12.4.3	Acoustic Centering	278
12.4.4	Comparisons to Single-Capture Measurements	280
12.4.5	Coherence Functions	284
12.4.6	Broader Bands	285
12.4.7	Pole Measurement Repeatability	287
12.4.8	Comparisons to Previous Works	290
12.4.9	Bandwidth Variations	291
12.4.10	Diffraction Effects	293
12.5	Directivity Database	295
12.6	Conclusions	297

IV	Modeling Sound Radiation	298
13	Point Source Modeling Transmission Matrix Method	299
13.1	Introduction	299
13.2	Theoretical Modeling	300
13.2.1	Point Source Model	300
13.2.2	Kirchhoff-Helmholtz Integral Equation	302
13.3	Measurements	302
13.4	Results	304
13.4.1	Theoretical Prediction	304
13.4.2	Directivity Measurements	305
13.5	Analysis	307
13.6	Conclusions	309
14	Multipole Modeling	310
14.1	Introduction	310
14.2	Methods	312
14.2.1	Measurements	312
14.2.2	Signal Processing	314
14.2.3	Spherical Harmonic Expansions	314
14.2.4	Multipole Representation	315
14.3	Results	317
14.3.1	Modal Extraction	317
14.3.2	Directivity Results	320
14.3.3	Low-frequency Modeling	321
14.4	Conclusions	324
15	Radiation From a Vibrating Cap on a Spherical Shell With a Circular Aperture	325
15.1	Introduction	325
15.2	Analytical Model	329
15.2.1	Formulation	329
15.2.2	Aperture Velocity Solution	331
15.2.3	Potential Layer Solution	334
15.3	Low-Frequency Approximations	335
15.3.1	Vibrating Cap Self and Mutual Impedance	335
15.3.2	Approximation using Eigenfunction Expansion	336
15.3.3	Network Representation	337
15.3.4	Aperture Volume Velocity	341
15.3.5	Multipole Moments	342
15.3.6	Radiated Sound Power	346
15.4	Theoretical Results	348
15.4.1	Comparison with BEM Results	348

15.4.2	General Directional Trends	349
15.4.3	Effect of Aperture Location	350
15.5	Experimental Validation	350
15.6	Analysis and Discussion	359
15.7	Conclusions	361
16	Directivity of Vibrating Caps With Nonaxisymmetric Surface Velocities	364
16.1	Introduction	364
16.2	Methods	366
16.2.1	Exterior Solution of the Helmholtz Equation	366
16.2.2	Spatial Masking	367
16.2.3	Spherical Cap Expansion	368
16.2.4	Series Truncations	369
16.3	Results	378
16.3.1	Two Opposite-Polarity Semicircular Caps	378
16.3.2	Single Semicircular cap	380
16.3.3	Four Alternating-Polarity Quarter-Circular Caps	380
16.3.4	More Complicated Mode Shape	382
16.3.5	Rectangular Cap	383
16.3.6	Stadium Cap	386
16.4	Discussion	387
16.5	Conclusions	388
V	Microphone Placement Techniques	389
17	Microphone Placement for Sound Power Spectra	390
17.1	Introduction	390
17.2	Theoretical Considerations	393
17.2.1	Sound Power	393
17.2.2	Directivity	394
17.2.3	Reverberation	395
17.2.4	Semi-Reverberant Environments	396
17.2.5	Source-Filter Representation	397
17.3	Optimal Microphone Placements For Sound Power Estimation and Reverberation Effects	398
17.3.1	Semi-Reverberant Environments	399
17.3.2	Free-field Environments	400
17.3.3	Reverberant Environments	402
17.4	Results	403
17.4.1	Source Directivity Characteristics	405
17.4.2	Source-Filter Effects	412

17.4.3 Microphone Placements	414
17.5 Discussion	426
17.6 Conclusions	427
18 Microphone Placement for Maximum Loudness	429
18.1 Introduction	429
18.2 Methods	431
18.2.1 Overall Sound Pressure and Weighted Levels	431
18.2.2 Zwicker Loudness	432
18.3 Results	436
18.3.1 Sound Power of Musical Instruments	436
18.3.2 Directivities	438
18.4 Analysis	442
18.5 Conclusions	445
 Bibliography	 446

List of Figures

1.1	Diagram of a radiating source with position and translation vectors.	10
1.2	The acoustic center of a point source on a sphere over dimensionless ka , where a is the sphere's radius.	19
1.3	Sound pressure field for $ka = 0.01$ around (a) a point source on a rigid sphere and (b) its equivalent point source.	20
1.4	Sound pressure field for $ka = 0.01$ around (a) a radially oscillating cap with cap angle $\theta_c = \arccos(1/3)$ on a rigid sphere and (b) its equivalent point source.	22
1.5	Low-frequency acoustic centers of a radially and axially oscillating cap on a sphere as a function of cap angle θ_c	23
1.6	Sound pressure field for $ka = 0.01$ around (a) an axially oscillating cap with cap angle $\theta_c = 0.7\pi$ on a rigid sphere and (b) its equivalent point source.	24
1.7	Low-frequency acoustic center predicted by Eq. (1.28) for two point sources at the opposing poles of a sphere as a function of the second source's relative strength.	26
1.8	Sound pressure field for $ka = 0.01$ produced by two point sources at the opposing poles of a rigid sphere with a source strength ratio of $\gamma = -0.8$	27
1.9	Pressure produced by a point source distribution and the associated acoustic center marked as a green dot.	33
1.10	KEMAR HATS seated within a directivity measurement system.	35

1.11 Objective functions in the median plane at 100 Hz: (a) J_{ss} , (b) J_{zo} , (c) J_{lo} , and (d) J_{ph} .
 The red \times is the low-frequency acoustic center from Eq. (1.59). 36

1.12 Objective functions in the median plane at 300 Hz: (a) J_{ss} , (b) J_{zo} , (c) J_{lo} , and (d) J_{ph} .
 The red \times is the low-frequency acoustic center from Eq. (1.59). 38

1.13 KEMAR HATS directivity. (a) $r = R = 1.17$ m measured, (b) far-field projected, and
 (c) $r = 1.5$ m centered at 100 Hz. (d) $r = R = 1.17$ m measured, (e) far-field projected,
 and (f) $r = 1.5$ m centered at 300 Hz. 40

2.1 A depiction of an acoustic source contained within a spherical Gaussian surface of
 radius $r = a$. Here, S denotes the body’s boundary and Ω denotes the acoustic fluid
 domain. The subspace Ω_a represents the region where the Helmholtz equation solution
 [Eq. (2.1)] is valid, as the spherical surface encloses all nonhomogenous terms. 50

2.2 A depiction of a translated acoustic source with associated position vectors. The dotted
 contour suggests the untranslated source position for reference. 54

2.3 Directivity patterns of a centered and translated 20 point-source dodecahedral dis-
 tribution at varying radial measurement distances compared to the far-field patterns.
 Centered source distribution at (a) measurement radius $r = 1$ m, (b) propagated to $r = 2$
 m, (c) propagated to $r = 10$ m, and (d) far-field pattern. Translated source distribution
 centered about $\mathbf{r}'' = (0.7, 0.0, 0.0)$ m at (e) measurement radius $r = 1$ m, (f) propagated
 to $r = 2$ m, (g) propagated to $r = 10$ m, and (h) far-field pattern. 57

2.4 Directivity L_{AWRMSD} from anticipated far-field omnidirectionality based on propagated
 far-field pressures from a displaced monopole as assessed by arrays with varying
 numbers of sampling positions. The solid lines show the actual L_{AWRMSD} values,
 whereas the dotted lines of similar colors help visualize the diverging slopes. 61

2.5	Changes in directivity patterns due to small differences between the acoustic center and the geometric center of the array for a (a) monopole, (b) dipole, and (c) lateral quadrupole. The polar plots are on a 10 dB scale to allow visualization of the small changes.	63
2.6	An illustration motivating the centering algorithm for a monopole source. (a) Diagram of source location (red dot), original sampling sphere (black circle), and extrapolated sampling spheres (green, blue, and purple circles). Directivities evaluated on the (b) original sampling sphere and the extrapolated (c) green-dotted sphere, (d) blue-dashed sphere, and (e) purple dash-dot sphere.	67
2.7	Contour plots of the objective function at 500 Hz in the x - y plane for a (a) monopole, (b) dipole, (c) longitudinal quadrupole, and (d) lateral quadrupole displaced to position $\mathbf{r}'' = (0.5, 0.5, 0.0)$ m.	70
2.8	Objective functions for the acoustic source centering of a three-monopole distribution at 50 Hz. (a) J_{ss} . (b) J_{lo} . (c) J_{ph} . (d) J of the present work.	72
2.9	Objective functions for the acoustic source centering of a three-monopole distribution at 500 Hz. (a) J_{ss} . (b) J_{lo} . (c) J_{ph} . (d) J of the present work.	73
2.10	Frequency-dependent acoustic center results for a point source on a rigid sphere of radius $a = 1$ m.	75
3.1	Far-field phase spheres for a monopole [(a)-(c)], dipole [(d)-(f)], and radially vibrating cap on a sphere [(g)-(i)]. These include cases for the sources located at the center of the measurement array [(a), (d), and (g)], translated to position (0.0,0.1,0.3) m [(b), (e), and (h)], and the phase differences between the untranslated and translated sources [(c), (f), and (i)].	83
3.2	Delay-and-sum beamformer output for the acoustic source centering problem.	85

3.3	Far-field color-mapped phase spheres for the (a) centered, (b) translated, and (c) translated dodecahedron using a simplified degree $N = 1$ expansion.	86
3.4	Centering results for dodecahedral RPL. Left: Objective function $J(\theta', \phi')$. Right: normalized delay-and-sum output using a fixed angular position and varying r_c	87
3.5	Trumpet player within measurement arc while playing with a cup mute.	88
3.6	Measured narrowband trumpet directivity patterns for the first [(a), (d), (g), and (j)], second [(b), (e), (h), and (k)] and third [(e), (f), (i), and (l)] partials. Figures (a)-(c) are FRF-based magnitude directivity patterns at the measurement surface. Figures (d)-(f) are the FRF-based phase patterns on the measurement surface. Figures (g)-(i) are the far-field magnitude patterns based on $N=34$ expansions. Figures (j)-(l) are the centered near-field magnitude patterns using the proposed algorithm.	90
4.1	Comparison of the previous and direct methods for acoustic source translation. (a) Cross-section representing the pressure \mathbf{p} of a displaced dipole. (b) Projection $\hat{\mathbf{p}}$ of the measured pressure based on an $N = 4$ spherical harmonic expansion. (c) Translated pressure $\hat{\mathbf{p}}'$ using the initial projection $\hat{\mathbf{p}}$ based on an $N = 4$ spherical harmonic expansion. (d) Translation of pressure using the original measurement \mathbf{p} based on an $N = 4$ spherical harmonic expansion.	98
4.2	Errors of the previous and direct methods for centering a displaced monopole over frequency. The computed centered pressures $\hat{\mathbf{p}}'$ are based on an $N = 4$ spherical harmonic expansion. For convenience, a curve corresponding a monopole displacement $r'' = \lambda$ is superposed on the plot for the previous method.	99
5.1	Spherical spectrum of the far-field propagator $G_n^{(ff)}$	106

5.2	Spherical spectrum of the pressure produced by a radially vibrating cap on a rigid sphere of radius a , evaluated at two radial distances: (a) on the sphere's surface and (b) in the far field.	107
5.3	Spherical spectrum of the pressure produced by a radially vibrating cap on a rigid sphere centered at the point $\mathbf{r} = (0, 0, a)$	108
5.4	Spherical spectrum of the pressure produced by a point source located at the origin for two cases: (a) without a scattering sphere in the field and (b) with a scattering sphere of radius a centered at $\mathbf{r} = (0, 0, 2a)$	110
5.5	Spherical spectrum of a gamelan ageng lanang gong's far-field directivity.	113
5.6	Spherical spectrum of a female talker's measured directivity.	114
5.7	Narrowband female voice directivities at 500 Hz. (a) Measured FRF-based balloon. Far-field directivities based on (b) $N = 1$, (c) $N = 5$, and (d) $N = 34$ degree spherical harmonic expansions.	115
6.1	Illustrations of the spherical sampling positions for $K = 9$ (20°) dual equiangular sampling. (a) Chebyshev sampling. (b) Chebyshev-Lobatto sampling. (c) Chebyshev-Radau sampling.	125
6.2	Polar angle quadrature weights w_a for the case $K = 9$ (20° equiangular sampling) and three quadrature rules.	125
6.3	Numerically integrated $\langle Y_n^0, Y_n^0 \rangle$ for increasing sampling densities K and different quadrature schemes.	134
6.4	The RMSDs for spherical harmonic expansions of a unit cube function involving different quadrature weights, effective area weights, and increasing degree for $K = 36$ (5°) sampling.	135

6.5	Sound power per degree for a radially vibrating cap on a sphere derived from (a) theoretical expansion coefficients and (b) numerically determined expansion coefficients evaluated with an $n = 36$ Chebyshev-Lobatto scheme. (c) Analogous time-frequency aliasing effects.	139
6.6	Sound power per degree for two point sources measured with $K = 36$ Chebyshev-Lobatto polar-angle sampling and three distinct azimuthal resolutions: (a) $\Delta\phi = 2\Delta\theta$, (b) $\Delta\phi = \Delta\theta$, and (c) $\Delta\phi = \Delta\theta/2$	143
6.7	Directivity factor function deviation levels L_Q between the projected far-field directivity of a monopole displaced from the origin at $\mathbf{r} = (0.1, 0, 0)$ m and the theoretical omnidirectional far-field pattern. (a) Calculation involving all coefficients up to $n = N_{ch}$ and $n = N_{ch,l}$. (b) Calculation involving all coefficients up to $n = N_g$ and $n = N_{g,l}$	145
6.8	Sound pressure level plots for two point sources near an infinite rigid baffle in the x - y plane. Fields determined analytically for $z \geq 0$ in the x - z plane using the method of images with (a) $kd = 16$ and (c) $kd = 20$. Fields determined from numerically estimated expansion coefficients with (b) $kd = 16$ and (d) $kd = 20$	147
7.1	A microphone array used in measuring spherical directivities of musical instruments and speech. The array has 5° resolution in the polar angle. A full spherical directivity follows by rotating the musician or talker in 5° azimuthal steps and using a transfer function technique to address repetition variations.	150
7.2	Spherical, spheroidal, cylindrical, and rectangular prism arrays used in the numerical experiments. The number of unique sampling positions appears above each array.	154
7.3	The BEM results for the rectangular prism array at 1 kHz. (a) Evaluated pressure on the prism array surface. (b) Estimated far-field directivity using the HELS method. (c) Reference far-field array directivity.	156

7.4	Illustration of the bias-variance trade-offs that arise when estimating far-field directivity patterns from near-field sampled pressures. (a) Far-field directivity based on degree $N = 1$ expansion. (b) Far-field directivity based on degree $N = 6$ expansion. (c) Far-field directivity based on degree $N = 15$ expansion. (d) Far-field reference directivity.	157
7.5	Selected results at 100 Hz, 2 kHz, 3 kHz, and 5 kHz for the far-field reference array in comparison to the spheroidal, cylindrical, and rectangular prism arrays.	159
7.6	The AWD levels for the BEM experiments involving different array types.	160
7.7	Experimental validation setup for the Fender Princeton Reverb amplifier, showing the 14 microphone near-field array. Of note is the gap in the microphone placement near the bottom of the guitar amplifier.	161
7.8	Directivity results for the Fender Princeton Reverb amplifier at 100 Hz. (a) Estimated spherical far-field directivity pattern from the HELS method based on degree $N = 3$ expansion, with the transverse polar directivity overlaid as a green dashed line. (b) Measured transverse far-field directivity and estimated transverse directivity.	162
7.9	Directivity results for the Fender Princeton Reverb amplifier at 1 kHz without regularization. (a) Estimated spherical far-field directivity pattern based on a degree $N = 8$ expansion, with the transverse polar directivity overlaid as a green dashed line. (b) Measured transverse far-field directivity and estimated transverse directivity from the HELS method. Of note is the large lobe below the guitar amplifier shown in (a), where the sampling was sparse.	163

7.10	Directivity results for the Fender Prinecton Reverb amplifier at 1 kHz with regularization. (a) Estimated spherical far-field directivity pattern based on a degree $N = 8$ expansion, with the transverse polar directivity overlaid as a green dashed line. (b) Measured transverse far-field directivity and estimated transverse directivity from the HELS method. Regularization has removed the large bottom lobe seen in Fig. 7.9a and increased the agreement between the estimated and measured transverse directivities.	164
7.11	Directivity results for the Fender Twin Reverb amplifier at 1.5 kHz. (a) Spherical far-field directivity pattern based on a degree $N = 12$ expansion and regularization, with the transverse polar directivity overlaid as a green dashed line. (b) Measured transverse far-field directivity and estimated transverse directivity from the HELS method.	165
8.1	An ageng lanang gamelan gong within the rotating directivity measurement array.	172
8.2	An bebende gamelan gong within the rotating directivity measurement array.	173
8.3	Spherical spectrum of the agneng lanag gamelan gong. Each rectangle indicates the energy contained in a given expansion coefficient summed over all orders m for fixed degree n calculated in 100 Hz steps.	177
8.4	Propagated and normalized far-field directivities for the ageng lanang's lowest five modal frequencies. (a) 63 Hz. (b) 94 Hz. (c) 104 Hz. (d) 130 Hz. (e) 168 Hz. Out-of-plane surface velocity for the same modal frequencies. (f) 63 Hz. (g) 94 Hz. (h) 104 Hz. (i) 130 Hz. (j) 168 Hz.	180
8.5	Propagated and normalized far-field directivities for select higher frequency modes of the lanang ageng. (a) 198 Hz. (b) 376 Hz. (c) 420 Hz. (d) 566 Hz. (e) 650 Hz. Out-of-plane surface velocity for the same modal frequencies. (f) 198 Hz. (g) 376 Hz. (h) 420 Hz. (i) 566 Hz. (j) 650 Hz.	182

8.6	Propagated and normalized far-field directivities for the bebende gong's lowest five modal frequencies. (a) 144 Hz. (b) 226 Hz. (c) 239 Hz. (d) 389 Hz. (e) 469 Hz. Out-of-plane surface velocity for the same modal frequencies. (f) 144 Hz. (g) 226 Hz. (h) 239 Hz. (i) 389 Hz. (j) 469 Hz.	183
8.7	Propagated and normalized far-field directivities for select higher frequency modes of the bebende. (a) 592 Hz. (b) 849 Hz. (c) 1112 Hz. (d) 1180 Hz. (e) 1204 Hz. Out-of-plane surface velocity for the same modal frequencies. (f) 592 Hz. (g) 849 Hz. (h) 1112 Hz. (i) 1180 Hz. (j) 1204 Hz.	184
8.8	Normalized time-averaged sound power spectrum radiated from the ageng lanang gong when excited by a shaker.	185
8.9	Normalized time-averaged sound power spectrum radiated from the kemur gong when excited by a shaker.	186
8.10	(a) Maximum DI over frequency. (b) Angular location of the direction of strongest radiation.	190
8.11	Directivity Index as a function of (a) angular node number (b) radial node number. . .	191
8.12	Deviations between measured and symmetrized data about the median plane.	193
9.1	Scattering effects on the directivity of a point source without and with the presence of a rigid sphere for selected ka . <i>Top row</i> : Magnitude pressure. <i>Bottom row</i> : Polar plot of the far-field directivity.	198
9.2	Directivity balloons of the violin (a)-(c) and human speech (d)-(f) for the 400 Hz [(a), (d)], 500 Hz [(b), (e)], and 800 Hz [(c), (f)] 1/3rd-octave bands. The vantage point is from behind the body, and all balloons are based on a degree $N = 18$ spherical harmonic expansions.	199
9.3	Normalized shading function W_L for various levels of attenuation L	201

9.4	Values of attenuation based on scattering from a rigid sphere of radius a due to a point source placed at position $r = a_0$	202
9.5	Shading function W_s for various ka with $(\theta_0, \phi_0) = (\pi/2, 0)$. Increasing frequency leads to increasing attenuation behind the source, as well as the appearance of diffraction spot.	203
9.6	Three measurement set-ups. (a) Isolated clarinet and blowing apparatus. (b) Clarinet and blowing apparatus attached to KEMAR HATS. (c) Clarinetist.	204
9.7	Far-field projected directivity balloons for the fundamental of E4. (a) Isolated and artificially excited clarinet. (b) Artificially excited clarinet attached to a mannequin. (c) Clarinet played by a musician. All balloons are based on degree $N = 17$ spherical harmonic expansions. The vantage point is from the right side of the instrument.	205
9.8	Far-field projected directivity balloons for the fifth partial of E4. (a) Isolated and artificially excited clarinet. (b) Artificially excited clarinet attached to a mannequin. (c) Clarinet played by a musician. The balloons are based on degree $N = 17$ spherical harmonic expansions. The vantage point is from the right side of the instrument.	206
9.9	Shading applied to the fifth partial of E4. Directivity balloons of the (a) isolated instrument rotated to be in the same orientation as the mannequin, (b) shaded isolated instrument, and (c) instrument and mannequin combination. The balloons are based on degree $N = 17$ spherical harmonic expansions. The vantage point is from the right side of the instrument.	207
9.10	Shading applied to the 3rd partial of E4. Directivity balloons of the (a) isolated instrument rotated to be in the same orientation as the mannequin, (b) shaded isolated instrument (c) instrument and mannequin combination. The balloons are based on degree $N = 17$ spherical harmonic expansions. The vantage point is from the right side of the instrument.	208
10.1	A KEMAR HATS within the rotating directivity measurement system.	211

10.2	Directivity balloons for the 1.6 kHz 1/3-octave band. (a) Theoretical model of a radially vibrating cap set in a rigid sphere. (b) Isolated KEMAR HATS head. (c) Complete KEMAR HATS (including torso) with the head oriented toward $\psi_h = 0^\circ$. (d) Averaged live speech of seated talkers. The vantage point is from the right side of the sphere, HATS, and average talker so the mouth axis is toward the 0° azimuthal marker.	215
10.3	Directivities of the KEMAR HATS with head orientations $\psi_h = 0^\circ, 30^\circ, 60^\circ,$ and 90° as viewed from a fixed vantage point at $(45^\circ, 20^\circ)$. <i>Top row:</i> 1 kHz 1/3-octave band. <i>Bottom row:</i> 4 kHz 1/3-octave band. The blue arrows indicate the mouth axis directions.	216
10.4	Frequency-dependent directivity deviations between the reference directivities at various azimuthal head orientation angles ψ_h and the forward-facing head orientation $\psi_h = 0^\circ$. In all cases, the torso faced forward toward $\phi = 0^\circ$	218
10.5	Frequency-dependent directivity deviations between the reference directivities and the isolated head (no torso) rotated towards ψ_h	219
10.6	Frequency-dependent directivity deviations between the reference directivities and directivities measured with the head and torso rotated together as a single unit towards ψ_h	220
11.1	Directivity measurement system with a musician and trumpet.	225
11.2	Directivity measurement system with an artificially excited trumpet and manikin.	227
11.3	Trumpet narrowband directivities at 699 Hz based on (a) autospectral levels from the array microphone signals and (b) frequency-response functions between the reference and array microphone signals.	233
11.4	FRF-based directivity balloons for the (a)-(d) played and (e)-(h) artificially excited trumpet with manikin.(a) and (e): 233 Hz. (b) and (f): 311 Hz. (c) and (g): 438 Hz (d) and (h): 524 Hz.	234

11.5	FRF-based directivity balloons for the (a)-(d) played trumpet and (e)-(h) artificially excited trumpet with a manikin. (a) and (e): 589 Hz. (b) and (f): 737 Hz. (c) and (g): 932 Hz (d) and (h): 1160 Hz.	235
11.6	Played trumpet directivities at 695 Hz (F4, 2nd partial) based on (a) $N = 3$, (b) $N = 4$, (c) $N = 6$, (d) $N = 8$, and (e) $N = 12$ degree spherical harmonic expansions, and (f) the raw FRF-based directivity.	237
11.7	Directivity factor function deviation levels between measured FRF-based and spherical-harmonic-expansion-based directivities over expansion degree N for selected partials.	238
11.8	Spherical spectrum (E_n) for the (a) played and (b) artificially excited trumpet.	239
11.9	Directivity at 1315 Hz (E4 4th partial) based on (a) raw narrowband FRFs and (b) an $N = 13$ degree spherical harmonic expansion.	240
11.10	Directivity balloons based on (a)-(c) raw narrowband FRFs and (b)-(c) far-field propagated spherical harmonic expansions. (a) and (d): 394 Hz. (b) and (e): 986 Hz . (c) and (f): 1558 Hz.	242
11.11	Frequency-dependent trumpet directivity properties: (a) Directivity index and (b) maximum radiation axis elevation.	244
11.12	Directivity factor function deviations at the zenith microphone position between the 72 repeated captures.	245
11.13	Directivity factor function deviation levels between the played and artificially excited FRF-based directivity results.	247
11.14	Directivity factor function deviation levels between measured and symmetrized partials.	248
11.15	Played trumpet directivity balloons derived from Weinerziel et al. at (a) 279 Hz, (b) 738 Hz, (c) 1314 Hz, and (d) 1871 Hz. Far-field projected directivity balloons from the present work at (a) 277 Hz, (b) 737 Hz, (c) 1315 Hz, and (d) 1869 Hz.	249

11.16	Played trumpet directivity indices from Weinzierl et al. and the present work.	250
12.1	Directivity measurement system.	260
12.2	Sampling positions of the directivity measurement system. Effective sampling areas differed, as suggested by those illustrated about the points labeled $V_{w_{0,6}}$, $w_{9,6}$, and $w_{15,6}$. For convenience in summations, $w_{0,v}$ and $w_{36,v}$ segmented the sampling areas of the two poles into V equal sectors. The total polar sampling areas were then $V_{w_{0,v}}$ and $V_{w_{36,v}}$	263
12.3	Narrowband (1 Hz bandwidth) flute directivities for the note C4. Autospectral balloons for the (a) first partial (262 Hz), (b) third partial (787 Hz), and (c) fifth partial (1310 Hz). FRF-based balloons for the (d) first partial (262 Hz), (e) third partial (787 Hz), and (f) fifth partial (1310 Hz).	276
12.4	Narrowband directivity for the 2nd partial of the note D2 (292 Hz) from a tenor saxophone. Directivities derived from the smaller $R = 1.22$ m array based on (a) FRF measurements, (b) an $N = 18$ degree spherical harmonic expansion of the FRF measurements, and (c) the calculated far-field estimate. Directivities derived from the larger $R = 1.83$ m array based on (d) FRF measurements, (b) an $N = 18$ degree spherical harmonic expansion of the FRF measurements, and (e) the calculated far-field estimate.	279
12.5	Acoustic source centering effects for the bassoon for the note A2 (110 Hz). Magnitude directivity pattern based on (a) an $N = 18$ degree spherical harmonic expansion from the measurement at the array surface, (b) a point source placed at the estimated acoustic center of the bassoon, and (c) propagated far-field pressure. Constant-radius color-mapped phase directivity pattern based on (d) an $N = 18$ degree spherical harmonic expansion from the measurement at the array surface, (e) a point source placed at the estimated acoustic center of the bassoon, and (f) propagated far-field pressure.	281

12.6	Bass clarinet directivity for the 5th partial of C3 (657 Hz) based on (a) an $N = 18$ expansion of a 2,522-point multiple-capture measurement, (b) a truncated $N = 4$ expansion of the same a 2,522-point multiple-capture measurement, and (c) a maximum $N = 4$ expansion of a 32-point single-capture measurement. The polar plots show the transverse (green), median (blue), and frontal (magenta) plane results.	283
12.7	Normalized effective input auto-spectrum and spherically averaged coherence for the trombone playing the note B2. The vertical solid yellow line at 108 Hz, the dash-dot red line at 186 Hz, and the dashed green line at 744 Hz are frequency markers for the balloons in Fig. 12.8	284
12.8	Narrowband FRF-based directivity balloons and coherence balloons for the played note B2 (1 Hz resolution) of a trombone. Directivity balloons at (a) 108 Hz, (b) 186 Hz, and (c) 744 Hz. Coherence balloons at (d) 108 Hz, (e) 186 Hz, and (f) 744 Hz. (See the frequency markers in Fig. 12.7)	286
12.9	One-third-octave-band tuba directivities. Autospectral balloons for (a) 250 Hz, (b) 400 Hz, and (c) 630 Hz. Related OECOS balloons for (a) 250 Hz, (b) 400 Hz, and (c) 630 Hz.	288
12.10	Standard deviations of 1/3rd-octave-band directivity factor functions for the north and south pole measurements and narrowband spherically averaged coherence for the French horn.	290

12.11 Viola 1/3rd-octave-band directivities. Results for the 400 Hz band viewed from the side based on (a) an $N = 4$ expansion of measurements performed by Weinzierl et al. using a 32-point single-capture array, (b) an $N = 4$ expansion of measurements performed for the present work using a 32-point single-capture array, and (c) an $N = 18$ expansion performed for the present work using a 2,522-point multiple capture array. Results for the 1.6 kHz band viewed from above based on (d) an $N = 4$ expansion of measurements performed by Weinzierl et al. using a 32-point single-capture array, (e) an $N = 4$ expansion of measurements performed for the present work using a 32-point single-capture array, and (f) an $N = 18$ expansion of measurements performed for the present work using a 2,522-point multiple capture array. 292

12.12 Cello directivities over various bandwidths. (a) Narrowband (1 Hz resolution) OECOS at 415 Hz. (b) 400 Hz 1/6th-octave band (46 Hz bandwidth). (c) 400 Hz 1/3rd-octave band (92 Hz bandwidth). (d) Narrowband (1 Hz resolution) OECOS at 1kHz. (e) 1 kHz 1/6th-octave band (116 Hz bandwidth). (f) 1 kHz 1/3rd-octave band (232 Hz bandwidth). All directivities utilized $N = 18$ spherical harmonic expansions. 294

12.13 Violin and speech directivities in 1/3rd-octave bands. Violin directivities for the (a) 400 Hz, (b) 500 Hz, and (c) 800 Hz bands. Speech directivities for the (d) 400 Hz, (e) 500 Hz, and (f) 800 Hz bands. A slight viewpoint rotation of the violin balloons has allowed better comparisons of the diffraction patterns behind the seated musician with the seated talker. All directivities have employed $N = 18$ spherical harmonic expansions. 296

13.1 Spherical (a) and cylindrical (b) microphone arrays used to assess the radiated fields of two organ pipes. 303

13.2 Simulated directivity balloons of the open metal pipe using Eq. (1) for the first six partials: (a) 331 Hz, (b) 662 Hz, (c) 993 Hz, (d) 1323 Hz, (e) 1654 Hz, and (f) 1985 Hz. 304

13.3	Measured directivity balloons of the open metal pipe for the first six partials: (a) 331 Hz, (b) 662 Hz, (c) 993 Hz, (d) 1323 Hz, (e) 1654 Hz, and (f) 1985 Hz.	305
13.4	Measured directivity balloons for the measured closed wooden pipe for the first six partials: (a) 335 Hz, (b) 670 Hz, (c) 1005 Hz, (d) 1340 Hz, (e) 1675 Hz, and (f) 2010 Hz.	306
13.5	Pressure on the cylindrical scanning surface for the fundamental of the closed wooden pipe. (a) TMM-based point-source model simulation. (b) BEM simulation using only the first term of the KHIE. (c) BEM simulation using the full KHIE. (d) Measured pressure.	308
14.1	An ageng lanang gamelan gong within the rotating directivity measurement array. . .	313
14.2	Source locations, amplitudes, and polarities for an equivalent point source model involving seven point sources.	317
14.3	Normalized effective time-averaged sound power spectrum radiated from the gong when excited by a shaker.	318
14.4	Normalized out-of-plane gong surface velocity at the sound power spectral peaks based on SLDV scan data and assumed modal numbers. (a) 63 Hz. (b) 94 Hz. (c) 104 Hz. (d) 130 Hz. (e) 168 Hz. (f) 175 Hz. (g) 188 Hz. (h) 198 Hz.	319
14.5	Propagated and normalized far-field directivities for the gong's lowest eight modal frequencies: (a) 63 Hz, (b) 94 Hz, (c) 104 Hz, (d) 130 Hz, (e) 168 Hz, (f) 175 Hz, (g) 188 Hz, and (h) 198 Hz.	322
14.6	Simulated far-field gong directivities based on superpositions of monopole and dipole fields for the modal frequencies (a) 63 Hz, (b) 94 Hz, (c) 104 Hz, (d) 130 Hz, (e) 168 Hz, (f) 175 Hz, (g) 188 Hz, and (h) 198 Hz.	323
14.7	Area-weighted directivity factor function deviations L_Q between simulated and propagated far-field patterns for the lowest eight modes.	323

15.1	Depiction of a vibrating cap (red) on a rigid spherical shell (gray) with an open aperture (dotted line).	330
15.2	Self acoustic reactances of a vibrating cap on a closed sphere: (a) external side and (b) internal side. The red dashed curves represent low-frequency approximations.	340
15.3	Magnitude and phase of the aperture volume velocity.	343
15.4	Calculated sound power levels of vibrating cap on a sphere.	348
15.5	Directivity factor deviation levels L_Q between a BEM solution and the low-frequency approximation.	349
15.6	Far-field directivity balloons for a vibrating cap on a rigid spherical shell and a circular aperture on the opposing side. The results, based on the low-frequency model, are for (a) $ka = 0.1$, (b) $ka = 0.2$, (c) $ka = 0.4$ (near the Helmholtz resonance frequency), (d) $ka = 1$, (e) $ka = 1.5$, and (f) $ka = 2$	351
15.7	Far-field directivity of a vibrating cap on a spherical cap for $(\theta_a, \phi_a) =$ (a) $(90^\circ, 180^\circ)$, (b) $(90^\circ, 198^\circ)$, (c) $(90^\circ, 216^\circ)$, (d) $(90^\circ, 234^\circ)$, (e) $(90^\circ, 252^\circ)$, (f) $(90^\circ, 270^\circ)$	352
15.8	Directivity measurement system assessing the radiation of a spherical loudspeaker positioned at its center. The white disc controls the aperture size.	353
15.9	Spherically-averaged magnitude response of the spherical loudspeaker with three distinct aperture sizes. The vertical lines show estimated Helmholtz and closed-cavity air resonance frequencies.	355
15.10	Directivity balloons at 100 Hz ($ka = 0.2$) for a modeled (a)-(c) and measured (d)-(f) spherical loudspeaker with circular aperture angles (a), (d) $\alpha_a = 15^\circ$; (b), (e) $\alpha_a = 23^\circ$; and (c), (f) $\alpha_a = 33^\circ$	356
15.11	Directivity balloons at 700 Hz ($ka = 1.5$) for a modeled (a)-(c) and measured (d)-(f) spherical loudspeaker with circular aperture angles (a), (d) $\alpha_a = 15^\circ$; (b), (e) $\alpha_a = 23^\circ$; and (c), (f) $\alpha_a = 33^\circ$	357

15.12 Directivity balloons at 1 kHz ($ka = 2.2$) for a modeled (a)-(c) and measured (d)-(f) spherical loudspeaker with circular aperture angles (a), (d) $\alpha_a = 15^\circ$; (b), (e) $\alpha_a = 23^\circ$; and (c), (f) $\alpha_a = 33^\circ$	358
15.13 Directivity balloons at 1.5 kHz ($ka = 3.2$) for a modeled (a)-(c) and measured (d)-(f) spherical loudspeaker with circular aperture angles (a), (d) $\alpha_a = 15^\circ$; (b), (e) $\alpha_a = 23^\circ$; and (c), (f) $\alpha_a = 33^\circ$	360
15.14 Directivity factor function deviation levels between the measured and modeled directivities with (a) aperture velocity U_a (b) lumped-element aperture velocity approximation \tilde{U}_a	362
16.1 Spherical spectrum of the far-field propagator W_n	372
16.2 Illustration of the low-pass filtering effect of the far-field propagator W_n . Normal velocity distribution on a rigid sphere of radius a with a radially vibrating cap of angle $\mu = \pi/6$ using up to degree (a) $N = 5$ and (b) $N = 100$ spherical harmonic expansions. Far-field directivities for $ka = 2$ using up to degree (c) $N = 5$ and (d) $N = 100$ spherical harmonic expansions.	373
16.3 Values of the truncation parameter ε for increasing expansion degree N and various cap edge half-angles.	375
16.4 Spectrum of a unit-amplitude spherical cap as a function of cap edge half-angle. . . .	376
16.5 Surface velocities for the (a) dipole-like mask function, (b) single radially vibrating cap on a sphere, and (c) product of the mask and cap distributions to create the two opposite-polarity semicircular caps. Normalized far-field directivities for the two opposite-polarity semicircular caps at (d) $ka = 1$, (e) $ka = 5$, (f) $ka = 10$, and (g) $ka = 15$.	379

16.6 Surface velocity for the (a) two opposite-polarity semicircular caps, (b) single cap on a sphere, and (c) summation of the surface velocities in (a) and (b) to cancel the negative polarity region. Normalized far-field directivities for the semicircular cap at (d) $ka = 1$, (e) $ka = 5$, (f) $ka = 10$, and (g) $ka = 15$ 381

16.7 Surface velocity for the (a) quadrupole-like mask function, (b) single cap on a sphere, and (c) product of mask and cap distributions to create the four alternating-polarity quarter-circular caps. Normalized far-field directivities for the alternating-polarity cap at (d) $ka = 1$, (e) $ka = 5$, (f) $ka = 10$, and (g) $ka = 15$ 382

16.8 Surface velocity for the (a) diametric node masking function, (b) circular node masking function, and (c) product of the two masks. Normalized far-field directivities for the composite cap at (d) $ka = 1$, (e) $ka = 5$, (f) $ka = 10$, and (g) $ka = 15$ 383

16.9 Surface velocity for the (a) latitudinal strip of width $2\theta_s$, (b) longitudinal strip of width $2\phi_s$, and (c) rectangular cap. Normalized far-field directivities for the rectangular cap at (d) $ka = 1$, (e) $ka = 5$, (f) $ka = 10$, and (g) $ka = 15$ 385

16.10 Surface velocity for the (a) rectangular cap, (b) two semicircular caps, and (c) sum of the rectangular and two semicircular caps. Far-field directivities for the stadium cap at (d) $ka = 1$, (e) $ka = 5$, (f) $ka = 10$, and (g) $ka = 15$ 386

17.1 An energetic source-filter model representing the Hopkins-Stryker equation. Both the source directivity factor for a given angle and the frequency-dependent room constant color the sound power spectrum to produce the locally averaged total mean-squared pressure spectrum at the observation position. 398

17.2 Decibel plots $10\log_{10}[4/R(f)]$ of the inverted and scaled room constants, measured in 1/3-octave bands in a classroom and dance studio. The classroom values below $f_S = 154$ Hz (see Table 17.1) are less reliable than the higher-frequency values. 404

17.3	Directivity index function color spheres for the 1.6 kHz, 1/3-octave band for (a) trumpet, (b) French horn, (c) trombone, and (d) tuba.	406
17.4	Directivity index function color spheres for the 1 kHz, 1/3-octave band for (a) flute, (b) bassoon, (c) tenor saxophone, and (d) baritone saxophone.	408
17.5	Directivity index function color spheres for the 400 Hz, 1/3-octave band for (a) violin, (b) viola, (c) cello, and (d) double bass.	410
17.6	Speech directivity index function color spheres for the (a) 400 Hz, (b) 630 Hz, (c) 1.6 kHz, and (d) 2.5 kHz 1/3-octave bands.	411
17.7	The 1/3-octave-band sound power spectrum of a trombone scaled by $\rho_0 c$ and estimated mean-squared pressure spectra under different directional and room conditions at a radius of $r_m = 5.0$ m.	413
17.8	A color-mapped projection of the free-field objective function $J_{ff}(\vartheta, \phi)$ for speech. The green dot shows the location for the objective function minimum. Post-processing symmetrized the data set about the median plane.	415
17.9	Measured sound power spectrum and estimated single-channel sound power spectra for speech at various positions in a free-field environment. The mean-squared pressure of the source has been normalized so that the measured sound power level at 160 Hz is 0 dB. The measurement radius was $r_m = 1.21$ m.	416
17.10	Objective function $J_{ff}(\vartheta, \phi)$ for trumpet.	417
17.11	Objective function $J_{ff}(\vartheta, \phi)$ for tenor saxophone.	418
17.12	Objective function $J_{ff}(\vartheta, \phi)$ for violin.	419
17.13	Objective function $J_{sr}(\vartheta, \phi)$ for trombone at a microphone placement distance $r_m = 1.83$ m in a dance studio.	420
17.14	Objective function $J_{sr}(\vartheta, \phi)$ for trombone at a microphone placement distance $r_m = 10$ m in a dance studio.	422

17.15 Measured and estimated 1/3-octave band sound power spectra for the trombone at $r_m = 10$ m in the dance studio using the optimal angular position shown in Fig. 17.14. Normalization of the mean-squared pressure set the sound power value at 160 Hz to 0 dB.	423
17.16 Objective function $J_{sr}(\vartheta, \phi)$ for speech at $r_m = 1.21$ m in a classroom. Post-processing symmetrized the data set about the median plane.	424
17.17 Objective function $J_{sr}(\vartheta, \phi)$ for speech at $r_m = 1.21$ m in a dance studio. Post-processing symmetrized the data set about the median plane.	425
18.1 Broadband bassoon directivities based on the OASPL formulation. (a) Unweighted. (b) A-weighted. (c) C-weighted. (d) D-weighted.	433
18.2 Bassoon directivities based on the OASPL formulation for varying bandwidths about a 500 Hz center frequency. (a) 1 Hz narrowband. (b) 1/3-octave band. (c) 1/1-octave band. (d) Full broadband measurement bandwidth.	434
18.3 OASPL-based directivity of the trombone.	438
18.4 Loudness-based directivity of the trombone.	439
18.5 Loudness-based directivity for the flute.	440
18.6 Loudness-based directivity for the tenor saxophone.	440
18.7 Loudness-based directivity for the viola.	441
18.8 Sound power estimate deviations for the brass family.	443
18.9 Sound power estimate deviations for the woodwind family.	443
18.10 Sound power estimate deviations for the string family.	444

List of Tables

1.1	Definitions of four normalized spherical harmonics commonly used in this work. . . .	14
1.2	Tabulated amplitudes and locations for five point sources inside a measurement sphere of radius $R = 1$ m.	33
6.1	Polar-angle quadrature weights w_k for three equiangular quadrature rules. Each empty spaces indicates that no sampling node falls at the angle for the given sampling type and K value.	126
7.1	Sampling scheme radii for the various near-field arrays.	155
8.1	Lanang gong mode order based on SLDV measurements.	187
8.2	Bebende gong mode order based on SLDV measurements.	188
14.1	Lowest eight modal frequencies of the gong and assumed modal numbers.	319
16.1	Parameters for the dipole-like mask made from two spherical caps.	379
16.2	Parameters for the rotated dipole-like mask made from two caps.	382

16.3	Parameters for the four masking functions used to generate the (3, 2) type mode distribution. The first three masking functions (rows one through six) produce the diametrical nodal mask. The final masking function (rows seven and eight) produce the circular nodes where μ_1 is the total cap edge half-angle and $\mu_2 < \mu_1$ is the angle for the circular node.	384
16.4	Parameters for the longitudinal and latitudinal strips of width $2\theta_s$ and $2\phi_s$, respectively.	385
17.1	Geometrical and acoustical properties of the classroom and dance studio used in the semi-reverberant field examples.	404
18.1	Measured sound power levels for the mezzo-forte dynamic marking [1] compared to previously published values for the pianissimo and fortissimo dynamic markings [2]. .	437

Preface

Acoustic directivity is the physical phenomenon by which energy transported by sound waves varies angularly over a spherical observation surface. Sound radiated from most acoustic sources exhibits directional behavior. Common examples include the radiation from the human voice [3–6], musical instruments [7–9], and loudspeakers [10–13]. The necessity of valid directional data for practical applications, including microphone placements [14–17], auralizations [18, 19], and room acoustical designs [20, 21], has motivated decades of research into source radiation and directional properties. This dissertation presents several additional developments in the theory, measurement, modeling, and applications of sound source directivities. Because its chapters include self-contained coverage in several areas, the following paragraphs present a general overview of the dissertation and its organization in five parts.

Part I develops the concept of an acoustic source center. Although the acoustic center finds applications in transducer calibrations [22–24], assessments of anechoic chamber properties [25, 26], and other areas, it is fundamental in directivity measurements. Evaluating a source’s directivity requires a suitable observation or measurement surface. The source’s placement relative to this surface can create significant differences between measured patterns and the desired far-field directional response. Careful source placement may mitigate these effects when the source’s acoustic center coincides with the measurement coordinate origin. Nonetheless, a source’s acoustic center is generally unknown before measurement, requiring post-processing techniques to correct source

placement errors. Although previous works have proposed some computationally intensive methods to evaluate the center [27–29], the algorithms remain robust only for roughly omnidirectional sources at low frequencies. They generally fail to converge or provide meaningful results at higher frequencies with more complex radiation patterns.

Chapter 1 illustrates how the acoustic center coincides with a single equivalent point source for omnidirectional radiators at low frequencies. This result helps improve acoustic centering efforts and provides a closed-form solution for the acoustic center from the source’s spherical harmonic expansion coefficients. Chapter 2 shows that the far-field directivity pattern’s magnitude is invariant to the source placement. This crucial development allows a numerical optimization procedure for identifying the acoustic center at higher frequencies, even for sources with complex radiation patterns. Chapter 3 illustrates how the far-field phase relations of a translated source likewise lead to its acoustic center. Finally, Chapter 4 compares numerical approaches for calculating a source’s spherical harmonic expansion coefficients in translated frames, which is beneficial for post-processing directivities in the centered reference frame.

Part II considers several topics pertinent to directivity measurement theory. Despite the growing interest in directivity research in recent years, studies have employed dramatically different numbers of sampling positions over a sphere, from fewer than a hundred [3, 30–32] to over a thousand [1, 6, 33, 34]. The significant discrepancies in sampling densities highlight the investigators’ uncertainties about the resolutions required for meaningfully evaluating directivity functions. Even standardized spherical sampling densities [33] provide little insight into the usable bandwidths for given sources. Spherical measurement surfaces are ubiquitous in these standards and published works. However, the application of arbitrarily shaped surfaces for directivity measurements remains ambiguous.

Chapter 5 explores the number of sampling positions realistically needed to evaluate a given source’s directivity. The results confirm that source dimensions and geometry strongly influence that number and suggest that for many common sources, such as musical instruments and speech, even

currently standardized high resolutions [33] may be insufficient over the audible bandwidth. Next, Chapter 6 develops Chebyshev quadrature rules applicable to these standardized dual-equiangular sampling densities. The results clarify the benefits of this sampling approach and demonstrate the robustness of Chebyshev sampling compared to Gaussian sampling. Lastly, Chapter 7 demonstrates a method to extrapolate directivity results measured on arbitrarily shaped surfaces to spherical far-field directivity patterns.

Part III presents selected high-resolution directivity results. Chapter 8 reports the characteristics of two gamelan gongs. Due to the difficulties in measuring played musical instrument directivities, authors have often resorted to measuring artificially excited instruments to achieve high-resolution results [35–37]. However, their approaches have ignored critical musician effects, including the absorption and diffraction produced by musicians’ bodies and chairs. Chapter 9 explores such effects by comparing the directivities of an artificially excited and a musician-played clarinet. The results confirm that the musician’s absorption and diffraction significantly impact the directional results, even at low frequencies. Chapter 10 explores the typically overlooked but significant effects of diffraction about the human head and torso and their influence on speech directivity. Chapter 11 shows how a multiple-capture transfer function method [6] adapts to musical instrument directivities with a specific application to the trumpet. Measured directivities produced by an artificially excited and played trumpet validate the technique and highlight its robustness for high-resolution results. Finally, Chapter 12 describes the development of an archival database [38] of musical instrument directivities for researchers and practitioners working in audio, room acoustics, and other areas of acoustics.

Part IV details several approaches to modeling sound source directivities. The models provide insights into the underlying physical phenomena governing sound radiation and provide convenient simplifications to representing directivities. Chapter 13 illustrates how commonly applied transmission matrix methods [39, 40] adapt to point-source models and help predict the sound radiation

from organ pipes. Chapter 14 illustrates how spherical harmonic expansions yield equivalent point-source models based on multipole expansions of the pressure field. Chapter 15 develops a low-frequency model for the sound radiation from a radially vibrating cap on a rigid spherical shell with a circular aperture. The model provides insights into the low-frequency sound radiation of cavity-like geometries at low frequencies, including dipolar radiation in the limit of incompressible fluid flow, monopolar radiation near the cavity's Helmholtz resonance frequency, and more complex radiation at higher frequencies. Lastly, Chapter 16 illustrates how spherical-harmonic-domain operators provide closed-form solutions to several interesting nonaxisymmetric surface velocities, including rectangular pistons, semi-circular pistons, and pistons with imposed mode shapes. These models help explain the directional behaviors of various sources, including the gamelan gong.

Part V concludes this work by considering the impacts of sound source directivities on microphone placements. While audio engineers typically place microphones by ear or convention, the extensive information provided by measured directivity functions provides additional insights into optimal microphone placements. Chapter 17 demonstrates how a single-channel measurement can estimate the sound power spectrum of a source from its directivity function. Chapter 18 explains how a directivity function yields the microphone position with the loudest perceived sound over a sphere.

Part I

The Acoustic Center

Chapter 1

Low-Frequency Acoustic Center

This chapter demonstrates that at low frequencies, the acoustic centers of omnidirectional radiators relate to their dipole and monopole moments. This relation provides a closed-form solution to the acoustic center based on a source's spherical harmonic expansion coefficients.

1.1 Introduction

The acoustic source center has been a topic of considerable interest to researchers and practitioners for decades. Standards now describe it as “the position of the virtual point source from which sound pressure varies inversely as distance” [41] and “the point from which . . . spherical wavefronts . . . appear to diverge” [42]. These concepts apply to transducer calibrations [22–24], sound attenuation [43], assessments of anechoic chamber properties [25, 26], source placements for directivity measurements [27–29, 44], and many other applications in acoustics. The primary focus of the present work is the accurate placement of the low-frequency acoustic center.

Some early treatments of the acoustic center considered a source's far-field directional characteristics [45–47]. However, Trott asserted that a more specific definition is the “locus of the equivalent point source that yields the same far-field pressure in magnitude and phase in a specified direction”

rather than “an arbitrary center of rotation for determining the farfield directional response in terms of sound pressure magnitude” [48]. Jacobsen et al. later noted that most centering definitions seem to be grounded in the “idea of replacing a real, extended source by an equivalent point source” [49]. Nevertheless, they argued that the positioning of this equivalent point source is “deceptively simple” since different approaches yield inconsistent results. For example, definitions of the acoustic center based on matching $1/r$ decays [50–52], phase shifts [48, 53], group delays [22], or wavefronts [23] produce different acoustic centers for both a radially oscillating sphere or a theoretical point source on a sphere—even when the various methods apply to identical sources [49].

Vanderkooy justified using an equivalent point source by exploiting the location where one takes a multipole expansion of the Kirchhoff-Helmholtz integral equation (KHIE) to remove the dipole moment [54]. If the higher-order (e.g., quadrupole) terms are negligible, only the monopole moment subsequently remains. This concept leads to a global characterization of the sound field rather than an attempted matching of the amplitude decay, phase, or similar properties in specified directions. While Vanderkooy’s approach thus provided a unique acoustic center, it required knowledge of the source boundary pressure and particle velocity, which are generally unknown.

Noting that “theoretical results are difficult to work out,” Vanderkooy assumed far-field omnidirectional radiation to estimate the acoustic center based on the pressure difference between two equally distant points from the coordinate origin [54]. He did not directly apply the KHIE to determine acoustic centers but showed, via simulations, good agreement with the underlying centering concepts, including constant contours of $1/r$ decay about the center and constant wavefronts. His results also improved near-field agreement with far-field polar patterns whenever a source appropriately aligned with the acoustic center [55]. Near-field measurements of a small loudspeaker verified anticipated quasi-omnidirectional behavior when it rotated about the estimated acoustic center [54]. Thus, contrary to Trott’s assertion, Vanderkooy’s results suggested that the

point of rotation is not arbitrary; its optimal position coincides with the location of the equivalent point source.

Later research improved upon the two-point estimation method and applied the theory to microphones, a point source on a rigid sphere, and measurements of a KEMAR head-and-torso simulator [56,57]. These efforts showed that the concepts are consequential but applicable only to sources whose radiation patterns become omnidirectional in the far field. They are not particularly beneficial for dipolar, cardioid-like, or more complex patterns [54].

Aarts and Janssen derived the low-frequency acoustic centers of radially and axially oscillating caps on a rigid sphere using Vanderkooy's two-point estimation method [58]. Their general formula is a closed-form solution based on Legendre polynomial pressure expansion coefficients, applying to axisymmetric spherical sources with far-field omnidirectional radiation patterns. Their results provided insights into the effects of loudspeaker driver sizes on the acoustic center. However, more general radiation cases remained unresolved.

Because of the importance of acoustic centers for directivity measurements, other authors have attempted to exploit pressure field spherical harmonic expansions to determine their locations [27–29, 44]. Such expansions allow sound field representations of arbitrary sources instead of only axisymmetric spherical sources [59]. However, rather than developing closed-form solutions similar to Aarts and Janssen's solutions, the authors minimized objective functions based on changing spherical harmonic expansion origins to predict the acoustic centers [27,28]. Other efforts incorporated phase differences [27,29]. Because a close relationship exists between the first few multipole terms and spherical harmonic expansions at low frequencies [59–61], the approaches that minimize higher-order expansion terms [27,28] are somewhat analogous to Vanderkooy's approach of eliminating the dipole moment.

The advantage of these recent techniques is that they deduce an acoustic center directly from data measured by a surrounding spherical microphone array. Thus, the methods apply to measured

sources with general radiation patterns. Even so, the approaches come at the cost of computationally expensive optimization procedures that have difficulties centering sources at higher frequencies when the far-field omnidirectional radiation assumption breaks down [28]. In some cases, the phase-based approaches may extend the usable bandwidth [29].

Despite the importance and applicability of past work in acoustic centering, further conceptual development for general source radiation remains necessary. This work accordingly revisits and expands upon Vanderkooy's discussions and demonstrates that sound radiators with primarily omnidirectional far-field directivity patterns have low-frequency acoustic centers defined by their dipole-to-monopole moment ratios. Additional application of the KHIE to the sphere reveals that these moments follow from the spherical harmonic expansion coefficients of the surface particle velocities. A proposed centering method yields closed-form solutions for the low-frequency acoustic centers of several theoretical sources. It also produces center-of-mass-like formulas and provides bounds on acoustic center locations relative to source geometries. The results are general enough to handle both axisymmetric and nonaxisymmetric radiation.

After exploring the theoretical concept of the low-frequency acoustic center and providing several clarifying examples, the following sections generalize low-frequency acoustic centering to arbitrarily shaped sources via spherical harmonic expansion coefficients of radiated pressure fields and multipole moments. The generalization yields the acoustic center through a closed-form solution rather than an optimization procedure. The approach is thus applicable to measurements made by surrounding spherical microphone arrays, which are becoming increasingly ubiquitous for measuring sound radiation from arbitrarily-shaped sources. Experimental results based on a KEMAR head and torso simulator (HATS) validate the proposed technique and show it to be in excellent agreement with the optimization procedures developed in previous works. The results enhance theoretical understanding and will improve the practical applications of acoustic centering.

1.2 Theory of the Low-Frequency Acoustic Center

Consider an arbitrary acoustic source radiating into free space as suggested by Fig. 1.1. The KHIE with no volume sources present yields the complex pressure amplitude on the exterior domain as a function of the normal particle velocity $u_n(\mathbf{r}_s)$ and surface pressure $p(\mathbf{r}_s)$ on the boundary S : [62]

$$p(\mathbf{r}) = \iint_S \left[iz_0 k u_n(\mathbf{r}_s) G(\mathbf{r}, \mathbf{r}_s) + \frac{\partial}{\partial n_s} G(\mathbf{r}, \mathbf{r}_s) p(\mathbf{r}_s) \right] dS, \quad (1.1)$$

where

$$G(\mathbf{r}, \mathbf{r}_s) = \frac{e^{-ik|\mathbf{r}-\mathbf{r}_s|}}{4\pi|\mathbf{r}-\mathbf{r}_s|} \quad (1.2)$$

is the free space Green's function, $z_0 = \rho_0 c$ is the characteristic specific acoustic impedance of the medium, and k is the wavenumber. This convention assumes the normal direction is into the domain and assumes $e^{i\omega t}$ time dependence.

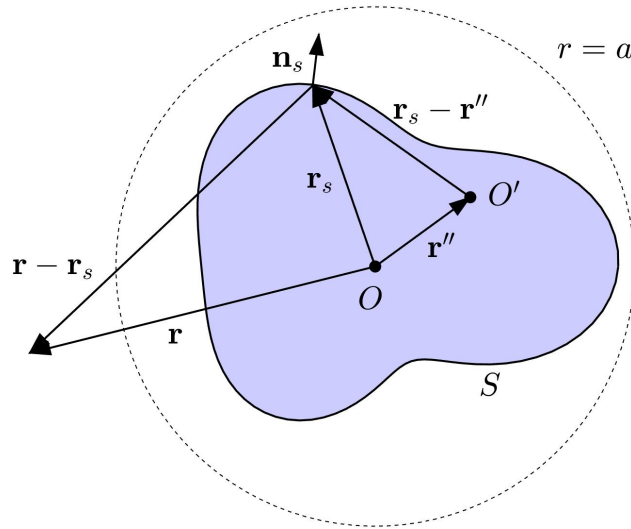


Figure 1.1 Diagram of a radiating source with position and translation vectors.

If the source falls within a notional observation sphere of radius a , indicated by the dashed circle in Fig. 2.1, a Taylor's series expansion of the free-space Green's function about the point \mathbf{r}'' sets up a convergent series of multipole moments when $ka \ll 1$ [62]. Considering only the first two terms

of the expansion, the monopole and dipole terms, the pressure becomes

$$p(\mathbf{r}) \approx MG(\mathbf{r}, \mathbf{r}'') + ikG(\mathbf{r}, \mathbf{r}'') \left(1 - \frac{i}{kR}\right) \mathbf{D}(\mathbf{r}'') \cdot \hat{\mathbf{R}}, \quad (1.3)$$

where M is the monopole moment

$$M = iz_0k \iint_S u_n(\mathbf{r}_s) dS, \quad (1.4)$$

\mathbf{D} is the dipole moment

$$\mathbf{D}(\mathbf{r}'') = \iint_S [iz_0k(\mathbf{r}_s - \mathbf{r}'')u_n(\mathbf{r}_s) + \hat{\mathbf{n}}_s p(\mathbf{r}_s)] dS, \quad (1.5)$$

$\mathbf{R} = \mathbf{r} - \mathbf{r}''$, and $\hat{\mathbf{R}}$ is the unit vector in the direction of \mathbf{R} . While the monopole moment is invariant to the point about which one takes the Taylor's series expansion, the dipole and higher-order moments are not.

To replace an extended source by a single point source, Vanderkooy allowed the expansion origin to vary [54]. He defined the acoustic center \mathbf{r}_c as the expansion origin (\mathcal{O}' in Fig. 1.1) about which the dipole moment vanishes, i.e.,

$$\mathbf{D}(\mathbf{r}_c) = \mathbf{0}. \quad (1.6)$$

When $\mathbf{r}'' = \mathbf{r}_c$, Eq. (1.3) then reduces to the simple form

$$p(\mathbf{r}) \approx MG(\mathbf{r}, \mathbf{r}_c). \quad (1.7)$$

This equation describes the field of a point source located at the acoustic center \mathbf{r}_c whose strength is proportional to the volume velocity of the original source. Thus, at low frequencies, it is possible to replace a “real, extended source by an equivalent point source” [49], simply by exploiting the point of KHIE multipole expansion.

With some deviations to Vandkerooy's solution for \mathbf{r}_c , one may express the acoustic center in terms of the monopole and dipole moments. Specifically, to determine \mathbf{r}_c from the surface velocity

and pressure, choosing $\mathbf{r}'' = \mathbf{r}_c$ in Eq. (1.5), applying Eq. (1.6), and rearranging terms shows that

$$\mathbf{r}_c i z_0 k \iint_S u_n(\mathbf{r}_s) dS = \iint_S [i z_0 k \mathbf{r}_s u_n(\mathbf{r}_s) + \hat{\mathbf{n}}_s p(\mathbf{r}_s)] dS. \quad (1.8)$$

Since the dipole moment with the origin as the expansion point is

$$\mathbf{D}(\mathbf{0}) = \iint_S [i z_0 k \mathbf{r}_s u_n(\mathbf{r}_s) + \hat{\mathbf{n}}_s p(\mathbf{r}_s)] dS, \quad (1.9)$$

the acoustic center follows as

$$\mathbf{r}_c = \frac{\mathbf{D}(\mathbf{0})}{M}. \quad (1.10)$$

Thus, one may define the low-frequency acoustic center simply as the dipole-to-monopole moment ratio.

This formula is effective for sources whose far-field radiation patterns are approximately omnidirectional, i.e., such that Eq. (1.7) yields an adequate representation of the far-field pressure. However, it does not restrict near-field directional patterns. Because the derivation requires $\mathbf{D}(\mathbf{r}_c) = \mathbf{0}$, it cannot apply to sources that produce dipole, cardioid, or more complex far-field patterns. Nevertheless, far-field omnidirectional radiation is common to many sources at low frequencies, including loudspeakers [10, 11, 63], speech [3, 6, 64], and some musical instruments [1, 7, 30, 35]. Reciprocity extends the approach to sound receivers with low-frequency omnidirectional reception, including certain microphones [10, 65, 66] and the human head [57, 67–69].

While one typically considers an acoustic center to be a real-valued quantity, Eq. (1.10) allows the possibility of a complex value in some cases. The following sections touch on this characteristic, which previous studies overlooked, but a complete understanding of its significance and ramifications requires additional research beyond the scope of the present work.

1.3 Application to Spherical Source Configurations

Although Eq. (1.10) provides a straightforward method to determine the acoustic center, calculating $\mathbf{D}(\mathbf{0})$ and M requires surface integrals involving the normal particle velocity and pressure, which are often unknown. This difficulty led Vanderkooy to adopt his fitting procedure for measured pressure values rather than evaluating the integrals. In their work on spheres with oscillating caps, Aarts and Janssen did not directly evaluate the surface integrals either. However, this section shows that sources with spherical geometries have spherical harmonic expansion coefficients for their normal surface velocity and matched particle velocity distributions that relate closely to the monopole and dipole moments. They consequently allow low-frequency acoustic centering via closed-form solutions.

If the surface S is that of a sphere of radius a , Eq. (15.56) becomes

$$M = iz_0ka^2 \int_0^{2\pi} \int_0^\pi u_n(\theta, \phi) \sin \theta d\theta d\phi \quad (1.11)$$

and Eq. (1.9) becomes

$$\mathbf{D}(\mathbf{0}) = a^2 \int_0^{2\pi} \int_0^\pi \hat{\mathbf{r}}_s [iz_0kau_n(\theta, \phi) + p(\theta, \phi)] \sin \theta d\theta d\phi, \quad (1.12)$$

where $\hat{\mathbf{r}}_s = \mathbf{r}_s/a$ is the outward-pointing unit normal vector. Spherical harmonic expansions applied to the normal particle velocity and pressure further simplify these integrals.

The normalized spherical harmonics

$$Y_n^m(\theta, \phi) = \sqrt{\frac{2n+1}{4\pi} \frac{(n-m)!}{(n+m)!}} P_n^m(\cos \theta) e^{im\phi} \quad (1.13)$$

of degree n and order m constitute an orthogonal basis on the sphere [70]. Here, P_n^m are the associated Legendre functions, which include the Condon-Shortley phase. Because the following derivation and subsequent applications employ spherical harmonics of degrees $n = 0$ and $n = 1$ extensively, Table 1.1 includes their definitions for convenience.

Table 1.1 Definitions of four normalized spherical harmonics commonly used in this work.

$$\begin{aligned}
 Y_0^0(\theta, \phi) &= \sqrt{\frac{1}{4\pi}} \\
 Y_1^{-1}(\theta, \phi) &= \sqrt{\frac{3}{8\pi}} \sin \theta e^{-i\phi} \\
 Y_1^0(\theta, \phi) &= \sqrt{\frac{3}{4\pi}} \cos \theta \\
 Y_1^1(\theta, \phi) &= -\sqrt{\frac{3}{8\pi}} \sin \theta e^{i\phi}
 \end{aligned}$$

The normal particle velocity at the spherical surface has the expansion

$$u_n(\theta, \phi) = \sum_{n=0}^{\infty} \sum_{m=-n}^n U_n^m Y_n^m(\theta, \phi), \quad (1.14)$$

where

$$U_n^m = \int_0^{2\pi} \int_0^{\pi} u_n(\theta, \phi) [Y_n^m(\theta, \phi)]^* \sin \theta d\theta d\phi \quad (1.15)$$

and * denotes complex conjugation. To find the monopole moment, one may substitute Eq. (1.14) into Eq. (1.11) to produce the result

$$M = iz_0 ka^2 \sum_{n=0}^{\infty} \sum_{m=-n}^n U_n^m \int_0^{2\pi} \int_0^{\pi} Y_n^m(\theta, \phi) \sin \theta d\theta d\phi. \quad (1.16)$$

With the integrand factor $1 = \sqrt{4\pi} [Y_0^0(\theta, \phi)]^*$ (see Table 1.1), orthogonality conditions yield

$$\int_0^{2\pi} \int_0^{\pi} Y_n^m(\theta, \phi) \sin \theta d\theta d\phi = \sqrt{4\pi} \delta_{n,0}^{m,0}, \quad (1.17)$$

where $\delta_{n,n'}^{m,m'}$ is the Kronecker delta, such that

$$M = iz_0 ka^2 \sqrt{4\pi} U_0^0. \quad (1.18)$$

The dipole moment requires the surface pressure distribution in addition to the velocity distribution. Applying Euler's equation to the exterior solution of the Helmholtz equation [59] yields

$$p(\theta, \phi) = -iz_0 \sum_{n=0}^{\infty} \sum_{m=-n}^n U_n^m \frac{h_n^{(2)}(ka)}{h_n^{(2)'}(ka)} Y_n^m(\theta, \phi), \quad (1.19)$$

where $h_n^{(2)}(ka)$ are the spherical Hankel functions of the second kind. Substituting Eqs. (1.19) and (1.14) into Eq. (1.12) then produces the dipole moment

$$\mathbf{D}(\mathbf{0}) = iz_0 a^2 \sum_{n=0}^{\infty} \sum_{m=-n}^n U_n^m \left[ka - \frac{h_n^{(2)}(ka)}{h_n^{(2)'}(ka)} \right] \int_0^{2\pi} \int_0^{\pi} \hat{\mathbf{r}}_s Y_n^m(\theta, \phi) \sin \theta d\theta d\phi. \quad (1.20)$$

From Table 1.1,

$$\hat{\mathbf{r}}_s = \begin{bmatrix} x_s/a \\ y_s/a \\ z_s/a \end{bmatrix} = \begin{bmatrix} \sin \theta \cos \phi \\ \sin \theta \sin \phi \\ \cos \theta \end{bmatrix} = \sqrt{\frac{2\pi}{3}} \begin{bmatrix} Y_1^{-1}(\theta, \phi) - Y_1^1(\theta, \phi) \\ i(Y_1^{-1}(\theta, \phi) + Y_1^1(\theta, \phi)) \\ \sqrt{2}Y_1^0(\theta, \phi) \end{bmatrix}^*. \quad (1.21)$$

Consequently, the orthogonalities of the respective spherical harmonics simplify the integral to

$$\int_0^{2\pi} \int_0^{\pi} \hat{\mathbf{r}}_s Y_n^m(\theta, \phi) \sin \theta d\theta d\phi = \sqrt{\frac{2\pi}{3}} \begin{bmatrix} \delta_{n,1}^{m,-1} - \delta_{n,1}^{m,1} \\ -i(\delta_{n,1}^{m,-1} + \delta_{n,1}^{m,1}) \\ \sqrt{2}\delta_{n,1}^{m,0} \end{bmatrix}. \quad (1.22)$$

Substituting this result into Eq. (1.20) then gives the result

$$\mathbf{D}(\mathbf{0}) = iz_0 a^2 \sqrt{\frac{2\pi}{3}} \begin{bmatrix} ka - \frac{h_1^{(2)}(ka)}{h_1^{(2)'}(ka)} \\ -i(U_1^{-1} + U_1^1) \\ \sqrt{2}U_1^0 \end{bmatrix}. \quad (1.23)$$

While Eq. (1.23) is valid for all frequencies, the small-argument approximations [70]

$$h_n^{(2)}(ka) \approx i \frac{(2n)!}{2^n n!} \frac{1}{(ka)^{n+1}}, \quad ka \ll 1 \quad (1.24)$$

and

$$h_n^{(2)'}(ka) \approx -i(n+1) \frac{(2n)!}{2^n n!} \frac{1}{(ka)^{n+2}}, \quad ka \ll 1 \quad (1.25)$$

provide further simplification at low frequencies. The ratio of the spherical Hankel function and its derivative simplifies to

$$\frac{h_n^{(2)}(ka)}{h_n^{(2)'}(ka)} \approx -\frac{ka}{(n+1)}, \quad ka \ll 1, \quad (1.26)$$

such that the dipole moment becomes

$$\mathbf{D}(\mathbf{0}) = iz_0 \frac{3}{2} ka^3 \sqrt{\frac{2\pi}{3}} \begin{bmatrix} U_1^{-1} - U_1^1 \\ -i(U_1^{-1} + U_1^1) \\ \sqrt{2}U_1^0 \end{bmatrix}. \quad (1.27)$$

Finally, the substitution of Eqs. (1.18) and (1.27) into Eq. (1.10) yields the acoustic center

$$\mathbf{r}_c = \frac{a}{2U_0^0} \sqrt{\frac{3}{2}} \begin{bmatrix} U_1^{-1} - U_1^1 \\ -i(U_1^{-1} + U_1^1) \\ \sqrt{2}U_1^0 \end{bmatrix}. \quad (1.28)$$

This result is significant because it presents a closed-form solution for the low-frequency acoustic center of a generally vibrating spherical source, and it is straightforwardly dependent on only a few particle velocity expansion coefficients.

For axisymmetric spherical sources, $U_n^m = 0$ when $m \neq 0$, so it is common to express the normal surface velocities in terms of Legendre polynomials for the $m = 0$ terms:

$$u_n(\theta) = \sum_{n=0}^{\infty} V_n P_n(\cos \theta). \quad (1.29)$$

The expansion coefficients V_n relate to the spherical harmonics expansion coefficients via the addition theorem [70]

$$U_n^m = V_n \frac{4\pi}{(2n+1)} [Y_n^m(\theta_0, \phi_0)]^*, \quad (1.30)$$

where (θ_0, ϕ_0) is the configuration rotation angle. With no rotation, the source remains axisymmetric about $\hat{\mathbf{z}}$, such that $(\theta_0, \phi_0) = (0, 0)$, $U_0^0 = \sqrt{4\pi}V_0$, and $U_1^0 = \sqrt{4\pi/3}V_1$ (see Table 1.1). The expression for the acoustic center then simplifies to

$$\mathbf{r}_c = a \frac{V_1}{2V_0} \hat{\mathbf{z}}, \quad (1.31)$$

which concurs with Ref. [58], Eq. (40).

1.4 Examples of Spherical Source Configurations

A radially oscillating sphere [62], a point source on a sphere [60], a radially vibrating cap on a sphere [10, 60], and an axially vibrating cap on a sphere [10, 71] all represent sources with known expansion coefficients. This section explores the low-frequency acoustic centers of these sources and those of other interesting configurations involving more than one point source on a rigid sphere.

1.4.1 Radially Oscillating Sphere

A radially oscillating sphere of radius a is a prototypical omnidirectional radiator with simple symmetry and uniform normal surface velocity $u_n(\theta, \phi) = u_0$. Its velocity expansion coefficients are all zero except $U_0^0 = u_0\sqrt{4\pi}$. Equation (1.28) thus requires that $\mathbf{r}_c = \mathbf{0}$, meaning the low-frequency acoustic center falls at the sphere's center, as suggested by its symmetry. When $ka \ll 1$, the sphere behaves as a simple source at the geometric origin [62].

1.4.2 One Point Source on a Rigid Sphere

The radiation from a point source on a rigid sphere is an important case because it yields the Green's function for the associated geometry [59]. It also illustrates basic diffraction effects [72] and has applications in areas such as the simple modeling of head-related transfer functions [56, 57, 73].

The velocity expansion coefficients for a point source of strength Q_s and position (θ_s, ϕ_s) on the sphere are [59]

$$U_n^m = \frac{Q_s}{a^2} [Y_n^m(\theta_s, \phi_s)]^* . \quad (1.32)$$

The monopole moment [Eq. (1.18)] is then

$$M = iz_0 k Q_s \quad (1.33)$$

and the dipole moment [see Eqs. (1.21) and (1.27)] is

$$\mathbf{D}(\mathbf{0}) = iz_0 \frac{3}{2} ka Q_s \hat{\mathbf{r}}_s, \quad (1.34)$$

where $\hat{\mathbf{r}}_s$ is the unit vector in the direction of (θ_s, ϕ_s) [compare Ref. [59], p. 216]. The acoustic center follows from Eq. (1.10) as

$$\mathbf{r}_c = \frac{3}{2} a \hat{\mathbf{r}}_s. \quad (1.35)$$

Vanderkooy used a numerical example of his method to estimate the low-frequency acoustic center of a point source on the surface of a 170 mm diameter rigid sphere. The calculated center fell at 42.4 mm [57], which has an implicit value of $r_c = 1.50a$, consistent with Eq. (1.35).

Figure 1.2 shows the concurrence of this center with results presented by Jacobsen et al. [49]. Their work evaluated three methods for determining the acoustic center of a point source on a rigid sphere. The solid black curve represents the acoustic center based on matching the amplitude of an equivalent point source [Ref. 49, Eq. (18)], the dashed red curve represents the acoustic center based on an reciprocal $1/r$ decay fit [Ref. 49, Eq. (19)], and the dot-dash blue curve represents the acoustic center based on a phase approach [Ref. 49, Eq. (21)]. In all cases, the far-field observation distance is $r = 1$ km.

In the low-frequency limit, both amplitude matching approaches converge to the center given by Eq. (1.35) and represented by the dotted green line. Additionally, it appears that in the far field both methods converge to the same value at all frequencies. As discussed in Ref. [49], the phase method places the acoustic center behind the source. However, the authors found that modifying the phase method by multiplying both the numerator and denominator in Ref. 49 Eq. (21) by a factor of -1 ensured only positive phase values. The resultant acoustic center appears as the purple curve with diamond markers; it does converge to the low-frequency limit. Because the formulations of the present work apply only to low-frequency radiation, deviations in the acoustic center's position occur at higher frequencies. However, at higher frequencies, the phase based

method does not concur with the two amplitude matching methods, highlighting the ambiguity in replacing a distributed source with an equivalent point source at high frequencies [49].

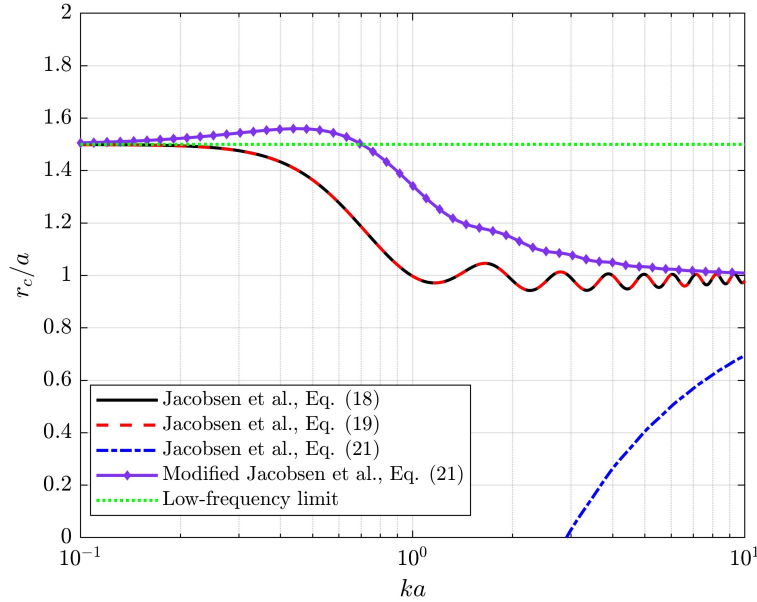


Figure 1.2 The acoustic center of a point source on a sphere over dimensionless ka , where a is the sphere's radius.

Figure 1.3(a) depicts the pressure field surrounding a point source on a rigid sphere for $ka = 0.01$. The figure includes contours in 3 dB increments to illustrate the constant $1/r$ decay. The green dot represents the acoustic center, and the green dashed circle represents a sphere of radius $5a$. The latter aligns well with the contours of constant $1/r$ decay, which is a necessary validation of the acoustic center's location. For this example, the near-field pattern is directional, and the acoustic center lies away from the sphere. However, with sufficient distance, the directivity converges to an omnidirectional far-field pattern. Figure 1.3(b) depicts the pressure field produced by an equivalent point source in free space. The far-field agreement between both fields highlights the method's effectiveness for low frequencies.

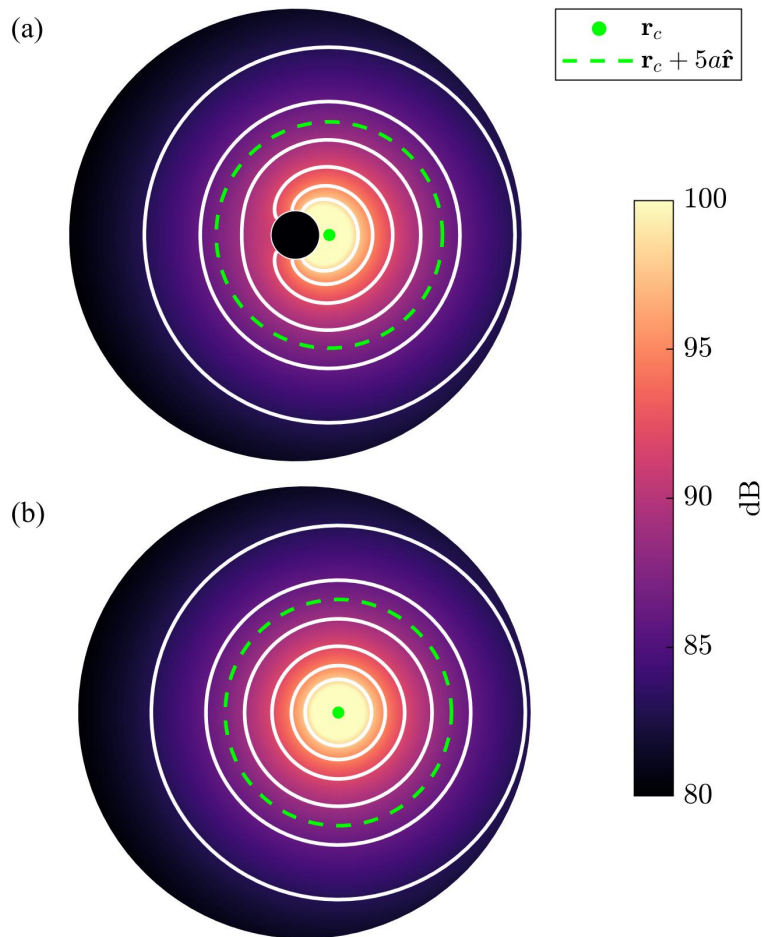


Figure 1.3 Sound pressure field for $ka = 0.01$ around (a) a point source on a rigid sphere and (b) its equivalent point source.

1.4.3 Radially Oscillating Cap on a Rigid Sphere

The radially oscillating cap on a rigid sphere [60] has helped researchers better understand the radiation of speech, loudspeakers, horns, and other sources [4, 6, 10–12]. It also bridges the previous two examples. In the limiting small cap-angle case, $\theta_c \rightarrow 0$ and the arrangement behaves as a point source on the sphere. However, when $\theta_c \rightarrow \pi$, it behaves as a radially oscillating sphere.

For a cap oriented toward the zenith, $u_n(\theta, \phi) = u_0$ for $0 < \theta < \theta_c$ and zero otherwise. The first two Legendre polynomial series expansion coefficients are then [10, 60] $V_0 = u_0(1 - \cos \theta_c)/2$ and $V_1 = 3u_0(1 - \cos^2 \theta_c)/4$, which yield the acoustic center $\mathbf{r}_c(\theta_c) = 3a(1 + \cos \theta_c)\hat{\mathbf{z}}/4$ via Eq. (1.31), in agreement with the result of Aarts and Janssen [58]. This function appropriately interpolates the acoustic center between $r_c = 3a/2$ and $r_c = 0$, the limiting $\theta_c \rightarrow 0$ and $\theta_c \rightarrow \pi$ cases, respectively.

Figure 1.4(a) depicts the acoustic pressure field around the source configuration for $ka = 0.01$ and $\theta_c = \arccos(1/3)$, so that the acoustic center lies at $r_c = a$. Figure 1.4(b) shows the pressure field produced by an equivalent point source in free space. Although there is significant diffraction around the sphere, the pressure produced by the equivalent point source at the acoustic center shows good far-field agreement.

1.4.4 Axially Oscillating Cap on a Rigid Sphere

An axially oscillating cap on a rigid sphere is another instructive example. A very small cap angle again produces the pressure field of a point source on a sphere, but a large cap angle $\theta_c \rightarrow \pi$ forms a transversely oscillating sphere with a significant dipole moment [62]. Attempting to replace a dipole field with a monopole field is equivocal, so one may anticipate that Eq. (1.28) diverges as $\theta_c \rightarrow \pi$ and $M \rightarrow 0$. This condition highlights a potential weakness of defining the acoustic center only in terms of the locus of an equivalent point source.

The normal surface velocity of an axially vibrating cap is $u_n(\theta, \phi) = u_0 \cos \theta$ for $0 < \theta < \theta_c$ and zero otherwise. The first two Legendre polynomial series expansion coefficients are [10, 71]

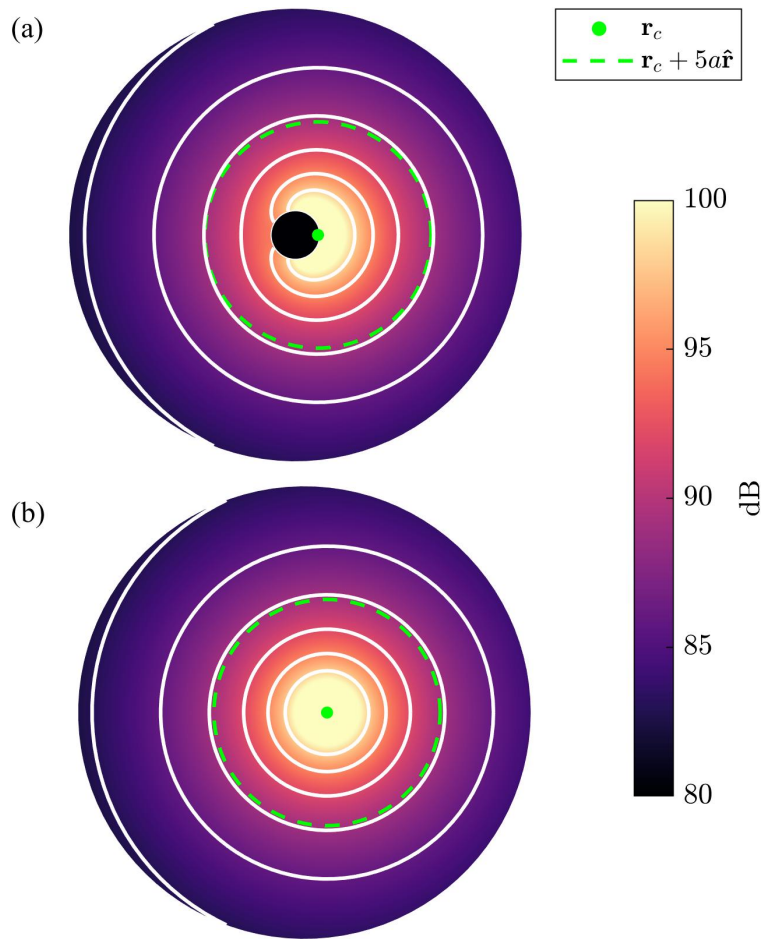


Figure 1.4 Sound pressure field for $ka = 0.01$ around (a) a radially oscillating cap with cap angle $\theta_c = \arccos(1/3)$ on a rigid sphere and (b) its equivalent point source.

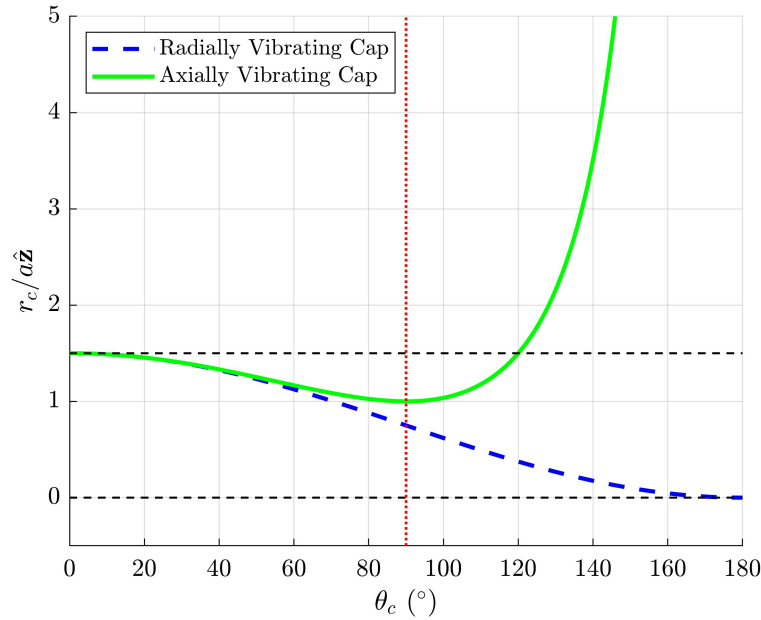


Figure 1.5 Low-frequency acoustic centers of a radially and axially oscillating cap on a sphere as a function of cap angle θ_c .

$V_0 = u_0(1 - \cos^2 \theta_c)/4$ and $V_1 = u_0(1 - \cos^3 \theta_c)/2$, which give the acoustic center $\mathbf{r}_c(\theta_c) = a(1 + \cos \theta_c + \cos \theta_c^2)\hat{\mathbf{z}}/(1 + \cos \theta_c)$ via Eq. (1.35), in agreement with the result of Aarts and Janssen [58].

Figure 1.5 plots the acoustic center as a function of the cap angle from the zenith for both the radially and axially vibrating caps. The acoustic center of the radially vibrating cap, shown as the blue dashed line, interpolates between the two limiting values, shown as horizontal black dashed lines, of $r_c = 3a/2$ and $r_c = 0$. As for the radially vibrating cap, shown as a solid green line, when $\theta_c \rightarrow 0$, the acoustic center of the axially vibrating cap becomes that of a point source on the sphere. However, as $\theta_c \rightarrow \pi$, $M \rightarrow 0$ [see Eqs. (15.56) and (1.11)], and $r_c \rightarrow \infty$ [see Eq. (1.10)]. The vertical dotted red line marks the threshold up to which $u_n(\theta, \phi) \geq 0$; in the range $\pi/2 < \theta \leq \theta_c$, $u_n(\theta, \phi)$ takes on a 180°-degree phase shift. Consequently, as θ_c increases beyond $\pi/2$, the monopole moment progressively diminishes and the acoustic center moves significantly farther from the sphere's geometric center.

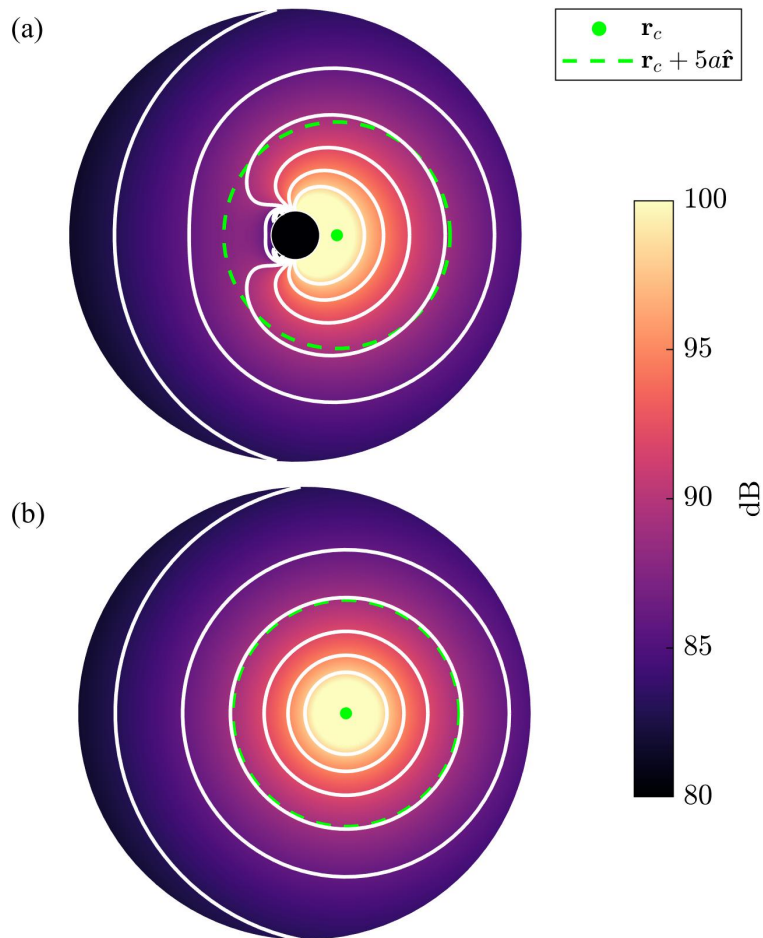


Figure 1.6 Sound pressure field for $ka = 0.01$ around (a) an axially oscillating cap with cap angle $\theta_c = 0.7\pi$ on a rigid sphere and (b) its equivalent point source.

Figure 1.6(a) depicts the pressure field around the sphere for $ka = 0.01$ and $\theta_c = 0.7\pi = 126^\circ$. The plot shows considerable near-field interference, diffraction, and the acoustic center at $r_c = 1.84a$. Figure 1.6(b) shows the pressure field produced by an equivalent point source in free space. Despite the very directional near-field pattern in Fig. 1.6(a), as the observation distance increases to the far field, the radiated fields agree and are both omnidirectional.

1.4.5 Two Point Sources on a Rigid Sphere

The concept of substituting a point source for a real source is only valid in the far field when the directivity pattern is omnidirectional. The radiation from two point sources at opposing poles of a rigid sphere helps clarify the difficulty introduced by a dipole moment. As in the preceding section, the first source at $(\theta_s, \phi_s) = (0, 0)$ has strength Q_s . The second source at $(\theta_s, \phi_s) = (\pi, 0)$ has strength γQ_s , where γ may vary as a real number. Through superposition, the velocity expansion coefficients become

$$U_n^m = \frac{Q_s}{a^2} ([Y_n^m(0, 0)]^* + \gamma [Y_n^m(\pi, 0)]^*). \quad (1.36)$$

However, because the source is axisymmetric, all $m \neq 0$ terms vanish. Equation (1.13) and the relation $P_n^0(-1) = (-1)^n$ then lead to the result

$$U_n^0 = \frac{Q_s}{a^2} \sqrt{\frac{2n+1}{4\pi}} [1 + \gamma(-1)^n], \quad (1.37)$$

such that

$$U_0^0 = \frac{Q_s}{a^2} \sqrt{\frac{1}{4\pi}} (1 + \gamma) \quad (1.38)$$

and

$$U_1^0 = \frac{Q_s}{a^2} \sqrt{\frac{3}{4\pi}} (1 - \gamma). \quad (1.39)$$

The acoustic center follows from Eqs. (1.30) and (1.31) as

$$\mathbf{r}_c = \frac{3}{2}a \left(\frac{1 - \gamma}{1 + \gamma} \right) \hat{\mathbf{z}}. \quad (1.40)$$

This expression also follows from Eqs. (1.33) and (1.34), since by superposition, the net monopole moment is $M = iz_0 k Q_s (1 + \gamma)$ and the net dipole moment is $\mathbf{D} = iz_0 k Q_s 3/2a (1 - \gamma) \hat{\mathbf{z}}$.

Figure 1.7 plots the acoustic center as a function of the source strength ratio γ and shows several significant trends. First, when the second source's strength is much larger than the first ($|\gamma| \gg 1$), the acoustic center converges to a single point at $(\theta_0, \phi_0) = (\pi, 0)$, such that $\mathbf{r}_c = -3a/2\hat{\mathbf{z}}$. Second, when the second source's strength is zero ($\gamma = 0$), the acoustic center is that of a single point source

located at $(\theta_0, \phi_0) = (0, 0)$, such that $\mathbf{r}_c = 3a/2\hat{\mathbf{z}}$. Third, the acoustic center falls at the center of the sphere when the second source's strength equals the first ($\gamma = 1$), as one might anticipate from symmetry. Fourth, when the two amplitudes are equal but the polarities are opposite ($\gamma = -1$), the acoustic center has an infinite discontinuity to $-\infty$ as $\gamma \rightarrow -1^-$ and $+\infty$ as $\gamma \rightarrow -1^+$.

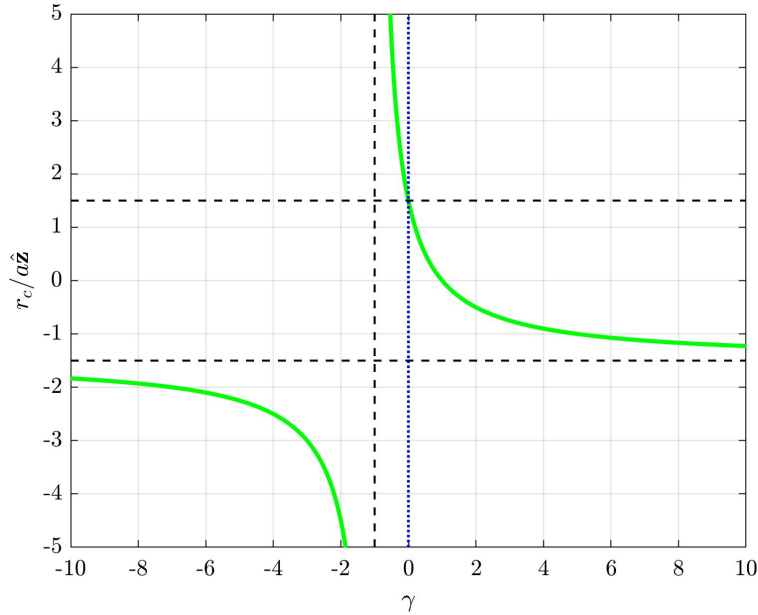


Figure 1.7 Low-frequency acoustic center predicted by Eq. (1.28) for two point sources at the opposing poles of a sphere as a function of the second source's relative strength.

The potentially large acoustic center radii for $\gamma \rightarrow 1$ in Fig. 1.7 do not necessarily suggest a nonphysical situation, provided that the source remains nearly omnidirectional in the far field. Figure 1.8 depicts the pressure field produced by the two point sources for $ka = 0.01$ and $\gamma = -0.8$. The plot ranges over $240a$ in both the x - and y -directions. As in Fig 1.3, the contours of equal $1/r$ decay appear in 3 dB increments; however, near the source configuration, which appears as a small black dot, the contours are missing for better visualization.

The cardioid-like equal-level contours in the near field suggest a strong dipole component, which moves the acoustic center to $r_c = 13.5a$, a significant distance from the sphere. Nevertheless, as suggested by the circular contours in the far field, this position coincides with the origin of

spherical wavefronts of constant amplitude. The pattern evolution from the near field to the far field apparently requires about $50a$ of propagation. In fact, because $ka = 0.01$, the acoustic far field lies beyond $100a$.

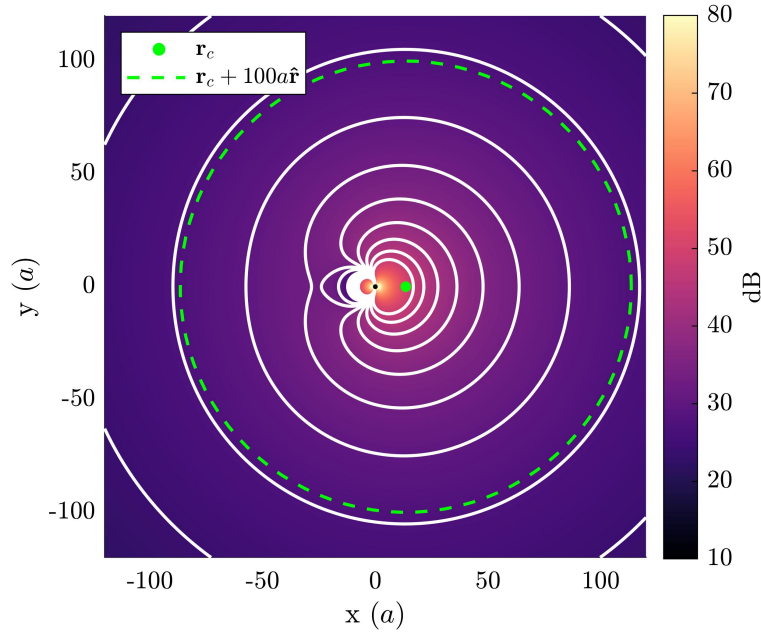


Figure 1.8 Sound pressure field for $ka = 0.01$ produced by two point sources at the opposing poles of a rigid sphere with a source strength ratio of $\gamma = -0.8$.

1.4.6 Multiple Point Sources on a Rigid Sphere and Related Extensions

Equations (1.33) and (1.34) further generalize the result in Eq. (1.40) to N point sources at arbitrary locations on a sphere. From

$$M = iz_0ka^2 \left(\sum_{i=1}^N Q_i \right) \quad (1.41)$$

and

$$\mathbf{D}(\mathbf{0}) = iz_0ka^2 \left(\frac{3}{2}a \sum_{i=1}^N Q_i \hat{\mathbf{r}}_i \right), \quad (1.42)$$

the acoustic center becomes

$$\mathbf{r}_c = \frac{3}{2}a \left(\frac{\sum_{i=1}^N Q_i \hat{\mathbf{r}}_i}{\sum_{i=1}^N Q_i} \right). \quad (1.43)$$

If the relative source strength ratios of all point sources are real valued, i.e., either in phase or 180° out of phase, the acoustic center likewise remains real valued as in Sec. 1.4.5. Other source strength configurations could lead to a complex-valued acoustic center (see Sec. 16.4). A striking feature of this equation is that it simplifies the challenge of determining $\mathbf{D}(\mathbf{0})$ from required surface pressure and velocity distributions. Spherical harmonics and spherical Hankel functions recast the dipole moment only in terms of source strengths and associated local surface velocities.

To better understand why a knowledge of the surface pressure p_i for the i^{th} source is unnecessary, one may work backwards from Eq. (1.42) to show that

$$\mathbf{D}(\mathbf{0}) = a^3 \sum_{i=1}^N \left(iz_0 k \frac{3}{2} Q_i \hat{\mathbf{r}}_i \right) \quad (1.44)$$

$$= a^3 \sum_{i=1}^N \left(iz_0 k Q_i \hat{\mathbf{r}}_i + \frac{1}{2} iz_0 k Q_i \hat{\mathbf{r}}_i \right). \quad (1.45)$$

For the i^{th} point source, the sifting property yields

$$\int_0^{2\pi} \int_0^\pi Q_i \hat{\mathbf{r}}_s \delta(\cos \theta - \cos \theta_i) \delta(\phi - \phi_i) \sin \theta d\theta d\phi = Q_i \hat{\mathbf{r}}_i, \quad (1.46)$$

so it is also true, by definition [see Eq. (1.12)], that

$$\mathbf{D}(\mathbf{0}) = a^3 \sum_{i=1}^N \left[iz_0 k Q_i \hat{\mathbf{r}}_i + \int_0^{2\pi} \int_0^\pi \hat{\mathbf{r}}_s p_i(\theta, \phi) \sin \theta d\theta d\phi \right]. \quad (1.47)$$

Consequently,

$$\int_0^{2\pi} \int_0^\pi \hat{\mathbf{r}}_s p_i(\theta, \phi) \sin \theta d\theta d\phi = \frac{1}{2} iz_0 k Q_i \hat{\mathbf{r}}_i. \quad (1.48)$$

This development shows that diffraction about the rigid sphere increases the dipole moment by 50%, moving the acoustic center farther from the surface. Equation (1.48) is thus a theoretical proof

of Vanderkooy's qualitative assertion that the KHIE pressure term moves the acoustic center away from the origin [54].

Treating a quasi-arbitrary, continuous surface velocity distribution $u_n(\theta, \phi)$ as a distribution of point sources allows further generalization of Eq. (1.43) to

$$\mathbf{r}_c = \frac{3}{2}a \left[\begin{array}{c} \frac{2\pi \pi}{0 \ 0} \int \int u_n(\theta, \phi) \hat{\mathbf{r}}_s \sin \theta d\theta d\phi \\ \frac{2\pi \pi}{0 \ 0} \int \int u_n(\theta, \phi) \sin \theta d\theta d\phi \end{array} \right] = \frac{3}{2} \left[\begin{array}{c} \frac{2\pi \pi}{0 \ 0} \int \int u_n(\theta, \phi) \mathbf{r}_s \sin \theta d\theta d\phi \\ \frac{2\pi \pi}{0 \ 0} \int \int u_n(\theta, \phi) \sin \theta d\theta d\phi \end{array} \right]. \quad (1.49)$$

This key result provides an upper bound to the acoustic center's radial distance given that $u_n(\theta, \phi)$ has the same phase. The maximum distance $r_c = 3a/2$ occurs when all volume velocity concentrates at a single point.

1.5 Generalization to Nonspherical Source configurations

While the surface velocity and pressure in the KHIE provided the bases for the preceding spherical-source acoustic centering developments, one may generalize the approach using a notional observation sphere of minimal radius a that entirely envelops an acoustic source of arbitrary shape. Because of the uniqueness of the exterior solution in spherical coordinates, the pressure *or* particle velocity on the sphere will infer both the monopole and dipole moments (for $ka \ll 1$) directly from its expansion coefficients [59, 61]. If a monopole and dipole field uniquely determine the pressure produced by the source, the pressure or particle velocity on the sphere will provide the unique solution for $r \geq a$ [59]. Consequently, a multipole expansion applied to the observed quantity must converge to the same monopole and dipole moments of the isolated source. Researchers have applied similar concepts in other works [66, 74, 75]; however, the nonuniqueness of the field inside the sphere requires additional consideration [76].

Because multipole expansions and pressure-field expansions involving spherical harmonics and spherical Bessel functions have similar terms [59–61], an equating of terms allows one to establish

the relationships between the multipole moments and the pressure expansion coefficients. This approach is valid for constructing the exterior field, as the following sections demonstrate, but the calculated monopole and dipole moments only have the physical meanings defined by Eqs. (15.56) and (15.57) in the limit of $ka \ll 1$. The surface integrals and spherical harmonic expansion coefficients do not have guaranteed relationships for higher frequencies, but this fact presents little problem for the following developments because the formulation of Eq. (1.10) is already in the limit of $ka \ll 1$.

1.5.1 General Formulation

The Helmholtz equation solution in spherical coordinates is [59]

$$p(r, \theta, \phi, k) = \sum_{n=0}^{\infty} \sum_{m=-n}^n C_n^m h_n^{(2)}(kr) Y_n^m(\theta, \phi), \quad r \geq a, \quad (1.50)$$

where

$$C_n^m = \frac{1}{h_n^{(2)}(ka)} \int_0^{2\pi} \int_0^{\pi} p(a, \theta, \phi) [Y_n^m(\theta, \phi)]^* \sin \theta d\theta d\phi. \quad (1.51)$$

In practice, the expansion coefficients follow from discrete measurements of the pressure field around the source and numerical integration or a least-squares fit [77, 78]. Significantly, because the present work's formulation requires only expansion degrees up to $n = 1$, the low-frequency acoustic center could follow from only four sampled positions [77].

Comparing Eqs. (1.50) and (1.19) reveals that

$$U_n^m = -\frac{1}{iz_0} C_n^m h_n^{(2)'}(ka). \quad (1.52)$$

Substitution of this result into Eqs. (1.14) and (1.11) yields the monopole moment

$$M = -ka^2 h_0^{(2)'}(ka) \sqrt{4\pi} C_0^0. \quad (1.53)$$

However, since $ka \ll 1$,

$$h_0^{(2)'}(ka) \approx -\frac{i}{(ka)^2} \quad (1.54)$$

and the monopole term simplifies to

$$M \approx i \frac{\sqrt{4\pi}}{k} C_0^0 \quad (1.55)$$

[compare Ref. [59], p. 198].

For the dipole moment,

$$\mathbf{D}(\mathbf{0}) = -\frac{3}{2}ka^3 h_1^{(2)'}(ka) \sqrt{\frac{2\pi}{3}} \begin{bmatrix} C_1^{-1} - C_1^1 \\ -i(C_1^{-1} + C_1^1) \\ \sqrt{2}C_1^0 \end{bmatrix}. \quad (1.56)$$

Using the $ka \ll 1$ approximation

$$h_1^{(2)'}(ka) \approx -\frac{2i}{(ka)^3}, \quad (1.57)$$

the dipole term simplifies to

$$\mathbf{D}(\mathbf{0}) = \frac{i\sqrt{6\pi}}{k^2} \begin{bmatrix} C_1^{-1} - C_1^1 \\ -i(C_1^{-1} + C_1^1) \\ \sqrt{2}C_1^0 \end{bmatrix}. \quad (1.58)$$

The acoustic center then follows from Eq. (1.10) as

$$\mathbf{r}_c = \frac{1}{kC_0^0} \sqrt{\frac{3}{2}} \begin{bmatrix} C_1^{-1} - C_1^1 \\ -i(C_1^{-1} + C_1^1) \\ \sqrt{2}C_1^0 \end{bmatrix}, \quad (1.59)$$

but it is now in terms of the pressure-field expansion coefficients.

1.5.2 Point Source Distribution

An arbitrary point source distribution with quasi-arbitrary, real-number-related source strengths provides a simple nonspherical evaluation case because one can infer the exact value of r_c from the

standard monopole and dipole moment definitions for point sources in free space [54, 62]. For N point sources, the monopole moment is

$$M = iz_0k \sum_{i=1}^N Q_i, \quad (1.60)$$

the dipole moment is

$$\mathbf{D}(\mathbf{0}) = iz_0k \sum_{i=1}^N Q_i \mathbf{r}_i, \quad (1.61)$$

and the acoustic center is

$$r_c = \left(\frac{\sum_{i=1}^N Q_i \mathbf{r}_i}{\sum_{i=1}^N Q_i} \right). \quad (1.62)$$

This center-of-mass-like formula [79] is similar to Eqs. (1.43) and (1.49) but without the $3a/2$ scaling factor. Previously, the factor arose from the dipole moment formed from the diffraction around the spherical rigid body, as shown by Eq. (1.48) [also compare Ref. 80]. However, center-of-mass-like formulas for nonspherical rigid boundaries and their velocity distributions will likely differ. Also similar to Eq. (1.43), a real-valued acoustic center follows when the relative source strength ratios of all point sources are real valued.

Suppose a spherical array of radius $R = 1.0$ m and 5° equiangular spacing in both the polar and azimuthal angles samples the pressure field produced by five point sources with the amplitudes and positions listed in Table 1.2 at $kR = 0.01$. The spherical harmonic expansion coefficients follow from Chebyshev numerical integration [78], such that Eq. (1.59) yields the acoustic center $\mathbf{r}_c = (0.92, -1.58, -0.20)$ m. This calculated value from the expansion coefficients agrees with that produced by Eq. (1.62) to less than a thousandth of a percent. As $kR \rightarrow 0$, the error decreases to machine precision.

Figure 1.9 depicts the resultant field produced by the point sources. The solid black circle denotes the sampling sphere in which all contours are missing to allow better visualization for $r < R$. The specific source amplitudes and positions create a strong dipole moment, causing the acoustic

center to fall outside the sampling sphere. However, its location does not impact the validity of the spherical harmonic expansion in Eq. (1.50). The only requirement is that all nonhomogenous terms, i.e., the point sources, fall within the sphere so that the region $r \geq R$ satisfies the homogenous Helmholtz equation.

Table 1.2 Tabulated amplitudes and locations for five point sources inside a measurement sphere of radius $R = 1$ m.

Q_i (m ³ /s)	x (m)	y (m)	z (m)
1.0	0.3	-0.1	-0.2
-0.6	0.3	0.3	0
0.7	0.2	-0.3	0
-0.8	-0.3	0.3	-0.1
0.2	-0.2	-0.3	0.1

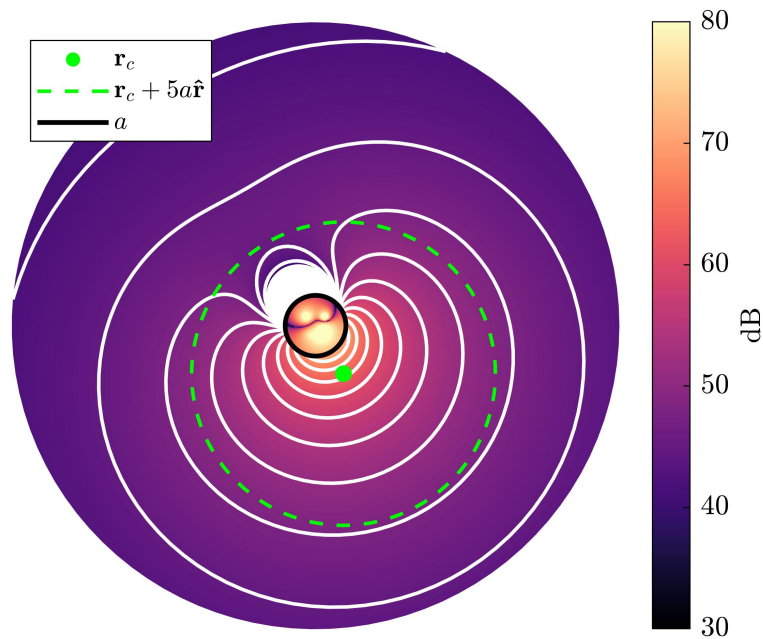


Figure 1.9 Pressure produced by a point source distribution and the associated acoustic center marked as a green dot.

1.6 Experimental Example

The results of a pertinent acoustic centering experiment and comparisons with the results of other centering methods provide further validation of the preceding developments. The authors employed a rotating semicircular microphone array to sweep out a sphere of sampled pressure data and evaluate the directivities of a KEMAR HATS with and without an attached torso and with varying head orientations [81]. The measurement and signal-processing techniques were similar to those used earlier for live speech [6]. The processing employed complex-valued frequency response functions (FRFs) and numerical integration [78] to produce the pressure expansion coefficients C_n^m described in Eq. (1.51). An $N = 10$ expansion ensured that the area-weighted directivity factor function deviation (AWDFFD) level L_Q [81] between the measured and expanded pressure remained less than 0.1 dB for the frequencies of interest.

As shown in Fig. 1.10, this HATS experiment extended the earlier work to consider the effects of attached manikin legs and a chair. The minimum sphere encompassing the entire arrangement had a radius $a \approx 0.75$ m with a center offset from the array's geometric center. However, if one considers the low-frequency scattering of selected manikin and chair parts to be negligible, a could become considerably smaller. To accommodate the configuration, the microphone radius increased from $R = 0.97$ m, used in Ref. [81], to $R = 1.17$ m. However, the enlarged radius still prohibited the exact alignment of the HATS mouth, the geometric center of the manikin's radiating region, at the array's geometric center. Consequently, post-processed acoustic centering became particularly important for correcting the measured directivity patterns (see Sec. 1.6.2).

1.6.1 Centering Results

In addition to calculating the source low-frequency acoustic center via Eq. (1.59), the authors considered four previously proposed acoustic centering algorithms to predict the acoustic center



Figure 1.10 KEMAR HATS seated within a directivity measurement system.

at various frequencies. The latter work involved minimizing the objective functions J_{ss} [Ref. [27] Eq. (7.1)], based on the coherent summation of the complex pressure; J_{Io} [Ref. [27] Eq. (7.3) and Ref. [28] Eq. (34)], which penalizes energy in higher degree expansion terms; J_{zo} [Ref. [28] Eq. (30)], which favors energy in the C_0^0 coefficient; and J_{ph} [Ref. [29] Eq. (58)], which considers phase symmetries. Technically, one should evaluate J_{ph} for phase symmetries in three orthogonal planes; however, radiation symmetry allowed optimization over the median (x - z) plane to suffice for the present example.

Figure 1.11 plots the objective functions in the median plane at 100 Hz ($ka \lesssim 1.4$). The solid black circle represents the measurement sphere circumference, whereas the surface colors and contours indicate the relative levels of the objective functions. Normalization between 0 and 1 for all objective functions facilitates simpler comparisons. The red \times at $\mathbf{r}_c = (x, z) = (0.00, 0.27)$ m indicates the low-frequency acoustic center in this plane calculated from Eq. (1.59). As mentioned in Sec. 1.2, this equation may sometimes produces a complex-valued acoustic center (also see Sec. 16.4). At this frequency, the imaginary part from the measured data was smaller by more than an

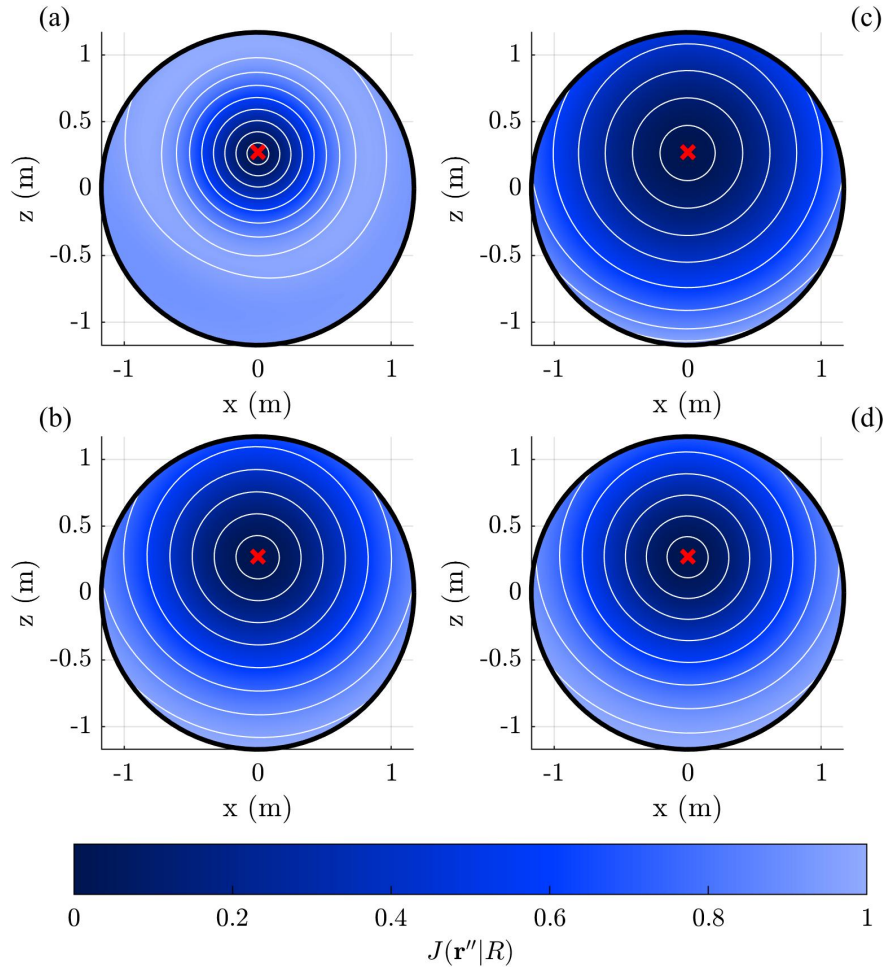


Figure 1.11 Objective functions in the median plane at 100 Hz: (a) J_{ss} , (b) J_{zo} , (c) J_{lo} , and (d) J_{ph} . The red \times is the low-frequency acoustic center from Eq. (1.59).

order of magnitude than the real part and was consequently considered negligible. The calculated acoustic center aligns well with all objective function minima, producing excellent agreement with the outcomes of the previous works. The RMS deviations between the global objective function minima and low-frequency acoustic center were all less than 1 cm even though the localized acoustic center from Eq. (1.59) resulted from a simple closed-form solution rather than a computationally expensive optimization routine.

Figure 1.12 plots the four objective functions at 300 Hz ($ka \lesssim 4.1$) and the calculated low-frequency center appearing at $\mathbf{r}_c = (0.00, 0.25)$ m. Although this frequency exaggerates the low-

frequency assumption, it is still instructive to consider the robustness of the calculated acoustic center. Because the radiation is slightly more directional at this frequency, local minima appear in some of the objective functions, although their global minima remain clear. The low-frequency acoustic center generally aligns well with the global minima but the agreement is not as exact at this frequency. Additionally, while the imaginary part of the calculated acoustic center is still relatively small, it has risen to within an order of magnitude of the real part, which further suggests that the low-frequency approximation has begun to break down. The RMS deviations between the global minima of the objective functions and the calculated acoustic center are less than 2 cm for J_{ss} and J_{zo} and 1 cm for J_{lo} and J_{ph} . For higher frequencies, the low-frequency acoustic center could serve as a viable initialization position to help the centering optimization routines achieve faster convergences.

1.6.2 Directivity Correction

Figure 1.13 presents the normalized directivity balloons for the seated HATS at 100 and 300 Hz and illustrates the effectiveness of acoustic centering to correct near-field directivity pattern anomalies. The balloons employ colors and radii to depict relative levels on a 40 dB scale. The vantage point is from the right-hand side of the manikin, which faces the 0° azimuthal marker.

Figure 1.13(a) shows the measured 100 Hz directivity pattern at the array surface, expanded via spherical harmonics to degree $N = 10$. Although one would anticipate omnidirectional radiation at this frequency [6], the source placement within the array causes the directivity to appear directional. As discussed by the authors in Ref. [82], far-field projection of the measured results allows the correction of such near-field anomalies. Figure 1.13(b) shows the 100 Hz far-field directivity balloon, projected via the $N = 10$ degree expansion. The far-field directivity is essentially omnidirectional, although the levels below the talker are minimally reduced, perhaps due to diffraction about the manikin's body and chair. Figure 1.13(c) plots the directivity evaluated at $r = 1.5$ m ($kr \approx 2.7$ and $r/2a \gtrsim 1.0$) but recentered about the low-frequency acoustic center presented in Fig. 1.11. Despite

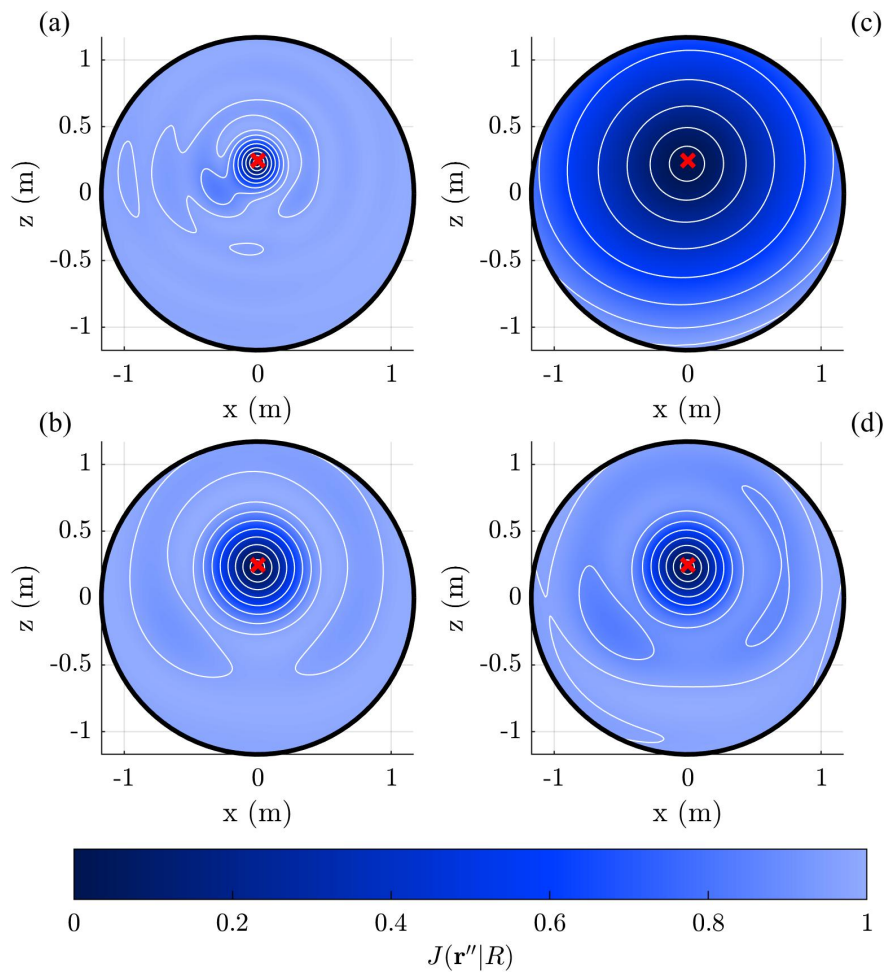


Figure 1.12 Objective functions in the median plane at 300 Hz: (a) J_{ss} , (b) J_{zo} , (c) J_{lo} , and (d) J_{ph} . The red \times is the low-frequency acoustic center from Eq. (1.59).

not being at a far-field evaluation distance, the directivity pattern appears nearly identical to the projected far-field pattern. The AWDFFD L_Q is only 0.1 dB between the far-field and $r = 1.5$ m centered patterns but 1.6 dB between the far-field and $r = R = 1.17$ m measured patterns.

Fig. 1.13(d) shows the measured 300 Hz directivity pattern at the array surface, again expanded to degree $N = 10$. At this higher frequency, diffraction led to reduced levels behind and below the manikin and chair [6, 72]. The axis of maximum radiation appears upward in elevation from the mouth axis, which is not characteristic for this particular frequency [6]. Figure 1.13(e) shows the projected far-field directivity, determined using the $N = 10$ expansion, with the axis of maximum radiation falling directly in front of the manikin's mouth. Finally, Fig. 1.13(f) shows the centered directivity pattern evaluated at $r = 1.5$ m ($kr \approx 8.2$ and $r/2a \gtrsim 1.0$). The centering improved L_Q from 1.4 dB to 0.7 dB relative to the projected far-field pattern.

1.7 Discussion

The low-frequency acoustic center provides a valuable and straightforward means to treat a distributed source as a single point source. However, its validity depends upon the nature of the source and the observation distance. For example, a radially oscillating sphere whose acoustic center falls at the origin has an equivalent point source representation valid in the near and far fields. On the other hand, two point sources at opposing poles on a sphere with a strength ratio $\gamma = -0.8$ (see Sec. 1.4.5) have an equivalent point source representation not valid until the observation distance is many times the sphere radius. Thus, while the low-frequency acoustic center is generally valid at a sufficient distance for sources producing omnidirectional far-field directivities, it is judicious to consider the minimum distance at which the equivalent representation becomes acceptable for practical applications.

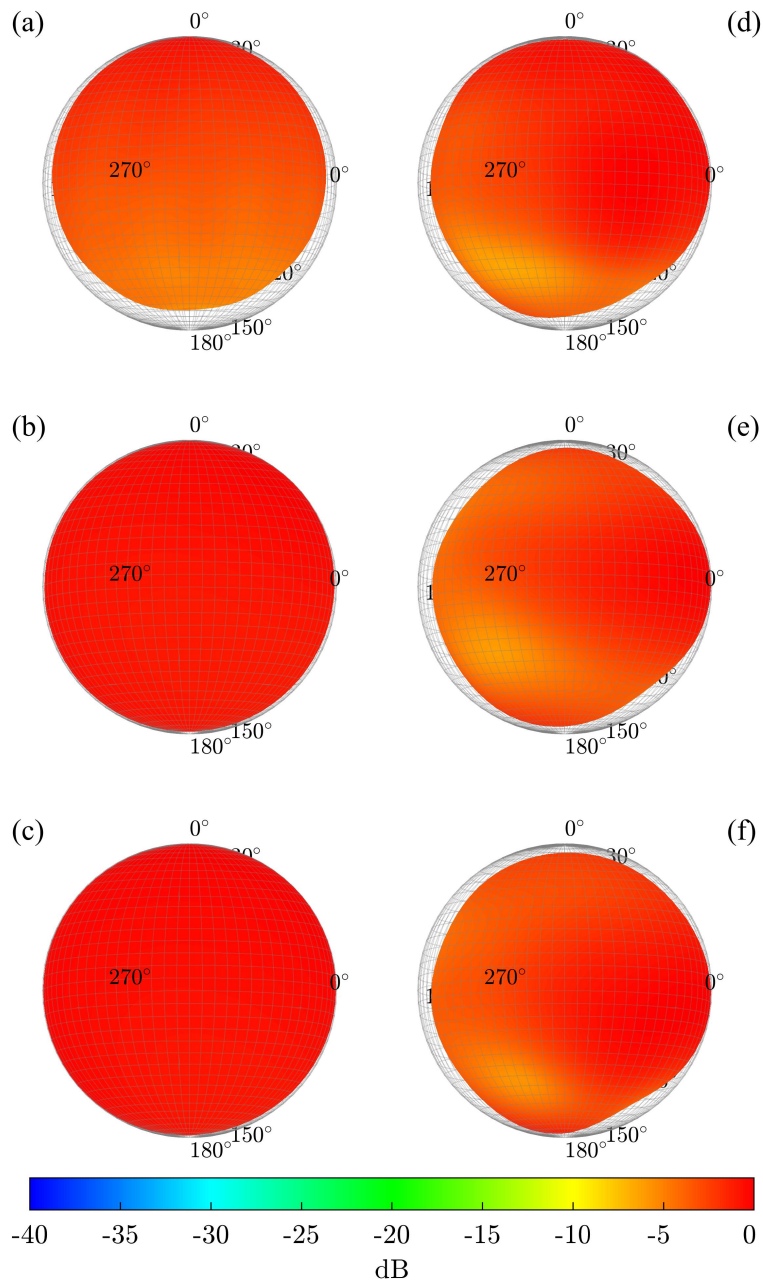


Figure 1.13 KEMAR HATS directivity. (a) $r = R = 1.17$ m measured, (b) far-field projected, and (c) $r = 1.5$ m centered at 100 Hz. (d) $r = R = 1.17$ m measured, (e) far-field projected, and (f) $r = 1.5$ m centered at 300 Hz.

The low-frequency centering method discussed in this work permits the direct use of spherical harmonic expansion coefficients from the acoustic pressure or particle velocity over an observation sphere. This resource is advantageous because it supports the direct determination of an acoustic center without requiring computationally expensive centering algorithms. Although it is not valid at higher frequencies, the low-frequency acoustic center may be a good starting point to improve the performance of higher-frequency optimization techniques.

Defining the acoustic center in terms of the location of an equivalent point source can become problematic in some situations, despite the concept's simplicity and common effectiveness. The replacement of an extended source with an equivalent point source requires first that $ka \ll 1$ and second that the far-field source radiation is omnidirectional [54]. These conditions highlight certain definitional weaknesses. To begin with, because many sources produce complicated directional patterns at higher frequencies, replacing their respective pressure fields with a single equivalent point source is equivocal for broad bandwidths. Indeed, Jacobsen et al. showed that different definitions stemming from the monopolar assumption of $1/r$ decay and constant-phase wavefronts led to conflicting acoustic centers at higher frequencies [49]. More recent centerings of higher-frequency musical instrument directivities have likewise given inconsistent results for the same sources when employing different objective functions [27–29].

Furthermore, even at low frequencies, some sources do not radiate omnidirectionally in the far field. For example, Weinreich's "sound hole sum rule," developed during his violin directivity studies, showed that sources with sound holes or ports connecting an interior cavity to the exterior domain may develop intense dipole moments and vanishing monopole moments [83]. These and other directional low-frequency source configurations [62] further limit the centering approach. For Eq. (1.7) to remain valid, one must ostensibly define what type of radiation is sufficiently omnidirectional.

Finally, the center-of-mass-like formulas of Secs. 1.4.6 and 1.5.2 reveal that some source distributions with complex-valued source strengths or surface velocities may lead to complex-valued acoustic centers with ambiguous meanings. A simple example of such a configuration is a loudspeaker with two drivers driven 90° out of phase. Accordingly, the low-frequency acoustic centering developments of this work require careful implementation. Using quasi-arbitrary, real-number-related source strengths and surface velocities kept the acoustic centers real. The experimental results in Sec. 1.6.1 yielded acoustic centers that were also nearly real. However, based on Eq. (1.10), some sources may have undefined low-frequency acoustic centers or centers that are considerably distant from the source body.

Hence, Trott's redefinition of the acoustic center from "an arbitrary center of rotation for determining the farfield directional response" to "the locus of the equivalent point source that yields the same farfield pressure in magnitude and phase in a specified direction" [48] should perhaps apply only as a limiting case for low-frequency radiation from primarily far-field omnidirectional sources. The need remains for a more consistent definition of the acoustic center, applying to all sources and generalizing to all frequencies. In principle, it should reduce to Trott's redefinition and the acoustic center discussed in this work for low frequencies and far-field omnidirectional sources.

1.8 Conclusions

This work has revisited the concept of a low-frequency acoustic source center and set forth a straightforward centering formula based on monopole and dipole moments. Application to the sphere produced a simple closed-form solution for the acoustic center of a quasi-generally vibrating spherical source. Spherical harmonic expansions of pressure fields from quasi-arbitrary source distributions also allow the determination of their acoustic centers, and center-of-mass-like formulas yield insights into the center locations for many source configurations.

The concept of an acoustic center corresponding to a single point source limits the method for some distributed sources because it precludes application to higher frequencies or sources with vanishing monopole moments. Future research could address this problem and clarify the meaning of the acoustic center for all sources and frequencies. It could also apply centering techniques to other theoretical or measured sources to produce additional insights. The authors encourage further work in these areas.

Chapter 2

Acoustic Centering Using Acoustical Holography

This chapter demonstrates that the magnitude of a source's far-field directivity pattern is invariant to source translation. This fundamental result allows far-field propagation to replace acoustic centering algorithms. Knowing a source's far-field magnitude response allows one to determine its acoustic center even at high frequencies and for complex radiation patterns.

2.1 Introduction

Directivities are crucial characteristics of sound sources with applications in auralization [18, 19], room acoustical design [20, 21], microphone placement [14, 15, 17], sound system design [84, 85], source modeling [86–88], and other areas. With the growing availability and usage of directivity data for many sound sources, researchers and practitioners would benefit from increased understanding of concepts and the improved tools for directivity measurements, post-processing, and implementation. This paper addresses this need in two specific areas: radial directivity dependence and acoustic centering via acoustical holography.

A directivity function characterizes a source's spatio-spectral radiation amplitude dependence and has standardized definitions such as “the . . . level . . . as a function of the direction of propagation of the radiated . . . sound . . . at a specified frequency” [41]. Beranek judiciously noted that it also depends upon “a stated distance r ” [10], with radial dependence vanishing only in the source's acoustic and geometric far field. Even though some of the earliest directivity measurements considered radial directivity dependences [3, 35, 89], most researchers and practitioners today employ directional data measured or modeled at constant radii of arbitrary distance as though they are radially independent far-field values, whether the assumption is technically valid or not. The AES56-2008 (r2019) standard formalized 5° and 10° angular resolutions for loudspeaker directivity measurements [33], and recent works have moved toward similar resolutions for live sources, including speech and played musical instruments [1,6]. Consequently, directivities with standardized angular resolutions are becoming more ubiquitous, but their proper usage and correction when they are not acoustically centered or measured in the far field have remained elusive.

Because of radial directivity dependence, the source alignment within a measurement array is significant and becomes particularly germane for measurement radii limitations due, for example, to the size of an anechoic chamber. Ureda [45] found that measurements constrained to the near field of a source have measured angular directivity patterns that change depending on the source's relative location. He then developed a method to determine the “apparent apex” of the source so that directivity measurements performed in the near field would “be representative of farfield performance.” However, in later works, he observed that deviations between the near-field and far-field directivity patterns persisted even with the source at the apparent apex [46]. Horn measurements showed that the measured pattern converged to the far-field directivity with increasing measurement radius, as theoretically anticipated [62]. In another work, Ureda [47] generalized his results from two-dimensional polar plots to three-dimensional directivity balloons. He made several salient observations, including (1) balloons change with measurement radius until converging to the

far-field pattern, (2) apparent apex shifts over frequency, and (3) “distance is more important than point of rotation” in making directivity measurements.

Other researchers developed different ideas about acoustic source centers, with applications outside of directivity measurements including transducer calibration [22–24], sound attenuation [43], and the anechoic properties of rooms [25, 26]. Trott [48] argued that a more specific definition of the acoustic center is the “locus of the point source that yields the same far-field pressure in magnitude and phase in a specified direction” rather than “an arbitrary center of rotation for determining the far-field directional response in terms of sound pressure magnitude.”

Indeed, most standardized definitions of the acoustic center, such as “the position of the virtual point source from which sound pressure varies inversely as distance” [41] or “the point from which ... spherical wavefronts ... appear to diverge” [42] seem to be grounded, as mentioned by Jacobsen et al., in the “idea of replacing a real, extended source by an equivalent point source” [49]. Determining the position of this equivalent point source is, they argued, “deceptively simple,” as different approaches do not give consistent results. Their analysis reviewed many techniques used in the literature to compute the acoustic center. The first, following the works of Cox and Rasmussen [50, 51], requires an analytical expression of the sound field to determine the equivalent source strength, from which one can fit the equivalent point source location. The second approach follows the standardized practice of fitting a measured or theoretical $1/r$ decay curve [52]. Other phase-based approaches considered uses of phase shift [48, 53], group delay [22], or matching wavefronts [23] to localize the acoustic center. However, Jacobsen et al. showed that these definitions could give markedly different acoustic center locations even for the *same* theoretical source, such as a pulsating sphere or a point source on a sphere.

Instead of using the approaches reviewed by Jacobsen et al., Vanderkooy and Henwood [54, 55] justified the location of an equivalent point source by exploiting the point about which one takes a multipole expansion of the Kirchhoff Helmholtz Integral Theorem (KHIT) to remove the dipole

moment. Assuming the higher-order (e.g., quadrupole) terms are negligible, only the monopole moment subsequently remains. Based on this concept, the authors developed a fitting procedure employing the measured pressure at two points and validated the concept with both numerical and experimental results, confirming many of the empirical results shown by Ureda. The outcomes included significant improvements in predicting the expected far-field behaviors from near-field measurements through proper source alignments. Vanderkooy and Henwood also showed that the far-field pattern requires sufficient radial measurement distance even with proper source alignment. However, because a multipole expansion converges rapidly when the acoustic wavelength is larger than the source dimensions [62], they noted that the approach is limited to low frequencies (up to around 200 Hz for loudspeakers). The technique only works for sources containing a monopole moment, although they contemplated a conceptual extension to dipole-like sources.

Other approaches have attempted to generalize the essence of Vanderkooy and Henwood's work to higher frequencies. Instead of using a multipole expansion, Deboy employed a spherical harmonic expansion as part of the Helmholtz equation exterior solution, which converges at all frequencies and allows theoretical extrapolation of the far-field pattern [27]. Because the low-degree terms of the spherical harmonic expansion correspond to multipole moments [59,61], Deboy defined the acoustic center as the expansion origin leading to "higher order components becom[ing] small." Unlike Vanderkooy's closed-form solution for the acoustic center, this approach required expansions about different origins and minimizing an objective function that penalized higher-degree terms through a weighted inner product. Deboy used the technique to center the simulated directivities of a theoretical monopole and dipole source. He also showed that the objective functions of measured musical instrument directivities tended to have well-defined global minima up to around 1 kHz. However, the low sampling density used in the spherical directivity measurements (64 samples compared to the AES standard's 2,522 samples) led to spatial aliasing limitations that did not allow validation of the objective function applied to complex sources at higher frequencies.

Ben Hagai et al. studied the same objective function proposed by Deboy more rigorously, plus four other optimization criteria applied to spherical harmonic expansions to define the acoustic center [28]. One criterion involved maximizing the power of the degree-zero term, which, because it corresponds to the monopole moment, is analogous to Vanderkooy's approach. Nevertheless, because the study's array employed only 32 sampling positions, the results for measured data were even more limited than those produced by Deboy; the authors noted that they achieved consistent results only up to around 400 Hz.

Besides such expansion-based techniques, another acoustic centering approach involved algorithmic searches for the location that minimize the tangential components of the acoustic intensity [44]. Yet other methods have attempted, through various means, to exploit phase differences over the sphere to localize the acoustic center [27, 29, 90].

While these past techniques are plausible for source centering at low and intermediate frequencies, they are not robust at all frequencies. Their lack of robustness results partly from underlying assumptions about acoustic sources that do not generalize to all frequencies. For example, Vanderkooy and Henwood's technique applies only to sources whose multipole expansions converge within a few terms. Methods that minimize energy in the pressure expansion coefficients based on spherical harmonics likewise involve limitations because low-degree energy assumptions are not valid for all sources at arbitrary frequencies. Similarly, although phase-based approaches may converge at higher frequencies, they generally require phase uniformity or symmetry, which limits their generalization [29].

In order to overcome these and other disadvantages, this work explores the effects of source translations on far-field directivities. Theoretical results confirm that the far-field magnitude patterns of both centered and translated directivities are equivalent. Consequently, numerical far-field propagation can replace source-centering algorithms for many practical applications. The work accordingly presents a source-centering method based on far-field directivity patterns. Because all

sources have fixed-magnitude far-field patterns at any specified frequency, the technique applies to arbitrary sources and frequencies. Theoretical models and measurements provide methodological validations. Experiments show that the algorithm performs correct centering for complex sources at high frequencies, although adequate sampling is critical to minimize spatial aliasing.

2.2 Theory

2.2.1 Far-field Nature of Radiating Sources

Consider a source with a defining boundary S radiating into an acoustic domain Ω as depicted in Fig. 2.1. If a spherical surface of radius $r = a$ entirely encloses the boundary, the unique solution to the Helmholtz equation for the spherical exterior domain, indicated here as $\Omega_a \subset \Omega$, is [59]

$$p(r, \theta, \phi, k) = \sum_{n=0}^{\infty} \sum_{m=-n}^n c_n^m(k) h_n^{(2)}(kr) Y_n^m(\theta, \phi), \quad r \geq a, \quad (2.1)$$

where k is the acoustic wavenumber, $c_n^m(k)$ are the frequency-dependent expansion coefficients, $h_n^{(2)}$ are the spherical Hankel functions of the second kind of order n (for outward-going waves with $e^{i\omega t}$ time dependence), i is the imaginary unit, and Y_n^m are the normalized spherical harmonics of degree n and order m . [70] The pressure expansion coefficients $c_n^m(k)$ follow by exploiting the orthogonality of the spherical harmonics on the $r = a$ boundary, such that

$$c_n^m(k) = \frac{1}{h_n^{(2)}(ka)} \int_0^{2\pi} \int_0^{\pi} p(a, \theta, \phi, k) Y_n^{m*}(\theta, \phi) \sin \theta d\theta d\phi, \quad (2.2)$$

where $*$ denotes complex conjugation.

It is critical to note here that there is no requirement placed on the location of the source defined by the boundary S , provided that the spherical surface fully encloses it. Equation (2.1) consequently remains valid even if the coordinate system origin and the acoustic source center (if it exists) are not aligned. The expansion coefficients may result from numerical integration of Eq. (2.2) or a

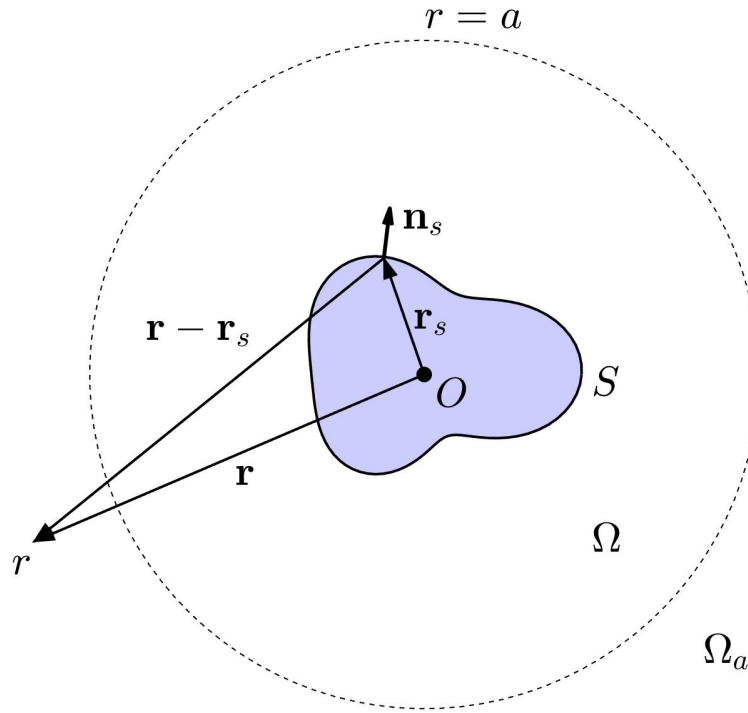


Figure 2.1 A depiction of an acoustic source contained within a spherical Gaussian surface of radius $r = a$. Here, S denotes the body's boundary and Ω denotes the acoustic fluid domain. The subspace Ω_a represents the region where the Helmholtz equation solution [Eq. (2.1)] is valid, as the spherical surface encloses all nonhomogenous terms.

least-squares approach [77,78]. Once known, these coefficients not only provide the unique solution on Ω_a but can also yield other field variables, including the particle velocity, time-averaged intensity, and time-averaged sound power. This extrapolation of field variables for $r > a$ corresponds to acoustical holography [59]. Near-field acoustical holography and other inverse methods allow extrapolation of field variables for $r < a$, although these techniques are limited due to their inherent nonuniqueness [59].

Many practical source directivity applications require only the far-field pressure, where r satisfies $kr \gg 1$ or $r \gg \lambda/2\pi$ (the acoustic far field) and $r \gg d$ (the geometric far field), with d representing the source's maximum spatial extent from the origin [62]. In the acoustic far field, the large-argument spherical Hankel function approximation allows separation of the radial portion

from the series expansion appearing in Eq. (2.1), such that

$$p(r, \theta, \phi, k) \approx \frac{e^{-ikr}}{r} \sum_{n=0}^{\infty} \sum_{m=-n}^n c_n^m(k) k^{-1} i^{n+1} Y_n^m(\theta, \phi), \quad kr \gg 1. \quad (2.3)$$

The form of this expression suggests several well-known features of spherical waves in the far field. First, the wave takes on spherical spreading, such that the sound pressure varies inversely with distance, thus being congruous with one common basis for determining the acoustic center. However, unlike a spherical wave produced by a simple source, the complex pressure has an angular dependence that is independent of the radial observation distance r . Additionally, while a simple source has constant phase across the spherical surface, the standard definition of a wavefront [41], the pressure described by Eq. (2.3) has no restriction on its phase. An unnormalized far-field directivity function $\tilde{D}_{ff}^H(\theta, \phi, k)$ characterizes the directivity as

$$\tilde{D}_{ff}^H(\theta, \phi, k) = \sum_{n=0}^{\infty} \sum_{m=-n}^n c_n^m(k) k^{-1} i^{n+1} Y_n^m(\theta, \phi), \quad (2.4)$$

so that the far-field pressure becomes

$$p_{ff}(r, \theta, \phi, k) = \frac{e^{-ikr}}{r} \tilde{D}_{ff}^H(\theta, \phi, k). \quad (2.5)$$

2.2.2 Effect of Source Translation on Far-field Directivity

To better explain the effects of misalignments between the coordinate reference frame origin and the acoustic center, this section investigates the effect of source translation through the Kirchhoff-Helmholtz integral theorem (KHIT) and the first directivity product theorem.

KHIT

The KHIT with no volume source terms describes the acoustic pressure within the exterior domain Ω in terms of the pressure $p_s(\mathbf{r}_s)$ and normal particle velocity $u_s(\mathbf{r}_s)$ on the domain boundary $\partial\Omega$

(see Fig. 2.1): [62]

$$p(\mathbf{r}) = \iint_S \left[p_s(\mathbf{r}_s) \frac{\partial}{\partial n_s} G(\mathbf{r}, \mathbf{r}_s) + iz_0 k u_s(\mathbf{r}_s) G(\mathbf{r}, \mathbf{r}_s) \right] dS, \quad (2.6)$$

where $z_0 = \rho_0 c$ is the characteristic specific acoustic impedance of the fluid, the surface normal \mathbf{n} points into Ω , and

$$G(\mathbf{r}, \mathbf{r}_s) = \frac{e^{-ik|\mathbf{r}-\mathbf{r}_s|}}{4\pi|\mathbf{r}-\mathbf{r}_s|} \quad (2.7)$$

is the free-space Green's function. It is important to note that while Eq. (2.1) is valid only over Ω_a , the KHIT is valid over the entire acoustic domain Ω .

In the acoustic and geometric far-field, application of the law of cosines and a subsequent binomial approximation allows simplification as

$$|\mathbf{r} - \mathbf{r}_s| = (r^2 + r_s^2 - 2rr_s \hat{\mathbf{r}}_s \cdot \hat{\mathbf{r}})^{1/2} \quad (2.8)$$

$$\approx r - \mathbf{r}_s \cdot \hat{\mathbf{r}}, \quad (2.9)$$

where $\hat{\mathbf{r}}$ is the unit vector in the directions of \mathbf{r} . Substituting this simplified form into the Green's function yields its far-field approximation

$$G_{ff}(\mathbf{r}, \mathbf{r}_s) \approx \frac{e^{-ikr}}{4\pi r} e^{ik\mathbf{r}_s \cdot \hat{\mathbf{r}}} \quad (2.10)$$

where the angular dependence in the denominator has been suppressed. The far-field pressure consequently becomes

$$p_{ff}(\mathbf{r}) \approx \frac{e^{-ikr}}{4\pi r} \iint_S \left[p_s(\mathbf{r}_s) \frac{\partial}{\partial n_s} e^{ik\mathbf{r}_s \cdot \hat{\mathbf{r}}} + iz_0 k u_s(\mathbf{r}_s) e^{ik\mathbf{r}_s \cdot \hat{\mathbf{r}}} \right] dS. \quad (2.11)$$

This result also confirms that the far-field pressure is the product of a spherical wave with a radially independent directivity function, since $\hat{\mathbf{r}}$ only depends on the angular direction (θ, ϕ) . The unnormalized, far-field directivity function produced from the KHIT is then

$$\tilde{D}_{ff}^{KHIT}(\theta, \phi, k) = \frac{1}{4\pi} \iint_S \left[p_s(\mathbf{r}_s) \frac{\partial}{\partial n_s} e^{ik\mathbf{r}_s \cdot \hat{\mathbf{r}}} + iz_0 k u_s(\mathbf{r}_s) e^{ik\mathbf{r}_s \cdot \hat{\mathbf{r}}} \right] dS. \quad (2.12)$$

Two approaches enable the consideration of source translations. The first is to shift the actual source location by \mathbf{r}'' and the second is to shift the observation position by $-\mathbf{r}''$. This section contains the derivation for the former.

As suggested by Fig. 2.2, if one shifts the source by \mathbf{r}'' in the same coordinate frame,

$$\mathbf{r}'_s = \mathbf{r}_s + \mathbf{r}'' . \quad (2.13)$$

The resulting pressure p' again follows from the KHIT, except with the integration performed over the shifted boundary S' :

$$p'(\mathbf{r}) = \iint_{S'} \left[p_s(\mathbf{r}'_s) \frac{\partial}{\partial n'_s} G(\mathbf{r}, \mathbf{r}'_s) + iz_0 k u_s(\mathbf{r}'_s) G(\mathbf{r}, \mathbf{r}'_s) \right] dS' . \quad (2.14)$$

With the new geometric far-field condition $r \gg d + r''$,

$$|\mathbf{r} - \mathbf{r}'_s| \approx r - \mathbf{r}'_s \cdot \hat{\mathbf{r}} \quad (2.15)$$

and the far-field pressure becomes

$$p'_{ff}(\mathbf{r}) \approx \frac{e^{-ikr}}{4\pi r} \iint_{S'} \left[p_s(\mathbf{r}'_s) \frac{\partial}{\partial n'_s} e^{ik\mathbf{r}'_s \cdot \hat{\mathbf{r}}} + iz_0 k u_s(\mathbf{r}'_s) e^{ik\mathbf{r}'_s \cdot \hat{\mathbf{r}}} \right] dS' . \quad (2.16)$$

This result is the same as that given in Eq. (2.11) but integrated over S' . Considering that $\mathbf{r}'_s = \mathbf{r}_s + \mathbf{r}''$, one may write the result as

$$p'_{ff}(\mathbf{r}) = \frac{e^{-ikr}}{4\pi r} e^{ik\hat{\mathbf{r}}'' \cdot \mathbf{r}} \iint_{S'} \left[p_s(\mathbf{r}'_s) \frac{\partial}{\partial n'_s} e^{ik\mathbf{r}_s \cdot \hat{\mathbf{r}}} + iz_0 k u_s(\mathbf{r}'_s) e^{ik\mathbf{r}_s \cdot \hat{\mathbf{r}}} \right] dS' . \quad (2.17)$$

The spatial variable \mathbf{r}'_s in Eq. (2.17) designates the points over the surface S' , whereas \mathbf{r}_s in Eq. (2.11) defines the points over the surface S . Because the surface pressure and normal particle velocity, surface normals, surface differentials, and other properties of the surface integrals are independent of \mathbf{r} and \mathbf{r}'' , the integrals in Eqs. (2.17) and (2.11) must be equal, such that

$$p'_{ff}(\mathbf{r}) = e^{ik\hat{\mathbf{r}}'' \cdot \mathbf{r}} p_{ff}(\mathbf{r}) . \quad (2.18)$$

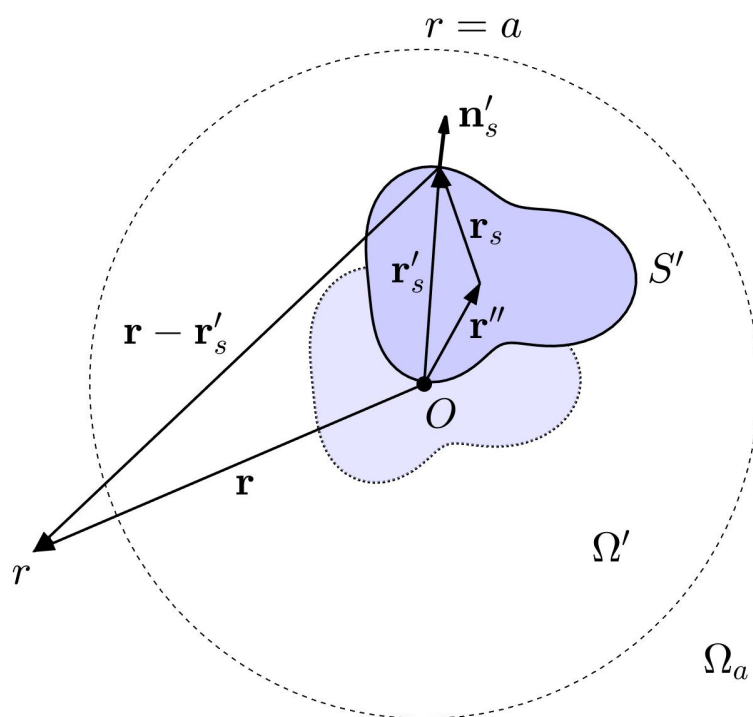


Figure 2.2 A depiction of a translated acoustic source with associated position vectors. The dotted contour suggests the untranslated source position for reference.

First Directivity Product Theorem

The same result follows from a shorter and less rigorous approach employing the first directivity product theorem [82]. Suppose $D_{ff}(\theta, \phi, k)$ is the normalized far-field directivity function of the source. The directivity of the translated source then follows by treating the untranslated source as a single-element array located at \mathbf{r}'' . The first product theorem gives the directivity of the translated source as [10, 59]

$$D'_{ff}(\theta, \phi, k) \propto G(\mathbf{r}, \mathbf{r}'') D_{ff}(\theta, \phi, k). \quad (2.19)$$

Finally, applying the far-field simplifying assumptions for the Green's function yields

$$D'_{ff}(\theta, \phi, k) \propto \frac{e^{-ik(r-\mathbf{r}'' \cdot \hat{\mathbf{r}})}}{4\pi r} D_{ff}(\theta, \phi, k) \quad (2.20)$$

$$\propto \frac{e^{-ikr}}{4\pi r} e^{ik\mathbf{r}'' \cdot \hat{\mathbf{r}}} D_{ff}(\theta, \phi, k) \quad (2.21)$$

$$(2.22)$$

and

$$D'_{ff}(\theta, \phi, k) = e^{ik\mathbf{r}'' \cdot \hat{\mathbf{r}}} D_{ff}(\theta, \phi, k), \quad (2.23)$$

where the last equation follows by ignoring any separable radial dependence. Additionally, the relation $|e^{-ik\mathbf{r}'' \cdot \hat{\mathbf{r}}}| = 1$ justifies the equality between the left and right-hand sides of the final equation since D_{ff} and D'_{ff} are both normalized.

Effect on Magnitude and Phase

Both approaches demonstrate that the far-field magnitude directivity patterns of translated and untranslated sources are equal:

$$|D'_{ff}(\theta, \phi, k)| = |D_{ff}(\theta, \phi, k)|. \quad (2.24)$$

This result also follows by considering a measurement array whose radius approaches infinity. Any small shift $r'' \ll r$ becomes negligible when considering the magnitude of the far-field pressure.

Section 2.4 exploits this critical detail in the development of an acoustic centering algorithm. However, a phase shift remains between the original and translated patterns as

$$\angle D'_{ff}(\theta, \phi, k) = k\mathbf{r}'' \cdot \hat{\mathbf{r}} + \angle D_{ff}(\theta, \phi, k)', \quad (2.25)$$

which is associated with the time delay caused by the source translation. Cox arrived at a similar result when he suggested that shifting a simple source by r'' along the z-axis would lead to a phase shift of $kr'' \cos \theta$ [50]. Thus, with a knowledge of the far-field directivity magnitude and phase, one may determine the far-field directivity after a source translation by simply modifying the directivity phase according to Eq. (2.25). Of course, obtaining the far-field directivity requires knowledge of the the source's far-field pressure, which results from measurements at a large enough radius or numerical propagation of the pressure to the far field using Eq. (6.44).

Figure 2.3 illustrates these directivity concepts for a theoretical point source distribution comprising 20 sources with equal complex amplitudes at dodecahedral vertices and a circumradius of $a_d = 0.2$ m centered about the origin. A radius $a = 1$ m array with 5° polar and azimuthal dual-equiangular spacing measured a 1.5 kHz ($\lambda \approx 0.2$ m) radiation from the distribution then repeated the measurement after the distribution translated spatially by $\mathbf{r}'' = (0.7, 0.0, 0.0)$ m, a significant shift relative to the array size. The angular resolution and degree $N = 35$ expansion derived from a Chebyshev quadrature rule [78] mitigated spatial aliasing effects. Equation (2.1) then propagated the measured pressure to surfaces of constant radii $r = 2$ and $r = 10$ m relative to the geometric array center. Finally, Eq. (2.4) produced the far-field directivity patterns $D_{ff}(\theta, \phi, k)$ for comparison.

The translated distribution's directivity pattern at the measurement radius initially appears much different than the untranslated distribution's pattern. However, following propagation to the far field, both source configurations yield the same magnitude directivities. The numerical propagation also illustrates properties of the acoustic and geometric far fields. For example, the spatial extent of the translated distribution is $d = 0.9$ m, meaning the geometric far-field requires roughly $r > 9$ m

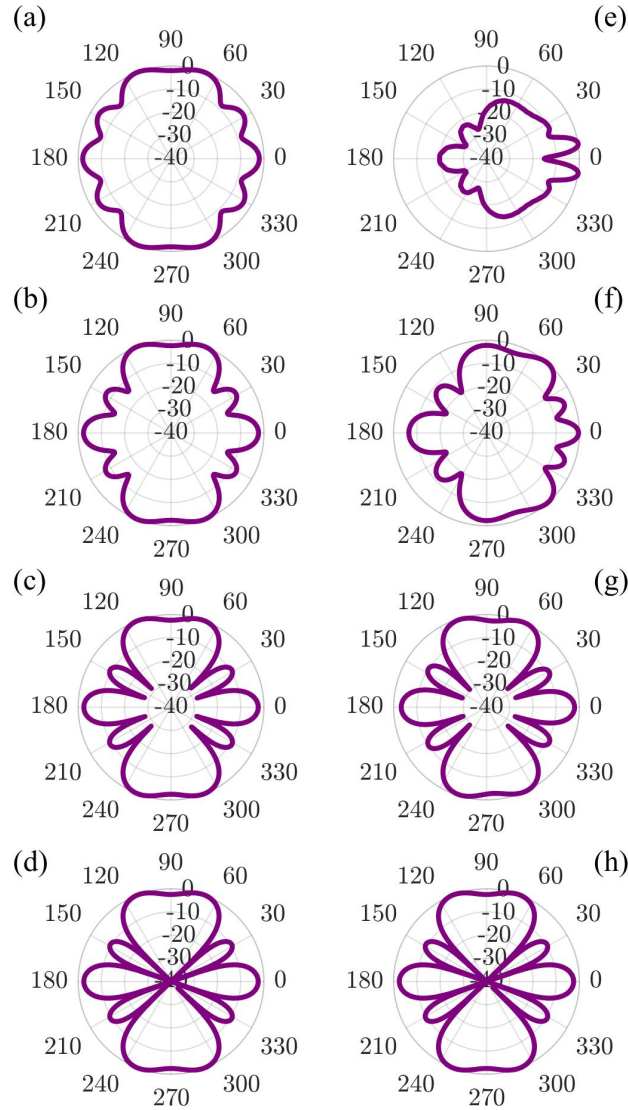


Figure 2.3 Directivity patterns of a centered and translated 20 point-source dodecahedral distribution at varying radial measurement distances compared to the far-field patterns. Centered source distribution at (a) measurement radius $r = 1$ m, (b) propagated to $r = 2$ m, (c) propagated to $r = 10$ m, and (d) far-field pattern. Translated source distribution centered about $\mathbf{r}'' = (0.7, 0.0, 0.0)$ m at (e) measurement radius $r = 1$ m, (f) propagated to $r = 2$ m, (g) propagated to $r = 10$ m, and (h) far-field pattern.

propagation. Both the untranslated and translated source radiation patterns converge to the same form at this intermediate distance and more closely resemble the far-field pattern than the patterns assessed at $r = 1$ m and $r = 2$ m.

Observing the centered directivity pattern's evolution over radial distance makes some acoustic near-field effects apparent. Its interference nulls are roughly 10 dB down from the maximum at the measurement radius but deepen with successively increasing evaluation distances until they become over 40 dB down in the far field. Distance-based evolutions illustrate that adequate radial distance is essential to overcome near-field effects even when a source is acoustically centered. This result highlights a deficiency in methods that only perform acoustic centering at the array measurement surface rather than properly propagating the pressure to the far field. Reference 82 includes other results for a monopole, dipole, and quadrupole.

Effect on Spatial Aliasing

While the far-field magnitude patterns of the acoustically centered and translated sources are equivalent, the phase shift introduced by misalignment can become problematic when considering spatial aliasing. In addition to resolving differences between measured near and far-field directivity patterns [27, 28], reducing spatial aliasing effects was a key motivation for recent works on source-centering. Shabtai et al. explored the undesirable effects of phase shifts due to source displacements at measurement radii [29]. However, without using far-field propagation, they did not account for the specific phase relationship governed by Eq. (2.25). This section reviews previously reported sampling and spatial aliasing concepts and considers how they apply to various sampling configurations.

The spherical Hankel function magnitude exhibits exponential-like decay for argument $kr < n$ and $1/r$ spherical spreading for $kr > n$. Consequently, for a source of greatest radial extent d and assumed uniform (white) energy in $c_n^m(k)$ for expansion at $r = d$, one anticipates that only terms with $n < kd$ will survive to the far field instead of decaying rapidly [59]. Thus,

$$N \approx kd \tag{2.26}$$

provides a rough approximation of the number of expansion terms required to represent the radiation of an acoustic source [83].

For a displacement of vector magnitude r'' , the required number of expansion terms increases by roughly [28, 91]

$$\Delta N \approx kr'' . \quad (2.27)$$

This result is understandable from Eq. (2.26) because a displacement r'' essentially increases the spatial source extent so that the required number of expansion terms becomes $N \approx k(d + r'')$. The far-field phase relation in Eq. (2.25) also confirms this result. Because the phase-shift factor $\exp(ik\hat{\mathbf{r}} \cdot \mathbf{r}'')$ in Eq. (2.23) has a form similar to that of a plane wave, one may equate relevant terms to show that the equivalent plane wave requires approximately $N_{pw} = kr''$ terms for accurate representation [59, 77]. Thus, if one approximates the original directivity by an N -degree polynomial, multiplication by an N_{pw} -degree polynomial also results in the ΔN given by Eq. (2.27).

Numerical experiments demonstrate the spatial aliasing effects of monopole translations on four $a = 1.0$ m radius measurement arrays with 32, 64, 614 (AES 10°), and 2,552 (AES 5°) sampling points each. The 32 and 64 sampling-point measurement arrays employ quasi-uniform sampling densities whereas the 614 and 2,552 sampling-point measurement arrays employ dual equiangular sampling. [33, 77] The point source location varies from $\mathbf{r}'' = (0.0, 0.0, 0.0)$ m to $\mathbf{r}'' = (0.8, 0.0, 0.0)$ m as it radiates at wavenumber $k = 50.0 \text{ m}^{-1}$ (2.7 kHz). After the arrays sample the pressure field, Eq. (6.44) numerically propagates the pressure to the far field. Figure 2.4 presents an area-weighted RMS deviation level, L_{AWRMSD} [6], from the anticipated omnidirectional far-field radiation plotted over kr'' . All curves show the same general trend. Initially, the number of sampling positions Q is sufficient to mitigate spatial aliasing errors. However, with sufficient source translation, deviations from omnidirectional behavior increase rapidly. As anticipated, the maximum practicable translation relates to the number of sampling positions; higher-density sampling densities (i.e., larger Q values) permit larger translations before aliasing. Using an arbitrary maximum L_{AWRMSD} value of 1.0 dB,

the 32, 64, 614, and 2,552-point arrays provide reasonable far-field projections up to $kr'' = 3.9$, $kr'' = 6.3$, $kr'' = 16.3$, and $kr'' = 33.7$, respectively. These results agree well with the anticipated maximum expansion degrees for each array [77, 78].

Another important observation follows by noting the increasing L_{AWRMSD} slope for each sampling configuration. Overlaid dotted lines of corresponding colors in Fig. 2.4 suggest this slope for each sampling configuration. Interestingly, as the number of sampling positions increases, the deviation slope successively decreases, suggesting that higher-density sampling configurations are more robust to source translations and their associated aliasing errors. As an initial attempt to explain this behavior, one may consider the necessity of $Q \geq (N + 1)^2$ sampling positions to assess radiation from a source of maximum degree N [77]. With the aid of Eq. (2.27), a source translation \mathbf{r}'' requires an additional $\Delta Q \geq 2(N + 1)\Delta N \gtrsim 2\sqrt{Q}kr''$ positions to minimize spatial aliasing errors. Because the ratio $\Delta Q/Q \gtrsim 2kr''/\sqrt{Q}$ is proportional to $1/\sqrt{Q}$, higher-density sampling is advantageous for measuring displaced sources. For example, if $kr'' = 1$, the AES standard 2,522 sampling positions require only 4% more sampling to remain robust and immune to spatial aliasing. In contrast, a 32-point array requires 35% more sampling. Lower-density sampling schemes thus appear to be more susceptible to spatial aliasing effects from source misalignments than higher-density schemes. This weakness derives not only from them accurately assessing only lower-degree (smaller N) source radiation to begin with but also because, for a given source displacement, the equivalent shift ΔN in the required number of expansion terms results in a disproportionate required number of new sampling positions. A more rigorous analysis of these effects would be worthwhile, but it is beyond the scope of the present work.

2.2.3 Effect of Small Translations

Another interesting case arises when a translated source remains relatively close to the geometric array center, such that $r'' \ll a$. If the array is in the acoustic and geometric far field of the centered

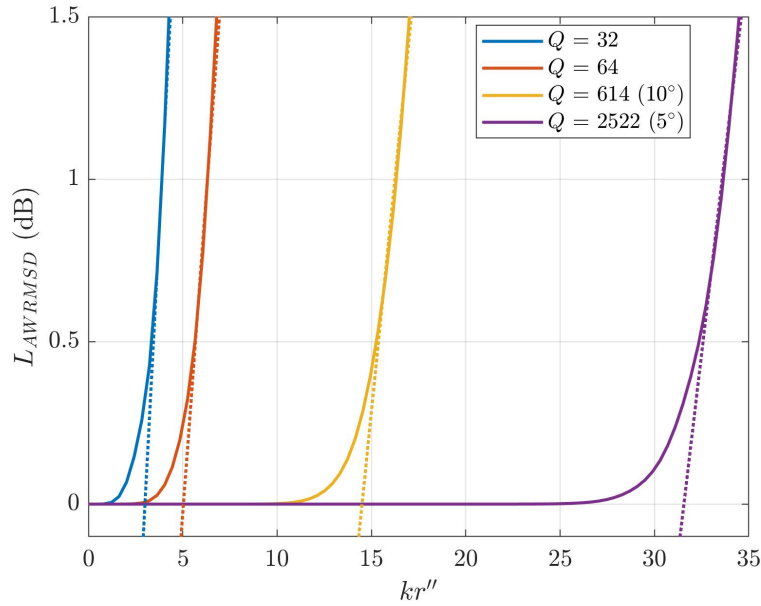


Figure 2.4 Directivity L_{AWRMSD} from anticipated far-field omnidirectionality based on propagated far-field pressures from a displaced monopole as assessed by arrays with varying numbers of sampling positions. The solid lines show the actual L_{AWRMSD} values, whereas the dotted lines of similar colors help visualize the diverging slopes.

source so that $a \gg \lambda/2\pi$ and $a \gg d$, it remains in the far field of the translated source because it still satisfies the required conditions $a \gg \lambda/2\pi + r''$ and $a \gg d + r''$. Thus, the magnitude directivity patterns of the centered and translated sources will be nearly equivalent. This result is significant for the experimentalist because it affirms that if one places the acoustic center sufficiently close to the center of a large measurement array, the directivity magnitude distortions are only slight.

Figure 2.5 illustrates this effect by comparing the simulated directivities of a monopole, dipole, and lateral quadrupole with varying displacements no greater than $r'' = 0.1a$. For all sources, even when the displacement reached $0.1a$, the maximum beam pattern error was less than 2 dB. The much more significant variations between measured and far-field patterns shown in Fig. 2.3 resulted from substantial source displacements relative to the array size, which a careful experimentalist can often avoid.

Previous works presented conflicting results for these effects. For example, while Pollow et al. stated that source translations have a greater effect on phases than magnitude patterns for typical measurements [90], Ben Hagai et al.'s experimental results showed dramatic changes in directional patterns of a trumpet for translations that were relatively small compared to the array radius [28]. However, most of the published directivities do not exhibit known features of trumpet radiation, including omnidirectional radiation at low frequencies, quasi-symmetry about the median plane, and a strong region of radiation in front of the bell at higher frequencies. This suggests that aliasing errors, asymmetries induced by the sampling positions [6], or other processing issues may have degraded the initial results, leading to further errors after translation. Later works tended to agree with the theoretical assertions; Shabtai and Vorländer's translated results only showed significant differences in phase rather than magnitude [29].

The results of this section have highlighted several significant trends related to the effects of source translations on directivity patterns. First, in the geometric and acoustic far field of a source, the magnitude directivity pattern is invariant to source translation. This effect implies that if the measurement array radius is sufficiently large and one positions the acoustic center near the array's center, deviations in magnitude patterns due to misalignments are small. Sound pressure propagation using Eq. (6.44) allows one to obtain the desired far-field magnitude pattern for smaller measurement radii. However, source displacements affect the directivity phase, which becomes problematic as the altered phase can increase the number of expansion terms required to represent the source adequately. This effect subsequently reduces the maximum usable frequency for a given sampling configuration.

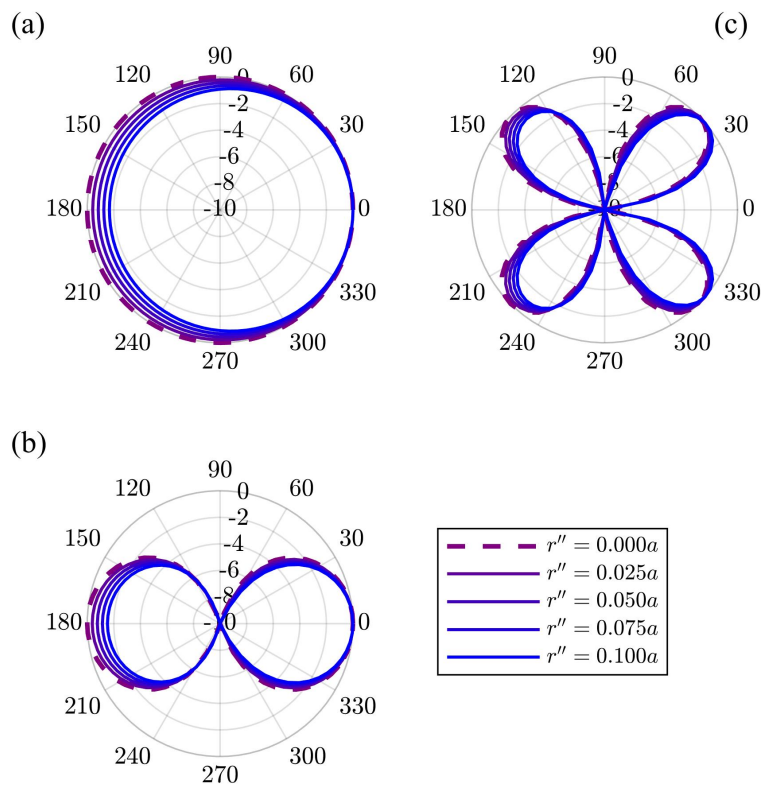


Figure 2.5 Changes in directivity patterns due to small differences between the acoustic center and the geometric center of the array for a (a) monopole, (b) dipole, and (c) lateral quadrupole. The polar plots are on a 10 dB scale to allow visualization of the small changes.

2.3 Acoustic Center Revisited

The KHIT and general exterior problem do not require an acoustic center to construct the unique solution to the Helmholtz equation. Furthermore, because different approaches to assessing acoustic centers may yield different locations for the same source [49], the definition, necessity, and benefit of an acoustic center may depend upon the application. For example, when considering the anechoic properties of a test room [26], one may find the definition of an acoustic center based on $1/r$ decay to be most beneficial. However, for directivities and their measurements, it seems most beneficial to define the acoustic center as follows:

The acoustic source center is the origin of the coordinate reference frame from which the observed angularly dependent pressure converges to its magnitude far-field pattern with the smallest observation distance r .

The examples of displaced sources in Fig. 2.3 and in Ref. 82 help motivate this interpretation. While the figures show that the centered and translated sources eventually yield the same far-field directivity pattern, the untranslated source patterns converge more rapidly, i.e., with the smallest radial propagation distance.

A converged far-field pattern allows one to safely ignore radial directivity dependence and employ a fixed directivity function dependent only upon the angular coordinates. A reference frame closest to the source that allows one to ignore radial directivity changes has clear advantages for computational applications. For example, Eq. (2.5) provides a more computationally efficient solution than the spherical harmonic expansion in Eq. (2.1) for wave-based simulations of the acoustic pressure. The benefit is especially opportune for sources generating complex radiation patterns that require many expansion coefficients. For ray-based methods that employ only far-field magnitude patterns, neglected near-field effects also become less significant.

As an elementary example, consider a monopole radiating at $k = 2 \text{ m}^{-1}$, translated to $\mathbf{r}'' = (0.5, 0, 0) \text{ m}$ so that $kr'' = 1$, and measured by an $a = 1.0 \text{ m}$ array. While its omnidirectional far-field magnitude pattern results from Eq. (2.1) without the need for centering, it is not until a propagation of distance of $r_{3dB} = 3.0 \text{ m}$ that Eq. (2.1) produces less than 3 dB deviations from the results of Eq. (2.5) and a distance of $r_{1dB} = 8.6 \text{ m}$ that it produces less than 1 dB deviations. If the monopole shifts closer to the origin, these distances become smaller until they reduce to $r_{3dB} = r_{1dB} = 0 \text{ m}$ when the monopole falls exactly at the origin.

The proposed definition of the acoustic center reduces to Trott's earlier redefinition for the case of an omnidirectional source at low frequencies. As discussed by Vanderkooy [54], such a source may be replaced by an equivalent point source located at its acoustic center. Then, by the arguments of the previous paragraph, the coordinate reference frame from which the observed pressure converges to its omnidirectional far-field pattern with the smallest observation distance r is the frame whose origin is the location of this equivalent point source. Importantly, this results suggests that the proposed definition should agree well with previous works at low frequencies.

2.4 Acoustic Centering Algorithm

The acoustic center definition in Sec. 2.3 serves as the basis for an objective function whose minimum occurs at the acoustic center. To better envision the function's behavior, consider the directivities assessed by spheres of *fixed* radius R , whose centers fall at varying origins \mathbf{r}'' . The green dotted, blue dashed, and purple dash-dotted circles in Fig. 2.6(a) suggest the cross-sections of three such candidate spheres for the case of a monopole displaced from the origin on the transverse plane. A red dot indicates the monopole's location and the solid black circle indicates the original measurement surface. Additionally, the colored \times symbols indicate each sphere's respective origin \mathbf{r}'' . Figure 2.6(b) shows the monopole's measured directivity on the array surface, with balloon

radius and color both indicating level on a relative logarithmic scale. Because of the source placement, the measured directivity pattern differs from the anticipated omnidirectional radiation pattern.

Figures 2.6(c) through 2.6(e) show the pressure evaluated on each of the candidate spheres, with the encircling colored line indicating the corresponding cross-section in Fig. 2.6(a). In practice, these directivities result by first measuring the pressure on the original sampling surface at $r = a$ and then evaluating the pressure on the translated spheres of radius R via acoustical holography. While the choice of the parameter R is somewhat arbitrary, to assess all translations within a maximal translation r''_m , R must be greater than $a + r''_m$ to ensure that the spherical evaluation surfaces remain in Ω_a , depicted as the gray region in Fig. 2.6(a). This requirement is necessary so that Eq. (2.1) remains valid. Additionally, R should be large enough to avoid near-field effects but not so large that deviations between evaluated directivities and the far-field pattern become negligible. Nevertheless, even for a choice of R an order of magnitude larger than a , it was found that enough differences between directivity patterns remained to detect the acoustic center.

As long as R is not in the far field, differences in directivity patterns on each sphere vary. Because all evaluated directivities result from the same spherical observation radius, the acoustic center definition implies that one reference frame will minimize deviations relative to the far-field directivity produced by Eq. (6.44). This finding consequently implies that one frame converges fastest to the far-field directivity. For the monopole case, only when the reference frame's center coincides with the source's acoustic center does the desired far-field pattern appear omnidirectional as in Fig. 2.6(d).

A deviation function similar to L_{AWRMSD} is adaptable as the objective function. In particular

$$J(\mathbf{r}''|R) = \frac{1}{4\pi} \int_0^\pi \int_0^{2\pi} (|D(r', \theta', \phi')| - |D_{ff}(\theta, \phi)|)^2 \sin \theta d\theta d\phi, \quad (2.28)$$

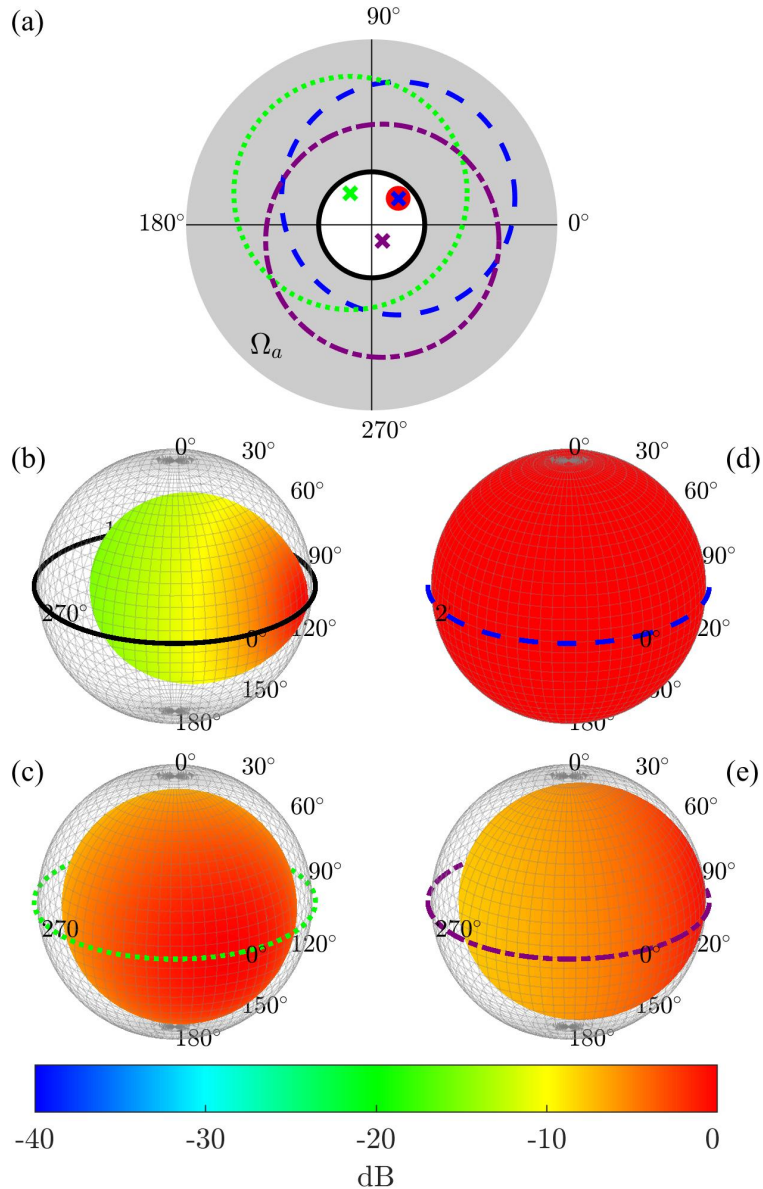


Figure 2.6 An illustration motivating the centering algorithm for a monopole source. (a) Diagram of source location (red dot), original sampling sphere (black circle), and extrapolated sampling spheres (green, blue, and purple circles). Directivities evaluated on the (b) original sampling sphere and the extrapolated (c) green-dotted sphere, (d) blue-dashed sphere, and (e) purple dash-dot sphere.

where $D(r', \theta', \phi')$ is the normalized directivity evaluated on a spherical surface of radius R with a center at \mathbf{r}'' , i.e., the vector

$$\mathbf{R}' = R\hat{\mathbf{r}} + \mathbf{r}'' \quad (2.29)$$

defines the evaluation sphere's surface. The far-field directivity function $D_{ff}(\theta, \phi)$ follows by normalizing Eq. (2.4). The acoustic center \mathbf{r}_c is then

$$\mathbf{r}_c = \underset{\mathbf{r}''}{\operatorname{argmin}} J(\mathbf{r}''|R). \quad (2.30)$$

In practice, numerical integration is necessary to evaluate the integrals in Eq. (2.28).

The acoustic center determined by this objective function is thus the origin of the reference frame with a directivity function evaluated at constant radius R most similar to the far-field directivity function. Similar to the formulations of Jacobsen et al., the acoustic center depends on the observation distance R [49], although with sufficiently large R the acoustic center becomes essentially independent of this parameter. Once the acoustic center is known, one can recompute the expansion coefficients in the new reference frame using the HELS method [75], as shown in Refs. 27 and 29, or by directly translating the expansion coefficients from one frame to another [28, 91]. In either case, it is important to note that the expansion coefficients provide the unique solution to the Helmholtz equation on Ω_a ; they only differ in the definitions of (r, θ, ϕ) when using Eq. (2.1).

2.5 Theoretical Results

2.5.1 Multipoles

For initial consideration, sources with simple geometries and well-defined acoustic centers include a displaced monopole, dipole, longitudinal quadrupole, and lateral quadrupole. For each simulation, the source's center falls at $\mathbf{r}'' = (0.5, 0.5, 0)$ m, and it radiates at 500 Hz ($kr'' \approx 6.4$). An $a = 1$ m

array having 5° resolution in the polar and azimuthal angles measures the radiated field. An $N = 20$ expansion minimizes spatial aliasing effects, and the centering algorithm uses $R = 10$ m.

Figure 2.7 shows the objective function with overlaid contours for each source in the x - y plane. The solid black curve indicates the array radius, and the color of the objective surface indicates its relative level. In all cases, the objective function minimum is the source location and the acoustic source center. At the stated frequency, the objective functions appear convex over the entire cross-section of the sphere. However, the surfaces of constant value do not appear to be quadratic with respect to the spatial coordinates and depend on the source. For example, the monopole shows a spherically-symmetric objective function, whereas the dipole and longitudinal quadrupoles have elongated patterns in the directions of the dipole and quadrupole moments. The lateral quadrupole has a rhombus-like pattern. When centered, the source representations follow in terms of the degree zero, one, and two eigenfunctions [59, 61], so they are low-order sources.

2.5.2 Point Source Distribution

While multipoles represent increasingly higher-order sources, they concentrate at a single point in space. In contrast, a point source distribution approaches the case of a more realistic, distributed source, meaning a centering algorithm's effectiveness for a point source distribution is particularly interesting.

Suppose an $a = 1$ m array having 5° resolution in the polar and azimuthal angles measures the radiated field of a three-monopole distribution at 50 Hz. The sources fall at $\mathbf{r}_c = (0.5, 0.2, 0.0)$ m, $\mathbf{r}_c = (-0.5, 0.2, 0.0)$ m, and $\mathbf{r}_c = (-0.1, -0.3, 0.0)$ m, with the respective source strengths $2.0 \text{ m}^3/\text{s}$, $1.0 \text{ m}^3/\text{s}$, and $1.0 \text{ m}^3/\text{s}$. At low frequencies, the acoustic center follows as $\mathbf{r}_c = (0.150, 0.075, 0.000)$ m from the center-of-mass formula [54].

Figure 2.8 plots several objective function surfaces in the x - y plane based on an $N = 20$ degree pressure expansion. Three functions are from previous works, and one is from the present work.

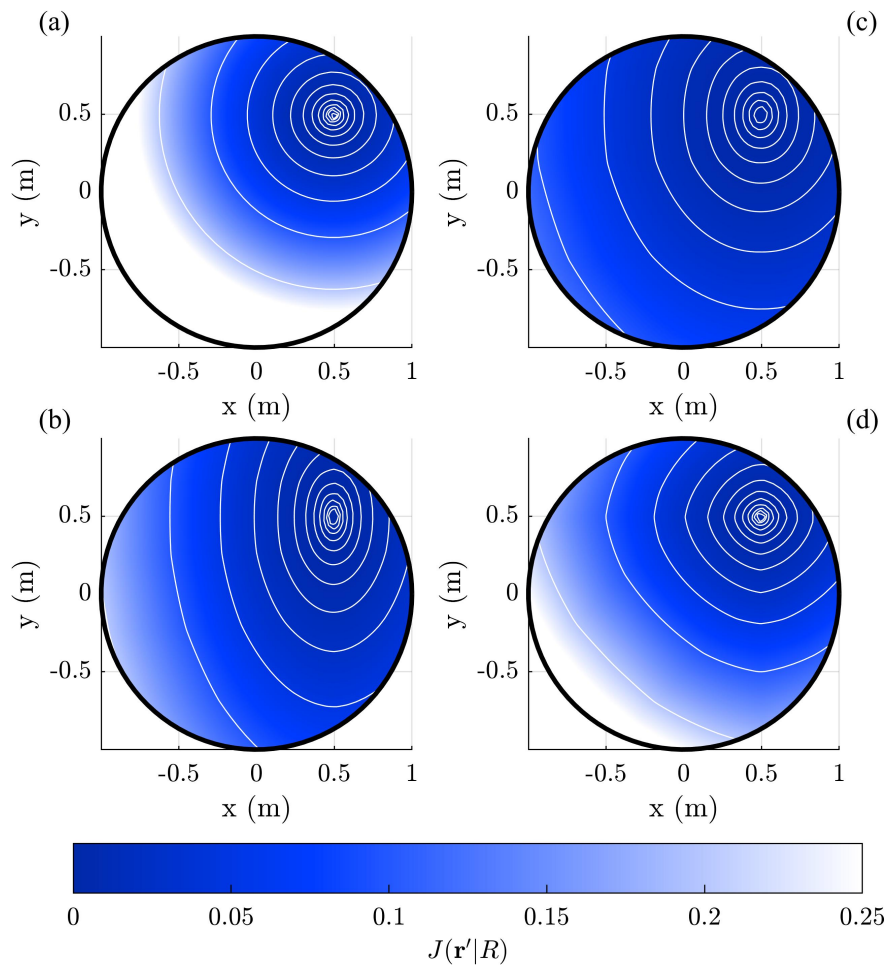


Figure 2.7 Contour plots of the objective function at 500 Hz in the x - y plane for a (a) monopole, (b) dipole, (c) longitudinal quadrupole, and (d) lateral quadrupole displaced to position $\mathbf{r}'' = (0.5, 0.5, 0.0)$ m.

Normalization of all objective functions ensures fair comparisons. Figure 2.8(a) plots J_{ss} , an objective function based on the coherent summation of the complex pressure [see Ref. 27, Eq. (7.1)]. Figure 2.8(b) plots J_{lo} , an objective function that penalizes energy in higher-degree expansion terms [see Ref. 27, Eq. (7.3) and Ref. 28, Eq. (34)]. Fig. 2.8(c) plots J_{ph} , an objective function based on phase contours in the x - y plane [see Ref. 29, Eq. (50)]. Finally, Fig. 2.8(d) plots the objective function proposed in the present work. The three green dots indicate the point source locations, while the red \times indicates the theoretical low-frequency acoustic center. The objective functions remain similarly convex in all cases, and their global minima coincide with the low-frequency acoustic center.

Figure 2.9 presents results for the same numerical experiment but at 500 Hz ($kr'' = 4.93$). Since kr'' is not small, the low-frequency acoustic center does not apply. As anticipated, the previously proposed algorithms struggle to identify a meaningful acoustic center. Numerous local minima appear in both J_{ss} and J_{lo} , similar to results reported in Refs. 27 and 28; some of the most significant local minima occur at the point source locations. Conversely, J_{ph} gives a single minimum; however, it converges to the point source with the largest amplitude. Only the proposed method of the present work identifies a single acoustic center located between the point sources, as one would expect.

The previous works formulated the objective functions J_{ss} , J_{lo} , and J_{ph} based on assumptions of radiation from a single point source, including coherent phase across spherical wavefronts and a low-order representation. Other research demonstrated that these assumptions remain valid for arbitrary sources with omnidirectional radiation at low-frequencies [54]. Consequently, all three objective functions converged to the true low-frequency acoustic center as seen in Fig. 2.8. However, the assumptions break down at higher frequencies and when radiation is no longer omnidirectional. Consequently, it is not surprising that all three functions identified individual point source locations rather than meaningful acoustic centers.

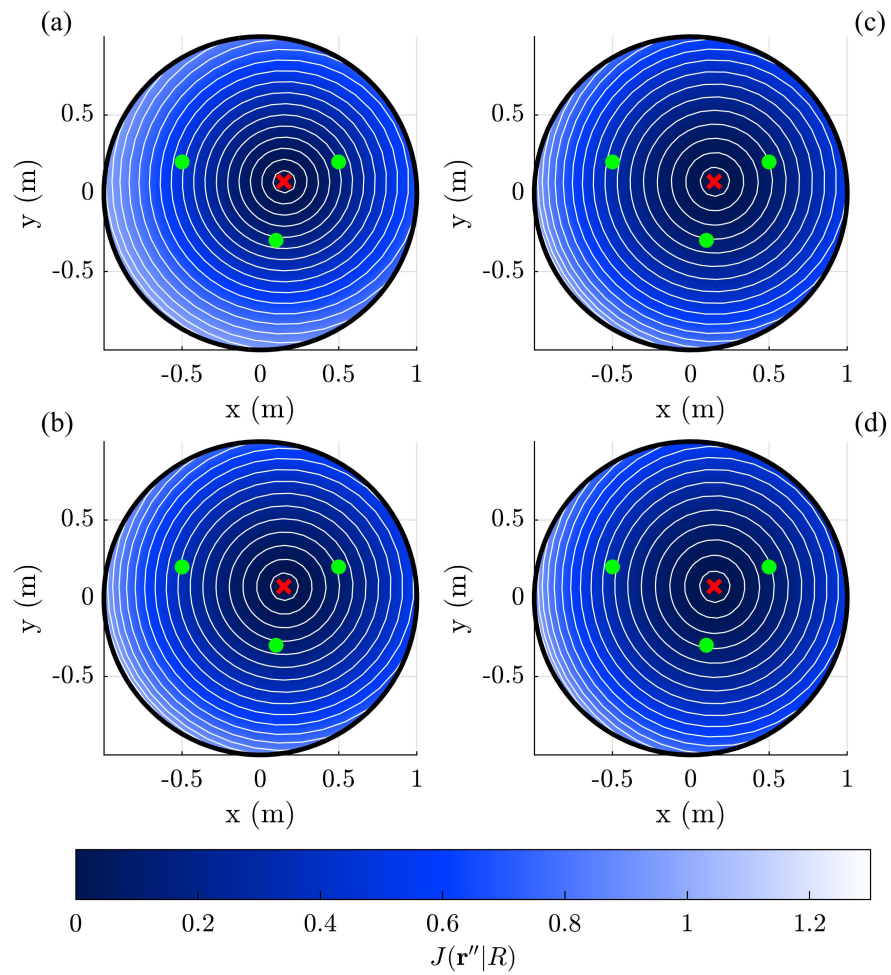


Figure 2.8 Objective functions for the acoustic source centering of a three-monopole distribution at 50 Hz. (a) J_{ss} . (b) J_{lo} . (c) J_{ph} . (d) J of the present work.

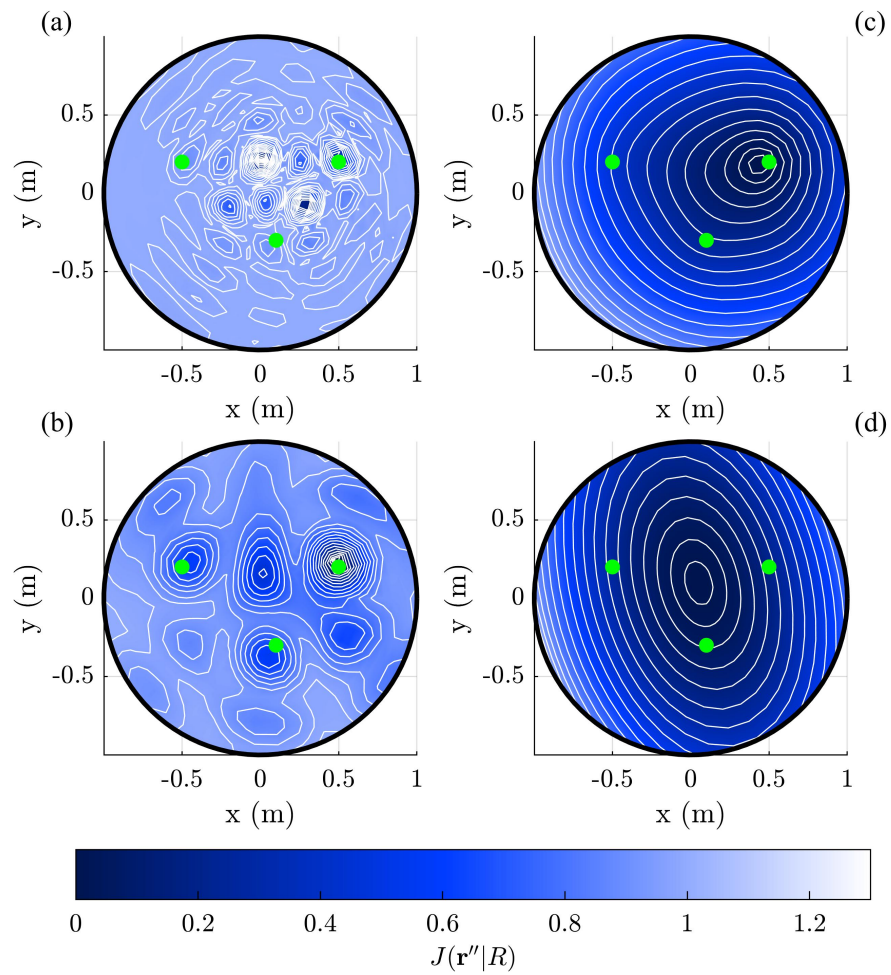


Figure 2.9 Objective functions for the acoustic source centering of a three-monopole distribution at 500 Hz. (a) J_{ss} . (b) J_{lo} . (c) J_{ph} . (d) J of the present work.

2.5.3 Point Source on a Sphere

This section compares the proposed algorithm's results to those presented by Jacobsen et al. for the acoustic center of a point source on a rigid sphere of radius a . This arrangement yields a more complex high-order source requiring roughly $N \approx ka$ expansion terms. Additionally, unlike the multipole cases, symmetry arguments cannot determine the exact position of the acoustic center. In fact, for this specific configuration, each of the centering approaches used by Jacobsen et al. yielded different acoustic centers over frequency.

Fig. 2.10 plots the acoustic center over frequency along the axis from the sphere's center, through the point source, and beyond. The blue dashed line indicates the position of the point source $r = a$, which is the acoustic center in the absence of the rigid sphere. The green dash-dotted line indicates the low-frequency acoustic center. The solid black curve shows a theoretical center based on matching $1/r$ decay with an equivalent monopole [Ref. 49, Eq. (18)]. The red dotted curve indicates the acoustic center determined from this work's proposed technique. For both Jacobsen et al. Eq. (18) and the proposed method, the formulations apply an observation distance of $R = 100$ m. Because the formulations and definitions of the acoustic center differ, one anticipates some differences between the curves. The acoustic center of Jacobsen et al. Eq. (18) follows from a single, on-axis observation point, whereas the proposed method uses a global approach that evaluates the source pressure in all directions. Nonetheless, while the curves do not agree perfectly, they have marked similarities. Both converge to the low-frequency acoustic center for $ka \ll 1$. As ka approaches unity, the curves dip toward $r_c = a$. For $ka \geq 1$, the predicted centers undulate about $r_c = a$ then slightly below $r_c = a$.

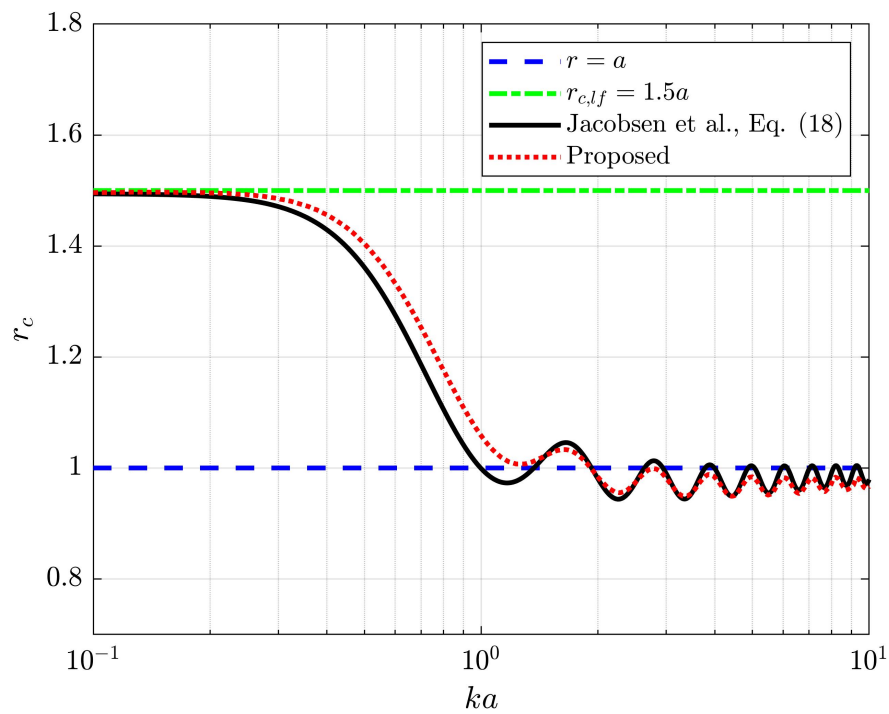


Figure 2.10 Frequency-dependent acoustic center results for a point source on a rigid sphere of radius $a = 1$ m.

2.6 Discussion

A key motivation for developing the acoustic center concepts and source-centering techniques has been the need to obtain reliable directivity patterns. This work's results have highlighted several related points. First, with a sufficiently large measurement radius and careful attention to the location of the source within an array, one can generally minimize deviations in magnitude patterns from actual far-field patterns. If one cannot place the array sufficiently far from the source or when the expected acoustic center cannot align with the geometric array center, far-field propagation of the measured results leads to the centered far-field magnitude pattern. Consequently, for applications where only magnitude values are essential, such as for many implementations of geometrical acoustics [92], one can generally overcome the effects of source misalignments without needing an acoustic centering procedure.

With the inclusion of directional phase information, several matters require careful consideration. If only the complex far-field pressure is necessary, source translations follow by simply modifying the far-field phase data via Eq. (2.25). For spherical harmonic expansions at variable radii, it is first essential to note that a change in the coordinate frame origin (e.g., to align the origin with the acoustic center) does not change the unique solution to the Helmholtz equation given by Eq. (2.1). Both the translated and centered directivities and their associated expansions are equally valid. The primary advantage of source translation is that it may yield a simplified source representation using fewer expansion coefficients [27, 28].

A simplified source representation has clear computational advantages when implementing spherical harmonic expansions in some time-domain, wave-based simulations [87] for which only a single expansion origin per source is practicable. The acoustic center's frequency-dependent nature implies that one cannot choose the acoustic center as this single expansion origin. Instead, one must consider which expansion origin provides the simplest spherical harmonic representation across all desired frequencies.

If low-frequency radiation is of interest, this origin may coincide with the low-frequency acoustic center. However, the acoustic center of a point source on a sphere in Sec. 2.5.3 shows that the optimal expansion origin likely differs from the low-frequency acoustic center for higher frequencies. Consequently, the optimal acoustic center may fall at an intermediate position for a broadband simulation. Determining a single optimal expansion origin goes beyond the scope of the present work, but it would be a worthwhile topic for future research. Such a location would also be beneficial for choosing a source placement when performing directivity measurements.

As the preceding sections have demonstrated, the proposed source-centering algorithm succeeds for both large displacements and high frequencies. However, the developments also pointed to the algorithm's limitations. Specifically, adequate spatial sampling is necessary to minimize spatial aliasing because the far-field pressure follows from acoustical holography. This fact implies that the total number and distribution of sampling positions constrain the technique's upper-frequency limit. Consequently, the method may not significantly increase usable bandwidth with low-density sampling schemes compared to other techniques. However, with higher-density sampling schemes, one can employ the technique to perform acoustic centering to much higher frequencies than via previously proposed methods. This benefit extends to complex radiation patterns, which typically require many expansion coefficients.

2.7 Conclusions

This work has provided perspectives on source translations, acoustic centering, and their effects on measured and far-field directivities. The results demonstrate that far-field magnitude patterns of translated sources are equivalent to those of centered sources, while phase shifts compensate for associated time delays. The work has presented an acoustic source-centering algorithm that specifically seeks the reference frame from which the sound pressure field converges fastest to the

far-field pattern. Theoretical multipoles, a point source distribution, and a point source on a sphere all validated the technique. The algorithm objective function appears convex at all tested frequencies, and its minimum agrees well with known acoustic centers. However, sampling resolution limits bandwidth because the approach extrapolates the sound pressure to the far field using acoustical holography. High-resolution sampling is essential to leverage the algorithm's full potential and perform acoustic centering at higher frequencies.

Experimentalists will benefit by performing source directivity measurements with large-radius spherical sampling, high sampling density, and source locations within the sphere. However, measurement surfaces should also be close to sources to improve signal-to-noise ratios for some applications, such as source imaging or near-field acoustical holography. High-density sampling is vital for small measurement radii if one desires to propagate measured directivities to the far field.

Future research could explore other approaches to acoustic centering based on far-field phase relations or more robust methods for spatial aliasing cases. Investigations addressing the best use of frequency-dependent acoustic source centers for source placements during measurements would also be beneficial.

Chapter 3

Phase Algorithm for Acoustic Centering

While Ch. 2 developed an acoustic centering algorithm based on the magnitude of a source's far-field directivity, this chapter applies far-field phase relations to develop an alternative acoustic centering technique. The chapter previously appeared as

S. D. Bellows and T. W. Leishman, "A spherical beamforming algorithm for acoustic centering and phase correction of source directivities," Proc. 24th Int. Conf. Acoust., ABS-0244, (2022).

3.1 Introduction

The directivity of a sound source characterizes the spatial dependence of its acoustic radiation over frequency. Understanding the directional characteristics of sources has broad applications, including auralizations, room acoustical design, microphone placement, and source modeling. Directivity measurements are typically performed by sampling at a constant-radius spherical surface with a specified sampling density, such as the 5 or 10-degree angular resolution suggested by the AES sampling standard [33]. Of practical concern when measuring the directivity of a source is the location of the source relative to the geometric center of the microphone array. Source misalignment within the array can lead to several undesirable effects. First, the measured pressure on the array

surface may not be representative of the desired far-field directivity pattern [45]. Additionally, source translations increase the number of expansion terms required, which in turn increase the likelihood of spatial aliasing [27, 28]. Thus, proper source positioning within the array is essential for practical directivity measurements.

More recently, the authors have shown that in the far-field, the magnitude pattern of centered and translated sources are equivalent [82]. One can exploit this equivalence to determine the reference frame from which the near-field pattern converges most rapidly to the known far-field magnitude pattern. While this approach is robust at higher frequencies and useful for complex sources, its computational expense is limiting because the formulation requires extraction of magnitude patterns in the spatial domain rather than an efficient spherical-harmonic-based process. To improve upon these limitations, this work presents an acoustic centering algorithm based on a source's far-field phase patterns. The relations between the far-field phases of centered and translated sources can cast the acoustic centering problem as the detection of arrival (DOA) of a local plane-wave with efficient solutions using spherical-harmonic-domain beamforming. Theoretical results help validate the robustness of the approach, and the technique successfully centers measured trumpet directivities.

3.2 Algorithm

3.2.1 Far-field Phase Relationship

Consider an acoustic source radiating into free space. If a closed spherical surface of radius $r = a$ entirely encompasses the source, the exterior solution to the Helmholtz equation in spherical coordinates yields the pressure for $r \geq a$ [59]:

$$p(r, \theta, \phi, k) = \sum_{n=0}^{\infty} \sum_{m=-n}^n c_n^m(k) h_n^{(2)}(kr) Y_n^m(\theta, \phi) \quad (3.1)$$

where k is the wavenumber, $h_n^{(2)}(kr)$ are the spherical Hankel functions of the second kind of order n , $Y_n^m(\theta, \phi)$ are the normalized spherical harmonics of degree n and order m , and $c_n^m(k)$ are the frequency-dependent expansion coefficients. Exploiting the orthogonality of the spherical harmonics over the sphere yields the expansion coefficients:

$$c_n^m(k) = \frac{1}{h_n^{(2)}(ka)} \int_0^{2\pi} \int_0^\pi p(a, \theta, \phi, k) [Y_n^m(\theta, \phi)]^* \sin \theta d\theta d\phi \quad (3.2)$$

where $*$ indicates complex conjugation. In the acoustic and geometric far-field of the source, where $kr \gg 1$ and $r \gg d$, with d being the spatial extent of the source, the asymptotic form of the spherical Hankel functions simplifies Eq. (3.1) to the form

$$p(r, \theta, \phi, k) = \frac{e^{-ikr}}{kr} \sum_{n=0}^{\infty} \sum_{m=-n}^n c_n^m i^{n+1} Y_n^m(\theta, \phi) \quad (3.3)$$

The far-field simplification allows separation of the pressure field's angular and radial dependence, yielding an unnormalized directivity function

$$\tilde{D}(\theta, \phi, k) = \sum_{n=0}^{\infty} \sum_{m=-n}^n c_n^m i^{n+1} Y_n^m(\theta, \phi). \quad (3.4)$$

Next, one may assume that the source has an acoustic center and let $D_c(\theta, \phi, k)$ denote its far-field normalized directivity function with the origin of the coordinate system aligned with the acoustic center. One may further let $D(\theta, \phi, k)$ denote the sources' far-field directivity function measured with the acoustic center located at position r_c . The first directivity product theorem then relates these two directivity functions as [59, 82]

$$D(\theta, \phi, k) = e^{ik\mathbf{r}_c \cdot \hat{\mathbf{r}}} D_c(\theta, \phi, k) \quad (3.5)$$

where $\hat{\mathbf{r}}$ is the unit vector in the direction of r . This key result shows that in the far-field, the magnitude directivity patterns of the centered and uncentered source are equivalent. However, the phase shift factor $e^{ik\mathbf{r}_c \cdot \hat{\mathbf{r}}}$ between the centered and uncentered patterns remains. Figure 3.1 illustrates this shift through color-mapped far-field phase spheres for a monopole, dipole, and radially vibrating

cap set on a rigid sphere. Each constant-radius plot describes the phase of the pressure using a cyclical color scheme. Figures 3.1(a), 3.1(d), and 3.1(g) show the far-field phase of each source when aligned with the array center. For the case of the vibrating cap on a sphere, the center of the sphere aligns with the array center. Next, Figs. 3.1(b), 3.1(e), and 3.1(h) show the far-field phase for each source after a translation of $r_c = (0.0, 0.1, 0.3)$ m. Finally, Figs. 3.1(c), 3.1(f), and 3.1(i) show the difference in phase pattern between the translated and untranslated cases. The numerical results verify that regardless of how simple or complex the initial phase of an untranslated source may be, the phase difference depends only on the translation and wavenumber as described in Eq. (3.5).

3.2.2 Phase-based Centering Algorithm

Previous work exploited the equivalence of the far-field directivity magnitudes to develop a centering algorithm that is robust even at high frequencies and for complex sources [82]. However, a disadvantage of the algorithm is that its use of magnitude patterns produces a computationally expensive approach in the spatial domain. This section leverages phase relationships between far-field directivities to yield a more computationally efficient algorithm with less robustness.

To begin with, for some sources one may assume that the phase of the centered pattern is roughly constant so that the measured far-field phase of the translated source is

$$\Psi(\theta, \phi, k) \approx k \mathbf{r}_c \cdot \hat{\mathbf{r}} \quad (3.6)$$

The pressure of a unit-amplitude plane wave is

$$p(r, \theta, \phi, k) = e^{-i\mathbf{k} \cdot \mathbf{r}} = e^{-ir\mathbf{k} \cdot \hat{\mathbf{r}}} \quad (3.7)$$

where \mathbf{k} is the wavenumber vector with magnitude k , which points in the direction of propagation. By associating the term $k \mathbf{r}_c$ of the far-field phase with the $-ir\mathbf{k}$ term of the plane wave, one may cast the acoustic centering problem as determining the direction of arrival (DOA) of the plane wave. One

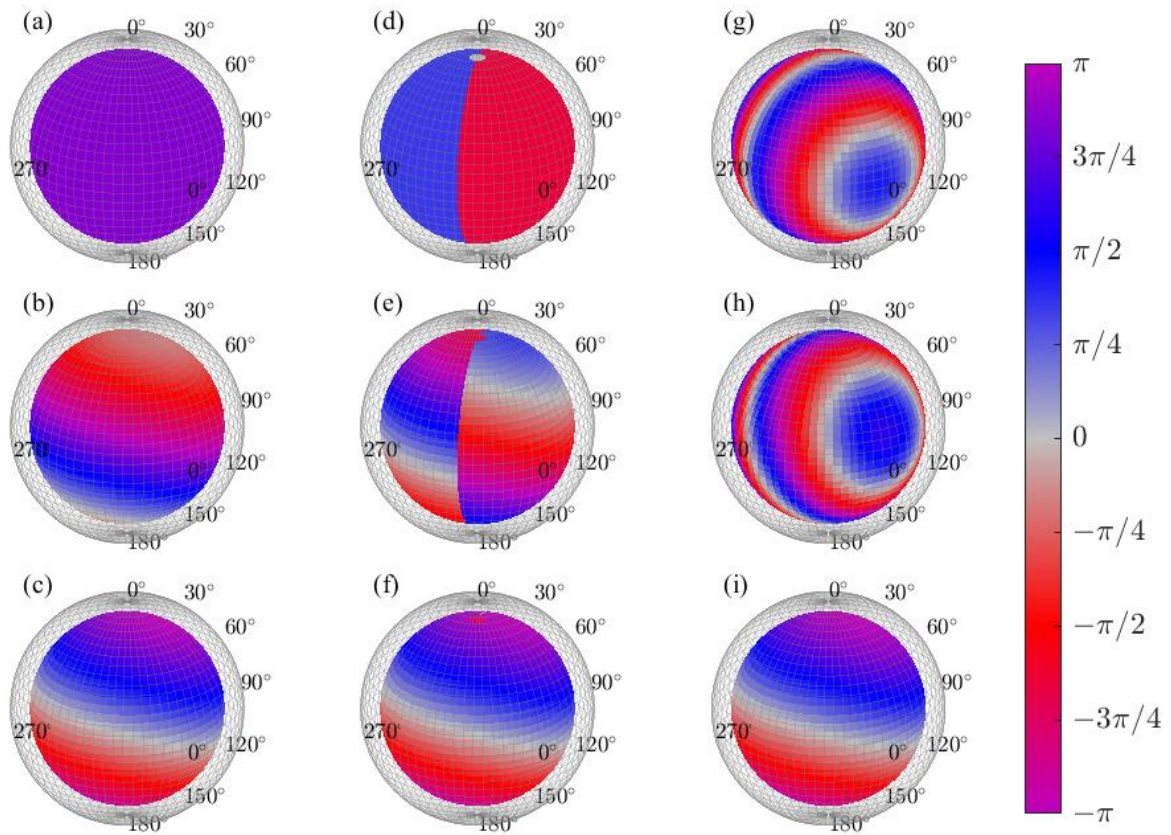


Figure 3.1 Far-field phase spheres for a monopole [(a)-(c)], dipole [(d)-(f)], and radially vibrating cap on a sphere [(g)-(i)]. These include cases for the sources located at the center of the measurement array [(a), (d), and (g)], translated to position (0.0, 0.1, 0.3) m [(b), (e), and (h)], and the phase differences between the untranslated and translated sources [(c), (f), and (i)].

key difference between the two problems is that for the plane-wave DOA, r is typically known, so the steering need only be performed over the angular coordinates θ and ϕ . However, for the source centering problem, r_c is unknown; the varying radial positions require additional consideration.

A straightforward approach to the problem is to use a delay-and-sum beamformer. In this case one may let y be the output of the beamformer so that [77]

$$y = \mathbf{w}_{nm}^H \mathbf{p}_{nm}. \quad (3.8)$$

Here, p_{nm} is a vector containing the spherical harmonic expansion coefficients of the far-field phase $e^{i\mathcal{P}}$ and \mathbf{w}_{nm} are the spherical harmonic coefficients of the beamforming weights,

$$w_{nm} = 4\pi i^n j_n(-kr) [Y_n^m(\theta, \phi)]^*, \quad (3.9)$$

where j_n are the spherical Bessel functions of order n . The position (r, θ, ϕ) that maximizes the beamformer output y is then the acoustic source center. Figure 3.2 illustrates this approach for a monopole located at $r_c = 0.3$ m and $(\theta_c, \phi_c) = (45^\circ, 90^\circ)$ with wavenumber $k = 10$ m⁻¹. Six different spherical projections for varying radial steering positions r_c show the beamformer output. The color scheme of each projection is kept constant to highlight that the acoustic center must be determined not only from the angular portion but also from the radial component. The beamformer's maximum output coincides with the monopole's true location, indicated by a red dot.

While the formulation based on Eq. (3.8) provides a satisfactory result, one can further improve the algorithm's computational efficiency by noting the strong axial symmetry of the far-field phase as seen in Figs. 3.2(c), (f), and (i). Because the order $m = 0$ spherical harmonics are axially symmetric about $\hat{\mathbf{z}}$ for any degree n , the rotation of the far-field phase function that maximizes the energy in the p_n^0 coefficients can determine the direction in which \mathbf{r}_c points. The Wigner-D rotation matrices $\mathbf{D}(\theta, \phi, \psi)$ allow this rotation to be carried out in the spherical harmonic domain [77]. By letting

$$\mathbf{q}_{nm}(\theta, \phi, \psi) = \mathbf{D}(\theta, \phi, \psi) \mathbf{p}_{nm} \quad (3.10)$$

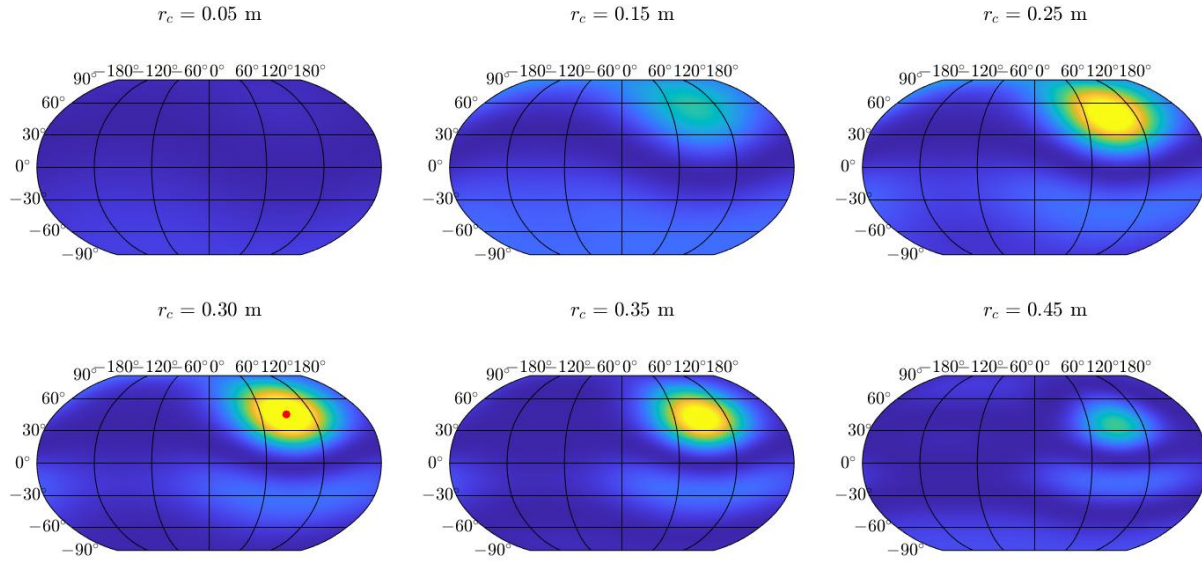


Figure 3.2 Delay-and-sum beamformer output for the acoustic source centering problem.

be the far-field phase spherical harmonic expansion coefficients after rotation, one finds that maximizing the objective function

$$J(\theta', \phi') = \sum_{n=0}^{\infty} |q_{n0}(\theta', \phi', 0)|^2 \quad (3.11)$$

yields the rotation required to orient the phase so that it is axially symmetric about $\hat{\mathbf{z}}$. Once this rotation is known, the direction (θ_c, ϕ_c) can be determined, and the delay-and-sum equation weights can be used with fixed angular components and varying radial components. The ambiguity in the rotation angle between $\hat{\mathbf{z}}$ and $-\hat{\mathbf{z}}$ resolves by allowing r_c to vary over both positive and negative ranges. Furthermore, because the degree $n = 1$ expansion terms contain the relevant directional information for a single plane wave, the expansion coefficients p_{nm} may be truncated to a maximal $N = 1$ expansion, with the associated Wigner-D rotation matrices being of size 4×4 for increased computational efficiency.

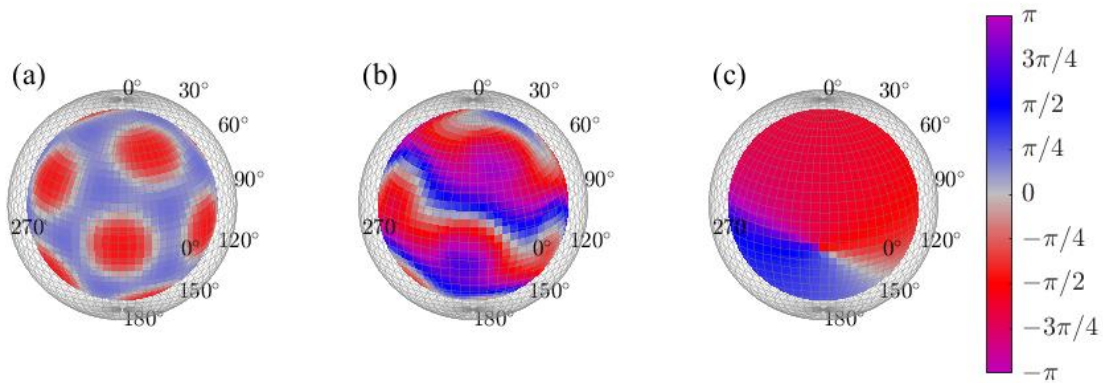


Figure 3.3 Far-field color-mapped phase spheres for the (a) centered, (b) translated, and (c) translated dodecahedron using a simplified degree $N = 1$ expansion.

3.3 Theoretical Results

The dodecahedron regular polyhedron loudspeaker (RPL) is an interesting source to study because, even though it behaves much like a simple source at low frequencies, its directivity becomes complex at high frequencies [13]. If one assumes the source has a single acoustic center, it must fall at the RPL center due to geometrical arguments. Thus, the RPL provides an ideal case of a complex radiator with a known acoustic center. Figure 3.3(a) shows the centered far-field phase of a simulated dodecahedron RPL for wavenumber $k = 30\text{m}^{-1}$ and RPL radius $a = 0.2$ m. Strong phase shifts are evident for each driver from the red patches in the general sphere of blue. Figure 3.3(b) shows the far-field phase after a source translation to $r_c = (0.0, 0.1, 0.2)$ m. Figure 3.3(c) then shows the simplified phase using the degree $N = 1$ expansion, which correctly identifies the direction of translation.

Figure 3.4 shows the centering results. The projected sphere plots the objective function $J(\theta', \phi')$ applied to the simplified phase shown in Fig. 3.3(c). The red dot indicates the true angular direction of the translation whereas the black x indicates the predicted direction. The line plot shows the

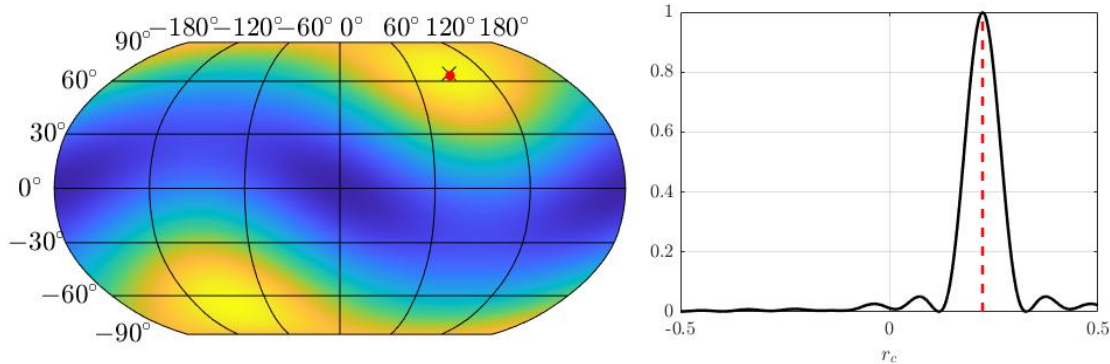


Figure 3.4 Centering results for dodecahedral RPL. Left: Objective function $J(\theta', \phi')$. Right: normalized delay-and-sum output using a fixed angular position and varying r_c .

delay-and-sum output using the identified direction and varying the radial parameter r_c . The vertical dashed red line indicates the true radial position.

3.4 Experimental Results

A radius $a = 1.17$ m rotating semi-circular microphone array measured the directivity of a played trumpet with various mutes. The microphone array consisted of 36 12.7 mm (0.5") precision microphones that were relatively calibrated to a dedicated channel. The microphones were placed in 5° polar angle increments. Subsequent arc rotations in 5° azimuthal increments swept out a sphere with sampling density consistent with the AES standard on loudspeaker directivities [33], minus the nadir (south pole) measurement position. A near-field reference microphone normalized varying excitation levels between the repeated measurements through frequency response functions (FRFs) as outlined in Ref. [6]. A head restraint and laser mounted to the instrument restricted the musician's movements for greater consistency between measurements. Figure 3.5 shows the trumpet player within the measurement system.

Because of the small arc radius, placement the trumpet's bell close to the array's center was not practical. Consequently, the authors anticipated source misalignment between the instrument's



Figure 3.5 Trumpet player within measurement arc while playing with a cup mute.

acoustic center and the array's geometric center. Figure 3.6 shows the raw FRF-based directivity balloons with 1 Hz narrowband resolution for the first three partials of the note E4: 329 Hz, 658 Hz, and 988 Hz, respectively. Color and radius both depict levels on the surface of constant $r = a$, with the 0° marker indicating the direction in front of the musician. Figures 3.6(a)-(c) show the magnitude of the FRF-based balloon, whereas Figs.

Figures 3.6(g)-(i) show the far-field magnitude directivities after propagation via Eq. (3.3) using an $N = 34$ expansion, the maximal possible for the given sampling configuration. The directivity is much less directional, implying that many of the features evident in Figs. 3.6(a)-(c) are likely near-field effects. In addition, the principal axis of radiation lowers slightly.

The phase-based centering algorithm determined the acoustic center of each partial to be at (0.25, 0.00, 0.43) m, (0.25, 0.00, 0.42) m, and (0.29, 0.00, 0.34) m, respectively. While the acoustic center is generally considered to be frequency dependent, the position remains relatively consistent for the three partials. Figures 3.6(j)-(l) show the corresponding centered directivities of Figs. 3.6(a)-(c) based on expanding the pressure about the estimated acoustic center at a $a = 1.7$ m radius. Importantly, they show strong similarities with the far-field pattern, even though these are not far-field directivities. This result shows the effectiveness of the centering algorithm, as the pressure measured about the acoustic center should quickly converge to the far-field pattern [82]. The area-weighted RMS deviation values [6] show that the deviations between the centered patterns of 3.6(j)-(l) and the far-field patterns of 3.6(g)-(i) were only 1.3, 1.7, and 2.0 dB compared to 1.9, 2.1, and 2.5 dB for the measured patterns of Fig. 3.6(a)-(c). Thus, the centering algorithm effectively reduces deviations between far-field directivities and nearer-field measurements.

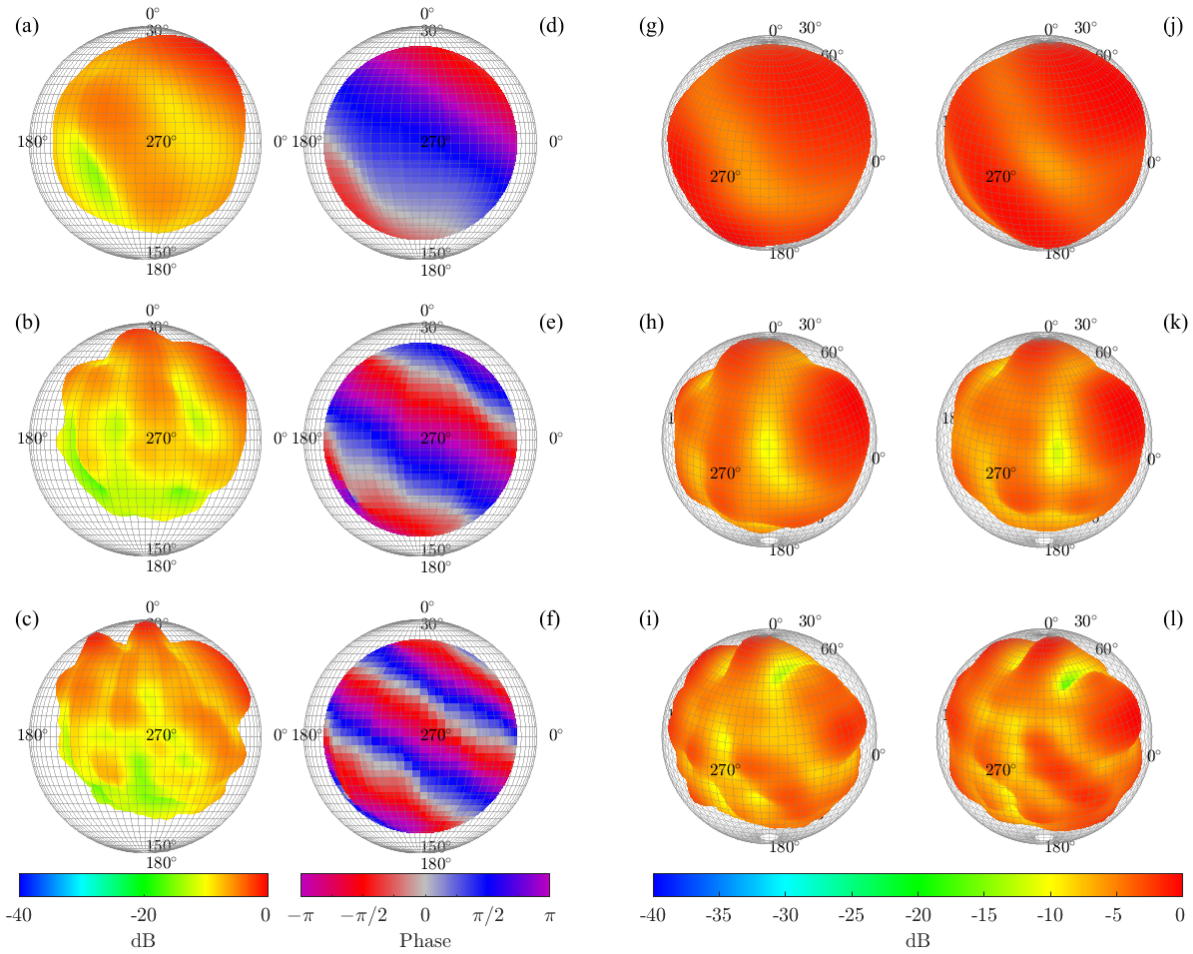


Figure 3.6 Measured narrowband trumpet directivity patterns for the first [(a), (d), (g), and (j)], second [(b), (e), (h), and (k)] and third [(e), (f), (i), and (l)] partials. Figures (a)-(c) are FRF-based magnitude directivity patterns at the measurement surface. Figures (d)-(f) are the FRF-based phase patterns on the measurement surface. Figures (g)-(i) are the far-field magnitude patterns based on N=34 expansions. Figures (j)-(l) are the centered near-field magnitude patterns using the proposed algorithm.

3.5 Conclusions

This work has presented an acoustic centering algorithm based on the far-field phases of sources. It allows the acoustic centering problem to be reformulated in terms of a spherical beamforming problem. Theoretical directivities and measured musical instrument directivities validate the method. Future work could include the application of the algorithm to other sound sources and exploring other approaches for sources with more complex phase patterns.

Chapter 4

Comparison of Pressure Field Translation

Methods

While Chapters 1, 2, and 3 developed techniques to determine a source's acoustic center from measured data, it is useful to translate the coordinate origin frame to align with this center for some applications. This chapter compares two methods for calculating the spherical harmonic expansion coefficients in a translated frame.

4.1 Introduction

Acoustic source centering is a post-processing technique for improving the quality of directivity measurements. When a sound source is measured, such as with a multichannel surrounding spherical microphone array, the acoustic center of the source may not perfectly align with the geometric center of the array, which can lead to distorted directivity patterns. Furthermore, because the acoustic center is generally frequency dependent [49], even if the geometric or acoustic centers were aligned at one frequency, they may not be at others. Several works have studied techniques for localizing and translating the acoustic center when measured by a surrounding spherical array [27–29, 93].

Once an algorithm determines the acoustic center, it may be desirable to translate the pressure field so that the coordinate origin and the acoustic center align. This work compares methods for numerically translating the acoustic pressure field from an uncentered to a centered reference frame.

4.2 Expansion Coefficients of Pressure Field

The general approach to identifying an acoustic source center in previous studies has been to use the measured pressure at the array sampling points to estimate the pressure expansion coefficients $c_n^m(k)$ of the Helmholtz equation in different coordinate reference frames. Using spherical coordinates, the pressure p may be written as

$$p(r, \theta, \phi, k) = \sum_{n=0}^{\infty} \sum_{m=-n}^n c_n^m(k) h_n^{(2)}(kr) Y_n^m(\theta, \phi), \quad (4.1)$$

where r is the radius, θ is the polar angle, ϕ is the azimuthal angle, k is the wave number, $c_n^m(k)$ are the pressure expansion coefficients, $h_n^{(2)}(kr)$ are the spherical Hankel functions of the second kind of order n and $Y_n^m(\theta, \phi)$ are the spherical harmonics of degree n and order m [70]. Assuming the measurements are made with a spherical microphone array of radius a , the formulation allows for the calculation of the pressure in the region $r \geq a$ [59]. If the source is assumed to be band-limited to order $n = N$, one may express Eq. 4.1 in matrix form as

$$\mathbf{p} = \Psi \mathbf{c}, \quad (4.2)$$

where

$$\mathbf{p} = \begin{bmatrix} p(r_1, \theta_1, \phi_1, k) \\ \vdots \\ p(r_Q, \theta_Q, \phi_Q, k) \end{bmatrix}, \quad (4.3)$$

$$\Psi = \begin{bmatrix} h_0^{(2)}(kr_1)Y_0^0(\theta_1, \phi_1) & \dots & h_N^{(2)}(kr_1)Y_N^N(\theta_1, \phi_1) \\ \vdots & \ddots & \vdots \\ h_0^{(2)}(kr_Q)Y_0^0(\theta_Q, \phi_Q) & \dots & h_N^{(2)}(kr_Q)Y_N^N(\theta_Q, \phi_Q) \end{bmatrix}, \quad (4.4)$$

$$\mathbf{c} = \begin{bmatrix} c_0^0(k) \\ \vdots \\ c_N^N(k) \end{bmatrix}, \quad (4.5)$$

and (r_q, θ_q, ϕ_q) represent the Q sampling positions.

Because of the double index over n and m in Eq. 4.1, \mathbf{p} is of size $Q \times 1$, Ψ is of size $Q \times (N+1)^2$, and \mathbf{c} is of size $(N+1)^2 \times 1$. In order to avoid ill-conditioning of the matrix Ψ , it has been suggested that $Q \geq (N+1)^2$ [28,77], allowing for the pressure coefficients \mathbf{c} to be solved for in the least-squares sense:

$$\mathbf{c} = \Psi^\dagger \mathbf{p}, \quad (4.6)$$

where Ψ^\dagger denotes the pseudoinverse of Ψ , defined as $(\Psi^H \Psi)^{-1} \Psi^H$.

In order to expand the pressure about a point (r'', θ'', ϕ'') different than the array's geometric center, the solution to the Helmholtz equation can be rewritten as

$$p(r', \theta', \phi', k) = \sum_{n=0}^{\infty} \sum_{m=-n}^n c_n^m(k) h_n^{(2)}(kr') Y_n^m(\theta', \phi'), \quad (4.7)$$

where the primed coordinates (r', θ', ϕ') are the radius, polar angle, and azimuthal angle, respectively, of the new coordinate system with origin (r'', θ'', ϕ'') , and $c_n^m(k)$ are the pressure expansion coefficients in this new reference frame. Letting Ψ' , \mathbf{c}' , and \mathbf{p}' be the same as Ψ , \mathbf{c} , and \mathbf{p} , except with primed coordinates (r', θ', ϕ') in place of the original reference frame coordinates (r, θ, ϕ) , and assuming that the pressure coefficients in the primed reference frame are also band-limited to N , the latter are given similarly:

$$\mathbf{c}' = \Psi'^\dagger \mathbf{p}'. \quad (4.8)$$

Because the pressure must be identical at the measurement points, independent of an arbitrary choice of reference frame, the expressions related to Eq. 4.2 can be equated, yielding

$$\Psi' \mathbf{c}' = \Psi \mathbf{c}, \quad (4.9)$$

which leads to the method for translating the pressure expansion coefficients from the original reference frame to the primed reference frame given in Ref. [28]:

$$\mathbf{c}' = \Psi'^{\dagger} \Psi \mathbf{c}. \quad (4.10)$$

The matrix $\Psi'^{\dagger} \Psi$ represents an approximate version of analytic translation matrices and is simpler to compute [28].

Once the expansion coefficients are computed in the new reference frame, an objective function is applied, typically related to the distribution of energy in the coefficients of \mathbf{c}' . The position in space that minimizes the objective function is then declared to be the acoustic center of the source. While much research has been done in exploring the convergence and effectiveness of various objective functions [28, 29], the focus of the present work is on comparing the algorithms for computing the pressure expansion coefficients in \mathbf{c}' .

4.3 Direct Method

From Eq. 4.6, it is apparent that $\Psi \mathbf{c} = \Psi \Psi^{\dagger} \mathbf{p} = \hat{\mathbf{p}}$ is the projection of the vector \mathbf{p} onto the range space of Ψ , $\mathcal{R}(\Psi)$ [94]. If one chooses an expansion order N such that $Q > (N + 1)^2$ to avoid ill-conditioning of the matrix Ψ , the rank of Ψ may not be sufficient to represent \mathbf{p} , as it is possible that $\mathbf{p} \notin \mathcal{R}(\Psi)$. If the resultant error $\mathbf{e} = \Psi \mathbf{c} - \mathbf{p}$ in the projection is non-zero, Eq. 4.9 is not strictly true, as $\mathbf{p}' = \mathbf{p} \neq \hat{\mathbf{p}}$. In the case that \mathbf{e} is small, such that $\mathbf{p} \approx \hat{\mathbf{p}}$, the expansion coefficients \mathbf{c} may still provide meaningful results; however, as the error of the projection grows, the expansion coefficients do not accurately reflect the original measured pressure, carrying errors over into the computation of \mathbf{c}' when using Eq. 4.10.

Similarly, even if \mathbf{p} is sufficiently represented by the coefficients \mathbf{c} when using the expansion of Eq. 4.2, there remains the challenge that the computation of \mathbf{c}' requires yet another least-squares approximation. If $\Psi' \mathbf{c}' = \Psi' \Psi'^{\dagger} \mathbf{p}' = \hat{\mathbf{p}}'$, the projection of the pressure \mathbf{p}' onto $\mathcal{R}(\Psi')$ has significant error, the expansion coefficients \mathbf{c}' do not accurately reflect the pressure \mathbf{p}' . This leads to distortions in the finalized acoustically centered directivity patterns. The problem is further exacerbated because, unlike $\mathcal{R}(\Psi)$, which is determined by the number of sampling positions Q , their fixed locations and the maximal order of the expansion N , $\mathcal{R}(\Psi')$ also depends on the choice of reference frame origin (r'', θ'', ϕ'') , as the entries of Ψ' are dependent on (r', θ', ϕ') . Thus, while $\mathcal{R}(\Psi)$ remains constant during the source centering procedure, $\mathcal{R}(\Psi')$ changes depending on the desired reference frame. Consequently the expansion error $\hat{\mathbf{p}}' - \mathbf{p}'$ can vary over position, complicating the validity of the position-dependent objective functions.

Another difficulty of the previous method is that the order of the expansion N must be assumed to be equal in both frames. However, in general this cannot be assumed. For example, a monopole field is band-limited to order $N = 0$ when located at the origin; however, when it is displaced from the origin, it requires an infinite number of terms to represent its field [28]. This means that in order to accurately represent the uncentered pressure, a higher N would be required than that necessary in the centered frame. Consequently, the second least-squares approximation to translate the coefficients to the new reference frame would have too many terms, which can lead to over-fitting errors [78, 95].

These and other errors were considered in Ref. [28], leading to the conclusion that if one assumes the translation is relatively small, the translation errors are negligible. The direct approach frees this constraint, allowing source centering to be performed over larger translational distances.

It is apparent that there are two sets of errors, one from the initial least-squares approximation of \mathbf{p} represented by $\hat{\mathbf{p}}$, and the second arising from the second least-squares approximation of \mathbf{p}' represented by $\hat{\mathbf{p}}'$. In the formulation of the translation algorithm, Eq. 4.9 was built on the assumption that $\mathbf{p}' = \mathbf{p}$; however, when using the least-squares method to determine the coefficients

\mathbf{c} , the actual relation used is $\mathbf{p}' = \hat{\mathbf{p}}$, yielding

$$\mathbf{c}' = \Psi'^{\dagger} \hat{\mathbf{p}}, \quad (4.11)$$

arrived at by substituting $\Psi\mathbf{c} = \hat{\mathbf{p}}$ into Eq. 4.10. Nevertheless, because \mathbf{p} is already known, it is unnecessary to use $\hat{\mathbf{p}}$, and the original pressure measurements can be directly used, giving the direct method for computing the expansion coefficients in the new reference frame [27]:

$$\mathbf{c}' = \Psi'^{\dagger} \mathbf{p}. \quad (4.12)$$

This approach uses only one least-squares approximation, reducing total errors. Upon careful inspection, it is apparent that the proposed method is merely a variation and application of the Helmholtz-Equation Least-Squares (HELs) method, which is developed in more detail by Wu [75]. In some cases, such as when only the pressure expansion coefficients \mathbf{c} are available, this formulation is not possible; however, when the original measured pressure \mathbf{p} is available, it may be used to directly compute the translated pressure coefficients and provide the most accurate results.

4.4 Results

This section presents case studies to illustrate the methodological improvements. First, a numerical experiment demonstrates the reduction of distortion in a centered directivity pattern. A dipole is placed 0.5 m from the origin and measured with a 32-point surrounding spherical array based on the angular positions of a Catalan pentakis dodecahedron with a constant radius of 1 m. The wave number is $k = 7.3 \text{ m}^{-1}$ (400 Hz with a sound speed of 343 m/s) so that the displacement of the dipole is significant relative to the array size and wavelength. The translation should fail according to the limitations previously discussed.

Figure 4.1(a) shows a cross-section of the pressure field caused by the displaced dipole, plotted on a decibel scale. Figure 4.1(b) shows the projection $\hat{\mathbf{p}}$ of the pressure \mathbf{p} onto $\mathcal{R}(\Psi)$ based on

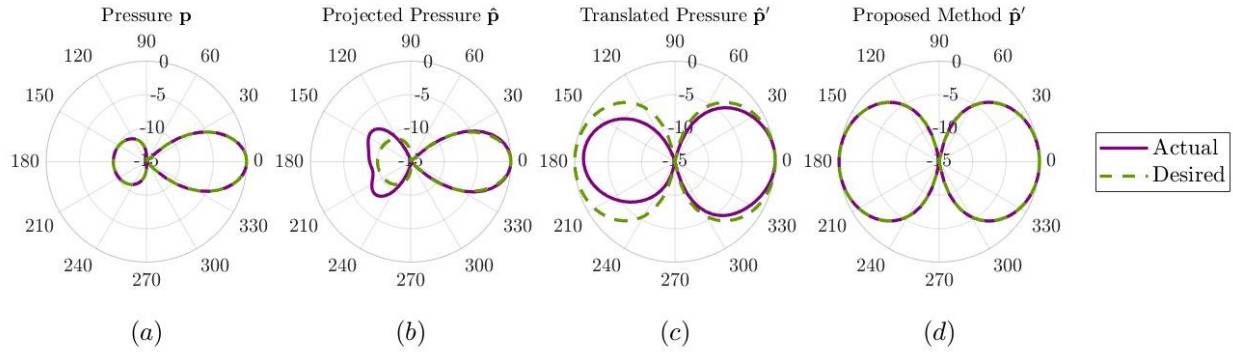


Figure 4.1 Comparison of the previous and direct methods for acoustic source translation. (a) Cross-section representing the pressure \mathbf{p} of a displaced dipole. (b) Projection $\hat{\mathbf{p}}$ of the measured pressure based on an $N = 4$ spherical harmonic expansion. (c) Translated pressure $\hat{\mathbf{p}}'$ using the initial projection $\hat{\mathbf{p}}$ based on an $N = 4$ spherical harmonic expansion. (d) Translation of pressure using the original measurement \mathbf{p} based on an $N = 4$ spherical harmonic expansion.

an $N = 4$ expansion. This intermediate step in the original source centering algorithm reveals that because the acoustic center is too far from the center of the array, the $N = 4$ expansion is too low in order to adequately represent \mathbf{p} . Figure 4.1(c) shows the resultant translated pressure of $\hat{\mathbf{p}}$ at the known acoustic center. The errors of the projection have led to a distortion in the final directivity pattern. Figure 4.1(d) shows the results of the proposed method, which computes the pressure expansion coefficients directly from the measured pressure. By circumventing the initial projection $\hat{\mathbf{p}}$, the true directivity pattern is recovered, even though the displacement of the dipole is significant.

The second numerical experiment illustrates the advantages in both physical displacement and bandwidth that are possible using the new method. The source is a monopole. A 1 m radius measurement array is based on dual-equiangular sampling with 5° resolution in both the azimuthal and polar angles, as commonly employed in loudspeaker directivity measurements [33]. The higher resolution helps prevent spatial aliasing errors. To avoid over-fitting, an order $N = 4$ expansion is used. A monopole is displaced from the origin up to 0.9 meters while the frequency is increased from 100 Hz to 1 kHz. The error between the translated pressure \mathbf{p}' and the known pressure \mathbf{p}_{true} is

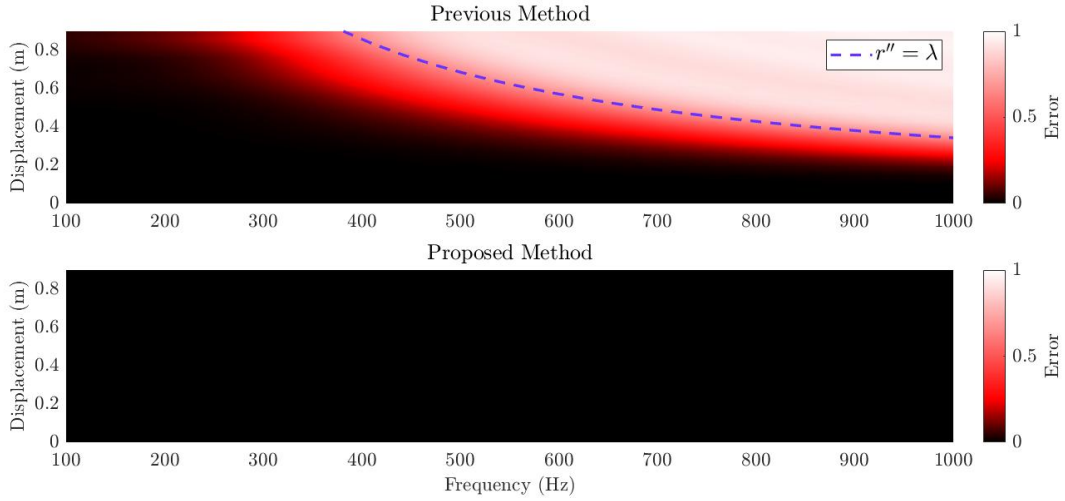


Figure 4.2 Errors of the previous and direct methods for centering a displaced monopole over frequency. The computed centered pressures $\hat{\mathbf{p}}'$ are based on an $N = 4$ spherical harmonic expansion. For convenience, a curve corresponding a monopole displacement $r'' = \lambda$ is superposed on the plot for the previous method.

computed using a root-mean-square deviation with quadrature weights w_q to equitably weight the uneven distribution of sampling points as outlined in Refs. [13, 78]:

$$E = \left(\sum_q w_q |p'_q - p_{q,true}|^2 \right)^{1/2}. \quad (4.13)$$

The results are graphically depicted in Figure 4.2, where the abscissa is frequency, the ordinate is monopole displacement and the translation error is represented through color. Furthermore, the curve representing the value of when the displacement of the source r'' equals a wavelength is included on the plot for the previous method. This experiment confirms the assertions of Ref. [28], in that as long as the translation remains small relative to wavelength, the translation errors can be neglected. However, the direct method is free from these constraints and shows no significant errors over this displacement and frequency range for the given array size and order.

4.5 Analysis

The direct method has several advantages over the approximate translation matrix method. By directly computing the translated coefficients \mathbf{c}' , projection errors in the coefficients are reduced, which leads to better results when used with the various objective functions. Furthermore, the direct method allows for testing of acoustic centers much farther away from the origin and at higher frequencies, both of which were limitations in past works. Another benefit is that the translated directivities have less distortion, as illustrated by the comparisons between Figs. 4.1(c) and (d). With the approximate translation matrix method, the order of the radiating source must be assumed to be the same in both the uncentered and centered reference frames; however, the direct method allows for the order of the expansion to be chosen only with regard to the centered reference frame, reducing the possibility of over-fitting errors.

4.6 Conclusions

This work has compared centering methods for translating the pressure of an acoustically uncentered reference frame to an acoustically centered reference frame. The direct method has been shown to increase the possible displacements and bandwidths of source translations while minimizing distortion errors in centered directivity patterns. It is a straightforward tool as long as the original sampled pressure is available. Future research could include studying the effect of the direct method when used with the previously proposed objective functions.

Part II

Measurement Theory

Chapter 5

Spatial Aliasing and Source Order

This chapter explores the close relationship between source dimensions and the number of required spherical harmonic expansion coefficients to represent its far-field directivity pattern. It also develops methods to estimate a source's effective acoustic dimension based on measured data.

5.1 Introduction

Directivity measurements are an important means of assessing the spatial dependence of sound source radiation. The resultant directional data has applications in room acoustical design [20,21], auralizations [18, 19], microphone placement [14, 15, 17], and sound source modeling [86, 88]. Despite the significance of directional data for these and other applications, the number of discrete sampling positions employed for published measurements has varied dramatically from fewer than a hundred [3, 30–32] to over a thousand [1, 6, 33, 34]. Meanwhile, AES-standardized directivity measurements with 10° and 5° dual-equiangular resolutions [33] have become ubiquitous for loudspeaker assessments and room-acoustical simulation software [96, 97]. Nevertheless, the standard provides little guidance on the maximum usable frequency for a given source using either sampling resolution. Furthermore, sampling scheme inconsistencies between published works

highlight a general ambiguity regarding the most suitable number of sampling positions required for effective directivity measurements.

Researchers have long applied spherical harmonic expansions of measured acoustic pressure in directivity applications [31, 83]. The expansions allow a continuous, rather than discrete, representation of the pressure field and serve as the angular component of the Helmholtz equation's solution in spherical coordinates [59]. Previous works have identified relations between the number of discretely sampled positions and the maximum spherical harmonic degree feasible in such expansions without significant spatial aliasing effects [77]. Other works have aimed to relate source geometry and other properties to the maximum degree required for source representations, e.g., through multipole expansions [62, 83]. Nevertheless, researchers and practitioners would benefit from a more concrete development and understanding of sampling considerations for making successful directivity measurements, including methods to determine limiting frequencies due to spatial aliasing.

This work approaches spatial sampling considerations by considering the effect of far-field propagation on a source's radiated pressure spectrum. The results confirm that far-field propagation behaves as a frequency-dependent low-pass spatial filter. This model of sound radiation allows a simple description of the relation between the maximum spherical harmonic degree and source geometry. Two methods for estimating source order based on measured directivity functions yield practical approaches for researchers and practitioners to understand when spatial aliasing limits applications of spherical harmonic expansions. Results for various musical instruments and speech serve as case studies of the theory's application in practical scenarios.

5.2 Source Order

5.2.1 Far-Field Propagation as a Filter

Consider an arbitrarily-shaped body radiating into free space and completely bounded by a notional sphere of radius d centered at the origin. The pressure p for any radius $r \geq d$ follows as [59]

$$p(r, \theta, \phi) = \sum_{n=0}^{\infty} \sum_{m=-n}^n \frac{h_n^{(2)}(kr)}{h_n^{(2)}(kd)} Y_n^m(\theta, \phi) \int_0^{2\pi} \int_0^{\pi} p(d, \theta, \phi) [Y_n^m(\theta, \phi)]^* \sin \theta d\theta d\phi, \quad (5.1)$$

where k is the wavenumber, $h_n^{(2)}$ are the spherical Hankel functions of the second kind of order n , and Y_n^m are the spherical harmonics of degree n and order m [70]. The integral

$$\int_0^{2\pi} \int_0^{\pi} p(d, \theta, \phi) [Y_n^m(\theta, \phi)]^* \sin \theta d\theta d\phi = p_n^m \quad (5.2)$$

yields the spherical harmonic expansion coefficients p_n^m of the pressure on the sphere of radius d such that

$$p(d, \theta, \phi) = \sum_{n=0}^{\infty} \sum_{m=-n}^n p_n^m Y_n^m(\theta, \phi). \quad (5.3)$$

When considering wave propagation from concentric spheres centered about the origin, the quotient

$$G_n(r) = \frac{h_n^{(2)}(kr)}{h_n^{(2)}(kd)}, \quad r > d \quad (5.4)$$

serves as a “propagator” [59], modifying the pressure observed at radius d to that represented at radius r . Consequently, the propagator behaves as a spatial filter between the two positions, with filtering dependent upon the choice of radial observation distance r and spherical Hankel order n .

Applying the large-argument relation for the spherical Hankel functions [70] yields the far-field result

$$p_{ff}(r, \theta, \phi) = \frac{e^{-ikr}}{kr} \sum_{n=0}^{\infty} \sum_{m=-n}^n \frac{i^{n+1}}{h_n^{(2)}(kd)} p_n^m Y_n^m(\theta, \phi), \quad (5.5)$$

so that the far-field propagator becomes

$$G_n^{(ff)} = \frac{i^{n+1}}{h_n^{(2)}(kd)}. \quad (5.6)$$

The source's unnormalized far-field directivity function follows as

$$D_{ff}(\theta, \phi) = \sum_{n=0}^{\infty} \sum_{m=-n}^n a_n^m Y_n^m(\theta, \phi), \quad (5.7)$$

where

$$a_n^m = G_n^{(ff)} p_n^m \quad (5.8)$$

are the far-field directivity expansion coefficients.

The use of far-field directivities in acoustical applications motivates an examination of how far-field propagation filters the observed pressure's angular response. For $n \gg kd$, the large-order relations of the Bessel functions give [70]

$$H_n^{(2)}(kd) \approx i \sqrt{\frac{2}{\pi n}} \left(\frac{ekd}{2n} \right)^{-n}, n \gg kd \quad (5.9)$$

where $H_n^{(2)}$ are the Hankel functions of the second kind. Applying the definition of the spherical Bessel functions gives the approximation

$$\frac{i^{n+1}}{h_n^{(2)}(kd)} \approx i^n kd \left(\frac{e}{2} \right)^{1/2} \left[\frac{ekd}{2n+1} \right]^n, n \gg kd. \quad (5.10)$$

When $ekd < 2n + 1$ such that $n > ekd/2 - 1/2 \approx 1.4kd - 0.5$, the far-field propagator's magnitude decays rapidly. Thus, far-field propagation has a low-pass filtering effect, significantly reducing the magnitudes of expansion coefficients p_n^m when $n \gg kd$. This low-pass effect coincides with Weinreich's observation that a source of maximum dimension d requires roughly up to spherical Hankel function order $N \approx kd$ for its representation [83]. The maximum order N required for sufficient representation is the source order. It is frequency dependent and linearly related to the source geometry.

To illustrate the frequency-dependent, low-pass filter response of G_n^{ff} , Fig. 5.1 plots the spectrum of the far-field propagator as a function of kd and n . Color indicates the relative level on a 30 dB scale normalized to the maximum value for each frequency considered. White indicates the most significant coefficients, whereas black indicates the least significant coefficients. An overlaid green

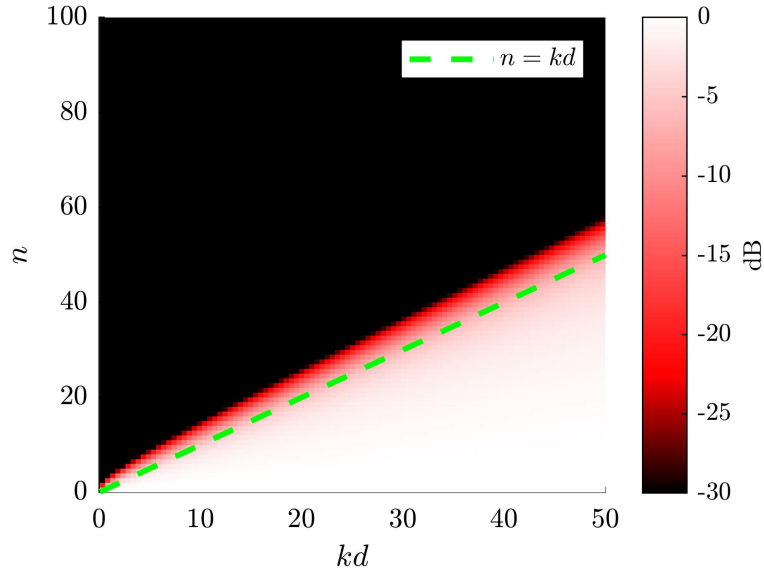


Figure 5.1 Spherical spectrum of the far-field propagator $G_n^{(ff)}$.

dashed line represents $n = kd$, the approximate maximum order limit. Although the large-order relation guarantees a strong filtering effect for $n \gg kd$, the filter response decays rapidly to below -30 dB for $n \gtrsim kd$.

Theoretical models provide additional insights into this spatial filtering effect. A radially vibrating cap on a rigid sphere of radius a is a straightforward model with frequency-dependent directivity [60]. Its applications have included estimating radiation from loudspeakers [10, 58], horns [12], and speech [6]. Figure 5.2(a) plots the p_n^m spectrum on a sphere's surface of radius a with a cap conical half-angle of $\theta_0 = \pi/10$. Significant expansion coefficients appear above the overlaid line $n = ka$ for this near-field evaluation distance. In contrast, the far-field directivity spectrum in Fig. 5.2(b) demonstrates that the far-field propagation filters out the coefficients with $n \gtrsim ka$.

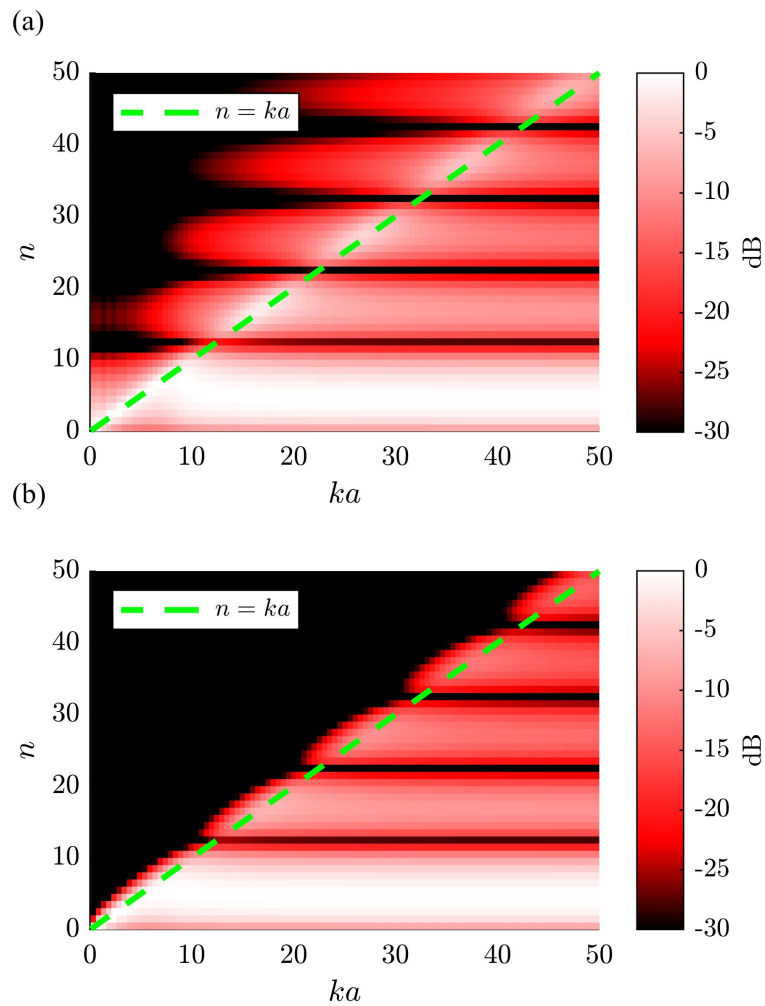


Figure 5.2 Spherical spectrum of the pressure produced by a radially vibrating cap on a rigid sphere of radius a , evaluated at two radial distances: (a) on the sphere's surface and (b) in the far field.

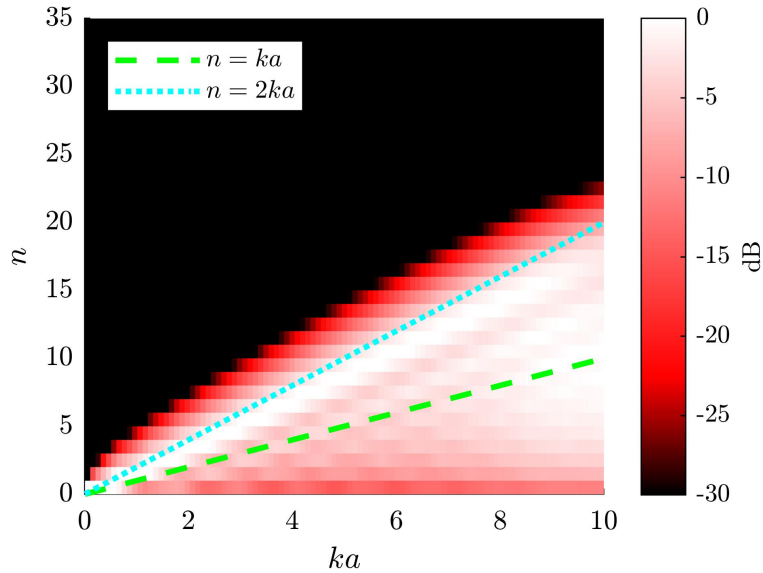


Figure 5.3 Spherical spectrum of the pressure produced by a radially vibrating cap on a rigid sphere centered at the point $\mathbf{r} = (0, 0, a)$.

5.2.2 Effect of Source Translation

Another consideration for source order is the effect of source translation. Previous work has suggested that a source translation of distance r'' from its acoustic center increases the source order by roughly kr'' [28]. To illustrate this principle, Fig. 5.3 plots the spherical spectrum of the vibrating cap on a sphere (see Fig. 5.2) but after a translation $r'' = a$ in the z direction. This translation suggests that the new source order should be $N \approx ka + kr'' = 2ka$, as indicated by the additionally overlaid blue dotted line in Fig. 5.3. As anticipated, the source translation does increase the source's order by roughly kr'' .

5.2.3 Effect of Body Diffraction

Another point of interest is how a diffracting or scattering body alters the source order. The ubiquity of musical instrument and voice directivity measurements without the human body, e.g., from an isolated and artificially excited instrument or dummy head, motivates further investigation of these

effects. Because diffraction about the human body significantly changes musical instrument [72] and voice [81] directivities, one may anticipate that it modifies source orders as well.

A point source in the presence of a rigid spherical scatterer [10] serves as a straightforward theoretical model to explore these effects. Figure 5.4(a) plots the spherical spectrum of the incident field from the source in the far field (i.e., the free field without the presence of the rigid scattering sphere). For a monopole centered at the origin, only the degree $n = 0$ terms are necessary for all frequencies, meaning the low-order representation appears as a solid white band at $n = 0$ in the figure. However, Fig. 5.4(b) plots the far-field spectrum with a rigid sphere of radius a centered at a point $3a$ from the source. Interestingly, even though the rigid sphere does not actively vibrate, it modifies the spherical spectrum, as indicated by the red region delimited approximately by the line $n = ka$. Although the coefficients are significantly smaller than those of the incident field, they illustrate how the diffracting body modifies the spherical spectrum and increases the effective source order.

5.3 Methods for Estimating the Effective Source Dimension from Data

The simple geometries of theoretical models permit straightforward source-order predictions based on physical arguments. However, there are benefits to determining the source orders of more complexly shaped bodies from measured data, which in each case requires predicting d , a source's effective acoustic dimension. This section proposes two methods of estimating this value based on measured or calculated pressure fields. Both attempt to fit the line $n = kd$ to the source's spherical spectrum. The first method applies a fit based on the convergence of norms, while the second involves a fit based on the convergence of the directivity factor function.

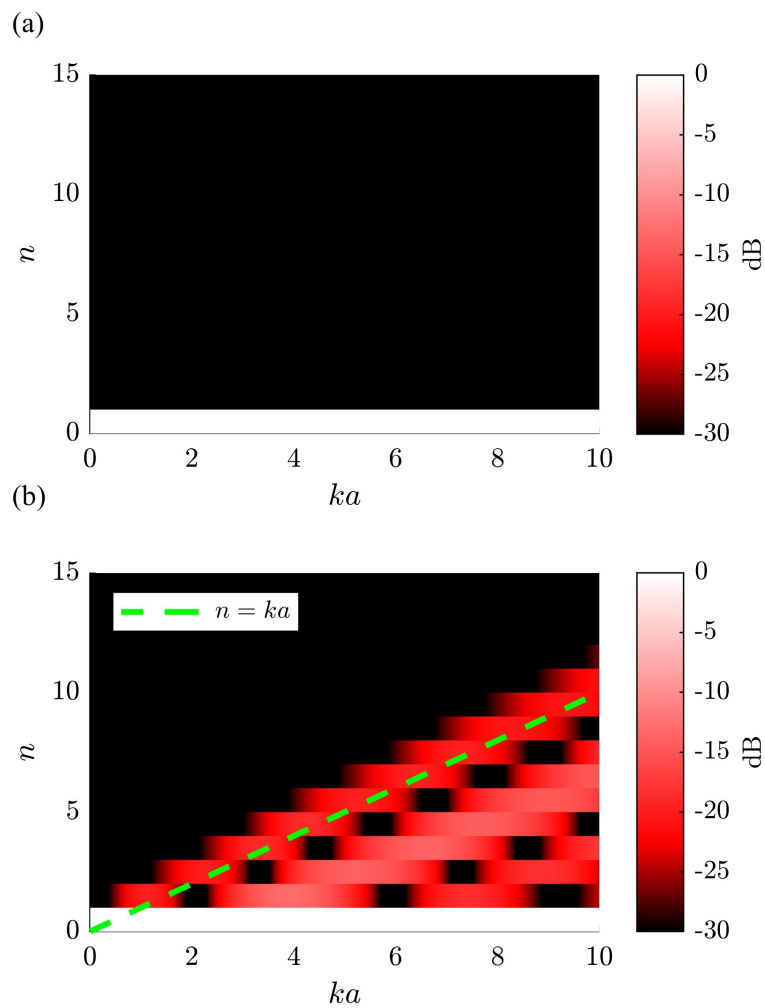


Figure 5.4 Spherical spectrum of the pressure produced by a point source located at the origin for two cases: (a) without a scattering sphere in the field and (b) with a scattering sphere of radius a centered at $\mathbf{r} = (0, 0, 2a)$.

5.3.1 Spectral Energy Method

Directly evaluating ratios of signal energies in the expansion coefficients serves as one approach to estimating the source order. The degree-dependent truncation parameter

$$\gamma(N, k) = \frac{\sum_{n=0}^N \sum_{m=-n}^n |a_n^m(k)|^2}{\sum_{n=0}^{\infty} \sum_{m=-n}^n |a_n^m(k)|^2} \quad (5.11)$$

represents the signal energy lost by truncating the spherical harmonic expansion to degree N . Selecting a threshold value γ determines the minimum source order required to represent the source for a given fidelity. For example, $\gamma = 0.98$ ensures that an expansion loses no more than 0.1 dB of the original signal energy. Evaluating N for several discrete k permits a least-squares fit to $N = kd$ to predict the source's effective acoustic dimension for arbitrary frequency.

5.3.2 Directivity Deviation Method

While Eq. (5.11) provides a spherical-harmonic-domain approach to estimating a source's effective acoustic dimension, a spatial-domain approach ensures that the expanded pressure converges to the measured pressure. To see the effect, let D_N be a directivity function truncated to degree N :

$$D_N(\theta, \phi, k) = \sum_{n=0}^N \sum_{m=-n}^n a_n^m(k) Y_n^m(\theta, \phi). \quad (5.12)$$

An alternative metric is subsequently

$$\mu(N, k) = E[D_N(\theta, \phi, k), D(\theta, \phi, k)], \quad (5.13)$$

where E can be any suitable deviation function, such as a directivity factor function deviation [81] or an area-weighted root-mean-square deviation [6]. Like the spectral energy truncation parameter γ , the threshold value μ determines the required N to represent the measured pattern. However, μ may be more advantageous than γ because it directly relates to deviations in directivity functions. For example, a choice of $\mu = 0.1$ dB would ensure that an expanded directivity function deviates

from its measured data by no more than 0.1 dB in any direction. In contrast, γ does not have a clear physical interpretation. An associated lack of physical understanding could become problematic in situations like that presented in Fig. 5.4, where a poor choice of γ could lead to the exclusion of significant, albeit low-amplitude coefficients. Nonetheless, the spectral energy method is much more computationally efficient because it does not require repeated evaluations of spherical harmonic expansions.

5.4 Results

5.4.1 Musical Instruments

An interesting musical instrument directivity example involves the previously reported radiation from a gamelan ageng lanang gong [98] with the spherical spectrum shown in Fig. 5.5. The overlaid cyan circles indicate the degree at which $\gamma = 0.98$ for 35 modal peaks under 1.5 kHz. The overlaid green dashed line shows the associated least-squares fit to $n = kd$ with $d = 0.54$ m. The latter value corresponds well to a rough geometrical estimate for d based on the gong's 0.41 m radius and the additional support structures used to suspend the instrument. Assuming a maximum $N = 34$ expansion afforded by the measurement's 5° dual-equiangular sampling scheme would limit spherical harmonic analysis to about 3.4 kHz without spatial aliasing.

5.4.2 Speech

Because voice directivity is critical for audio, telecommunications, and acoustical room designs, understanding spatial sampling requirements for speech has many practical benefits. Much like the scattering of sound from a point source by a rigid sphere, human speech radiates from a small radiating region near a much larger diffracting body. Figure 5.6 plots the spherical spectrum at the measurement radius for a female talker [6]. Interestingly, the spectrum shows a strong white band

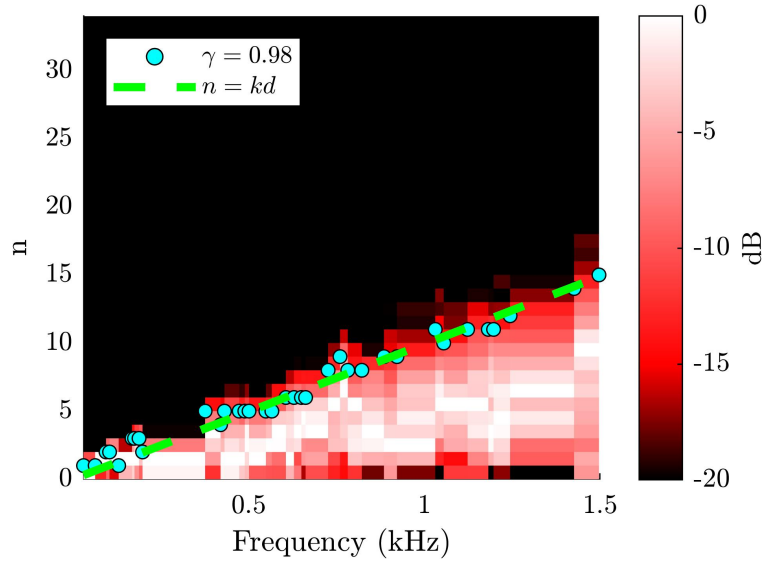


Figure 5.5 Spherical spectrum of a gamelan ageng lanang gong's far-field directivity.

that does not exceed $n = 5$ by 4 kHz. This feature is similar to the prominent band in the spectrum of the point source in the presence of the rigid sphere [see Fig. 5.4(b)].

The cyan dotted line in Fig. 5.6 is $n = kd_h$, where $d_h = 0.09$ m from the head alone provides an initial estimate of the source order. The most significant magnitude coefficients fall below this line. However, because including the entire diffracting human body modifies voice directivity [81], the green dashed line in the figure represents $n = kd_b$, where $d_b = 0.44$ m estimates the source order based on a $\gamma = 0.98$ truncation parameter (see Sec. 5.3.2). This $d_b = 0.44$ m agrees with rough geometrical approximations considering the average spatial extent of a seated human talker.

Figure 5.7 compares various narrowband (1 Hz resolution) speech directivity balloons at 500 Hz to explore the impact of neglecting the lower-amplitude coefficients above $n = kd_h$. Figure 5.7(a) plots the FRF-based directivity acquired from a multiple-capture transfer-function method on the measurement surface [6]. Even at this lower frequency, significantly reduced levels behind the seated talker appear.

The values $k = 9.16 \text{ m}^{-1}$ at 500 Hz and $d_h = 0.09$ m suggest that $N = \lceil kd_h \rceil = 1$ is sufficient for the source representation, where $\lceil \cdot \rceil$ is the ceiling function. Accordingly, Fig. 5.7(b) plots the

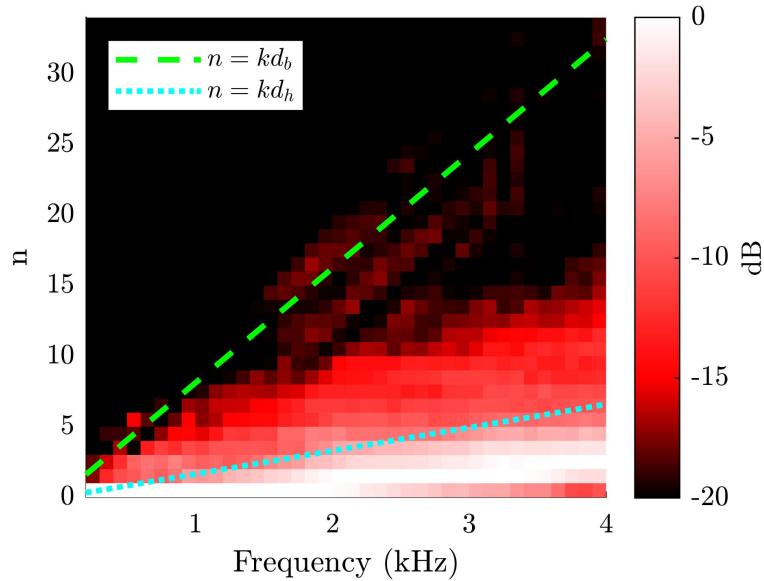


Figure 5.6 Spherical spectrum of a female talker's measured directivity.

propagated far-field directivity based on an $N = 1$ degree expansion. While the expansion preserves some essential directional characteristics, it loses other crucial details, including the distinctive effects of diffraction and absorption about the seated body and chair.

In contrast, using the full-body source dimension estimate $d_b = 0.44$ m yields $N = \lceil kd_b \rceil = 5$ as the expansion limit for the improved directivity approximation in Fig. 5.7(c). Finally, Fig. 5.7(d) plots the far-field propagated directivity based on an $N = 34$ expansion. These final two directivities show much better agreement with the raw data and include the locations of reduced sound levels due to diffraction about the body. The directivity factor deviation function levels [81] between the $N = 34$ degree far-field directivity expansion and the $N = 1$ and $N = 5$ degree expansions are 1.2 dB and 0.5 dB, respectively.

From this example, it is apparent that estimating a source's effective dimension requires careful consideration. For $d_b = 0.44$ m, spatial aliasing limits spherical-harmonic analysis on complex-valued narrowband data beyond 4.2 kHz. This limits assumes that this frequency is sufficiently in

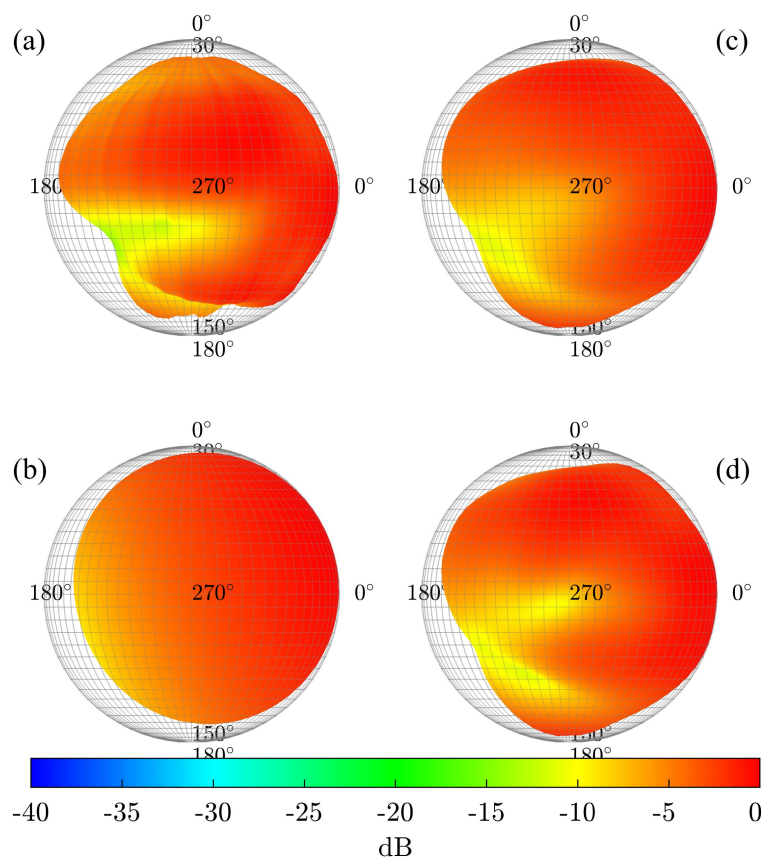


Figure 5.7 Narrowband female voice directivities at 500 Hz. (a) Measured FRF-based balloon. Far-field directivities based on (b) $N = 1$, (c) $N = 5$, and (d) $N = 34$ degree spherical harmonic expansions.

the far-field for the given measurement radius. Because far-field propagation filters higher-order terms, a near-field measurement radius may further restrict the usable measurement frequency.

5.5 Discussion and Conclusions

Plotting the spherical spectrum of a source is a powerful tool for analyzing sampling limitations and source orders. This work's theoretical and experimental results confirm that an effective acoustic dimension may help characterize source order. The presented techniques allow researchers and practitioners to estimate the required number of sampling positions for a given source while highlighting limitations to current sampling standards.

For the sources considered in this work, AES 5° dual-equiangular sampling [33], currently the highest standardized directivity resolution, is often only sufficient to allow spherical-harmonic-based analysis up to a few kilohertz. Comprehensive, spherical-harmonic-based analysis of complex-valued narrowband data over the entire audio bandwidth would require significantly higher sampling density. For example, using the effective source dimension of $d = 0.44$ m given in Sec. 5.4.2, analysis up to 20 kHz ($k \approx 370$ m⁻¹) would require $N \approx 162$ degree expansions. Dual-equiangular sampling with 1° resolution and 64,082 unique positions over a sphere would satisfy this requirement [77, 78]. However, this density would dramatically increase the numbers of sampling positions used in current sampling standards and practices.

Future work could consider other methods for estimating a source's effective acoustic dimension. Efforts that tabulate these dimensions for common sources would benefit experimentalists in their measurement designs.

Chapter 6

Quadrature for Dual-Equiangular Sampling

This chapter compares three quadrature rules for equiangular sampling. The results highlight the utility of equiangular sampling compared to Gaussian sampling and demonstrate the benefits of dual-equiangular sampling.

6.1 Introduction

Audio engineers and acousticians have long acknowledged the importance of source directivity measurements for characterizing the frequency-dependent angular properties of radiated sound fields in free space. The measurements are pertinent for many areas of audio, including room acoustics [20,21], auralizations [18,19,99], sound systems [84], microphone placements [14,15,17], and others. Obtaining meaningful directivity data requires sampling at numerous locations about a source. However, regardless of the acquisition method, all directivity assessments yield data with finite sampling points or contours. Thorough leveraging of sampled data requires effective quadrature rules (or least-squares techniques) for the most meaningful processing and analysis [31,59,77].

Spherical directivity measurements typically fall into single-capture or multiple-capture categories. Single-capture measurements employ a fixed number of array microphones, e.g., 13, 32, or 64, sampling the radiated field simultaneously, often with relatively uniform distributions [18, 31, 100, 101]. This approach is especially beneficial for live sources, e.g., played musical instruments or speech, whose sound radiation is not as repeatable or controllable as that of loudspeakers or other transducers. Its primary drawback is the infeasible number of microphones, cables, channels, and support structures required for high-resolution results.

By contrast, multiple-capture measurements employ repeated source radiations and sectional spherical acquisitions to scan sound fields sequentially over the observation surface. They involve individual moving microphones, rotating microphone arrays, or sources attached to computer-controlled rotation apparatuses. Microphone arrays are often semi-circular or quarter-circular for longitudinal acquisitions [5, 13, 21, 34, 102–104], but other configurations are also possible [37, 105–107]. Most multiple-capture schemes encompass and parameterize a spherical or hemispherical surface via selected polar and azimuthal sampling angles. Array microphone spacings often control the polar-angle resolution, while rotational increments often control the azimuthal-angle resolution. Sampling is often equiangular for each coordinate [21, 34, 102], but irregular polar sampling schemes are also possible [5, 26, 103].

The AES56-2008 (r2019) standard has regulated loudspeaker directivity measurements via *dual*-equiangular sampling having 5° or 10° resolution for *both* angles [33]. Recent efforts have applied similar sampling to live sources [1, 6]. However, development and clarification of suitable quadrature rules for these and other spherical measurement schemes would benefit from numerical integration for the calculations of sound power [26, 62], directivity deviation metrics [6, 13], spherical harmonic expansions [9, 31, 77, 78], and other results.

An early numerical integration method over the sphere applied Gauss-Legendre quadrature to the polar angle [108]. It has become pertinent to many fields of investigation and remains popular

today because of its accuracy [109]. The method's primary drawback is that its sampling nodes fall at Legendre polynomial zeros, leading to uneven and inconvenient spacings in the polar angle. Consequently, the approach has seen relatively limited use in audio and acoustical applications compared to the AES dual-equiangular scheme, although notable exceptions exist [110, 111].

The exploration of spherical equiangular quadrature rules dates back at least to the work of Shukowsky [112], but several texts reference the work of Driscoll and Healy [113] in relationship to spherical signal processing [77, 114]. A significant disadvantage of the latter is that the zenith (north-pole) and nadir (south-pole) weights are always zero, meaning the approach does not leverage the full potential of the AES standard. Later improvements avoided pole sampling by shifting the sampling positions a half interval (e.g., such that the first sample falls at 2.5° for 5° polar equiangular sampling) [115] as in Shukowsky's earlier method [112].

A quadrature rule directly applicable to AES56-2008 (r2019) would be valuable, as would rules addressing practical variations, such as those that include only one pole position at the zenith or nadir or hemispherical sampling. Furthermore, Driscoll and Healy's original equiangular rule applies to an azimuthal angle sampling density that is only half that of the polar angle density, e.g., 10° azimuthal spacing for 5° polar spacing [113]. The possible benefits of doubling their sampling density, as in the AES dual-equiangular scheme [33], have remained unclear.

This work addresses the various deficiencies of past methods by first demonstrating that the Driscoll and Healy rule falls under the class of Clenshaw-Curtis quadrature rules [116], based on Chebyshev polynomials of the second kind. It then develops two rules for equiangular sampling based on Chebyshev polynomials of the first and third kinds. The former is a Lobatto-type rule derived initially by Imhof [117], using both the zenith and nadir positions; the latter is a Radau-type rule, using only one of the two poles. Additional modifications extend the quadrature rules to hemispherical measurements.

Numerical experiments illustrate the improved robustness of the proposed rules, including for applications that employ spherical harmonic expansions. The developments verify that the performances of Chebyshev-type quadrature rules are quite similar to those of Gaussian quadrature rules [118], allowing converging expansions to higher degrees than previously considered. Simulations based on theoretical models provide insights into spatial aliasing limitations, further confirming their performances. The results suggest that the AES56-2008 (r2019) approach of equal polar and azimuthal angular resolutions is beneficial. The following sections clarify these and other matters pertinent to equiangular and dual-equiangular sampling and provide resources for researchers and practitioners to evaluate associated spherical integrals more effectively for directivity-related applications.

6.2 Numerical Integration For Equiangular Sampling Schemes

The parameterization of the sphere via equiangular polar and azimuthal sampling allows calculation of a spherical integral as [108]

$$\int_0^{2\pi} \int_0^\pi f(\theta, \phi) \sin \theta d\theta d\phi = \sum_{a=1}^A \sum_{b=1}^B w_a w_b f(\theta_a, \phi_b) + E[f(\theta, \phi)], \quad (6.1)$$

where $f(\theta, \phi)$ is a function over the sphere, θ_a and ϕ_b are the discrete polar and azimuthal-angle sampling nodes, respectively, and w_a and w_b are the associated quadrature weights. The error functional $E[f(\theta, \phi)]$ pertains to the specific quadrature scheme in question. When $E[f(\theta, \phi)] = 0$ for numerical integration of any polynomial up to degree M , the scheme is exact to that degree.

6.2.1 Azimuthal Sampling

The azimuthal-angle quadrature weights allow integral calculations of the form

$$\int_0^{2\pi} f(\phi) d\phi = \sum_{b=1}^B w_b f(\phi_b) + E[f(\phi)] \quad (6.2)$$

for 2π -periodic $f(\phi)$. With equiangular sampling, the nodes fall at

$$\phi_b = \frac{2\pi(b-1)}{B} = (b-1)\Delta\phi, \quad b = 1, 2, \dots, B, \quad (6.3)$$

where $\Delta\phi = 2\pi/B$. The quadrature weights are [108, 109]

$$w_b = \frac{2\pi}{B} = \Delta\phi \quad (6.4)$$

and are exact to degree B [108].

The weights are rotationally invariant because the integrand is periodic and the sampling nodes are evenly spaced. Since they are exact in integrating a constant, i.e., a degree zero polynomial,

$$\int_0^{2\pi} d\phi = \sum_{b=1}^B w_b = 2\pi, \quad (6.5)$$

such that the sum of the weights equals the integration interval.

6.2.2 Polar Sampling

The polar-angle weights enable integral calculations of the form

$$\int_0^\pi f(\theta) \sin \theta d\theta = \int_{-1}^1 f(x) dx = \sum_{a=1}^A w_a f(x_a) + E[f(x)], \quad (6.6)$$

using the transformation $x = \cos \theta$. This equation is unlike Eq. (6.2) in that there is no required symmetry that produces a simple integral formula. Hence, various quadrature rules may arise, depending on the collocation points θ_a . However, similar to Eq. (6.5), when the weights are exact for integrating a constant,

$$\int_0^\pi \sin \theta d\theta = \int_{-1}^1 dx = \sum_{a=1}^A w_a = 2, \quad (6.7)$$

such that

$$\int_0^{2\pi} \int_0^\pi \sin \theta d\theta d\phi = \sum_{a=1}^A \sum_{b=1}^B w_a w_b = 4\pi. \quad (6.8)$$

This equation provides a useful means to verify the proper scaling of the quadrature weights.

For positive integer K , the $\Delta\theta = \pi/K$ spacing of equiangular polar sampling nodes coincides with the zeros and extrema of the Chebyshev polynomials [116]. Consequently, Chebyshev quadrature rules are natural choices for equiangular sampling on the sphere. The following sections propose three quadrature rules based more specifically on Clenshaw-Curtis Chebyshev quadrature [116, 119, 120]. Although the rules follow from well-established mathematical methods, they require distinct applications for their derivations. In particular, they require well-considered choices for two components: (1) a discrete orthogonality relation for the Chebyshev polynomials and (2) an appropriate integral weighting function.

Mason and Handscomb noted that there are at least sixteen discrete orthogonality relations [116], allowing a rich variety of rule possibilities. This work presents relations based on Chebyshev polynomials of the first, second, and third kinds of degree n , which are bases for its three rules. With the transformation $x = \cos \theta$, the respective polynomials have the forms

$$T_n(x) = T_n(\cos \theta) = \cos n\theta, \quad (6.9)$$

$$U_n(x) = U_n(\cos \theta) = \frac{\sin(n+1)\theta}{\sin \theta}, \quad (6.10)$$

and

$$V_n(x) = V_n(\cos \theta) = \frac{\cos(n + \frac{1}{2})\theta}{\cos \frac{1}{2}\theta}. \quad (6.11)$$

For numerical integration over the sphere, the weighting function in

$$\int_{-1}^1 f(x)W(x)dx \quad (6.12)$$

is conveniently $W(x) = 1$.

6.2.3 Chebyshev Quadrature

As illustrated in Fig. 6.1(a), the first spherical quadrature scheme relies on equally spaced points not including the zenith and nadir endpoints. The weights reduce to those presented by Driscoll and

Healy [113], with minor modifications. The $K - 1$ sampling points are

$$x_k = \cos \theta_k = \cos \frac{k\pi}{K}, \quad k = 1, 2, \dots, K - 1, \quad (6.13)$$

such that $A = K - 1$ in the general quadrature rule of Eq. (6.6). The discrete orthogonality rule [116]

$$d_{nm} = \sum_{k=1}^{K-1} (1 - x_k^2) U_n(x_k) U_m(x_k) = \begin{cases} 0 & n \neq m \\ \frac{1}{2}K & n = m \end{cases} \quad (6.14)$$

applies to Chebyshev polynomials of the second kind for degrees $0 \leq n \leq K - 2$.

If $f(x)$ is a function of maximum polynomial degree $M = K - 2$,

$$f(x) = \sum_{n=0}^{K-2} a_n U_n(x), \quad (6.15)$$

where a_n are the expansion coefficients and

$$\begin{aligned} \int_{-1}^1 f(x) dx &= \sum_{n=0}^{K-2} a_n \int_{-1}^1 U_n(x) dx \\ &= \sum_{n=0}^{K-2} a_n u_n, \end{aligned} \quad (6.16)$$

where

$$\begin{aligned} u_n &= \int_{-1}^1 U_n(x) dx \\ &= \begin{cases} \frac{2}{n+1}, & n = 0, 2, 4, \dots \\ 0, & n = 1, 3, 5, \dots \end{cases}. \end{aligned} \quad (6.17)$$

The coefficients result from multiplying both sides of Eq. (6.15) by $(1 - x_k^2)U_m(x_k)$ and summing over the discrete indices to yield

$$\begin{aligned} \sum_{k=1}^{K-1} (1 - x_k^2) U_m(x_k) f(x_k) &= \sum_{n=0}^{K-2} a_n \sum_{k=1}^{K-1} U_n(x_k) U_m(x_k) (1 - x_k^2) \\ &= a_n d_{nm}, \end{aligned} \quad (6.18)$$

such that

$$a_n = \frac{2}{K} \sum_{k=1}^{K-1} (1 - x_k^2) U_n(x_k) f(x_k). \quad (6.19)$$

Through this definition and Eq. (6.17), Eq. (6.16) becomes

$$\begin{aligned} \int_{-1}^1 f(x) dx &= \frac{2}{K} \sum_{k=1}^{K-1} f(x_k) \sum_{n=0}^{K-2} u_n U_n(x_k) (1 - x_k^2) \\ &= \sum_{k=1}^{K-1} w_k f(x_k), \end{aligned} \quad (6.20)$$

which, using $U_n(x)$ defined in Eq. (6.10) and the relation $(1 - x_k^2) = \sin^2 \theta_k$, shows that the quadrature weights are

$$w_k = \frac{4}{K} \sin \theta_k \sum_{\substack{n=0 \\ n \text{ even}}}^{K-2} \frac{\sin(n+1)\theta_k}{n+1}. \quad (6.21)$$

The indexing of n to include zero and skip odd values in Eq. (6.21) yields agreement with the weights presented by Driscoll and Healy, with a few adjustments. First, the Driscoll and Healy weights and those of Refs. [77] and [114] include a sampling node at $\theta = 0$. However, because $\sin \theta_k$ multiplies the sum in Eq. (6.21), any sampling node at the poles is zero and therefore unnecessary. Additionally, there is a slight scaling variation as reported in Ref. [114] due to differing definitions of the orthogonality relations. The weights presented here conform to the relation in Eq. (6.7), so that their sum is 2. Finally, Driscoll and Healy only contemplated K as a power of two for compatibility with fast-Fourier transforms. However Eq. (6.21) remains valid for any K .

As suggested earlier, these weights fall into the general family of Clenshaw-Curtis quadrature rules developed decades before Driscoll and Healy's work on spherical sampling. For equiangular spacing $\Delta\theta = \pi/K$, the $K - 1$ sampling nodes of Eq. (6.13) and their weights in Eq. (6.21) guarantee an exact quadrature rule for up to at least degree $M = K - 2$ polynomials. Figure 6.2 plots the Chebyshev weights for the case of $K = 9$ (20°) equiangular sampling as a red dash-dot line. Table 6.1 provides numerical values for the $K = 9$ (20°), $K = 18$ (10°), and $K = 36$ (5°) equiangular sampling weights.

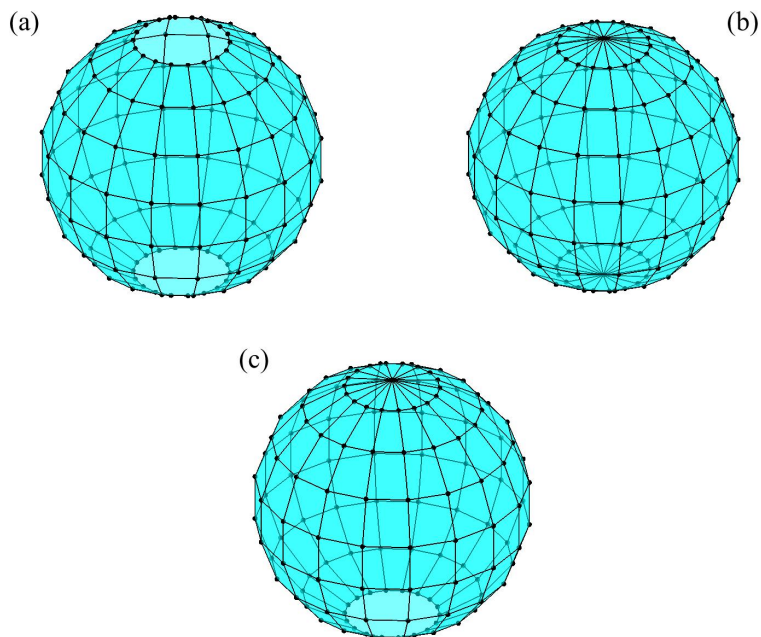


Figure 6.1 Illustrations of the spherical sampling positions for $K = 9$ (20°) dual equiangular sampling. (a) Chebyshev sampling. (b) Chebyshev-Lobatto sampling. (c) Chebyshev-Radau sampling.

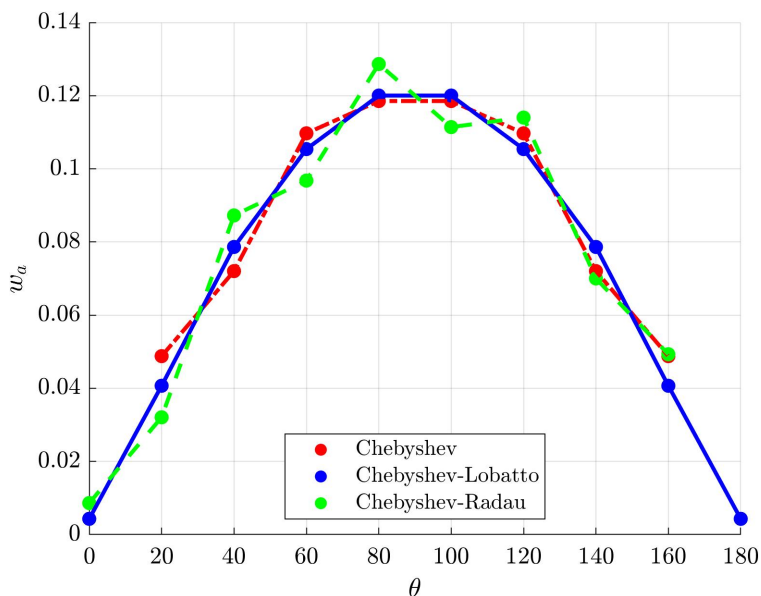


Figure 6.2 Polar angle quadrature weights w_a for the case $K = 9$ (20° equiangular sampling) and three quadrature rules.

Table 6.1 Polar-angle quadrature weights w_k for three equiangular quadrature rules. Each empty space indicates that no sampling node falls at the angle for the given sampling type and K value.

θ_w	Chebyshev			Chebyshev-Lobatto			Chebyshev-Radau		
	$K = 36$	$K = 18$	$K = 9$	$K = 36$	$K = 18$	$K = 9$	$K = 36$	$K = 18$	$K = 9$
0°				0.0008	0.0031	0.0123	0.0000	0.0000	0.0247
5°	0.0090			0.0074			0.0090		
10°	0.0137	0.0358		0.0152	0.0296		0.0137	0.0358	
15°	0.0241			0.0226			0.0241		
20°	0.0283	0.0538	0.1398	0.0299	0.0600	0.1166	0.0283	0.0538	0.0919
25°	0.0384			0.0369			0.0384		
30°	0.0421	0.0933		0.0436	0.0871		0.0421	0.0933	
35°	0.0516			0.0500			0.0516		
40°	0.0546	0.1061	0.2064	0.0561	0.1123	0.2253	0.0546	0.1061	0.2500
45°	0.0632			0.0617			0.0632		
50°	0.0653	0.1398		0.0669	0.1336		0.0653	0.1398	
55°	0.0730			0.0715			0.0730		
60°	0.0740	0.1450	0.3143	0.0756	0.1512	0.3019	0.0740	0.1450	0.2772
65°	0.0806			0.0791			0.0806		
70°	0.0805	0.1702		0.0820	0.1640		0.0805	0.1702	
75°	0.0858			0.0843			0.0858		
80°	0.0844	0.1657	0.3396	0.0859	0.1719	0.3439	0.0844	0.1657	0.3686
85°	0.0885			0.0869			0.0885		
90°	0.0857	0.1807		0.0873	0.1745		0.0857	0.1807	
95°	0.0885			0.0869			0.0885		
100°	0.0844	0.1657	0.3396	0.0859	0.1719	0.3439	0.0844	0.1657	0.3192
105°	0.0858			0.0843			0.0858		
110°	0.0805	0.1702		0.0820	0.1640		0.0805	0.1702	
115°	0.0806			0.0791			0.0806		
120°	0.0740	0.1450	0.3143	0.0756	0.1512	0.3019	0.0740	0.1450	0.3266
125°	0.0730			0.0715			0.0730		
130°	0.0653	0.1398		0.0669	0.1336		0.0653	0.1398	
135°	0.0632			0.0617			0.0632		
140°	0.0546	0.1061	0.2064	0.0561	0.1123	0.2253	0.0546	0.1061	0.2006
145°	0.0516			0.0500			0.0516		
150°	0.0421	0.0933		0.0436	0.0871		0.0421	0.0933	
155°	0.0384			0.0369			0.0384		
160°	0.0283	0.0538	0.1398	0.0299	0.0600	0.1166	0.0283	0.0538	0.1413
165°	0.0241			0.0226			0.0241		
170°	0.0137	0.0358		0.0152	0.0296		0.0137	0.0358	
175°	0.0090			0.0074			0.0090		
180°				0.0008	0.0031	0.0123			

6.2.4 Chebyshev-Lobatto Quadrature

While the equiangular quadrature scheme of the preceding section is clearly useful, its unfortunate zero pole weights effectively discard two beneficial sampling positions from the AES standard [33]. An alternative scheme employs a Lobatto-type quadrature rule that includes both pole positions. As suggested in Fig. 6.1b,

$$x_k = \cos \frac{k}{K\pi}, \quad k = 0, 1, \dots, K, \quad (6.22)$$

comprising $K + 1$ equiangular sampling points [$A = K + 1$ in Eq. (6.6)].

The discrete orthogonality relation for Chebyshev polynomials of the first kind is [116]

$$\begin{aligned} d_{nm} &= \sum_{k=0}^K \varepsilon_{0k} \varepsilon_{Kk} T_n(x_k) T_m(x_k) \\ &= \begin{cases} 0 & n \neq m \\ \frac{K}{2\varepsilon_{0n} \varepsilon_{Kn}} & n = m \end{cases}, \end{aligned} \quad (6.23)$$

where

$$\varepsilon_{nk} = \begin{cases} 1, & n \neq k \\ \frac{1}{2} & n = k \end{cases}. \quad (6.24)$$

Following the steps in Sec. 6.2.3 and using the relation

$$\int_{-1}^1 T_n(x) dx = \begin{cases} \frac{2}{1-n^2}, & n = 0, 2, 4, \dots \\ 0, & n = 1, 3, 5, \dots \end{cases} \quad (6.25)$$

yields the quadrature weights

$$w_k = \varepsilon_{0k} \varepsilon_{Kk} \frac{4}{K} \sum_{\substack{n=0 \\ n \text{ even}}}^K \varepsilon_{0n} \varepsilon_{Kn} \frac{\cos(n\theta_k)}{1-n^2}. \quad (6.26)$$

Imhof [117] originally derived these weights in 1963 but they have not generally appeared in audio and acoustical applications involving spherical sampling [77, 114]. For the equiangular

spacing $\Delta\theta = \pi/K$, the $K + 1$ sampling nodes of Eq. (6.22) and weights of Eq. (6.26) guarantee exact quadrature up to at least degree $M = K$ instead of degree $M = K - 2$ for the straight Chebyshev quadrature. The nodes and weights are also fully compatible with the AES directivity measurement standard. Figure 6.2 plots the Chebyshev-Lobatto quadrature weights for $K = 9$ as a solid blue line and Table 6.1 presents the numerical weight values for $K = 9$, $K = 18$, and $K = 36$.

6.2.5 Chebyshev-Radau Quadrature

In some measurement applications, a support structure or rotation apparatus may obstruct the sampling at one of the poles. In this case, dropping that sampling position while utilizing all other positions, including the opposite pole, would be ideal. A Radau-type quadrature rule enables this adaptation.

The K equiangular points that include the zenith but not the nadir are

$$x_k = \cos \frac{k}{K\pi}, \quad k = 0, 1, \dots, K - 1 \quad (6.27)$$

[$A = K$ in Eq. (6.6)]. The discrete orthogonality relation for Chebyshev polynomials of the third kind is [116]

$$\begin{aligned} d_{nm} &= \sum_{k=0}^{K-1} \varepsilon_{0k} (1 + x_k) V_n(x_k) V_m(x_k) \\ &= \begin{cases} 0 & n \neq m \\ K & n = m \end{cases}, \end{aligned} \quad (6.28)$$

where $0 \leq n \leq K - 1$. The relation

$$\int_{-1}^1 V_n(x) dx = \begin{cases} 2, & n = 0 \\ \frac{(-1)^n (1 + 2n) - 1}{n(n+1)}, & n > 1 \end{cases}, \quad (6.29)$$

yields the quadrature weights

$$\begin{aligned} w_k &= \varepsilon_{0k} \frac{(1 + \cos \theta_k)}{K \cos \frac{1}{2} \theta_k} \sum_{n=0}^{K-1} v_n \cos \left(n + \frac{1}{2} \right) \theta_k \\ &= \varepsilon_{0k} \frac{2}{K} \cos \frac{1}{2} \theta_k \sum_{n=0}^{K-1} v_n \cos \left(n + \frac{1}{2} \right) \theta_k, \end{aligned} \quad (6.30)$$

where the last line results from the cosine half-angle formula.

For the equiangular spacing $\Delta\theta = \pi/K$, the K sampling nodes of Eq. (6.27) and the respective weights of Eq. (6.30) guarantee an exact quadrature rule for polynomials up to at least degree $M = K - 1$. Figure 6.2 plots the Chebyshev-Radau quadrature weights for $K = 9$ as a dashed green line and Table 6.1 presents values of the quadrature weights for $K = 9$, $K = 18$, and $K = 36$.

When K is even so that a sampling position falls at $\theta = \pi/2$, the zenith weight becomes zero and the Chebyshev-Radau weights reduce to the Chebyshev weights of Eq. (6.21). As shown in Table 6.1, this is the case for $K = 36$ (5°) and $K = 18$ (10°). However, for odd $K = 9$ (20°), Eq. (6.30) yields a unique set of weights, including a nonzero zenith weight.

Applying a discrete orthogonality relation of the Chebyshev polynomials of the fourth kind yields a quadrature rule for equiangular sampling points that include the nadir but not the zenith. However, the respective weights are those of Eq. (6.30) but reflected across $\theta = \pi/2$ as one may anticipate from symmetry arguments.

6.2.6 Hemispherical Quadrature Rules

Researchers have applied hemispherical measurements to the piano [102], harp [104], Korean traditional musical instruments [21], gamelan gongs and metallophones [31], axial cooling fans [103], drones [121], and many other sources. The ISO 3745 standard also specifies a hemispherical method for evaluating the sound power of a source [26]. Such widespread use of hemispherical sampling justifies a brief treatment here to help optimize associated measurements and improve their utility.

The key to producing an applicable quadrature rule for the hemisphere is to enforce a fictitious symmetry about $\theta = \pi/2$. With reference to Eq. (6.6), a function $g(\theta)$ that includes the reflection of a hemispherical ($0 \leq \theta \leq \pi/2$) function $f(\theta)$ leads to the integral relationship

$$\begin{aligned} \int_0^{\pi/2} f(\theta) \sin \theta d\theta &= \frac{1}{2} \int_0^{\pi} g(\theta) \sin \theta d\theta \\ &= \frac{1}{2} \sum_{a=1}^A w_a g(\theta_a) \\ &= \sum_{a=1}^A w'_a f(\theta_a), \end{aligned} \quad (6.31)$$

where

$$w'_a = \begin{cases} w_a & \theta_a \neq \frac{\pi}{2} \\ \frac{1}{2}w_a & \theta_a = \frac{\pi}{2} \end{cases} \quad (6.32)$$

and w_a represents the weights of any of the quadrature rules discussed in Secs. 6.2.3 through 6.2.5. In other words, only the weight at $\pi/2$ requires modification.

From a practical standpoint, it may be challenging to sample the field at exactly $\theta = \pi/2$ when the hemisphere extends to a rigid boundary at the x - y plane, e.g., the floor of a hemi-anechoic environment. Consequently, sampling with odd K is beneficial to avoid a sampling node at this position.

6.3 Spherical Harmonic Expansions

A key application of spherical numerical integration involves evaluating spherical harmonic expansion coefficients [77, 110, 114]. The coefficients find uses in numerous operations, including smoothing, spatial filtering, and interpolating directivity functions [59]. As angular solutions to the Helmholtz equation, spherical harmonic expansions have many applications, including field extrapolations via acoustical holography and acoustic source centering [27, 28, 59]. Hence, it is

difficult to overstate the importance of reliably deriving expansion coefficients from discretely sampled data.

The normalized spherical harmonics

$$Y_n^m(\theta, \phi) = \sqrt{\frac{2n+1}{4\pi} \frac{(n-m)!}{(n+m)!}} P_n^m(\cos \theta) e^{im\phi} \quad (6.33)$$

of degree n and order m include the associated Legendre functions $P_n^m(\cos \theta)$ of the same degree and order [70], and form a complete orthogonal basis for $L^2(\mathcal{S}^2)$, the space of (Lebesgue) square-integrable functions on the sphere. The inner product on this space is [114]

$$\langle f, g \rangle = \int_0^\pi \int_0^{2\pi} f(\theta, \phi) g^*(\theta, \phi) \sin \theta d\theta d\phi \quad (6.34)$$

which induces the norm

$$\|f\|_{L^2}^2 = \int_0^\pi \int_0^{2\pi} |f(\theta, \phi)|^2 \sin \theta d\theta d\phi. \quad (6.35)$$

Any function $f \in L^2(\mathbb{S}^2)$ admits a spherical harmonic representation

$$f(\theta, \phi) = \sum_{n=0}^{\infty} \sum_{m=-n}^n f_n^m Y_n^m(\theta, \phi), \quad (6.36)$$

where f_n^m are the expansion coefficients, which follow from orthogonality:

$$f_n^m = \langle f, Y_n^m \rangle = \int_0^\pi \int_0^{2\pi} f(\theta, \phi) [Y_n^m(\theta, \phi)]^* \sin \theta d\theta d\phi. \quad (6.37)$$

The norm in the space of square summable sequences ℓ^2 is

$$\|f_n^m\|_{\ell^2}^2 = \sum_{n=0}^{\infty} \sum_{m=-n}^n |f_n^m|^2, \quad (6.38)$$

where

$$\|f_n^m\|_{\ell^2} = \|f\|_{L^2} \quad (6.39)$$

from Parseval's theorem.

Discrete sampling positions limit the number of expansion coefficients one may reliably calculate [77]. While a least-squares fit for the coefficients is viable, quadrature rules provide valuable and

practical insights into the maximum expansion degree N . Substitution of Eq. (6.36) into Eq. (6.37) yields

$$f_n^m = \sum_{p=0}^{\infty} \sum_{q=-p}^p f_p^q \langle Y_p^q, Y_n^m \rangle, \quad (6.40)$$

which represents an infinite sum of integrals of spherical harmonics with integrand degree $n + p$. When analytically evaluated, the inner products reduce to Kronecker deltas due to orthogonality, such that these integrals vanish when $p \neq n$ or $q \neq m$. However, quadrature errors arise with discrete sampling and numerical integration, leading to spatial aliasing errors [77].

If f has maximum degree N , the integrand's degree in Eq. (6.37) will become $2N$ for evaluating spherical harmonic expansion coefficients of degree N . Thus, to exactly evaluate the expansion coefficients up to degree N , the quadrature rule must be exact to degree $M = 2N$. Therefore, for spherical harmonic expansions, the Chebyshev sampling scheme should be exact to at least $N_{ch} = \lfloor (K - 2)/2 \rfloor = \lfloor K/2 - 1 \rfloor$, where $\lfloor \cdot \rfloor$ indicates rounding down to the nearest integer [113]. Similarly, the Chebyshev-Lobatto scheme should be exact to at least $N_{ch,l} = \lfloor K/2 \rfloor$, and the Chebyshev-Radau scheme should be exact to at least $N_{ch,r} = \lfloor (K - 1)/2 \rfloor$. For example, $K = 36$ sampling (AES 5° resolution) yields an exact Chebyshev-Lobatto result to at least degree $N_{ch,l} = 18$.

It is also instructive to consider the limit of Gaussian quadrature using the same number of sampling nodes. Gaussian quadrature is exact to degree $M = 2A - 1$ for A nodes [108]. Thus, for the same number of nodes as Chebyshev quadrature, $N_g = \lfloor (2(K - 1) - 1)/2 \rfloor = K - 2$. For the same number of nodes as Chebyshev-Lobatto quadrature, $N_{g,l} = \lfloor (2(K + 1) - 1)/2 \rfloor = K$.

To illustrate these concepts, Fig. 6.3 plots values of $\langle Y_n^0, Y_n^0 \rangle$ as a function of degree n and four sampling densities: $K = 9$ (20°), $K = 18$ (10°), $K = 36$ (5°), and $K = 45$ (4°). Setting $m = 0$ ensures consideration of only the polar angle weight accuracy. (Section 6.4.2 explores the impact of azimuthal sampling density.) In addition to the three types of Chebyshev quadrature presented earlier, a rule based on geometrically approximated effective sampling areas [13] provides an additional reference for comparison. The black dashed vertical line indicates the exact maximum

degree N_{ch} expected for regular Chebyshev sampling, and the black dotted vertical line indicates the corresponding degree N_g for the Gaussian quadrature.

Several significant trends in the plots are noteworthy. First, the Chebyshev-type quadrature rules remain exact to the anticipated degrees. Second, the errors above those degrees remain minimal ($< 0.1\%$) up to nearly the Gaussian-quadrature limit, especially for higher K schemes. Third, when K is odd so that the Chebyshev-Radau weights differ from the Chebyshev weights ($K = 9$ and $K = 45$), their performance is better, achieving accuracy similar to the Chebyshev-Lobatto weights. Fourth, relative error decreases as K increases, highlighting that accuracy and exactness are not equivalent.

While it is often straightforward to define exactness mathematically, accuracy is more difficult to characterize. Previous work has shown that while Clenshaw-Curtis Chebyshev quadrature rules are not exact to the same degree as Gaussian quadrature rules, they remain robust and comparable in reliability while affording more convenient sampling configurations [78, 118]. Indeed, Trefethen found that “the supposed factor-of-2 advantage of Gauss quadrature is rarely realized” [118]. The performance of the effective sampling area weights further validates this concept. While the weights originated from simple geometrical arguments, they perform comparably with the Chebyshev methods. Thus, while a degree of exactness is valuable, one should also consider the general performance accuracy of any quadrature rule.

To further explore the proposed schemes’ accuracies, Fig. 6.4 plots their spherical harmonic expansion convergences for a unit cube function [78]. This function is interesting and convenient because of its flat faces, sharp edges, and corners, which require high-degree spherical harmonics. A fine $K = 100$ Chebyshev-Lobatto sampling grid serves as a reference for the exact evaluation of the expansion coefficients f_n^m to degree $N = 50$. The root-mean-square deviation (RMSD) curves follow by calculating the estimated expansion coefficients \hat{f}_n^m to increasing degree N for the three Chebyshev quadrature schemes and the effective area scheme when $K = 36$ (5°). The RMSD thus

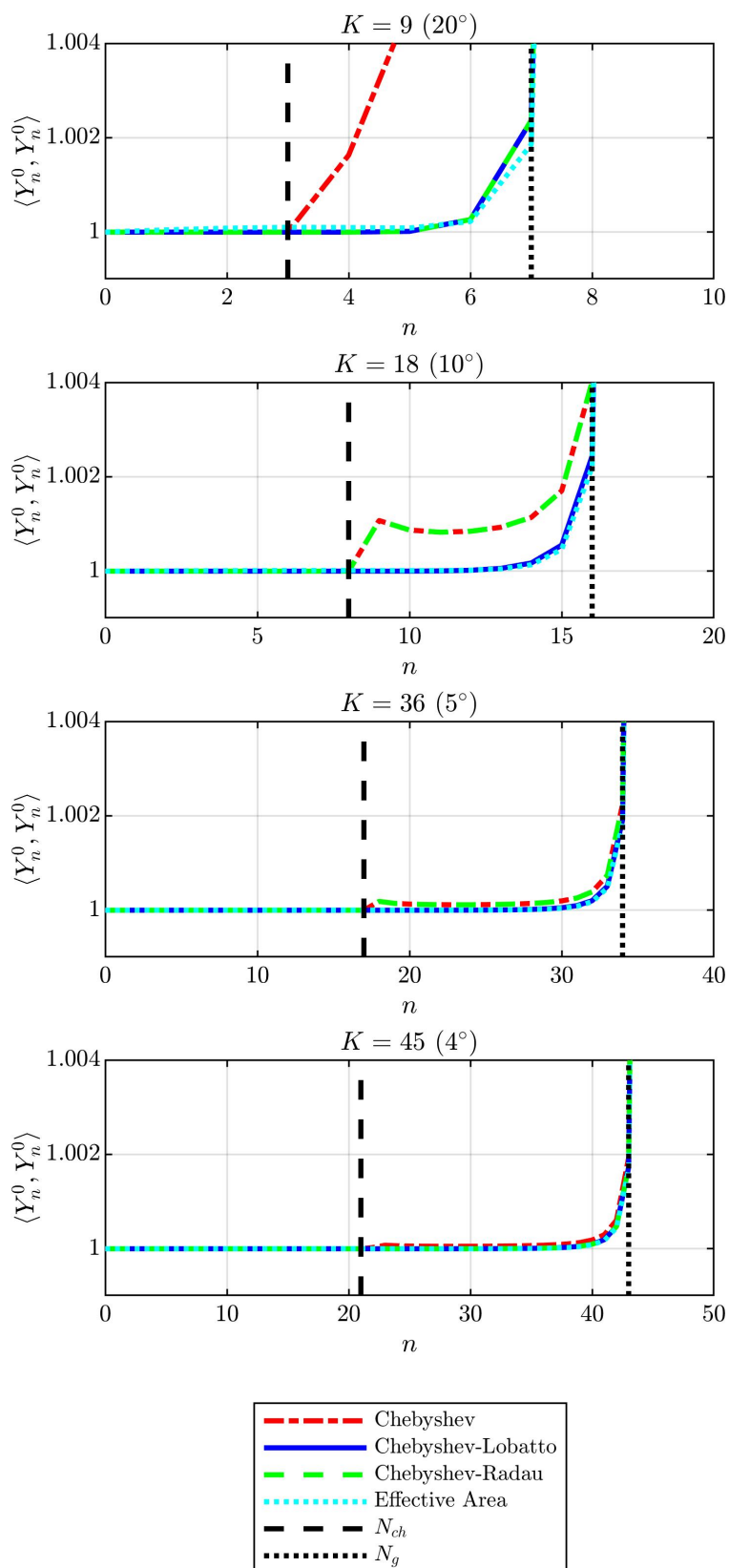


Figure 6.3 Numerically integrated $\langle Y_n^0, Y_n^0 \rangle$ for increasing sampling densities K and different quadrature schemes.

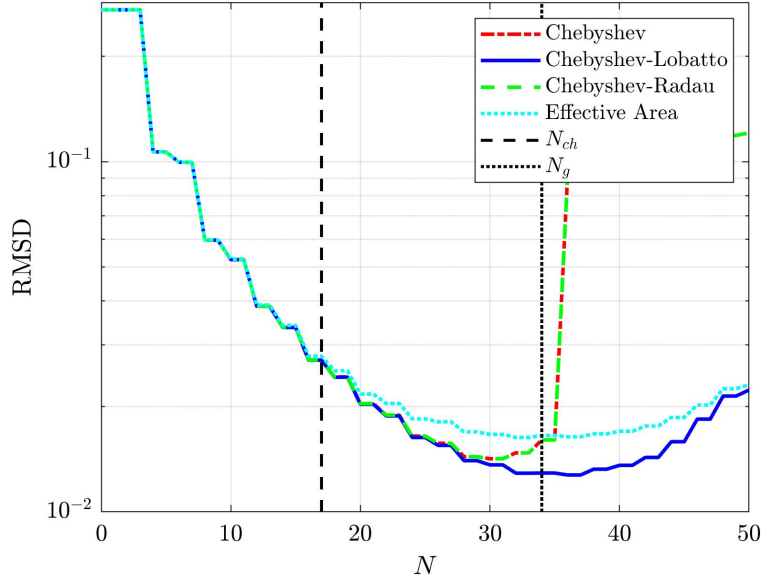


Figure 6.4 The RMSDs for spherical harmonic expansions of a unit cube function involving different quadrature weights, effective area weights, and increasing degree for $K = 36$ (5°) sampling.

becomes

$$\begin{aligned}
 RMSD(N) &= \sqrt{\int_0^\pi \int_0^{2\pi} |\hat{f} - f|^2 \sin \theta d\theta d\phi} \\
 &= \sqrt{\sum_{n=0}^N \sum_{m=-n}^n |f_n^m|^2 + |\hat{f}_n^m|^2 - \hat{f}_n^m [f_n^m]^* - f_n^m [\hat{f}_n^m]^*}, \quad (6.41)
 \end{aligned}$$

where the last line follows from Parseval's theorem. As the expansion coefficients converge to their exact values, $RMSD(N) \rightarrow 0$.

The plotted curves illustrate several important trends. First, all schemes produce similar expansion deviations up to approximately $N = N_{ch} = 17$, the maximum exact degree for regular Chebyshev sampling. Second, although one may initially anticipate that the deviations will increase beyond N_{ch} , the curves actually show that the deviations continue to *decrease*. This remarkable result shows that increasing the expansion degree above the maximum exact degree is beneficial. Third, beyond $N = 17$, the effective area weights do not perform as well as the quadrature weights. Fourth, the Chebyshev and Chebyshev-Radau quadratures achieve maximum convergence at $N = 30$;

beyond $N_g = 34$, their deviations increase substantially. Fifth, the Chebyshev-Lobatto quadrature produces its best approximation at $N = N_{g,l} = 36$.

These outcomes and those of Fig. 6.3 suggest that for equiangular Chebyshev sampling, no aliasing errors occur up to N_{ch} , $N_{ch,l}$, and $N_{ch,r}$, the maximum degrees for exact quadrature. In the range of N_{ch} to N_g , minor aliasing errors occur, but better convergence follows by adding more expansion terms. The aliasing arises simply because the quadrature rule is no longer exact, but the results remain very accurate, i.e., the quadrature errors remain small. For example, in Fig. 6.3, errors for the numerically evaluated inner product were less than 0.5% for many $n > N_{ch}$ values. Near N_g and beyond, significant quadrature errors prohibited further convergence. It is also noteworthy that the effective sampling area scheme performs reasonably well even though it is not exact for some degrees (see, for example, the $K = 9$ case in Fig. 6.3). Again, this highlights the importance of evaluating a quadrature rule's overall performance in addition to its exactness.

6.4 Pressure-Field Expansions

For a measurement radius R , the continuous solution to the Helmholtz equation on the exterior domain $r \geq R$ is [59]

$$p(r, \theta, \phi) = \sum_{n=0}^{\infty} \sum_{m=-n}^n p_n^m \frac{h_n^{(2)}(kr)}{h_n^{(2)}(kR)} Y_n^m(\theta, \phi), \quad r \geq R, \quad (6.42)$$

where p_n^m are the pressure expansion coefficients determined via orthogonality at $r = R$:

$$p_n^m = \int_0^\pi \int_0^{2\pi} p(R, \theta, \phi) [Y_n^m(\theta, \phi)]^* \sin \theta d\theta d\phi. \quad (6.43)$$

As $r \rightarrow \infty$, the large-argument form of the spherical Hankel functions yields [59]

$$p_{ff}(r, \theta, \phi) = \frac{e^{-ikr}}{kr} \sum_{n=0}^{\infty} \sum_{m=-n}^n p_n^m \frac{i^n}{h_n^{(2)}(kR)} Y_n^m(\theta, \phi), \quad (6.44)$$

such that the unnormalized far-field directivity pattern becomes

$$D_{ff}(r, \theta, \phi) = \sum_{n=0}^{\infty} \sum_{m=-n}^n p_n^m \frac{i^n}{h_n^{(2)}(kR)} Y_n^m(\theta, \phi). \quad (6.45)$$

If an infinite rigid baffle lies in the x - y plane, the boundary condition $\partial p / \partial z|_{z=0} = 0$ precludes the spherical harmonics that are not symmetric about $\theta = \pi/2$ for the hemispherical space $z \geq 0$. Since

$$P_n^m(-x) = (-1)^{m+n} P_n^m(x), \quad (6.46)$$

the expansion then becomes

$$p(r, \theta, \phi) = \sum_{n=0}^{\infty} \sum_{m=-n}^n \xi_n^m p_n^m(k) \frac{h_n^{(2)}(kr)}{h_n^{(2)}(kR)} Y_n^m(\theta, \phi), \quad r > R, \theta < \frac{\pi}{2}, \quad (6.47)$$

where

$$\xi_n^m = \begin{cases} 1, & \text{even } n+m \\ 0, & \text{odd } n+m \end{cases}. \quad (6.48)$$

6.4.1 Spatial Aliasing

An essential consideration for any directivity measurement is the number of sampling positions required to represent the frequency-dependent radiation pattern adequately. Consider a source of maximum extent d from the origin with expansion coefficients p_n^m produced from a notional observation sphere at radius $R = d$. The nature of the spherical Hankel functions for orders $n \gtrsim kd$ causes the magnitude of the associated expansion coefficients to rapidly decay as the pressure propagates to the far-field [59]. This effect leads to the result that a source of maximum extent d from the origin requires coefficients up to degree $n \approx kd$ to represent its far-field radiation [59, 83].

One may explore these effects in more detail by combining the time-averaged sound power in terms of the expansion coefficients [59] and an energy-per-degree metric [114] to create the following time-averaged sound power per expansion degree:

$$\langle W_n(k) \rangle_t = \frac{1}{2z_0 k^2} \sum_{m=-n}^n |c_n^m(k)|^2, \quad (6.49)$$

where $z_0 = \rho_0 c$ is the characteristic specific acoustic impedance of the medium, and $c_n^m(k) = p_n^m(k)/h_n^{(2)}(kR)$. The time-averaged sound power of a source at a given wavenumber follows as

$$\langle W(k) \rangle_t = \sum_{n=0}^{\infty} \langle W_n(k) \rangle_t. \quad (6.50)$$

Equation (6.49) provides a valuable metric to understand how much signal power each expansion coefficient contains and the relative importance of higher-degree coefficients.

An interesting example involves the axisymmetric acoustic pressure produced by a radially vibrating cap on a rigid sphere of radius a and cap circumference angle $\theta_c = 10^\circ$. Researchers have applied this model to understand the general directional characteristics of sources such as loudspeakers [10], horns [11, 12], and speech [4, 6]. Figure 6.5(a) plots $\langle W_n(k) \rangle_t$ for the closed-form theoretical expansion coefficients [10] as functions of ka and expansion degree n . The plotted color indicates the relative radiated power for each expansion degree on a normalized logarithmic scale. White represents the highest energy (most important expansion coefficients), and black represents the lowest energy (least important expansion coefficients). The overlaid green line $N \approx ka$ represents the predicted number of required expansion coefficients based on the simple source geometry mentioned earlier. As anticipated, most of the significant expansion coefficients lie below this line while the energy of higher-degree coefficients drops off quickly, e.g., to 40 dB or more below the maximum, above it.

Figure 6.5(b) plots $\langle W_n(k) \rangle_t$ based on numerically determined expansion coefficients from Eq. (6.37) and $K = 36$ Chebyshev-Lobatto quadrature, which exemplifies the 5° AES sampling standard. The sampled pressure followed by analytically expanding the pressure via Eq. (6.42) at the fixed angular locations and radial distance $R = 20$ m. The dashed cyan line represents $N_{ch,l}$, whereas the dotted cyan line indicates $N_{g,l}$ (Compare Figs. 6.3 and 6.4).

Section 6.3 suggested that $N_{g,l}$, the Gaussian quadrature limit for the same number of sampling nodes as Chebyshev-Lobatto quadrature, is the limiting degree for viable expansion. In the region $n < N_{g,l}$ and $ka \lesssim 30$, the calculated $\langle W_n(k) \rangle_t$ are essentially identical to those derived analytically

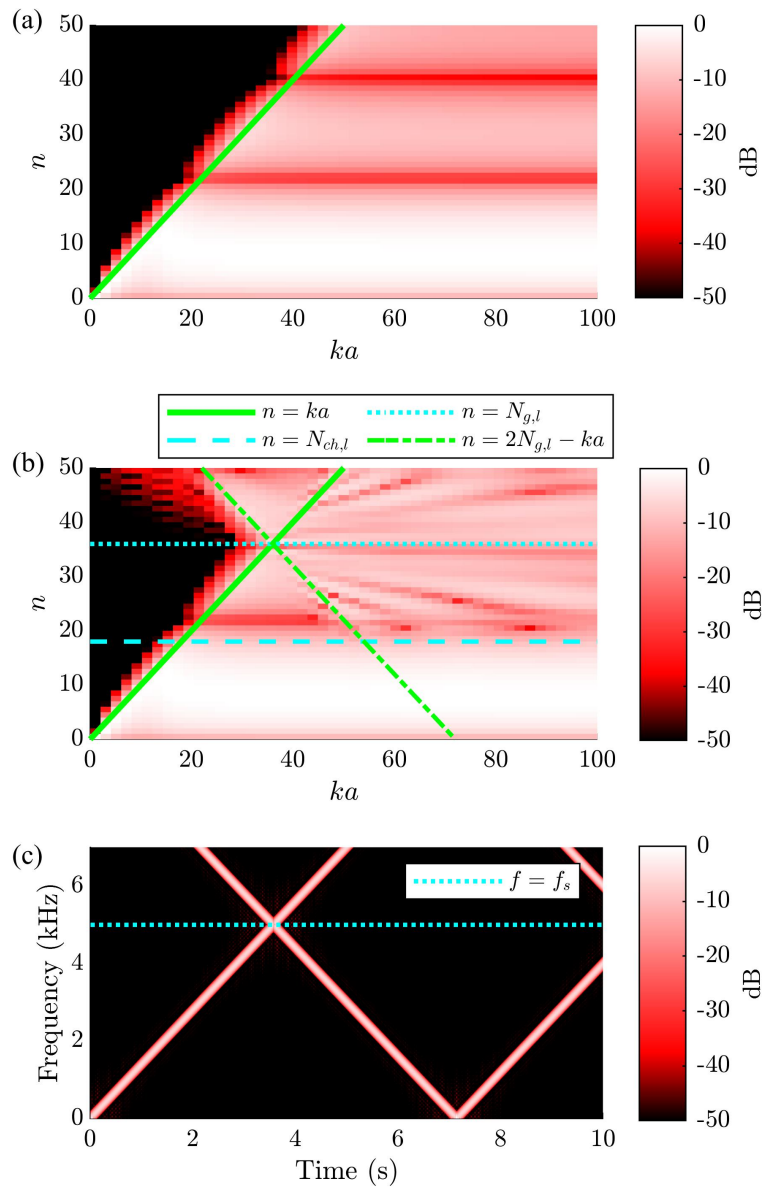


Figure 6.5 Sound power per degree for a radially vibrating cap on a sphere derived from (a) theoretical expansion coefficients and (b) numerically determined expansion coefficients evaluated with an $n = 36$ Chebyshev-Lobatto scheme. (c) Analogous time-frequency aliasing effects.

for Fig. 6.5(a). The region $n > N_{g,l}$ and $ka \lesssim 30$ does show deviations between the analytical values due to quadrature errors for coefficients whose degrees n exceed $N_{g,l}$. In practice, evaluating the expansion for degrees no greater than $N_{g,l}$ eliminates these errors. Additionally, a comparison with the analytical values shows that a truncated expansion at $N_{g,l}$ loses no significant coefficients for this frequency range.

However, the intersection of the lines $n = N_{g,l}$ and $n = ka$ yields a reference point about which deviations begin to occur for $n < N_{g,l}$. Because the expansion requires roughly $n \approx ka$ terms to adequately represent the pressure field, when ka approaches and exceeds $N_{g,l}$, significant aliasing effects arise. In the region $n < N_{g,l}$ and $ka > N_{g,l}$, deviations between the analytically and numerically evaluated $\langle W_n(k) \rangle_t$ values become apparent. These deviations appear mainly beyond $n = 2N_{g,l} - ka$, the reflection of the line $n = ka$ across $n = N_{g,l}$ and represented by the dash-dotted green line. Interestingly, these deviations appear to have a quasi-reflectional symmetry about the line $n = N_{g,l}$.

Because the deviations appear mainly beyond $n = 2N_{g,l} - ka$, one could attempt to truncate the expansion up to this line. However, this approach is problematic because it does not include necessary higher-degree terms, leading to a significant loss of signal energy. Consequently, for $ka > N_{g,l}$ the expansion is not valid because first, the expansion requires coefficients with $n > N_{g,l}$ for proper convergence and second, coefficients with $n < N_{g,l}$ may be corrupted due to spatial aliasing effects. As a result, in practical situations the expansion can only be applied in the frequency range of $N_{g,l} < ka$.

These aliasing effects are analogous to time-frequency aliasing about the Nyquist frequency, wherein a signal with frequency $f_s/2 + \Delta f$ aliases with a frequency $f_s/2 - \Delta f$ for the sampling rate f_s . To aid in conceptualizing the similarities between the spatial and frequency aliasing, Fig. 6.5(c) plots the short-time Fourier transform (STFT) of the function $y(t) = \sin(1400\pi t^2)$ sampled

at $f_s = 10$ kHz. With a Nyquist frequency of 5 kHz, aliasing occurs when $t = 3.6$ s, leading to reflected energy across the line $f = f_s/2$.

The expansion coefficients and frequency bins calculated above lines $n = N_{g,l}$ and $f = f_s/2$ in Figs. 6.5(b) and 6.5(c), respectively, are erroneous and discardable. Consequently, an expansion based on the AES 5° sampling standard has an absolute upper bound of $N_{g,l} = 36$. Since aliased energy corrupts an expansion and reduces its reliability, the maximum usable wavenumber is roughly $k = N_{g,l}/a$. These results also demonstrate that identifying the reflection lines in a $\langle W_n(k) \rangle_t$ plot over frequency helps establish when spatial aliasing occurs and estimate when a spherical harmonic expansion is no longer valid.

6.4.2 Effect of Azimuthal Sampling Density

The preceding sections have focused on the accuracies of polar-angle quadrature rules. In principle, the azimuthal resolution should cause the azimuthal quadrature rule to be exact to the same degree as the polar-angle rule. Driscoll and Healy used this concept to choose the azimuthal spacing $\Delta\phi = 2\Delta\theta = 2\pi/K$ [113]. The K azimuthal sampling positions allow spherical harmonic expansions up to degree $N = \lfloor K/2 \rfloor$, close to the Chebyshev limit $N_{ch} = \lfloor K/2 - 1 \rfloor$ of the polar-angle resolution.

However, the preceding sections also suggested that the Chebyshev quadrature rules allow converging spherical harmonic expansions up to about degree N_g for practical applications. Thus, a dual-equiangular $\Delta\phi = \Delta\theta$ spacing should be advantageous. Conveniently, the AES sampling standard already applies this approach.

A simple numerical experiment illustrates the significance of the azimuthal sampling density and the advantage of $\Delta\phi = \Delta\theta$ sampling. Figure 6.6 presents the $\langle W_n(k) \rangle_t$ produced by two equi-strength point sources radiating simultaneously at $\mathbf{r} = (-0.1, 0.3, -0.1)$ m and $\mathbf{r} = (0.1, 0.2, 0.2)$ m. Equivalent point source models such as this are useful for representing the directivities of tone-hole instruments, organ pipes, and other sources [40, 86, 88, 89]. A $K = 36$ Chebyshev-Lobatto

scheme samples the pressure field produced by the two point sources with three distinct azimuthal spacings: $\Delta\phi = 2\Delta\theta$, $\Delta\phi = \Delta\theta$, and $\Delta\phi = \Delta\theta/2$. The maximum-degree spherical harmonics, considering only the azimuthal resolution, are then $N = 18$, $N = 36$, and $N = 72$, respectively.

Figures 6.6(a) and (b) show the results for $\Delta\theta = 2\Delta\phi$ and $\Delta\phi = \Delta\theta$, respectively. In each case, the overlaid green line is $n = kd$, where $d = 0.33$ m is the distance of the point source farthest from the origin. As for the vibrating cap on the rigid sphere, the most important coefficients lie below this line. When $\Delta\phi = 2\Delta\theta$, spatial aliasing occurs near $n = N_{ch,l} = 18$. However, when $\Delta\phi = \Delta\theta$, it occurs much higher near $n = N_{g,l} = 36$. Even though the polar sampling positions remain the same, the discrepancy arises because azimuthal sampling with $\Delta\phi = 2\Delta\theta$ and $\Delta\phi = \Delta\theta$ limit the expansions to a maximum degrees $N = 18$ and $N = 36$, respectively. Thus, halving the azimuthal spacing from that corresponding to $N_{ch,l}$ to that corresponding to $N_{g,l}$ effectively doubles the usable bandwidth of the spherical harmonic expansion.

Figure 6.6(c) shows $\langle W_n(k) \rangle_t$ for $\Delta\phi = \Delta\theta/2$. The spectrum is nearly identical to that for $\Delta\phi = \Delta\theta$ in Fig. 6.6(b), with aliasing occurring at the same degree. This additional doubling of the azimuthal sampling density is insignificant because the polar-angle resolution limits the maximum usable expansion degree to roughly $N_{g,l}$.

6.4.3 Far-field Projection

While the previous sections have suggested that a maximum expansion degree approaching the Gaussian limit is preferable for computing Chebyshev-type spherical harmonic expansion coefficients, it is essential to understand how minor aliasing errors between N_{ch} and N_g over the sphere may degrade the far-field pattern determined from Eq. (6.45). A straightforward example quantifies these types of deviations for radius $R = 1$ m and $K = 36$ Chebyshev and Chebyshev-Lobatto dual-equiangular sampling schemes assessing the field produced by a point source displaced from the origin to $\mathbf{r} = (0.1, 0, 0)$ m. As with the results in Sec. 6.4.2, the anticipated maximum degree of this

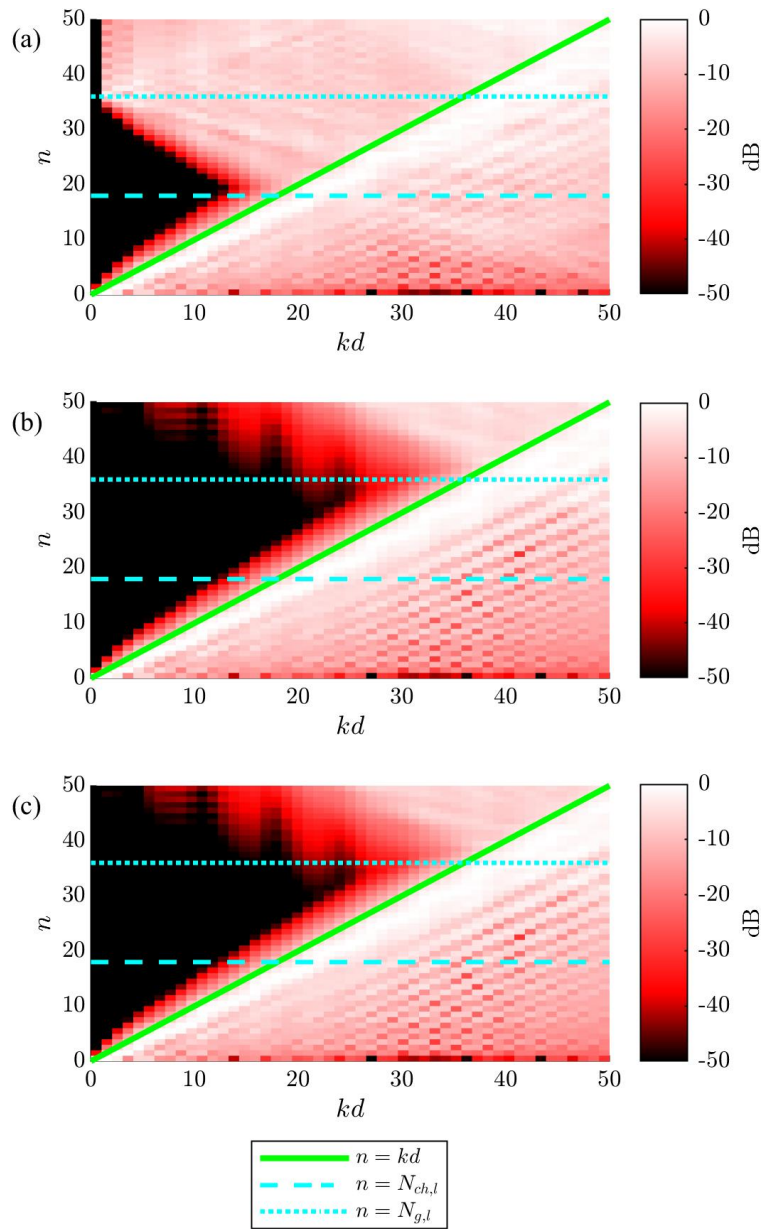


Figure 6.6 Sound power per degree for two point sources measured with $K = 36$ Chebyshev-Lobatto polar-angle sampling and three distinct azimuthal resolutions: (a) $\Delta\phi = 2\Delta\theta$, (b) $\Delta\phi = \Delta\theta$, and (c) $\Delta\phi = \Delta\theta/2$.

source will be roughly $n = kd = 0.1k$. However, the source's far-field directivity magnitude pattern should remain omnidirectional despite its displacement [82]. A directivity factor function deviation level L_Q [81] characterizes any deviations between the projected far-field directivity factor function and its omnidirectional counterpart as a function of kd .

Figure 6.7(a) shows L_Q calculated with all coefficients satisfying $n \leq N_{ch} = 17$ for Chebyshev sampling and $n \leq N_{ch,l} = 18$ for Chebyshev-Lobatto sampling. Because the schemes are exact up to these limits, the deviations below $kd = N_{ch}$ and $kd = N_{ch,l}$ are approximately negligible. However, serious deviations arise above these thresholds, showing that the far-field projections have failed.

Figure 6.7(b) shows L_Q calculated with all coefficients satisfying $n < N_g = 34$ for Chebyshev sampling and $n < N_{g,l} = 36$ for Chebyshev-Lobatto sampling. For the Chebyshev sampling, minor deviations (e.g., < 0.5 dB) occur below $kd = 30$ because the higher-degree coefficients include minor aliasing errors. Even up to $kd = 30$, the deviations remain below 0.1 dB. The deviations over the same region for Chebyshev-Lobatto sampling are significantly smaller and nearly negligible. Beyond $kd = 30$, the deviations increase for both schemes, becoming greater than 1 dB beyond $kd = 34$ for the Chebyshev sampling and $kd = 35$ for the Chebyshev-Lobatto sampling.

It is important to note that the far-field projection using only $n \leq N_{ch}$ coefficients is reliable to roughly $kd = N_{ch}$. On the other hand, the projection using $n < N_g$ coefficients is reliable to roughly $kd = N_g$, with minor errors for $kd < N_{ch}$. These results suggest that including the $N_{ch} < n < N_g$ coefficients will benefit the expanded far-field pressure by nearly doubling its usable bandwidth. However, the source order should also inform the maximum practical degree. For example, if kd is small over the desired bandwidth, calculating up to N_{ch} may be preferable to avoid introducing minor aliasing errors. If necessary, one may estimate d using $\langle W_n(k) \rangle_t$ and the related developments of the preceding sections.

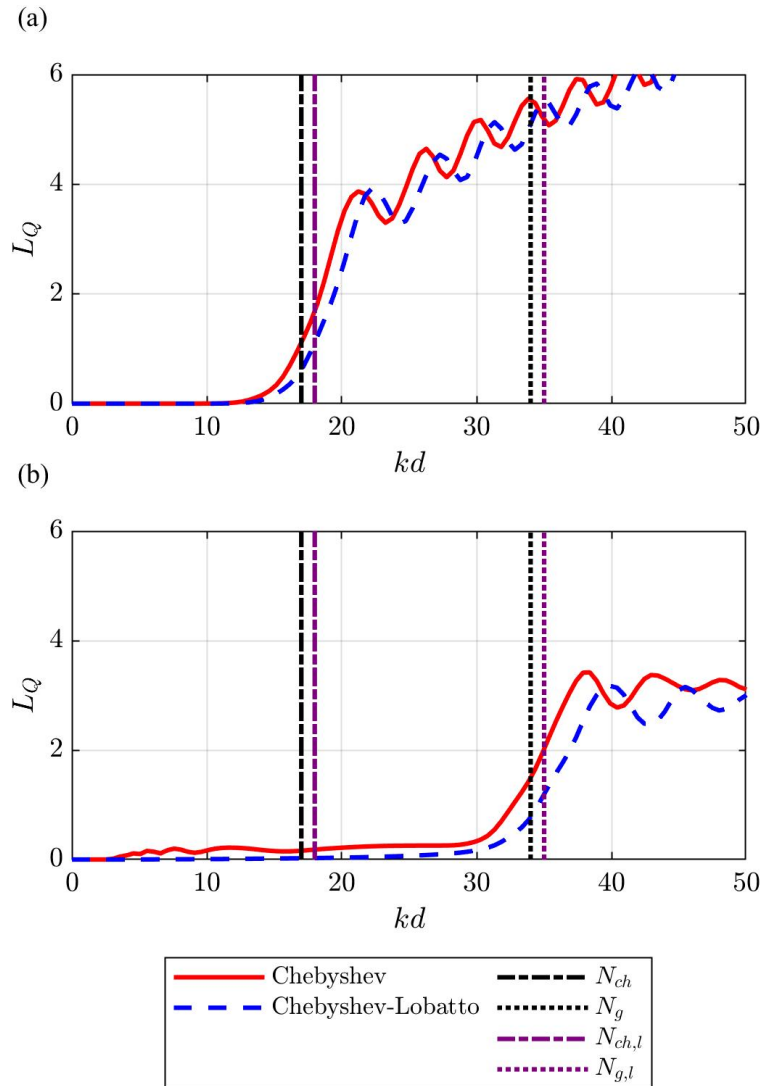


Figure 6.7 Directivity factor function deviation levels L_Q between the projected far-field directivity of a monopole displaced from the origin at $\mathbf{r} = (0.1, 0, 0)$ m and the theoretical omnidirectional far-field pattern. (a) Calculation involving all coefficients up to $n = N_{ch}$ and $n = N_{ch,l}$. (b) Calculation involving all coefficients up to $n = N_g$ and $n = N_{g,l}$.

6.4.4 Hemispherical Directivities

A final illustrative example considers two point sources of equal strengths located at $\mathbf{r} = (\sqrt{2}/2, 0, \sqrt{2}/2)$ m and $\mathbf{r} = (-\sqrt{2}/2, 0, \sqrt{2}/2)$ m above an infinite rigid baffle in the x - y plane. The equivalent field follows by placing fictitious image sources symmetrically below the x - y plane in free space [62]. All sources remain within the maximum distance $d = 1$ m from the origin, so that the anticipated crucial coefficients are $n \leq k$.

A $K = 18$ Chebyshev-Lobatto hemispherical scheme samples the field at $R = 1.5$ m, and the resultant expansion coefficients follow from numerical integration. Based on the results from the previous sections, if one calculates the coefficients up to $n < N_{g,l} = 18$, the source order suggests that for $k < 18 \text{ m}^{-1}$, the expansion will remain approximately valid, while serious deviations are likely to arise for $k > 18 \text{ m}^{-1}$.

Figure 6.8 plots the pressure fields around the sources in the x - z plane for two wavenumbers: $k = 16 \text{ m}^{-1}$ and $k = 20 \text{ m}^{-1}$. Figures 6.8(a) and 6.8(c) plot the fields as determined analytically from the method of images for $kd = 16$ and $kd = 20$, respectively. Color indicates the relative sound pressure level on a decibel scale, whereas the white semi-circle indicates the sampling radius. In each case, two bright red patches localize the positions of the point sources. Wave interactions from the sources, including reflections from the baffle, lead to constructive and destructive interference regions.

Figure 6.8(b) plots the pressure field calculated via Eq. (6.47) from numerically estimated expansion coefficients for $kd = 16$. A comparison with Fig. 6.8(a) shows excellent agreement of relative levels and locations of interference lobes. Figure 6.8(d) plots a similar result for $kd = 20$. Even though kd is only slightly higher, reproduction is poor. Spatial aliasing effects have contaminated the expansion coefficients and thus render the expansion less meaningful. These results highlight the importance of understanding a given sampling scheme's limits and identifying when spatial aliasing occurs.

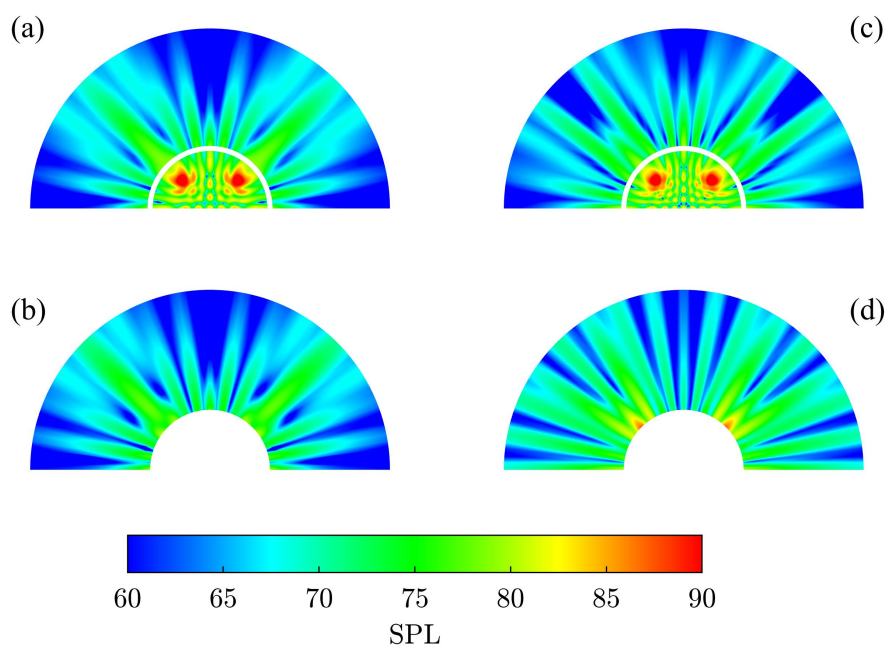


Figure 6.8 Sound pressure level plots for two point sources near an infinite rigid baffle in the x - y plane. Fields determined analytically for $z \geq 0$ in the x - z plane using the method of images with (a) $kd = 16$ and (c) $kd = 20$. Fields determined from numerically estimated expansion coefficients with (b) $kd = 16$ and (d) $kd = 20$.

6.5 Conclusions

This work has developed two spherical quadrature schemes based on equiangular sampling and compared their performances to previously proposed rules. The first scheme adapts Imhof's Chebyshev-Lobatto rule, while the second is a Chebyshev-Radau rule derivation. The Chebyshev-Lobatto rule, which applies directly to the AES56-2008 (r2019) measurement standard, performs best. However, the Chebyshev-Radau rule allows the deletion of a polar sampling node to allow for a support structure or rotation apparatus that may obstruct sampling at that position.

Numerical integration experiments have illustrated that while the rules are exact to about half the limit of Gaussian quadrature, they remain similarly robust up to the Gaussian degree limit, effectively doubling the viable bandwidth compared to previous assumptions. The results demonstrate that choosing an azimuthal angular resolution equal to the polar angular resolution (dual-equiangular sampling) is a beneficial enhancement that improves upon the equiangular rule recommended by Driscoll and Healy. This work has also demonstrated how sound power per expansion degree is a valuable metric for identifying spatial aliasing in directivity measurements. Numerical simulations explored the impacts of spatial aliasing errors on far-field projections, demonstrating the importance of considering such effects for proper sampling of fields produced by practical sources.

Chapter 7

Spherical Directivities from Arbitrarily Shaped Arrays

This chapter demonstrates how one may employ arbitrarily shaped arrays for directivity measurements and outlines some benefits and drawbacks of several array types. The chapter previously appeared as:

S. D. Bellows and T. W. Leishman, "Obtaining far-field spherical directivities of guitar amplifiers from arbitrarily shaped arrays using the Helmholtz equation least-squares method," Proc. Mtgs. Acoust., 42, 055005, (2020). doi: 10.1121/2.0001410.

7.1 Introduction

Directivity measurements describe the spatial dependence of free radiated pressure fields, making them essential tools for characterizing sound sources. Researchers and practitioners have utilized various approaches for measuring directivities, but most methods currently involve constant-radius polar or spherical sampling, typically designed or assumed to be in the source far fields. The AES standard for measuring loudspeaker directivities specifies either 10° or 5° spherical resolution in the

polar and azimuthal angles, leading to 614 or 2,522 unique sampling positions, respectively [33]. File structures such as the common loudspeaker format (CLF) [96] or EASE GLL [97] facilitate the sharing of the spherical data with support for various bandwidths, including narrowband or 1/1 or 1/3-octave bands. Figure 7.1 shows a directivity measurement array with microphones spaced at 5° in the polar angle. Full spherical data results by rotating the sound source azimuthally using a computer-controlled system. Recently, specialized transfer function techniques have allowed the 5° resolution standard to be applied to live sources such as musical instruments and speech [1, 6], with the resulting data being freely available in an archival database [38].

While measuring directivities with spherical arrays is a straightforward process, there are several potential advantages to using arbitrarily shaped arrays, including those conforming more closely to

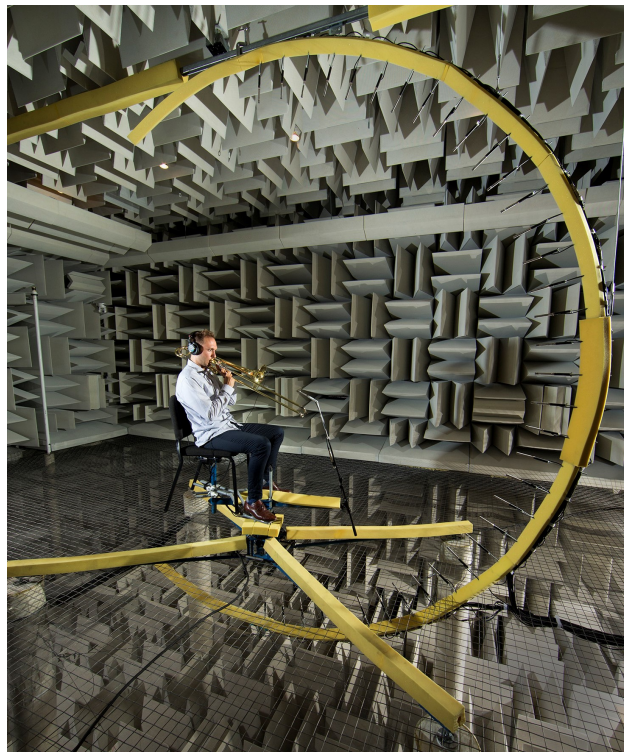


Figure 7.1 A microphone array used in measuring spherical directivities of musical instruments and speech. The array has 5° resolution in the polar angle. A full spherical directivity follows by rotating the musician or talker in 5° azimuthal steps and using a transfer function technique to address repetition variations.

radiators' geometries. For loudspeakers, this allows enhanced vibro-acoustic analysis using inverse methods such as near-field acoustical holography (NAH) [59], inverse boundary element method (I-BEM) [122], or the Helmholtz equation least-squares (HELs) method [75] to study cone velocity, cone breakup, and other characteristics. Near-field measurements also allow increased signal-to-noise ratios and the potential to make assessments in smaller measurement rooms or other nonideal environments. Arrays with relatively simple geometries permit directivity measurements without highly specialized apparatuses. While the underlying principles and techniques necessary for using arbitrarily shaped arrays to measure far-field directivities have been available for decades [123], they remain relatively obscure for the measurement of loudspeakers. This work illustrates how one may obtain reliable far-field spherical directivities from sampling using arbitrarily shaped arrays by measuring several guitar amplifiers' directivities. The approach proceeds from the HELs method, and the results include both numerical and experimental validations.

7.2 Formulation

7.2.1 HELs Method

The exterior pressure solution to the Helmholtz equation in spherical coordinates is [59]

$$p(r, \theta, \phi, k) = \sum_{n=0}^{\infty} \sum_{m=-n}^n c_n^m(k) h_n^{(2)}(kr) Y_n^m(\theta, \phi), \quad (7.1)$$

where $p(r, \theta, \phi, k)$ is the pressure, $h_n^{(2)}(kr)$ are the spherical Hankel functions of the second kind of order n , $Y_n^m(\theta, \phi)$ are the spherical harmonics of degree n and order m [70], and $c_n^m(k)$ are the pressure expansion coefficients. To estimate the $c_n^m(k)$, one may employ the HELs method, wherein Q measurements of the pressure appear as linear combinations of the selected basis functions $\Psi(\mathbf{r}, k)$, which, in spherical coordinates, are the products of spherical Hankel functions

and spherical harmonics:

$$\Psi_n^m(r, \theta, \phi, k) = h_n^{(2)}(kr) Y_n^m(\theta, \phi). \quad (7.2)$$

By considering only eigenfunctions up to a maximal expansion degree N , the system of equations takes the matrix form

$$\mathbf{p} = \Psi \mathbf{c} + \mathbf{e}, \quad (7.3)$$

where

$$\mathbf{p} = \begin{bmatrix} p(\mathbf{r}_1, k) & p(\mathbf{r}_2, k) & \cdots & p(\mathbf{r}_Q, k) \end{bmatrix}^T, \quad (7.4)$$

$$\mathbf{c} = \begin{bmatrix} c_0^0(k) & c_1^{-1}(k) & \cdots & c_N^N(k) \end{bmatrix}^T, \quad (7.5)$$

$$\Psi = \begin{bmatrix} \Psi_0^0(\mathbf{r}_1, k) & \Psi_1^{-1}(\mathbf{r}_1, k) & \cdots & \Psi_N^N(\mathbf{r}_1, k) \\ \Psi_0^0(\mathbf{r}_2, k) & \Psi_1^{-1}(\mathbf{r}_2, k) & \cdots & \Psi_N^N(\mathbf{r}_2, k) \\ \vdots & \vdots & \ddots & \vdots \\ \Psi_0^0(\mathbf{r}_Q, k) & \Psi_1^{-1}(\mathbf{r}_Q, k) & \cdots & \Psi_N^N(\mathbf{r}_Q, k) \end{bmatrix}, \quad (7.6)$$

\mathbf{e} is a column vector representing the least-squares errors, and \mathbf{r}_q , with $q = 1, 2, \dots, Q$, represent the Q arbitrary sampling positions. If the number of positions exceeds the number of required coefficients, the least-squares solution to the overdetermined system follows as

$$\mathbf{c} = \Psi^\dagger \mathbf{p}, \quad (7.7)$$

where the pseudo-inverse Ψ^\dagger is

$$\Psi^\dagger = (\Psi^H \Psi)^{-1} \Psi^H. \quad (7.8)$$

For the present work, a regularized least-squares fit was sometimes beneficial, particularly when sparse sampling densities occurred in particular spatial regions. The Tikhonov regularization (ridge regression) was well suited, in which the regularized pseudo-inverse Ψ_λ^\dagger is [95]

$$\Psi_\lambda^\dagger = (\Psi^H \Psi + \lambda \mathbf{I})^{-1} \Psi^H, \quad (7.9)$$

where $\lambda > 0$ is the regularization parameter, determined ad hoc.

7.2.2 Far-Field Directivity Pattern

By applying the large-argument relation of the spherical Hankel functions,

$$h_n^{(2)}(kr) \approx i^{n+1} \frac{e^{-ikr}}{kr}, \quad kr \gg 1, \quad (7.10)$$

the far-field pressure becomes

$$p(r, \theta, \phi, k) \approx \frac{e^{-ikr}}{kr} \sum_{n=0}^{\infty} \sum_{m=-n}^n c_n^m(k) i^{n+1} Y_n^m(\theta, \phi), \quad (7.11)$$

comprising a spherical wave with the unnormalized far-field directivity function

$$\tilde{D}_{\infty}(\theta, \phi, k) = \sum_{n=0}^{\infty} \sum_{m=-n}^n c_n^m(k) i^{n+1} Y_n^m(\theta, \phi). \quad (7.12)$$

Thus, to compute the far-field spherical directivity, one first measures the acoustic pressure at Q distinct near-field positions. Next, the HELS method produces the expansion coefficients $c_n^m(k)$ using an overdetermined system of equations. Finally, the spherical harmonic expansion of Eq. (7.12) represents the far-field directivity pattern.

7.3 Numerical Results

7.3.1 Array Sampling Schemes

A simple loudspeaker model provided a convenient means to numerically validate the method for four distinct near-field arrays, each with plausible geometries. Figure 7.2 shows the selected arrays surrounding the model. The first is a spherical array with 10° resolution in the polar and azimuthal angles and 614 unique sampling positions, which coincides with the AES standard. The second is a prolate-spheroidal grid based on a sampling resolution similar to that of the spherical array, having

the same number of positions. The third is a cylindrical array with a flat top and bottom and 602 unique sampling positions. The final array comprises a rectangular prism (cuboid), also with 602 unique sampling positions. The number of sampling positions for each array is approximately equal but constrained by their different shapes.

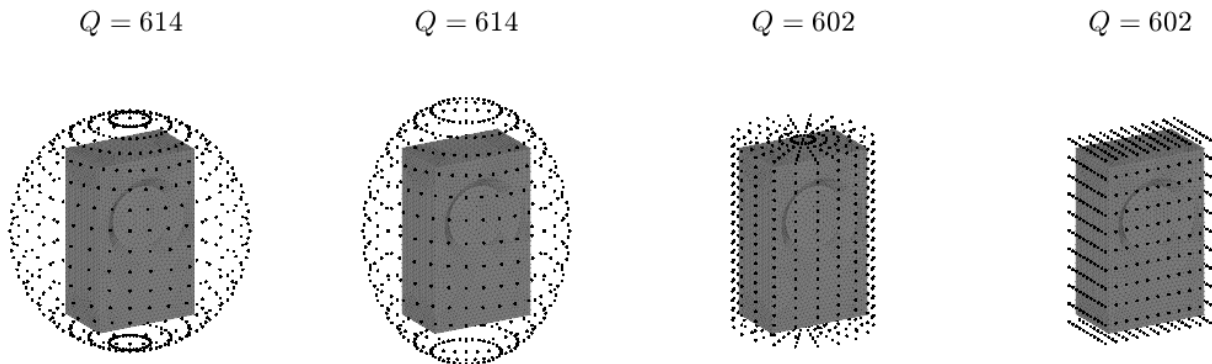


Figure 7.2 Spherical, spheroidal, cylindrical, and rectangular prism arrays used in the numerical experiments. The number of unique sampling positions appears above each array.

The array's dimensions allowed them to nearly graze the $40 \text{ cm} \times 25 \text{ cm} \times 15 \text{ cm}$ loudspeaker model with the nearest microphones of the array at 10% of its maximum extent. Finally, a far-field spherical reference array with 5 m radius and 5° resolution validated the HELS method's spherical directivities. Table 7.1 reports the smallest, mean, and largest radial positions of each near-field sampling scheme as measured from the origin.

7.3.2 BEM Results

The boundary element method (BEM) produced the pressure at each sampling position of each array over a 100 Hz to 5 kHz bandwidth for the numerical experiments. From the calculated pressures, the HELS method estimated the expansion coefficients $c_n^m(k)$. Finally, propagating the pressure results

to the far-field enabled the evaluation of the directivity through a 5° degree polar and azimuthal sampling scheme and subsequent comparison to the reference spherical array results.

Figure 7.3 shows the results for the rectangular prism array at 1 kHz. Figure 7.3a gives the relative sound pressure level on the array surface, Fig. 7.3b shows the estimated far-field spherical directivity using a degree $N = 6$ expansion, and Fig. 7.3c shows the reference far-field directivity without any expansion. All plots appear on a normalized 40 dB scale relative to the maximum pressure. The far-field patterns are very similar, albeit with some discrepancies behind the loudspeaker, which appear in the balloons' green-colored regions. This trend was consistent for various numerical experiments, as the regions that were many dB down from the maximum were challenging to estimate with high accuracy.

An essential part of the far-field estimation process is the selection of the expansion degree N . The choice is critical because it helps minimize the error of the associated directivity pattern. Figure 7.4 shows the results for the rectangular prism array at 2 kHz and compares the effects of various expansion degrees. When the degree is too small, such as $N = 1$ in Fig. 7.4a, the pattern does not accurately represent the measured pressure because of excess bias caused by too few degrees of freedom in the eigenfunction expansion. As the degree increases, the bias reduces, and the results agree better with the measured pressure, such as with the $N = 6$ balloon shown in Fig. 7.4c. However, if the degree becomes too high, such as for the $N = 15$ balloon in Fig. 7.4c, it produces

Table 7.1 Sampling scheme radii for the various near-field arrays.

Array Shape	Smallest Radial Position (m)	Mean Radial Position (m)	Largest Radial Position (m)
Spherical	0.27	0.27	0.27
Spheroidal	0.24	0.27	0.31
Cylinder	0.16	0.22	0.27
Prism	0.08	0.20	0.27

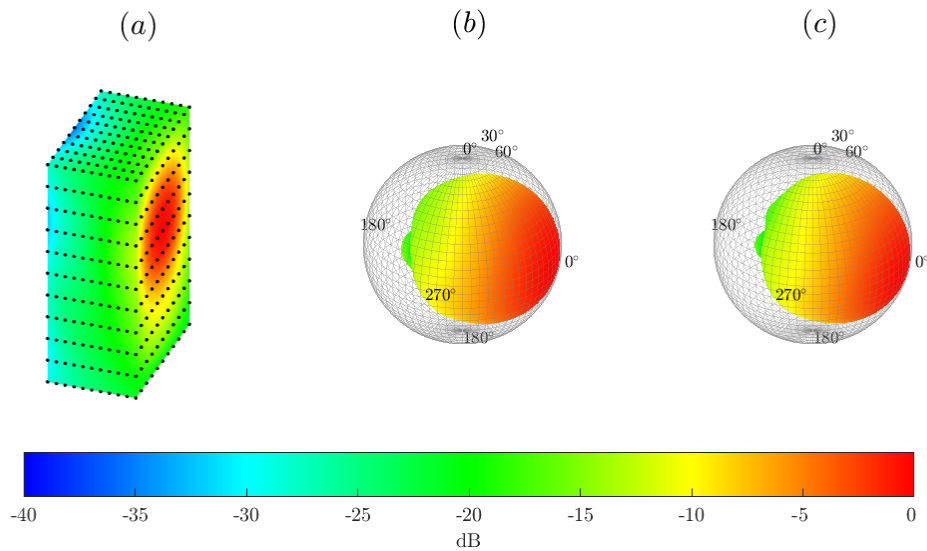


Figure 7.3 The BEM results for the rectangular prism array at 1 kHz. (a) Evaluated pressure on the prism array surface. (b) Estimated far-field directivity using the HELS method. (c) Reference far-field array directivity.

too much variance, and the overfitting causes the model to deviate from the measured pressure. The degree $N = 6$ balloon was the best fit for this particular frequency. Its features are similar to those of the measured far-field balloon, but it still has some notable differences. In practice, as one does not know the far-field pattern beforehand, it is necessary to monitor the expansion's degree carefully. A model degree $N = kd$, where d is the maximum dimension of the radiating object, seemed to give a reasonable initial estimate. This prediction approximately represented the maximum degree of the spherical eigenfunctions that did not rapidly evanesce before reaching the far-field [59].

7.3.3 Numerical Experimental Errors

One way to establish the frequency-dependent error between the directivity results of the various array types and the reference far-field pattern is to compute the spherically area-weighted deviation

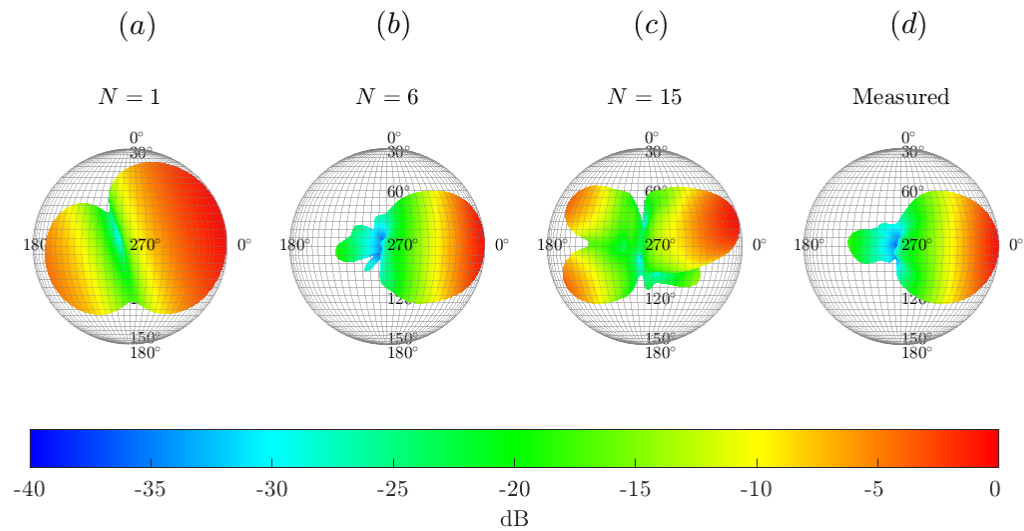


Figure 7.4 Illustration of the bias-variance trade-offs that arise when estimating far-field directivity patterns from near-field sampled pressures. (a) Far-field directivity based on degree $N = 1$ expansion. (b) Far-field directivity based on degree $N = 6$ expansion. (c) Far-field directivity based on degree $N = 15$ expansion. (d) Far-field reference directivity.

(AWD) [13],

$$\sigma_{AWD}^2 = \sum_i w_i \left[\frac{|\tilde{D}(\theta, \phi, k)| - |\tilde{D}_{ref}(\theta, \phi, k)|}{|\tilde{D}_{ref}(\theta, \phi, k)|} \right]^2, \quad (7.13)$$

where \tilde{D} represents the normalized directivity, \tilde{D}_{ref} is the normalized reference directivity, and w_i are Chebyshev quadrature weights for the 5° sampling [78]. On a logarithmic scale, the deviation becomes

$$L_{AWD} = 10 \log_{10}(1 + \sigma_{AWD}^2). \quad (7.14)$$

For each array type, the best estimations of the far-field directivity pattern at each frequency resulted from increasing the expansion degree N to select the lowest error between it and the known far-field pattern. While this is not generally possible under experimental conditions, since the far-field pattern is unknown, this procedure provided the best-case scenario for a given array at a given frequency. Figure 7.5 compares selected directivity balloons from the arrays at 100 Hz, 2 kHz, 3 kHz, and 5 kHz. The top figure row shows the far-field spherical reference array results, while the subsequent rows show the propagated results from the spheroidal, cylindrical, and rectangular prism arrays. When the directivity patterns are simple and nearly omnidirectional at low frequencies, they all show good agreement. However, as frequency increases, the patterns' deviations become more apparent, particularly for the cylindrical and prism arrays.

As shown in Fig. 7.6, the errors between all array results and the reference pattern are consistently small at low frequencies across the sampling schemes. However, as frequency increases, the varied array performances become more evident. In particular, the near-field spherical array performed best, followed in order by the spheroidal, cylindrical, and rectangular prism arrays. These trends suggest that the closer a near-field array is to a spherical geometry, the better it enables pressure propagation to the far field to match the spherical far-field directivity pattern. One may note that the spherical and spheroidal arrays had an additional twelve sampling positions; however, since this represents only about 2% of the total number of sampling positions for the cylindrical and prism arrays, the related effect is presumably negligible. The errors begin to increase above about 2

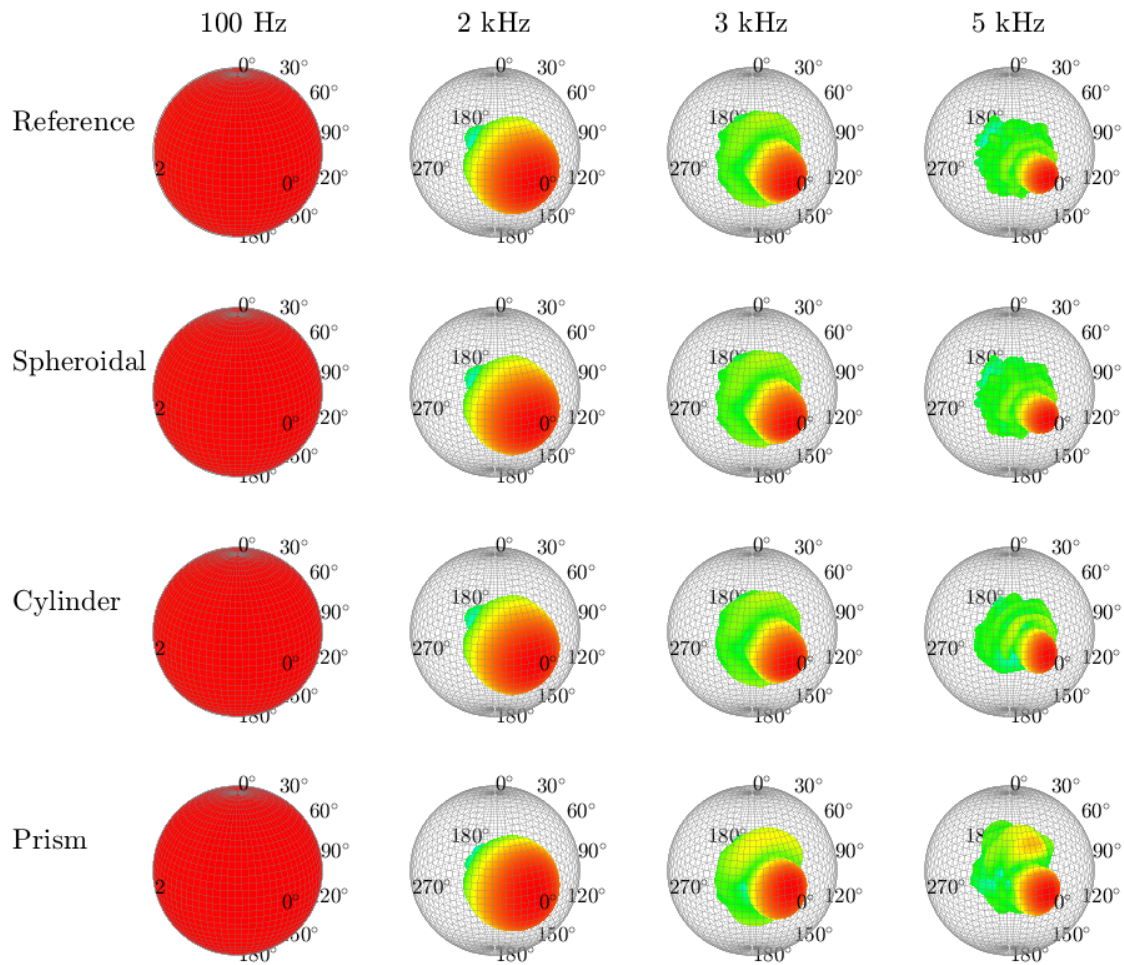


Figure 7.5 Selected results at 100 Hz, 2 kHz, 3 kHz, and 5 kHz for the far-field reference array in comparison to the spheroidal, cylindrical, and rectangular prism arrays.

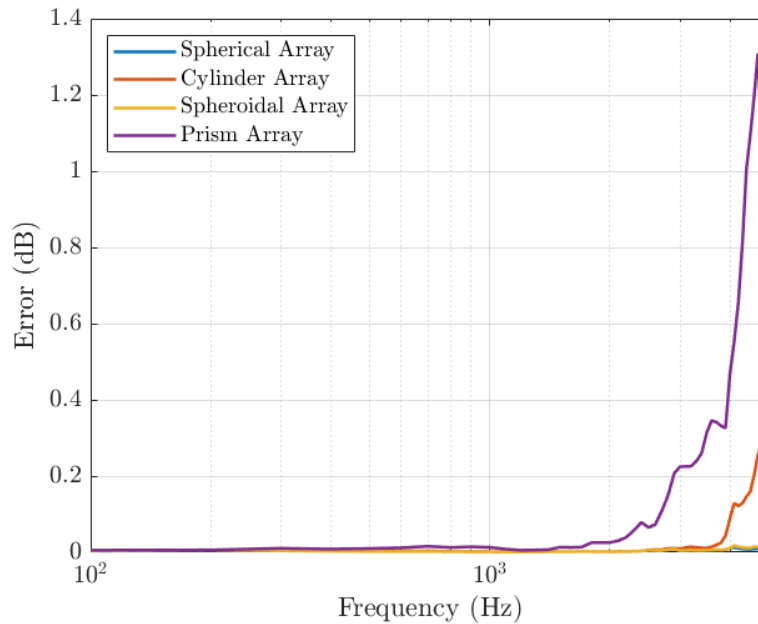


Figure 7.6 The AWD levels for the BEM experiments involving different array types.

kHz for the given sampling positions of all arrays, which corresponds to a value of $kd \approx 9$. However, the spheroidal and spherical arrays' deviations remain well below 0.1 dB for all frequencies below 5 kHz.

7.4 Experimental Results

The experimental validation included four guitar amplifiers' measured directivities: Fender Princeton Reverb, Fender Twin Reverb, Fender Deluxe Reverb, and VOX AC30. The experimental array shown in Fig. 7.7 consisted of 14 microphones arranged for cylindrical scanning. One near-field microphone produced a reference signal for computing frequency response functions, and one far-field microphone produced a signal for validating propagated results in the transverse plane. The entire cylindrical sampling surface developed gradually as the amplifier rotated in 5° degree azimuthal increments, resulting in 937 unique sampling positions on the array surface and 72 unique

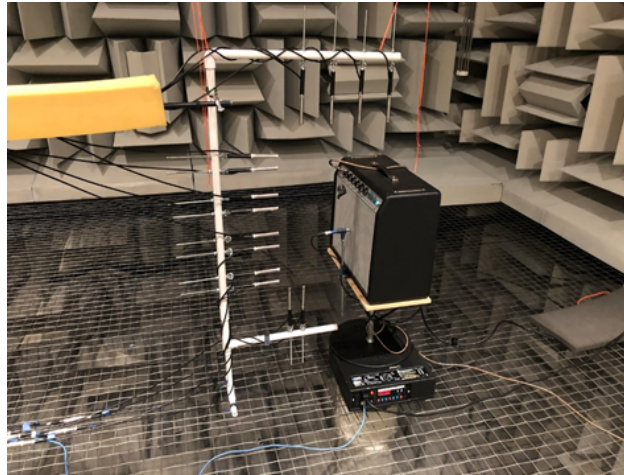


Figure 7.7 Experimental validation setup for the Fender Princeton Reverb amplifier, showing the 14 microphone near-field array. Of note is the gap in the microphone placement near the bottom of the guitar amplifier.

sampling positions for reference in the transverse plane. In the initial configuration shown in Fig. 7.7, the microphone arrangement below the guitar amplifier created a sparsely sampled region that allowed the investigation of associated effects. For later measurements, the bottom microphone nearest to the guitar amplifier shifted closer to it.

7.4.1 Princeton Reverb

Figure 7.8 shows directivity results for the Fender Princeton Reverb at 100 Hz based on a degree $N = 3$ expansion. Because the amplifier has an open back, the radiation pattern at low frequencies has dipole-like characteristics, evident in both the estimated far-field spherical directivity of Fig. 7.8a and the transverse-plane polar directivity of Fig. 7.8b. The measured and estimated far-field transverse directivities in Fig. 7.8b show good agreement.

As frequency increased, the use of regularization helped mitigate errors due to sparse sampling. Figure 7.9 shows the results at 1 kHz using a degree $N = 8$ expansion. In Fig. 7.9b, the transverse-plane measured and estimated directivities agree well in front of and behind the amplifier, but less

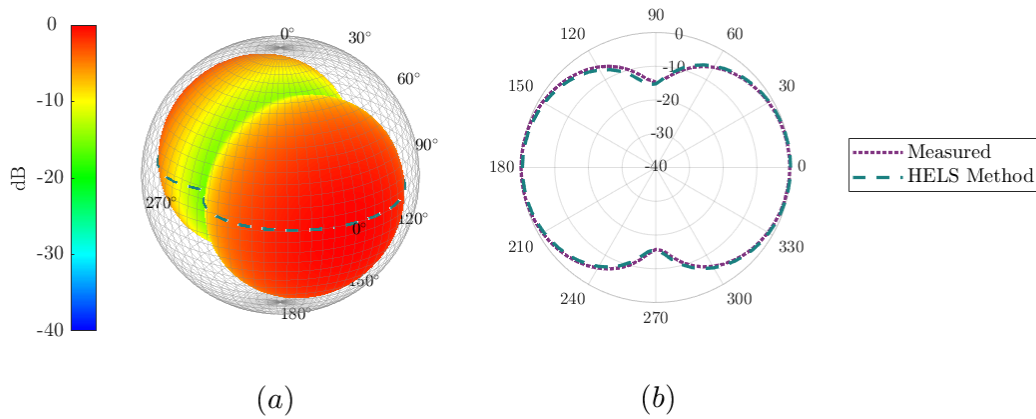


Figure 7.8 Directivity results for the Fender Princeton Reverb amplifier at 100 Hz. (a) Estimated spherical far-field directivity pattern from the HELS method based on degree $N = 3$ expansion, with the transverse polar directivity overlaid as a green dashed line. (b) Measured transverse far-field directivity and estimated transverse directivity.

so within the null regions toward the sides. Interestingly, a large lobe has formed below the guitar amplifier, despite no dominant radiation in that direction. This effect results from a lack of sampling constraints directly below the amplifier, which allows the least-squares fit to reduce the error at other array positions at the expense of higher error in the unconstrained region. Regularization mitigates this outcome by penalizing the prevailing norm of the expansion coefficients. Figure 7.10 shows improved directivity results for the same frequency and expansion degree but with coefficients computed using the regularized pseudo-inverse. The large lobe below the amplifier in Fig. 7.9a is no longer visible in Fig. 7.10a, whereas the main lobe caused by the true amplifier radiation remains intact. The measured and estimated transverse-plane directivities in Fig. 7.10b also show better general agreement, including significantly improved correspondence in the side null regions.

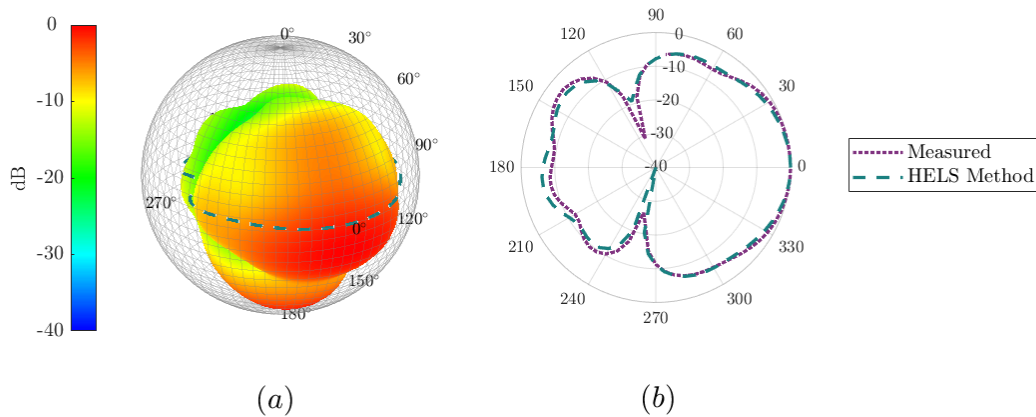


Figure 7.9 Directivity results for the Fender Princeton Reverb amplifier at 1 kHz without regularization. (a) Estimated spherical far-field directivity pattern based on a degree $N = 8$ expansion, with the transverse polar directivity overlaid as a green dashed line. (b) Measured transverse far-field directivity and estimated transverse directivity from the HELS method. Of note is the large lobe below the guitar amplifier shown in (a), where the sampling was sparse.

7.4.2 Twin Reverb

An array reconfiguration that better distributed the bottom microphone positions improved measurement performance and reduced the sparse sampling errors. However, because the bottom microphones were still unable to measure radiation directly beneath the amplifier, regularization remained necessary. Figure 7.11 shows the results for the Fender Twin Reverb at 1.5 kHz. Similar to the Princeton Reverb, the Twin Reverb is an open-back amplifier. However, unlike the Princeton Reverb, the Twin Reverb includes two front-facing loudspeaker drivers. In the directivity balloon shown in Fig. 7.11a, these drivers create an interesting interference pattern with three frontal lobes. The estimated far-field directivity followed from a degree-12 expansion with regularization. There is good agreement between the measured and estimated transverse far-field directivities as shown in Fig. 7.11b. However, within regions more than 10 dB down from the maximum, the method is less reliable.

7.5 Discussion

This work's numerical and experimental results indicate that estimating sound sources' far-field spherical directivities using arbitrarily shaped near-field arrays is plausible. The error curves from BEM results suggest that while all the tested arrays performed roughly the same at low frequencies, the more spherical arrays performed better at higher frequencies. More rigorous analysis is necessary to strengthen this observation and determine the usable bandwidths and other limitations of near-field array types for specific source shapes and dimensions. The work's BEM and experimental results showed that the method's performance began deteriorating above about 2 kHz. As frequency increased, estimation errors also increased but were concentrated primarily in regions that were many dB down from the directivity maximum. For some applications, these errors may be negligible, provided there is an accurate estimation of the directivity in regions where the most sound energy radiates. Future evaluation metrics may benefit from weighting errors by

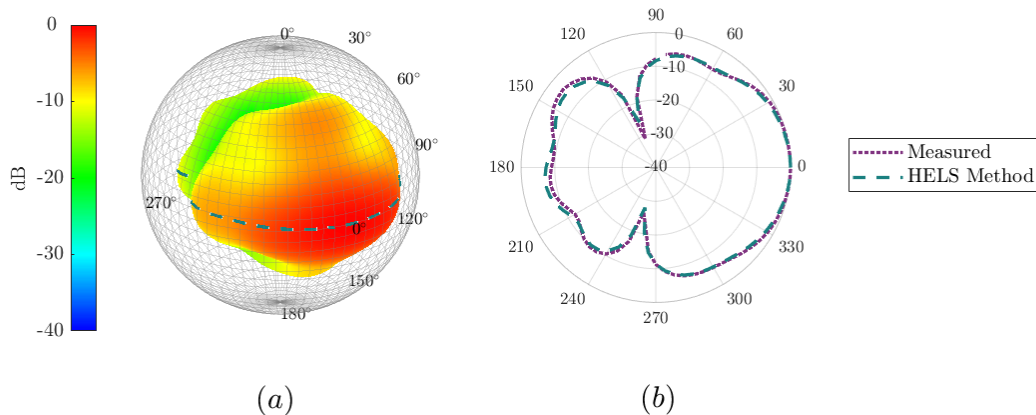


Figure 7.10 Directivity results for the Fender Prinecton Reverb amplifier at 1 kHz with regularization. (a) Estimated spherical far-field directivity pattern based on a degree $N = 8$ expansion, with the transverse polar directivity overlaid as a green dashed line. (b) Measured transverse far-field directivity and estimated transverse directivity from the HELS method. Regularization has removed the large bottom lobe seen in Fig. 7.9a and increased the agreement between the estimated and measured transverse directivities.

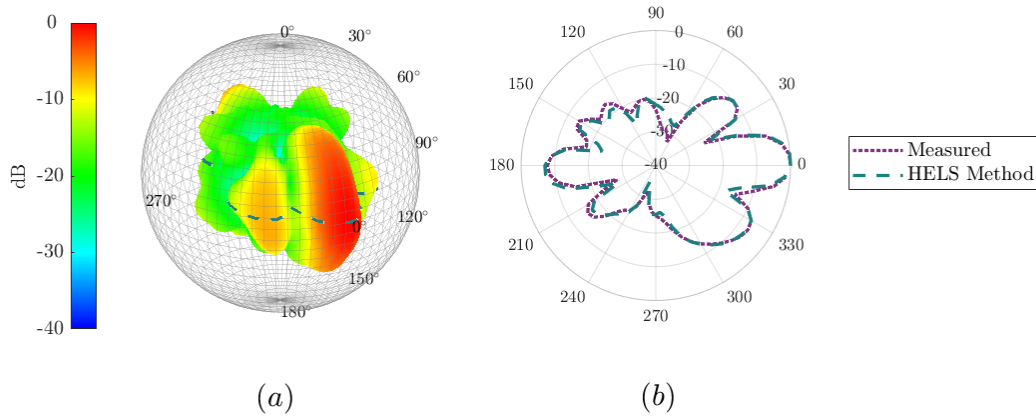


Figure 7.11 Directivity results for the Fender Twin Reverb amplifier at 1.5 kHz. (a) Spherical far-field directivity pattern based on a degree $N = 12$ expansion and regularization, with the transverse polar directivity overlaid as a green dashed line. (b) Measured transverse far-field directivity and estimated transverse directivity from the HELS method.

the intensities in given directions, thus penalizing substantial radiation regions more than weaker ones. In the numerical experiments, the method tended to perform better when sampling positions were within the radiating source's near-field. Consequently, as frequency increases, it may also become desirable to utilize a hybrid approach with far-field propagators [124]. To optimize the model degree, the authors found that $N = kd$ gave a reasonable initial estimate that may benefit from further refinement. Regularization helped improve the quality of the estimated patterns, mainly when sampling was sparse.

7.6 Conclusions

This work has illustrated, both numerically and experimentally, how to obtain far-field spherical directivity patterns of sources using arbitrarily shaped near-field arrays and the HELS method, especially at lower frequencies. However, one must ensure that the expansion degree and regularization are sufficient to provide meaningful results. Future work could include theoretical and experimental

exploration of additional sampling configurations and the validation of experimental results using a known spherical directivity instead of only a polar directivity in a single plane. This work's arrays formed specific shapes, viz., spheres, spheroids, cylinders, and rectangular prisms. It could be of interest to study randomly distributed sampling positions, although this would most likely provide more theoretical insight than practical use in future directivity measurements.

Part III

Directivity Measurement Results

Chapter 8

Gamelan Gong Directivity

This chapter presents directivity measurement results for two gamelan gongs. The results reveal that while at low frequencies the gong's radiation is roughly dipolar, complex directional patterns appear at higher frequencies.

8.1 Introduction

Sound radiation from musical instruments is an essential aspect of their unique sound and musical style. It also contributes to how an instrument portrays musical culture and tradition. Measured directivity patterns, a valuable tool in characterizing sound radiation, have numerous applications such as in room and concert hall acoustical designs [20,21], auralizations [19,99], and microphone placements [14,17]. Previous directivity research has largely concentrated on Western orchestral instruments [1, 7, 20, 125, 126] although there are notable exceptions [21, 31, 127]. Nonetheless, many musical instruments with unique acoustic features, such as Indonesian gamelan gongs, have unresolved radiation characteristics.

Gamelan gongs, primarily found in the Bali and Java regions of Indonesia, are an essential part of the gamelan ensemble of percussion instruments, reflecting the region's rich and complex culture.

Several types of gamelan gongs exist. The *gong ageng*, which translates to “large gongs” or “great gongs”, is the lowest pitch and comes in two variants: *lanang* (male) and *wadon* (female). The *wadon* and *lanang gong ageng* are struck with soft mallets on strong beats in Balinese gamelan music and are left to ring during musical transitions. Several smaller gongs also exist in the gamelan ensemble and have different musical purposes than the *gong ageng*. For example, the *kempur* is played with a soft mallet but is a higher pitch than the *ageng*, while the *bebende* is played with a small wooden hammer and is used for syncopation on off-beats. All are hand-made (traditionally from bronze) and therefore have non-constant thickness. Gamelan gongs differ from other gongs, such as the *tam-tam*, in that the edge of the rim is extended, wrapping backward a distance roughly equal to half the radius of the gong. Gamelan gongs also have a raised dome (polished gold color) called a *boss* in their center. The height and size of the boss vary between the gamelan gong types.

The structural acoustics of gamelan gongs have been the focus of several studies. McLachlan [128] measured changes in the acoustic outputs of gongs constructed of different materials due to his interest in the gong’s tuning procedure. His results determined that the boss beaten into the gong’s face raised its fundamental frequency, whereas thinning lowered it. His finite-element method (FEM) models illustrated how the boss shape, gong rim thickness, and rim angle all modified and tuned modal frequencies.

Krueger et al. [129] investigated *ombak*, an acoustic beating phenomenon of the *wadon gong ageng* that occurs when struck on the boss.¹⁵ Microphone and scanning laser Doppler vibrometer (SLDV) measurements helped identify the natural frequencies of the instrument. In addition to determining the frequencies of the first two axisymmetric modes, they found frequency peaks at the second and third harmonics of the first mode, suggesting that nonlinear effects exist. Other peaks at sum and difference frequencies of these modes were also detected. Subsequent measurements using increasing excitation force confirmed that nonlinear interactions occurred and were responsible for creating the *ombak* effect.

Perrin et al. [130] studied a small gamelan gong. Their analysis employed finite-element method (FEM) modeling, electronic speckle pattern interferometry (ESPI), and SLDV scans to tabulate its modal frequencies. Although discrepancies in the modal frequencies arose between the measurement modalities, the authors generally found that the “modified Chladni’s law” gave predictions in good agreement with the ESPI data. They confirmed nonlinear behavior and identified three modes as the most acoustically significant: the radial (0, 1) mode and the pair of angular-radial (1, 1) modes.

While many studies have thus provided more knowledge regarding the structural modes of gamelan gongs, their acoustic radiation patterns have remained unclear. Zotter [31] measured the directivity of an ageng gamelan gong using a 10-channel microphone array and assuming axial symmetry. He found dipole-like directivity for the first two axial modes of the instrument. He also included results for time-varying directivities due to beating effects. However, the symmetry assumption limited the analysis to only two modes.

This work compares the directivity patterns of an ageng lanang and a bebende Balinese gamelan gong evaluated by a high-resolution spherical directivity measurement system. Driving the gongs at low amplitude by a shaker ensured that nonlinear effects such as *ombak* did not occur. Subsequent SLDV scans accompany the directivity results and reveal connections between the gong’s far-field radiated patterns and its mode shapes. The results show that differences in the radiation patterns occur between the gongs for similar surface velocity distributions. Comparisons between computed directivity index (DI) values at resonance peaks to those of dipole and quadrupole sources highlight the gongs’ multidirectional radiation. Similar to Zotter’s results, the directivities show dipole-like radiation for the first two modes. Other low-order modes exhibit dipole-like radiation, while higher-order modes radiate with more complex directivity patterns. The sound power of each gong illustrates how structural mode ordering may relate to the musical purpose of the two gongs.

8.2 Methods

8.2.1 Measurements

Figure 15.8 shows the lanang gong within the measurement system, whereas Fig. 8.2 shows the bebende gong. Both gongs are hand-made from bronze, with a thickness ranging from 2 to 4 mm. The radius of the lanang's face is about 41 cm, while the radius of the bebende's face is about 25 cm. In contrast to typical Javanese gongs, only the gong's boss is polished to a gold color. While the lanang's boss is pronounced, with a height of about 4 cm and a radius of 8.5 cm, the bebende's 6 cm radius boss is sunken to a height of 0.3 cm. The sides extend backwards 24 cm for the lanang and 17.5 cm for the bebende. These elongated sides form a circular cavity behind the gong about 35 cm in radius for the lanang and 20.5 cm in radius for the bebende. This unique geometry due to the boss and elongated sides is less common, found primarily in Indonesia.

A rotating semicircular microphone array measured the directivity of the gamelan gongs. The microphone array consisted of 36 12.7 mm (0.5 in) precision microphones spaced in 5° degree increments in the polar angle. Array rotations in 5° azimuthal steps allowed a full spherical scan of 2,521 unique sampling positions, consistent with the AES directivity sampling standard [33], with the omission of the nadir position. A near-field reference microphone provided an acoustic input signal for calculating frequency response functions (FRFs) between it and the output of each array microphone signal. Frequency-dependent relative calibrations between the array and reference microphones ensured proper level normalizations in subsequent post-processing which would otherwise appear as latitudinal banding in directivity balloon plots.

Three repetitions of a 5 second linear swept-sine input signal sent to a shaker (LDS V203) excited the gong over the audible bandwidth. Although the large gamelan gong's have interesting non-linear vibrations, this work applied low-amplitude levels to ensure operation over the linear regime of the gong. A small moveable mount positioned the shaker behind the gong, allowing



Figure 8.1 An ageng lanang gamelan gong within the rotating directivity measurement array.

several measurements with different contact points. The contact position used in the following analysis was placed on the back side of the gong's face between the boss and rim wall, as this position excited several modes which do not appear when the shaker attached directly to the gong's boss. Each of the 72 azimuthal positions produced 37 24-bit, 48 kHz recordings using Focusrite Rednet4 digital audio interfaces.

The structural vibrations of the gong determine its directional behavior. Thus, visualizations of the gongs' surface velocity provide insight into the gong's directivity. To better understand how the gong's modal shapes influenced its directivity, additional measurements followed from an SLDV scan of the instruments. Similar to the directivity measurements, the shaker excited the instrument

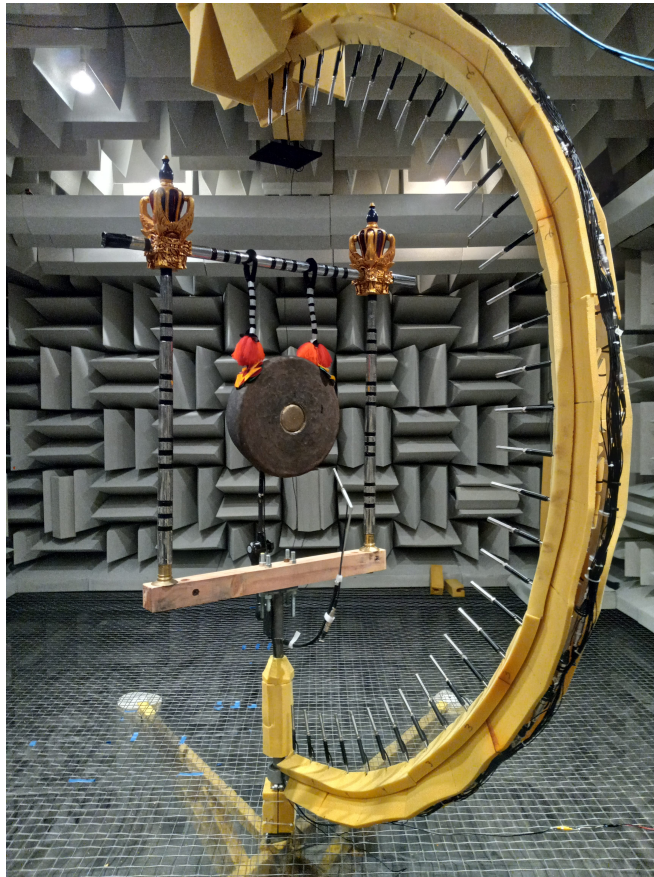


Figure 8.2 An bebende gamelan gong within the rotating directivity measurement array.

while the SLDV laser head scanned 977 positions on the gong's front face. The shaker's position was in a similar location so that all measured modes of interest appeared in both the SLDV scan and directivity results. The spatial resolution allowed modal analysis well above 1.5 kHz, although this work primarily focuses on results up to this frequency.

8.2.2 Signal Processing

While the shaker input excitation signal is more repeatable than that of played musical instruments, FRFs nonetheless increase extraneous noise immunity and provide a convenient normalization to address any variations that might occur between measurement rotations [1]. The near-field input autospectrum $G_{aa,v}$ for the v^{th} rotation and the FRF H_{uv} for the u^{th} array microphone and v^{th} rotation followed from standard spectral estimation and deconvolution procedures. [131, 132]

The radiated sound power of the source provides a straightforward method to identify the gong's modal frequencies. Because the spherical surface followed from multiple rotations of the measurement system, the effective input autospectrum [6],

$$G_{aa,eff}(f) = \frac{\sum_{u=0}^{U-1} \sum_{v=0}^{V-1} w_{uv} G_{aa,v}(f) |H_{uv}(f)|^2}{\sum_{u=0}^{U-1} \sum_{v=0}^{V-1} w_{uv} |H_{uv}(f)|^2}, \quad (8.1)$$

where w_{uv} are quadrature weights for numerical integration over the sphere [78, 133], yielded an averaged input autospectrum over the azimuthal rotations. The time-averaged sound power radiated by the gong was then [62, 131]

$$\langle W(f) \rangle_t = R^2 \frac{G_{aa,eff}(f)}{\rho_0 c} \sum_{u=0}^{U-1} \sum_{v=0}^{V-1} w_{uv} |H_{uv}(f)|^2, \quad (8.2)$$

where R is the measurement radius. Peaks of $\langle W(f) \rangle_t$ indicated the gong's modal frequencies for further analysis.

Coherence functions at each sampling position γ_{uv}^2 also helped quantify noise levels and indicated when the instrument excitation levels were no longer sufficient to produce meaningful directivity

functions [6]. The spatially averaged coherence follows by averaging the coherence function over the sphere

$$\langle \gamma^2(f) \rangle_S = \sum_{u=0}^{U-1} \sum_{v=0}^{V-1} w_{uv} \gamma_{uv}^2(f). \quad (8.3)$$

It provides a useful metric for evaluating the signal-to-noise ratio over the entire measurement surface for a particular frequency. The averaged value over all modes considered was $\langle \gamma^2(f) \rangle_S = 0.97$, indicating acceptable signal-to-noise ratios over the frequencies of interest.

8.2.3 Spherical Harmonics and Directivity Functions

The spherical harmonics provide an orthonormal basis for expanding directivities over the spherical evaluation surface [31, 114]. As the angular component of the Helmholtz-equation solution on the exterior domain, they find important applications in wave-based modeling of sound fields [59]. The normalized spherical harmonics of degree n and order m are defined here as [70]

$$Y_n^m(\theta, \phi) = \sqrt{\frac{2n+1}{4\pi} \frac{(n-m)!}{(n+m)!}} P_n^m(\cos \theta) e^{im\phi}, \quad (8.4)$$

where P_n^m are the associated Legendre functions of degree n and order m .

The pressure field for $r \geq R$ is [59]

$$p(r, \theta, \phi, k) = \sum_{n=0}^{\infty} \sum_{m=-n}^n c_n^m(k) h_n^{(2)}(kr) Y_n^m(\theta, \phi), \quad r \geq R, \quad (8.5)$$

where $h_n^{(2)}(kr)$ are the spherical Hankel functions of the second kind (for outward propagation and $e^{i\omega t}$ time dependence). The expansion coefficients follow by exploiting the spherical harmonic's orthogonality over the sphere:

$$c_n^m(k) = \frac{1}{h_n^{(2)}(kR)} \int_0^{2\pi} \int_0^\pi p(R, \theta, \phi, k) [Y_n^m(\theta, \phi)]^* \sin \theta d\theta d\phi, \quad (8.6)$$

where $*$ indicates complex conjugation. Numerical quadrature allows evaluation of the integral [133].

The sampling density applied in this work permits expansions up to a maximal degree $N = 34$ expansion [78].

Because the measurement system produces discretely sampled directivity functions, considering the frequency range under which the sampling density remains sufficient for analysis is important. For spherical harmonics applications, spatial aliasing effects may limit the usable bandwidth. One approach to identifying spatial aliasing is to consider the magnitude of the spherical harmonic coefficients of a given degree. Because the maximum degree n necessary for representation at a given wavenumber k is roughly $n = ka$, where a is the source dimensions, one may estimate an initial limiting frequency based on geometric arguments [83]. For example, the ageng lanang gong radius is $a = 0.41\text{m}$ so that a maximal spherical harmonic expansion degree of $N = 34$ suggests an upper bound of around 4.5 kHz.

Figure 11.8 plots the spherical spectrum [59, 114] of the larger ageng lanang gong over expansion degree n and frequency f . Color indicates the relative level of each coefficient relative to the maximum for each frequency on a logarithmic scale. White indicates high energy (important) coefficients whereas black indicates low energy (unimportant) coefficients. As anticipated, the number of expansion coefficients required increases linearly with respect to frequency. The overlaid dashed line indicates the line $n = (0.41\text{m})k$, based off of geometrical arguments. The regions of coefficients with the largest magnitudes fall below this line. However, it is also apparent that there are some coefficients above this line which are non-negligible. To ensure the expansion has all coefficients with no less than -20 dB down from the maximum limits the maximum frequency range to about 2 kHz. This limiting frequency lies above the frequencies under analysis in the present work so that the sampling resolution is sufficient. Because the bebende gong is smaller than the ageng lanang, aliasing effects do not occur until an even higher frequency.

Once determined, the expansion coefficients allow computation of extrapolated far-field directivities via the large-argument representations of the spherical Hankel functions: [62]

$$D_{ff}(\theta, \phi) = \sum_{n=0}^{\infty} \sum_{m=-n}^n c_n^m(k) i^{n+1} Y_n^m(\theta, \phi). \quad (8.7)$$

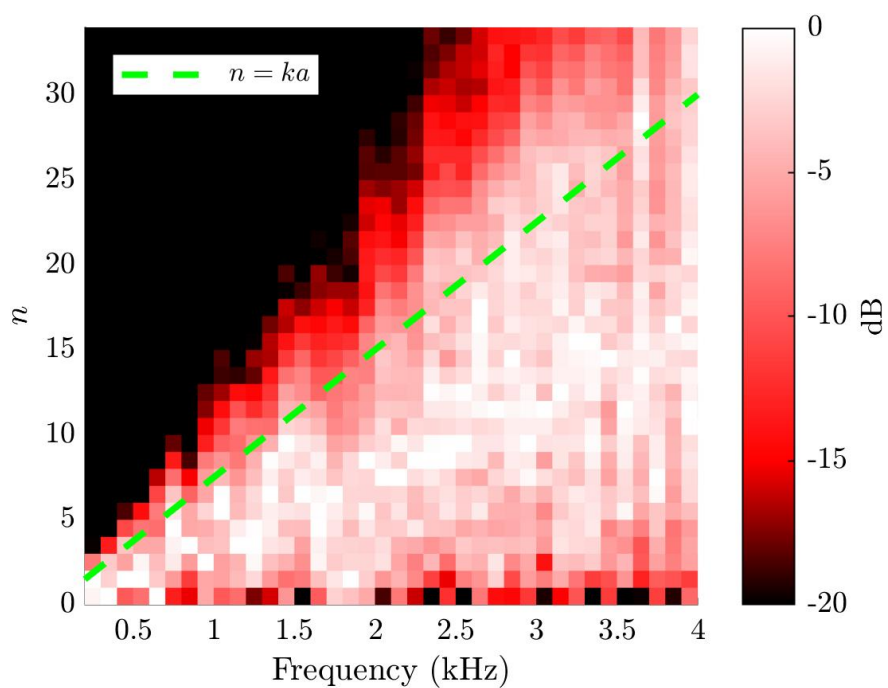


Figure 8.3 Spherical spectrum of the agneng lanag gamelan gong. Each rectangle indicates the energy contained in a given expansion coefficient summed over all orders m for fixed degree n calculated in 100 Hz steps.

Extrapolation of the complex pressure also allows far-field corrections for the sound power estimate when R is in the near-field of the source. Additionally, far-field propagation corrects near-field directivity variations due to possible source misalignment between the acoustic center of the source and the geometric center of the array [45, 82].

The directivity factor function, defined as

$$Q(\theta, \phi, f) = \frac{4\pi |D_{ff}(\theta, \phi, f)|^2}{\int_0^{2\pi} \int_0^\pi |D_{ff}(\theta, \phi, f)|^2 \sin \theta d\theta d\phi}, \quad (8.8)$$

represents the sound intensity in a given direction relative to the that of an omnidirectional source with the same sound power. [10] The directivity index DI expresses it on a logarithmic scale, i.e., $DI = 10 \log_{10} Q$.

An area-weighted, directivity factor function deviation σ_Q quantifies directivity deviations between two different patterns as [81]

$$\sigma_Q = \int_0^{2\pi} \int_0^\pi |Q_1(\theta, \phi) - Q_2(\theta, \phi)| \sin \theta d\theta d\phi. \quad (8.9)$$

It may be expressed on a logarithmic scale as

$$L_Q = 10 \log_{10}(1 + \sigma_Q) \quad (8.10)$$

where the addition of one maps a value of $\sigma_Q = 0$ to a deviation level $L_Q = 0$ dB. It is similar to the area-weighted root-mean-square deviation [6] except for directivity normalization by power instead of levels.

8.3 Results

8.3.1 Directivity Results

Ageng Lanang

Figure 8.4a-e shows the propagated and normalized far-field directivities at frequencies corresponding to the lowest five modal peaks. Color and balloon radius indicate the relative levels on a 40 dB scale and the overlaid grid indicates the angular locations of the sampling positions of the measurement system. The gong faced the 0° degree azimuthal angle marker during the measurements. All directivity balloons appear from the same vantage point, above and slightly to the left of the gong. Figure 8.4f-j plots the out-of-plane surface velocities as measured by the SLDV. The velocities are normalized to the maximum with red color indicating in-phase vibrations and blue indicating out-of-phase vibrations.

As seen in Figs. 8.4a through 8.4c, the directivity is roughly dipolar for the first three modes. At 63 Hz (Fig. 8.4a), the dipole moment falls to the x -direction (towards the 0° azimuthal marker) so that a null occurs in the plane of the gong face (yz -plane). However, for the other two frequencies, the dipole moment is directed towards the positive y - z -direction at 94 Hz (Fig. 8.4b) and the negative y - z -direction for 104 Hz (Fig. 8.4c). These latter two modes appear to be roughly variations of each other through a 90° rotation.

Visualization of the associated surface velocity provides some insights into the directional behavior. For example, at 63 Hz (Fig. 8.4f), the gong appears to be vibrating as a $(0, 1)$ mode. Consequently, the gong's face moves forwards and backwards along the x -axis. This vibration is similar to that of an oscillating disk which produces a dipole-like directivity. [62] Thus, the dipole-like directivity seen in Fig. 8.4a may be attributed to this motion.

Figures 8.4g and 8.4h show $(1, 1)$ modal patterns. Interestingly, the null lines in the dipole-radiation seen in Fig. 8.4b and 8.4c align with the apparent node lines on the gong's surface. Given

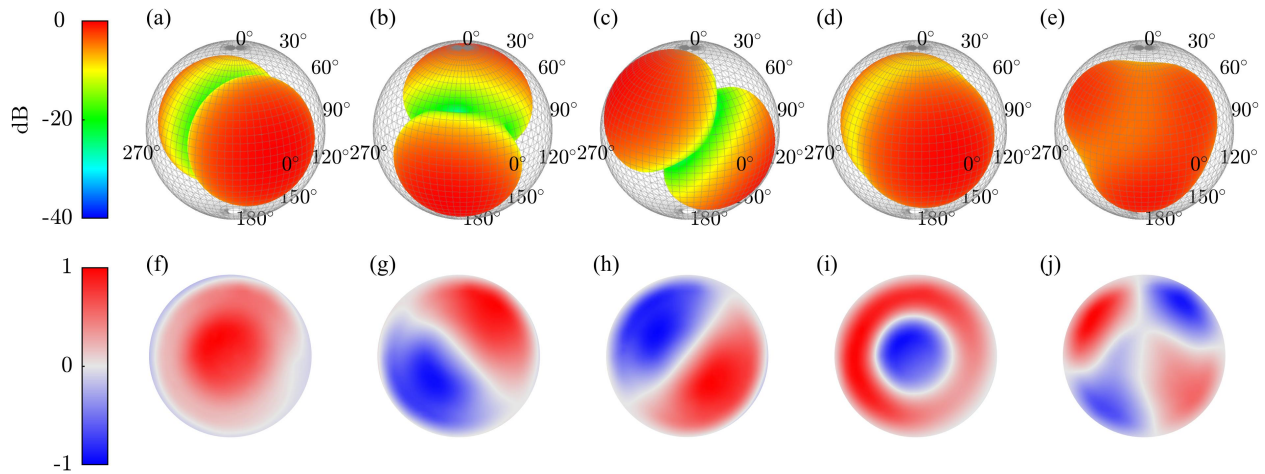


Figure 8.4 Propagated and normalized far-field directivities for the ageng lanang's lowest five modal frequencies. (a) 63 Hz. (b) 94 Hz. (c) 104 Hz. (d) 130 Hz. (e) 168 Hz. Out-of-plane surface velocity for the same modal frequencies. (f) 63 Hz. (g) 94 Hz. (h) 104 Hz. (i) 130 Hz. (j) 168 Hz.

that the surface velocity distribution on the back face of the gong has opposite polarity to the distribution on the front face, it is somewhat surprising that these modes do not form an angled lateral quadrupole.

At 130 Hz (Fig. 8.4d), the directivity is bi-directional, with the strongest radiation in front of and behind the gong. Although the pattern is somewhat similar to that of the dipole-like radiation at 63 Hz, the null between the two strongly radiating lobes is not as pronounced. At 63 Hz, the null is nearly 20 dB down from the maximum compared to only about 10 dB down at 130 Hz. The corresponding surface velocity (Fig. 8.4i) shows a $(0, 2)$ mode. Interestingly, these axisymmetric $(0, 1)$ and $(0, 2)$ modes at 63 Hz and 130 Hz share quasi-axisymmetric radiation patterns.

The directivity at 168 Hz (Fig. 8.4e) is more complex, with strong radiation in a broad region in front with reduced radiation behind the gong. Its associated surface velocity (Fig. 8.4j) shows four regions of in and out-of-phase vibration which appear as a distorted $(2, 1)$ pattern. Unlike for the other modes, there does not visually appear to be a direct correlation between surface null lines and the radiated pattern.

Figure 8.5 plots the directivity for select higher frequency modal peaks. While at lower frequencies the radiation is simpler and primarily dipolar for many modes, the directivity at higher frequencies becomes more complex. For example, at 367 Hz (Fig. 8.5b), the directivity pattern has four distinct lobes directed to the sides of the gong. The two lobes closest to the transverse (xy) plane are about 5 dB stronger than those falling along the median plane. Some slight radiation is also apparent behind the gong. The associated surface velocity (Fig. 8.5g) appears as a (2,2) mode with one radial node line and two angular node lines, leading to eight regions of in and out-of-phase vibration. The location of the angular node lines agrees with the location of the directivity nulls seen in Fig. 8.5b in a similar fashion to the dipole-like results at 94 Hz and 104 Hz (Fig. 8.4b and Fig. 8.4c).

In contrast, at 420 Hz (Fig. 8.5c) the radiation is primarily behind the gong and relatively little sound radiates to the sides. The surface velocity at 420 Hz (Fig. 8.5h) is more complex and does not appear to have a direct correspondence to the directional response. Figure 8.5d reveals that eight lobes which are roughly uniformly distributed around the gong form at 566 Hz. Interestingly, the radiation lobes behind the gong are stronger than those in front by about 3 dB. Despite its complex surface velocity distribution (Fig. 8.5i), there are four edge anti-nodal regions, which appear to correspond to the nulls between directional lobes in the radiated pattern.

At 650 Hz (Fig. 8.5e), a quasi-symmetric six-lobed pattern forms, with the strongest regions of radiation being to the sides of the gong. Again, six edge anti-nodal regions appear (Fig. 8.5j) and tend to align with the location of nulls between the directivity lobes. These few examples illustrate the complexity of the gong's radiation at higher frequencies. Additionally, the correspondence between edge anti-nodal regions and the number of directivity lobes forming at 94 Hz, 104 Hz, 420 Hz, 566 Hz, and 650 Hz strongly suggests their significant role in gamelan gong radiation.

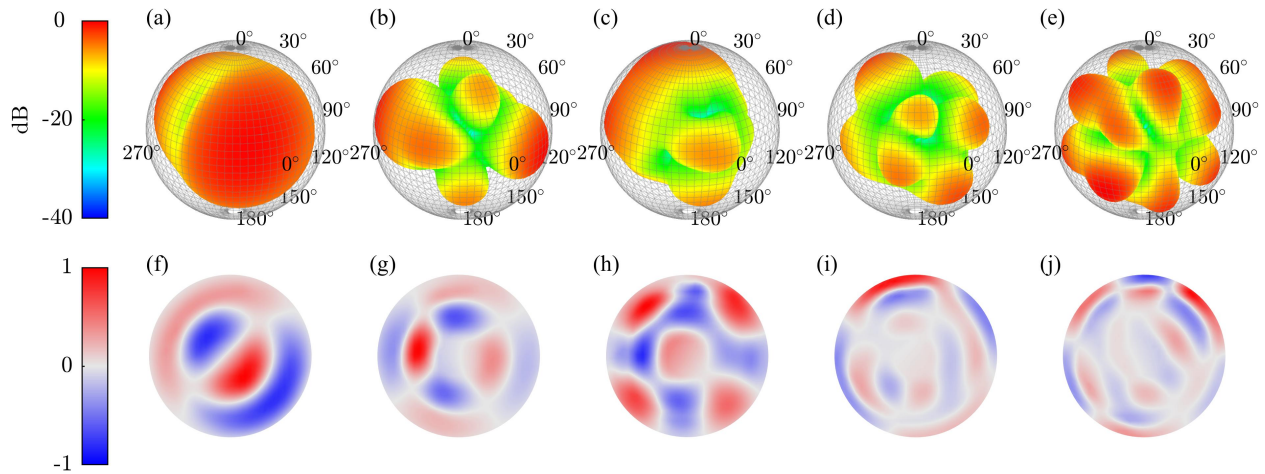


Figure 8.5 Propagated and normalized far-field directivities for select higher frequency modes of the lanang ageng. (a) 198 Hz. (b) 376 Hz. (c) 420 Hz. (d) 566 Hz. (e) 650 Hz. Out-of-plane surface velocity for the same modal frequencies. (f) 198 Hz. (g) 376 Hz. (h) 420 Hz. (i) 566 Hz. (j) 650 Hz.

Bebende

The bebende gong shows some similarities to the larger ageng lanang gong, although distinct differences remain. Figure 8.6 plots the directivity of the lowest five measured modal frequencies of the bebende gong. Similar to previous figures, the out-of-plane surface velocity for the same frequencies appear below for reference. Like the ageng lanang, the lowest mode at 144 Hz (Fig. 8.6a) corresponds to a dipole-like directivity, with the dipole moment on-axis and the null appearing in the plane of the gong. Both these modes correspond to a similar $(0, 1)$ mode-like surface velocity (Fig. 8.4f and Fig. 8.6f).

However, the next two modes present different directional characteristics than those corresponding to the same mode shape for the ageng lanang. At 226 Hz (Fig. 8.6b) and 239 Hz (Fig. 8.6c), the directivity remains quasi-dipole like with the dipole moment oriented slightly up and down, respectively. However, the surface velocities, which both appear as $(1, 1)$ modes in Fig. 8.6g and Fig. 8.6h, are similar to those of the ageng lanang seen in Fig. 8.4g and Fig. 8.4h. Despite the similarities of the surface velocity, the directivities appear very different.

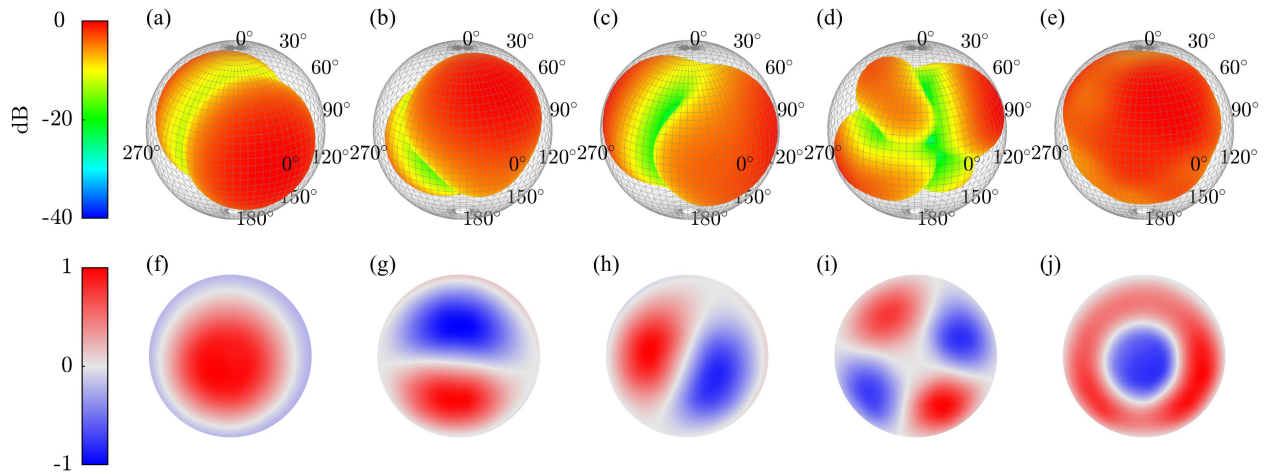


Figure 8.6 Propagated and normalized far-field directivities for the bebende gong's lowest five modal frequencies. (a) 144 Hz. (b) 226 Hz. (c) 239 Hz. (d) 389 Hz. (e) 469 Hz. Out-of-plane surface velocity for the same modal frequencies. (f) 144 Hz. (g) 226 Hz. (h) 239 Hz. (i) 389 Hz. (j) 469 Hz.

The mode ordering between the ageng lanang and the bebende is the same for the first three modes. For the next three, the order differs, with the $(1,2)$ mode appearing before the $(0,2)$ mode for the bebende gong. The different ordering is seen in the directivity patterns. At 389 Hz (Fig. 8.6d), the directivity balloon has four lobes roughly corresponding to the four anti-nodal regions seen in the $(1,2)$ mode shape. At 469 Hz (Fig. 8.6e), the directivity appears more omnidirectional than that for the corresponding mode shape for the ageng lanang (Fig. 8.4d).

Higher frequency results shown in Fig. 8.7 highlight unique radiation characteristics for the bebende gong. Similar to the results for the ageng lanang, the location and number of anti-nodal regions on the gongs face correspond to the number of lobes to the side of the gong for the directivity at the modal peaks at 592 Hz (Fig. 8.7a), 849 Hz (Fig. 8.7b), and 1112 Hz (Fig. 8.7c). The surface velocity distributions at these frequencies, seen in Fig. 8.7f-h, have two, four and eight anti-nodal edge regions which correspond to the location and position of the two, four and eight lobes seen in Fig. 8.7a-c. Thus, similar to the ageng lanang, at higher frequencies the radiation appears to be influenced by the number and location of anti-nodal edge regions.

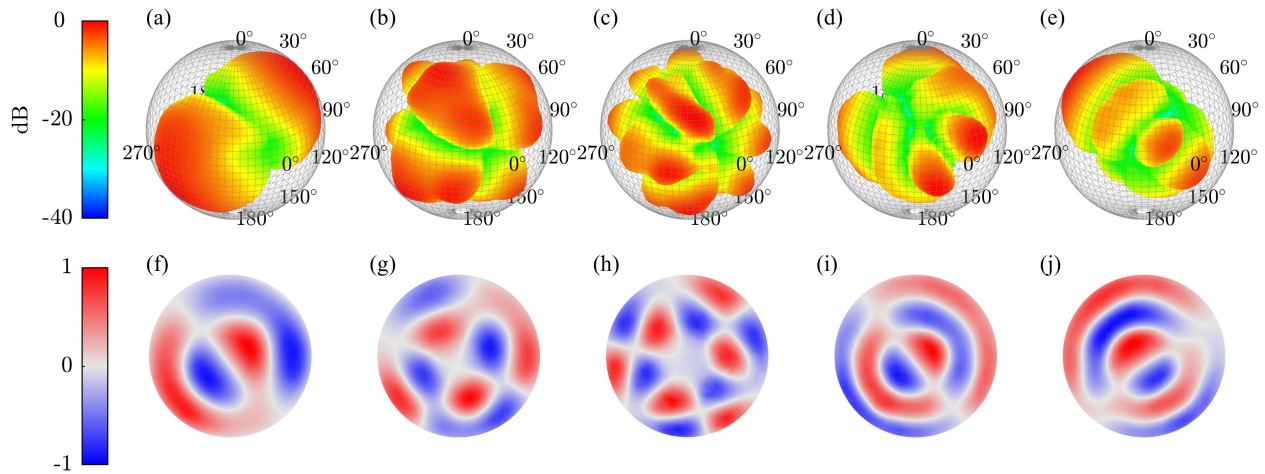


Figure 8.7 Propagated and normalized far-field directivities for select higher frequency modes of the bebende. (a) 592 Hz. (b) 849 Hz. (c) 1112 Hz. (d) 1180 Hz. (e) 1204 Hz. Out-of-plane surface velocity for the same modal frequencies. (f) 592 Hz. (g) 849 Hz. (h) 1112 Hz. (i) 1180 Hz. (j) 1204 Hz.

The directivity at 1180 Hz (Fig. 8.7d) and 1204 Hz (Fig. 8.7e) each have six lobes. Unlike those seen in Fig. 8.7a-c; however, the lobes do not fall in the plane of the gong's face (yz) plane. The associated normal particle velocity seen in Fig. 8.7i-j show an apparent $(1,3)$ mode, leading to six anti-nodal regions. The orientation of these anti-nodal regions corresponds very strongly to the six lobes visible in the far-field radiated pattern.

8.4 Analysis

8.4.1 Modal Frequencies

Despite belonging to the same instrument family, the directivity patterns of the ageng lanang and bebende gongs greatly differ even for similar surface velocities. These differences in part may be due to differing geometry and material inhomogeneity. For example, the ageng lanang has a deeper boss and shallower side walls. However, another important characteristic is the acoustic wavelength relative to the structural modal frequency.

To consider these differences, Fig. 14.3 plots the normalized $\langle W(f) \rangle_t$ radiated by the ageng lanang gong when excited by the shaker, plotted as a function of both frequency dimensionless ka , where $a = 0.41$ m is the gong's radius. As anticipated, the instrument's modal nature strongly characterizes its acoustic output. Below 200 Hz, eight sharp, distinct peaks evidence the gong's lowest modes. The spectral region from 200 Hz to around 350 Hz appears as a gap with no strongly radiating modes. The spectral region between 350 Hz and 1 kHz shows increased modal density with many modes radiating within 20 dB down from the maximum. Above 1 kHz, the radiated power rolls off at roughly 10 dB per octave.

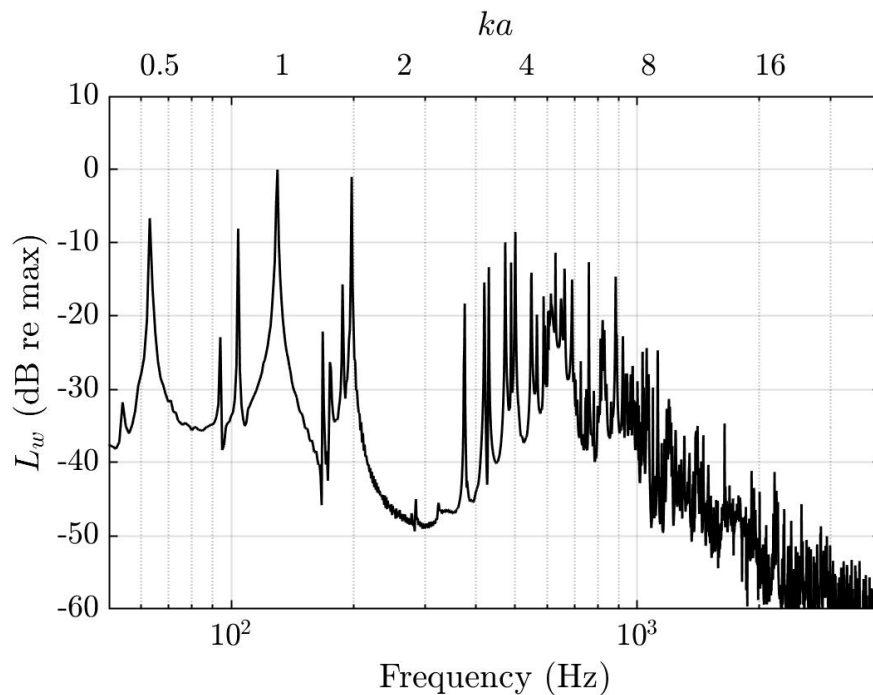


Figure 8.8 Normalized time-averaged sound power spectrum radiated from the ageng lanang gong when excited by a shaker.

Figure 8.9 plots the normalized $\langle W(f) \rangle_t$ radiated by the bebende gong when excited by the shaker, plotted as a function of both frequency dimensionless ka , where $a = 0.25$ m is the gong's radius. In contrast to the ageng lanang gong's result, there does not appear to be a band gap between

the lowest and higher modes. Additionally, the spacing between modal peaks and their relative wavelengths differ between the two gongs.

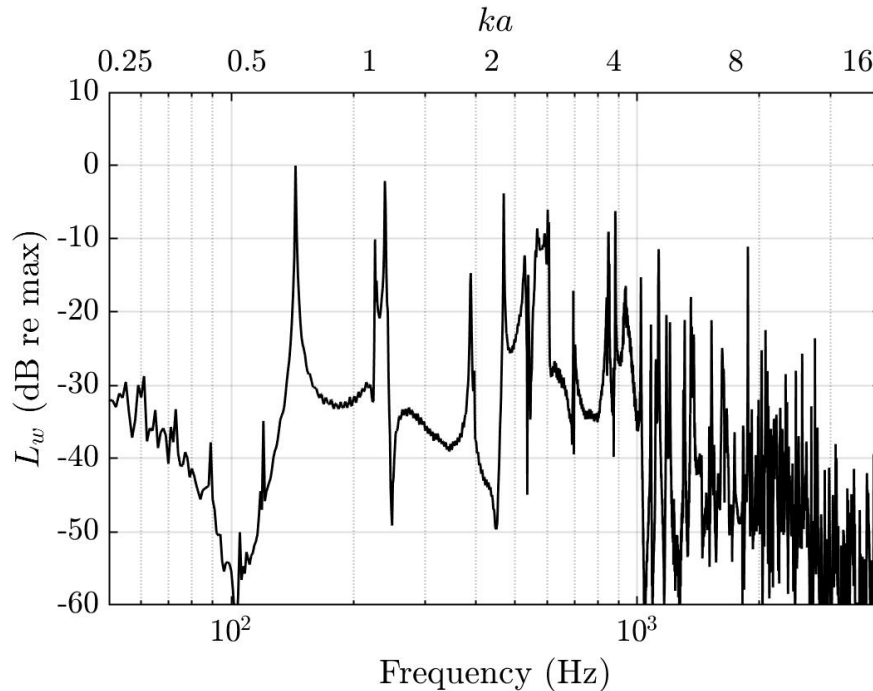


Figure 8.9 Normalized time-averaged sound power spectrum radiated from the kemur gong when excited by a shaker.

Tables 8.1 and 8.2 tabulate the modal frequencies, associated acoustic wavenumber, and estimated radial and angular node numbers for the first ten modes of the gongs. While the ordering of the first three modes is the same for both gongs, significant differences arise for the other higher modes. These ordering differences in turn lead to different acoustic wavelengths for the same mode number. Consequently, even if the gongs had similar sizes and geometry, the differing mode order relative to frequency would lead to distinct directivity patterns.

Besides variations in directivity patterns, differences in the gong's modal frequencies explains why the lanang produces ombak while the bebende does not. Krueger et al. [129] determined that ombak occurs because non-linear excitation of the first axisymmetric mode generates a harmonic near the second axisymmetric mode. For the lanang, the first axisymmetric mode (0, 1) appears at

64 Hz. Consequently, a non-linearly produced second harmonic would appear near 128 Hz. This is only slightly lower than the 130 Hz second axisymmetric mode (0, 2) and would lead to a 2 Hz beating when excited together. In contrast, the bebende's first axisymmetric mode resonates at 144 Hz so a non-linearly produced second harmonic would appear at 288 Hz. This frequency is not near the 472 Hz second axisymmetric mode nor any other measured modes. Thus, modal frequency location clarifies why the lanang produces a beating phenomena when strongly struck whereas the bebende does not.

Table 8.1 Lanang gong mode order based on SLDV measurements.

Frequency (Hz)	ka	Angular Number	Radial Number
64	0.5	0	1
94	0.7	1	1
104	0.8	1	1
130	1.0	0	2
168	1.3	2	1
174	1.3	2	1
188	1.4	1	2
198	1.5	1	2
276	2.1	3	1
284	2.1	3	1

8.4.2 Directivity Index

The directivity index (DI) provides a simple metric for quantifying how directional a source is. It is typically reported as a value along the principal axis of radiation, although some have considered its generalization to the entire sphere [10, 134]. For loudspeakers and other transducers, the principal

Table 8.2 Bebende gong mode order based on SLDV measurements.

Frequency (Hz)	ka	Angular Number	Radial Number
144	0.7	0	1
224	1.0	1	1
240	1.1	1	1
388	1.8	2	1
472	2.2	0	2
536	2.5	3	1
546	2.5	3	1
606	2.8	1	2
692	3.2	4	1
844	3.9	2	2

axis of radiation is usually obvious from source geometry. However, as evidenced by their complex, multi-directional radiation patterns, this is not the case for the gamelan gongs. To accommodate the complex radiation patterns of the gamelan gongs, this work extracts the maximum DI value over the sphere and its associated angular position similar to the approach applied in Ref. 135.

Figure 8.10a plots the maximum value of the DI over the sphere at each extracted modal peak. The DI values for the ageng lanang appear as circles whereas those for the bebende appear as diamonds. For a dipolar source, $D(\theta, \phi) \propto \cos \theta$ [62] so the DI is $10\log_{10} 3 \approx 4.77$ dB. This value is overlaid as a dashed line. The eight lowest modes of the ageng lanang and the lowest three modes and the fifth mode of the bebende fall into this range. This is in good agreement with the directivities seen in Fig. 8.4a-d and Fig. 8.6a-c, which have dipole-like radiation characteristics.

For a lateral quadrupole, $D(\theta, \phi) \propto \cos \theta \cos \phi$ [62] so the DI is $10\log_{10} 6 \approx 7.78$ dB. This value is overlaid as a dash-dot line. From around 200 Hz to 1 kHz, the DI climbs from levels

corresponding to dipole radiation to levels corresponding to quadrupole radiation. Above 1 kHz, the DI for some modes increases higher, approaching a level of 12 dB.

Figure 8.10b plots the direction of the strongest radiation over the sphere. Interestingly, the trends of both gongs is markedly different. For the ageng lanang, only a few modes (including the lowest) radiate strongest directly in front of the gong. Most of the other modes radiate strongly in the region $x < 0$ (behind the gong face's plane). For the bebende gong, more modes tend to radiate strongly in region $x > 0$ (in front of the gong face's plane) although many modes also radiate strongly to the side and behind. These results are also in good agreement with the select directivities seen in Figs. 8.4 - 8.7.

Because of the noted correlations between edge anti-nodal regions and the number of lobes, it is insightful to consider the DI as a function of both angular and radial node number rather than frequency. Figure 8.11 plots the DI values as a function of the estimated angular and radial node numbers for the extracted modal frequencies. Although there are some trends, such as general lower DI values for low angular node numbers, the spread of DI as a function of angular and radial node number is quite large. Nonetheless, it does appear, especially for angular numbers greater than three, that the DI may be correlated to the number of angular node lines. Nonetheless, the inclusions of even higher modes than considered in this study could modify this trend.

The DI values and positions quantify radiation trends visualized in the directivity balloons. First, at low frequencies, the radiation is primarily dipole-like. For intermediate and higher frequencies it rises to levels similar and exceeding quadrupole-like radiation. Thus, the gongs can be considered multi-directional radiators. In general, the strongest regions of radiation for many modes are to the side and behind the gong. Lastly, angular node number may be more strongly correlated with DI values than radial node number.

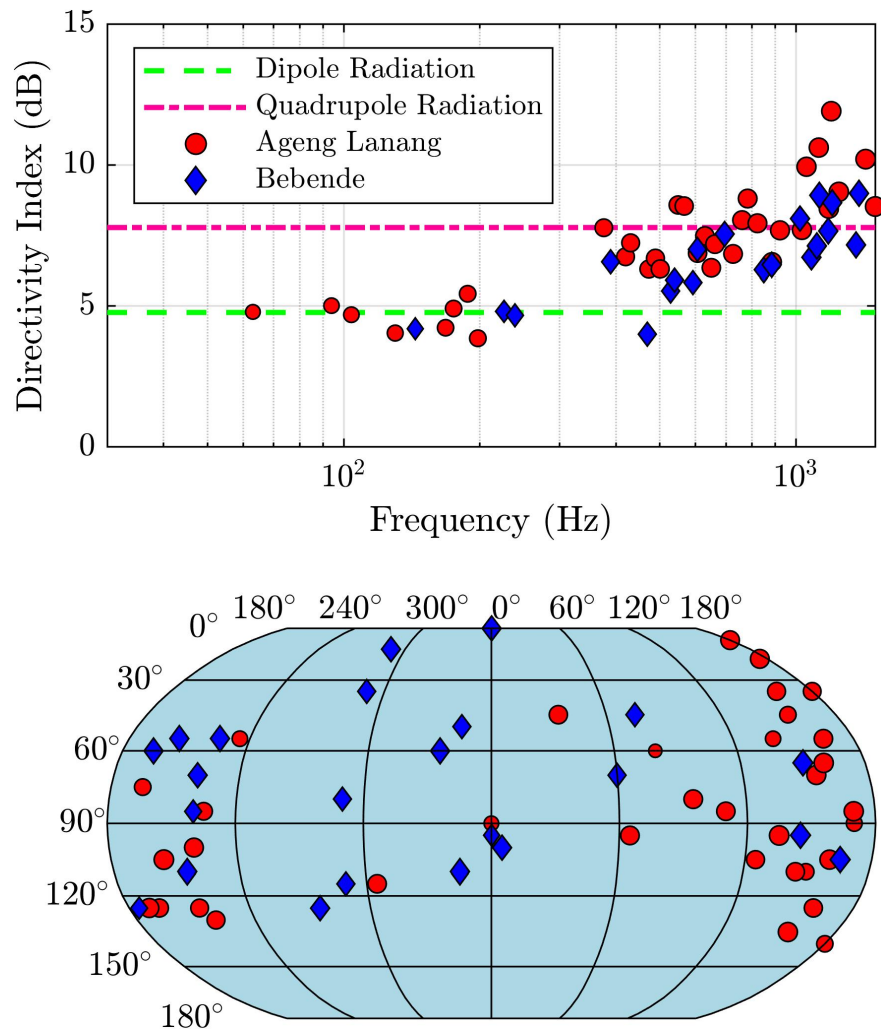


Figure 8.10 (a) Maximum DI over frequency. (b) Angular location of the direction of strongest radiation.

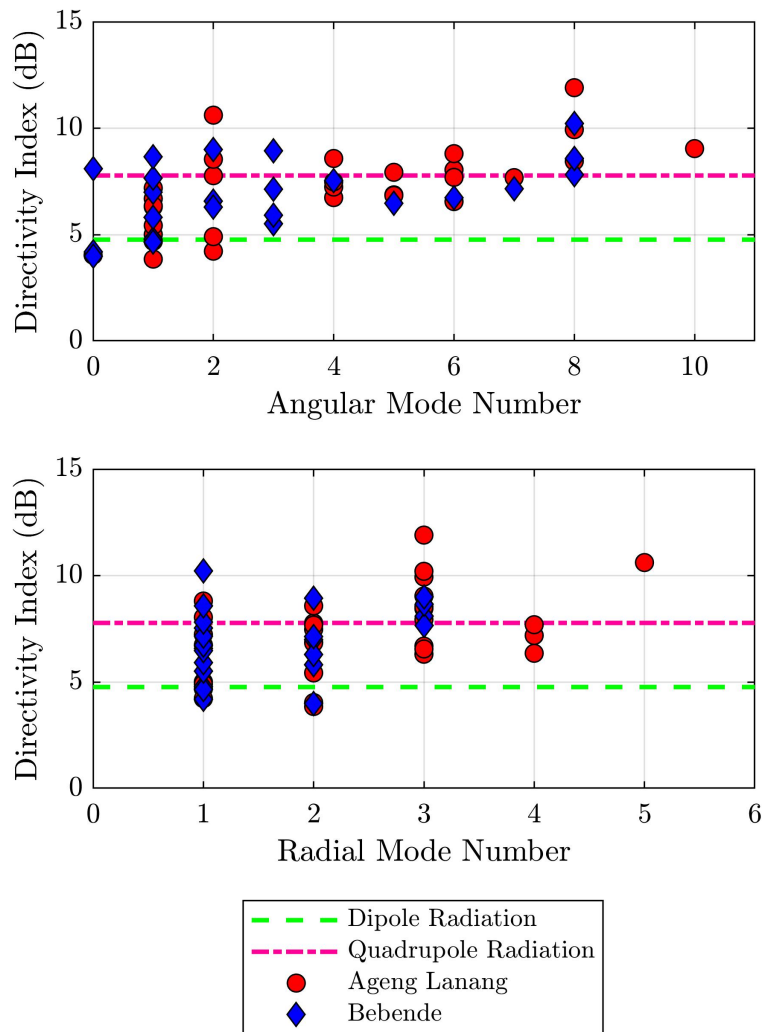


Figure 8.11 Directivity Index as a function of (a) angular node number (b) radial node number.

8.4.3 Impact of Side Walls on Median Plane Symmetry

If the gamelan gongs were flat plates with no side wall, one would anticipate strong symmetries about the median plane of the gong. However, the measured radiation patterns clearly show that the addition of the side walls as well as other inhomogeneities in the hammered gongs influence their directivity, leading to deviations from anticipated reflectional symmetries. Symmetry analysis helps quantify these deviations from an idealized source with no side walls.

To consider deviations from symmetry, let Q_s be the symmetrized directivity function

$$Q_s(\theta, \phi) = \frac{1}{2}(Q(\theta, \phi) + Q_r(\theta, \phi)), \quad (8.11)$$

where Q is defined in Eq. (8.8) and Q_r is the reflected directivity factor function across the median plane. Q_s thus represents the average value between both planes. Figure 11.14 plots L_Q (Eq. (12.13)) between the symmetrized and measured data. Only for a handful of modes is the measured reflectional symmetry strong enough to avoid differences less than 1.0 dB. Most modes fall into the range of 1 to 2 dB difference between measured and symmetrized data, although some modes approach and exceed 3 dB. Thus, the unique geometry of the gongs leads to deviations from anticipated symmetries of other gongs and percussion instruments.

8.5 Discussion

Sound radiation from gamelan gongs is complex. While at lower frequencies the radiation patterns are simple and dipole-like, higher modes develop complicated, multi-directional radiation. Often the number and location of edge anti-nodal regions correlates with the number of radiation lobes. Nonetheless, the unique construction and geometry of the gongs often leads to unanticipated directional behavior.

While somewhat similar in general shape, the ageng lanang and bebende gongs serve unique musical functions within the Balinese gamelan. As a result, the instruments' geometry and hand-

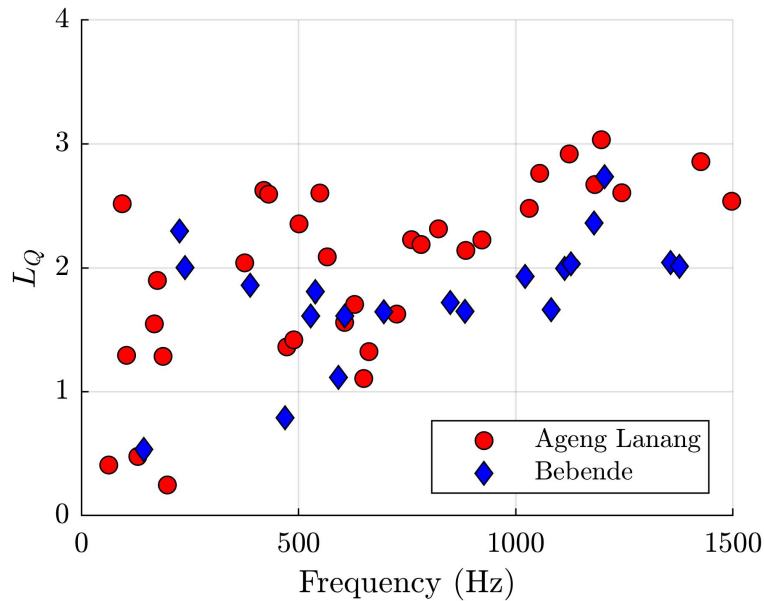


Figure 8.12 Deviations between measured and symmetrized data about the median plane.

tuned modal frequencies are distinctive to each instrument. These variations appear both in the ordering and relative location of modal frequencies and lead to differing acoustic impressions, such as the ombak present in the ageng lanang. In turn, changes in the structural modal frequencies relative to an acoustic wavelength create unique radiation patterns for the same modal frequencies. Disparate cavity depths, boss heights, and other properties lead to additional variations between the gongs' radiated patterns.

One difficulty in understanding gamelan gong radiation is the lack of theoretical models available to predict their behavior. While for a flat circular plate the radiation could be inferred directly from the mode shape, the gong side walls, varying shell thickness, and boss complicate their radiation characteristics. Common models, such as infinitely baffled pistons and their counterparts [10, 136, 137] fail to properly account for radiation behind the gong which plays a critical role in their radiation. On the other hand, rigid spherical models, such as a vibrating cap on a sphere and their counterparts [10, 60, 138] do not have closed-form solutions for non-axisymmetric radiation, severely limiting their application to only a few modes of the gong. They additionally neglect the

gong's open cavity geometry. Thus, better theoretical models which can account for both the open cavity geometry and non-axisymmetric solutions would benefit radiation analysis from the gamelan gongs.

8.6 Conclusions

The structural mode shapes of gamelan gongs often have close connections to their far-field directivity patterns. This work considered the radiation from two gongs, the ageng lanang and bebende gongs. At low-frequencies, the gongs have dipole-like radiation, while at high frequencies, the gong's become multi-directional. Modal frequency analysis revealed that differing modal frequency values and ordering between the gongs leads to unique radiation patterns even for similar mode shapes. The gong's side walls contribute to a loss of reflectional symmetry about the gong's face's plane. Furthermore, the direction of strongest radiation is not always consistent between the two gongs.

Future work includes considering how the gong's non-linear vibrations influence its directivity and improved theoretical modeling. Other interesting areas of research could include studying directivity variations between Balinese and Javanese gamelan gongs or directivity variations between gamelan gongs and other gongs such as the tam-tam.

Chapter 9

Influence of Musician Diffraction on Clarinet Directivity

This chapter studies the impact of a musician's body on directivity measurements. The results clarify the need for incorporating the diffraction and absorption caused by a musician's body in directivity measurements for specific applications. The chapter previously appeared as:

S. D. Bellows and T. W. Leishman, "Modeling musician diffraction and absorption for artificially excited clarinet directivity measurements," Proc. Mtgs. Acoust., 46, 035002, (2022). doi: 10.1121/2.0001586.

9.1 Introduction

Understanding the directional characteristics of musical instruments has many applications, including acoustical room design, auralizations, and sound source modeling. Typically, microphone arrays measure the musical instrument's directivity in an anechoic environment. To excite the instrument, previous works have employed both natural and artificial excitation. Additionally, researchers have evaluated the directivity of both isolated instruments, i.e., without a musician, and played musical

instruments. While studying the directivity of an isolated instrument has merits in its own right, for many practical applications, the impact of diffraction, scattering, and absorption due to the musician is critical to obtaining accurate and realistic results. Nonetheless, these effects generally receive little attention when performing directivity measurements and are often neglected.

When considering the isolated instrument, artificial excitation has several merits. The primary advantage of this excitation is that it allows a repeatable excitation signal, advantageous for when multiple captures are necessary to scan the instrument, such as when performing high-resolution measurements [34] or acoustical holography [139]. Nonetheless, while valuable, using artificial excitation requires a playing apparatus to be constructed for each instrument of interest and can even vary significantly for the same instrument. For example, artificially excited violin directivity measurements have employed reciprocity techniques [36], Lorentz-force-based techniques [140], and bowing machines [141]. Because the method of excitation influences how the instrument produces and radiates sound, care must be taken to ensure that the artificial excitation is as similar as possible to natural excitation for realistic results. In addition, the associated playing difficulties when using a playing apparatus can lead to extensive measurement times to consider the full range of the instrument and thus have limited many studies to a few notes and their associated partials.

In contrast, natural instrument excitation ensures that the instrument is excited as in normal playing conditions and facilitates the measurement of the full range of the instrument without technical difficulties. However, the lack of repeatability between multiple captures has generally limited the sampling resolution of played musical instrument directivity measurements. Consequently, most directivity measurements of played musical instruments use sampling based on a fixed number of microphone positions, e.g., 13, 32, or 64 [18, 32, 100]. However, various normalization schemes previously applied compensated to some degree for the playing variability of the instrument, allowing for multiple capture measurements. More recently, a frequency-response function (FRF)-based approach allowed the measurement of sixteen musical instruments conforming to the

AES loudspeaker directivity sampling standard [1, 33]. Nonetheless, even FRFs are limited in the frequency range due to high signal-to-noise ratios required and still cannot compensate for musician movements.

Another advantage of natural excitation is that it allows a streamlined approach to measuring multiple instruments using the same measurement setup. On the other hand, artificial excitation requires researchers to construct a new playing apparatus for each instrument or instrument family. Thus, methods employing natural excitation dominate the literature in terms of the number of instruments considered in each study, such as three in Ref. [18], four in Ref. [21], sixteen in Ref. [1], or forty-one in Ref. [32]. Finally, because natural excitation has typically employed musicians in their normal playing positions, they are best suited for many acoustical applications such as room acoustical design or auralizations. Indeed, the motivation of many naturally excited musical directivity studies was for these applications [18, 32, 99].

Recent works have aimed for high-resolution measurements of played musical instrument directivities for use in such applications. However, many directional data from previous studies of isolated instruments still exist. In addition, the repeatability of artificial excitation remains a significant advantage over natural excitation. Consequently, researchers would benefit from a greater understanding of how the presence of a musician alters the directivity of isolated instruments. This work studies the effects of musician absorption and diffraction on musical instrument directivities. It proposes several approaches that would allow experimentalists to perform measurements with artificial excitation while still accounting for the diffraction and absorption of the musician's body. The results will benefit researchers and practitioners using directivity data for various acoustical applications.

9.2 Musician Diffraction and Absorption

Enough time and resources can overcome many of the mentioned limitations of artificial excitation. However, musician diffraction plays an important role in musical instrument directivities and should not be ignored, particularly when used for applications such as auralizations or room acoustical design. To understand the effects that diffraction and scattering can have on the directivity of a source, consider a point source radiating into free-space compared to in the presence of a rigid spherical scatterer. Without the scattering body, the far-field directivity will be omnidirectional. However, the presence of the rigid sphere changes the directional features dramatically. Figure 9.1 illustrates this for various ka , with a being the radius of the sphere and k being the wavenumber. For large wavelengths ($ka \ll 1$), the scattering body has minimal effect on the directivity. However, as the wavelength becomes sizable to the scattering body, deviations from omnidirectionality become visible. Undulating levels indicate constructive and destructive interference regions due to varying path lengths. Behind the sphere, a diffraction spot appears, which is also apparent in, for example, speech directivity [6].

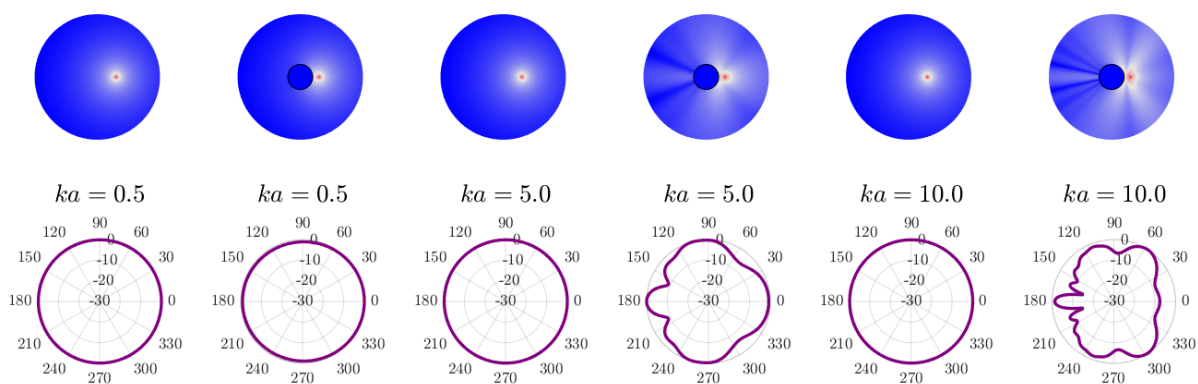


Figure 9.1 Scattering effects on the directivity of a point source without and with the presence of a rigid sphere for selected ka . *Top row:* Magnitude pressure. *Bottom row:* Polar plot of the far-field directivity.

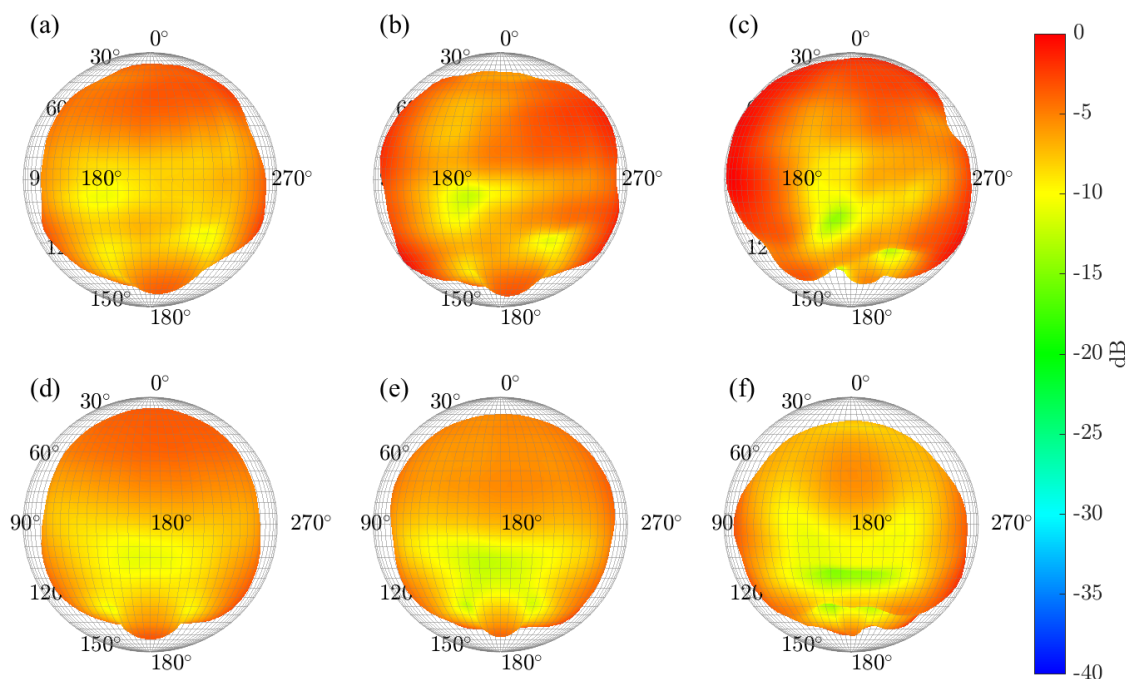


Figure 9.2 Directivity balloons of the violin (a)-(c) and human speech (d)-(f) for the 400 Hz [(a), (d)], 500 Hz [(b), (e)], and 800 Hz [(c), (f)] 1/3rd-octave bands. The vantage point is from behind the body, and all balloons are based on a degree $N = 18$ spherical harmonic expansions.

Comparisons of directivity patterns often reveal that despite differences in the mechanisms that generate sound, diffraction effects across instruments are remarkably similar. Figure 13.5 shows this effect for speech and the violin. It plots the 400, 500, and 800 Hz 1/3rd-octave-band directivity balloons for the violin and speech, with color and radius showing the relative levels on a 40 dB scale. While each source produces and radiates sound differently, the directional characteristics at these frequencies are very similar due to the diffraction of the human body. At higher frequencies, these similarities become less pronounced; nonetheless, they show that diffraction plays an important role in source directivities.

9.3 Modeling Absorption and Diffraction with Array Shading

Because the diffraction, scattering, and absorption of musicians can significantly affect the directivity of the sound source, in several applications, it is desirable to include these effects. When performing artificially excited musical instrument directivity measurements, a simple method would be to include a mannequin in the measurement setup. This approach has commonly been used with speech directivity measurements [4, 6, 142] but not for musical instrument directivity measurements.

However, in some situations, such as when the size of the measurement room limits the maximum size of the array, using a mannequin may not be feasible. One straightforward approach is to shade the isolated instrument's measured directivity pattern to imitate musician diffraction and absorption artificially. That is, based on a measured directivity function D , the shaded directivity function D_s is

$$D_s(\theta, \phi, f) = W(\theta, \phi, f)D(\theta, \phi, f), \quad (9.1)$$

where $W(\theta, \phi, f)$ is the shading function or weight. While shading is commonly used with arrays to control beam pattern performance, this section highlights two possible shading functions that mimic diffraction and absorption effects. Results for measured data appear in Sec. 16.3.

Some researchers have measured the frequency-dependent attenuation behind the musician [143], but have not developed formulations to apply it to isolated instruments. To accomplish this, a cardioid pattern motivates an initial shading function with attenuation behind the musician. Modifying the cardioid pattern to allow for variable attenuation in both angular components leads to

$$W_L(\theta, \phi, f) = \frac{\alpha(L(f)) + \sin \theta \cos \phi}{\alpha(L(f)) + 1} \quad (9.2)$$

where

$$\alpha(L(f)) = \frac{10^{-L(f)/20} + 1}{10^{-L(f)/20} - 1} \quad (9.3)$$

and $L(f)$ is the desired attenuation in dB. Figure 9.3 shows the associated normalized shading balloons for varying L .

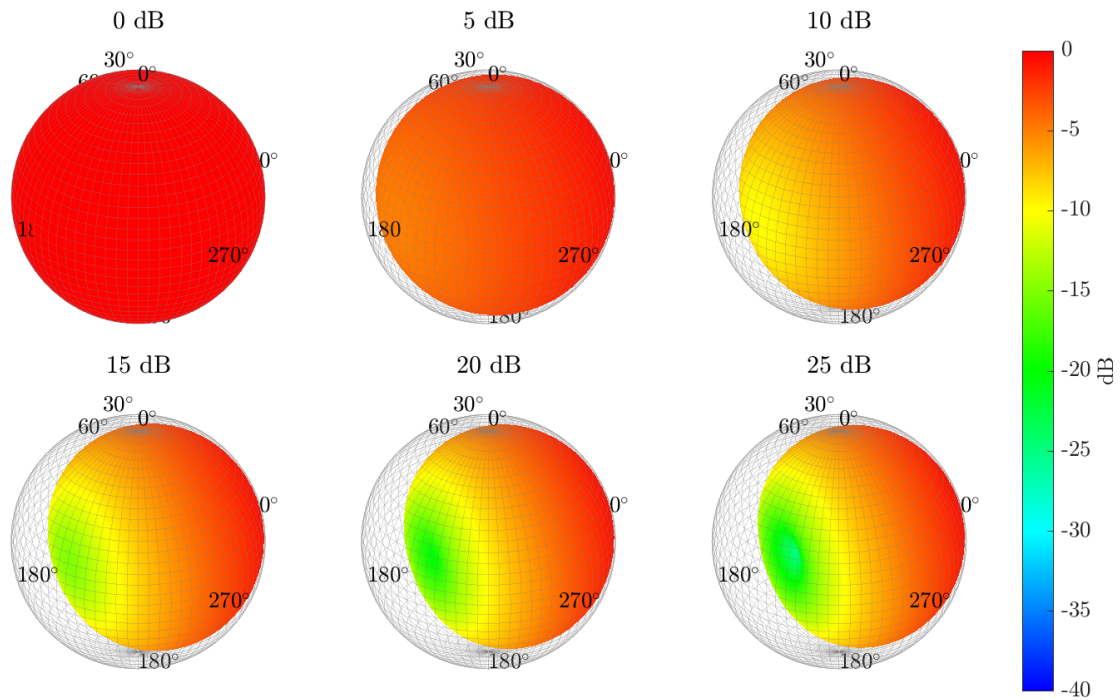


Figure 9.3 Normalized shading function W_L for various levels of attenuation L .

If the attenuation is unknown, a theoretical model can estimate the parameter α . For this work, a simple model of the scattering from a point source near a rigid sphere provided a basic understanding of the attenuation. The point source was placed at a radial position a_0 relative to the radius of the rigid sphere a . The difference between the maximum pressure and the pressure directly behind the sphere provided the attenuation estimate. To mitigate the effect of strongly fluctuating attenuation values due to strong diffraction lobes such as those seen directly behind the sphere in Figs. 9.1 and 9.5, a $N = 4$ expansion of the pressure smoothed these features. Figure 9.4 shows the resultant curves for the parameter α . The curves reveal that at low frequencies, the effect of the sphere adds minimal attenuation behind; however, at higher frequencies, the attenuation becomes more significant.

While Eq. (9.2) provides a simple shading function if the attenuation behind the musician is known, it does not include wave phenomena such as diffraction spots. An alternative shading

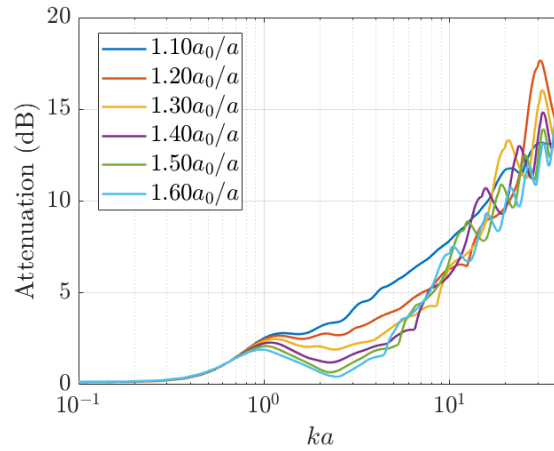


Figure 9.4 Values of attenuation based on scattering from a rigid sphere of radius a due to a point source placed at position $r = a_0$.

function that includes this effect is the radiation of sound from a point source on the sphere. The unnormalized weights are [59]

$$W_s(\theta, \phi) = \sum_{n=0}^{\infty} \sum_{m=-n}^n \frac{h_n^{(2)}(ka)}{h_n^{(2)'}(ka)} Y_n^m(\theta, \phi) [Y_n^m(\theta_0, \phi_0)]^*, \quad (9.4)$$

where k is the wavenumber, $h_n^{(2)}$ are the spherical Hankel functions of the second kind of order n , Y_n^m are the spherical harmonics of degree n and order m , $*$ denotes complex conjugation, and (θ_0, ϕ_0) is angular position of the point source on the sphere of radius a . For this shading function, the radius of the sphere controls the frequency-dependent nature of the attenuation. Thus, to apply this function, the parameter a could be estimated based on dimensions of the scattering body or through modeling. In this work, minimizing differences between measured directivities and W_s at low frequencies determined the effective radius of the body. First, the authors determined the directivity factor function of a given note's fundamental. The estimate of the effective radius follows by finding the value of a which minimizes the directivity factor deviation error between the measured directivity factor function and W_s . Figure 9.5 shows the shading functions for select ka . Notably, a diffraction spot appears in several of the directivity balloons.

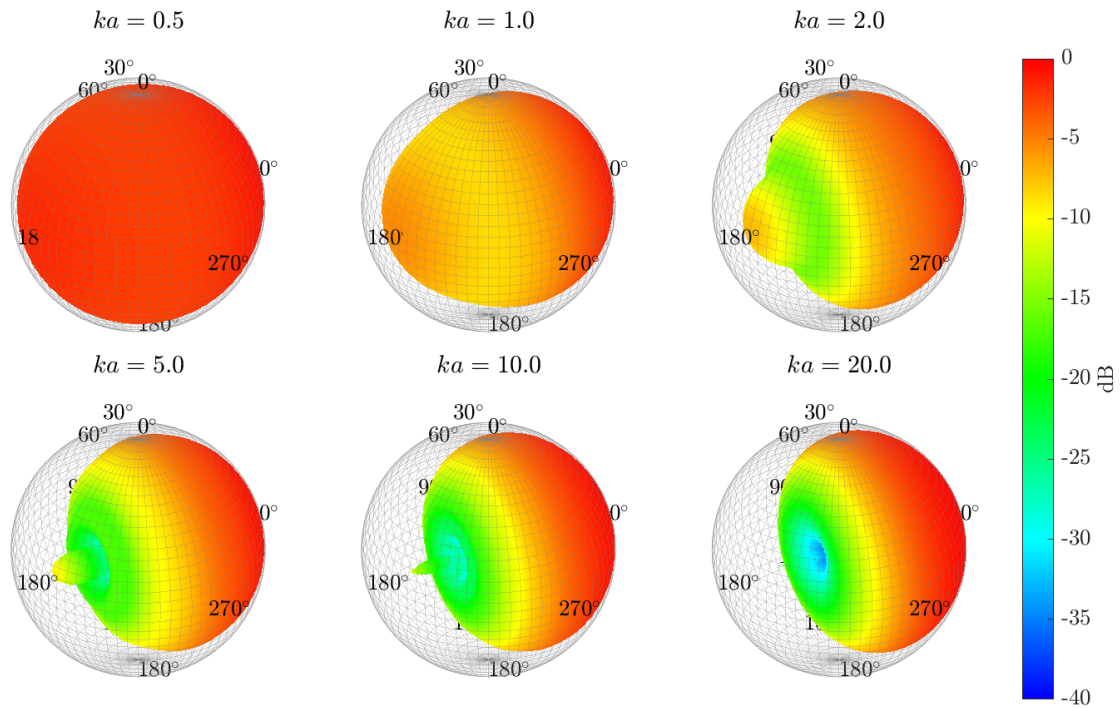


Figure 9.5 Shading function W_s for various ka with $(\theta_0, \phi_0) = (\pi/2, 0)$. Increasing frequency leads to increasing attenuation behind the source, as well as the appearance of diffraction spot.

9.4 Directivity Measurements

This work measured clarinet directivity using three different methods to study the effect of the musician's body on directivity. Figure 15.8 shows each measurement setup: the isolated instrument (upside-down), excited artificially using a blower, the instrument and blowing apparatus attached to a seated mannequin with the blowing apparatus replacing the head, and the instrument played by a musician. The semi-circular array included 36 12.7 mm (0.5 in.) microphones positioned in 5° polar angular spacing. Subsequent rotations in 5° azimuthal steps enabled a full-spherical measurement conforming to the AES sampling standard with the omission of the south pole measurement position [33]. Data processing with FRFs provided normalization for each capture, which was essential in the case of the played instrument [1, 6]. For the artificial blower, the measurement



(a)



(b)



(c)

Figure 9.6 Three measurement set-ups. (a) Isolated clarinet and blowing apparatus. (b) Clarinet and blowing apparatus attached to KEMAR HATS. (c) Clarinetist.

radius was $a = 0.98$ m, while for the musician, the radius was $a = 1.17$ m. Despite differing measurement radii, acoustical holography allowed far-field propagation of the pressure for equitable comparisons [59, 82].

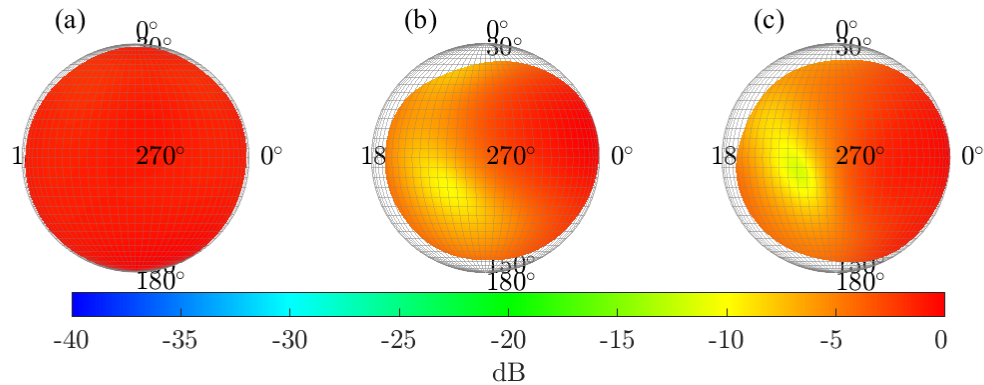


Figure 9.7 Far-field projected directivity balloons for the fundamental of E4. (a) Isolated and artificially excited clarinet. (b) Artificially excited clarinet attached to a mannequin. (c) Clarinet played by a musician. All balloons are based on degree $N = 17$ spherical harmonic expansions. The vantage point is from the right side of the instrument.

9.5 Results

9.5.1 Diffraction Effects

The measurements revealed apparent diffraction and absorption effects even at lower frequencies. Figure 9.7 shows far-field projected directivities for the fundamental of E4 (328 Hz). While the isolated instrument shown in Fig. 9.7(a) appears to be roughly omnidirectional, both the artificially excited instrument with the mannequin and the played instrument show that even at this frequency, there can be over 10 dB of attenuation due to the musician's body. The played instrument and the artificially excited instrument with the mannequin both show that the strongest radiation region occurs in front of the instrument. In contrast, the regions of greatest attenuation occur roughly to the side and behind the musician. Directly behind the musician, there are increased radiation levels, similar to the balloon shown in Fig. 9.5 for the cases $ka = 1$ and $ka = 2$.

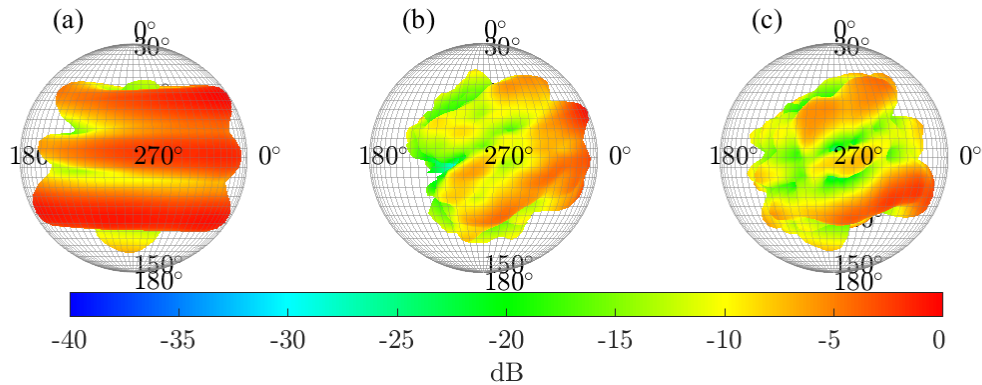


Figure 9.8 Far-field projected directivity balloons for the fifth partial of E4. (a) Isolated and artificially excited clarinet. (b) Artificially excited clarinet attached to a mannequin. (c) Clarinet played by a musician. The balloons are based on degree $N = 17$ spherical harmonic expansions. The vantage point is from the right side of the instrument.

At higher frequencies, the effects become more pronounced. Figure 9.8 shows the far-field projected directivities for the 5th partial of E4 (1641 Hz). For the isolated case, three distinct, quasi-axially symmetric interference lobes appear. For the case of the played and nonisolated instrument, wave effects behind the musician are apparent, although three lobes are still visible in front of the instrument in both cases.

9.5.2 Shading Results

Figure 9.9 compares directivity balloons with diffraction and absorption effects artificially added through the shading function W_L for the fifth partial of E4, the same partial used for Fig. 9.8. The theoretical curves shown in Fig. 9.4 determined the attenuation to be $L = 11.2$ dB. Figure 9.9 (a) shows directivity results from the isolated instrument, rotated with an orientation corresponding to the same angle as used with the blower-mannequin apparatus. Figure 9.9 (b) shows the shaded directivity of the isolated instrument, whereas Fig. 9.9 (c) shows the results of the artificially excited

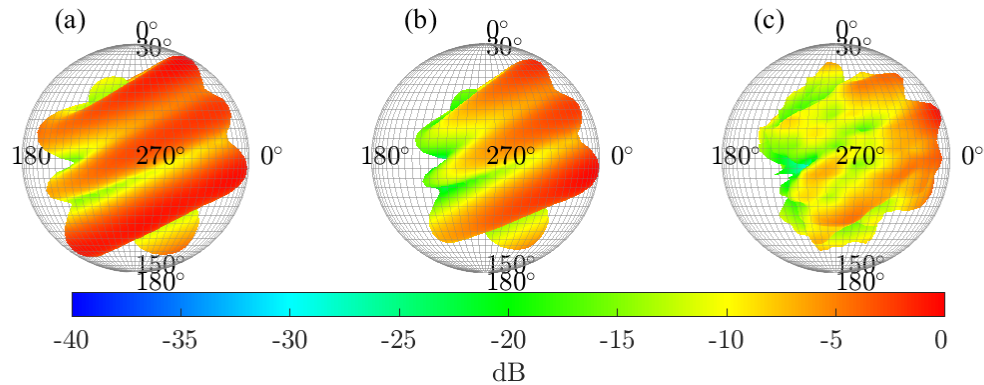


Figure 9.9 Shading applied to the fifth partial of E4. Directivity balloons of the (a) isolated instrument rotated to be in the same orientation as the mannequin, (b) shaded isolated instrument, and (c) instrument and mannequin combination. The balloons are based on degree $N = 17$ spherical harmonic expansions. The vantage point is from the right side of the instrument.

instrument with the mannequin. The shading greatly improves the isolated instrument's results, with W_L reducing strong radiation behind the instrument to levels comparable to those occurring with the mannequin.

While the shading function W_L mimics reduced levels behind the musician, it does not include some wave effects such as a diffraction spot. Figure 9.10 illustrates how using a shading function such as W_s adds these effects for the third partial of E4 (985 Hz) using an estimate of $a = 0.2$ m. Without shading, the isolated instrument's directivity balloon shown in Fig. 9.10(a) appears to be roughly omnidirectional even at this higher frequency. In contrast, the directivity produced by the mannequin-blower apparatus shows reduced levels and an apparent diffraction spot behind the mannequin as seen in Fig. 9.10(c). The shaded directivity shown in Fig. 9.10(b) includes a diffraction spot, reduced levels behind the instrument, and many other similarities.

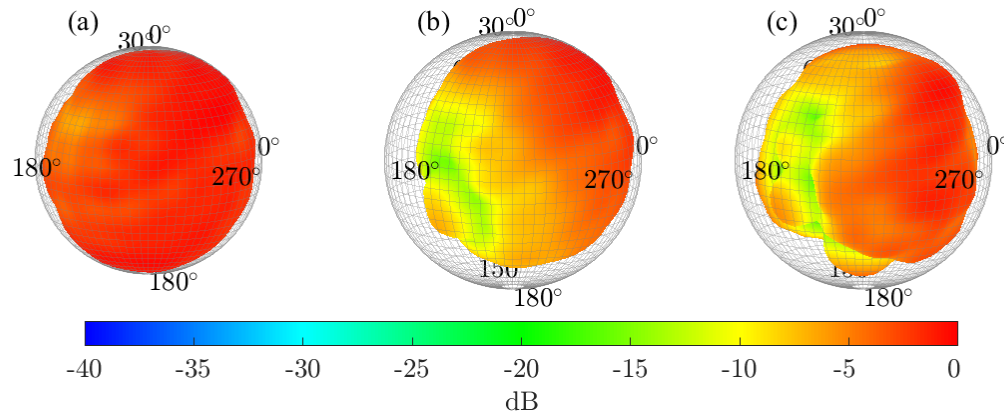


Figure 9.10 Shading applied to the 3rd partial of E4. Directivity balloons of the (a) isolated instrument rotated to be in the same orientation as the mannequin, (b) shaded isolated instrument (c) instrument and mannequin combination. The balloons are based on degree $N = 17$ spherical harmonic expansions. The vantage point is from the right side of the instrument.

9.6 Conclusions

The acoustical effects of a musician's body play a key role in the directivity of a played musical instrument. Incorporating these effects for applications such as auralizations or room acoustical design is essential. This work suggests that including a mannequin in the measurement set-up significantly improves the similarity between directivities of artificially excited and played instruments. In cases where using a mannequin is unfeasible, artificially adding wave effects through shading functions provides a reasonable yet less rigorous approximation. This work has demonstrated two possible shading functions. Future research may include studying other instruments and how a musician's body affects their directivities and developing other shading functions. Listening tests could validate whether musician diffraction and absorption effects are perceptually relevant.

Chapter 10

Effect of Head Orientation on Speech

Directivity

Speech directivity measurements typically involve the head in the same direction as the torso. This chapter explores the impacts of other head orientations on speech directivity results. It appeared previously as:

S. D. Bellows and T. W. Leishman, "Effect of Head Orientation on Speech Directivity," Proc. Interspeech 2022, 246-250, (2022). doi: 10.21437/Interspeech.2022-553.

10.1 Introduction

Human voice directivity has many applications in audio, telecommunications, room acoustical design, auralization, and other areas. The directional characteristics have been the focus of numerous studies over the past century, including studies on the directivity of seated talkers [3, 5, 144, 145], standing talkers [4, 142], and singers [64, 146–149], all using various sampling resolutions and measurement modalities. Recently, the authors have published work on spherical directivities of seated talkers with 5° resolution based on the AES sampling standard [6].

While the various studies have provided vital insights into the radiation of sound by the human voice and vaguely shown that diffraction about the human body plays an essential role in directivity patterns, they have not focused on the effects of head orientation on speech directivity. This work explores the differences in speech directivities due to changing head orientations with and without torso diffraction. The resulting data appears in an archival database for use by other researchers; they will be particularly beneficial in applications such as auralizations or virtual-reality simulations [150], where head orientation is relevant to obtaining realistic results.

10.2 Methods

10.2.1 Measurements

The directivity measurements took place in an anechoic environment with the semi-circular rotating microphone array shown in Fig 10.1. The measurement arc included 36 12.7 mm (0.5 in.) microphones at a $a = 0.97$ m radius and incrementally spaced at 5° increments in the polar angle θ . Due to obstructions from the measurement apparatus, the nadir ($\theta = 180^\circ$) did not include a microphone. Each microphone and its signal path had been relatively calibrated over frequency for post-processing of its channel data. The measurement arc rotated in 5° steps in the azimuthal angle ϕ to produce a full-spherical data set, conforming to AES sampling standard [33] (except the nadir position). With the 72 azimuthal sampling angles, the measurement consisted of 2,521 unique sampling positions over the sphere. The overhead turntable, measurement arc, and support structures included absorptive treatments of sufficient thickness to minimize the effects of undesirable scattering

The authors selected a G.R.A.S. KEMAR head and torso simulator (HATS) for the measurements. While a HATS differs from a human talker because of geometric characteristics, lack of arms or legs, a fixed mouth aperture, dissimilar skin absorption, and other properties, previous measurements



Figure 10.1 A KEMAR HATS within the rotating directivity measurement system.

of live speech from human talkers have shown that the directivity produced by the HATS is an acceptable approximation over the audible bandwidth [6]. Other authors have also employed mannequins for speech directivity studies [4, 142, 149, 151, 152]. The primary advantages of the HATS over human talkers for this investigation were its readily controlled and adjusted acoustic output and azimuthal head orientation angle ψ_h , which both yielded more reproducible results.

Three 5 s exponentially weighted swept-sine signals excited the mouth simulator, whose opening aligned with the array center. The first directivity measurements were of the isolated head, independent of the torso, with and without foam on the supporting stand. Measurement comparisons determined that the additional foam was beneficial for this and all subsequent measurements. The second measurement set included both the head and torso, with the mouth initially oriented toward $\psi_h = 0^\circ$ (i.e., facing directly forward), then rotated sequentially using the HATS neck angle scale

in 10° increments up to $\psi_h = 90^\circ$ (i.e., with the mouth over the left shoulder). Because of the left-right HATS symmetry, the measurements included only head orientations to one side. The second measurement set also included intermediate head orientations at 5° , 15° , 25° , and 35° . The complete experimental data thus consisted of full spherical directivity measurements of the isolated head and fourteen different head orientations with the attached torso.

10.2.2 Processing

The frequency response functions (FRF) $H(\theta, \phi, f)$ between the electric input signal $x(t)$ driving the HATS and each array microphone output signal $\tilde{y}(\theta, \phi, t)$ resulted by dividing the averaged cross-spectrum $G_{x\tilde{y}}(\theta, \phi, f)$ by the averaged input autospectrum $G_{xx}(f)$ [131]. Here, \tilde{y} indicates the possibility of uncorrelated noise in the output signal. The cross and auto spectra enabled the calculation of coherence functions and helped analyze signal-to-noise ratios and other measurement limitations or errors. Finally, broader-band (e.g., 1/3-octave band) results followed from the narrowband data by calculating the coherent output spectrum and then summing over the desired bandwidths [6, 131]. The 1/3rd-octave-band directivities used for analysis in this work are available for further exploration in an online archival database [38].

10.2.3 Directivity Functions

Directivity functions $D(\theta, \phi, f)$ followed by normalizing the FRFs by the maximum magnitude response for a given frequency [6]. Magnitude beam patterns $B(\theta, \phi, f)$ expressed directivity functions on a logarithmic scale.

Another beneficial directivity metric is the directivity factor function $Q(\theta, \phi, f)$ [10]:

$$Q(\theta, \phi, f) = \frac{4\pi |H(\theta, \phi, f)|^2}{\int_0^{2\pi} \int_0^\pi |H(\theta, \phi, f)|^2 \sin \theta d\theta d\phi}. \quad (10.1)$$

The directivity index function $DI(\theta, \phi, f)$ expresses the directivity factor function on a logarithmic scale as $DI(\theta, \phi, f) = 10 \log_{10} Q(\theta, \phi, f)$.

The directivity factor function allows for a straightforward deviation metric

$$\sigma_Q^2(f) = \frac{1}{4\pi} \int_0^{2\pi} \int_0^\pi |Q(\theta, \phi, f) - Q_{ref}(\theta, \phi, f)|^2 \sin \theta d\theta d\phi, \quad (10.2)$$

where $Q_{ref}(\theta, \phi, f)$ is a reference directivity factor function. On a logarithmic scale, the deviation level is

$$L_Q(f) = 10 \log_{10}[1 + \sigma_Q(f)]. \quad (10.3)$$

For convenience, one may average the deviation $\sigma_Q(f)$ over frequency to create a global, frequency-independent value.

10.3 Results

10.3.1 Head and Torso Diffraction

Comparisons of directivities from the HATS mouth simulator oriented toward $\psi_h = 0^\circ$, with and without the torso attached to the head, provide the first glimpse into associated radiation and diffraction effects. A theoretical and computational model of a 0.9 cm radius radially vibrating cap on a 8.5 cm radius rigid sphere provides additional insights, as this type of model has provided simple speech radiation predictions in previous works [4, 152]. Its simulations produced commensurate sound pressures and summations over the same bandwidths as the experimental measurements for equitable comparisons.

Figure 10.2 compares normalized directivity balloons of the four sources for the 1.6 kHz 1/3-octave band on a 40 dB scale. Plot color and radius both indicate level, while the encompassing spherical mesh indicates the maximum 0 dB reference level. The theoretical model's balloon in Fig. 10.2(a) shows an expected radiation pattern, with axial symmetry about the cap axis plus a region

of reduced level behind the sphere and a rear lobe due to diffraction. Figure 10.2(b) shows the directivity for the isolated KEMAR head, which has several features in common with the theoretical model, including a region of reduced levels behind the head due to diffraction. However, while the head maintains reflectional symmetry about the median plane, it does not produce axial symmetry about the mouth axis. This change presumably arises because the head is not a perfect sphere, and the mouth does not fall on the intersection of the transverse and median planes through the head's geometrical center. The direction of its most substantial radiation is *not* directly in front of the mouth at the 90° polar angle, which one might consider the primary radiation axis, but angles slightly upward. A similar feature appears for the speech directivity generated with the head and torso combination, as shown in Fig. 10.2(c). For this case, the shadow region behind the head is similar; however, a clear lobe has formed above the transverse mouth plane. Figure 10.2(d) shows the average directivity of live seated talkers from Ref. [6] for comparison. The pattern shares several features with the pattern produced by the HATS.

10.3.2 Head Orientations

The next step in the evaluation process was to assess the effects of head orientation on the HATS directivity. At low frequencies, the directivity changes with head rotation remained minimal, presumably due to the sizeable acoustic wavelength compared to the diffracting body. However, at higher frequencies, more pronounced changes arose. Figure 10.3 shows the directivity balloons for four head orientations ψ_h in 30° increments and from the same vantage points for the 1 kHz and 4 kHz 1/3-octave bands. The blue arrows indicate the mouth axis direction. The torso faced forward (i.e., toward $\phi = 0^\circ$) in all cases.

For the 1 kHz 1/3-octave band, differences between balloons are not extremely pronounced, although they do show a tendency for the dominant radiation and rear diffraction lobe directions to rotate with the changing head orientations. An upward-directed lobe for $\psi_h = 0^\circ$, similar to that

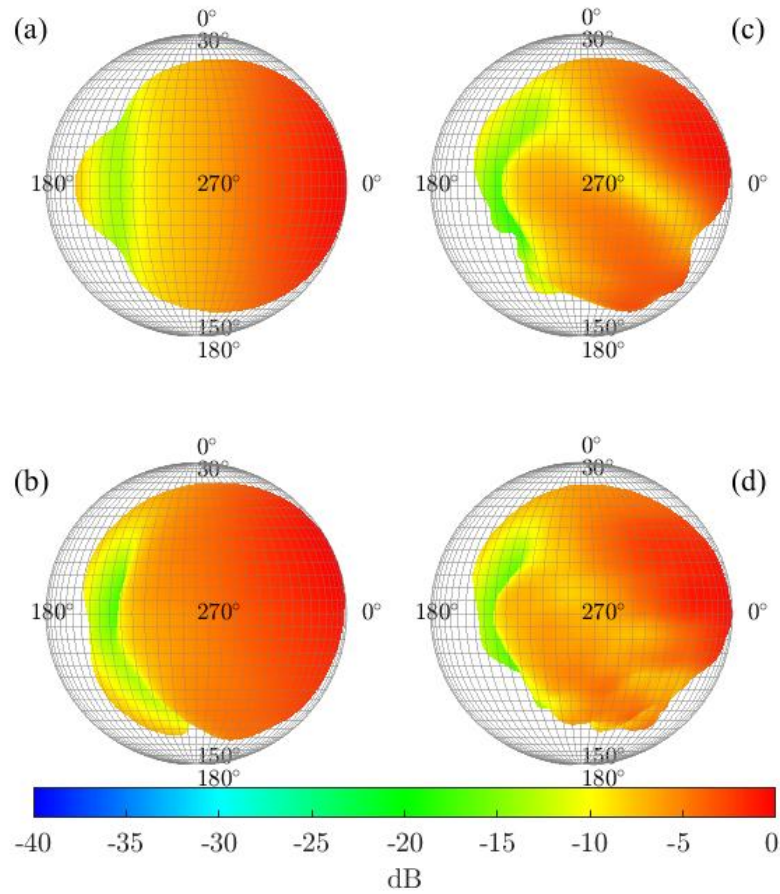


Figure 10.2 Directivity balloons for the 1.6 kHz 1/3-octave band. (a) Theoretical model of a radially vibrating cap set in a rigid sphere. (b) Isolated KEMAR HATS head. (c) Complete KEMAR HATS (including torso) with the head oriented toward $\psi_h = 0^\circ$. (d) Averaged live speech of seated talkers. The vantage point is from the right side of the sphere, HATS, and average talker so the mouth axis is toward the 0° azimuthal marker.

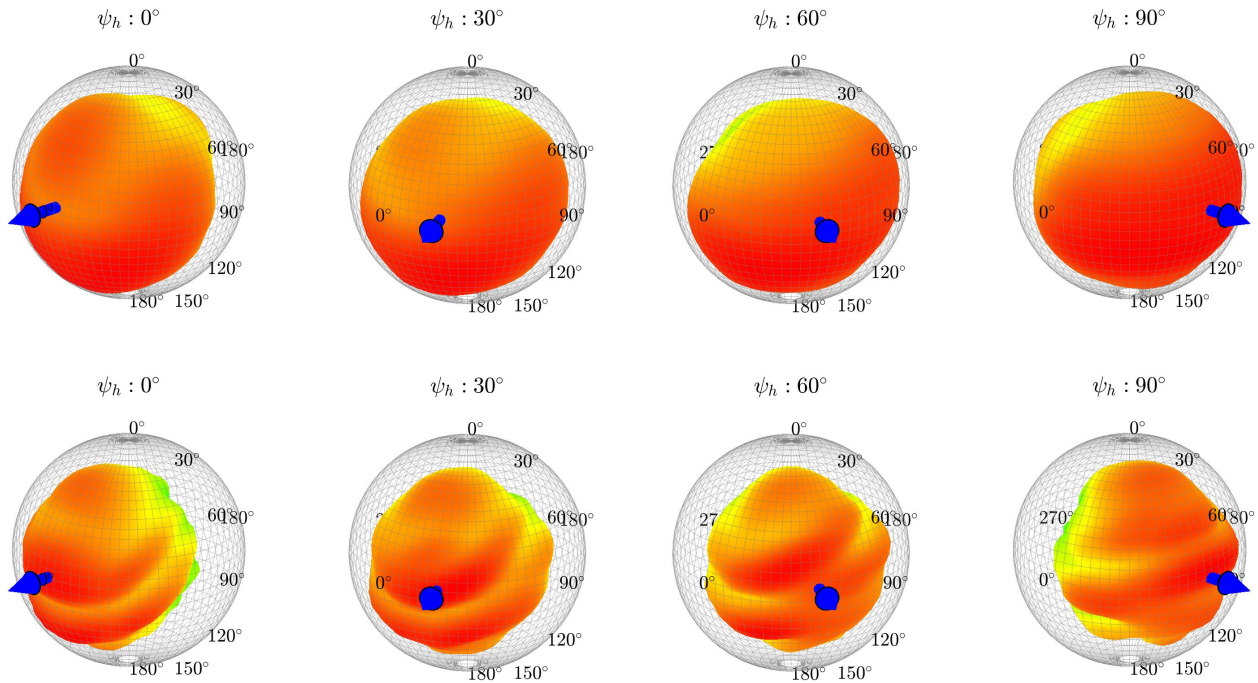


Figure 10.3 Directivities of the KEMAR HATS with head orientations $\psi_h = 0^\circ$, 30° , 60° , and 90° as viewed from a fixed vantage point at $(45^\circ, 20^\circ)$. *Top row*: 1 kHz 1/3-octave band. *Bottom row*: 4 kHz 1/3-octave band. The blue arrows indicate the mouth axis directions.

seen in Figs. 10.2(b)-(d), morphs with head rotation until only a single large lobe appears about the mouth axis at $\psi_h = 90^\circ$.

More notable changes occur for the 4 kHz 1/3-octave band. With the head facing forward, toward $\psi_h = 0^\circ$, two dominant lobes form in the polar angle and two smaller lobes form above and below. This behavior is typical for live speech radiation at this frequency [6] and changes little with head rotation up to $\psi_h = 30^\circ$. However, by $\psi_h = 60^\circ$, a third strong lobe appears, centered between the earlier two lobes and directed over the shoulder. At this head orientation, there is no quasi-symmetry about the median plane of the head. At $\psi_h = 90^\circ$, with the mouth almost directly over the shoulder, a strong lobe dominates the beam pattern along the mouth axis, with smaller side lobes above and below. These results illustrate how head orientation can change directivity, particularly when the mouth approaches the shoulder.

10.4 Analysis

This section explores errors occurring when one neglects torso diffraction and head orientation. Three different cases identify relevant scenarios and give rise to insightful frequency-dependent directivity deviations for select head orientations ψ_h . For all cases, the reference directivity data set Q_{ref} for Eq. (10.2) is that of the KEMAR HATS with its torso oriented forward toward $\phi = 0^\circ$ and head oriented in a specified direction ψ_h . Thus, the reference directivity data set represents the HATS directivity when both head orientation and torso diffraction are accounted for.

10.4.1 Neglecting Head Orientation

One set of deviations follows if one ignores the directional effects of changing head orientations and simply assumes the HATS directivity is that of the head and torso combination with both fixed and oriented forward towards $\phi = 0^\circ$. Figure 10.4 presents several frequency-dependent deviations between this configuration and selected reference head orientations. For the case of the smaller $\psi_h = 10^\circ$ orientation, the deviations remain under 2 dB up to 10 kHz; however, for the larger $\psi_h = 90^\circ$ orientation, the errors exceed 5 dB at 10 kHz. The frequency-averaged directivity deviations are 1.1, 2.0, 2.8, and 3.2 dB for the orientations $\psi_h = 10^\circ, 30^\circ, 60^\circ,$ and 90° , respectively. These errors and differences in associated beam patterns such as those shown in Fig. 10.3 indicate that the incorporation of head orientation is important for obtaining realistic directivity results.

10.4.2 Neglecting Torso Diffraction

The next deviation set contrasts the reference directivities with isolated head directivities having the same head orientations ψ_h but no simulator torso. Figure 10.5 shows several frequency-dependent results. The deviations are roughly consistent across the head orientations, increasing from around 1 dB at 200 Hz to 2 dB at 10 kHz. The frequency-averaged directivity deviations were 1.5, 1.6,

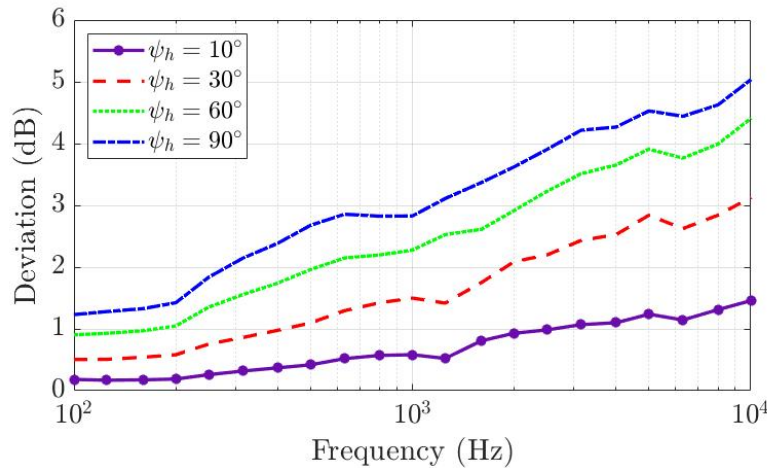


Figure 10.4 Frequency-dependent directivity deviations between the reference directivities at various azimuthal head orientation angles ψ_h and the forward-facing head orientation $\psi_h = 0^\circ$. In all cases, the torso faced forward toward $\phi = 0^\circ$.

1.6, 1.7 and 1.6 dB for the orientations $\psi_h = 0^\circ, 10^\circ, 30^\circ, 60^\circ,$ and 90° , respectively. Neglecting torso diffraction, therefore, produces significant directivity deviations. However, because the deviations are generally smaller than those that neglect head orientations (see Fig. 10.4), especially at higher frequencies, the results suggest that accounting for head orientation is more important than accounting for torso diffraction.

10.4.3 Neglecting Effect of Head Orientation on Torso Diffraction

The final deviation set contrasts the reference directivities with the directivities produced by the HATS when the head and torso rotate azimuthally together as a unit, so that the both the head and torso are in the same direction of ψ_h . This scheme treats head orientation as total-body rotation, as would be the case when one rotates a fixed directivity measurement via post processing to estimate the effects of varying head orientations. Figure 10.6 shows the frequency-dependent results. When the radiation is nearly omnidirectional at low frequencies, the limited deviations are smaller than those for the second deviation set shown in Fig. 10.5. As frequency increases, the deviations

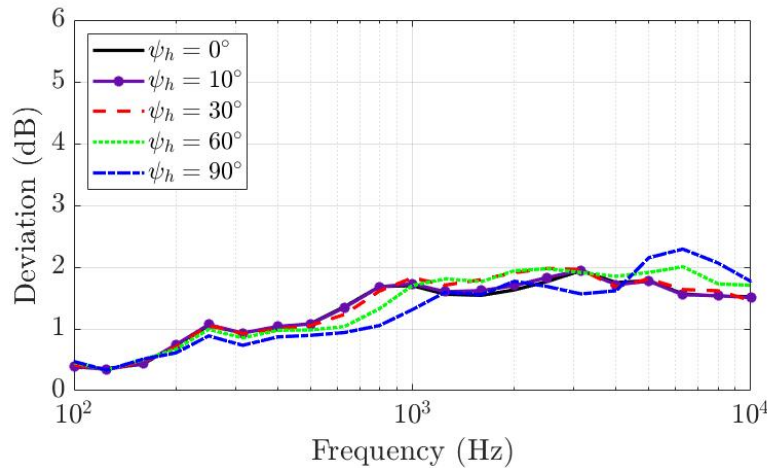


Figure 10.5 Frequency-dependent directivity deviations between the reference directivities and the isolated head (no torso) rotated towards ψ_h .

increase, level off, then undulate in correspondence with the formation of frequency-dependent diffraction lobes noted in previous studies on live speech directivities [6, 135]. The frequency-averaged deviation values are 0.8, 1.3, 1.6, and 1.7 dB for the orientations $\psi_h = 10^\circ$, 30° , 60° , and 90° , respectively. The deviations of the smaller head rotations are lower than those of the second deviation set, but are similar for larger head rotations. This suggests that a mimicking of smaller head rotations is possible via post-processing rotation of a fixed directivity measurement that includes torso diffraction. However, for larger head rotations, the benefits are no greater than using the directivity of an isolated head with no torso diffraction.

10.5 Conclusions

This work has investigated the effects of azimuthal head orientation and torso diffraction on the directivity of a KEMAR HATS. The results show that neglecting torso diffraction or head orientation relative to the torso can lead to significant differences in directivity beam patterns, including shifting diffraction lobes. Directivity deviations illustrated that while differences in directivity beam patterns

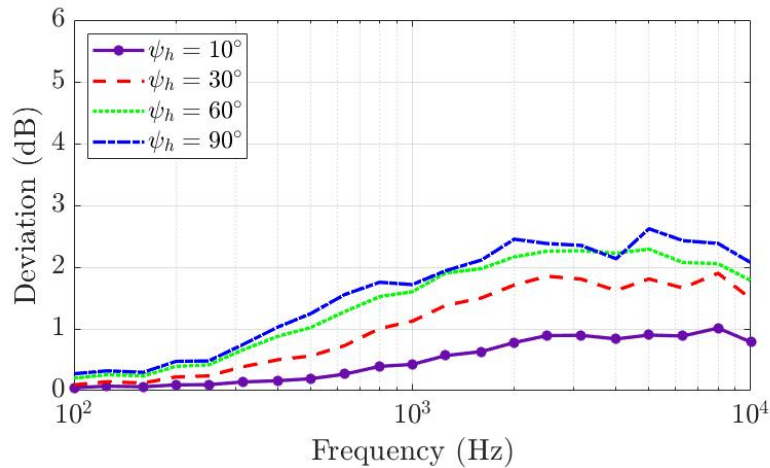


Figure 10.6 Frequency-dependent directivity deviations between the reference directivities and directivities measured with the head and torso rotated together as a single unit towards ψ_h .

at low frequencies are minor, they become more substantial above 1 kHz. The deviations also showed that incorporating correct head orientation is more important than including torso diffraction. For small head orientations, rotating a fixed directivity with torso diffraction in post-processing is more beneficial than using an isolated head directivity.

One limitation of this work is that the HATS constrained head rotation to only the azimuthal angle, meaning the work did not explore the effects of up-and-down head movements. Another limitation is that the investigation considered only the KEMAR HATS, whereas future work could include other HATS models, compare directivity results with those produced by live talkers, and consider differences between distinct phonemes. The study compared isolated head directivity with combined head and torso directivities for different head orientations, but it neglected the diffraction effects of legs and arms. The effects of the limbs, including differences in seated and standing positions, would also be a worthwhile topic in future speech directivity research. Other research could explore whether the noted directivity deviations are perceptually significant or not. The authors encourage further work in these areas.

Chapter 11

Trumpet Directivities Derived from a Multiple-Capture Method

This chapter demonstrates how a multiple-capture measurement technique allows the acquisition of high-resolution trumpet directivities. The technique incorporates several elements discussed in Chs. 2 and 5 to produce the results.

11.1 Introduction

Directional radiation is an essential aspect of played musical instruments. Musical instrument radiation characteristics influence many practical applications, including microphone placements [14–17], auralizations [18, 19], and concert hall designs [20, 21]. Nevertheless, properly acquiring and implementing source directivities for these and other applications requires sufficient spatial resolution. The AES56-2008 (r2019) [33] governs measured spherical directivities for loudspeakers with 5° angular resolution to enable successful electroacoustic and room-acoustical modeling and prediction. Commercially available room acoustical prediction software packages commonly

employ these standardized angular resolutions [96, 97]. However, the fine details afforded by comparable resolutions for musical instruments have remained obscure.

Musical instrument directivity measurements present several practical challenges [153]. For example, unlike loudspeakers, musicians cannot repeat notes exactly each time their orientations or scanning microphone positions change, and new measurements begin. Furthermore, while the position of a loudspeaker is easily controllable during a measurement sequence, a musician often shifts while playing. Aligning a principal loudspeaker axis toward desired polar and azimuthal angles is automatable, but practical considerations restrict the rotation of a live musician and his or her instrument to the horizontal plane (i.e., the azimuthal angle) only.

To evade these and other challenges, some researchers have resorted to artificial excitation of instruments, including horns [35, 154], the clarinet [72, 155, 156], bassoon [34, 143], violin [36, 37, 139–141, 156–158], guitar [157, 159], harp [104, 159], and piano [160, 161]. While the enhanced repeatability of artificial excitation increases the feasibility of higher-resolution measurements, the approach ignores the critical effects of live musicians, including their diffraction, absorption, and natural instrument excitation. More recently, Ref. 72 showed that diffraction and absorption of the human body significantly alter the directivities of isolated instruments, even at lower frequencies.

Meyer and Wogram correctly stressed that musicians and instruments are intrinsically integrated entities for practical directivity measurements [154]. In fact, while most of Meyer's published results emanated from artificially excited instruments, he also performed sparse measurements of played instrument directivities in some cases to evaluate the diffraction and absorption caused by musicians' bodies [143, 154].

One approach to evaluating *played* musical instruments' directivities is limiting measurement to individual multichannel recordings. This *single-capture method* fixes the positions and orientations of musicians and instruments within a stationary enveloping microphone array having limited (e.g., 13, 22, 32, or 64) total sampling positions over the measurement surfaces or contours [18, 31, 100,

101, 125, 127]. One of the most significant works to date involving directivity measurements of 41 modern and historical instruments employed a quasi-spherical microphone array with 32 nearly uniformly spaced positions [32].

Single-capture systems do not require playing repetitions and may claim better measurement repeatability. However, they are not feasible for high sampling densities. The 5° angular resolutions specified for standardized loudspeaker directivity measurements would require 2,522 unique sampling positions over a sphere, with accompanying microphones, support structures, cables, and data acquisition channels. Because this is an impractical number for single-capture measurements, multiple-capture systems employing moving microphones or sources are necessary to measure played musical instruments, just as they are to measure loudspeakers.

Researchers have previously employed multiple-capture methods in musical instrument directivity studies, such as for the piano [102], violin [105, 106], and traditional Korean musical instruments [21]. However, the works employing the approaches lacked complete spherical data, did not use excitation approaches applicable to all instruments, or did not use actual transfer functions to adequately compensate for differences between playing repetitions necessitated by incremental captures. Recently, two of the present authors published work on a multiple-capture, transfer-function method for measuring live speech directivity with a full-spherical, 5° resolution compatible with the AES standard [6]. Nevertheless, adaptations of multiple-capture methods to musical instruments come with unique challenges and differing results.

This work illustrates how the multiple-capture, transfer-function method adapts to musical instrument directivities by assessing a trumpet's sound radiation. The applied techniques enable 5° polar and azimuthal angular resolution measurements compatible with the AES directivity sampling standard [33]. Narrowband directivities, while confirming well-known general radiation characteristics, reveal intricate radiation patterns, diffraction lobes, and musician shadowing. Comparing results to those of an artificially played trumpet and seated manikin is similar to the approach

described in Ref. 72 and confirms the reliability of the multiple-capture, transfer-function method. Derived directivity indices confirm that the trumpet is a highly directional source at many frequencies. Additional results and discussions related to source centering and spatial aliasing highlight the benefits of the multiple-capture method in producing high-resolution, spherical directivities with broad applications.

11.2 Methods

11.2.1 Measurement Procedure

Several components of the directivity measurement system appear in Fig. 12.1, including a fixed reference microphone, a rotating semicircular microphone array, and a musician and instrument within an anechoic chamber ($f_c = 80$ Hz). The constant-radius $R = 1.17$ m array incorporated 36 12.7 mm (0.5 in.) precision free-field microphones at fixed 5° polar-angle increments. Relative frequency-dependent calibration of each microphone and its signal path to a dedicated channel minimized measurement errors that would otherwise appear as latitudinal bands in directivity balloon plots. Acoustically treated apparatuses suspended and supported the arc and rotation system. The musician's chair and footrests could adjust vertically, horizontally, and angularly within the rotating arc. Reference 1 includes more details about the measurement hardware and calibration procedures.

Because a structure did not support the trumpet rigidly, musician movements could potentially introduce spatial variances affecting the directivity measurement's quality. To mitigate these variances, a head restraint connected to the musician's chair ensured consistent head orientation. A laser attached to the instrument illuminated an acoustically unobtrusive ≈ 2 cm square target fixed to the chamber wall several meters away. The measurement procedure thus required that the musician hold the trumpet still to align with the target during the playing sequence.



Figure 11.1 Directivity measurement system with a musician and trumpet.

While oriented toward the initial azimuthal angle $\phi = 0^\circ$, the musician played a chromatic scale at mezzo-forte from B \flat 3 to F5, the typical playing range of the instrument, with each note held for 1 s, followed by a 1 s rest. A metronome signal in the musician's earphone ensured a consistent pace, while an electronic tuner helped maintain pitch consistency. The musician repeated any problematic notes of a scale for correction. Following a successful multichannel recording, the rotation system advanced 5° in the azimuthal angle ϕ , and the musician repeated the scale. This process continued until the directivity measurement system collected a complete sphere of sampled data via 72 multichannel recordings, each with 24-bit, 48 kHz sampling.

As an additional validation, the directivity measurement system evaluated the directivity of the trumpet when it was artificially excited by a small transducer coupled to the trumpet mouthpiece. Three repetitions of a five-second logarithmic swept sine served as the excitation signal. As suggested by Fig. 11.2, the artificial excitation apparatus was attached to a seated manikin. Although the manikin was somewhat smaller, lacked forearms and hands, and otherwise differed in geometry, it provided a rough approximation of the diffraction and absorption caused by the musician's body [72]. A support structure aligned the instrument and its laser to the same target on the anechoic chamber wall.

11.2.2 Data processing and analysis

Because even the best musicians play repeated notes with amplitude and spectral variations, imperfect repetitions seemingly pose an insurmountable problem for multiple-capture directivity measurements. However, when appropriately employed, frequency response functions (FRFs) between the reference and array microphone signals mitigate these effects. Previous research has demonstrated that FRFs establish directivity functions for loudspeakers [13], the human voice, [6, 162] and musical instruments [106, 107]. However, for musical instruments playing discrete notes (i.e., without glissandi), the FRFs must derive from spectrally sparse signals and are valid only at specific



Figure 11.2 Directivity measurement system with an artificially excited trumpet and manikin.

frequencies for which significant radiated sound energy arrives at both the reference and array microphones.

Narrowband

The FRFs for the u^{th} microphone at the v^{th} azimuthal rotation followed from the autospectral estimates $G_{aa_v}(f)$ of the reference microphone signal $a_v(t)$ and the cross-spectral estimates $G_{a\tilde{b}_{uv}}(f)$ between that signal and each array microphone signal $\tilde{b}_{u,v}(t)$, where the tilde indicates the possibility of uncorrelated noise in the array signals. For each note, the spectral estimates resulted from Welch's method [131, 163] and involved five 48,000-sample block sizes (1 s record length, 1 Hz narrow-band resolution), a Hann window, and 90% overlap. For each reference and array microphone pair, the least-squares FRF estimate

$$H_{uv}(f) = G_{a\tilde{b}_{uv}}(f)/G_{aa_v}(f) \quad (11.1)$$

provided an unbiased result with respect to uncorrelated noise in the output signals [131]. A normalized FRF-based directivity function follows as [6]

$$D_{uv}(f) = \frac{H_{uv}(f)}{H_{(uv)_{\max|H|}}(f)}, \quad (11.2)$$

where $(uv)_{\max|H|}$ represents the index pair with the maximum FRF magnitude for a given frequency.

The coherence function

$$\gamma_{a\tilde{b}_{uv}}^2(f) = |G_{a\tilde{b}_{uv}}|^2 / G_{aa_v}(f)G_{\tilde{b}\tilde{b}_{u,v}}(f) \quad (11.3)$$

and the related signal-to-noise ratio

$$SNR_{u,v}(f) = 10 \log_{10} \{ \gamma_{a\tilde{b}_{uv}}^2(f) / [1 - \gamma_{a\tilde{b}_{uv}}^2(f)] \} \quad (11.4)$$

utilized the array signal autospectral estimates $G_{\tilde{b}\tilde{b}_{u,v}}(f)$ in addition to the reference autospectral and cross-spectral estimates to provide necessary checks of FRF qualities. As the coherence function

ranged from 0 to 1, it represented the ratio of correlated to uncorrelated signal energy in the reference and array signals at frequency f [131]. The coherence thereby played a critical role in establishing statistical confidence in the FRF measurements as originating from linear, time-invariant (LTI) systems free of appreciable extraneous noise.

Spherical Harmonic Expansions

Frequency response functions provide frequency-dependent normalizations of levels between rotations and rejections of uncorrelated noise between the reference and array signals. Other helpful tools for improving measurement quality and overcoming measurement difficulties are spherical harmonic expansions. The normalized spherical harmonics $Y_n^m(\theta, \phi)$ of degree n and order m [70] form an orthonormal basis for expanding functions on the sphere. As the spherical harmonics are intrinsic angular wave function components of the Helmholtz equation solution in spherical coordinates, a spherical harmonic expansion applied to complex-valued narrowband data yields the unique solution on the exterior domain [59]:

$$\hat{p}(r, \theta, \phi, k) = \sum_{n=0}^{\infty} \sum_{m=-n}^n p_n^m(k) \frac{h_n^{(2)}(kr)}{h_n^{(2)}(kR)} Y_n^m(\theta, \phi), \quad r \geq R, \quad (11.5)$$

where \hat{p} is the complex pressure amplitude, r is the radial distance from the origin, R is the measurement sphere radius, k is the wavenumber, $h_n^{(2)}(kr)$ are the spherical Hankel functions of the second kind of order n (for outward-going waves with $e^{i\omega t}$ time dependence), and $p_n^m(k)$ are the pressure expansion coefficients. The expansion coefficients follow from orthogonality as

$$p_n^m(k) = \int_0^{2\pi} \int_0^\pi \hat{p}(r, \theta, \phi, k) [Y_n^m(\theta, \phi)]^* \sin \theta d\theta d\phi, \quad (11.6)$$

where $*$ indicates complex conjugation. In practice, discrete measurements allow only a finite number of expansion coefficients [77] Driscoll and Healy's [113] spherical quadrature weights adapt to the applied sampling density and allow expansions to $N_s = 34$ [78]. A continuous directivity

function on the measurement surface follows as [6]

$$D(\theta, \phi, k) = \frac{\hat{p}(R, \theta, \phi, k)}{\hat{p}[R, (\theta, \phi)_{\max|\hat{p}|}, k]}. \quad (11.7)$$

One practical consideration in directivity measurements is the location of the source within the measurement array. As evident in Fig. 12.1 and Fig. 11.2, the radiating portion of the trumpet did not align with the geometric center of the array. Improper placement may lead to deviations between near-field measured patterns and the desired far-field pattern [45]. Some past works have applied acoustic source-centering techniques to measured directivities [27–29, 32]. However, Refs. 82 and 164 have demonstrated that a far-field projection is sufficient to obtain a far-field directivity while correcting for undesired near-field deviations. Applying the large-argument asymptotic form of the spherical Hankel functions yields an unnormalized far-field directivity function as [59]

$$\tilde{D}_{ff}(\theta, \phi, k) = \sum_{n=0}^{\infty} \sum_{m=-n}^n \frac{i^{n+1}}{kh_n^{(2)}(kR)} P_n^m(k) Y_n^m(\theta, \phi). \quad (11.8)$$

The far-field directivity factor function subsequently follows as [10]

$$Q_{ff}(\theta, \phi, k) = \frac{4\pi |\tilde{D}_{ff}(\theta, \phi, k)|^2}{\int_0^{2\pi} \int_0^\pi |\tilde{D}_{ff}(\theta, \phi, k)|^2 \sin \theta d\theta d\phi}. \quad (11.9)$$

For a source enclosed by a notional sphere of radius $R = d$ centered at the origin, the evanescent nature of the spherical Hankel functions suggests that the relative contributions of the expansion coefficients with $n \gtrsim kd$ decay rapidly in the far-field. [59, 77, 83] As a result, a sound source with “effective radius” [83] d requires an expansion with terms up to $N \approx kd$. This simple relationship suggests that a source is spatially bandlimited [114], so that one may effectively truncate the infinite series in Eqs. 12.6 and 11.8 at a frequency dependent N . Spatial aliasing effects occur when the maximum degree for source representation N exceeds the sampling configuration’s maximum resolvable degree N_s .

Estimating d from measured data is essential to deduce the maximal usable frequency for spherical-harmonic-based analysis without spatial aliasing errors. The energy-per-degree metric

[114]

$$E_n(k) = \sum_{m=-n}^n |p_n^m(k)|^2 \quad (11.10)$$

serves as a useful tool for estimating the effective radius of a source from measured data. It represents the signal energy for a specified expansion degree and provides a measure of a source's spherical spectrum. Since a source with effective radius d radiates little energy to the far field for $n > kd$, the ratio for a given frequency

$$\gamma_N(k) = \frac{\sum_{n=0}^N E_n(k)}{\sum_{n=0}^{\infty} E_n(k)}, \quad (11.11)$$

represents the signal energy lost by the infinite series truncation to degree N . For a fixed threshold, e.g., $\gamma = 0.98$, computing N_f for several discrete wavenumber k values allows a least-squares fit to the line $N = kd$. To ensure spatial aliasing effects do not negatively impact the estimate, the maximum wavenumber considered in the least-squares fit should be no more than N_s/R , which corresponds to 1.6 kHz for the present work. This limit represents the maximum frequency for spherical-harmonic-based analysis applied to an arbitrarily-shaped source entirely contained within the measurement radius R . Of course, higher-frequency analysis is possible for sources with effective radii $d < R$.

Truncations of spherical harmonic expansions smooth directivity patterns, enabling spatial filtering to reduce measurement noise [59, 165]. Because the most important expansion coefficients and radiated energy tend to lie along and below $n = kd$, coefficients higher than this limit are prone to a lower signal-to-noise ratio, assuming Gaussian spatial noise. Truncation of these higher-degree coefficients according to

$$N = \lceil kd \rceil + 2 \quad (11.12)$$

thus allows appropriate spatial filtering of the measured data [59]. In Eq. 11.12, the ceiling function $\lceil \cdot \rceil$ rounds up to the nearest integer and the arbitrary addition of two helps preserve energy from the roll-off above $n = kd$ (See Sec. 11.3.3 and Fig. 11.8).

11.3 Results

11.3.1 Narrowband Frequency Response Functions

Figure 11.3 highlights the effectiveness of the FRF method by comparing narrowband (1 Hz resolution) normalized directivity functions derived from the array autospectral levels [Fig. 11.3(a)] with those derived from FRFs [Fig. 11.3(b)] for the 3rd partial of B \flat (699 Hz). Balloon colors and radii indicate relative levels on a decibel scale. The musician faces the 0° azimuthal marker, and the vantage point is upward and to the musician's right. Because the FRF-based balloon derives from the raw FRF results [Eq. 11.2], it does not incorporate spherical harmonic expansions or far-field propagation.

As one might anticipate, the first directivity pattern is hardly discernible without adequate compensations for playing repetitions and their associated captures at the azimuthal angle increments. The fixed reference microphone data indicated that level variations for this specific partial and frequency exceeded 30 dB. The input-level variations led to the strong longitudinal banding artifacts in the output measured by the array.

On the other hand, the FRFs between the reference and array microphone signals are robust to these variations, assuming that the pertinent sound propagation mechanisms comprise an LTI system. As evidenced by the FRF-based balloon in Fig. 11.3(b), the FRFs correctly compensated for these deviations, leading to a smooth directivity function with no visible banding effects. This typical result highlights the effectiveness of the transfer-function method for narrow bands (and broader bands) when properly applied to live sound sources.

Figure 11.4 plots narrowband (1 Hz resolution) FRF-based directivity balloons [Eq. 11.2] for four different partials from the played trumpet [Figs. 11.4 (a)-(d)] and the equivalent extracted frequencies for the artificially excited trumpet [Figs. 11.4 (e)-(g)]. At 233 Hz [B \flat 3, 1st partial, Figs. 11.4(a) and (e)], the radiation at the array surface is not particularly directional, although some

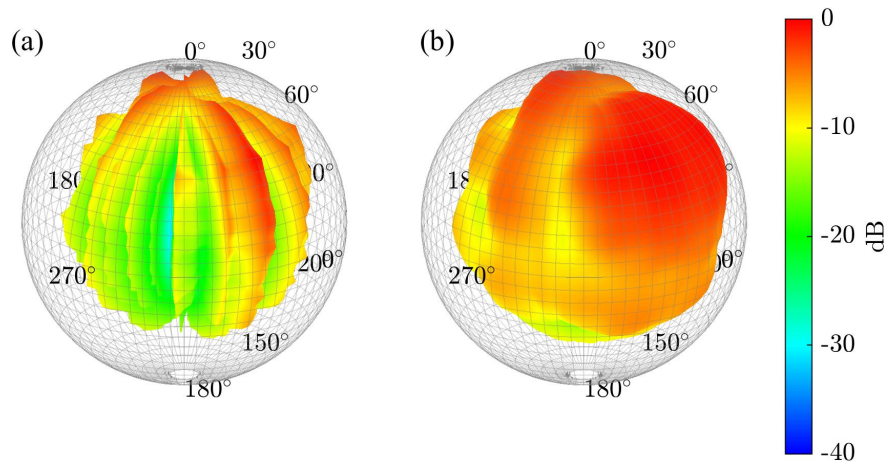


Figure 11.3 Trumpet narrowband directivities at 699 Hz based on (a) autospectral levels from the array microphone signals and (b) frequency-response functions between the reference and array microphone signals.

diffraction and shadowing behind the musician appear. At 311 Hz [Eb4, 1st partial, Figs. 11.4(b) and (f)], stronger radiation in front of the musician and a side lobe become apparent. Shadowing attenuation behind the musician exceeds 10 dB. These trends continue to develop at 438 Hz [A4, 1st partial, Figs. 11.4(c) and (g)], and 524 Hz [C4, 2nd partial, Figs. 11.4(d) and (h)]. At these frequencies, the strongest radiation regions concentrate in front of the trumpet, and reduced levels appear behind and in the directions of the musicians' legs. Similar diffraction features are visible in speech and clarinet directivity measurements [6, 72].

Despite the inherent differences between a musician and a manikin, the directivities derived from the played trumpet qualitatively agree with those derived from the artificially excited trumpet. Although some lobes' precise directions and locations show minor variations, the essential directional characteristics, including the numbers of lobes and regions of reduced levels, concur. The directivity factor function deviation level [81] (DFFDL) L_Q between the played and artificially excited directivities did not exceed 1.0 dB for these partials. The individual DFFDLs were 0.7 dB, 0.8 dB, 1.0 dB, and 1.0 dB for 233 Hz, 311 Hz, 438 Hz, and 524 Hz, respectively. These similarities and the absence of longitudinal banding highlight the FRF method's robustness in

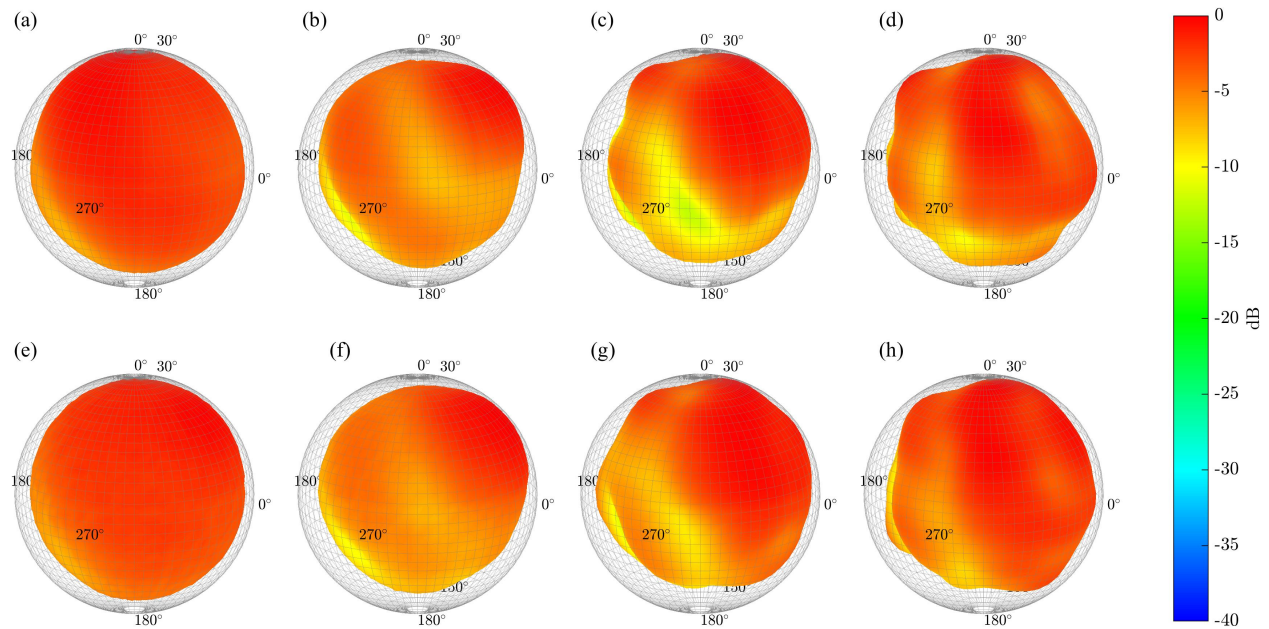


Figure 11.4 FRF-based directivity balloons for the (a)-(d) played and (e)-(h) artificially excited trumpet with manikin.(a) and (e): 233 Hz. (b) and (f): 311 Hz. (c) and (g): 438 Hz (d) and (h): 524 Hz.

compensating between repeated measurements and deriving high-resolution directivities of played musical instruments.

Figure 11.5 plots the directivity balloons of four higher-frequency partials for the played trumpet [Figs.11.5 (a)-(d)] and the equivalent extracted frequencies for the artificially excited trumpet [Figs.11.5 (e)-(g)]. The vantage point is upward and behind the musician and manikin to facilitate visualization of the diffraction and interference patterns around and behind the bodies. At 589 Hz [D4, 2nd partial, Figs. 11.5 (a) and (e)], the most substantial radiation concentrates directly in front of the musician, and two side lobes and a diffraction spot appear behind the musician's chair. Increased diffraction effects behind the body and complex regions of constructive and destructive interference characterize the directivity patterns at this higher frequencies, especially at 1160 Hz [Bb3, 5th partial, Figs. 11.5 (d) and (h)].

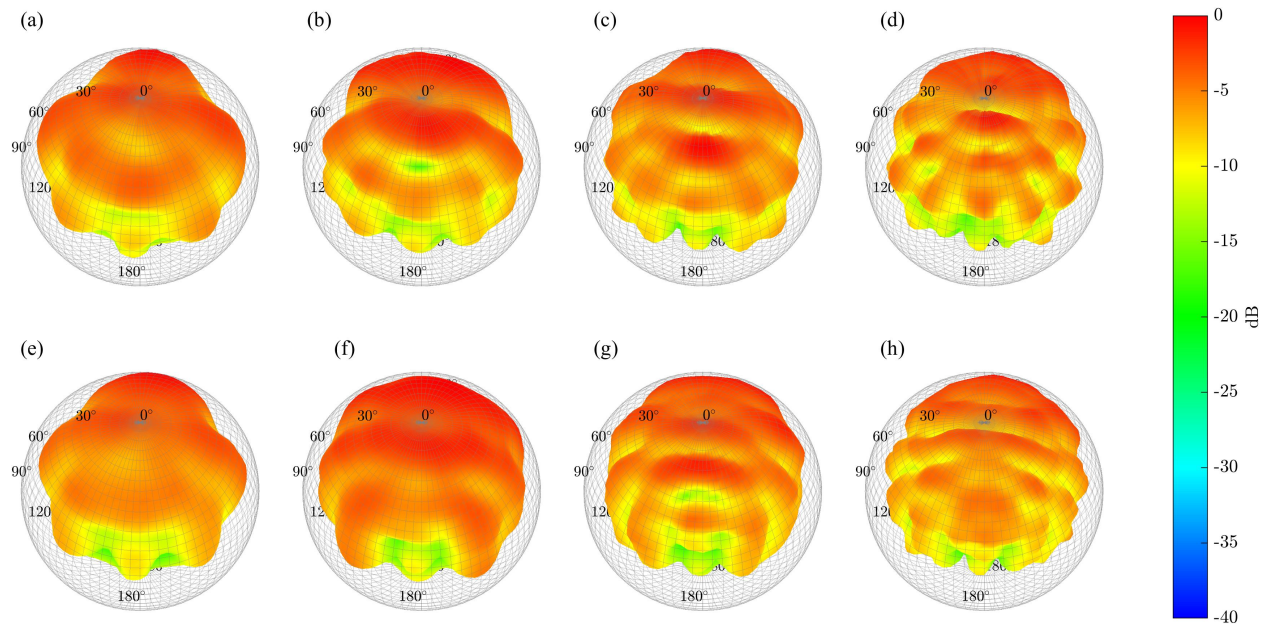


Figure 11.5 FRF-based directivity balloons for the (a)-(d) played trumpet and (e)-(h) artificially excited trumpet with a manikin. (a) and (e): 589 Hz. (b) and (f): 737 Hz. (c) and (g): 932 Hz (d) and (h): 1160 Hz.

The qualitative agreement continues between the general radiation characteristics of the played and artificially excited trumpets at these higher frequencies. However, some finer details appear to differ, potentially due to the inherent differences between the musician and the manikin. The DFFDLs were 1.2 dB, 1.5 dB, 1.6 dB, and 1.5 dB for 589 Hz, 737 Hz, 932 Hz, and 1160 Hz, respectively. Section 11.4.2 further considers deviations between played and artificially excited directivities.

11.3.2 Spherical Harmonic Expansions

Spherical harmonic expansions are beneficial for directivity interpolation, far-field propagation, and other processing applications. However, their implementation requires careful convergence analysis to ensure adequate expansion terms. Figure 11.6 plots the directivities derived from spherical harmonic expansions of the complex-valued FRFs over varying expansion degrees evaluated on the

measurement surface $r = R$ [Eq. 11.7] for the second partial of F4 (695 Hz). The expansions limited to $N = 3$ [Fig. 11.6(a)] or $N = 4$ [Fig. 11.6(b)] are insufficient to capture the general radiation trends at this particular frequency. The DFFDLs between the raw FRF-based directivity [Fig. 11.6(f)] and each of these expansion directivities are 4.4 dB and 3.9 dB, respectively. An $N = 6$ expansion [Fig. 11.6(c)] produces general directional characteristics that begin to resemble the original measured data and decreases the DFFDL to only 1.3 dB. The $N = 8$ [Fig. 11.6(d)] and $N = 12$ [Fig. 11.6(e)] expansions further decrease the DFFDL to 0.4 dB and 0.2 dB, respectively.

The number of required expansion coefficients depends on frequency. To highlight this concept, Fig. 11.7 plots L_Q between the original measured data and the expanded data for varying maximal expansion degree N and four partials. For the 233 Hz case (B \flat 3, 1st partial) shown by the solid red curve, the deviation levels decrease to below 1.0 dB with only an $N = 3$ degree expansion. However, for the 1315 Hz case (E4, 4th partial) shown by the purple dotted curve, the levels do not reach this same threshold until an $N = 13$ degree expansion. Thus, properly implementing spherical harmonic expansions requires careful monitoring of both frequency-dependent effects and convergence to measured patterns.

11.3.3 Spatial Aliasing

Considering a source's effective radius provides additional insight into the increasing number of expansion terms required with increasing frequency. Figure 11.8 plots the energy per degree E_n over frequency and expansion degree [see Eq. 11.10] for the played [Fig. 11.8(a)] and artificially excited [Fig. 11.8(b)] trumpet. Color indicates the relative level on a decibel scale, with white representing expansion coefficients with high levels and black representing expansion coefficients with low levels.

With a truncation factor of $\gamma = 0.98$ (see Sec. 11.2.2), least-squares fits estimated the effective radius of the played trumpet and musician and the artificially excited trumpet and manikin to be

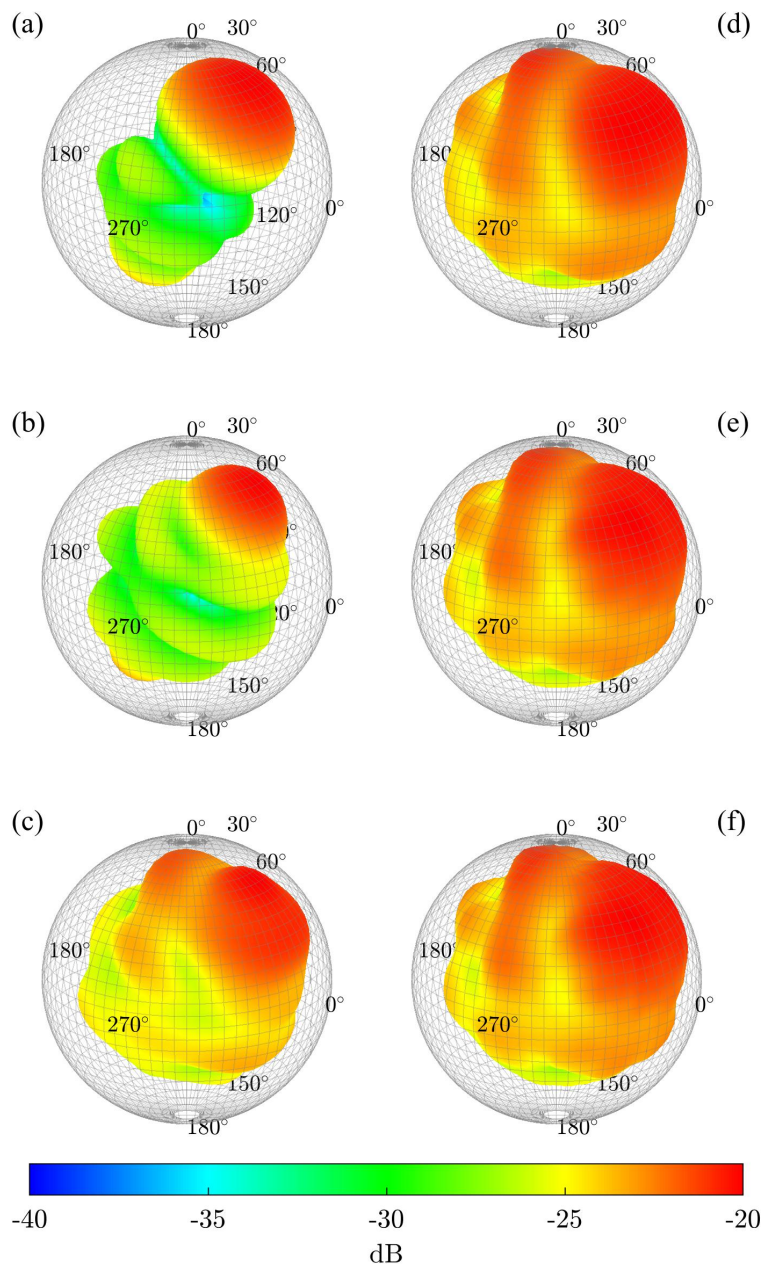


Figure 11.6 Played trumpet directivities at 695 Hz (F4, 2nd partial) based on (a) $N = 3$, (b) $N = 4$, (c) $N = 6$, (d) $N = 8$, and (e) $N = 12$ degree spherical harmonic expansions, and (f) the raw FRF-based directivity.

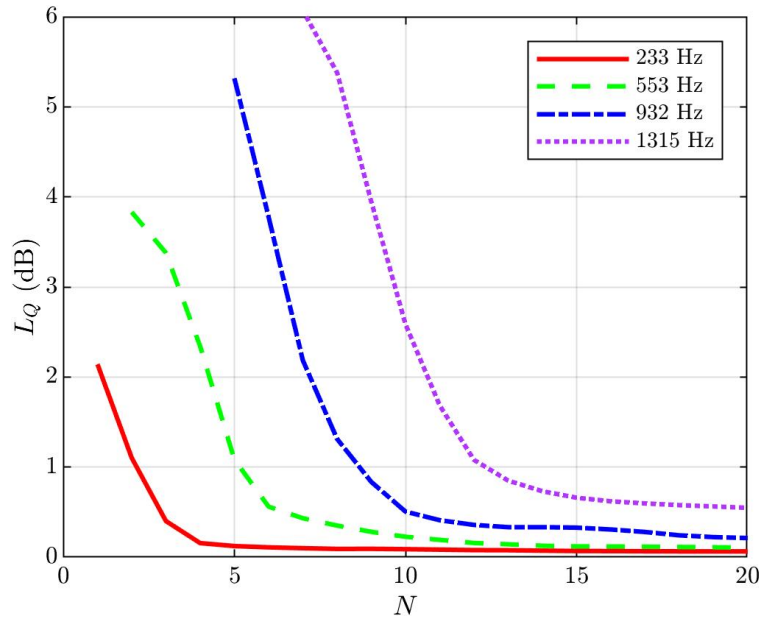


Figure 11.7 Directivity factor function deviation levels between measured FRF-based and spherical-harmonic-expansion-based directivities over expansion degree N for selected partials.

$d = 0.44$ m and $d = 0.45$ m, respectively. Overlaid blue dotted lines in Figs. 11.8(a) and (b) indicate the truncation curve $N = \lceil kd \rceil + 2$ that use these values. Below 3 kHz, most of the significant coefficients lie below this line. The essential expansion coefficients, indicated by the white streaks, follow the trend of $n = kd$.

The overlaid green dashed line represents the upper expansion degree without significant spatial aliasing, $N_s = 34$ [78, 113]. Near 4.5 kHz, significant signal energy reflects across this line $N = 36$, which is analogous to time-frequency domain aliasing, where the frequency $f = f_s/2 + \Delta f$ aliases to $f = f_s/2 - \Delta f$, where f_s is the sampling rate. Accordingly, the reflected energy in the plot is a key indicator of the reliable bandwidth without spatial aliasing. Using the intersection of $N = \lceil kd \rceil + 2$ with $N_s = 34$ yields an upper usable limit of 3.9 kHz. Above this frequency, spatial aliasing effects are significant and pressure field extrapolation or interpolation using spherical harmonic expansions may be unreliable.

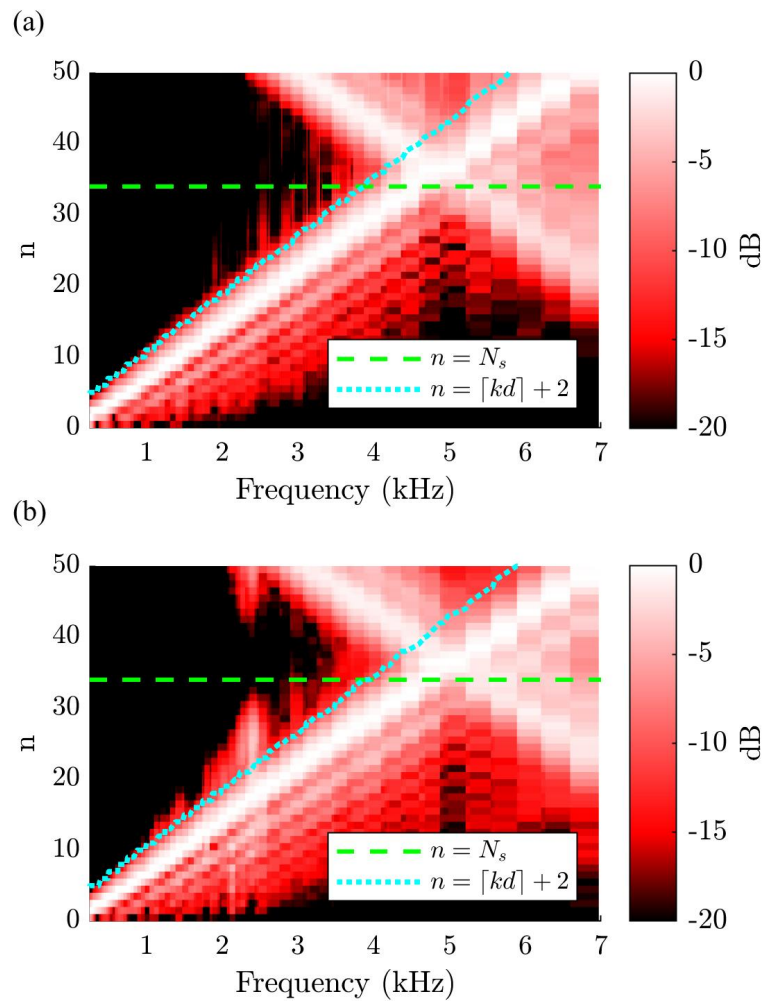


Figure 11.8 Spherical spectrum (E_n) for the (a) played and (b) artificially excited trumpet.

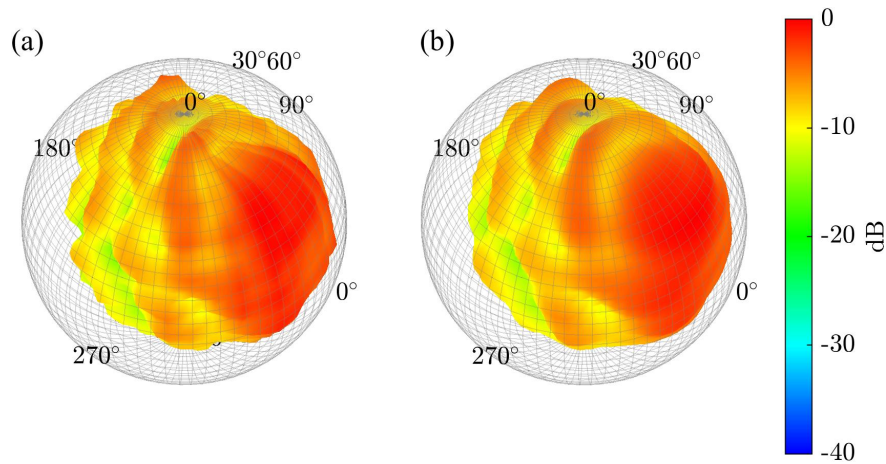


Figure 11.9 Directivity at 1315 Hz (E4 4th partial) based on (a) raw narrowband FRFs and (b) an $N = 13$ degree spherical harmonic expansion.

11.3.4 Spatial Filtering

With an estimate of the effective source radius in place, appropriately truncating the spherical harmonic expansion enables spatial filtering, which can remove undesirable measurement noise [59]. To illustrate this concept, Fig. 11.9(a) plots a raw FRF-based directivity balloon for the fourth partial of E4 (1315) Hz. Although the compensation by the FRF method is substantial compared, for example, to the directivities of Fig. 11.3, some minor longitudinal banding remains due to measurement inconsistencies between repeated captures. For this particular frequency, Eq. 11.12 with an effective radius of $d = 0.44$ suggests that a truncation at $N = 13$ will maintain the essential directional characteristics while eliminating measurement noise contained in higher-degree expansion coefficients and smoothing the residual banding. Fig. 11.9(b) plots the resultant directivity expanded to this degree.

11.3.5 Far-field Propagation

Far-field propagation via spherical harmonic expansions corrects for near-field variations due to, for example, source placement within the measurement array [82, 164]. Figure 11.10 illustrates how

far-field propagation may modify measured directivities for three select partials. Figure 11.10(a) shows the played trumpet directivity at 394 Hz (G4, 1st partial) while Fig. 11.10(d) shows its far-field projected pattern using an $N = 6$ degree expansion. The directional characteristics remain similar, but the radiated levels are stronger to the side and behind. Because the trumpet bell lies in front of ($+x$) and above ($+z$) the array's geometric center (see Fig. 12.1), the source placement suggests that the near-field directivity will have stronger levels directly in front of the bell than the far-field directivity, as is the case for a displaced monopole [82]. Similar changes are visible in Figs. 11.10(b) and (e), which compare the directivities at 986 Hz (E4, 3rd partial) with an $N = 10$ degree expansion.

Figure 11.10(c) shows the measured directivity at 1558 Hz (C5, 3rd partial). At this higher frequency, one may anticipate that the principal radiation axis will be in front of the musician, where body diffraction effects impact radiation less significantly [81]. However, the measured pattern indicates that the principal axis falls slightly above the direction of the bell at an elevation angle of approximately 25° (polar angle $\theta = 65^\circ$). In contrast, the far-field projected directivity Fig. 11.10(f) with an $N = 15$ degree expansion lowers the principal axis to an elevation angle of about 15° ($\theta = 75^\circ$).

11.3.6 Directivity Index

The directivity index (DI) has been a fundamental metric of source directivity for decades. Although one may calculate the DI and its associated directivity factor in any direction [10], most authors report it along a source's principal radiation axis only. This axis is clear for many sources, such as typical loudspeakers and horns. However, it is unrealistic for other more complicated sources, including many played musical instruments. Some sources are multidirectional [13]. Others have complex interference and diffraction patterns. Some, like the human voice, have maximum radiation directions that vary with frequency [135].

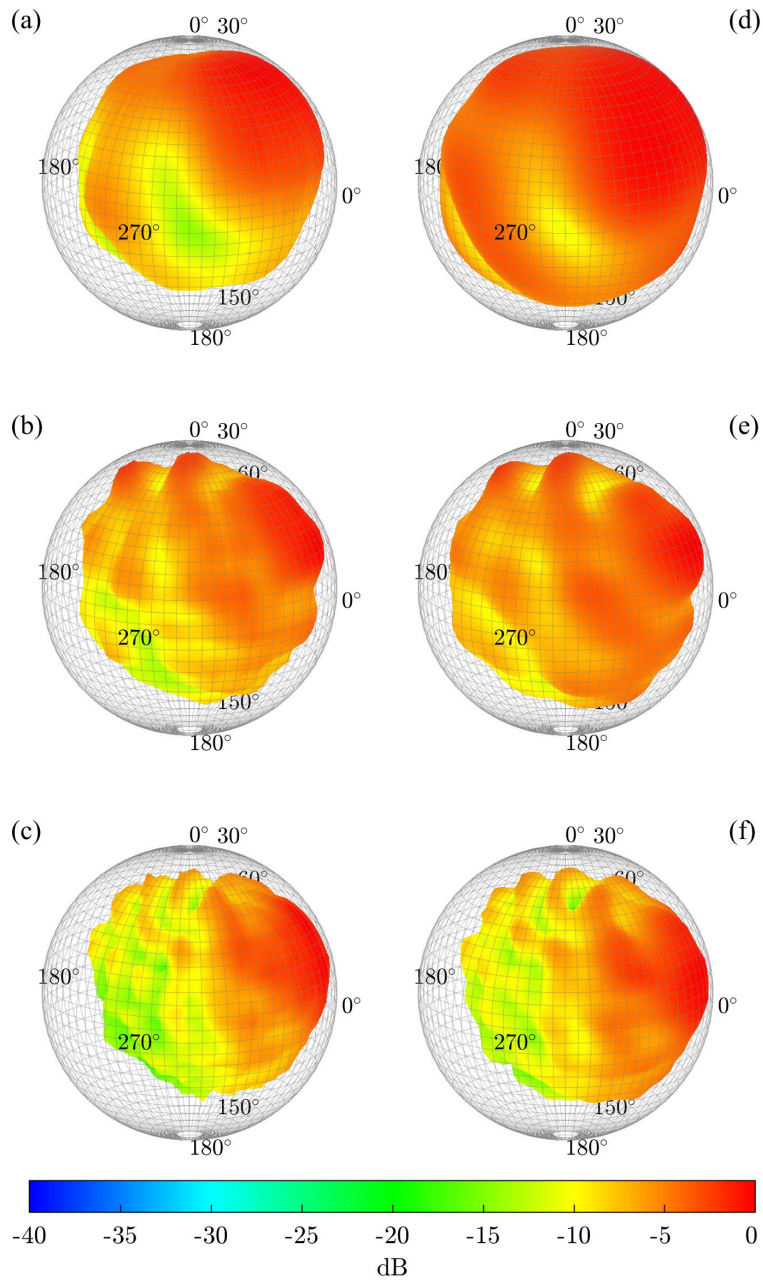


Figure 11.10 Directivity balloons based on (a)-(c) raw narrowband FRFs and (b)-(c) far-field propagated spherical harmonic expansions. (a) and (d): 394 Hz. (b) and (e): 986 Hz. (c) and (f): 1558 Hz.

Figure 11.11(a) plots the frequency-dependent DIs of the played and artificially excited trumpet. Figure 11.11(b) presents the frequency-dependent elevation angle for the maximum radiation axis. The markers represent two hundred extracted partials from the first ten harmonics of the twenty played notes. In both plots, the far-field corrected values appear only up to 4 kHz to eliminate higher-frequency values contaminated with spatial aliasing. The far-field corrections produce calculated DIs of about 1.5 dB at the lowest frequencies. The DIs slowly increase to about 5 dB at 1 kHz. Above 1 kHz, they increase by about 2 dB per octave until reaching approximately 15 dB at 5 kHz.

As mentioned in the preceding section, far-field corrections impact the direction of maximum radiation. The uncorrected direction angles never decrease to below 0° elevation. However, the corrected values fluctuate until converging near -5° at the highest frequencies. The uncorrected values converge to about 15° , indicating the importance of directional pattern correction via far-field propagation.

11.4 Analysis

11.4.1 Zenith Variance

The FRF method employed in this work operates under the assumption that the trumpet's sound radiation behaves as an LTI system. Because the zenith (north pole) microphone should remain at the same place relative to the trumpet during the array rotation, the variance of this microphone's directivity level provides insights into FRF variability and repeatability between the 72 repeated captures. A zenith directivity factor function deviation (ZDFFD) quantifies the variability as

$$\sigma_{Q_z} = \frac{[\sum_{v=0}^{V-1} |Q_{0v}(f) - \langle Q_{0v}(f) \rangle_v|^2]^{1/2}}{\langle Q_{0v}(f) \rangle_v}, \quad (11.13)$$

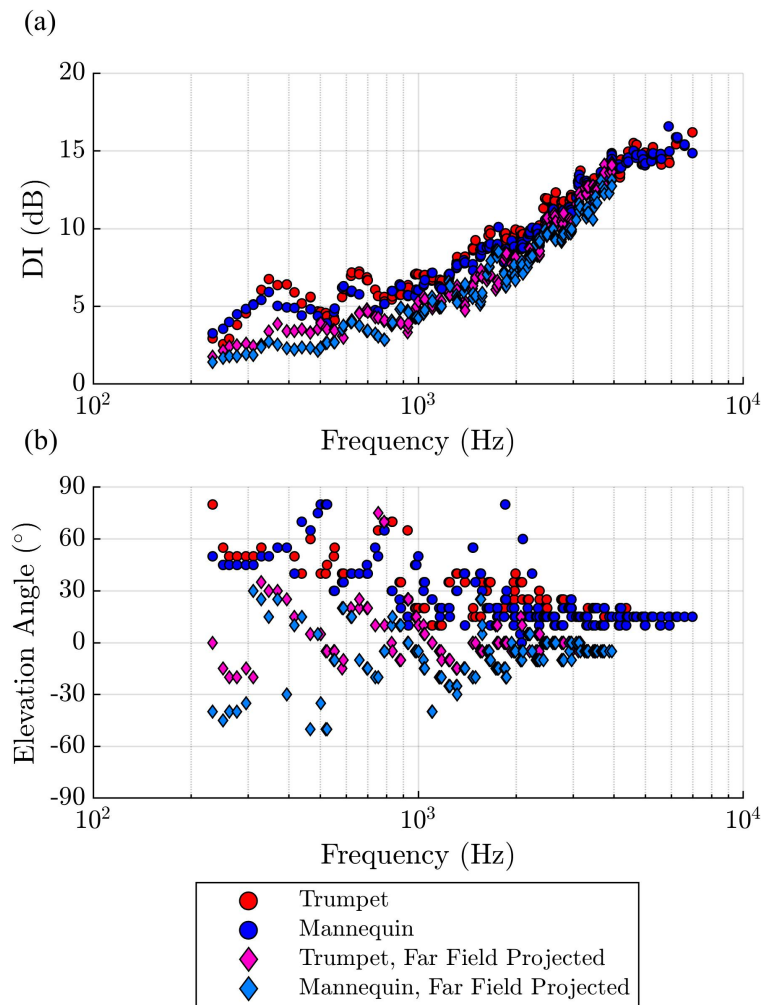


Figure 11.11 Frequency-dependent trumpet directivity properties: (a) Directivity index and (b) maximum radiation axis elevation.

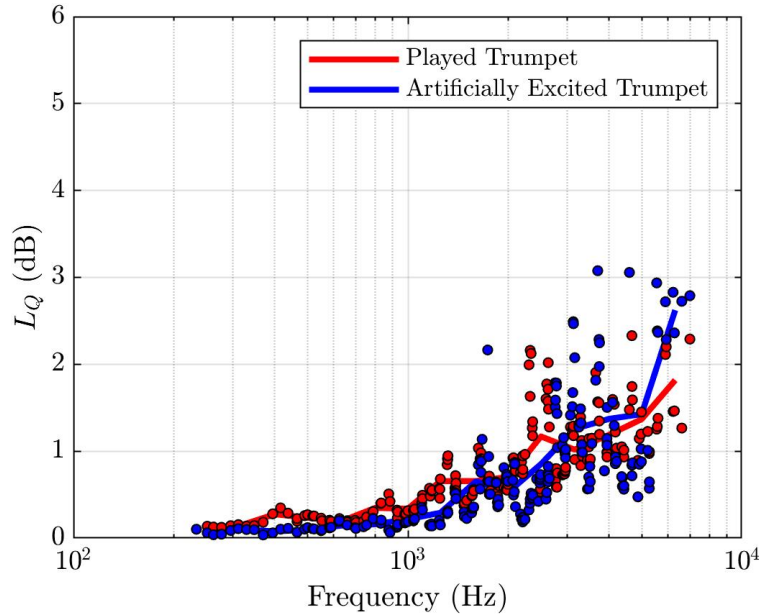


Figure 11.12 Directivity factor function deviations at the zenith microphone position between the 72 repeated captures.

where Q_{0v} is the directivity factor function at the zenith sampling position ($u = 0$) and $\langle Q_{0v}(f) \rangle_v$ is its azimuthally averaged value.

Figure 11.12 plots $L_{Q_z} = 10 \log_{10}(1 + \sigma_{Q_z})$ for two hundred extracted partials from both the musician and manikin-based directivities. Solid curves represent the average deviations over 1/3-octave bands to help visualize the frequency-dependent trends better. The deviations remain small up to 1 kHz; L_{Q_z} does not exceed 0.6 dB for the played instrument and 0.3 dB for the artificially excited instrument. Above 1 kHz, the deviations begin to increase, and by 4 kHz, they are consistently above 1.0 dB. However, the deviations for all played partials remain below 2.5 dB. The manikin-based deviations tend to be lower than those produced by the musician except at the highest frequencies. The average level over all frequencies is 0.8 dB for the musician and manikin. These results quantify the repeatability of the FRF-based method in compensating for varying repetition levels with restrained musician movements.

11.4.2 Comparison with Artificial Directivity

The artificially excited trumpet provides meaningful validation of the FRF-based multiple capture method and its high-resolution directivity measurements. Figure 11.13 plots the DFFDLs for the same two hundred partials to quantify deviations between the played and artificially excited directivity measurements. The levels follow from the raw FRF-based measurements with no spherical harmonic expansion or other post-processing applied. The red curve shows the 1/3-octave-band averages and better illustrates the general trends. For the lowest frequencies considered, the deviations remain below 1.0 dB. As frequency increases, they slowly rise to about 2.0 dB at 2 kHz. The deviations vary more significantly near and above 2 kHz, with some levels exceeding 3.0 dB and others dropping below 2.0 dB. The general frequency-dependent trend increases with increasing frequency. The average DFFDL across all partials is 2.1 dB.

The relatively low DFFDL over frequency highlights the efficacy of the FRF method. The increase of DFFDL with frequency does not necessarily suggest that the FRF method is becoming less valid; it may merely indicate that geometric and material differences between the musician and manikin lead to increased deviations at higher frequencies. For example, the directivities at 1160 Hz seen in Figs. 11.5(d) and (h) do not show any severe longitudinal banding in the FRF-based measurements; the reported deviations in Sec. 11.3.1 of around 1.5 dB appear to result from variations in the locations of diffraction lobes and attenuation regions around the musician. Indeed, the ZDFFD level L_{Q_z} at this frequency is only 0.4 dB, indicating high FRF repeatability. Nonetheless, while the pole variance may be a better indicator of measurement reliability, the relatively low L_Q between the played and artificially excited directivities over frequency provides an essential validation of the multiple-capture method.

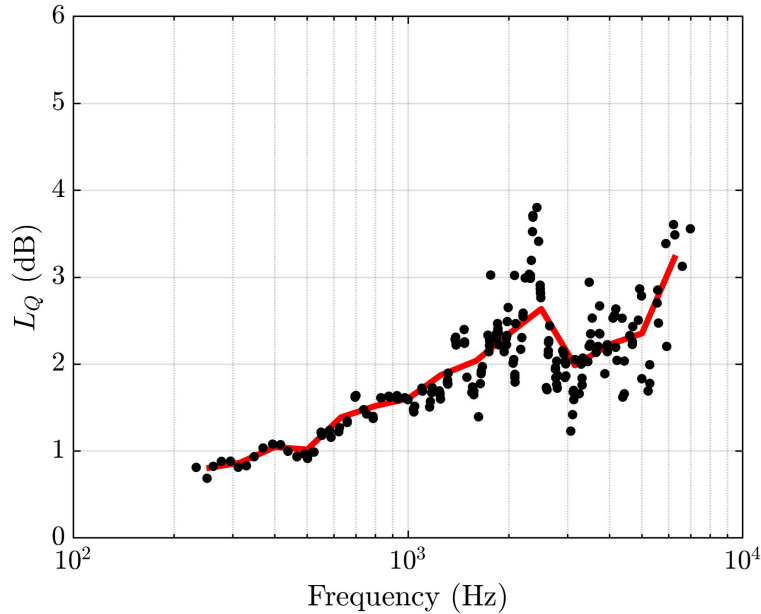


Figure 11.13 Directivity factor function deviation levels between the played and artificially excited FRF-based directivity results.

11.4.3 Symmetry

For many sources, symmetry is another key indicator of directivity validity, such as the quasi-symmetry about the median plane for speech. [6] From geometrical arguments, one would also expect quasi-symmetry about the median plane for the trumpet, especially at lower frequencies. The equiangular sampling scheme employed in the present work facilitates symmetrizing about the median plane. The process involves averaging data from opposing points on the measurement sphere so that the symmetrized directivity factor function becomes

$$Q_s(\theta, \phi, f) = \frac{1}{2} [Q(\theta, \phi, f) + Q(\theta, -\phi, f)], \quad (11.14)$$

where Q is the original function and Q_s is the symmetrized function. If a source exhibits high symmetry, deviations between the measured Q and symmetrized Q_s should be slight.

Figure 11.14 plots the DFFDLs between the measured and symmetrized data for the played and artificially excited trumpet. The symmetry levels in both cases are nearly the same below 1

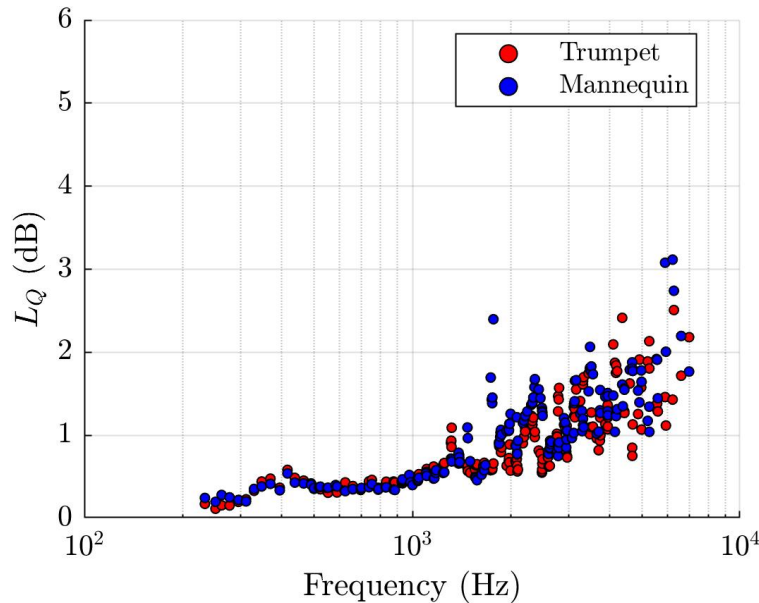


Figure 11.14 Directivity factor function deviation levels between measured and symmetrized partials.

kHz and consistently fall below 0.6 dB. As frequency increases, the DFFDLs and their differences tend to increase. However, the frequency averaged values are 0.9 dB and 1.0 dB for the played and artificially excited trumpet, respectively, indicating high symmetry.

11.4.4 Comparison of Results from Previous Work

Figure 11.15 compares played trumpet directivity results derived from the original recordings of Weinzierl et al. [126] with those of present work for selected partials. Although the number of sampling positions greatly varies (32 for Weinzierl et al. compared to 2,521 for the present work), the essential directional characteristics remain the same. The balloons show increasing directivity with increasing frequency and similar general diffraction and shadowing effects by the musician. The higher-resolution measurements provide significantly more detail and additional insights into the finer source radiation and diffraction features.

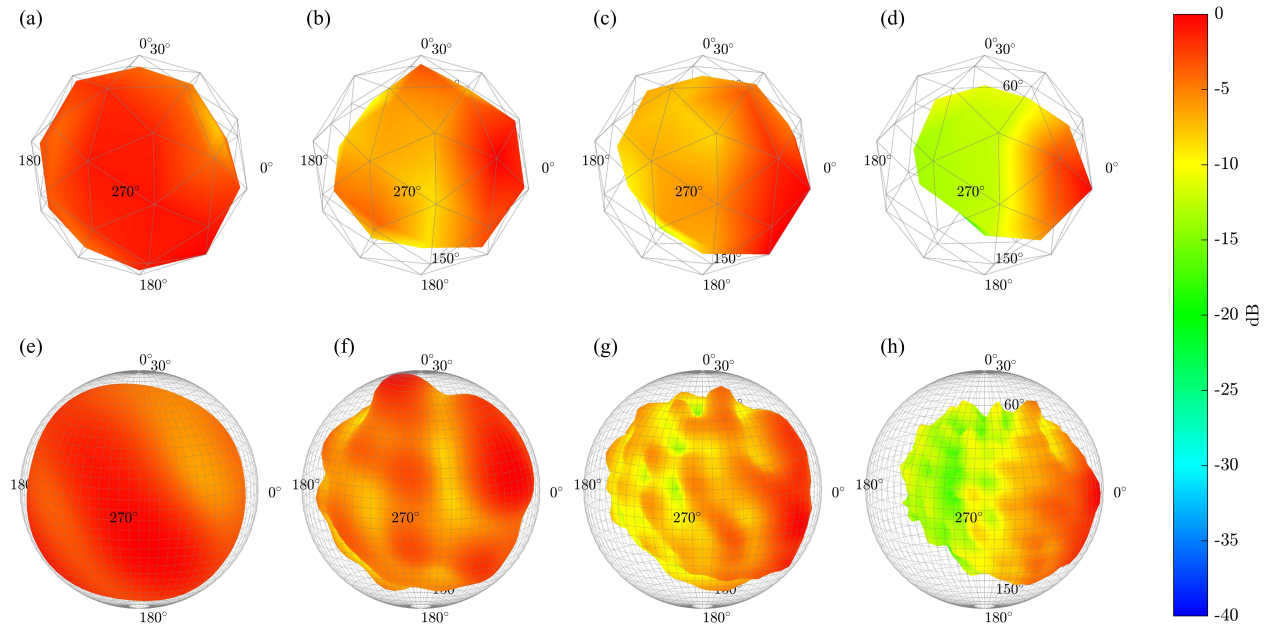


Figure 11.15 Played trumpet directivity balloons derived from Weinerziel et al. at (a) 279 Hz, (b) 738 Hz, (c) 1314 Hz, and (d) 1871 Hz. Far-field projected directivity balloons from the present work at (a) 277 Hz, (b) 737 Hz, (c) 1315 Hz, and (d) 1869 Hz.

Figure 11.16 compares the frequency-dependent DI values derived from Weinzierl et al. [126] with those of the present work for played trumpets. Both works show similar DI increases from around 2.5 dB at 250 Hz to 5 dB by 1 kHz and more than 10 dB by 3 kHz. More significant discrepancies arise above 3 kHz, but it is important to note that a 32-point measurement array can at most evaluate a DI of $10\log_{10}(32) \approx 15$ dB [63], meaning the DI values near and above that level are less reliable. Frequency-averaged deviations between the two data sets were less than 1.0 dB below 1 kHz but rose to 3.9 dB when considering all values below 4 kHz.

11.5 Discussion

The multiple-capture method provides a feasible means of assessing high-resolution played musical instrument directivities compatible with loudspeaker standards. Nonetheless, its procedures require careful implementation to achieve satisfactory results. A fundamental assumption is that the system

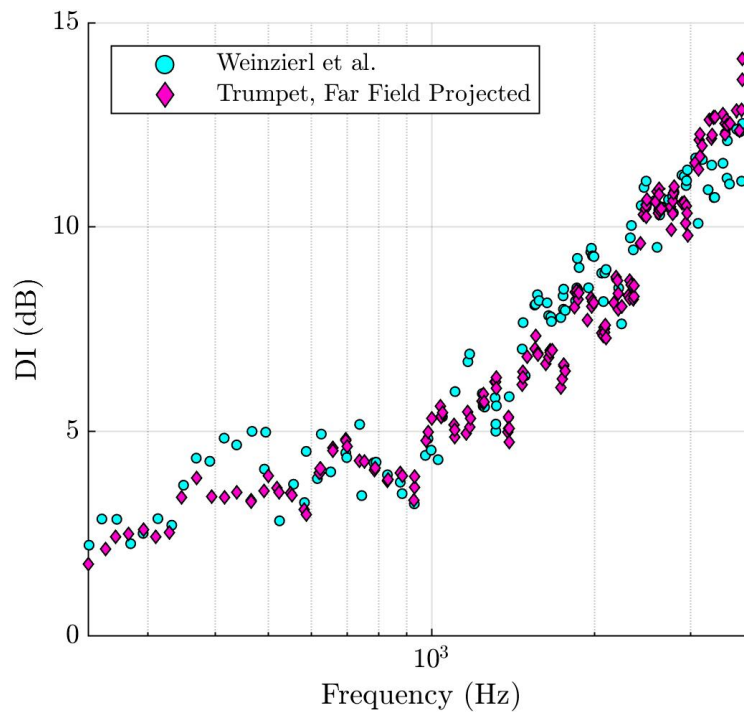


Figure 11.16 Played trumpet directivity indices from Weinzierl et al. and the present work.

between the reference microphone input and each array microphone output is approximately linear and time invariant. Because the exterior sound pressure levels produced by most musical instruments are sufficiently low to avoid nonlinear acoustic propagation effects, the assumption of a linear system between the reference microphone and each array microphone is generally realistic. However, the requirement of a time-invariant system introduces more practical challenges. Controlling instrument orientation and musician position between incremental rotations is essential to mitigate movements that can appear as longitudinal banding in the FRF-based directivity balloons.

Another practical challenge includes proper source placement within the array. While post-processing far-field propagation corrects for source misalignments, it requires spherical harmonic expansions. Consequently, sampling must be dense enough to mitigate spatial aliasing. Using the estimated source effective radius of $a = 0.44$ m, the resolution applied in this work enables spherical harmonic expansions up to around 4 kHz. The maximum frequency without spatial aliasing would

be significantly lower for lower-resolution schemes, such as those employed in single-capture measurements. For example, using the same source effective radius would limit the maximum frequency for narrowband spherical harmonic analysis to about 500 Hz and 900 Hz for 32-point and 64-point sampling schemes, respectively. These limitations could help explain why trumpet directivities interpolated via spherical harmonics and reported in Ref. 28 do not materialize to have anticipated symmetries or agree with the *uninterpolated* results in Fig. 11.15.

The existence of spatial aliasing limitations in directivity measurements constitutes a significant research area that requires further investigation. While some previous works have discussed this topic to an extent, actual sampling limitations have often remained ambiguous. This work has explored this concept in three significant ways: (1) studying the convergence of spherical harmonic expansions to the measured pressure, such as in Figs. 11.6 and 11.7; (2) plotting the source's spherical spectrum, such as in Fig. 11.8; and (3) estimating the source effective radii. Nevertheless, a need remains for additional research into methods that determine required sampling positions for musical instrument directivities. In addition, the results of this work suggest that even current loudspeaker sampling standards may be insufficient to achieve narrowband spherical harmonic expansions over the entire audible bandwidth.

11.6 Conclusions

This work has illustrated how a multiple-capture transfer function method allows the assessment of high-resolution played musical instrument directivities with spherical sampling compatible with current loudspeaker directivity standards. Measurements of played trumpet directivities have demonstrated good agreement with those produced by an artificially excited trumpet with an accompanying manikin and previously reported single-capture directivities of lower resolution. The results confirm the expectation that the played trumpet is a directional source with a directivity

index value exceeding 10 dB by 4 kHz. However, the results also demonstrate the importance of musician diffraction effects, which are essential in practical applications. Future work could explore the impacts of trumpet mutes on directivities and apply the measurement techniques to many other musical instruments. Further analysis of spatial aliasing limitations on directivity measurements would also enhance this vital area of acoustics.

Chapter 12

Development of a Musical Instrument Directivity Database

This chapter builds upon Ch. 11 to present high-resolution directivities of fourteen played musical instruments. The results appear in an archival database for use in architectural acoustics and other applications.

12.1 Introduction

While directional radiation has long been a defining characteristic of played musical instruments, serious scientific study of the topic began less than a century ago. Early investigations focused on rudimentary measurements of a few instruments, including the brass family [35] and organ pipes [89]. However, objective understanding of instrument directivities remained vague until Olson [7] and especially Meyer [8, 140, 143, 154, 155, 160, 166–168], published polar, beamwidth, and other basic directivity plots for many common musical instruments and frequencies. Even then, the fine details of spherical directivities remained obscure.

More recently, AES56-2008 (r2019) [33] standardized measured spherical directivities for loudspeakers with 5° angular resolution to enable better electroacoustic and room-acoustic modeling and prediction. Such measurements are feasible because loudspeaker responses are largely consistent and repeatable. It stands to reason that similar spatial resolutions should become available for played musical instrument directivities due to their significance in room-acoustic modeling, auralizations, microphone placements, and other applications. However, high-resolution directivity measurements of natural sources present many practical challenges [153]. For example, unlike loudspeakers, musicians cannot repeat notes exactly each time their orientations or scanning microphone positions are changed, and new measurements have begun. Furthermore, while the position of a loudspeaker is easily controlled during a measurement sequence, a musician often shifts while playing. Alignment of a principal loudspeaker axis toward desired polar and azimuthal angles is automatable, but practical considerations restrict rotation of a live musician and their instrument to the horizontal plane (i.e., the azimuthal angle) only.

To circumvent these and other challenges, some researchers have resorted to artificial excitation of instruments, including the clarinet [155, 156], bassoon [34, 143], violin [36, 37, 139–141, 156–158], guitar [157, 159], harp [104, 159], and piano [160, 161]. Their approaches enhanced the repeatability of radiated sounds and the feasibility of instrument reorientations or transducer repositionings between repetitions. However, while the resulting measurements supplied important information and insights into the sound radiation of the isolated instruments, they generally ignored the critical effects of live musicians (e.g., their diffraction, absorption, and natural instrument excitation) and thus altered the directivity patterns [6, 153]. Meyer and Wogram correctly stressed that musicians and instruments are intrinsically integrated entities for practical directivity measurements [154]. In fact, while the majority of Meyer's published results derived from artificially excited instruments, in some of his works he additionally performed sparse measurements of played instrument directivities to evaluate the absorption and diffraction caused by the musicians' body [143, 154]. Moreover,

because the musician effects have yet to be studied rigorously, the use of directivities derived from artificially excited instruments for applications such as room-acoustic modeling and auralization remains equivocal. In addition, while artificially excited instrument directivities sometimes allow for increased angular sampling resolutions, the associated studies have not involved consistent equipment setups and directivity measurement techniques that apply to many types of played instruments or allow researchers to study the entire pitch ranges of selected instruments efficiently. These limitations are partly due to the difficulties of designing and implementing apparatuses that perform the artificial excitation and control the played notes. Moreover, the excitation and supporting apparatuses often create unnatural scattering and diffraction effects, further distorting the directivity patterns from those produced by musicians.

Because of the complications of measuring *played* instrument directivities, researchers have struggled to assess spherically replete results successfully, e.g., high-resolution patterns compatible with current architectural acoustics simulation formats. The researchers have made several resourceful attempts with varying success, but improvements to the approaches have remained necessary to overcome their limitations. Most past methods measured directivities using fixed or rotating microphone arrays, although some have included alternative schemes, such as scanning pressure-velocity (PU) probes [107, 169]. Single-capture methods have employed musicians and instruments at fixed positions and orientations within stationary enveloping microphone arrays having limited total sampling positions (e.g., 13, 22, 32, or 64) over the measurement surfaces or contours [18, 31, 101, 125, 127]. One of the most significant works to date involved directivity measurements of 41 modern and historical instruments using a quasi-spherical microphone array with 32 positions [32].

While single-capture systems do not require playing repetitions and may claim better measurement repeatability, they are not feasible for high sampling densities. The 5° angular resolutions specified for standardized loudspeaker directivity measurements would require 2,522 unique sam-

pling positions over a sphere, with accompanying microphones, support structures, cables, and data acquisition channels. Because this is an impractical number for single-capture measurements, multiple-capture systems employing moving microphones or sources are necessary to measure played musical instruments, just as they are to measure loudspeakers.

Recently, two of the authors published work on a multiple-capture (rotate-and-repeat) method for measuring live speech directivity with a full-spherical, 5° resolution compatible with the AES standard [6]. The work also reviewed efforts of other authors regarding voice and speech directivity measurements. However, as described in the present work, adaptations of multiple-capture methods to musical instruments come with unique challenges and differing results. Initial experiments conducted by the authors' research group on high-resolution multiple-capture musical instrument directivity measurements [1, 170] led to the specific methods, validations, and results presented in this paper. Other examples of spherical, high-resolution, multiple-capture methods for musical instruments are scarce.

Bork et al. measured the directivity of a played piano by rotating it through both a seven-channel, vertical quarter-circle microphone array, and a seven-channel, horizontal quarter-circle array [102]. An eighth channel served as a reference. The measurement set-up allowed polar directivity measurements in the transverse plane and upper half of the frontal and median planes with 15° resolution for 45 unique sampling positions. While the measurements provided a detailed picture of piano sound radiation, the sampling was limited to measurement planes and did not comprise a full-spherical directivity assessment.

J. Štěpánek and Z. Otčenášek utilized a 16-channel circular array raised to various heights to scan five transverse polar directivities [105]. With the addition of nine microphones for the highest and lowest cross-sections, the entire measurement surface consisted of a closed cylinder with 98 total sampling positions. The researchers used microphone signals for normalization to compensate for differences between repeated measurements. While this approach provided more sampling

positions than many single-capture systems for played instrument directivities, it did not utilize a full-spherical scanning surface or transfer functions to better compensate for differences in repeated measurements.

Jeong et al. measured the directivities of three traditional Korean musical instruments and a pansori singer in a hemi-anechoic environment using a 10-channel, vertical, quarter-circle microphone array with 10° polar angular resolution [21]. The arc rotated in 10° azimuthal increments to sweep out a hemispherical surface with 315 unique sampling positions. The microphone directly above the musician provided a sound level reference. However, the approach employed only octave-band analysis and did not use narrowband transfer functions for compensation between repeated measurements.

Pérez Carillo et al. also utilized a repeated-capture approach for measuring violin directivities [106]. They mechanically rotated a violin within a 21-channel microphone array to achieve 1,260 sampling positions. The researchers excited the violin quasi-naturally using a glissando on the instrument's G string and utilized transfer functions between a piezoelectric pickup integrated with the instrument's bridge and the array microphone signals. While the approach enabled a significant sampling density improvement over single-capture systems, it involved several limitations. For example, to achieve a sampling scheme compatible with the AES standard, one must interpolate the resulting directivity values because of the irregularity of the sampling positions on the sphere. Furthermore, while glissandi are suitable for string instruments and a few other instruments, the playing technique is not readily adaptable to many other instruments. Finally, due to the mechanical apparatus used to rotate the violin, the researchers did not incorporate a typical upright seated playing position with the instrument. Consequently, the diffraction and scattering effects of the apparatus and musician varied from normal playing conditions.

A few researchers have thus leveraged repeated-capture methods to produce higher-resolution directivity results for played instruments than those produced by single-capture systems. However,

the works employing the approach have lacked complete spherical data, have not used excitation approaches applicable to all instruments, or have not used actual transfer functions to adequately compensate for differences between played repetitions with incremental captures. Moreover, the results of past studies are not typically available for public use in practical applications.

This paper describes a high-resolution multiple-capture transfer function method that produces spherical directivity measurements for many played instruments. The approach has several vital distinctions, including appropriately processing the tonal instrument spectra to produce broader band (e.g., $1/n$ -octave-band) directivities commonly required in architectural acoustics software. The sampled directivity functions, balloon plots, and polar plots follow from proper frequency response functions (FRFs or transfer functions) [13] between signals of reference microphones in the rotating reference frame and those of semicircular array microphones. Because these measurements derive from average cross-spectra and autospectra, they also yield coherence balloons that characterize measurement qualities over the measurement sphere and spectrum, thus facilitating the identification of possibly problematic directivity values. The approach enabled angular resolutions that meet or exceed those recommended for room acoustics simulations, auralizations, and other applications. The method provides a general approach for investigators to assess high-resolution directivities of various instruments over their entire working ranges without the need for specialized artificial excitation apparatuses. This work also addresses relevant issues to directivity measurements such as near-field effects and acoustic source centering, and presents a valuable quadrature method for use with its sampling scheme and the associated AES56-2008 (r2019) standard.

This work further contributes to musical instrument directivity research by providing an associated archival database for 14 played orchestral instruments of the string, woodwind, and brass families. The directivities incorporate 5° angular resolutions, following the AES56-2008 (r2019) standard, in tabulated $1/3$ rd-octave bands and file types commonly used in architectural acoustics simulations [96,97]. The results will enhance predictions of room-acoustic responses to instruments,

auralizations of rehearsal and performance venues, and inform microphone placement techniques for audio recordings, sound reinforcement applications, and musical acoustics research. They will also improve the general understanding of instrument radiations, the physical modeling of instruments, and their computer simulations. Because these applications and others require high-quality directivities to produce optimal results, the measurement techniques and results described in this work will enhance the theoretical and practical efforts of acoustical researchers, consultants, audio engineers, musicians, instrument makers, and other professionals seeking to better understand and work with played instruments. The following sections describe the measurement and signal processing methods, measurement validations, and selected results for several instruments.

12.2 Methods

12.2.1 Measurement system

Several components of the directivity measurement system appear in Fig. 12.1, including three adjustable-position reference microphones, the fixed semicircular microphone array, and the musician and instrument rotation system within an anechoic chamber. The constant-radius $R = 1.83$ m array incorporated 37 12.7 mm (0.5 in) precision free-field microphones positioned at fixed 5° polar-angle increments. An alternative array employed a smaller $R = 1.22$ m radius for a few additional measurements. Relative calibration of each microphone and its signal path over frequency to a dedicated channel reduced directivity errors that would otherwise appear as latitudinal bands in balloon plots.

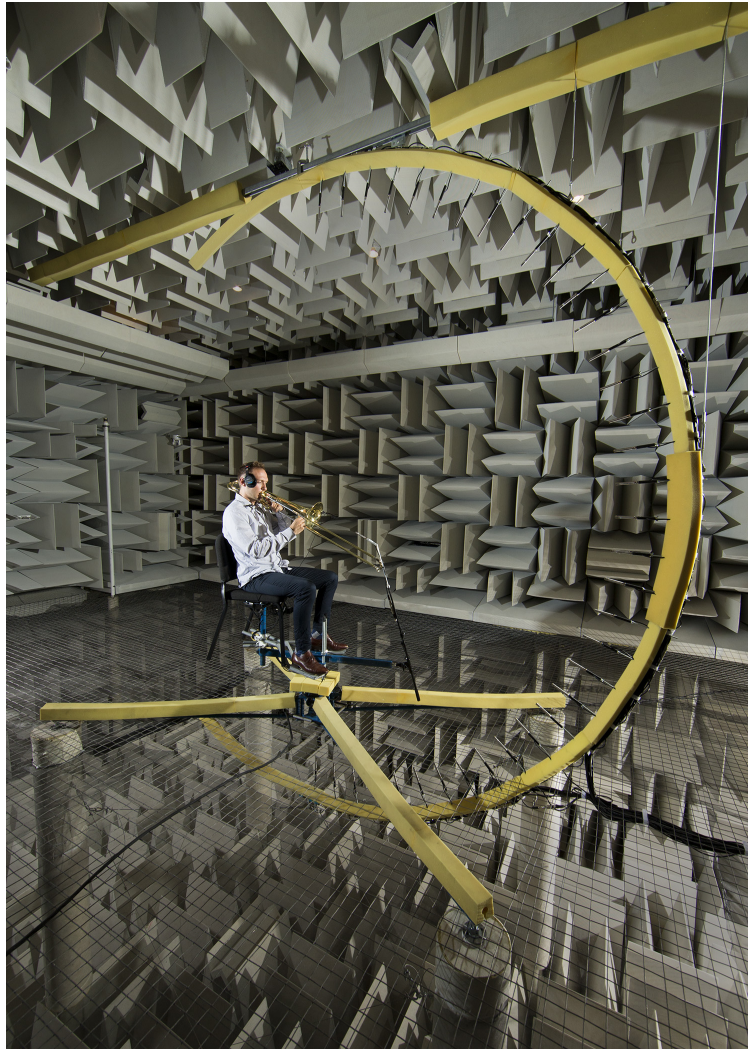


Figure 12.1 Directivity measurement system.

Acoustically treated apparatuses suspended and supported the arc and rotation system. The rotation system supported a musician chair and footrests, which adjusted vertically, horizontally, and angularly within the rotating reference frame. During the initial musician and instrument positioning, lasers facilitated geometric centering of the instrument's radiating portion (e.g., the trombone bell) at the measurement sphere's center.

12.2.2 Measurement procedure

Because a structure did not support the musical instruments rigidly within the rotating reference frame, musician movements could introduce spatial variances beyond those intended by the controlled rotations and thus affect the directivity measurements' qualities. Along with general instructions for the musicians to sit still and hold their instruments at consistent positions and orientations, a small laser attached to their instruments helped them maintain this consistency as the beam illuminated a small acoustically unobtrusive target within the rotating reference frame.

Musicians typically do move during practice or performance. However, their motions differ from one musician to another and from one playing circumstance to another. One might optically capture specific or average musician and instrument motions under live playing conditions [171]. Subsequent post-processing with the results could modify the still directivity data with motion simulation or spatiotemporal averaging, but this was beyond the present work's scope.

With the musician seated in the directivity measurement system at the appropriate height and orientation, a technician adjusted and secured the microphones within the rotating reference frame to produce useful reference signals. One microphone was attached to the musical instrument, another to the musician's lapel or shirt, and a third to a boom arm a short distance from the instrument. The exact position of a reference microphone was not particularly crucial, as long as its location was close to the instrument, consistent in the rotating reference frame throughout the recording sequence, and able to detect sufficient signal levels at desired frequencies. If one reference microphone failed to meet these requirements, the signal of another was helpful for subsequent processing.

While oriented toward the initial azimuthal angle $\phi = 0^\circ$, the musician played either a note at a specified pitch and dynamic marking or a chromatic scale at mezzo-forte over the complete working range of the instrument, with each note held for 1 s, followed by a 1 s rest. A metronome signal in the musician's earphone ensured a consistent pace, while an electronic tuner helped maintain pitch consistency. The musician repeated any problematic notes of a scale for correction.

Following a successful multichannel recording at the initial azimuthal angle, the rotation system advanced 5° in the azimuthal coordinate ϕ , and the musician repeated the note or scale for a second recording. This process continued until the directivity measurement system collected a complete sphere of sampled data via 72 multichannel recordings. The first and last azimuthal angles also repeated themselves at the 360° interval to allow a consistency check. The system likewise recorded repeated data at the polar angles of $\theta = 0^\circ$ and 180° for each azimuthal-angle increment. Thus, a complete data set comprised 2,701 array and 219 reference-channel recordings, each with 24 bit, 48 kHz sampling. However, as indicated earlier, the number of unique array recordings was 2,522. Figure 12.2 shows the associated sampling positions, with each polar angle increment indexed as $u = 0, 1, \dots, U - 1$, where $U = 37$ and each azimuthal angle increment indexed as $v = 0, 1, \dots, V - 1$, where $V = 72$.

12.2.3 Data processing

Because even the best musicians play repeated notes with amplitude and spectral variations, imperfect repetitions may seem at first glance to pose an insurmountable problem for multiple-capture directivity measurements. However, when appropriately employed, the FRFs between the reference and array microphone signals mitigate these effects. As demonstrated previously, FRFs provide effective means of establishing directivity functions for loudspeakers [13], the human voice [6, 162], and musical instruments [106, 107]. However, for musical instruments playing discrete notes (i.e., without glissandi), the FRFs must derive from spectrally sparse signals that are only valid at specific frequencies for which significant radiated sound energy arrives at both the reference and array microphones. The FRFs and associated directivity functions thus preserve desirable signal-to-noise ratios at the partial frequencies on a narrowband basis.

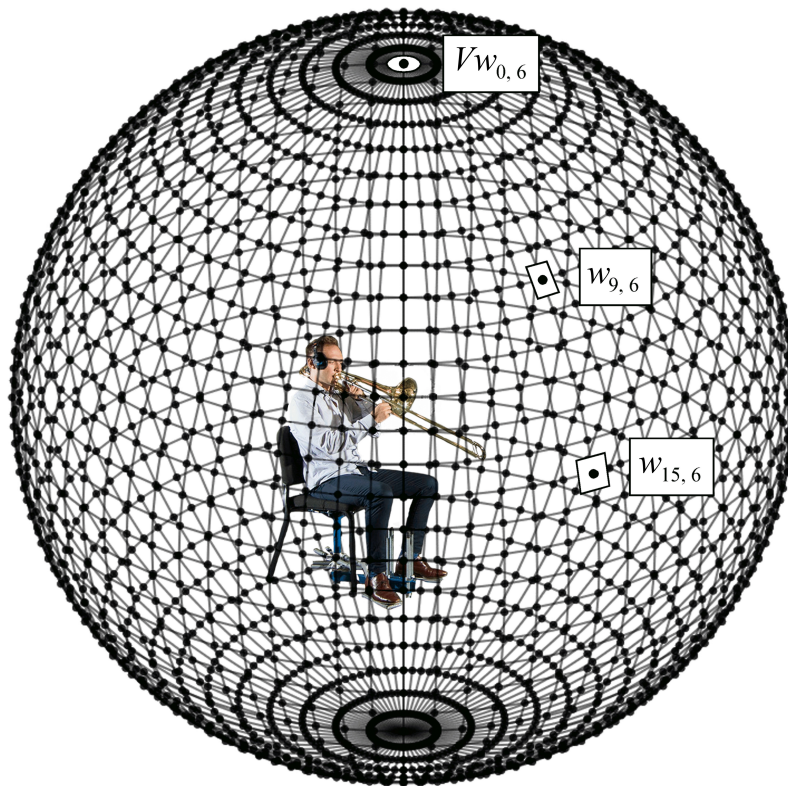


Figure 12.2 Sampling positions of the directivity measurement system. Effective sampling areas differed, as suggested by those illustrated about the points labeled $Vw_{0,6}$, $w_{9,6}$, and $w_{15,6}$. For convenience in summations, $w_{0,v}$ and $w_{36,v}$ segmented the sampling areas of the two poles into V equal sectors. The total polar sampling areas were then $Vw_{0,v}$ and $Vw_{36,v}$.

Narrowband

The FRFs followed from the autospectral estimates $G_{aa_v}(f)$ of the reference microphone signal $a_v(t)$ and the cross-spectral estimates $G_{a\tilde{b}_{u,v}}(f)$ between that signal and each array microphone signal $\tilde{b}_{u,v}(t)$, where the tilde indicates the possibility of uncorrelated noise in the array signals. For each note, the spectral estimates resulted from Welch's method [131, 163] and involved five 48,000-sample block sizes (1 s record length, 1 Hz narrow-band resolution), a Hann window, and 90% overlap. For each reference and array microphone pair, the least-squares FRF estimate $H_{uv}(f) = G_{a\tilde{b}_{u,v}}(f)/G_{aa_v}(f)$ provided an unbiased result with respect to uncorrelated noise in the output signals [131].

The coherence function $\gamma_{a\tilde{b}_{u,v}}^2(f) = |G_{a\tilde{b}_{u,v}}|^2 / G_{aa_v}(f)G_{\tilde{b}_{u,v}\tilde{b}_{u,v}}(f)$ and the related signal-to-noise ratio $SNR_{u,v}(f) = 10\log_{10}\{\gamma_{a\tilde{b}_{u,v}}^2(f)/[1 - \gamma_{a\tilde{b}_{u,v}}^2(f)]\}$ utilized the array signal autospectral estimates $G_{\tilde{b}_{u,v}\tilde{b}_{u,v}}(f)$ in addition to the reference autospectral and cross-spectral estimates to provide necessary checks of FRF quality. As it ranged from 0 to 1, the coherence function represented the ratio of correlated to uncorrelated signal energy in the reference and array signals at frequency f [131]. The coherence thereby played a critical role in establishing statistical confidence in the FRF measurements as originating from linear, time-invariant systems free from appreciable extraneous noise.

The coherence function also relates closely to the coherent output spectrum

$G_{bb_{uv}}(f) = G_{\tilde{b}_{u,v}\tilde{b}_{u,v}}(f)\gamma_{a\tilde{b}_{u,v}}^2(f) = G_{aa_v}(f)|H_{uv}(f)|^2$ [131], the energy of an array signal fully correlated with a reference signal. This spectrum is useful in directivity measurements because it minimizes the uncorrelated noise in each array signal and thus optimizes signal identification due to the input. These benefits assume that a reference microphone adequately detects the instrument signal produced by its physical mechanisms and yields a linearly related signal with negligible noise contamination. Combined with the array signals, the reference signal yields the same theoretical

coherent output spectrum as the true instrument source signal, despite modifications by linear transfer functions to the reference microphone and through its transduction mechanisms [131].

Because the reference signal autospectrum $G_{aa_v}(f)$ varies with each incremental rotation in ϕ due to imperfect playing repetitions, an effective input autospectrum based on sound power is valuable for some multiple-capture directivity calculations [6], as discussed further in Secs. 12.2.3 and 12.2.3. Assuming the measurement radius R is sufficiently in the far-field of the source, the time-averaged sound power spectrum is

$$\langle W(f) \rangle_t = \frac{R^2}{\rho_0 c} \int_0^{2\pi} \int_0^\pi \langle p^2(R, \theta, \phi, f) \rangle_t \sin \theta d\theta d\phi. \quad (12.1)$$

For a single-capture system, in which the reference signal autospectrum is the same for all azimuthal angles, the sound power is

$$\langle W(f) \rangle_t = \frac{R^2}{\rho_0 c} G_{aa}(f) \sum_{q=0}^{Q-1} w_q |H_q(f)|^2, \quad (12.2)$$

where Q is the total number of sampling positions and w_q are quadrature weights to approximate the integral over the sphere numerically. However, for a multiple-capture system, the time-averaged sound power measured by the system is

$$\langle W(f) \rangle_t = \frac{R^2}{\rho_0 c} \sum_{u=0}^{U-1} \sum_{v=0}^{V-1} w_{uv} G_{aa_v}(f) |H_{uv}(f)|^2. \quad (12.3)$$

By equating the sound power formulations for the single and multiple-capture measurements, one may solve for a reference signal autospectrum that would have produced the same sound power had it been consistent for all azimuthal angles. This *effective input autospectrum* has the form

$$G_{aa,eff}(f) = \frac{\sum_{u=0}^{U-1} \sum_{v=0}^{V-1} w_{uv} G_{aa_v}(f) |H_{uv}(f)|^2}{\sum_{u=0}^{U-1} \sum_{v=0}^{V-1} w_{uv} |H_{uv}(f)|^2}. \quad (12.4)$$

The *effective coherent output spectrum* then follows as

$$G_{bb,eff_{uv}}(f) = G_{aa,eff}(f) |H_{uv}(f)|^2. \quad (12.5)$$

The spatially averaged coherence function $\langle \gamma^2(f) \rangle_S$ is a convenient figure of merit calculated by averaging the coherence function over the sphere for a given frequency using quadrature weights to evaluate the spherical integral numerically. A spatially averaged SNR calculation subsequently replaces $\gamma_{ab_{uv}}^2(f)$ with $\langle \gamma^2(f) \rangle_S$. These metrics are especially beneficial at higher frequencies when the increasingly directional characteristics of some instruments cause coherence values to vary considerably over the sphere.

Broader Bands

While musical instrument radiation is primarily a harmonic narrowband process, some applications, including computational architectural acoustics simulations, require broader-band (e.g., 1/3-octave-band) directivities [96]. Spectral bands between radiated harmonics may contain little energy, resulting in lower coherence values. While one might employ a peak-detection algorithm to select high-amplitude frequencies and average their results together, this approach is problematic because it neglects nonharmonic instrument sound generation which should be considered a part of the instrument's directional characteristics [167]. Additionally, averaging partials may bias broadband directivities by favoring the directional behaviors at specific frequencies in the overall result. Broader-band directivity summations based on partials also have the severe limitation that if no partial falls within a bandwidth due to the spectrally sparse nature of the signals, it is not possible to create a valid directivity representation. Calculating directivity at a selected frequency through averaged FRFs across all played notes in a chromatic scale could also prove ineffective since, for a given frequency, one note may provide adequate excitation or signal level to produce a viable directivity while other notes may not.

The $G_{bb,eff_{uv}}(f)$ spectra in Eq. (12.4) prove especially useful to overcome these limitations for broader-band directivities. For this work, the authors computed these quantities for each note then averaged them across all played notes to produce a complete narrowband directivity representation

called the overall effective coherent output spectrum (OECOS). Broader-band directivities followed by summing the OECOS over desired bandwidths to represent the total band signal energy from the array microphones correlated with the reference microphone signal.

This approach has several advantages. To begin with, $G_{bb,eff_{uv}}(f)$ and the corresponding directivity for each note preserve the nonharmonic sound generated by the instrument, as detected by the reference microphone, while suppressing uncorrelated noise, such as the self-noise of the array microphones (see Sec. 12.2.3). In addition, through its narrowband average across all played chromatic scale notes, the OECOS effectively penalizes directional contributions produced by spectral gaps with low coherence values and signal-to-noise ratios while favoring the more substantial spectral contributions with high coherence values and signal-to-noise ratios. Consequently, one may interpret the summed narrowband OECOS over a broader band and the associated directivity as a weighted sum. The weights are proportional to how strongly the array microphone signals correlate with the reference microphone signal for the particular note and narrowband frequency. Furthermore, because the OECOS is a narrowband representation of the source directivity, it is straightforward to sum directivities into fixed, proportional, equivalent rectangular, or other bandwidths of interest.

Spherical Harmonic Expansions

The normalized spherical harmonics $Y_n^m(\theta, \phi)$ of degree n and order m [70] form an orthonormal basis for expanding functions on the sphere. Their expansions apply to both complex-valued narrowband data and magnitude-only narrowband or broadband data and are beneficial for compact representations, rotations, smoothing, and symmetrizing. [165] In addition, as the spherical harmonics are intrinsic wave function components of the solution to the Helmholtz equation in spherical coordinates, spherical harmonic expansions applied to complex-valued narrowband data yield the unique solution on the exterior domain [59]

$$\hat{p}(r, \theta, \phi, k) = \sum_{n=0}^{\infty} \sum_{m=-n}^n c_n^m(k) h_n^{(2)}(kr) Y_n^m(\theta, \phi), \quad r \geq R \quad (12.6)$$

where \hat{p} is the complex pressure amplitude, r is the radial distance from the origin, R is the measurement sphere radius, k is the wavenumber, $h_n^{(2)}(kr)$ are the spherical Hankel functions of the second kind (for outward-going waves with $e^{i\omega t}$ time dependence), and $c_n^m(k)$ are the pressure expansion coefficients. The coefficients follow by exploiting the orthogonality of the spherical harmonics over the sphere and have the form

$$c_n^m(k) = \frac{1}{h_n^{(2)}(kR)} \int_0^{2\pi} \int_0^\pi \hat{p}(R, \theta, \phi, k) Y_n^{*m}(\theta, \phi) \sin \theta d\theta d\phi, \quad (12.7)$$

where $*$ denotes complex conjugation.

Numerical integration of sampled complex pressures becomes feasible via appropriate quadrature weights or least-squares fits [77, 78]. This same approach applies to the sampled complex FRF estimates $H_{uv}(f) = H(R, \theta_u, \phi_v, f)$ in producing a degree-limited continuous $H(r, \theta, \phi, f)$.

Directivity Functions

For $r \geq R$, a complex normalized directivity function follows from $H(r, \theta, \phi, f)$ as

$$D(r, \theta, \phi, f) = \frac{H(r, \theta, \phi, f)}{H[r, (\theta, \phi)_{\max|H|}, f]}, \quad (12.8)$$

where $(\theta, \phi)_{\max|H|}$ is the angle with the maximum magnitude given by $\max_{\theta, \phi} |H(r, \theta, \phi, f)|$ for each frequency f [6, 13]. The decibel beam pattern for balloon and polar plots follows as

$$B(r, \theta, \phi, f) = 20 \log_{10} |D(r, \theta, \phi, f)|. \quad (12.9)$$

The normalizations for the directivity functions and decibel beam patterns of broadband magnitude data follow similarly. Some works have applied phases to loudspeaker 1/3-octave-band magnitude directivities [85, 172], but the value of such applications to musical instrument directivities is uncertain.

Of common interest is the far-field directivity function, which follows directly from Eq. (12.8) with $kr \gg 1$ and $r \gg d$, where d is the characteristic dimension of the instrument and the accompanying musician. One may also obtain a far-field result from Eq. (12.6) by first substituting the

asymptotic form of the spherical Hankel function then extracting the angular dependence to produce an unnormalized far-field directivity:

$$\tilde{D}_\infty(\theta, \phi, f) = \sum_{n=0}^{\infty} \sum_{m=-n}^n c_n^m(k) i^{n+1} Y_n^m(\theta, \phi). \quad (12.10)$$

One may define a directivity factor function as [10, 62]

$$Q(r, \theta, \phi, f) = \frac{|D(r, \theta, \phi, f)|^2}{\int_0^{2\pi} \int_0^\pi |D(r, \theta, \phi, f)|^2 \sin \theta d\theta d\phi}, \quad (12.11)$$

with a corresponding directivity index function $DI(r, \theta, \phi, f) = 10 \log_{10} Q(r, \theta, \phi, f)$. Both the beam pattern $B(r, \theta, \phi, f)$ and directivity index $DI(r, \theta, \phi, f)$ express source directionality on a decibel scale; the primary difference is the normalization of the beam pattern by the maximum value at a given frequency versus the normalization of the directivity index through the sound power. Consequently, while beam patterns are convenient for directivity visualizations, the directivity index is more beneficial for directivity error metrics.

For this work, the frequency-dependent deviation $\sigma_Q(f)$ between two directivity factor functions serves as a figure of merit:

$$\sigma_Q(f) = \left[\frac{1}{4\pi} \int_0^{2\pi} \int_0^\pi |Q_1(\theta, \phi, f) - Q_2(\theta, \phi, f)|^2 \sin \theta d\theta d\phi \right]^{1/2}. \quad (12.12)$$

One may also represent the result on a decibel scale as

$$L_{\sigma_Q}(f) = 10 \log_{10} [1 + \sigma_Q(f)]. \quad (12.13)$$

Acoustic Source Centering

Some past works have applied acoustic source centering techniques to measured directivities [27–29, 32]. The alignment of the instrument acoustic center, the point from which waves seem to diverge spherically [41], and the array geometric center has certain benefits. With unaligned centers, significant differences may arise between the far-field directivity pattern of the source and

that measured on the array surface. Another advantage to centering techniques is that the number of required expansion terms in Eq. (12.6) may reduce significantly while still producing adequate field representations.

The first directivity product theorem [10, 59] shows that the far-field magnitude patterns of centered and uncentered sources are equivalent [82]—an understandable result considering the limiting case of radiated sound measured by a hypothetical array of infinite radius. Because Eq. (12.10) allows one to propagate uncentered measured pressures to the far field, any difference introduced in the magnitude pattern by misalignment between the geometric array center and acoustic source center will vanish. A phase shift will remain, accounting for the difference between the centers.

These results are direct consequences of the uniqueness of the Helmholtz equation solution given by Eq. (12.6), which governs the pressure at any position $r \geq R$ and places no requirement on the relative position of the radiating and diffracting body or its acoustic center, provided that the spherical boundary at $r = R$ fully encompasses the body. Of course, one can change the underlying coordinate reference frame through translation, but the translation itself does not alter the pressure field generated by the source; it only alters the system referencing the field positions. Consequently, pressure or FRF propagation to the far field via Eq. (12.10) is sufficient to determine far-field source directivities.

This is particularly useful when only magnitude values are of importance, such as for some ray-tracing approaches. Furthermore, since both centered and uncentered complex-valued directivities provide the unique solution in their respective reference coordinate frames, it may be preferable in some cases to use uncentered directivities in wave-based simulations. This is because the uncentered directivities result from fixed geometric source placements, whereas centered directivities require moving source placements over frequency since the acoustic center is generally frequency dependent [49].

Although one can obtain far-field directivity patterns without the need for sophisticated centering algorithms, the ability to represent source radiation more efficiently through reduced numbers of required expansion terms has clear benefits for computational efficiency. However, the original expansion coefficients still provide a unique solution on the exterior domain, while the most commonly used architectural acoustics prediction software packages use tabulated magnitude broadband far-field directivity data [96] or impulse response measurements at discrete positions [97]. Consequently, because this work aims to provide these data, it does not consider centering for reduced-degree, spherical-harmonic-based pressure expansions but proposes it as future research.

Since the alignment of the acoustic source center and geometric array center can reduce the number of expansion terms needed to represent the pressure field adequately, one may exploit a priori knowledge of the acoustic center to reduce spatial aliasing errors. This advantage follows because there is a limit on the maximum measurable expansion degree N for a given array sampling density and configuration, with higher-degree terms spatially aliasing into lower-degree terms [77]. Therefore, placing the acoustic source center at the geometric array center for measurements can reduce the required N to represent the field using Eq. (12.6). This placement mitigates the effects of spatial aliasing in some instances, but because the acoustic centers of played instruments are generally frequency dependent, predetermined physical centering schemes have inherent limitations. Nonetheless, the authors propose source-placement recommendations for directivity measurements as future work.

12.3 Validation Experiments

While repeated capture measurements can produce high-resolution directivities, they typically require longer measurement sessions and may introduce errors due to playing inconsistencies. Extended sessions may not be not technically problematic, but they necessitate careful management

of musician fatigue. In addition, unavoidable playing inconsistencies require specialized signal processing and other mitigation procedures. If each system between the instrument excitation and sound production mechanism and an array microphone output is linear and time invariant (LTI), the techniques described in Sec. 12.2.3 effectively address the variations between captures. However, inconsistencies such as slight musician body movements, pitch shifts, and changes in playing style introduce time-varying features. Because most physical systems only approximate LTI systems, it is essential to understand the effects of these features on the directivity measurements to determine the conditions under which the latter are valid, reliable, and repeatable.

In this work, three principal validation methods addressed this need. First, calculated coherence balloons enabled visualizations and quantifications of influences due to noise, nonlinearity, and time variance in the overall system. Second, a 32-point single-capture measurement system similar to that used to measure musical instrument directivities in Ref. 32 produced comparative directivities. Third, the 2,522-point repeated-capture system evaluated loudspeaker directivities with controlled changes to loudspeaker excitation signals, positions, and orientations within the rotating reference frame to simulate variations common to played musical instruments and observe the effects. The following sections discuss these methods in greater detail. Section 16.3 provides examples of the first two methods and adds symmetry verifications assured by physical conditions and 1/3rd-octave-band normalized standard deviations of directivity factor functions at the measurement poles.

12.3.1 Coherence Balloons

Balloon plots of the coherence function over the sphere help viewers visualize and detect undesirable measurement effects, including excessive noise and distortion, faulty microphones or connections, and poor reference microphone placements [6]. Discernible low-coherence patterns with values less than some desired minimum (e.g., 0.9) serve to flag potentially problematic angles with

excessive FRF uncertainty, prompting additional efforts to improve the directivity measurements. As suggested earlier, the authors deployed multiple reference microphones at fixed locations in the rotating reference frame so that if one happened to fall at a position of low radiated pressure and reduced coherence, the signal of another might produce more acceptable results in post-processing. Low coherence values do not necessarily imply that a corresponding directivity value is erroneous, only that there is less confidence in the estimated FRF value at that particular angle. Therefore, the coherence function helps quantify measurement validity and assess assumptions of linearity, time-invariance, and negligible noise. Section 12.4.5 provides additional discussion.

12.3.2 Single-Capture System

In the past, researchers have used single-capture measurement systems to avoid the problems of playing repetition inconsistencies. In this work, the authors also configured a single-capture quasi-spherical array of 32 microphones at the same $R = 1.83$ m radius as the multiple-capture system for validation purposes. By comparing the directivities produced by the single and multiple-capture systems, the authors aimed to explore errors introduced by time-varying playing features. In some ways, direct comparisons between the systems' results were inequitable because the multiple-capture system had nearly 80 times as many sampling positions as the single-capture system. However, general directivity pattern trends were comparable, such as the directions of diffraction lobes. Illustrative results from the 32-point measurements follow in Secs. 12.4.4 and 12.4.8.

12.3.3 Perturbation Tests

Directivity measurements of a Tannoy System 800 loudspeaker included intentional perturbations to explore the influences of time-varying features on the multiple-capture method. The first test produced a repeatable benchmark directivity using a 20 Hz to 21.5 kHz linear chirp as the electrical excitation and reference signal, repeated five times at each azimuthal-angle increment

for measurement averaging. Subsequent tests changed the excitation signal to an anechoically recorded instrument chromatic scale and the reference signal to that produced by a near-field microphone in the rotating reference frame. Various applied perturbations caused minor differences in measured directivities and yielded several insights. The perturbation tests included random changes to the electrical input level (within 12 dB) and pitch (within ± 20 cents), plus changes to loudspeaker positions (within 1.25 cm) and angular orientation (within 0.75° for both the polar and azimuthal angles). The results showed several significant trends. First, the errors tended to be frequency-dependent, with higher frequencies having more significant directivity pattern errors. Second, position and orientation perturbations produced more substantial errors than amplitude and pitch perturbations. Visual inspection of the directivities revealed that position and orientation perturbations caused some longitudinal banding in the patterns, while amplitude and pitch perturbations did not. A frequency-dependent, area-weighted, root-mean-square deviation (AWRMSD) [6] indicated that up to 4 kHz or more, the errors remained below 1.5 dB. More detailed discussions of these validation measurements appear in Ref. 1.

12.4 Selected Results

The following sections present selected directivity results and observations for the flute, tenor saxophone, bassoon, bass clarinet, trombone, tuba, French horn, cello, violin, and viola. They also highlight several noteworthy aspects of the directivity measurements, spatial sampling methods, signal processing techniques, and validations.

12.4.1 Narrowband

As a linearly arrayed tone-hole instrument, the flute produces interesting directivity patterns with interference effects caused by sound emitting from its embouchure hole, open tone holes, and

end. Figure 12.3 shows several narrowband (1 Hz bin width) balloon plots from a Gemeinhardt Model 3SB flute playing the note C4. The first balloon column resulted from the array microphone signals' autospectra, whereas the second column resulted from the FRFs. The autospectral balloons' longitudinal bands demonstrate that the musician excited the frequencies differently with each rotation, mainly due to expected differences in playing level or spectrum. The autospectral balloons also exhibit more general roughness, suggesting the presence of uncorrelated measurement noise. The improvements of the FRF-based directivities are quite discernible; they compensate for changes in playing level and spectrum and reduce uncorrelated noise to render much smoother results. The directivity patterns show that interference lobes are a defining characteristic of sound radiation from flutes. There is one primary lobe for the fundamental frequency of this note. However, by the fifth partial, five interference lobes appear. Such anticipated effects were also apparent for other tone-hole woodwind instruments, such as the bassoon and tenor saxophone.

While the compensation provided by the FRF-based narrowband directivities is substantial, it sometimes leaves minor residual longitudinal banding. From the autospectral balloons in Figs. 12.3(a) through 12.3(c), it is apparent that changes in narrowband levels following each rotation varied more at higher frequencies, likely due to repetition spectral differences. The autospectral and cross-spectral estimates were also less consistent at higher frequencies, leading to poorer FRF estimates as demonstrated by the coherence functions. Compared to the first partial, the third and fifth partials had spherically-averaged SNR values 5.8 dB and 21.1 dB lower, respectively. These results suggest that the excitation levels required to maintain acceptable SNR values are also critical for reducing undesirable measurement noise in FRF-based balloons. Section 12.3.3 suggested that time-varying system properties related to small shifts in position and orientation of the instrumentalist could likewise contribute to residual longitudinal banding. However, while these anomalies may be apparent for 1 Hz narrowband data, they are essentially absent from directivities summed over wider bandwidths and smoothed via spherical harmonic expansions [6].

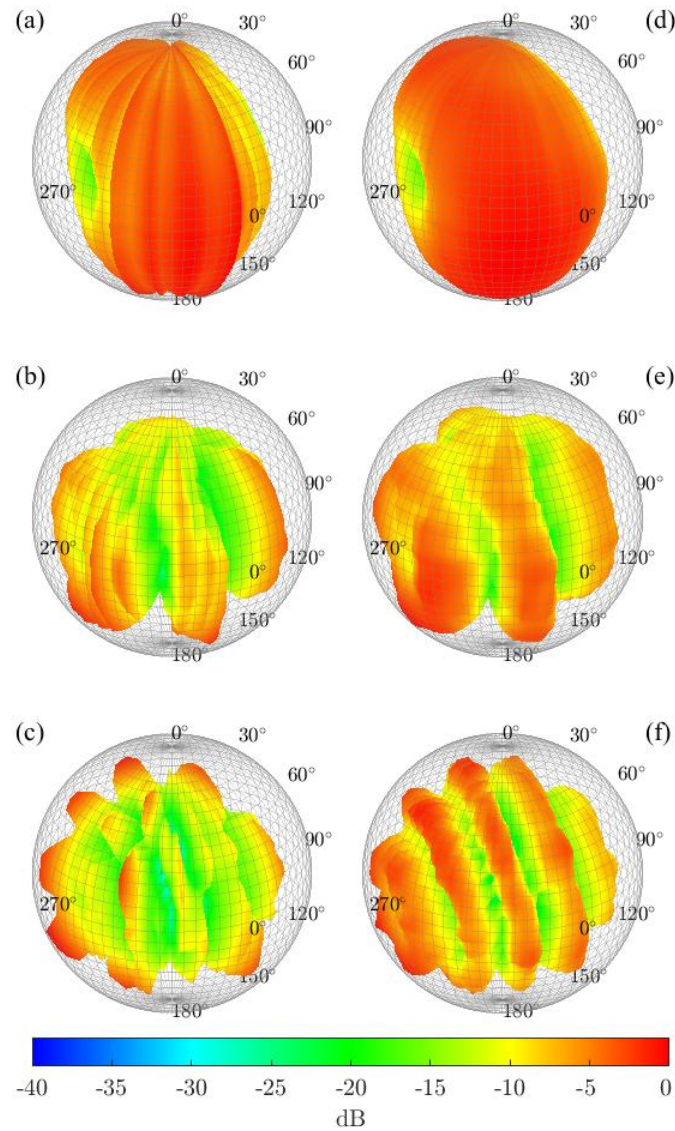


Figure 12.3 Narrowband (1 Hz bandwidth) flute directivities for the note C4. Autospectral balloons for the (a) first partial (262 Hz), (b) third partial (787 Hz), and (c) fifth partial (1310 Hz). FRF-based balloons for the (d) first partial (262 Hz), (e) third partial (787 Hz), and (f) fifth partial (1310 Hz).

12.4.2 Far-field Propagation

The $R = 1.83$ m radius of the measurement system array was as large as practicable for the anechoic chamber's working dimensions. However, it presented a practical challenge for large instruments or those radiating very low frequencies because the microphones were not in the geometric or acoustic far field. Measurements made with the $R = 1.22$ m radius array were even closer to the instrument and, consequently, in the near-field to higher frequencies. Implementing Eq. (12.10) thus became necessary to ensure the calculation of far-field directivity patterns. Because the authors made measurements of some instruments with both the $R = 1.22$ m and $R = 1.83$ m arrays, it was possible to compare directivity patterns at both measurement surfaces with those propagated to the far-field.

Figure 12.4 illustrates the results for the 2nd partial of a D2 (292 Hz, 1 Hz resolution) produced by a Cannonball Gerald Albright Signature tenor saxophone. Figure 12.4(a) shows the FRF-based balloon measured by the smaller $R = 1.22$ m radius array. The wavelength at this frequency is roughly 1.17 m, similar to the array's radius. As evidenced by the balloon, a strong lobe exists toward the top right of the musician, while a circular region of reduced directivity appears toward the top left. Figure 12.4(b) shows the directivity results from an $N = 18$ degree expansion of the complex FRFs at the array radius. Here, some of the slight longitudinal banding apparent in the original FRF-based balloon has become smooth. Such use of degree-limited spherical harmonic expansions for reducing spatial measurement noise is a regularization technique in spherical near-field acoustical holography. [59] Figure 12.4(c) presents the far-field directivity pattern obtained after applying Eq. (12.10) to the expansion. In this case, the pattern has become more omnidirectional, although most general radiation characteristics have remained the same. Figure 12.4(d) shows the measured FRF-based balloon for the same note and partial but assessed with the larger $R = 1.83$ m radius array. The directivity is similar to that measured by the smaller-radius array but appears to have features intermediate to the estimated far-field directivity. Figure 12.4(e) shows this result smoothed

with an $N = 18$ degree expansion. Finally, Fig. 12.4(f) shows the far-field pattern calculated from the larger array measurement.

The directivity patterns from the $R = 1.22$ m and $R = 1.83$ m radius measurements show similar trends, although the measurement closer to the source is more directional. With the pressure propagated to the far-field for both cases, the directivities converged to a similar pattern, as anticipated. The L_{σ_Q} between the directivities measured at the array surfaces was 0.9 dB, but the value dropped below 0.5 dB for the propagated far-field directivities. For reference, the L_{σ_Q} between the far-field patterns and an omnidirectional source was 1.5 dB for both the smaller and larger radius array. These results affirm that propagation to the far-field is a valuable technique to compensate for near-field measurement effects. In general, one may mitigate measured and far-field differences by using a larger radius array when possible. For example, L_{σ_Q} between the measured and far-field directivity results for the smaller array was 1.7 dB, whereas the value was only 1.2 dB for the larger array. In many cases, such as with small instruments at high frequencies, differences between array measurements and propagated far-field estimates are negligible. Nonetheless, the results illustrate the need to compensate appropriately for near-field effects when they are present.

12.4.3 Acoustic Centering

Another cause of variations between measured directivity patterns is the misalignment of the acoustic source center and geometric array center. However, as discussed in Sec. 12.2.3, the far-field pattern follows from computational far-field propagation, even when the two centers do not align. Figure 12.5 illustrates this effect for a Fox Model 601 bassoon playing the note A2 (110 Hz, 1 Hz resolution). Figure 12.5(a) shows the FRF-based magnitude directivity of the fundamental. One may expect the linearly-arrayed tone-hole instrument to produce roughly omnidirectional radiation at this low frequency [173]. However, the directivity looks more like that of a point source displaced from the geometric array center, suggesting that source centering is an issue at this frequency. Further

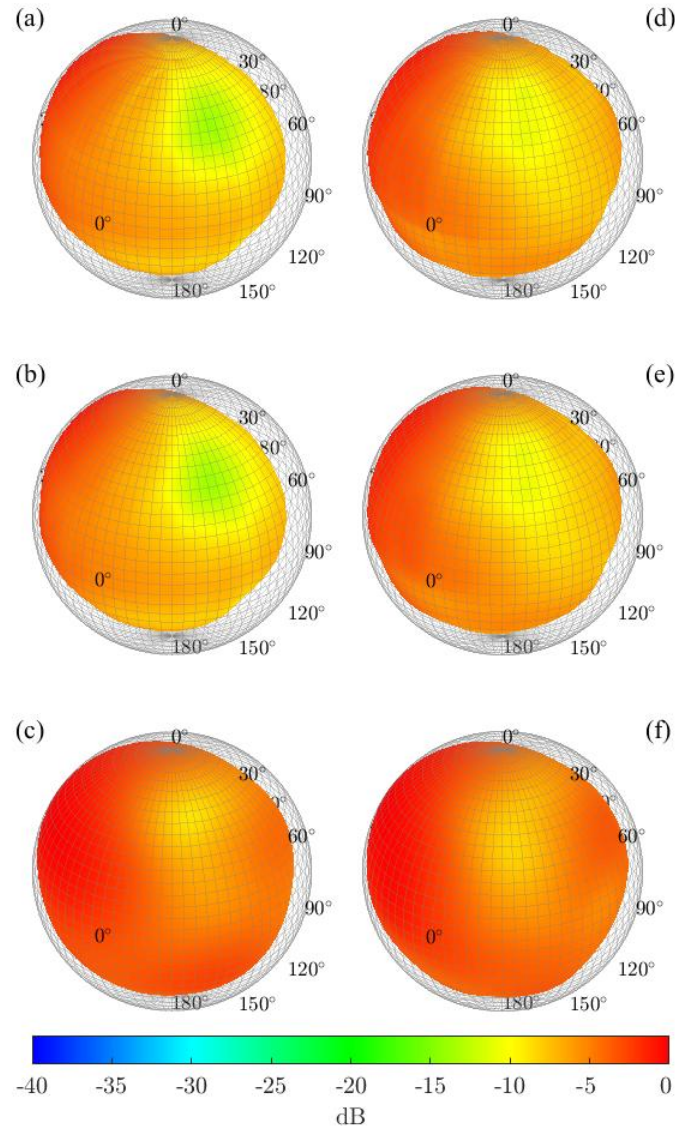


Figure 12.4 Narrowband directivity for the 2nd partial of the note D2 (292 Hz) from a tenor saxophone. Directivities derived from the smaller $R = 1.22$ m array based on (a) FRF measurements, (b) an $N = 18$ degree spherical harmonic expansion of the FRF measurements, and (c) the calculated far-field estimate. Directivities derived from the larger $R = 1.83$ m array based on (d) FRF measurements, (e) an $N = 18$ degree spherical harmonic expansion of the FRF measurements, and (f) the calculated far-field estimate.

investigation of the phase profile for the directivity shown in Fig 12.5(d) substantiates this assertion, as the phase has a roughly axisymmetric pattern about the direction of most substantial radiation with an approximately constant rate of phase decrease from that direction to the opposite side of the sphere.

Calculation of the acoustic source center utilized an algorithm proposed by two of the authors in Ref. 82. Figure 12.5(b) shows the magnitude pattern for a point source placed at that position, and Fig. 12.5(e) shows its phase pattern. Careful comparisons of the magnitude and phase profiles of both the bassoon and the displaced point source corroborate the assumption that at this frequency, the bassoon behaves as a simple point source displaced from the origin due to a misaligned acoustic center. Finally, Figs. 12.5(c) and 12.5(f) respectively show the calculated far-field magnitude and phase patterns for the bassoon measurement. The magnitude pattern demonstrates the anticipated quasi-omnidirectional behavior, whereas the phase profile remains roughly the same but becomes closer to that of the displaced point source, as anticipated [82]. Thus, while near-field effects and source misalignments can cause differences between measured and far-field patterns, these differences are resolvable using computational far-field propagation.

12.4.4 Comparisons to Single-Capture Measurements

Spherical harmonic expansions are valuable for analyzing and processing directivity measurements, but they require sufficiently high sampling densities to minimize spatial aliasing. [34, 77] Comparative instrument directivities produced by the higher-resolution multiple-capture system and lower-resolution single-capture systems (see Sec. 12.3.2) are instructive in this regard and provide limited validations for the multiple-capture system.

Figure 12.6 compares directivities based on spherical harmonic expansions of the 5th partial of C3 (657 Hz, 1 Hz resolution) produced by a Buffet Prestige B \flat bass clarinet. Figure 12.6(a) shows the balloon plot and transverse, median, and frontal-plane polar plots from the 2,522-point multiple-

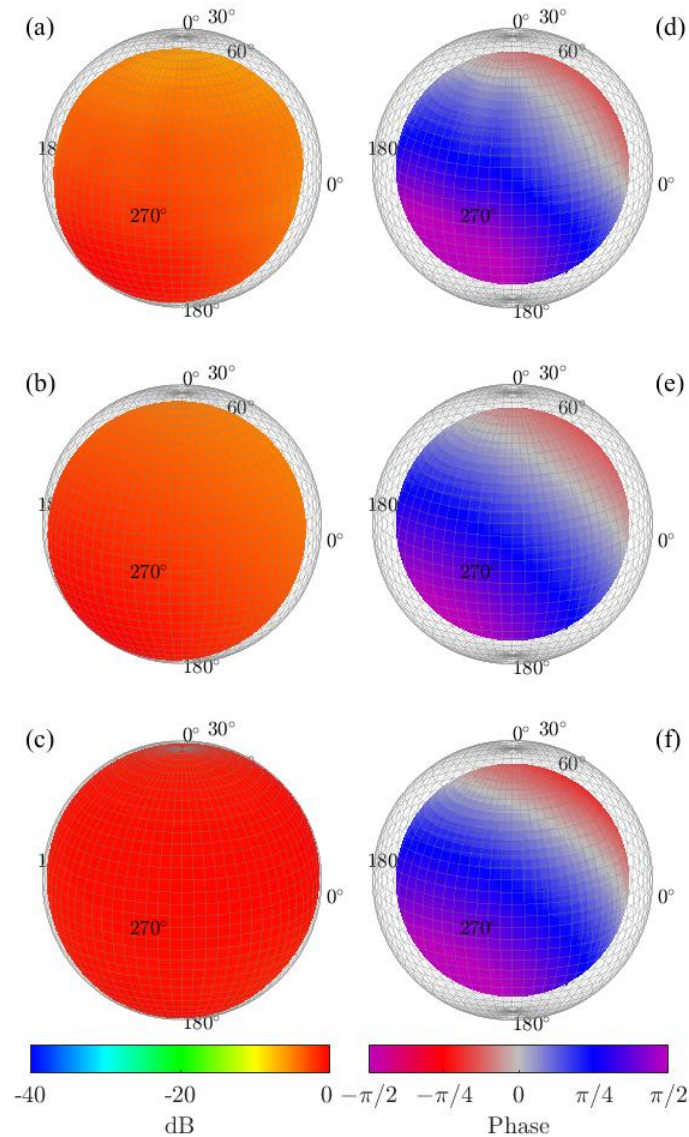


Figure 12.5 Acoustic source centering effects for the bassoon for the note A2 (110 Hz). Magnitude directivity pattern based on (a) an $N = 18$ degree spherical harmonic expansion from the measurement at the array surface, (b) a point source placed at the estimated acoustic center of the bassoon, and (c) propagated far-field pressure. Constant-radius color-mapped phase directivity pattern based on (d) an $N = 18$ degree spherical harmonic expansion from the measurement at the array surface, (e) a point source placed at the estimated acoustic center of the bassoon, and (f) propagated far-field pressure.

capture system, based on an $N = 18$ spherical harmonic expansion. Figure 12.6(b) shows the same measurement from the multiple-capture system but based on a truncated $N = 4$ spherical harmonic expansion. Both directivities show several similarities, including the locations and directions of the primary radiation lobe, a small diffraction spot (akin to a Poisson spot) behind the musician, and reduced levels in regions beyond the musician's legs. However, the truncation has produced a loss of finer pattern details. Figure 12.6(c) shows the directivity results from the 32-point single-capture system, expanded to the maximum-possible $N = 4$. While the general radiation features have survived from the lower-resolution measurement, several salient, previously noted features have vanished. The $N = 4$ degree expansions for the 32-point and 2,552-point measurements use the same number of expansion terms for their directivity representations, so the skewing and loss of detail of the lower-resolution measurement are presumably the results of spatial aliasing. These problematic effects persist for far-field directivities computed using Eq. (12.10).

A fundamental means of validating certain directivity measurement features is to verify symmetries assured by physical conditions. A bass clarinet played in its standard position serves as a good example. The instrument should produce a quasi-symmetric directivity pattern about the median plane, apparent in the transverse and frontal polar plots but not in the median polar plot. The high-resolution and truncated high-resolution results confirm these expectations, while the low-resolution results do so to a lesser extent. Similar effects occurred at other frequencies. The asymmetries for the lower-resolution measurements likely resulted from spatial-aliasing effects and the 32-point array's asymmetrical orientation about the median plane. [6] Thus, while the 32-point single-capture measurements helped validate the multiple-capture measurements, they also lacked critical features unique to the radiation and diffraction caused by the instrument and musician.

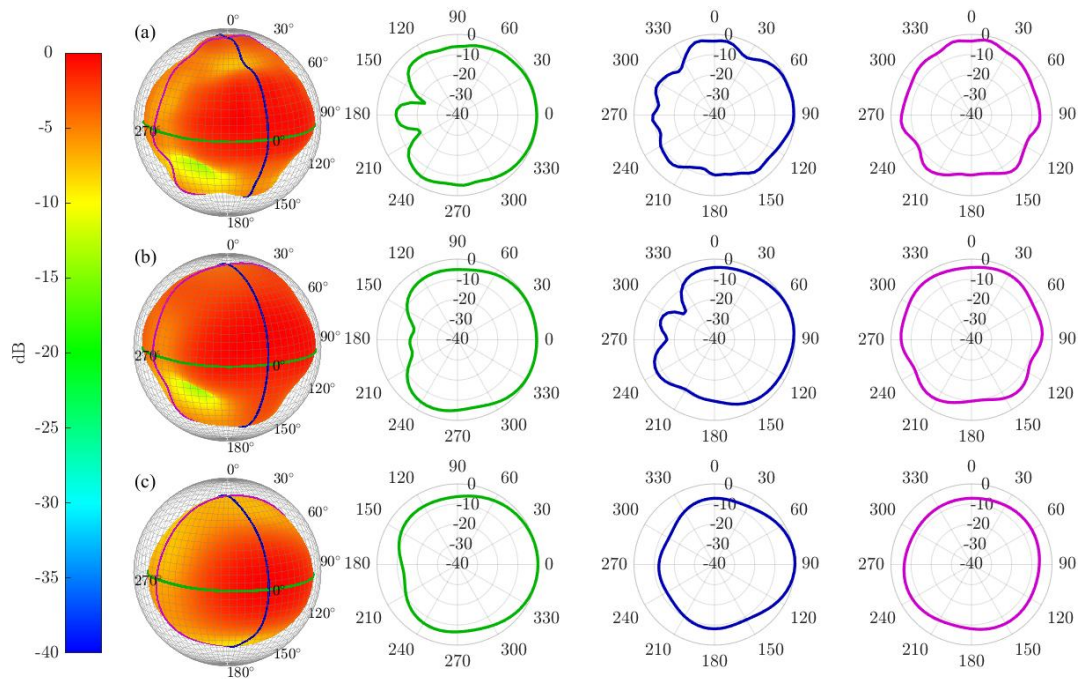


Figure 12.6 Bass clarinet directivity for the 5th partial of C3 (657 Hz) based on (a) an $N = 18$ expansion of a 2,522-point multiple-capture measurement, (b) a truncated $N = 4$ expansion of the same a 2,522-point multiple-capture measurement, and (c) a maximum $N = 4$ expansion of a 32-point single-capture measurement. The polar plots show the transverse (green), median (blue), and frontal (magenta) plane results.

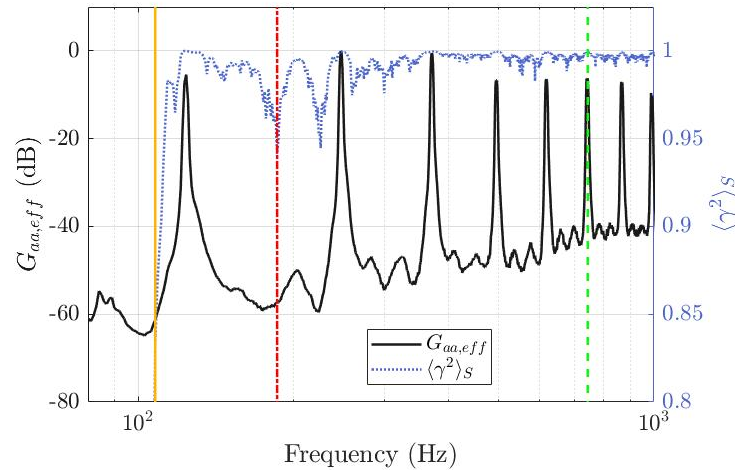


Figure 12.7 Normalized effective input auto-spectrum and spherically averaged coherence for the trombone playing the note B2. The vertical solid yellow line at 108 Hz, the dash-dot red line at 186 Hz, and the dashed green line at 744 Hz are frequency markers for the balloons in Fig. 12.8

12.4.5 Coherence Functions

Another validation of the 2,522-point measurements involves their spherically averaged coherence functions and coherence balloons. As mentioned earlier, these tools help identify frequencies and angles of reduced signal energy and SNR, along with nonlinearities and other nonideal measurement conditions. Figure 12.7 shows the normalized effective input autospectrum of an Edwards trombone playing the note B2 with an overlaid spherically averaged coherence curve. The autospectral peaks correspond to the fundamental and spaced harmonics. The spherically averaged coherence also has high values within the resonant-peak bandwidths and decreased values between them, where less energy generated by the instrument decreases the SNRs.

The paired FRF and coherence balloons in Fig. 12.8 further illustrate this concept. Figures 12.8(a) and 12.8(d) show the FRF-based directivity and coherence balloons, respectively, at 108 Hz, just below the fundamental resonance bandwidth (refer to Fig. 12.7). The trombone radiates little energy at this frequency, and the spatially averaged coherence value is low. The coherence

balloon has widely varying values, and the corresponding FRF-based directivity balloon shows poorly estimated values. Figures 12.8(b) and 12.8(e) show the directivity and coherence balloons for the off-resonance frequency 186 Hz between the first two harmonic peaks. At this frequency, the spatially averaged coherence value drops below 0.95. However, the coherence balloon suggests that there are presumably higher-level interharmonics and acceptable coherence values in front of the instrument, while behind the instrument, the coherence is less acceptable. The FRF-based directivity balloon likewise appears to vary smoothly and fittingly at the instrument's front, but the region of poor coherence corresponds to a rough region of questionable directivity values, with large fluctuations in estimated levels. Finally, Fig. 12.8(c) and 12.8(f) show the FRF and coherence balloons for the on-resonance sixth partial of B2 (744 Hz). Here, the coherence balloon has nearly optimal values approaching 1.0 over the balloon's entire surface, and the FRF-based balloon shows a clear directivity pattern with quasi-symmetric lobes around the instrument. Accordingly, coherence values and balloons can assist in validating directivity measurement qualities and reliabilities.

12.4.6 Broader Bands

Because many musical instruments are tonal sources, narrowband directivities are often sufficient to characterize the radiation patterns of distinct partials. However, for some applications, broader-band directivities are more suitable. As discussed in Sec. 12.2.3, it is desirable to calculate the total spectrum radiated by an instrument, including both harmonic and interharmonic energy, using the OECOS. The signal processing reduces the deleterious effects of extraneous noise-laden frequencies on directivities and is preferable to using energetic values measured only at the array surface. Summation over desired bandwidths then represents the total effective band energy radiated by the instrument that is coherent with the reference microphone signal.

Figure 12.9 illustrates the effectiveness of the OECOS for addressing this matter to characterize the directivity of a Yamaha YEB321 E \flat tuba for selected 1/3rd-octave bands. Figures 12.9(a)

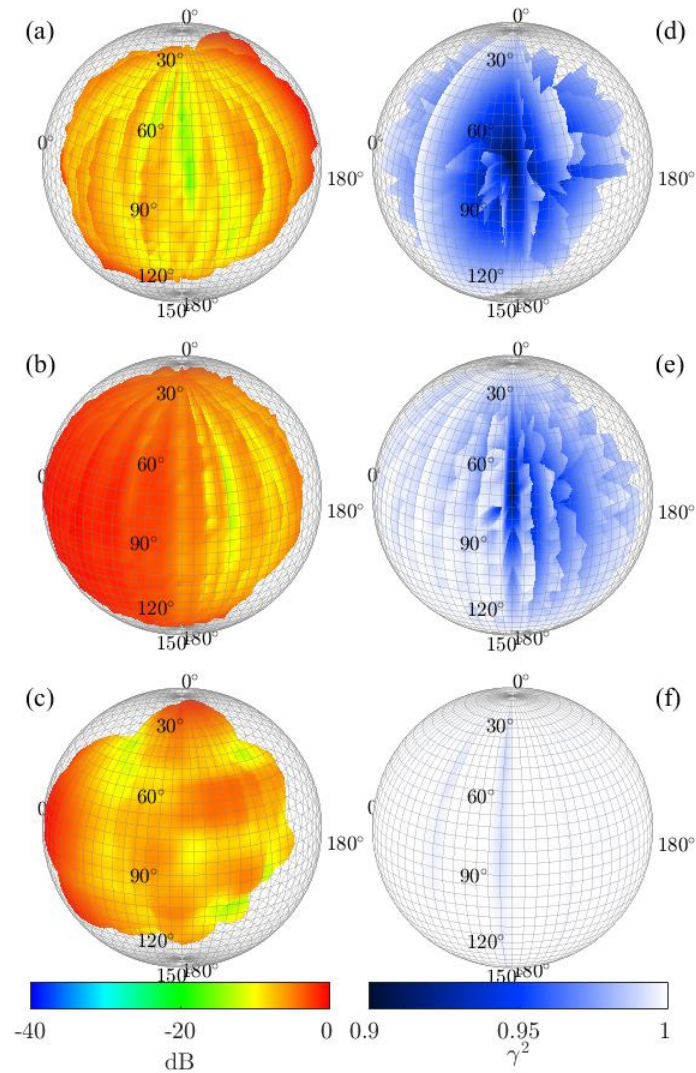


Figure 12.8 Narrowband FRF-based directivity balloons and coherence balloons for the played note B2 (1 Hz resolution) of a trombone. Directivity balloons at (a) 108 Hz, (b) 186 Hz, and (c) 744 Hz. Coherence balloons at (d) 108 Hz, (e) 186 Hz, and (f) 744 Hz. (See the frequency markers in Fig. 12.7)

through 12.9(c) show 1/3rd-octave-band directivities based on the measured array autospectra for the 400 Hz, 500 Hz, and 630 Hz bands, respectively. While these larger bandwidth summations generated smoother balloons than narrowband autospectral balloons (e.g., see Fig. 12.3), it is evident that some residual longitudinal banding remains. Figures 12.9(d) through 12.9(f) show 1/3rd-octave band directivities based on the OECOS for the same bands. The formulation has reduced the longitudinal banding, allowing for improved detection of features such as the diffraction spots and lobes in Figs. 12.9(e) and 12.9(f). As for narrowband directivities, spherical harmonic expansions can further smooth any minor residual banding over the magnitude data, but the authors have not utilized them for these plots.

12.4.7 Pole Measurement Repeatability

While spatially averaged coherences provide meaningful indicators of measurement validity and repeatability, measurements performed at the poles of the directivity measurement system provide another means of analyzing variance across the 72 repeated captures. The poles ostensibly remain at the same positions relative to the instrument and musician for each repetition, so one may assume that the frequency-dependent variations of the FRFs and OECOSs should be slight. To quantify these variations, the authors calculated normalized standard deviations of 1/3rd octave-band directivity factor functions derived from the OECOSs for the north and south poles. These deviations can then be mapped to a logarithmic scale using Eq. (12.13). Figure 12.10 provides the results for a Paxman 75.3L French horn. The narrowband spatially averaged coherence calculated for all notes also appears in the figure. The gray region represents the span between the fundamental frequencies of the lowest and highest played notes (F2 at 87 Hz to C#5 at 554 Hz), thus indicating where the excitation signal includes fundamentals and some higher harmonics. Several noteworthy trends are apparent. First, the standard deviation between pole measurements was low in the gray region, remaining well below 1.0 dB despite its gradual increase over frequency. Outside of the gray

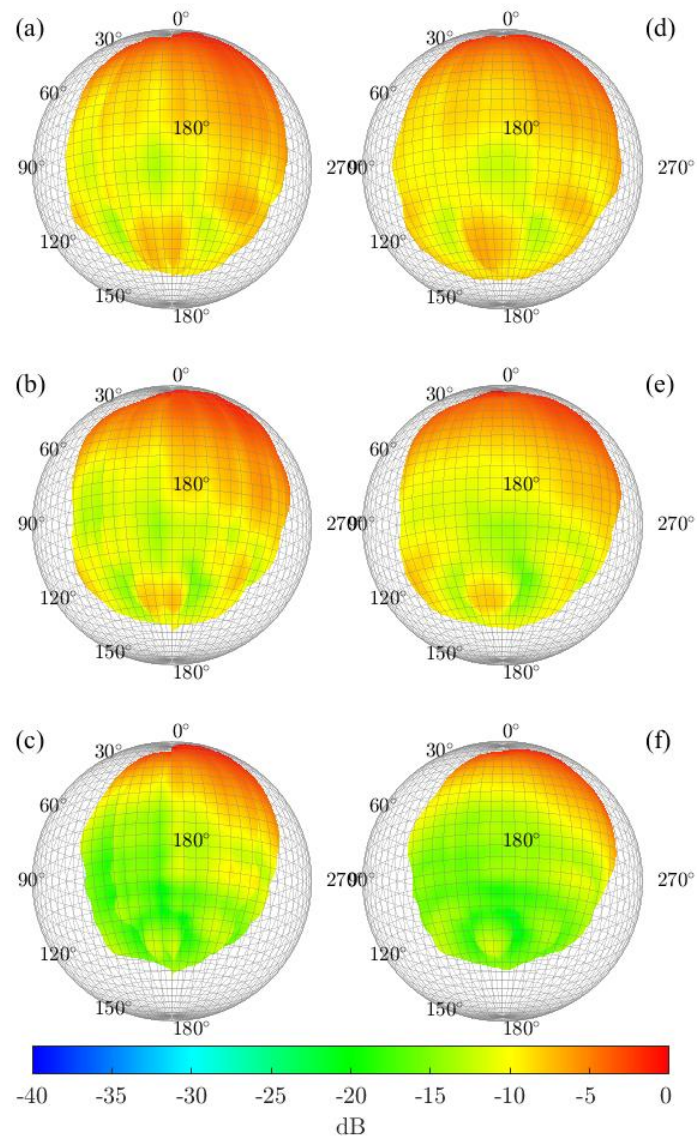


Figure 12.9 One-third-octave-band tuba directivities. Autospectral balloons for (a) 250 Hz, (b) 400 Hz, and (c) 630 Hz. Related OECOS balloons for (a) 250 Hz, (b) 400 Hz, and (c) 630 Hz.

region, where the excitation signal contains only partials and interharmonics, the spatially averaged coherence begins to decrease from near-optimal values, and the standard deviations continue to climb, reaching a value of about 3.0 dB near 5 kHz. Above 5 kHz, the spherically averaged SNR is less than 0 dB, indicating that the microphone signal contains significant uncorrelated noise, such as microphone self-noise. Thus, the interpretation of changes in deviations is less meaningful in this region since the decreasing standard deviations above 5 kHz are most likely due to the consistency of extraneous noise rather than instrument sounds.

Similar trends resulted for most instruments. Over the bandwidth in which the fundamentals contributed to the signal energy, variations in the pole directivity factor functions remained low. Outside of this range, spatially averaged coherence decreased and the standard deviations correspondingly increased. Lower spatially averaged coherence values at the highest frequencies indicated reduced measurement reliability. The trends also illustrated some of the limitations of the multiple-capture method. In order to correctly calculate the FRFs, which provide a theoretical elimination of uncorrelated noise, one must first obtain accurate estimates of the cross-spectra and autospectra. However, as frequency increases, the instrument produces less signal energy, meaning the accuracy of those estimates decreases. Consequently, the FRF estimates become less reliable and less repeatable, as illustrated by the falling coherence levels and increasing variability in the pole measurements.

Based on directivity factor function standard deviations, average spherical coherence, and unsmoothed directivity visual inspection, most instruments' 1/3rd octave-band directivities had acceptable reliability over a range of between 3 to 5 octaves (i.e., 9 to 15 1/3rd-octave bands). Numerical files for the 1/3rd-octave-band directivities are available at Ref. 38. They include tabulated data and file formats commonly used in architectural acoustics simulation software. Their calculations followed the methods described in this paper, including the use of OECOS, far-field corrections, particularly at low frequencies when the array was not in the acoustic far-field, and

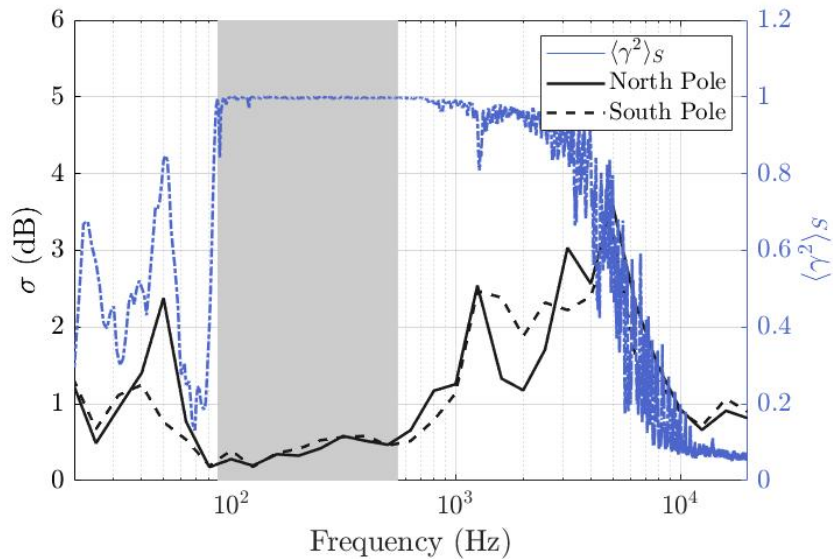


Figure 12.10 Standard deviations of 1/3rd-octave-band directivity factor functions for the north and south pole measurements and narrowband spherically averaged coherence for the French horn.

spherical harmonic expansions. The archive also provides directivity balloon animations that rotate and vary over frequency.

12.4.8 Comparisons to Previous Works

Figure 12.11 compares viola directivities for the 400 Hz and 1.6 kHz 1/3rd-octave bands, as measured by Weinzierl et al. [126] and the present authors using 32-point single-capture arrays and the present authors using the 2,522-point multiple-capture array. The single-capture directivities show similar features, such as strong radiation regions above the instrument and in the direction of the musicians' legs for the 400 Hz balloons. For the 1.6 kHz balloons, a broad directional lobe to the musician's left and a shadow region behind and slightly to the musician's right, opposite the instrument, are visible. Although the directivities measured by Weinzierl et al. resulted from a different instrument, musician, and array alignment, the L_{σ_Q} between the two 32-point measurements was only 1.3 dB for the 400 Hz 1/3rd-octave band and 2.2 dB for the 1.6 kHz 1/3rd-octave band. The

directivities acquired by the multiple-capture system shared similar general features but exhibited more detail. The L_{σ_Q} for the multiple-capture system directivities compared with those measured by Weinzierl et al. was 1.4 dB for the 400 Hz 1/3rd-octave band and 2.6 dB for the 1.6 kHz 1/3rd-octave band.

The similarities between all three balloons for the 400 Hz band suggest that despite individual differences between instrument models, playing positions, and musician diffraction effects, measured directivities provide a suitable general representation of played musical instrument radiation patterns. However, it is also apparent that the differences between the low and high-resolution balloons become more pronounced at higher frequencies, suggesting that increased sampling is also beneficial.

12.4.9 Bandwidth Variations

Because instrument directivities inherently change over frequency, comparing the results for various bandwidths is interesting. Figure 12.12 shows several cello directivity balloons derived from the 1 Hz resolution OECOS and $N = 18$ spherical harmonic expansions. Figures 12.12(a) through 12.12(c) show the 1 Hz resolution OECOS at 415 Hz ($A^{\flat}4$ fundamental), the 46 Hz bandwidth for the 400 Hz 1/6th-octave band, and the 92 Hz bandwidth for the 400 Hz 1/3rd-octave band, respectively. Figures 12.12(d) through 12.12(f) show the 1 Hz resolution OECOS at 1 kHz, the 116 Hz bandwidth 1 kHz 1/6th-octave band, and the 232 Hz bandwidth 1 kHz 1/3rd-octave band, respectively. Compared to other instrument families, string instruments tend to have more complicated directivity patterns, as evidenced by substantial interference regions and asymmetric diffraction lobes in the narrowband balloons.

Several strong directional features may smooth out and become lost with increasing bandwidth, while some dominant radiation features may remain. For example, the L_{σ_Q} between the narrowband 415 Hz directivity and the 400 Hz 1/6th-octave band [Figs. 12.12(a) and 12.12(b)] was only 0.2 dB,

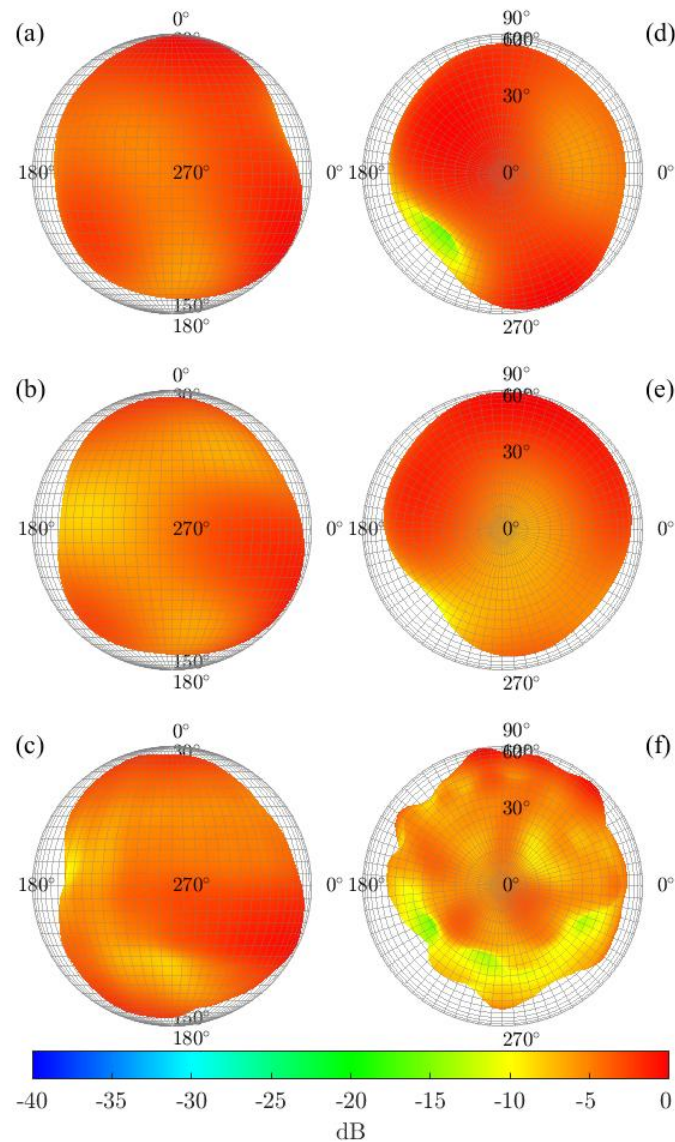


Figure 12.11 Viola 1/3rd-octave-band directivities. Results for the 400 Hz band viewed from the side based on (a) an $N = 4$ expansion of measurements performed by Weinzierl et al. using a 32-point single-capture array, (b) an $N = 4$ expansion of measurements performed for the present work using a 32-point single-capture array, and (c) an $N = 18$ expansion performed for the present work using a 2,522-point multiple capture array. Results for the 1.6 kHz band viewed from above based on (d) an $N = 4$ expansion of measurements performed by Weinzierl et al. using a 32-point single-capture array, (e) an $N = 4$ expansion of measurements performed for the present work using a 32-point single-capture array, and (f) an $N = 18$ expansion of measurements performed for the present work using a 2,522-point multiple capture array.

whereas the L_{σ_Q} between the narrowband 415 Hz directivity and the 400 Hz 1/3rd-octave band [Figs. 12.12(a) and 12.12(c)] was 2.1 dB. However, from all notes played in the chromatic scale, only two fundamentals and ten partials fell into the 400 Hz 1/6th-octave band, whereas four fundamentals and 19 partials fall into the 400 Hz 1/3rd-octave band.

The L_{σ_Q} between the narrowband 1 kHz directivity and the 1 kHz 1/6th-octave band [Figs. 12.12(d) and 12.12(e)] was 2.3 dB, whereas that between the narrowband 1 kHz directivity and the 1 kHz 1/3rd-octave band [Figs. 12.12(d) and 12.12(f)] was 2.6 dB. Both deviations are higher than those from the 400 Hz 1/ n th-octave bands. This effect is likely a result of the larger bandwidths and more summed partials (29 for the 1 kHz 1/6th-octave band and 58 for the 1 kHz 1/3rd-octave band). Thus, while broader-band 1/3rd-octave magnitude data can serve as a suitable approximation for complex narrowband data, it is important to consider the loss of detail over the larger bandwidths.

12.4.10 Diffraction Effects

Played instruments produce directivities that account for musicians' natural diffraction and absorption, which many studies have neglected. In many cases, these effects can be profound and strongly influence the radiated fields. Figure 12.13 illustrates this point by comparing the 1/3rd-octave-band directivities produced by the violin and by live human speech (as reported in Ref. 6). Although the radiation mechanisms of the violin and the human voice are markedly different, the directivity patterns share similar characteristics due to the diffraction of the human body. For example, one observes a diffraction spot behind and below the seated musician or talker in all six balloons. Similar diffraction spots were apparent for other instruments, including brasses and woodwinds. The tuba directivity balloons in Figs. 12.9(e) and 12.9(f) and the bass clarinet transverse polar plot in Fig. 12.6(a) show the effect clearly.

Other similarities are also apparent, including stronger radiation toward the bottom left and right, visible in the 400 Hz band balloons of Figs. 12.13(a) and 12.13(d) and reduced radiation in a region

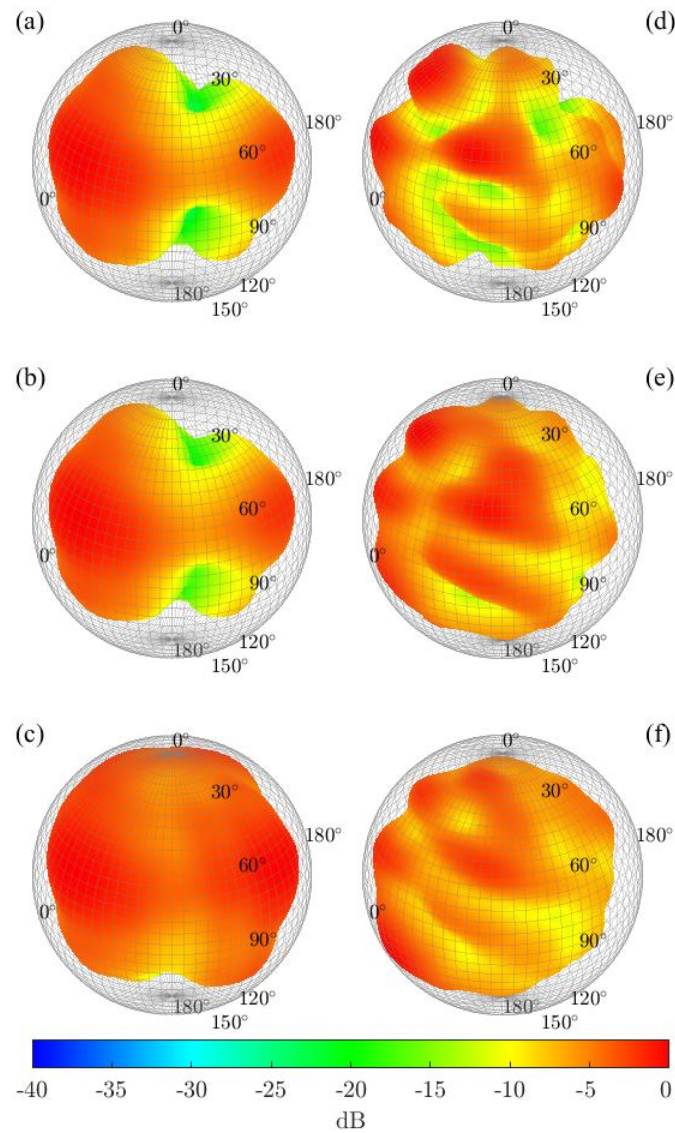


Figure 12.12 Cello directivities over various bandwidths. (a) Narrowband (1 Hz resolution) OECOS at 415 Hz. (b) 400 Hz 1/6th-octave band (46 Hz bandwidth). (c) 400 Hz 1/3rd-octave band (92 Hz bandwidth). (d) Narrowband (1 Hz resolution) OECOS at 1 kHz. (e) 1 kHz 1/6th-octave band (116 Hz bandwidth). (f) 1 kHz 1/3rd-octave band (232 Hz bandwidth). All directivities utilized $N = 18$ spherical harmonic expansions.

directly behind the body. The direction and orientation of diffraction lobes are consistent with the primary source radiations, directly in front of the talker for speech and slightly off to the musician's side for the violin. Despite the unique characteristics in the directivity patterns, such as stronger radiation above and to the musician's left, as evidenced in Fig. 12.13(c), the overall similarities and shared features suggest that the body plays a significant role in the directivity of musical instruments. Several previous works on artificially excited violin directivities suggested that below 500 Hz, the radiation of the violin without a musician was roughly omnidirectional. [141, 158, 168] However, this behavior is not characteristic of played violin directivities in the 400 Hz and 500 Hz bands. The measured directivities instead show that the diffraction and absorption of the musician's body have caused the directivities to deviate from an omnidirectional result, with some directions exceeding 10 dB down from the maximum. The L_{σ_Q} between the measured patterns and an omnidirectional pattern is 1.6 dB for both the 400 Hz and 500 Hz bands and 2.0 dB for the 800 Hz band. Thus, as suggested earlier in Sec. 15.1, practical directivity applications, such as architectural acoustics modeling and microphone placement, should consider the intrinsically integrated effects of musicians' bodies.

12.5 Directivity Database

Directional data is essential in many acoustics applications. An archival database stored at Ref. [38] contains directivities of 14 played orchestral instruments of the string, woodwind, and brass families. The directivities incorporate 5° angular resolutions, following the AES56-2008 (r2019) standard. The 1/3rd-octave band data followed from summation of the OECOS over the desired bandwidths. Instruments that radiate significant energy at low-frequencies, such as the tuba and string bass, include far-field corrections. The data includes tabulated directivities and file types commonly used in architectural acoustics simulations [96, 97].

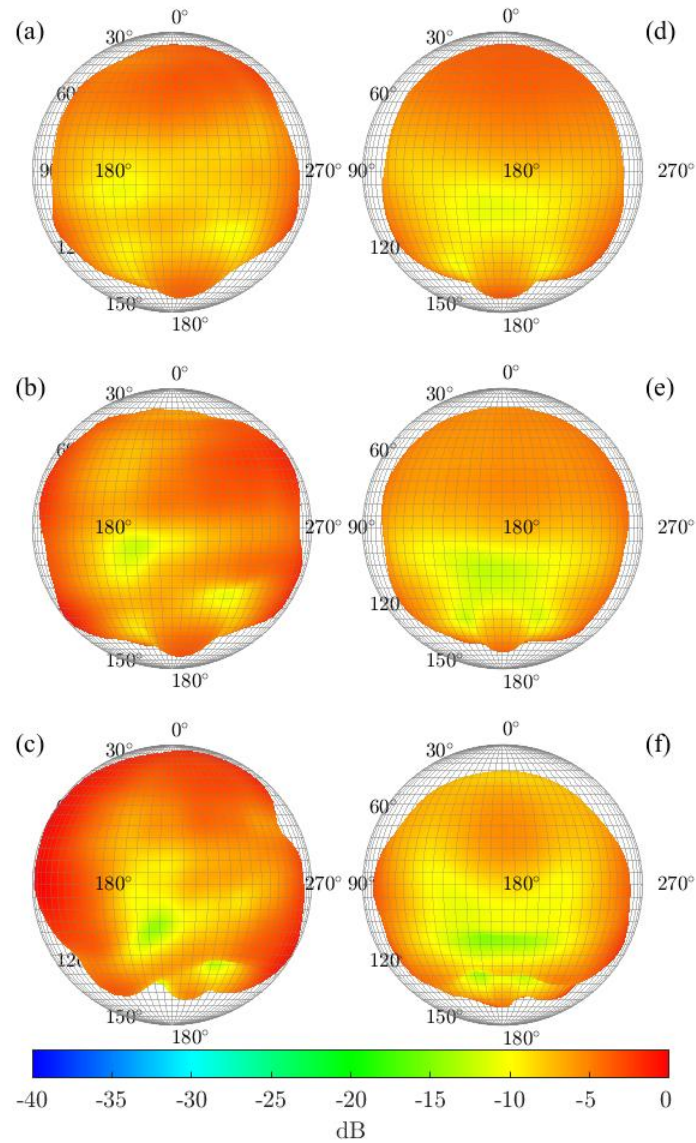


Figure 12.13 Violin and speech directivities in 1/3rd-octave bands. Violin directivities for the (a) 400 Hz, (b) 500 Hz, and (c) 800 Hz bands. Speech directivities for the (d) 400 Hz, (e) 500 Hz, and (f) 800 Hz bands. A slight viewpoint rotation of the violin balloons has allowed better comparisons of the diffraction patterns behind the seated musician with the seated talker. All directivities have employed $N = 18$ spherical harmonic expansions.

12.6 Conclusions

The multiple-capture transfer function technique presented in this paper produces reliable high-resolution directivity measurements of played musical instruments, despite the inherent difficulties caused by their natural excitation. The method allows for sampling densities consistent with published loudspeaker standards, namely 5° degree polar and azimuthal equiangular sampling. This work has presented a quadrature method for the sampling scheme and addressed other directivity measurement issues such as acoustic source centering. The formulated narrowband OECOS generates broader-band directivities, even from the tonal spectra radiated by many musical instruments. Coherence balloons, spatially averaged coherence values, and repeated 1/3rd-octave band directivity factor functions at the sampling poles delineate spectral regions with valid and invalid directivities. Perturbation tests, measurements with a single-capture system, and comparisons to previous works also substantiated the multiple-capture technique's reliability, repeatability, and limitations. The 1/3rd-octave-band directivities of several musical instruments produced from the method are available in an online archival database. The authors encourage the use of the methods and results for acoustical applications and additional research in this area.

Part IV

Modeling Sound Radiation

Chapter 13

Point Source Modeling Transmission Matrix

Method

This chapter illustrates how point-source models using the impedance translation theorem can predict the directional radiation of organ pipes. It also considers limitations to the approach, including deviations due to diffraction around the pipe. The chapter previously appeared as:

S. D. Bellows and T. W. Leishman, "Modeling and measurements of organ pipe sound radiation," Proc. 24th Int. Conf. Acoust., ABS-0243, (2022).

13.1 Introduction

The transmission matrix method (TMM) represents a complex system as a one-dimensional transmission line, allowing a simple yet robust approach to modeling many musical instruments [39]. Because the one-dimensional model is approximately valid as long as the instrument bore remains small compared to the acoustic wavelength, this approach is particularly useful in predicting the frequencies produced using various fingerings of wind instruments even for higher frequencies. While it is common to utilize the TMM to predict played frequencies and input impedance curves,

the approach also helps predict the directional characteristics of musical instruments. Nonetheless, the effectiveness of the TMM in predicting directivities have remained inconclusive, partly due to the lack of high spatial resolution directivity measurements for comparisons.

This work contrasts TMM-based directivity models to measured spherical directivities. In particular, this investigation applies the TMM to organ pipes due to their simple natures. Results show that the TMM-based techniques successfully predict directivities at low frequencies. However, BEM simulations and near-field cylindrical scans reveal that the neglecting of diffraction effects limits the effectiveness of the approach.

13.2 Theoretical Modeling

13.2.1 Point Source Model

At low frequencies, a simple point-source model reasonably describes the radiation of sound from the organ pipes [40, 89]. For open pipes, two sources are necessary: one at the mouth and one at the open end. For a closed pipe, only a single source at the mouth is necessary. For time-harmonic radiation, the pressure at a point r is

$$p(\mathbf{r}, k) = iz_0 k \sum_{n=1}^N U_n G(\mathbf{r}, \mathbf{r}_n) \quad (13.1)$$

where N is the number of openings, U_n is the frequency-dependent volume velocity at the n th opening, i is the imaginary unit, $z_0 = \rho_0 c$ is the characteristic specific acoustic impedance of the fluid, k is the wavenumber, and

$$G(\mathbf{r}, \mathbf{r}_n) = \frac{e^{-ikR_n}}{4\pi R_n} \quad (13.2)$$

is the free-space Green's function with

$$R_n = |\mathbf{r} - \mathbf{r}_n| \quad (13.3)$$

being the distance from the observation position r to the location r_n of the n th opening.

When considering normalized far-field directivities, the volume velocity of the mouth is arbitrary for a closed pipe with only one opening. However, for an open pipe, the impedance translation theorem relates the volume velocity between the two openings [39, 40]. The TMM simplifies the numerical implementation for more complex sources with many openings [40]. The acoustic radiation impedance of the open end of the pipe can be modeled as an unflanged tube:

$$Z_{AR,O} = \frac{z_0}{S} (0.25(ka)^2 + i0.61ka) \quad (13.4)$$

The acoustic radiation impedance of the mouth can be roughly modeled as a baffled circular piston:

$$Z_{AR,M} = \frac{z_0}{S} \left(1 - \frac{J_1(2ka)}{ka} + i \frac{H_1(2ka)}{ka} \right) \quad (13.5)$$

Translating the impedance of the open end through length L to the mouth opening yields

$$Z_A = Z_{A0} \frac{Z_{AR,O} + iZ_{A0} \tan(kL)}{Z_{A0} + iZ_{AR,O} \tan(kL)} \quad (13.6)$$

where $Z_{A0} = z_0/S$ and S being the pipe's cross sectional area. A current divider gives the volume velocity at the mouth as

$$U_m = U_{in} \frac{Z_A}{Z_A + Z_{AR,M}}, \quad (13.7)$$

where U_{in} is an arbitrary input volume velocity. Finally, the volume velocity at the open end is given by

$$U_o = (U_{in} - U_m) \frac{-iZ_{A0} \csc(kL)}{iZ_{A0}(\tan(kL/2) - \csc(kL)) + Z_{AR,O}}. \quad (13.8)$$

Thus, a simple model can estimate the volume velocities at the pipe openings for predicting far-field directivities using Eq. (13.1).

13.2.2 Kirchhoff-Helmholtz Integral Equation

A more complete representation of the pressure field follows from the Kirchhoff-Helmholtz Integral Equation (KHIE) [62]:

$$p(\mathbf{r}) = iz_0k \iint_S u_n(\mathbf{r}_s)G(\mathbf{r}, \mathbf{r}_s)dS + \iint_S p(\mathbf{r}_s) \frac{\partial}{\partial n} G(\mathbf{r}, \mathbf{r}_s)dS \quad (13.9)$$

where u_n is the normal particle velocity, the integral is taken over the boundary S and n is the normal direction into the domain. In this form, the first integral of the KHIE can be roughly interpreted as the radiation of sound from the source due to surface vibrations, whereas the second integral can be interpreted as the pressure field due to diffraction and scattering effects of the boundary.

If one considers the boundary surface S to fully enclose the exterior of the pipe, it is evident that Eq. (13.1) approximates the first integral of the KHIE with

$$U_n = \iint_{S_n} u_n(\mathbf{r}_s)dS \quad (13.10)$$

where S_n is the surface bounding the n th pipe opening. With this approach, the openings of the pipe behave as vibrating pistons of effective areas S_n . This approximation should remain valid provided that the acoustic wavelength is larger than the pipe openings. However, Eq. (13.1) neglects the second integral in the KHIE. Thus, when this term becomes important, deviations between the modeled and measured directivities will arise. Section 15.6 explores this limitation by comparing measured results with a BEM simulation, which numerically evaluates Eq. (13.9).

13.3 Measurements

The authors employed spherical and cylindrical arrays to measure the pressure fields produced by two organ pipes: one open metal pipe and closed wood pipe. The spherical array, shown with the closed wooden pipe in Fig. 15.8(a), consisted of 36 12.7 mm (0.5 in) microphones placed in 5-degree increments in the polar angle at a radius of $a = 0.97$ m. The cylindrical array, shown with

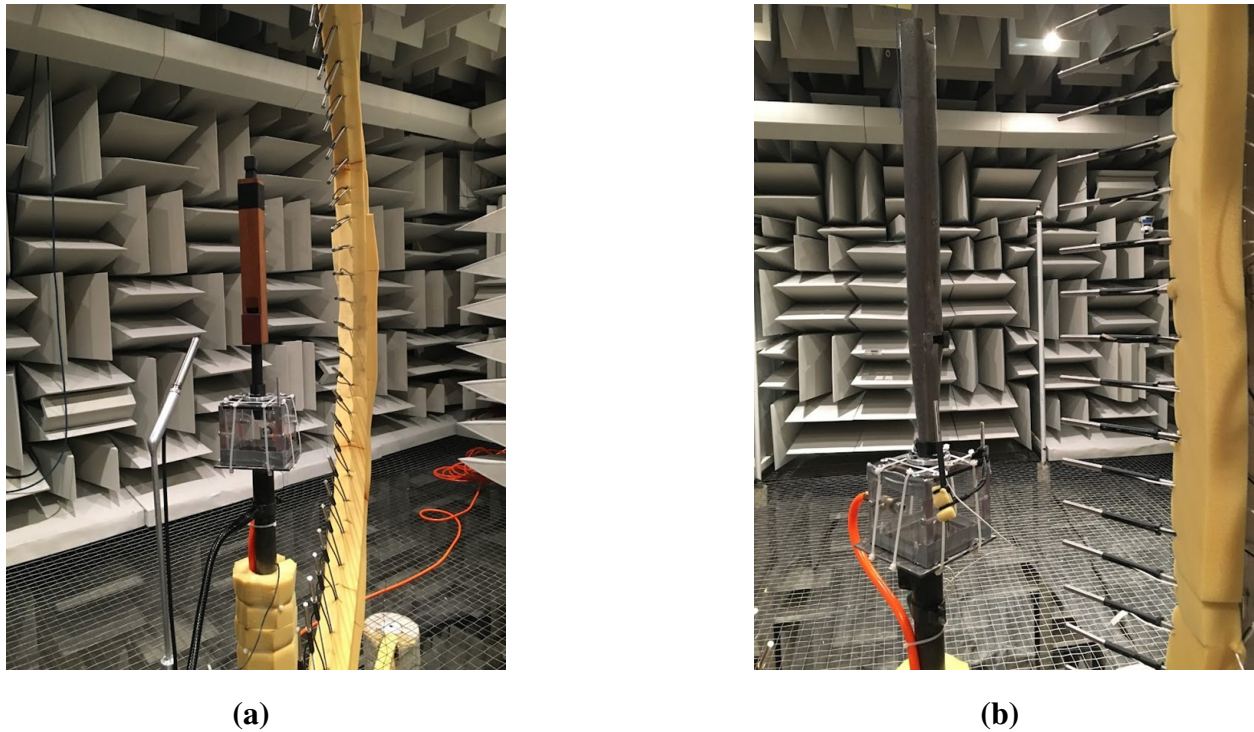


Figure 13.1 Spherical (a) and cylindrical (b) microphone arrays used to assess the radiated fields of two organ pipes.

the open metal pipe in Fig. 15.8(b), consisted of 36 6.35 mm (0.25 in) microphones placed in 5 cm increments at a circular radius of $\rho = 0.25$ m. A turntable rotated each array in 5-degree azimuthal steps. Relative calibrations for each microphone array and a near-field reference microphone ensured normalization between the repeated measurements using frequency-response functions (FRFs) [13].

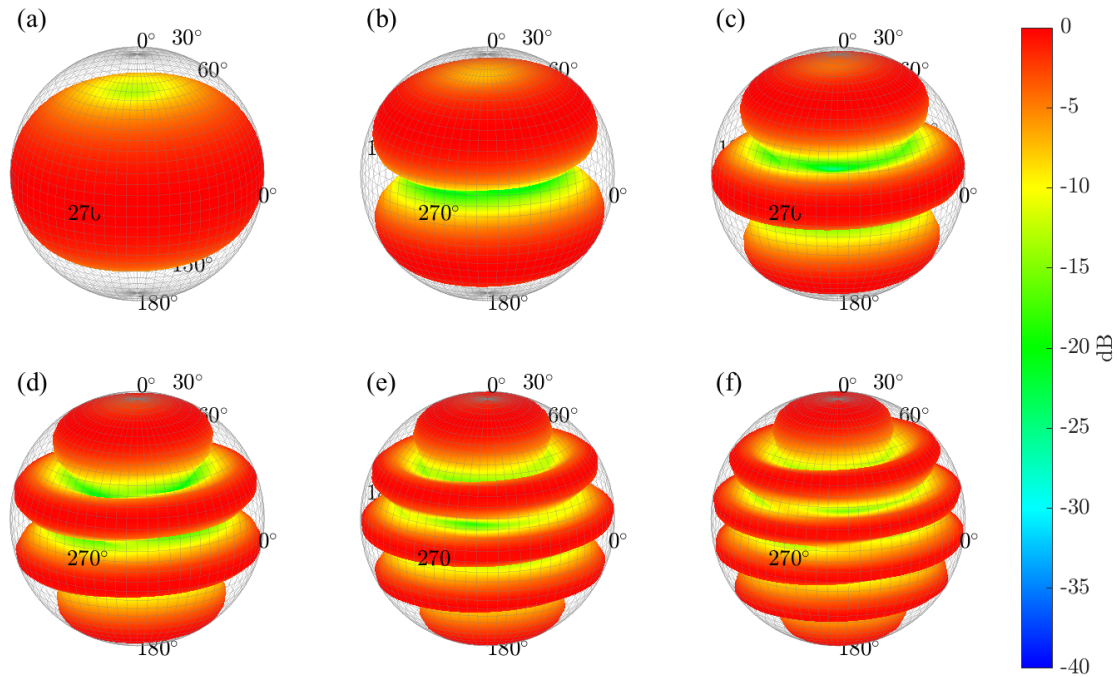


Figure 13.2 Simulated directivity balloons of the open metal pipe using Eq. (1) for the first six partials: (a) 331 Hz, (b) 662 Hz, (c) 993 Hz, (d) 1323 Hz, (e) 1654 Hz, and (f) 1985 Hz.

13.4 Results

13.4.1 Theoretical Prediction

Figure 13.2 shows simulated directivity balloons for the first through sixth partials of the open metal pipe using Eq. (13.1) with $L = 0.46$ m. Both radius and color indicate levels on a 40 dB scale. The mouth of the pipe faces the $\phi = 0^\circ$ azimuthal marker. For the fundamental, the directivity appears as a single disc-like shape. As anticipated for a two point-source model, as frequency increases, the number of lobes also increases. The directivity patterns are nearly axisymmetric about the line connecting the center of the top opening of the pipe with the mouth. Because the wooden pipe has only one radiating opening, the simulated directivity pattern for all frequencies is omnidirectional.

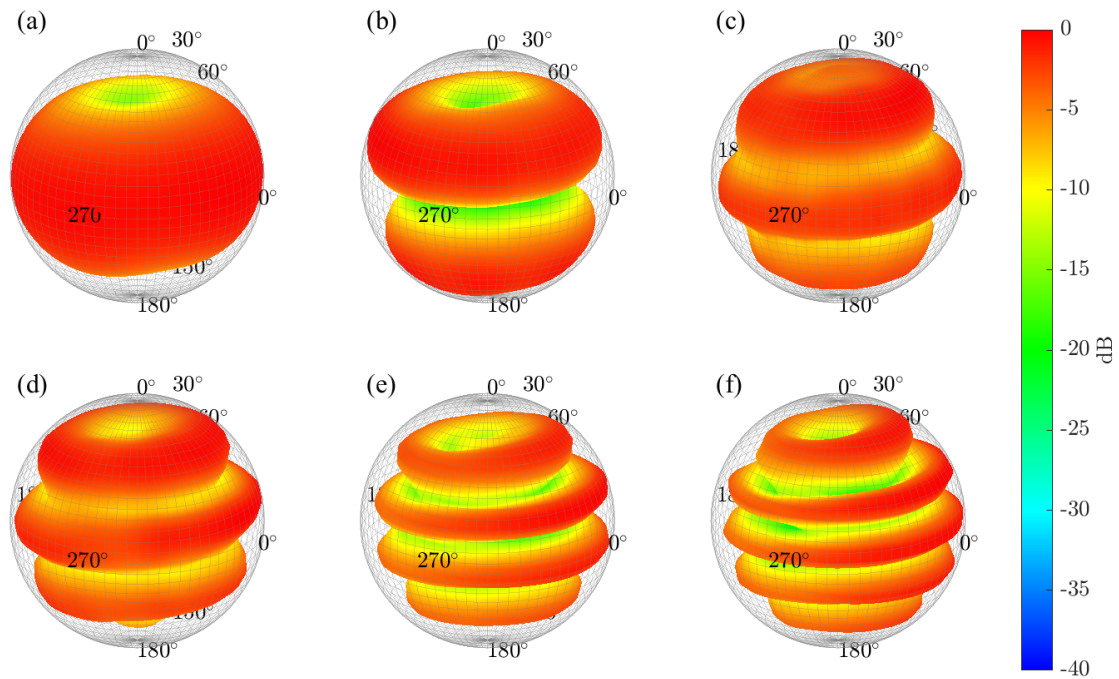


Figure 13.3 Measured directivity balloons of the open metal pipe for the first six partials: (a) 331 Hz, (b) 662 Hz, (c) 993 Hz, (d) 1323 Hz, (e) 1654 Hz, and (f) 1985 Hz.

13.4.2 Directivity Measurements

Figure 13.3 shows the directivity balloons of the measured metal pipe. The patterns are remarkably similar, especially for the first three partials below 1 kHz. As for the simulated case, the balloons are roughly axisymmetric about the axis connecting the openings. However, at higher frequencies, reduced levels appear behind the pipe (near $\phi = 180^\circ$) that reduce the axial symmetry.

Figure 13.4 shows the measured closed wooden pipe. While for the fundamental, the radiation is roughly omnidirectional, at higher frequencies, particularly above 1 kHz, the radiation is significantly reduced behind the instrument. Small undulations appear, although they are weak and not nearly as pronounced as for the open pipe.

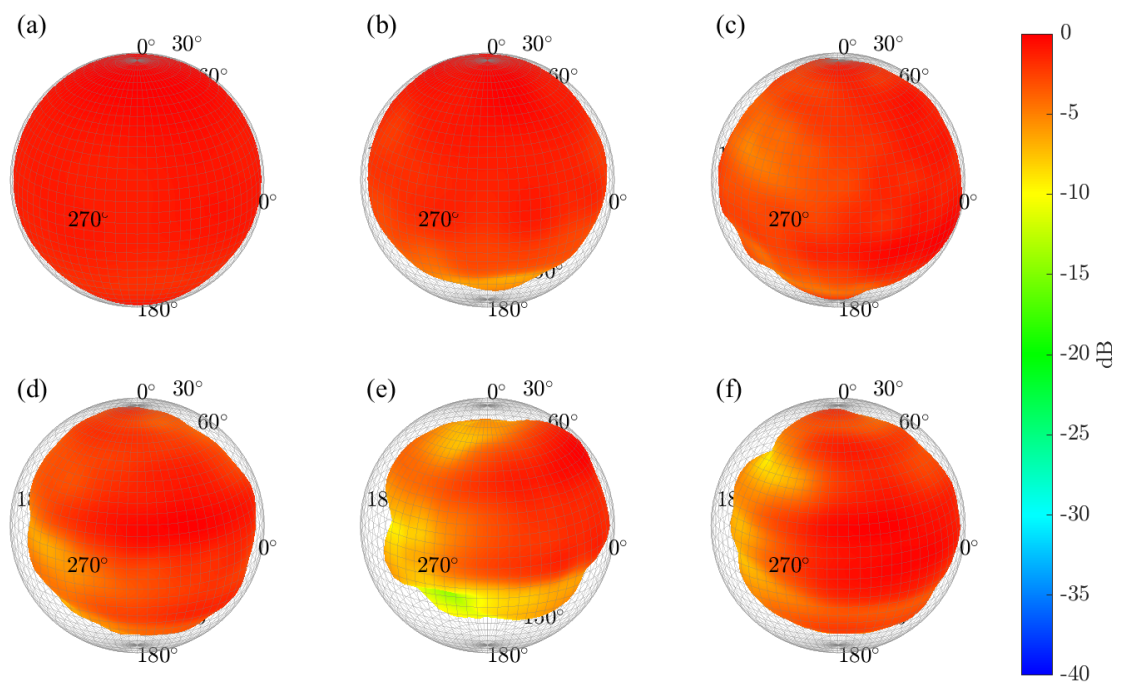


Figure 13.4 Measured directivity balloons for the measured closed wooden pipe for the first six partials: (a) 335 Hz, (b) 670 Hz, (c) 1005 Hz, (d) 1340 Hz, (e) 1675 Hz, and (f) 2010 Hz.

13.5 Analysis

As suggested by the measurement results, simple point-source models provide reasonable estimates of source directivities at lower frequencies. However, reduced levels behind the pipes suggest that diffraction around the pipe itself may play an important role in the radiation patterns, particularly at higher frequencies. An enhanced model using a BEM evaluation of the KHIE provides additional insights into this assertion.

To simulate the pressure while maintaining similarity to the modeling approach used in Eq. (13.1), a single boundary enveloping the exterior of the pipe describes the source geometry. This approach divides the pipe into an exterior and interior portion so that the openings of the pipes become inhomogeneous Neumann (velocity) boundary conditions. Then, as shown in Eq. (13.10), the net volume velocity used in Eq. (13.1) is the surface integral of the particle velocity at each opening. The TMM method predicts the particle velocity at each opening by dividing the predicted values from Eqs. (13.7) and (13.8) by the area S_n of the opening. While a more accurate model would follow from treating the pipes as thin-walled structures and allowing the computational domain to include both the interior and exterior of the pipe, this method is useful because it maintains a consistent approach between the simple point-source model of Eq. (13.1) and the first term of the KHIE. The second term of the KHIE, numerically evaluated using BEM, can then be seen as a correction term to the original model.

Because the field produced by the second term decays at a faster rate than the $1/r$ dependence of the first term due to the normal derivative of the Green's function, this field is more apparent in the near-field of the source. Consequently, measurements produced by the cylindrical array are beneficial for identifying the effects of the second term in the KHIE.

Figure 13.5 plots results for the fundamental of the closed wooden pipe. Figure 13.5(a) shows the pressure evaluated on the cylindrical sampling surface as simulated by Eq. (13.1) with the point source centered at the mouth of the instrument. As anticipated, the pressure is nearly uniform for

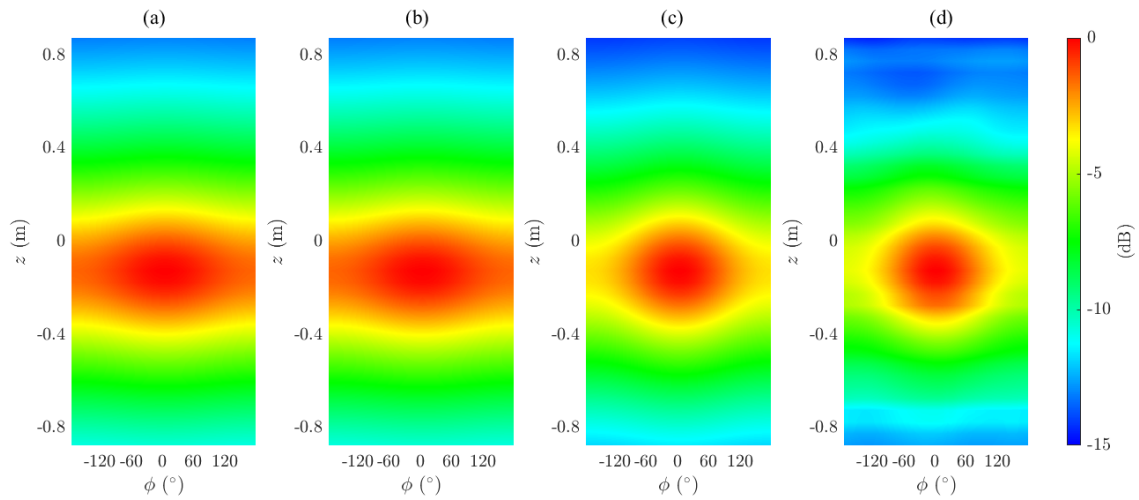


Figure 13.5 Pressure on the cylindrical scanning surface for the fundamental of the closed wooden pipe. (a) TMM-based point-source model simulation. (b) BEM simulation using only the first term of the KHIE. (c) BEM simulation using the full KHIE. (d) Measured pressure.

constant height z , although the levels slightly increase in front of the pipe mouth and decrease behind the pipe as the mouth is not directly at the center of array. Figure 13.5(b) shows the simulated pressure using only the first term of the KHIE. Because the wavelength is much larger than the opening, Eq. (13.10) remains a reasonable approximation and the pressure remains similar to that predicted by the point-source model. Figure 13.5(c) shows the simulated pressure when both terms in the KHIE are included. The inclusion of the second term significantly decreases the levels behind the instrument, and the area in front of the mouth is clearly seen as a red circular patch. The BEM simulation agrees well with the measured data shown in Fig 13.5(d), which also has a similar red circular patch in front of the pipe mouth. Thus, including the second term would improve the accuracy of the TMM-based point-source model.

13.6 Conclusions

This work explored limitations in modeling the directivities of organ pipes using equivalent point-sources combined with the TMM. The results show that while there is excellent agreement between simulations and measurements at low frequencies, significant deviations occur at higher frequencies. Near-field cylindrical scans and BEM simulations reveal that neglecting diffraction effects around the pipe can cause these deviations. Future work could include applying the method to more complex sources such as woodwind instruments and developing simplified approaches to model diffraction effects.

Chapter 14

Multipole Modeling

This chapter illustrates how select gamelan gong directivities discussed in Ch. 8 may be modeled using the superposition of a monopole and dipole field as part of a multipole expansion. The chapter appeared earlier as:

S. D. Bellows, D. T. Harwood, K. L. Gee, and T. W. Leishman, "Low-frequency directional characteristics of a gamelan gong," *Proc. Mtgs. Acoust.*, 50, 035003, (2022). doi: 10.1121/2.0001722.

14.1 Introduction

Measured directivity patterns are valuable resources to characterize the sound radiation from musical instruments. They have additional applications in room acoustical designs [20, 21], auralizations [19, 99], and microphone placements [14]. While research has provided some understanding of the directional characteristics of Western orchestral instruments [1, 7, 20, 125, 126], there remains much less understanding, with notable exceptions [21, 31, 127], regarding the radiation of instruments from other music cultures.

The structural acoustics of Indonesian gamelan gongs have received considerable attention due to their unique characteristics. Due to his interest in the tuning procedure of gamelan gongs,

McLachlan [128] measured the acoustic outputs of gongs made of different materials. He found that the boss (hemispherical dome at the gong's center) beaten into the gong's face raised its fundamental frequency, whereas thinning lowered the frequency. His finite-element method (FEM) models illustrated how the boss shape, gong rim thickness, and rim angle all modified and tuned modal frequencies.

Krueger et al. [129] investigated *ombak*, an acoustic beating phenomenon of a large ageng wadon Balinese gamelan gong. Both acoustical and scanning laser Doppler vibrometer (SLDV) measurements identified its lowest modal frequencies. Despite the agreement between the acoustic and structural measurements, the researchers found that the acoustic signal contained frequency peaks near the sum and difference frequencies of the first gong axial modes. They additionally discovered second and third harmonics of the fundamental axial mode that suggested significant nonlinear effects. Subsequent measurements using increasing excitation force confirmed that nonlinear interactions between the modes were a primary cause of *ombak*.

Perrin et al. [130] studied a small gamelan gong. Their analysis employed finite-element method (FEM) modeling, electronic speckle pattern interferometry (ESPI), and SLDV scans to tabulate its modal frequencies. Although discrepancies in the modal frequencies arose between the measurement modalities, the authors generally found that the “modified Chladni's law” gave predictions in good agreement with the ESPI data. They confirmed nonlinear behavior and identified three modes as the most acoustically significant: the radial (0, 1) mode and the pair of angular-radial (1, 1) modes.

While many studies have thus provided more knowledge regarding the structural modes of gamelan gongs, their acoustic radiation patterns have remained unclear. Zotter [31] measured the directivity of an ageng gamelan gong using a 10-channel microphone array and assuming axial symmetry. He found dipole-like directivity for the first two axial modes of the instrument. He

also included results for time-varying directivities due to beating effects. However, the symmetry assumption limited the analysis to only two modes.

This work presents the directivity patterns of an ageng lanang Balinese gamelan gong assessed by a high-resolution spherical directivity measurement system. Subsequent SLDV scans revealed close connections between the gong's far-field radiated patterns and mode shapes. Similar to Zotter's results, the directivities reveal dipole-like radiation at the lowest frequencies. At higher frequencies, the sound radiation takes on more complex patterns. Spherical harmonic and subsequent multipole expansions allow equivalent point source representations of the gong's acoustic radiation at the lowest frequencies.

14.2 Methods

14.2.1 Measurements

As shown in Fig. 15.8, a rotating semicircular microphone array assessed the directivity of the ageng lanang gamelan gong. The microphone array consisted of 36 12.7 mm (0.5 in) precision microphones spaced in 5° degree increments in the polar angle. Array rotations in 5° azimuthal steps allowed a full spherical scan of 2,521 unique sampling positions, consistent with the AES directivity sampling standard [33], with the omission of the nadir position.

A swept-sine input signal sent to a shaker excited the gong over the audible bandwidth. Several measurements employed varying shaker contact points to ensure the excitation of numerous normal modes of vibration. A near-field reference microphone provided a directivity input signal for calculating frequency response functions (FRFs) between it and the output of each array microphone signal. While the shaker input excitation signal is notably more repeatable than that of played musical instruments [1], FRFs nonetheless increase extraneous noise immunity and provide a convenient normalization to address any variations that might occur between measurement rotations.



Figure 14.1 An ageng lanang gamelan gong within the rotating directivity measurement array.

To better understand how the gong's modal shapes influenced its directivity, additional measurements followed from an SLDV scan of the instrument. As for the directivity measurements, the shaker excited the instrument while the laser head scanned 977 positions on the gong's front face. The spatial resolution allowed modal analysis well above 1.5 kHz, although this work primarily focuses on results for lower frequencies.

14.2.2 Signal Processing

The directivity near-field input autospectrum $G_{aa,v}$ for the v^{th} rotation and the FRF H_{uv} for the u^{th} array microphone and v^{th} rotation followed from standard spectral estimation and deconvolution procedures. [131, 132] The effective input autospectrum [6],

$$G_{aa,eff}(f) = \frac{\sum_{u=0}^{U-1} \sum_{v=0}^{V-1} w_{uv} G_{aa,v}(f) |H_{uv}(f)|^2}{\sum_{u=0}^{U-1} \sum_{v=0}^{V-1} w_{uv} |H_{uv}(f)|^2}, \quad (14.1)$$

where w_{uv} are quadrature weights for numerical integration over the sphere [78, 133], yielded an averaged input autospectrum over the azimuthal rotations. The total effective time-averaged sound power [62, 131] radiated by the gong was

$$\langle W(f) \rangle_{t,eff} = R^2 \frac{G_{aa,eff}(f)}{\rho_0 c} \sum_{u=0}^{U-1} \sum_{v=0}^{V-1} w_{uv} |H_{uv}(f)|^2, \quad (14.2)$$

where R is the measurement radius. Peak extraction of $\langle W(f) \rangle_{t,eff}$ allowed determination of the gong's modal frequencies from the acoustic signals.

14.2.3 Spherical Harmonic Expansions

The spherical harmonics provide an orthonormal basis for expanding directivities over the spherical evaluation surface [31, 114]. As the angular component of the Helmholtz-equation solution on the exterior domain, they find important applications in wave-based modeling of sound fields [59]. The

normalized spherical harmonics of degree n and order m are defined here as [70]

$$Y_n^m(\theta, \phi) = \sqrt{\frac{2n+1}{4\pi} \frac{(n-m)!}{(n+m)!}} P_n^m(\cos \theta) e^{im\phi}, \quad (14.3)$$

where P_n^m are the associated Legendre functions of degree n and order m .

The pressure field for $r \geq R$ is [59]

$$p(r, \theta, \phi, k) = \sum_{n=0}^{\infty} \sum_{m=-n}^n c_n^m(k) h_n^{(2)}(kr) Y_n^m(\theta, \phi), \quad r \geq R, \quad (14.4)$$

where $h_n^{(2)}(kr)$ are the spherical Hankel functions of the second kind (for outward propagation and $e^{i\omega t}$ time dependence). The expansion coefficients follow by exploiting the spherical harmonic's orthogonality over the sphere:

$$c_n^m(k) = \frac{1}{h_n^{(2)}(kR)} \int_0^{2\pi} \int_0^\pi p(R, \theta, \phi, k) [Y_n^m(\theta, \phi)]^* \sin \theta d\theta d\phi, \quad (14.5)$$

where $*$ indicates complex conjugation. Numerical quadrature allows evaluation of the integral [133]. Once determined, the expansion coefficients allow computation of extrapolated far-field directivities via the large-argument representations of the spherical Hankel functions [62]:

$$D_{ff}(\theta, \phi) = \sum_{n=0}^{\infty} \sum_{m=-n}^n c_n^m(k) i^n Y_n^m(\theta, \phi). \quad (14.6)$$

Extrapolation of the complex pressure also allows far-field corrections for the sound power estimate when R is in the near-field of the source.

14.2.4 Multipole Representation

A multipole expansion of the Kirchhoff Helmholtz Integral Equation (KHIE) yields a simplified representation of the source's sound field [40, 62]. The monopole moment is [62]

$$M = \iint_S i z_0 k u_n(\mathbf{r}) dS \quad (14.7)$$

and the dipole moment is

$$\mathbf{D} = \iint_S [iz_0 k \mathbf{r} u_n(\mathbf{r}) + \hat{\mathbf{n}} p(\mathbf{r})] dS, \quad (14.8)$$

where u_n and p are the normal velocity and pressure on the radiating body's boundary surface S , respectively. At low-frequencies and neglecting higher order moments (e.g. quadrupole), the resultant field becomes

$$p(\mathbf{r}) \approx p_m(\mathbf{r}) + p_d(\mathbf{r}), \quad (14.9)$$

where

$$p_m(\mathbf{r}) = M \frac{e^{-ikr}}{4\pi r} \quad (14.10)$$

is the monopole field and

$$p_d(\mathbf{r}) = ik \frac{e^{-ikr}}{4\pi r} \left(1 - \frac{i}{kr}\right) \mathbf{D} \cdot \hat{\mathbf{r}} \quad (14.11)$$

is the dipole field.

One may use the spherical harmonic expansion coefficients to infer the multipole moments of the source [59, 61, 103]. For example, the following matrix equation converts the degree $n = 0$ and $n = 1$ expansion coefficients into the monopole and dipole moments:

$$\begin{bmatrix} M \\ D_x \\ D_y \\ D_z \end{bmatrix} = \frac{i\sqrt{\pi}}{k^2} \begin{bmatrix} 2k & 0 & 0 & 0 \\ 0 & \sqrt{6} & 0 & -\sqrt{6} \\ 0 & -i\sqrt{6} & 0 & -i\sqrt{6} \\ 0 & 0 & 2\sqrt{3} & 0 \end{bmatrix} \begin{bmatrix} c_0^0 \\ c_1^{-1} \\ c_1^0 \\ c_1^1 \end{bmatrix}. \quad (14.12)$$

The matrix entries result from equating the multipole and spherical harmonic expansion terms [59]. However, only in the limit of $kR \ll 1$ do the derived multipole moments correspond to the integrals in Eqs. (15.56) and (15.57) [83].

Notably, the known monopole and dipole moments of the gong allow a representation of the sound field using an equivalent point-source model [61]. Such models are often more convenient for numerical simulations using directivities [86]. Figure 14.2 illustrates the locations and amplitudes

of a seven-point-source model that reconstructs the pressure field for $kR \ll 1$ with high accuracy provided that $k\epsilon \ll 1$, where ϵ is the separation distance of opposing point sources. The single point source at the origin represents the monopole field, whereas the three orthogonal opposite-polarity pairs represent the dipole field. Consequently, one may readily construct a low-frequency equivalent point source representation of a source once its spherical harmonic expansion coefficients are known.

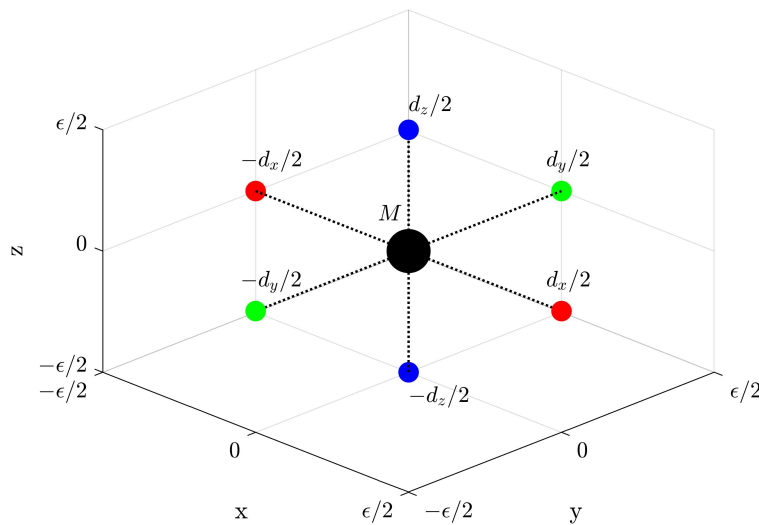


Figure 14.2 Source locations, amplitudes, and polarities for an equivalent point source model involving seven point sources.

14.3 Results

14.3.1 Modal Extraction

Figure 14.3 shows an example of the normalized $\langle W(f) \rangle_{t,eff}$ radiated by the gong when excited by the shaker, plotted as a function of both frequency dimensionless ka , where $a = 0.4$ m is the gong's radius. As anticipated, the instrument's modal nature strongly characterizes its acoustic output. Below 200 Hz, eight sharp, distinct peaks evidence the gong's lowest modes. The spectral region

from 200 Hz to around 350 Hz appears as a gap with no strongly radiating modes. Increased modal density occurs above 350 Hz, although the radiated level is generally lower than for the lowest eight modes.

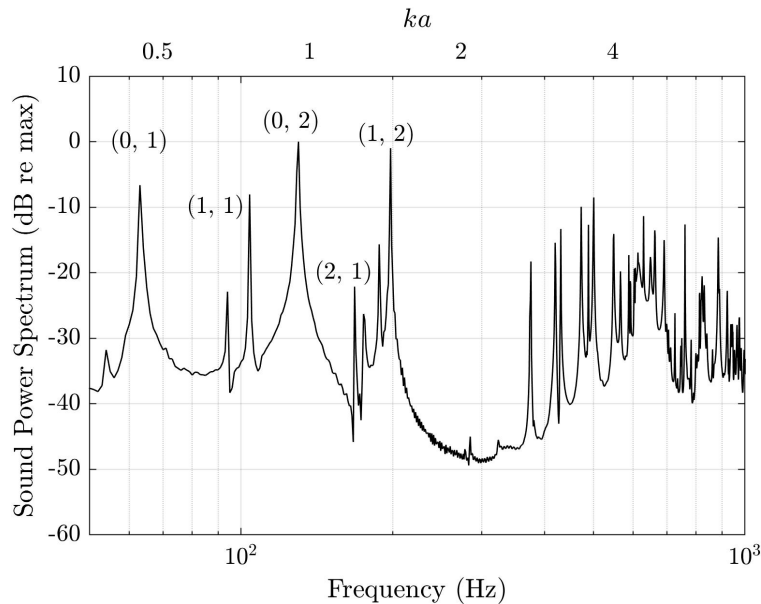


Figure 14.3 Normalized effective time-averaged sound power spectrum radiated from the gong when excited by a shaker.

Figure 14.4 plots the surface velocity of the gong as measured by the SLDV for the frequencies of the eight lowest modal peaks. Additionally, Table 14.1 reports the corresponding modal frequencies as extracted acoustically from the microphone output and structurally from the SLDV measurements. The two measurement modalities produced excellent agreement for the extracted modal frequencies; only the (0, 1) mode had a 1 Hz discrepancy in its value.

Perrin et al. [130] identified the (0, 1) and (1, 1) modes as being among the most acoustically significant for small gamelan gongs. These mode shapes for the ageng lanang gamelan gong used in the present work appear in Figs. 14.4(a) through 14.4(c) and occur at 63 Hz, 94 Hz, and 104 Hz, respectively. From the radiated sound power spectrum shown in Fig. 14.3, both the 63 Hz (0, 1) mode and the 104 Hz (1, 1) mode radiate at similar levels. The reduced level for the 94 Hz (1, 1)

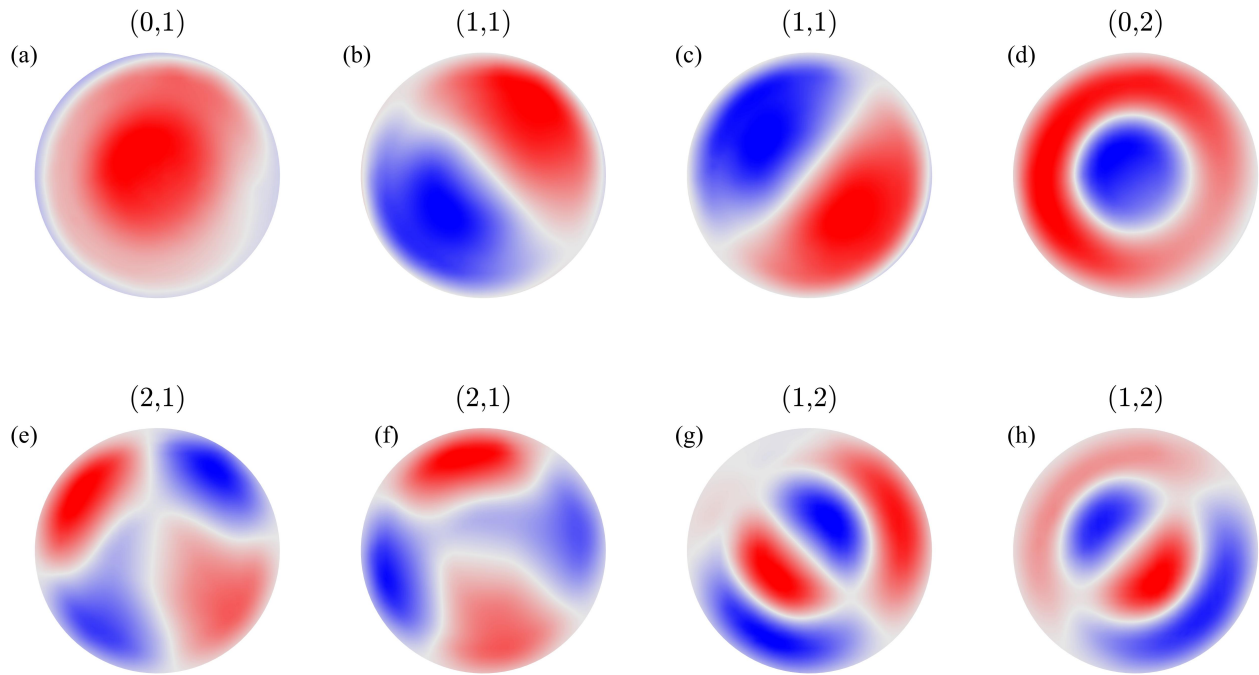


Figure 14.4 Normalized out-of-plane gong surface velocity at the sound power spectral peaks based on SLDV scan data and assumed modal numbers. (a) 63 Hz. (b) 94 Hz. (c) 104 Hz. (d) 130 Hz. (e) 168 Hz. (f) 175 Hz. (g) 188 Hz. (h) 198 Hz.

Table 14.1 Lowest eight modal frequencies of the gong and assumed modal numbers.

Frequency (Acoustic)	Frequency (SLDV)	Angular	Radial
63	64	0	1
94	94	1	1
104	104	1	1
130	130	0	2
168	168	2	1
174	174	2	1
188	188	1	2
198	198	1	2

mode may have been caused by the stinger placement, as the nodal lines were unknown before the measurements.

Krueger et al. [129] determined that the nonlinearly generated harmonics of the (0, 1) mode interacting with the (0, 2) mode create ombak for some large gamelan gongs. Thus, the (0, 2) mode should be acoustically significant in addition to the (0, 1) and (1, 1) modes identified by Perrin et al. Its mode shape appears in Fig. 14.4(d) and has a modal frequency of 130 Hz. Its radiated sound power level shown in Fig. 14.3 is the highest of all modes, confirming its importance to the gong's overall sound.

The next highest modes in Table 14.1 are the two (2, 1) modes at 168 and 174 Hz. However, from the radiated sound power curves, these modes do not appear to radiate efficiently compared to the other low-frequency modes. Their relatively weak radiation contrasts with the two strongly radiating (1, 2) modes occurring at 188 Hz and 198 Hz. The level of the 198 Hz (1, 2) mode is within 1 dB of the (0, 2) mode's level.

14.3.2 Directivity Results

Figure 14.5 shows the propagated and normalized far-field directivities for the lowest eight modes, where both color and balloon radius indicate the relative levels on a 40 dB scale. The gong faced the 0° degree azimuthal angle marker during the measurements.

As seen in Figs. 14.5(a) through 14.5(c), the directivity is dipolar for the (0, 1) and (1, 1) modes. For the (0, 1) mode, the out-of-phase velocities of the front and back gong faces produce a dipole moment in the x -direction (towards the 0° azimuthal marker). The (1, 1) modal patterns in Fig. 14.4 have node lines on the gong surface that approximately define the far-field directivity nulls. The velocity distribution on the front face of the gong determines the dipole moment in roughly the positive y - z -direction for the 94 Hz (1, 1) mode and the negative y - z -direction for the 104 Hz (1, 1) mode. Given that the surface velocity distribution on the back face of the gong has opposite

polarity to the distribution on the front face, it is somewhat surprising that these modes do not form an angled lateral quadrupole.

The dominant (0, 2) mode shown in Fig. 14.5(d) also has dipole-like directivity, but its null is not as well defined. The effect is possibly due to an increasing monopole moment [83]. Zotter [31] also observed dipole-like directivity for the (0, 1) and (0, 2) modes, although his symmetry assumptions did not allow identification of the dipolar nature of the (1, 1) modes.

The directivity at the next four modal peaks, shown in Figs. 14.5(e) through 14.5(h), have more complex directivity patterns with regions of strong and weak radiation. The directivity at the 168 Hz modal peak has more omnidirectional-like radiation except for a null running along the direction of the gong's right side. The directivity at the 175 Hz modal peak has a null dividing the most substantial radiation between the positive and negative x - z directions. The directivity at the 188 Hz modal peak is similar to that of the 94 Hz (1, 1) mode. Comparison of the out-of-plane velocity distribution of these two modes in Figs. 14.4(b) and 14.4(g) confirms that the location of the angular node line falls at a similar position on the gong's face. However, for the directivity at the 198 Hz modal peak is not similar to that of its corresponding 104 Hz (1, 1) mode.

14.3.3 Low-frequency Modeling

The gong's lowest four modes fall in the frequency regime corresponding to $ka < 1$. Additionally, the far-field directivities suggest that only a monopole and dipole field may reasonably represent the lowest four modes. The next four modes have more complex surface velocity distributions and far-field patterns; thus, higher-order moments may be necessary to model their fields adequately.

Figure 14.6 shows the far-field directivity for each gong mode based on a superposition of the monopole and dipole fields. Comparisons with the measured far-field directivities in Fig. 14.5 reveals good agreement for the lowest four mode. In each case, the direction of radiation lobes and

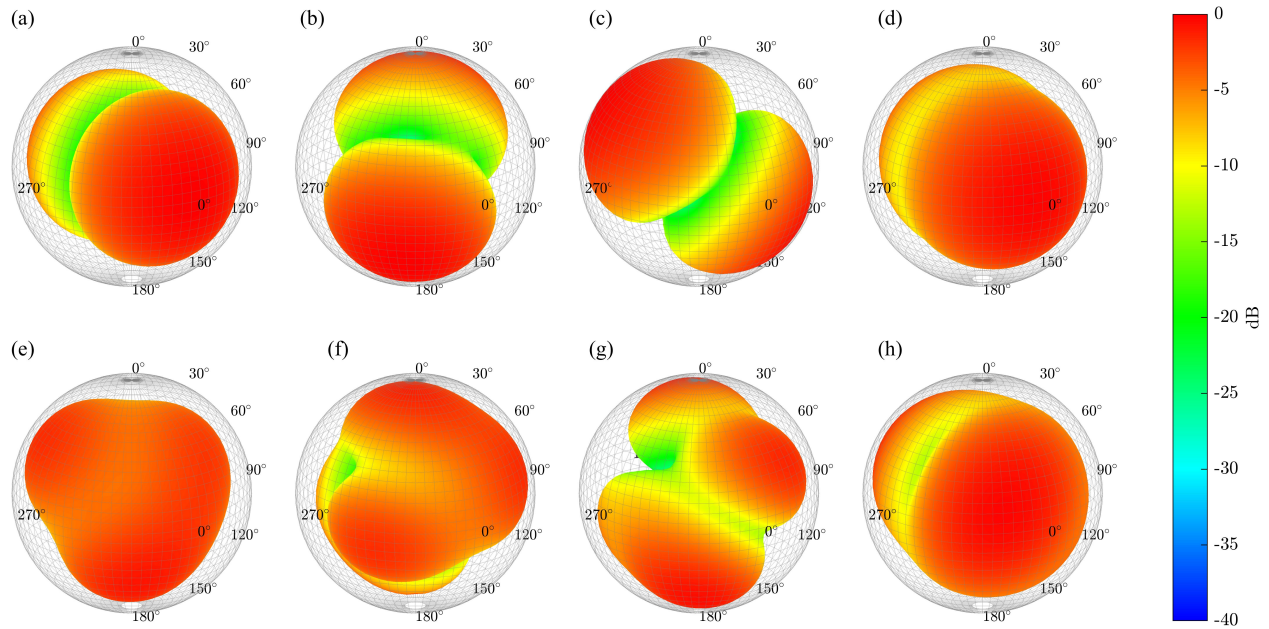


Figure 14.5 Propagated and normalized far-field directivities for the gong's lowest eight modal frequencies: (a) 63 Hz, (b) 94 Hz, (c) 104 Hz, (d) 130 Hz, (e) 168 Hz, (f) 175 Hz, (g) 188 Hz, and (h) 198 Hz.

nulls align. For the higher four modes, the agreement is not as good. While some general qualitative features remain, there are discrepancies in the locations and strengths of the various lobes and nulls.

An area-weighted directivity factor function deviation quantifies the differences between the measured and modeled propagated far-field patterns as a single level L_Q [81]. Figure 15.14 shows the value of L_Q for each mode. The deviations for the lowest four modes remain below 1.0 dB, again showing that they tend to have the best agreement. The deviations for the higher four modes are larger, approaching values closer to 3 dB. Consequently, for $ka > 1$, the accuracy declines for multipole representations using only the monopole and dipole fields.

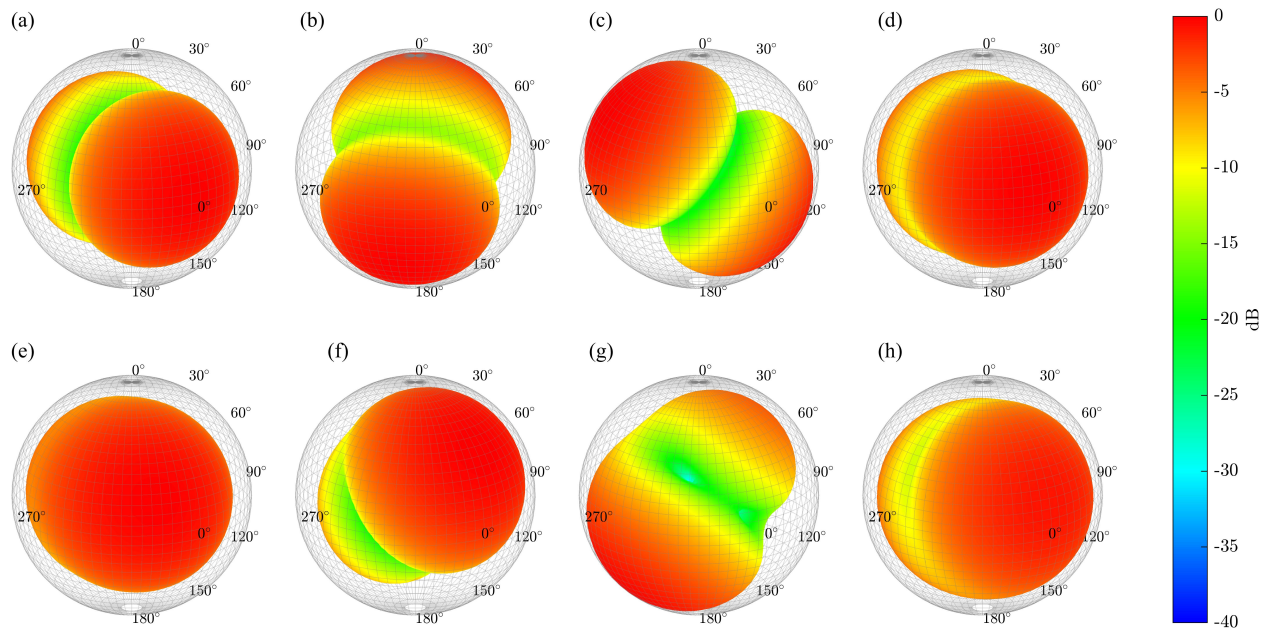


Figure 14.6 Simulated far-field gong directivities based on superpositions of monopole and dipole fields for the modal frequencies (a) 63 Hz, (b) 94 Hz, (c) 104 Hz, (d) 130 Hz, (e) 168 Hz, (f) 175 Hz, (g) 188 Hz, and (h) 198 Hz.

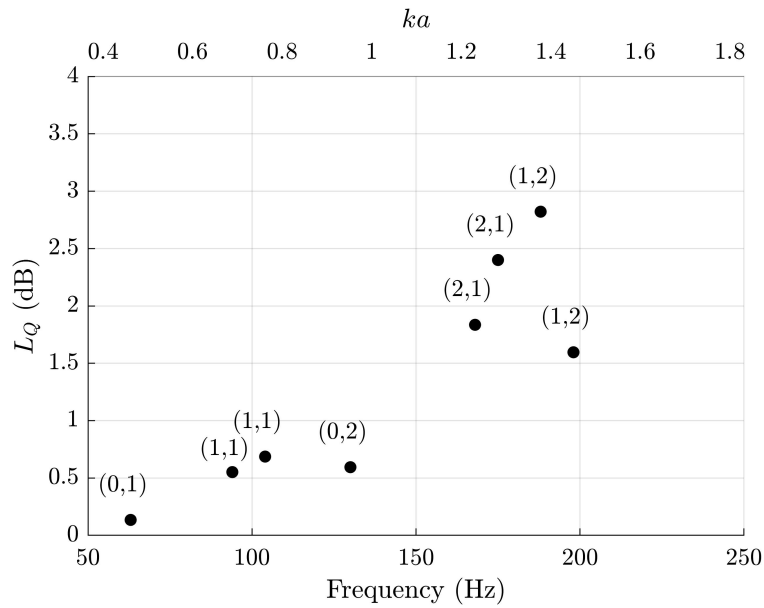


Figure 14.7 Area-weighted directivity factor function deviations L_Q between simulated and propagated far-field patterns for the lowest eight modes.

14.4 Conclusions

The structural mode shapes of the gamelan gong often have close connections to their far-field directivity patterns. The ageng lanang Balinese gamelan gong measured in this work has a set of eight modes over 150 Hz bandwidth spanning the musical notes B1 to G3 (20 semitones). Above this region, a 150 Hz band gap occurs. A spectral regime with increasing modal densities follows this gap.

The surface velocity distributions and nodal lines of the lowest four modes allow qualitative predictions of dipole-like far-field directivity patterns. Multipole expansions using only monopole and dipole fields represent the gong's radiation patterns for these modes with high accuracy. However, higher modes take on more complex patterns that are more difficult to represent with only two contributing field types.

This work only considered the modeling of gong directivity patterns with monopole and dipole fields. Future research could include higher-order (e.g., quadrupole) fields or applying more general equivalent point source methods. Considering the radiation from nonlinearly excited modes would provide a better understanding of the gong's acoustic radiation under normal playing conditions. Another interesting area of future research might include comparing the behaviors of other gongs to gain insights into how the results of this work generalize to other ensemble instruments.

Chapter 15

Radiation From a Vibrating Cap on a Spherical Shell With a Circular Aperture

This chapter derives a low-frequency solution for the radiation from a vibrating cap on a rigid spherical shell with an open circular aperture. The model demonstrates that sources with a cavity or enclosure connected to the exterior domain through a port or aperture have dipole-like directivities at very low frequencies, omnidirectional radiation near the source's Helmholtz resonance frequency, and more complex radiation patterns at higher frequencies. The work relates to the low-frequency results discussed in Ch. 7 for open-back guitar amplifiers.

15.1 Introduction

Theoretical models based on simple spherical geometries have long been used to improve understanding of the directional characteristics of sound sources. Their usefulness primarily results from their geometries, which allow spherical harmonic expansions of the pressure field with analytically determined expansion coefficients. The primary advantage of spherical models over the circular cap in an infinite plane rigid baffle and its counterparts [136, 137, 174] is that they incorporate diffraction

about finite bodies, yielding more realistic approximations over three-dimensional space for practical applications. Consequently, spherical models are desirable for their reliability, computational clarity, and increased realism.

Morse and Ingard derived analytical results for a radially vibrating “cap” (spherical cap or spherical segment of one base) and a point source on a rigid sphere [60, 175]. Among other effects, their results showed omnidirectional radiation for long wavelengths and shadowing behind the sphere, both of which are helpful for understanding basic diffraction effects ranging from those of loudspeaker cabinets [176] to musicians’ bodies [72]. Skudrzyk derived results for an axially vibrating spherical cap and a plane circular cap set in a sphere [71]. The latter employed a least-squares approximation to the expansion coefficients based on a technique developed by Williams et al. [66]. Beranek and Mellow considered radiation from a rectangular cap on a sphere [10], with results that required numerical integration to determine the final values of the expansion coefficients. Aarts and Janssen provided results for axisymmetric velocity distributions by introducing the Zernike polynomials to provide solutions for various Stenzel velocity profiles [138]. Other authors have explored variations such as surrounding a vibrating cap with a pressure-release spherical baffle [177] or a pressure-release belt set in a rigid spherical baffle [178].

Numerous authors have applied spherical models successfully to predict directivities of practical sources. For example, Johansen found in his horn studies that a radially oscillating cap set in a rigid sphere provided excellent agreement with his boundary element method (BEM) simulations [11]. Other authors implemented spherical models to simulate the directivities of regular polyhedron loudspeakers (RPLs) [179–181]. Through superposition, one can easily place multiple vibrating caps, representing loudspeaker drivers of varying sizes and locations, on an otherwise rigid spherical body. When they are combined in this way, the resultant directivities no longer produce a single axis of principal radiation at small wavelengths but instead take on more complex multi-directional

patterns [13]. Beyond loudspeakers, authors have employed the model of a radially vibrating cap on a sphere to represent the radiation and directivity of speech [4, 6, 81, 152].

While each spherical model has included different underlying assumptions about the cap velocity distribution or boundary conditions on the spherical baffle, they all qualitatively suggest the same general directional characteristics: (1) omnidirectional radiation for long wavelengths and (2) strong directivity in front of the vibrating cap with accompanying shadowing behind the sphere for short wavelengths. Consequently, despite their broad applicability and utility in approximating selected source radiation characteristics, they cannot satisfactorily represent other sources without further adaptations. For example, more challenging problems include some ported loudspeakers, open-back guitar amplifiers, and many musical instruments that may not behave as omnidirectional sources at low frequencies. Their lack of omnidirectional behavior is due to the “sound hole sum rule” discussed by Weinreich in his work on the violin [83].

The sound hole sum rule states that when the wavelength is large so that the air motion behaves as an incompressible fluid, source configurations with ports or sound holes connecting the interior cabinet or cavity to the exterior domain have a vanishing monopole moment. This effect occurs as any incompressible flow produced by a vibrating surface is exactly canceled by flow entering through the opening. This volume velocity cancellation allows more complex radiation patterns at low-frequencies, such as dipolar radiation for the violin. As a monopole moment can only form when inertial effects disrupt the exact cancellation of the velocity flow, the Helmholtz resonance of such configurations distinguishes varying directional behavior [83].

Previous works have considered geometries relevant to these problems to a limited extent, although they primarily focused on sound scattering. For example, Miles explored the scattering of a plane wave by a hollow, rigid spherical shell with a circular aperture [182]. Because the resultant boundary value problem (BVP) led to mixed boundary conditions, he presented both a long wavelength approximation and numerically evaluated variational solutions. Elias and

Malb  que considered scattering from a point source located at the center of a similar structure using both the BEM and the method of analytical reduction (MAR) [183], a valuable technique for efficient solutions with both long and short wavelengths [184]. Their results included an analysis of the Helmholtz resonance, radiated sound power, and directivity. More recently, Vinogradava considered scattering from a spherical barrel (a hollow sphere with two circular apertures), also using MAR [185].

Despite its potential to support many modeling applications, one arrangement lacks significant analysis in the literature: the sound radiation from a vibrating cap set on a rigid spherical shell with an open circular aperture. Knowledge of the solution to this problem will benefit researchers and practitioners in several areas of acoustics, whose explorations include relevant vibrations and radiations from cavity-like structures with apertures.

This work develops a solution in the following ways. First, Sec. 15.2 presents the problem formulation and derives two integral equations that solve the BVP, following the general approach used by Miles. The first equation, based on an aperture-velocity formulation, is most useful when the aperture size is smaller than the wavelength. The second equation, based on a potential-layer formulation, reduces to thin-walled boundary integral equations and is more suitable for larger aperture sizes.

While one may discretize both integral equations and numerically solve them using BEMs, Sec. 15.3 instead focuses on a low-frequency approximation based on the concepts of self and mutual radiation impedances between the vibrating cap and aperture. The motivation for this choice follows from a statement by Shaw in his work on the violin. While numerical methods are commonly used in acoustics to solve complex problems, “the cost is high in terms of effort and in the loss of contact with fundamental concepts.” [186] The low-frequency approximation leads to a superposition of two caps on a rigid sphere, one of whose velocity is the given vibrating cap velocity and the other is the aperture particle velocity. Analytical solutions to the self and mutual impedances reveal that

these two equivalent caps vibrate out of phase at low frequencies, while at the Helmholtz resonance frequency, they vibrate in phase.

Further simplification of the self and mutual impedances leads to their lumped-element approximations, including the interior and exterior end corrections for a cap set in a sphere. The lumped element parameters predict essential system characteristics, including the Helmholtz resonance. A multipole expansion of the radiation reveals the low-frequency directional characteristics, including dipole radiation at large wavelengths and quasi-omnidirectionality at the Helmholtz resonance frequency. Finally, Sec. 15.5 validates the results experimentally through directivity measurements of a spherical loudspeaker with a single driver and a variable enclosure aperture.

15.2 Analytical Model

15.2.1 Formulation

Consider a rigid, spherical shell of radius $r = a$ and negligible wall thickness, as depicted in Fig. 15.1. The shell includes a circular aperture of cone half angle α_a centered about (θ_a, ϕ_a) . It also includes a radially vibrating spherical cap of cone half angle α_c centered about (θ_c, ϕ_c) with constant normal surface velocity u_c .

Denote the exterior domain Ω^+ as the region $r > a$ and the interior domain Ω^- as the region $r < a$. Additionally, let Γ_c be the surface of the vibrating cap, Γ_a be the spherical surface of the aperture, and Γ_s be the the surface of the remaining spherical shell.

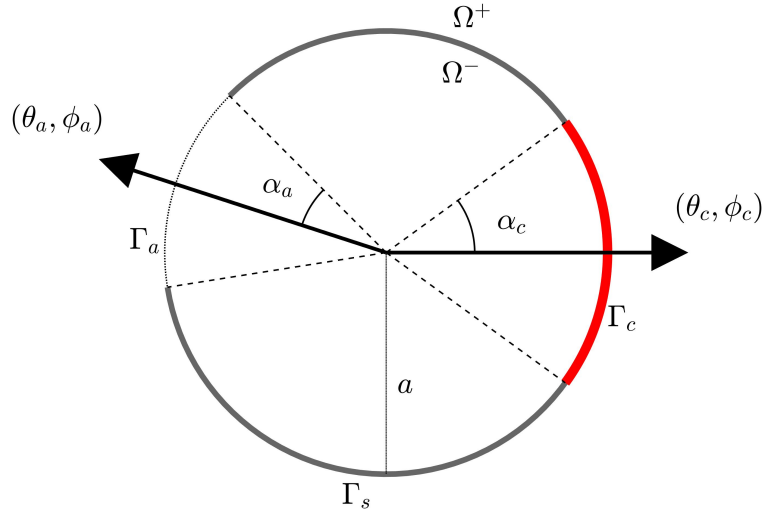


Figure 15.1 Depiction of a vibrating cap (red) on a rigid spherical shell (gray) with an open aperture (dotted line).

The following BVP describes the time-harmonic pressure (for $e^{i\omega t}$ time dependence):

$$\nabla^2 p(r, \theta, \phi) + k^2 p(r, \theta, \phi) = 0, \quad \Omega^+, \Omega^- \quad (15.1)$$

$$\lim_{r \rightarrow \infty} \left(r \left[\frac{\partial p(r, \theta, \phi)}{\partial r} + ikp(r, \theta, \phi) \right] \right) = 0 \quad (15.2)$$

$$u_n(a, \theta, \phi) = \begin{cases} u_c, & \Gamma_c \\ 0, & \Gamma_s \end{cases} \quad (15.3)$$

$$p^+(a, \theta, \phi) = p^-(a, \theta, \phi), \quad \Gamma_a \quad (15.4)$$

$$u_n^+(a, \theta, \phi) = u_n^-(a, \theta, \phi), \quad \Gamma_a, \quad (15.5)$$

where u_n is the particle velocity normal to the spherical surface. Equation 15.2 represents the Sommerfeld radiation condition [62] and Eqs. 15.4 and 15.5 respectively enforce the continuities of pressure and particle velocity across the aperture connecting the interior and exterior domains.

The following sections present two distinct integral equations that solve the BVP, reflecting the general approach of Miles [182]. The first follows from an aperture velocity formulation, whereas the second employs a potential-jump formulation across the surface at $r = a$. The work presents

both methods because the first leads to a low-frequency approximation derived in a later section; the second relates to common boundary integral equations.

15.2.2 Aperture Velocity Solution

One approach to the solution is to superpose two rigid, closed spheres with vibrating caps, as in techniques used to model RPLs and their directivities [180]. The first cap's normal velocity u_c is constant and the second cap's normal velocity $u_a(\theta, \phi)$ is the unknown aperture particle velocity, which generally varies over Γ_a and satisfies the remaining boundary conditions. The total pressure from both caps is

$$p(\mathbf{r}) = p_1(\mathbf{r}) + p_2(\mathbf{r}), \quad (15.6)$$

where p_1 is the pressure produced by the sphere with cap velocity u_c and p_2 is the pressure produced by the sphere with cap velocity (aperture particle velocity) $u_a(\theta, \phi)$.

An eigenfunction expansion yields the pressure p_1 for a radially vibrating cap on a rigid sphere. Expanding the associated particle velocity u_1 in terms of spherical harmonics gives

$$u_1(\theta, \phi) = \sum_{n=0}^{\infty} \sum_{m=-n}^n U_n^m Y_n^m(\theta, \phi), \quad (15.7)$$

where $Y_n^m(\theta, \phi)$ are the normalized spherical harmonics of degree n and order m [70] and

$$U_n^m = u_c Q_n(\alpha_c) \frac{4\pi}{(2n+1)} [Y_n^m(\theta_c, \phi_c)]^*, \quad (15.8)$$

where $*$ denotes complex conjugation. The coefficients Q_n are [10]

$$Q_n(\alpha_c) = \begin{cases} \frac{1}{2}(1 - \cos \alpha_c), & n = 0 \\ \frac{1}{2}[P_{n-1}(\cos \alpha_c) - P_{n+1}(\cos \alpha_c)], & n > 0 \end{cases}, \quad (15.9)$$

where P_n are the Legendre polynomials, such that

$$\sum_{n=0}^{\infty} Q_n(\alpha_c) P_n(\cos \theta) = \begin{cases} 1, & \theta < \alpha_c \\ 0, & \theta > \alpha_c \end{cases}. \quad (15.10)$$

Additionally, the surface area of a cap of angle α_c is

$$S_c = 2\pi a^2(1 - \cos \alpha_c). \quad (15.11)$$

Equation 16.15 provides the Legendre polynomial expansion coefficients of a unit amplitude cap for the axisymmetric case $(\theta_c, \phi_c) = (0, 0), u_c = 1$. Additionally, Eq. 15.8 uses the spherical harmonic addition theorem [70]

$$P_n(\cos \Theta) = \sum_{m=-n}^n Y_n^m(\theta, \phi) [Y_n^m(\theta', \phi')]^*, \quad (15.12)$$

where Θ is the angle between (θ, ϕ) and (θ', ϕ') , to rotate the vibrating cap to arbitrary (θ_c, ϕ_c) .

Applying Euler's equation yields the pressure both inside and outside the sphere:

$$p_1(r, \theta, \phi) = \begin{cases} -iz_0 \sum_{n=0}^{\infty} \sum_{m=-n}^n U_n^m \frac{j_n(kr)}{j_n(ka)} Y_n^m(\theta, \phi), & r < a \\ -iz_0 \sum_{n=0}^{\infty} \sum_{m=-n}^n U_n^m \frac{h_n^{(2)}(kr)}{h_n^{(2)'}(ka)} Y_n^m(\theta, \phi), & r > a, \end{cases} \quad (15.13)$$

where j_n and $h_n^{(2)}$ are the spherical Bessel and Hankel functions of order n and $z_0 = \rho_0 c$ is the characteristic specific acoustic impedance of the medium. By allowing $r \rightarrow \infty$, the large-argument relation for the spherical Hankel function yields an unnormalized far-field directivity pattern $\tilde{D}(\theta, \phi)$:

$$\tilde{D}(\theta, \phi) = \sum_{n=0}^{\infty} \sum_{m=-n}^n c_n^m i^{n+1} Y_n^m(\theta, \phi). \quad (15.14)$$

The pressure p_2 produced by the cap second representing the aperture particle velocity follows similarly. The spherical harmonic expansion coefficients relate to $u_a(\theta, \phi)$ through the orthogonality of the spherical harmonics:

$$V_n^m = \int_0^{2\pi} \int_0^\pi u_a(\theta, \phi) [Y_n^m(\theta, \phi)]^* \sin \theta d\theta d\phi. \quad (15.15)$$

The integral vanishes outside of Γ_a and the resultant pressure is

$$p_2(r, \theta, \phi) = \begin{cases} -iz_0 \sum_{n=0}^{\infty} \sum_{m=-n}^n V_n^m \frac{j_n(kr)}{j_n(ka)} Y_n^m(\theta, \phi) & r < a \\ -iz_0 \sum_{n=0}^{\infty} \sum_{m=-n}^n V_n^m \frac{h_n^{(2)}(kr)}{h_n^{(2)'}(ka)} Y_n^m(\theta, \phi) & r > a \end{cases}. \quad (15.16)$$

Continuity boundary conditions across the aperture determine $u_a(\theta, \phi)$ and its expansion coefficients V_n^m . To derive the result, first let δp_1 be the pressure difference of p_1 across the boundary $r = a$ of the closed sphere with a radially vibrating cap:

$$\delta p_1(\theta, \phi) = -iz_0 \sum_{n=0}^{\infty} \sum_{m=-n}^n \zeta_n U_n^m Y_n^m(\theta, \phi), \quad (15.17)$$

where, with the aid of the Wronskian relationship

$$j'_n(ka)h_n(ka) - h'_n(ka)j_n(ka) = \frac{i}{(ka)^2}, \quad (15.18)$$

the expansion coefficient is

$$\zeta_n = \frac{i}{j'_n(ka)h'_n(ka)(ka)^2}. \quad (15.19)$$

The pressure difference δp_2 caused by the aperture cap has a form similar to Eq. 15.17 but with U_n^m replaced by V_n^m . The total pressure difference δp is then

$$\begin{aligned} \delta p(\theta, \phi) &= \delta p_1(\theta, \phi) - \delta p_2(\theta, \phi) \\ &= \delta p_1(\theta, \phi) - iz_0 \sum_{n=0}^{\infty} \sum_{m=-n}^n \zeta_n V_n^m Y_n^m(\theta, \phi). \end{aligned} \quad (15.20)$$

Applying continuity of pressure ($\delta p = 0$) at the boundary yields

$$iz_0 \sum_{n=0}^{\infty} \sum_{m=-n}^n \zeta_n V_n^m Y_n^m(\theta, \phi) = \delta p_1(\theta, \phi), \quad (\theta, \phi) \in \Gamma_a, \quad (15.21)$$

so that substituting Eq. 15.15 into Eq. 15.21 gives the integral equation

$$\iint_{\Gamma_a} u_a(\theta', \phi') K_a(\cos \Theta) \sin \theta' d\theta' d\phi' = \delta p_1(\theta, \phi), \quad (\theta, \phi) \in \Gamma_a \quad (15.22)$$

where

$$K_a(\cos \Theta) = iz_0 \sum_{n=0}^{\infty} \zeta_n \frac{2n+1}{4\pi} P_n(\cos \Theta). \quad (15.23)$$

The integral equation only requires evaluation on Γ_a . Equation 15.22 corresponds to Ref. 182 Eq. (26), except with a different definition of δp because Miles' formulation considered the pressure

jump due to a plane wave and not a vibrating cap on a rigid sphere. Standard numerical procedures can discretize and solve the integral equation for u_a since K_a and δp_1 are known [182, 187].

Finally, extrapolating Eq. 15.16 to the far field and applying Eq. 15.15 gives the far-field directivity produced by the aperture

$$\tilde{D}_a(\theta, \phi) = \int_0^{2\pi} \int_0^\pi u_a(\theta', \phi') K_{ff}(\cos \Theta) \sin \theta' d\theta' d\phi', \quad (15.24)$$

with

$$K_{ff}(\cos \Theta) = z_0 \sum_{n=0}^{\infty} \frac{i^n}{h'_n(ka)} \frac{2n+1}{4\pi} P_n(\cos \Theta). \quad (15.25)$$

15.2.3 Potential Layer Solution

The potential layer approach determines the pressure as a result of a pressure jump δp across the spherical boundary $r = a$. Expressing the potential layer δp in terms of a spherical harmonic expansion and then applying Euler's equation and the associated boundary conditions yields another integral equation, this time over $\Gamma_c \cup \Gamma_s$: [182]

$$\iint_{\Gamma_c \cup \Gamma_s} \delta p(\theta', \phi') g_s(\cos \Theta) \sin \theta' d\theta' d\phi' = iz_0 u_n(\theta, \phi), \quad (\theta, \phi) \in \Gamma_c \cup \Gamma_s. \quad (15.26)$$

where

$$g_s(\cos \Theta) = \sum_{n=0}^{\infty} \zeta_n^{-1} \frac{2n+1}{4\pi} P(\cos \Theta). \quad (15.27)$$

This integral equation coincides with Ref. 182 Eq. (57).

Given the expression for the free-space Green's function in terms of spherical harmonics [182],

$$G(\mathbf{r}, \mathbf{r}') = - \sum_{n=0}^{\infty} ikh_n^{(2)}(kr) j_n(kr') \frac{2n+1}{4\pi} P(\cos \Theta), \quad (15.28)$$

when \mathbf{r} and \mathbf{r}' are on the surface $r = a$,

$$\frac{\partial^2}{\partial r \partial r'} G(\mathbf{r}, \mathbf{r}') = - \frac{k}{a^2} g_s(\cos \Theta) \quad (15.29)$$

and one obtains

$$\iint_{\Gamma_c \cup \Gamma_s} \delta p(\mathbf{r}') \frac{\partial^2}{\partial n \partial n'} G(\mathbf{r}, \mathbf{r}') dS = -iz_0 k u_n(\mathbf{r}), \quad (15.30)$$

which is a thin-body formulation of the hyper-singular boundary integral equation [188–190]. Reference 187 contains more details concerning its numerical implementation and the necessary handling of the kernel's singularities.

Importantly, one solves Eq. 15.22 over Γ_a whereas one solves Eq. 15.30 over $\Gamma_c \cup \Gamma_s$. Consequently, when considering the total number of discretized unknowns, Eq. 15.22 is more appropriate for a small aperture size, whereas Eq. 15.30 is more appropriate for a large aperture size.

15.3 Low-Frequency Approximations

15.3.1 Vibrating Cap Self and Mutual Impedance

Consider the aperture velocity formulation presented in Sec. 15.2.2. Assuming the aperture velocity is roughly constant at low frequencies allows a simplified approximation based on the superposition of two radially vibrating caps on a sphere. Determining the aperture velocity amplitude requires the self and mutual impedances between these two caps. Consequently, this section develops the self and mutual impedances between two radially vibrating caps on a sphere. The first has a cone half angle α_1 and surface area S_1 , while the second has a cone half angle α_2 and surface area S_2 .

On the exterior side, the self acoustic impedance of the first cap is [10, 191]

$$Z_{A,11}^+ = \frac{\langle p_1 \rangle_{S_1}^+}{U_1} \Big|_{U_2=0} = \frac{-i4\pi a^2 z_0}{S_1^2} \sum_{n=0}^{\infty} \frac{h_n^{(2)}(ka)}{h_n^{(2)'}(ka)} \frac{Q_n^2(\alpha_1)}{(2n+1)}. \quad (15.31)$$

On the interior side, the self impedance follows by replacing the spherical Hankel functions with spherical Bessel functions:

$$Z_{A,11}^- = \frac{\langle p_1 \rangle_{S_1}^-}{U_1} \Big|_{U_2=0} = \frac{-i4\pi a^2 z_0}{S_1^2} \sum_{n=0}^{\infty} \frac{j_n(ka)}{j_n'(ka)} \frac{Q_n^2(\alpha_2)}{(2n+1)}. \quad (15.32)$$

The self impedances of the second cap follow similarly.

The exterior mutual acoustic impedance between the first and second caps is [191]

$$\begin{aligned} Z_{A,12}^+ &= \left. \frac{\langle p_1 \rangle_{S_1}^+}{U_2} \right|_{U_1=0} \\ &= \frac{-i4\pi a^2 z_0}{S_1 S_2} \sum_{n=0}^{\infty} P_n(\cos \Theta_{12}) \frac{h_n^{(2)}(ka)}{h_n^{(2)'}(ka)} \frac{Q_n(\alpha_1) Q_n(\alpha_2)}{(2n+1)}, \end{aligned} \quad (15.33)$$

where Θ_{12} is the angle between the centers of the two caps. For the interior side, the mutual impedance is

$$\begin{aligned} Z_{A,12}^- &= \left. \frac{\langle p_1 \rangle_{S_1}^-}{U_2} \right|_{U_1=0} \\ &= \frac{-i4\pi a^2 z_0}{S_1 S_2} \sum_{n=0}^{\infty} P_n(\cos \Theta_{12}) \frac{j_n(ka)}{j_n'(ka)} \frac{Q_n(\alpha_1) Q_n(\alpha_2)}{(2n+1)}. \end{aligned} \quad (15.34)$$

The mutual impedances $Z_{A,21}^+ = Z_{A,12}^+$ and $Z_{A,21}^- = Z_{A,12}^-$ from acoustic reciprocity, which is apparent from the formulas.

15.3.2 Approximation using Eigenfunction Expansion

At low frequencies, the self and mutual impedances relate the cap volume velocity $U_c = u_c S_c$ to the unknown aperture volume velocity U_a in the following way. The total spatially-averaged pressure at the aperture opening due to both caps is

$$\langle p_a \rangle_{S_a}^{\pm} = U_a Z_{A,aa}^{\pm} + U_c Z_{A,ac}^{\pm}, \quad (15.35)$$

where $Z_{A,aa}$ is the self impedance, $Z_{A,ac}$ is the mutual impedance, and the \pm symbol indicates that the expression holds for both the exterior and interior sides. Replacing the point-wise continuity of the pressure (Eq. 15.4) with continuity of the spatially averaged pressure requires that

$$U_a = -U_c \left(\frac{Z_{A,ac}^+ - Z_{A,ac}^-}{Z_{A,aa}^+ - Z_{A,aa}^-} \right). \quad (15.36)$$

Thus, under the approximation of uniform aperture particle velocity ($u_a S_a = U_a$), the low-frequency representation of V_n^m becomes

$$V_n^m \approx u_a \frac{4\pi R_n(\alpha_a)}{(2n+1)} [Y_n^m(\theta_a, \phi_a)]^* . \quad (15.37)$$

The total pressure field becomes

$$p(r, \theta, \phi, k) = \sum_{n=0}^{\infty} \sum_{m=-n}^n g_n^m(k) h_n^{(2)}(kr) Y_n^m(\theta, \phi) \quad (15.38)$$

where

$$g_n^m = \frac{-iz_0}{h_n^{(2)'}(ka)} \frac{4\pi}{(2n+1)} \{ u_c R_n(\alpha_c) [Y_n^m(\theta_c, \phi_c)]^* + u_a R_n(\alpha_a) [Y_n^m(\theta_a, \phi_a)]^* \} . \quad (15.39)$$

15.3.3 Network Representation

Equation 15.36 allows an approximation of the aperture volume velocity for wavelengths large compared to the aperture size by relating the self and mutual impedances of the vibrating cap and aperture to each other. Additional simplification follows by representing each impedance as a lumped-element component. The lumped-element representation is particularly beneficial for estimating the Helmholtz resonance of the cavity and understanding the low-frequency behavior of the aperture volume velocity.

For long wavelengths, the small-argument approximation of the ratio [70]

$$\frac{h_n^{(2)}(ka)}{h_n^{(2)'}(ka)} \approx \frac{-ka}{n+1}, \quad ka \ll 1 \quad (15.40)$$

in Eq. 15.31 yields

$$\begin{aligned} Z_{A,11}^+ &\approx \tilde{Z}_{A,11}^+ \\ &= \frac{i4\pi a^3 z_0 k}{S_1^2} \sum_{n=0}^{\infty} \frac{Q_n^2(\alpha_1)}{(2n+1)(n+1)} \\ &= \frac{i\omega \rho_0 l_1^+}{S_1}, \end{aligned} \quad (15.41)$$

where \tilde{Z} indicates a lumped-element impedance approximation and

$$l_1^+ = \frac{4\pi a^3}{S_1} \sum_{n=0}^{\infty} \frac{Q_n^2(\alpha_1)}{(2n+1)(n+1)} \quad (15.42)$$

is the exterior end correction. Thus, the exterior self-impedance of the vibrating cap involves only an acoustic mass-like element.

The acoustic impedance of the same cap looking in to the cavity involves both acoustic compliance and acoustic mass elements in series. The compliance stems from the $n = 0$ expansion term, whereas the mass follows from the $n > 0$ terms. The $n = 0$ term reduces by applying small-argument approximations to the spherical Bessel functions [70], such that

$$\frac{j_0(ka)}{j'_0(ka)} \approx \frac{-3}{ka} \quad (15.43)$$

and Eq. 15.32 becomes

$$\begin{aligned} \frac{-i4\pi a^2 z_0}{S_1^2} \frac{j_0(ka)}{j'_0(ka)} Q_0^2(\alpha_1) &\approx \frac{i12\pi a z_0}{k} \frac{R_0^2(\alpha_1)}{S_1^2} \\ &= \frac{i3\rho_0 c^2}{4\pi a^3 \omega}, \end{aligned} \quad (15.44)$$

since $R_0(\alpha_1) = \frac{1}{2}(1 - \cos \alpha_1)$ and $S_1^2 = 2\pi a^2(1 - \cos \alpha_1)$. The terms for $n > 0$ reduce through the approximation

$$\frac{j_n(ka)}{j'_n(ka)} \approx \frac{ka}{n}, \quad ka \ll 1, \quad n > 0, \quad (15.45)$$

such that

$$\begin{aligned} \frac{-i4\pi a^2 z_0}{S_1^2} \sum_{n=1}^{\infty} \frac{j_n(ka)}{j'_n(ka)} \frac{Q_n^2(\alpha_1)}{(2n+1)} &\approx \frac{-i4\pi a^3 k z_0}{S_1^2} \sum_{n=1}^{\infty} \frac{R_n^2(\alpha_1)}{n(2n+1)} \\ &= \frac{-i\omega\rho_0 l_1^-}{S_1}, \end{aligned} \quad (15.46)$$

where l_1^- is the interior end correction

$$l_1^- = \frac{4\pi a^3}{S_1} \sum_{n=1}^{\infty} \frac{Q_n^2(\alpha_1)}{n(2n+1)}. \quad (15.47)$$

Combining both terms yields

$$Z_{A,11}^- \approx \tilde{Z}_{A,11}^- = -\frac{\rho_0 c^2}{i\omega V} - \frac{i\omega\rho_0 l_1^-}{S_1}, \quad (15.48)$$

where $V = 4\pi a^3/3$ is the sphere's volume. Interestingly, only the acoustic mass depends on the cap cone half angle α_1 . The negative signs appearing in Eq. 15.48 result from the definition of the normal direction of the sphere. For example, at very low frequencies where the acoustic compliance dominates, a negative cap velocity should lead to a compression in the cavity.

The mutual impedances simplify in a similar manner. On the exterior side,

$$Z_{A,12}^+ \approx \tilde{Z}_{A,12}^+ = \frac{i\omega\rho_0 l_{12}^+}{S_2}, \quad (15.49)$$

which is again mass like, with an exterior mutual end correction

$$l_{12}^+ = \frac{4\pi a^3}{S_1} \sum_{n=0}^{\infty} P_n(\cos\Theta_{12}) \frac{R_n(\alpha_1)R_n(\alpha_2)}{(2n+1)(n+1)}. \quad (15.50)$$

The mutual impedance inside the sphere incorporates an acoustic compliance and mass in series:

$$Z_{A,12}^- \approx \tilde{Z}_{A,12}^- = -\frac{\rho_0 c^2}{i\omega V} - \frac{i\omega\rho_0 l_{12}^-}{S_2} \quad (15.51)$$

where the interior mutual end correction is

$$l_{12}^- = \frac{4\pi a^3}{S_1} \sum_{n=1}^{\infty} P_n(\cos\Theta_{12}) \frac{R_n(\alpha_1)R_n(\alpha_2)}{n(2n+1)}. \quad (15.52)$$

Figure 15.2 plots the normalized self acoustic reactances on the exterior and interior and exterior sides of a vibrating cap on a sphere with cone half angle $\alpha_1 = 10^\circ$. The black curves represent the values from the expansions given in Eqs. 15.31 and 15.32. The dashed red curves represent the low-frequency approximations from Eqs. 15.44 and 15.48. For the exterior reactance, the low-frequency approximation remains reasonable even for $ka > 1$; however, the presence of modes within the spherical cavity limit the low-frequency approximation for the interior reactance.

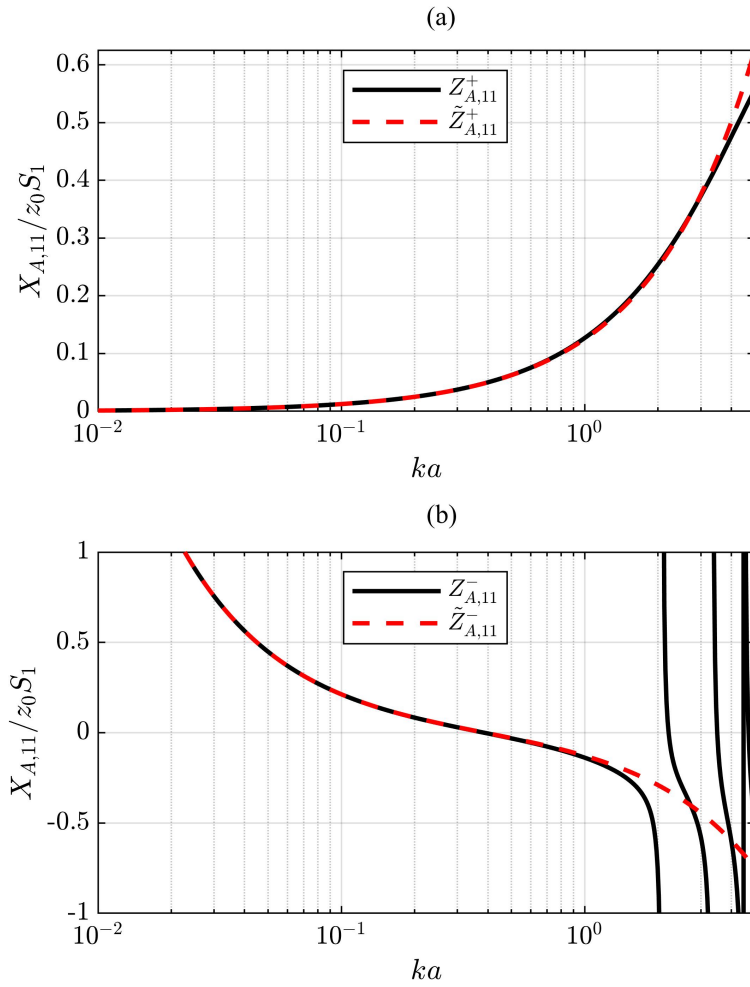


Figure 15.2 Self acoustic reactances of a vibrating cap on a closed sphere: (a) external side and (b) internal side. The red dashed curves represent low-frequency approximations.

15.3.4 Aperture Volume Velocity

Using the lumped-element impedance representations in Eq. 15.36 produces the following estimate for the aperture volume velocity:

$$\tilde{U}_a = -U_c \left[\frac{S_a - k^2 V (l_{ac}^+ + l_{ac}^-)}{S_a - k^2 V (l_a^+ + l_a^-)} \right]. \quad (15.53)$$

In the case that $ka \ll 1$ the aperture volume velocity becomes

$$\tilde{U}_a = -U_c. \quad (15.54)$$

Thus, as one may anticipate from near-incompressible flow at low-frequencies, the fluid externally displaced by the vibrating cap equals the fluid entering through the aperture. This equation consequently verifies Weinreich's "sound hole sum rule" [83] for this spherical geometry and leads to a strong dipole moment at these frequencies [See Sec. 15.3.5].

Finally, from Eq. 15.53 one can estimate the Helmholtz resonance frequency in terms of the lumped element parameters by solving for the zero of the denominator. From Eq. 15.36 it is apparent that the zero occurs when $Z_{A,a}^+ = Z_{A,a}^-$. Applying the lumped-element values yields the Helmholtz resonance frequency [192]

$$\tilde{f}_H = \frac{c}{2\pi} \sqrt{\frac{S_a}{V(l_a^+ + l_a^-)}}. \quad (15.55)$$

This equation highlights the importance of including the cavity inertance, represented by the interior end correction l_a^- , for predicting f_H . [193]

Figure 15.3 plots the magnitude and phase of the aperture volume velocity for the parameters $\alpha_c = 10^\circ$, $(\theta_c, \phi_c) = (90^\circ, 0^\circ)$, $\alpha_a = 12^\circ$, $(\theta_a, \phi_a) = (90^\circ, 180^\circ)$, and $u_c = 1$ mm/s. The blue curve presents the aperture volume velocity calculated from Eq. 15.36, whereas the green dashed curve shows the lumped-element prediction of the volume velocity from Eq. 15.53. The horizontal black dash-dot line indicates the volume velocity of the cap U_c , and the vertical red dotted line shows the estimated Helmholtz resonance frequency \tilde{f}_H from the lumped-element parameters.

For very small ka , both U_a and U_c converge to the same magnitude value but are 180° out of phase as described by Eq. 15.54. As frequency increases, the magnitude has a sharp peak very near \tilde{f}_H , at which point the aperture volume velocity changes to being in phase with the cap volume velocity. Above \tilde{f}_H , the lumped-element representation predicts that $|\tilde{U}_a|$ from Eq. 15.53 will continue to decrease; however, the curve representing $|U_a|$ from Eq. 15.36 shows that after dropping below $|U_c|$, $|U_a|$ increases again. Nonetheless, the results suggest that for $ka < 1$, the lumped-element approximation \tilde{U}_a gives a reasonable approximation to U_a . This simplification may be beneficial for other cavity geometries where the exact forms of the self and mutual impedances are unknown but one may estimate parameters such as cavity volume, surface area, and end-corrections.

15.3.5 Multipole Moments

At low frequencies, it is possible to predict the directional behavior of the source by considering its multipole representation [62]. The multipole expansion follows from a Taylor series approximation of the Green's function employed in the Kirchhoff Helmholtz integral theorem. This allows computation of the monopole, dipole, and higher-order moments from surface integrals based on the known pressure and normal particle velocity on the boundary [40, 62].

For example, the monopole moment is

$$M = \iint i z_0 k u_n(\mathbf{r}) dS, \quad (15.56)$$

whereas the dipole moment is

$$\mathbf{D} = \iint i z_0 k \mathbf{r} u_n(\mathbf{r}) + \mathbf{n} p(\mathbf{r}) dS. \quad (15.57)$$

Based on these two moments, the resultant field is then

$$p(\mathbf{r}) \approx p_m(\mathbf{r}) + p_d(\mathbf{r}) \quad (15.58)$$

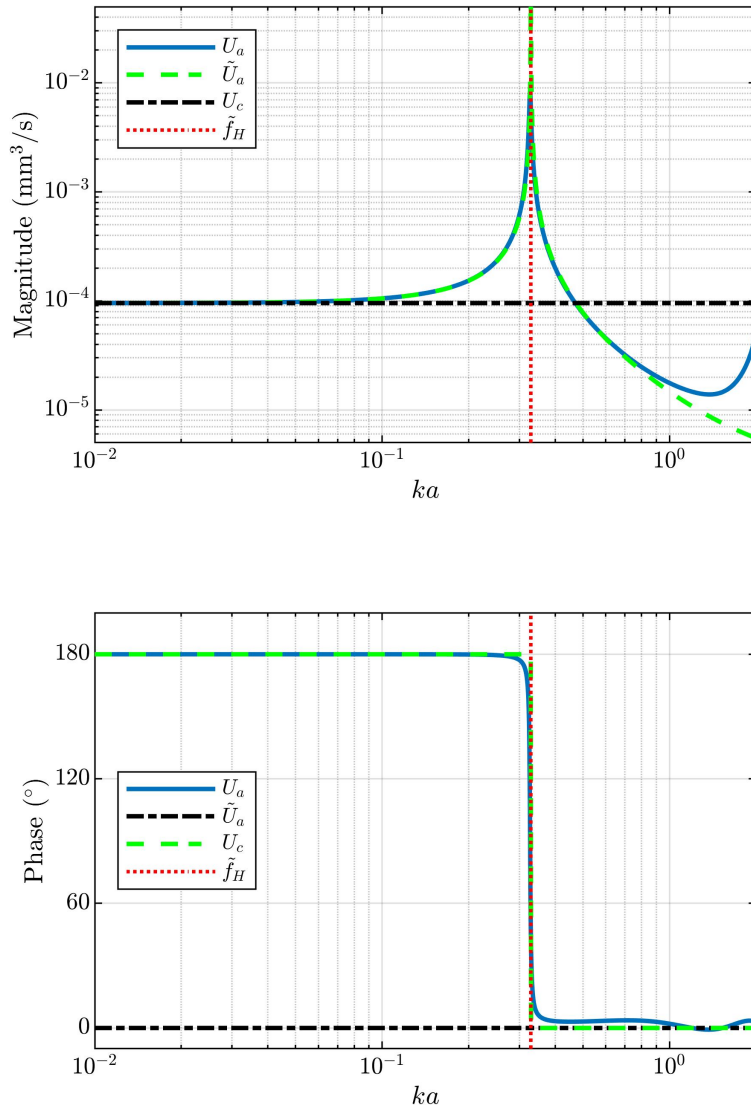


Figure 15.3 Magnitude and phase of the aperture volume velocity.

where

$$p_m(\mathbf{r}) = M \frac{e^{-ikr}}{4\pi r} \quad (15.59)$$

and

$$p_d(\mathbf{r}) = ik \frac{e^{-ikr}}{4\pi r} \left(1 - \frac{i}{kr}\right) \mathbf{d} \cdot \mathbf{e}_r. \quad (15.60)$$

Because of the similarity between the multipole sources and the spherical wave functions comprised of spherical harmonics and spherical Hankel functions, it is possible to assign values of the expansion coefficients to respective multipole moments [59,61]. However, only in the limit of $ka \ll 1$ do the relations between the expansion coefficients and the values produced by the surface integrals in Eqs. 15.56 and 15.57 become equal.

Consider the monopole moment $M = iz_0 k U_m$, where U_m is the equivalent monopole source strength (volume velocity). By equating terms in the spherical harmonic expansion to the pressure field of Eq. 15.59, it is evident that [59]

$$U_m = \frac{\sqrt{4\pi}}{z_0 k^2} g_0^0(k). \quad (15.61)$$

By substituting the value for $g_n^m(k)$ from Eq. 15.39 and using $Y_0^0(\theta, \phi) = 1/\sqrt{4\pi}$ and $S_i = 4\pi a^2 Q_0(\alpha_i)$, one arrives at the result

$$U_m = \frac{-i(U_c + U_a)}{(ka)^2 h_0^{(2)'}(ka)}. \quad (15.62)$$

If $ka \ll 1$, then the derivative of the spherical Hankel function simplifies the expression further so that

$$U_m \approx U_c + U_a. \quad (15.63)$$

This result shows that for long wavelengths, the equivalent monopole volume velocity is the net volume velocity on the spherical surface as shown by Eq. 15.56. Because of the results in Sec. 15.3.4, when $ka \ll 1$, $U_m \rightarrow 0$ and the monopole moment vanishes.

Similarly, the source's dipole moment follows by equating terms from the dipole pressure expression and the expansion components. Because the dipole moments in the \mathbf{e}_x and \mathbf{e}_y directions both contribute to the positive and negative-order spherical harmonic of degree one, it is convenient to express the relation to the expansion coefficients using the matrix form

$$\begin{bmatrix} d_x \\ d_y \\ d_z \end{bmatrix} = \frac{i\sqrt{6\pi}}{k^2} \begin{bmatrix} 1 & 0 & -1 \\ -i & 0 & -i \\ 0 & \sqrt{2} & 0 \end{bmatrix} \begin{bmatrix} g_1^{-1} \\ g_1^0 \\ g_1^1 \end{bmatrix}. \quad (15.64)$$

While this result describes the most general relation between the degree-one expansion coefficients and the dipole moment, it is worthwhile to consider the special case where the cap and aperture align on the z-axis [i.e., $(\theta_c, \phi_c) = (0^\circ, 0^\circ)$ and $(\theta_a, \phi_a) = (180^\circ, 0^\circ)$]. Then by symmetry, the dipole components d_x and d_y become zero and the z-component of the dipole moment becomes

$$d_z = \frac{3\pi z_0}{h_1^{(2)'}(ka)k^2} (u_c \sin^2 \alpha_c - u_a \sin^2 \alpha_a), \quad (15.65)$$

where the development used $Q_1(\alpha_i) = 3/4 \sin^2 \alpha_i$ and $Y_1^0(\theta, \phi) = \sqrt{3/4\pi} \cos(\theta)$. For $ka \ll 1$, the expression simplifies further to

$$d_z \approx iz_0 k \frac{3\pi a^3}{2} (u_c \sin^2 \alpha_c - u_a \sin^2 \alpha_a). \quad (15.66)$$

This term relates directly to Eq. 15.57 in the following manner. Suppose the dipole moment results from a single vibrating cap of angle α_c , oriented at $(\theta_c, \phi_c) = (0, 0)$, and with constant normal velocity u_i . The integral of Eq. 15.57 splits into two integrals, one for the normal component of the particle velocity and one for the pressure. The first integral becomes

$$I_1 = iz_0 k 2\pi a^3 u_c \int_0^{\alpha_c} \cos \theta \sin \theta d\theta \quad (15.67)$$

$$= iz_0 k u_c \pi a^3 \sin^2 \alpha_c, \quad (15.68)$$

where $z = a \cos \theta$. For the second integral, one must use the entire expansion of Eq. 16.5 for the pressure. However, because the z component of the sphere's unit normal vector is $n_z = \cos \theta =$

$\sqrt{3/4\pi}Y_0^1(\theta, \phi)$, only the c_0^1 term remains due to orthogonality, such that

$$I_2 = -i4\pi z_0 a^2 \frac{h_1(ka)}{3h_1^{(2)'}(ka)} u_i Q_1(\alpha_i) \frac{3}{4\pi} \quad (15.69)$$

$$= iz_0 k a^3 \frac{\pi}{2} u_i \sin^2 \theta, \quad (15.70)$$

provided that $ka \ll 1$. Thus, the total moment for a single cap becomes

$$L_i = iz_0 k \frac{3\pi a^3}{2} u_i \sin^2 \alpha_i, \quad (15.71)$$

from which one can generalize that for N caps, each directed toward \mathbf{n}_i ,

$$\mathbf{d} = \sum_{i=1}^N \mathbf{n}_i L_i, \quad ka \ll 1. \quad (15.72)$$

Substituting appropriate values of \mathbf{n}_i and L_i for the cap and aperture aligned on the z axis yields

$$\mathbf{d} = (L_c - L_a) \mathbf{e}_z, \quad ka \ll 1, \quad (15.73)$$

which is equivalent to Eq. 15.66.

Equations 15.63 and 15.72 are simplifications to the more general problem. However, they are useful for clarifying the directional nature of the source, which the upcoming sections will explore in greater detail.

15.3.6 Radiated Sound Power

Once the expansion coefficients g_n^m are known, the time-averaged sound power radiated by the source relates as [59]

$$\langle W(k) \rangle_t = \frac{1}{2z_0 k^2} \sum_{n=0}^{\infty} \sum_{m=-n}^n |g_n^m(k)|^2. \quad (15.74)$$

The power radiated by the $n = 0$ term, associated with the monopole moment, is

$$\langle W(k) \rangle_t^{(m)} = \frac{z_0 k^2 |U_m|^2}{8\pi}, \quad (15.75)$$

which tends to 0 for low frequencies since U_m vanishes. The power radiated from the $n = 1$ terms, associated with the dipole moment, is

$$\langle W(k) \rangle_t^{(d)} = \frac{k^2}{24\pi z_0} \sum_{\mu=1}^3 |d_\mu|^2. \quad (15.76)$$

When the cap and aperture are aligned on the z axis, the expression simplifies to

$$\langle W(k) \rangle_t^{(d)} \approx \frac{z_0 3\pi (ka)^4}{32} |u_c a \sin^2 \alpha_c - u_a a \sin^2 \alpha_a|^2. \quad (15.77)$$

Finally, when the cap and aperture have the same size ($\alpha_c = \alpha_a$) and in the case that $ka \ll \ll 1$ so $u_c = -u_a$,

$$\langle W(k) \rangle_t^{(d)} \approx \frac{z_0 3\pi (ka)^4}{8} |u_c|^2 a^2 \sin^4 \alpha_c. \quad (15.78)$$

Figure 15.4 shows several calculated sound power level curves for an equal-sized cap and aperture ($\alpha_c = \alpha_a = 20^\circ$) placed on opposing sides $[(\theta_c, \phi_c) = (90^\circ, 0^\circ)$ and $(\theta_a, \phi_a) = (90^\circ, 180^\circ)]$ of a sphere of radius $a = 1$ m, with cap particle velocity $u_c = 1.0$ mm/s. The black curve shows the total sound power level calculated from Eq. 17.15. The green dotted line indicates the contribution from the monopole-associated term $n = 0$ [Eq. 15.75], and the red dashed line indicates the contribution from the dipole-associated terms with $n = 1$ [Eq. 15.76]. Finally, the blue line shows the low-frequency approximation for the dipole term from Eq. 15.78.

With the sound power contribution of the monopole and dipole moments separated, it is possible to predict the directional nature of the source qualitatively, provided that the aperture size is small enough that all assumptions remain valid. Well below the Helmholtz resonance frequency, indicated by the vertical red dotted line in Fig. 15.4, most of the radiated sound power is from the dipole term, such that dipolar radiation is likely [83]. As frequency approaches the Helmholtz resonance frequency, the directivity becomes more monopolar. Finally, above resonance, the relative contributions of the monopole and dipole terms vary, suggesting more complex directivity patterns.

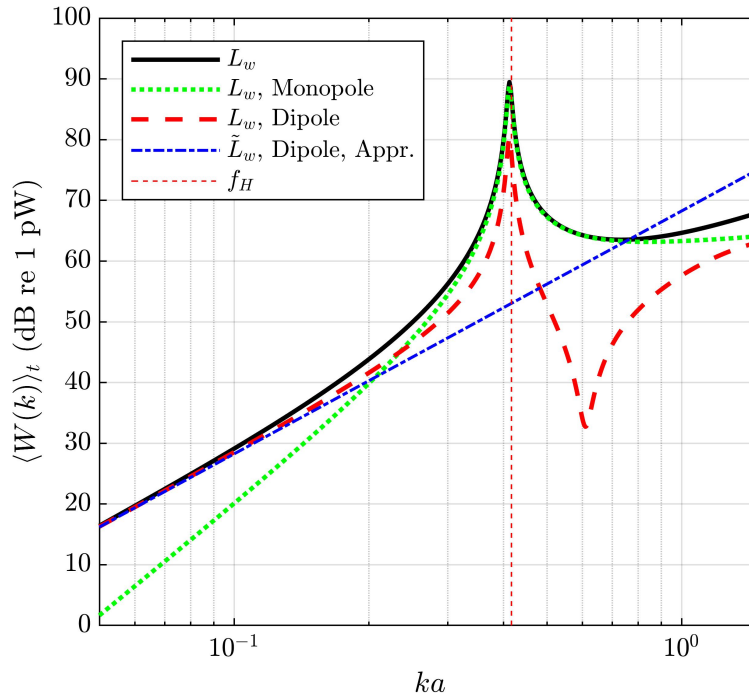


Figure 15.4 Calculated sound power levels of vibrating cap on a sphere.

15.4 Theoretical Results

15.4.1 Comparison with BEM Results

A BEM implementation of Eq. 15.22 allows a numerical validation of the low-frequency approximation. Figure 15.5 shows area-weighted directivity factor function deviation levels [81] L_Q between the BEM solution and the low-frequency approximation for three different Θ_{ca} values and $\alpha_c = \alpha_a = 18^\circ$. For $ka < 1$, the low-frequency approximation and BEM solution show excellent agreement; a frequency-averaged deviation over this range is less than 0.1 dB. For $ka > 1$, the deviations depend upon Θ_{ca} . When the cap and aperture are on opposing sides of the sphere ($\Theta_{ca} = 180^\circ$), they are generally small, remaining below 1.0 dB up to at least $ka = 10$. However, when $\Theta_{ca} = 90^\circ$ or $\Theta_{ca} = 135^\circ$, deviations greater than 1 dB occur above $ka = 3$. When the cap and aperture align, only axisymmetric particle velocity distributions occur at the aperture surface;

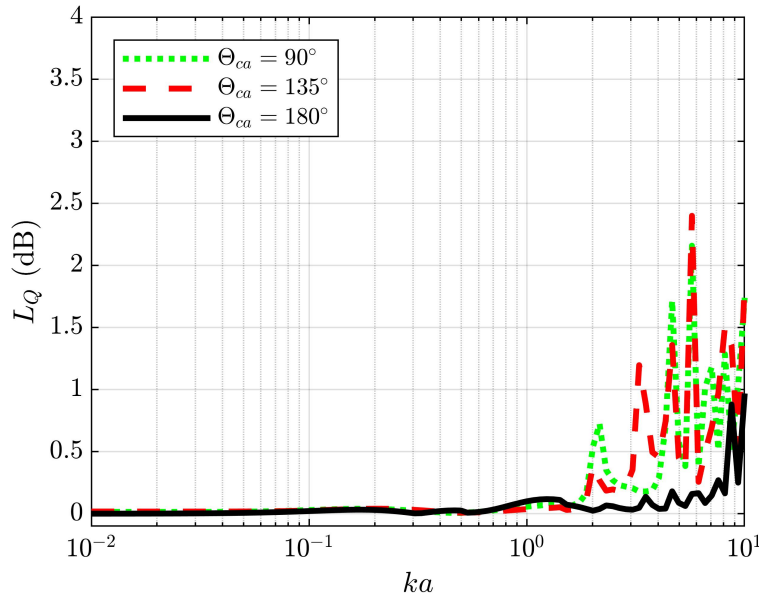


Figure 15.5 Directivity factor deviation levels L_Q between a BEM solution and the low-frequency approximation.

thus, one may anticipate that reasonable agreement follows by modeling the aperture as a cap with constant velocity. However, when the cap and aperture do not align, the aperture surface may coincide with nodal lines inside the sphere, leading to a nonaxisymmetric velocity distribution on its surface. Accordingly, the simple assumption of constant velocity over the aperture becomes less reliable, leading to larger deviations for $ka > 1$.

15.4.2 General Directional Trends

Figure 15.6 shows directivity balloons based on the low-frequency model with $\alpha_c = \alpha_a = 18^\circ$, $(\theta_c, \phi_c) = (90^\circ, 0^\circ)$, and $(\theta_a, \phi_a) = (90^\circ, 180^\circ)$ for selected ka values. Color and radius both indicate the levels on a decibel scale. Assuming the cap center represents the front of the sphere, the vantage point is upward and to the sphere's right. As anticipated, the directional characteristics are essentially dipolar for very small for ka , as shown by Fig. 15.6(a); the dipole moment aligns with the cap and aperture. However, as the frequency approaches the Helmholtz resonance frequency, the strong

dipolar characteristics weaken, and the directivity becomes more ellipsoidal or bean-shaped, as suggested by Fig. 15.6(b). At the Helmholtz resonance frequency, there is increased volume velocity at the aperture, and the directivity is essentially monopolar, as suggested by Fig. 15.6(c). Above resonance, the directivity patterns take on forms similar to those produced by a cap on a rigid closed sphere, such as Fig. 15.6(e), with reduced levels behind the sphere. However, radiation from the aperture does cause differing patterns from the closed-sphere case, such as the mushroom-like directivity patterns seen in Fig. 15.6(f).

15.4.3 Effect of Aperture Location

The aperture's relative size and location determine the source's dipole moment at low frequencies. Figure 15.7 shows far-field polar directivities in the transverse plane when $ka = 0.001$, $\alpha_c = 20^\circ$, $(\theta_c, \phi_c) = (90^\circ, 0^\circ)$, and $\alpha_a = 5^\circ$. The aperture location varies in six steps from $(\theta_a, \phi_a) = (90^\circ, 180^\circ)$ (the opposing side of the sphere from the cap) to $(\theta_a, \phi_a) = (90^\circ, 270^\circ)$ (the right side of the sphere). In each plot, the blue line indicates (θ_c, ϕ_c) and the red line indicates (θ_a, ϕ_a) . The green-dotted line denotes the pattern's null, which falls between (θ_c, ϕ_c) and (θ_a, ϕ_a) . The results show how the aperture location alters the source's directivity pattern so that the maximum radiation direction may not align with the direction of the vibrating cap.

15.5 Experimental Validation

A 3D-printed spherical loudspeaker of exterior radius $a = 0.12$ cm and 5 mm wall thickness served as a tool to experimentally validate the directional characteristics of the theoretical model. The loudspeaker included a single driver positioned at $(\theta_c, \phi_c) = (90^\circ, 0^\circ)$ with a 7 cm effective radiating diameter and cap angle $\alpha_c \approx 36^\circ$. In addition to the spherical loudspeaker's $\alpha_a \approx 33^\circ$ aperture at $(\theta_a, \phi_a) = (90^\circ, 0^\circ)$, two variable-sized ($\alpha_a \approx 15^\circ$ and $\alpha_a \approx 23^\circ$), open spherical shell segments

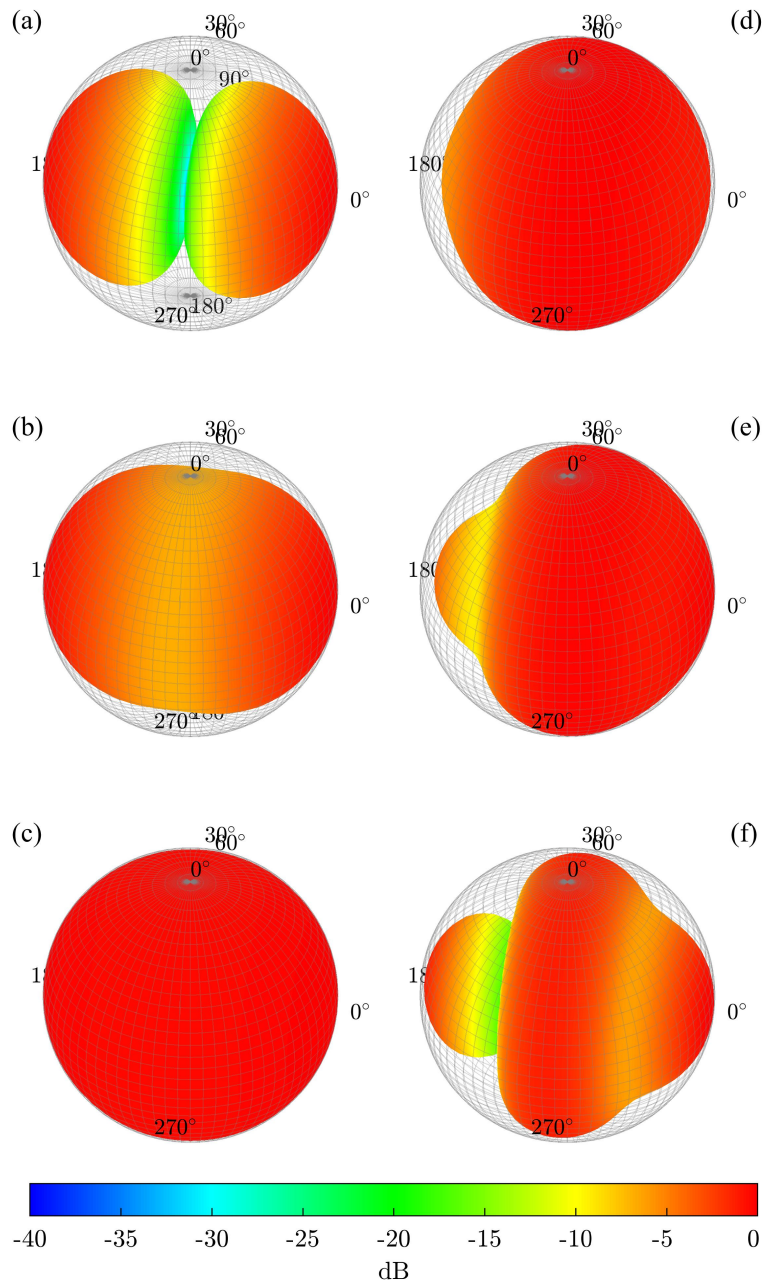


Figure 15.6 Far-field directivity balloons for a vibrating cap on a rigid spherical shell and a circular aperture on the opposing side. The results, based on the low-frequency model, are for (a) $ka = 0.1$, (b) $ka = 0.2$, (c) $ka = 0.4$ (near the Helmholtz resonance frequency), (d) $ka = 1$, (e) $ka = 1.5$, and (f) $ka = 2$.

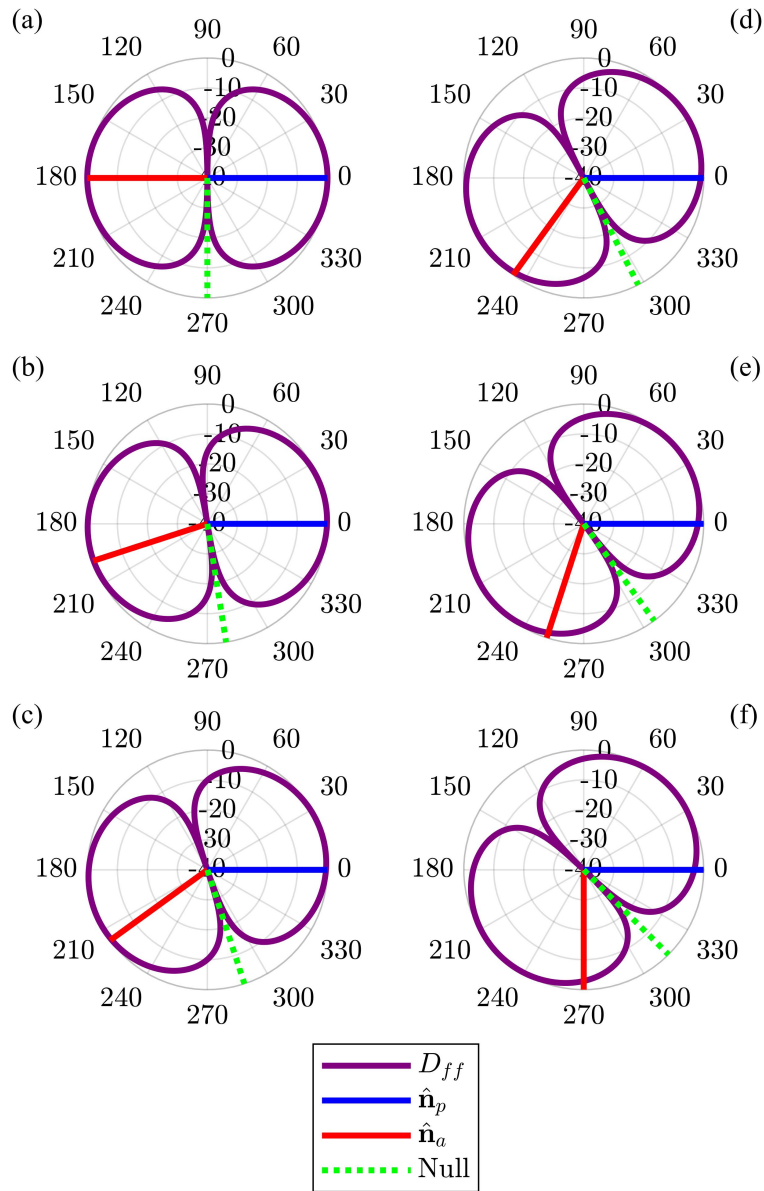


Figure 15.7 Far-field directivity of a vibrating cap on a spherical cap for $(\theta_a, \phi_a) =$ (a) $(90^\circ, 180^\circ)$, (b) $(90^\circ, 198^\circ)$, (c) $(90^\circ, 216^\circ)$, (d) $(90^\circ, 234^\circ)$, (e) $(90^\circ, 252^\circ)$, (f) $(90^\circ, 270^\circ)$.



Figure 15.8 Directivity measurement system assessing the radiation of a spherical loudspeaker positioned at its center. The white disc controls the aperture size.

attach to the back and allow a total of three different aperture sizes. A 1.17 m radius rotating microphone array with 36 12.7 mm (0.5 in.) microphones measured the directivity in 5° resolution in both the polar and azimuthal angles, consistent with the AES sampling standard [33]. The array omitted the nadir (south pole) measurement position because of the obstruction caused by the loudspeaker support structure. Figure 15.8 shows the spherical loudspeaker (black) in the measurement system with one of the spherical shell segments (white) attached.

The experimental spherical source embodiment involved several inconsistencies with the theoretical model. First, it employed a cone loudspeaker rather than an ideal radially vibrating cap. Second, its shell had a finite rather than infinitesimal thickness. Third, to accommodate an interchanging of various fittings, the aperture has a flat baffle rather than a curved baffle. These practical limitations created some ambiguity in establishing the proper values for the sphere radius a and aperture angle

α_a . However, rather than considering separate interior and exterior values for these parameters, the averaged value yielded a reasonable approximation.

Figure 15.9 shows the spherically averaged [6, 78] frequency-response function between the electrical input signal and the array microphones for the three different aperture areas over a frequency range near the Helmholtz resonance frequency. The vertical dashed lines indicate the estimated f_H frequencies using Eq. 15.55. In all cases, the predicted resonance frequencies are less than 5% from the measured values.

Two additional vertical lines, labeled as f_{A1} and f_{A2} , indicate the first two air resonance frequencies of a closed, rigid cavity. Peaks in the spherical loudspeaker response are evident just above these values. The smaller the aperture size, the closer the measured resonance frequencies approach the rigid, closed-cavity values.

A small resonance peak appears near $ka = 1$. Because numerical finite-element method (FEM) simulations of the spherical enclosure suggest structural resonances in this spectral region, the resonance is likely due to either structural cavity properties or an electro-acoustic resonance of the driver. The preceding developments have already accounted for the Helmholtz and higher acoustic resonances, and the smaller resonance was not visible in the rigid-walled BEM simulations.

Figure 15.10 plots several modeled and measured source directivities at 100 Hz ($ka = 0.2$) for the three aperture sizes. The directivity is nearly omnidirectional for the smallest size because the measurement frequency is close to the Helmholtz resonance frequency $f_H = 159$ Hz ($\tilde{f}_H = 165$ Hz). As the aperture sizes increase, the resonance frequencies shift higher to 213 Hz and 267 Hz, meaning the fixed 100 Hz measurement frequency becomes relatively low, and the directivities become successively dipolar (compare Fig. 15.6). The levels L_Q of directivity factor function deviations between the measured and modeled patterns are 0.6 dB, 0.4 dB, and 0.3 dB for the smallest to largest aperture sizes, respectively. Thus, the low-frequency modeling approximations agree well with the measurements at this frequency.

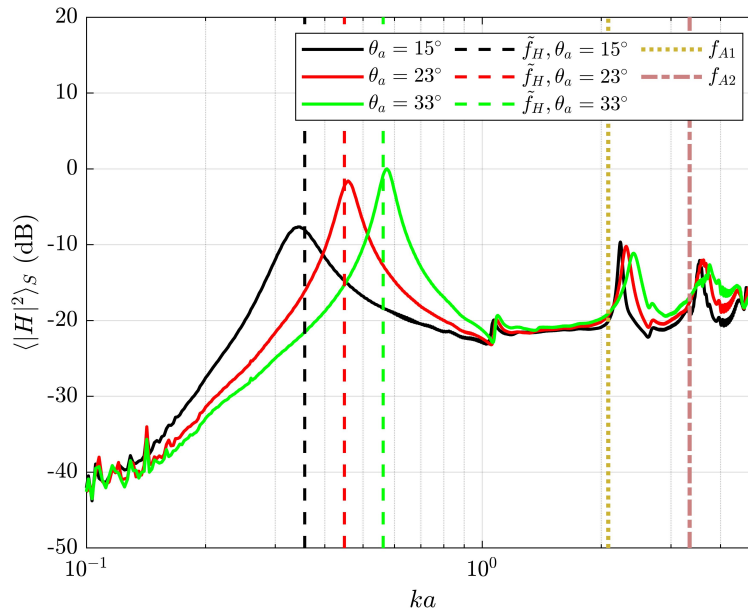


Figure 15.9 Spherically-averaged magnitude response of the spherical loudspeaker with three distinct aperture sizes. The vertical lines show estimated Helmholtz and closed-cavity air resonance frequencies.

Figure 15.11 plots modeled and measured directivities for the source at 700 Hz ($ka = 1.5$). Although $ka > 1$, the good agreement remains between the modeled and measured directivities, with L_Q being 0.3 dB, 0.3 dB, and 0.4 dB for the smallest to largest aperture sizes, respectively. The directivity patterns are similar to the mushroom-like shapes in Fig. 15.6.

Figure 15.12 plots modeled and measured directivities for the source at 1 kHz ($ka = 2.2$). More significant deviations are visible between the simulated and measured patterns at this higher frequency. The deviation level L_Q has become 1.1 dB, 0.8 dB, and 0.8 dB for the smallest to largest aperture sizes, respectively. However, despite the larger deviations, the essential directional characteristics remain credible for the modeled behavior. The measured directivity patterns show three distinct lobes, with substantial radiation behind the loudspeaker.

Figure 15.13 plots modeled and measured directivities for the source at 1.5 kHz ($ka = 3.2$). As anticipated, the deviations have increased; the L_Q values are 1.5 dB, 1.7 dB, and 1.4 dB for the smallest to largest aperture sizes, respectively. However, a general qualitative agreement between

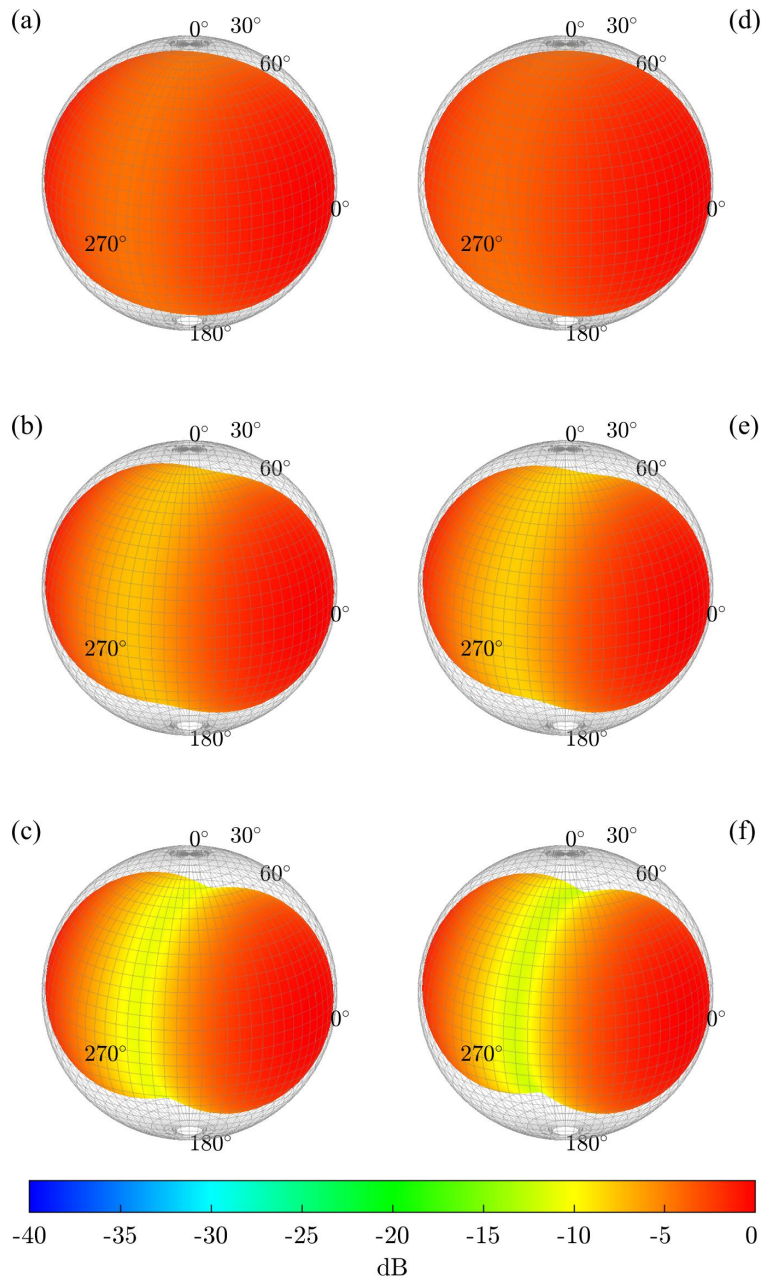


Figure 15.10 Directivity balloons at 100 Hz ($ka = 0.2$) for a modeled (a)-(c) and measured (d)-(f) spherical loudspeaker with circular aperture angles (a), (d) $\alpha_a = 15^\circ$; (b), (e) $\alpha_a = 23^\circ$; and (c), (f) $\alpha_a = 33^\circ$.

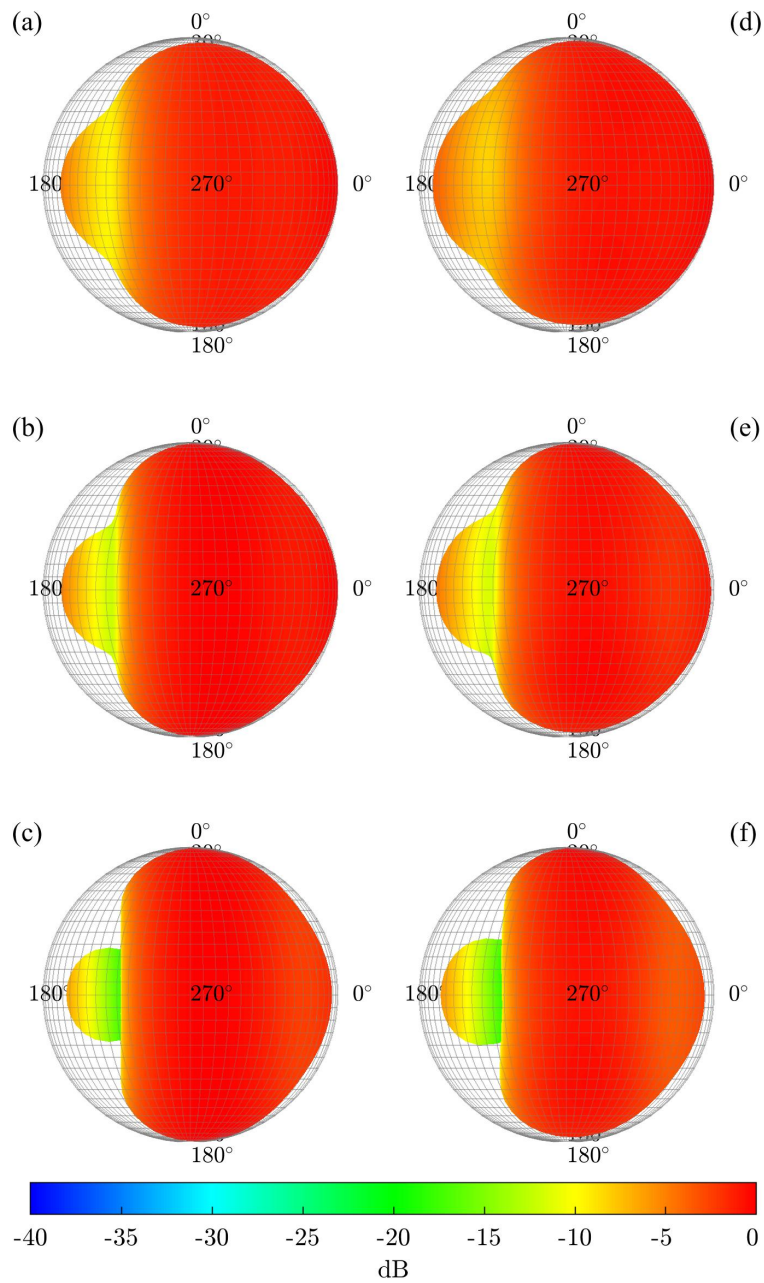


Figure 15.11 Directivity balloons at 700 Hz ($ka = 1.5$) for a modeled (a)-(c) and measured (d)-(f) spherical loudspeaker with circular aperture angles (a), (d) $\alpha_a = 15^\circ$; (b), (e) $\alpha_a = 23^\circ$; and (c), (f) $\alpha_a = 33^\circ$.

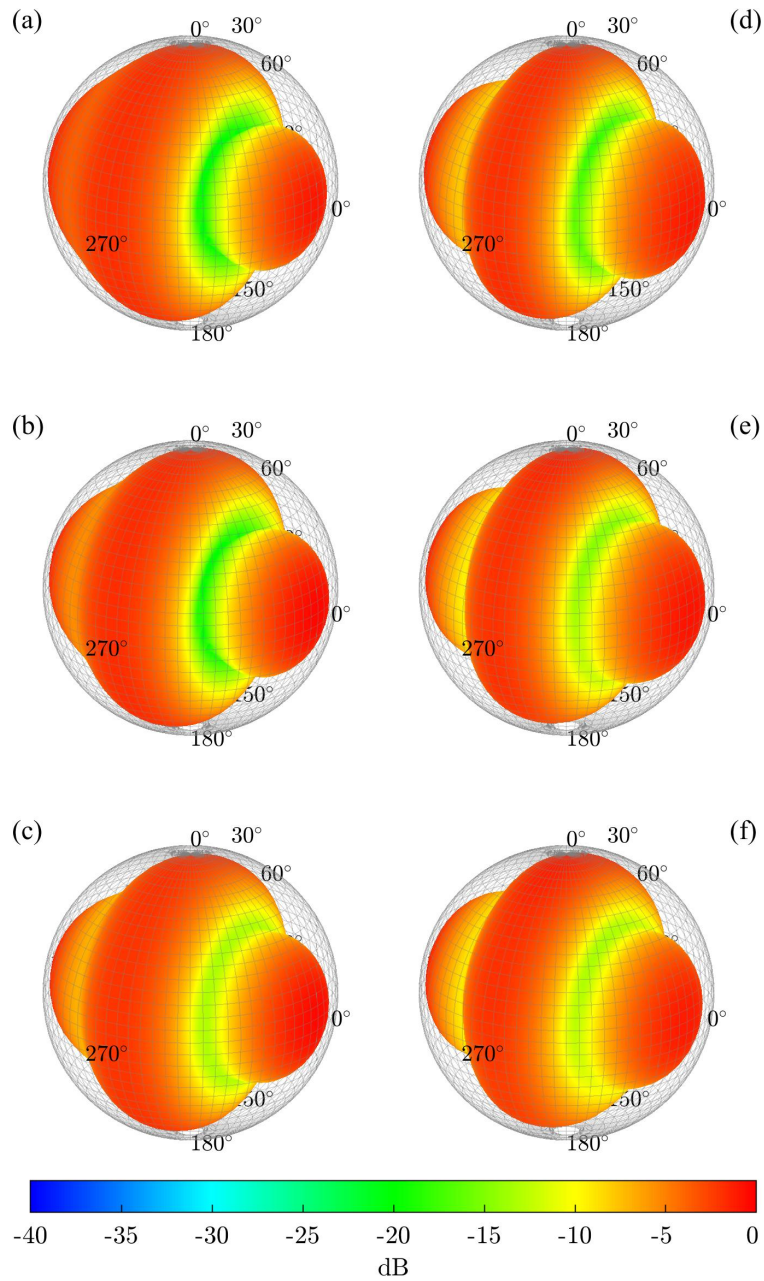


Figure 15.12 Directivity balloons at 1 kHz ($ka = 2.2$) for a modeled (a)-(c) and measured (d)-(f) spherical loudspeaker with circular aperture angles (a), (d) $\alpha_a = 15^\circ$; (b), (e) $\alpha_a = 23^\circ$; and (c), (f) $\alpha_a = 33^\circ$.

simulated and measured directivities remains. The measured directivity has a unique form with distinct lobes and a mushroom-shaped region of intense radiation directly in front of the loudspeaker driver. For the larger apertures, the most substantial radiation is behind the loudspeaker rather than in front.

15.6 Analysis and Discussion

Figure 15.14 shows graphs of L_Q values between the simulated and measured data for each of the three aperture sizes. Figure 15.14(a) shows the results for simulated directivities using U_a for the aperture velocity, as derived from the self and mutual impedances in Eq. 15.36. With two exceptions, the directivity deviations remain below 1.0 dB up to $ka = 2$. The sharp deviation peak near $ka = 1$ corresponds to the resonance peak in Fig. 15.9. The smaller peak near $ka = 0.8$ also coincides with a small bump in the black curve and, to a lesser extent, in the red curve of Fig. 15.9. Visual inspection of the measured directivities at these frequencies reveals a “lumpy” characteristic to the balloons, indicative of wave interference. As discussed in Sec. 15.5, these anomalies are likely due to structural or other resonances not accounted for in the rigid-wall model assumption. This assertion receives additional validation because the deviations occur at the same frequencies regardless of the aperture size and thus appear independent of the strictly acoustic source properties. Above $ka = 2$, the deviations between measurements and the model continue to grow, exceeding 3.0 dB by around $ka = 6$. Vertical dashed lines in the figure represent the resonance frequencies of a closed, rigid-walled sphere. Near these resonances, spikes in the deviation curves are apparent.

Figure 15.14(b) shows similar L_Q graphs for directivities simulated using \tilde{U}_a for the aperture velocity, as derived from lumped-element parameters in Eq. 15.53. The deviations for $ka < 1$ are virtually identical to those derived from U_a . However, for $ka > 1$, the deviations rise to near 2.0 dB by $ka = 2.0$ and quickly rise to over 3.0 dB before $ka = 3.0$. As suggested by Fig. 15.3, \tilde{U}_a

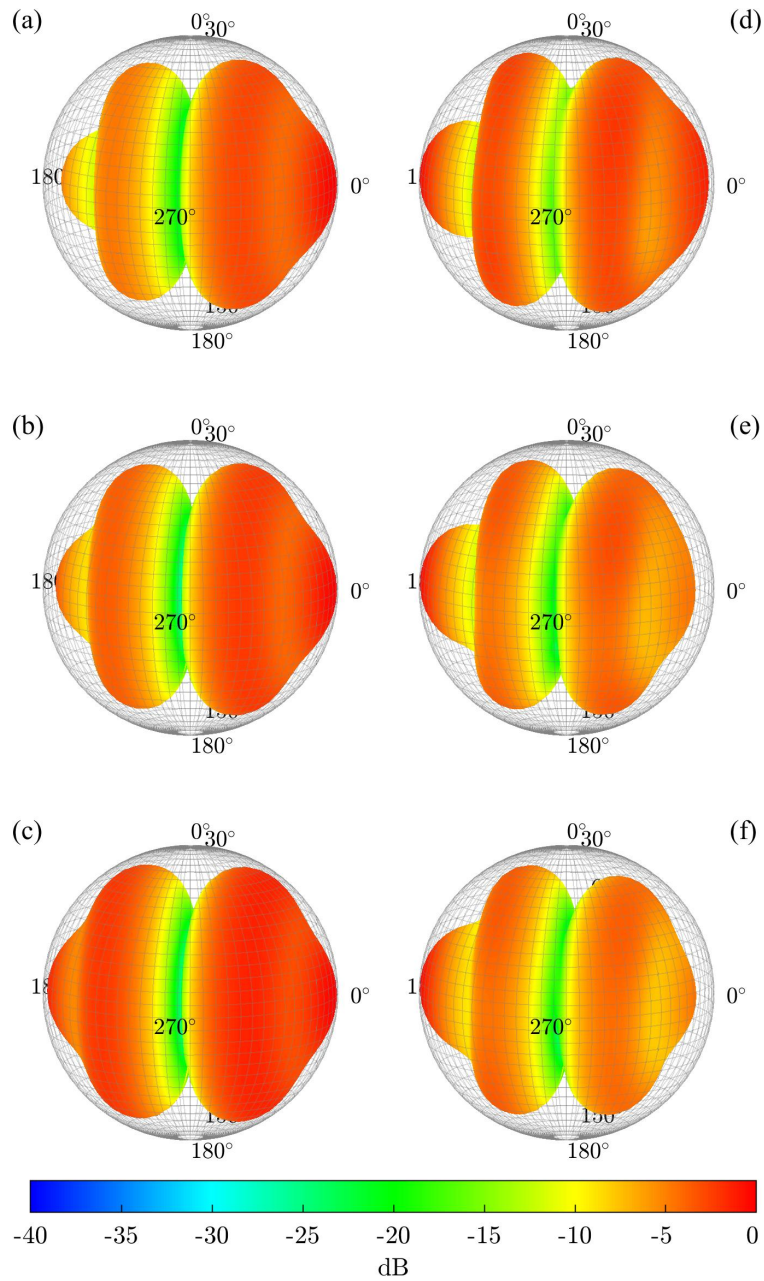


Figure 15.13 Directivity balloons at 1.5 kHz ($ka = 3.2$) for a modeled (a)-(c) and measured (d)-(f) spherical loudspeaker with circular aperture angles (a), (d) $\alpha_a = 15^\circ$; (b), (e) $\alpha_a = 23^\circ$; and (c), (f) $\alpha_a = 33^\circ$.

tends gradually to zero above resonance, whereas U_a rises again. Thus, using U_a over \tilde{U}_a becomes important above the source's Helmholtz resonance frequency. Below this range, \tilde{U}_a gives a reliable estimate, which is beneficial when exact formulas for self and mutual impedances are unknown due to differing cavity and cap shapes.

These results, the BEM deviations, and the results from Sec. 15.5 suggest the following rules of thumb. Below $ka = 1$, the low-frequency model quantitatively agrees well with the complete solution and measurements. In this spectral region, the lumped-element parameters reasonably estimate the aperture volume velocity so that $\tilde{U}_a \approx U_a$. Above $ka = 1$, the low-frequency approximation using U_a gives good agreement up to at least $ka = 10$ when the cap and aperture align. However, the agreement is less reliable when the cap and aperture do not align. Additionally, above $ka = 1$, the lumped-element estimate \tilde{U}_a is unreliable even when the cap and aperture align.

15.7 Conclusions

This work has developed a low-frequency approximation to a vibrating cap on a spherical shell with a circular aperture. The key idea has been to model the aperture as a second vibrating cap with a velocity determined by the self and mutual impedance between the aperture and the primary vibrating cap. Lumped-element approximations of the self and mutual impedances provided a simplified formula for the aperture volume velocity and Helmholtz resonance frequency. Multipole moments extracted from the derived spherical harmonic coefficients reveal that at very low frequencies, the directivity is dipolar. Approaching the Helmholtz resonance frequency, the directivity becomes more monopolar until it reaches a quasi-omnidirectional state at resonance. Above resonance, the directivity takes on more complex forms. Both numerical BEM simulations and measurements of a comparable spherical loudspeaker validated the low-frequency approximation, yielding good quantitative agreement up to approximately $ka = 2.0$.

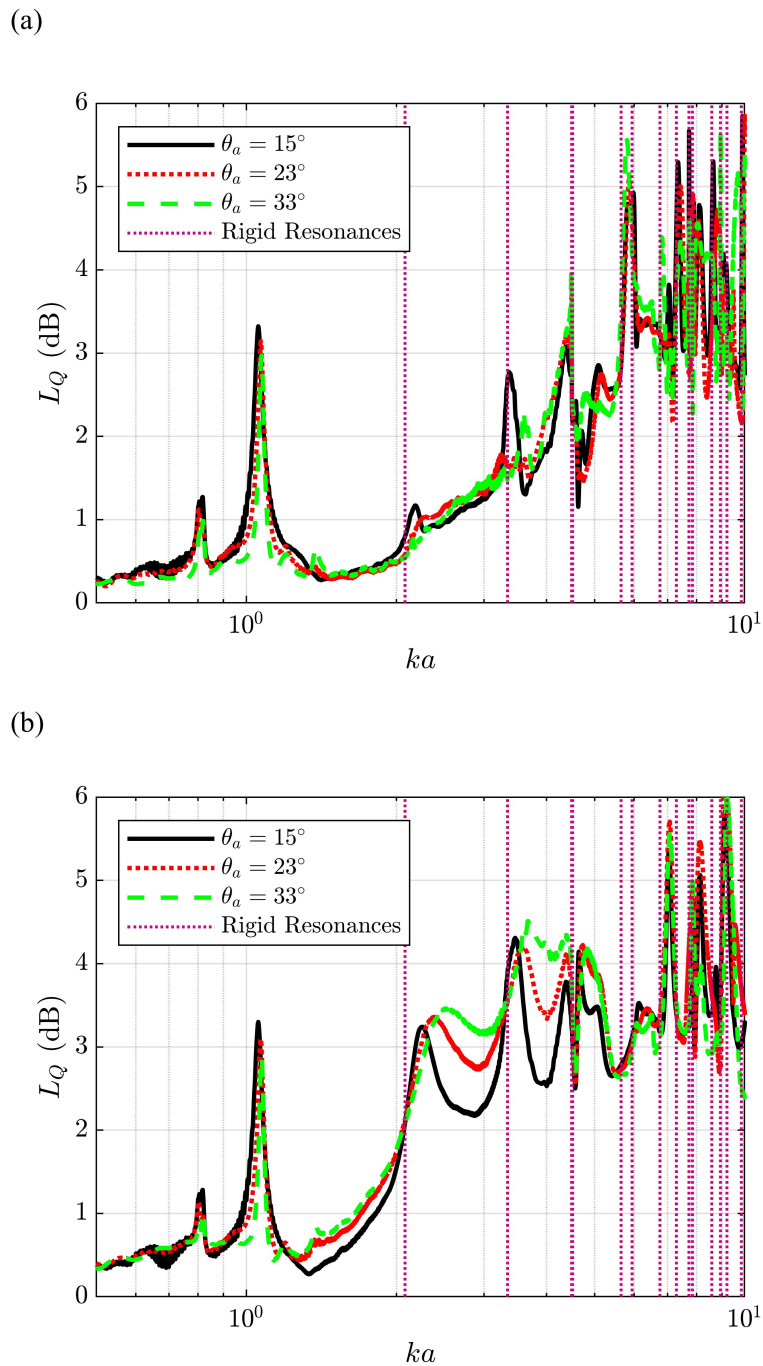


Figure 15.14 Directivity factor function deviation levels between the measured and modeled directivities with (a) aperture velocity U_a (b) lumped-element aperture velocity approximation \tilde{U}_a .

The model's results will be beneficial for understanding and predicting the directivities of sources with apertures, such as musical instruments with sound holes, guitar amplifiers with open backs, or loudspeakers with vents. Because this work focused on low-frequency approximations, future research could develop a numerical method such as MAR to obtain results valid for $ka \gg 1$. Other research could consider models for multiple caps and apertures.

Chapter 16

Directivity of Vibrating Caps With Nonaxisymmetric Surface Velocities

This chapter develops a technique to calculate the radiation from spheres with nonaxisymmetric velocity distributions. The method provides analytic solutions to vibrating caps with imposed mode shapes, rectangular caps, and other interesting vibrational patterns.

16.1 Introduction

One important class of theoretical models deals with acoustic radiation from spherical geometries. An essential feature of the models is a spherical baffle, which incorporates diffraction about the body, as opposed to the infinite plane rigid baffle or its counterparts [136, 137, 174]. Over the decades, researchers have developed several axisymmetric spherical theoretical models based on Fourier-Legendre series expansions of surface velocities. However, nonaxisymmetric spherical sources with analytic solutions are uncommon.

The known exact axisymmetric solutions include radiation from a point source [60, 175], a radially vibrating cap [60, 175], and an axially vibrating cap [10, 71], which are useful for

various purposes. Their applications have included modeling loudspeakers [10], horns [11], and speech [4, 6, 81, 152]. The models also provide a basic understanding of the diffraction effects produced by loudspeaker cabinets [176], musicians' bodies [72], and other obstacles. Other more advanced modeling configurations have included a vibrating cap with a pressure-release spherical baffle [177] or with a pressure-release belt set in a rigid spherical baffle [178]. More recently, Aarts and Janssen considered other axisymmetric velocity distributions by utilizing Zernike polynomials and developing solutions for various Stenzel velocity profiles [138].

One technique for creating specific nonaxisymmetric solutions has involved rotating and superposing the radiation from an axisymmetric radially vibrating cap on a rigid sphere several times to simulate the directivity of a regular polyhedral loudspeaker (RPL) [179–181]. While this has been useful for creating a theoretical source with quasi-omnidirectional and multidirectional characteristics [13], the method cannot represent arbitrarily shaped, e.g., rectangular or elliptical, caps or caps with arbitrary phases. While Aarts and Janssen contemplated extending their method, e.g., to consider phase distributions, the problematic integrals between the associated Legendre polynomials and the Zernike polynomials prohibited further consideration of the approach. Some researchers have resorted to numerical integration to overcome difficulties due to integrals of associated Legendre functions, such as for studying the radiation from a rectangular cap on a sphere [10]. Nonetheless, analytic solutions for many nonaxisymmetric spherical models remain unresolved.

This work presents a method for evaluating the expansion coefficients for various nonaxisymmetric velocity distributions. The technique applies a “spatial masking operator” [114] to assess the product of functions on the sphere in terms of their spherical harmonic expansions. Judicious choices of cap orientations and amplitudes yield analytic solutions to various problems, including a rectangular cap, a semicircular cap, and caps with imposed mode shapes on spheres. The method will help researchers and practitioners develop more useful theoretical models for sound radiation studies.

16.2 Methods

16.2.1 Exterior Solution of the Helmholtz Equation

Consider the radiation of sound from a sphere of radius a with known normal particle velocity u_n on its surface described by the following boundary-value problem (BVP) in spherical coordinates:

$$\begin{aligned} \nabla^2 p(r, \theta, \phi) + k^2 p(r, \theta, \phi) &= 0, \quad r \geq a \\ \frac{\partial}{\partial n} p(a, \theta, \phi) &= -iz_0 k u_n(\theta, \phi) \\ \lim_{r \rightarrow \infty} r \left(\frac{\partial}{\partial r} + ik \right) p(r, \theta, \phi) &= 0, \end{aligned} \quad (16.1)$$

where $z_0 = \rho_0 c$ is the characteristic specific acoustic impedance of the medium, k is the wavenumber, and the time dependence is $e^{i\omega t}$. The unique solution on the exterior domain $r \geq a$ follows from a spherical harmonic expansion of the normal velocity [59]

$$u_n(\theta, \phi) = \sum_{n=0}^{\infty} \sum_{m=-n}^n U_n^m Y_n^m(\theta, \phi), \quad (16.2)$$

where

$$Y_n^m(\theta, \phi) = \sqrt{\frac{2n+1}{4\pi} \frac{(n-m)!}{(n+m)!}} P_n^m(\cos \theta) e^{im\phi} \quad (16.3)$$

are the normalized spherical harmonics of degree n and order m . [70] The expansion coefficients U_n^m are

$$U_n^m = \int_0^{2\pi} \int_0^\pi u(\theta, \phi, k) [Y_n^m(\theta, \phi)]^* \sin \theta d\theta d\phi, \quad (16.4)$$

where * indicates complex conjugation.

The pressure follows from Euler's equation as [59]

$$p(r, \theta, \phi) = -iz_0 \sum_{n=0}^{\infty} \sum_{m=-n}^n U_n^m \frac{h_n^{(2)}(kr)}{h_n^{(2)'}(ka)} Y_n^m(\theta, \phi), \quad r \geq a. \quad (16.5)$$

where $h_n^{(2)}(kr)$ are the spherical Hankel functions of the second kind of order n .

16.2.2 Spatial Masking

Although the velocity expansion coefficients U_n^m uniquely define the pressure for $r \geq a$, their determination requires integrals incorporating the associated Legendre functions P_n^m , making them difficult to evaluate analytically. One may overcome this limitation for nonaxisymmetric surface velocity distributions by taking the product of two axisymmetric but rotated functions. This section shows how one may write the expansion coefficients of the product in terms of the individual expansion coefficients of each function, yielding analytic solutions to nonaxisymmetric radiation problems.

Suppose that the normal velocity is the product of two functions, $f(\theta, \phi)$ and $g(\theta, \phi)$:

$$u_n(\theta, \phi) = g(\theta, \phi)f(\theta, \phi). \quad (16.6)$$

If the spherical harmonic coefficients of f and g are F_n^m and G_n^m , respectively, it is convenient to determine the expansion coefficients U_n^m in terms of F_n^m and G_n^m . With each function written in terms of its respective spherical harmonic expansion, Eq. (16.2) becomes

$$u_n = \sum_{w=0}^{\infty} \sum_{w=-v}^v U_w^v Y_w^v(\theta, \phi) = \left(\sum_{s=0}^{\infty} \sum_{s=-t}^t G_s^t Y_s^t(\theta, \phi) \right) \times \left(\sum_{p=0}^{\infty} \sum_{p=-q}^q F_p^q Y_p^q(\theta, \phi) \right). \quad (16.7)$$

Multiplying both sides of this expression by $[Y_n^m(\theta, \phi)]^*$, integrating over the sphere, and applying the orthogonality of the spherical harmonics on the left-hand side then yields

$$U_n^m = \sum_{p=0}^{\infty} \sum_{s=0}^{\infty} \sum_{q=-p}^p \sum_{s=-t}^t \Lambda_{n,p,s}^{m,q,t} G_s^t F_p^q, \quad (16.8)$$

where

$$\Lambda_{n,p,s}^{m,q,t} = \int_0^{2\pi} \int_0^{\pi} Y_p^q(\theta, \phi) Y_s^t(\theta, \phi) [Y_n^m(\theta, \phi)]^* \sin \theta d\theta d\phi \quad (16.9)$$

$$= (-1)^m \sqrt{\frac{(2p+1)(2s+1)(2n+1)}{4\pi}} \begin{pmatrix} p & s & n \\ 0 & 0 & 0 \end{pmatrix} \begin{pmatrix} p & s & n \\ q & t & -m \end{pmatrix}, \quad (16.10)$$

which incorporates the Wigner $3j$ symbols [114]. The symbol $\Lambda_{n,p,s}^{m,q,t}$ represents a scalar value for the selected degrees n , p , and s and orders m , q , and t .

One may consider Eq. (16.8) to represent an infinite-dimensional “spatial-masking” operator acting on F_p^q to produce U_n^m [114]. Specifically, if

$$B_{n,p}^{m,q} = \sum_{s=0}^{\infty} \sum_{t=-s}^s \Lambda_{n,p,s}^{m,q,t} G_s^t \quad (16.11)$$

are the operator elements,

$$U_n^m = \sum_{p=0}^{\infty} \sum_{q=-p}^p B_{n,p}^{m,q} F_p^q, \quad (16.12)$$

which means $B_{n,p}^{m,q}$ describes how F_p^q maps to U_n^m . In this spatial-masking procedure, the function $g(\theta, \phi)$, whose expansion coefficients appear in Eq. (16.11), is the mask. The operator elements $B_{n,p}^{m,q}$ thus depend on the choice of masking function. Because multiplication commutes, one may interchange f and g freely.

16.2.3 Spherical Cap Expansion

One particularly useful function for modeling sound radiation and for use as a spatial mask is a uniform, unit-amplitude spherical cap, defined by its edge half-angle μ and cap orientation (ϑ, φ) . For a cap centered at $(\vartheta, \varphi) = (0, 0)$ (i.e., the zenith), the function is

$$q(\theta, \phi; \mu, 0, 0) = \begin{cases} 1, & \theta < \mu \\ 0 & \theta > \mu \end{cases}. \quad (16.13)$$

Expanding Eq. (16.13) in terms of Legendre polynomials yields [10]

$$q(\theta, \phi; \mu, 0, 0) = \sum_{n=0}^{\infty} \sum_{m=-n}^n Q_n(\mu) P_n(\cos \theta) \quad (16.14)$$

where

$$Q_n(\mu) = \begin{cases} \frac{1}{2}(1 - \cos \mu), & n = 0 \\ \frac{1}{2}(P_{n-1}(\cos \mu) - P_{n+1}(\cos \mu)), & n > 0. \end{cases} \quad (16.15)$$

Applying the spherical harmonic addition theorem [70]

$$P_n(\cos \Theta) = \sum_{m=-n}^n \frac{4\pi}{(2n+1)} Y_n^m(\theta, \phi) [Y_n^m(\vartheta, \varphi)]^* \quad (16.16)$$

allows one to orient the cap in arbitrary direction (ϑ, φ) . The spherical harmonic expansion coefficients become

$$Q_n^m(\mu, \vartheta, \varphi) = Q_n(\mu) \frac{4\pi}{(2n+1)} [Y_n^m(\vartheta, \varphi)]^*. \quad (16.17)$$

For a radially vibrating cap on a sphere of velocity amplitude u_0 , edge half-angle μ , and orientation to (ϑ, φ) , the velocity expansion coefficients in Eq. (16.2) are

$$U_n^m = u_0 Q_n^m(\mu, \vartheta, \varphi), \quad (16.18)$$

such that the exterior acoustic pressure in Eq. (16.5) becomes

$$p(r, \theta, \phi, k) = -iz_0 u_0 \sum_{n=0}^{\infty} \sum_{m=-n}^n Q_n^m(\mu, \vartheta, \varphi) \frac{h_n^{(2)}(kr)}{h_n^{(2)'}(ka)} Y_n^m(\theta, \phi), \quad r \geq a. \quad (16.19)$$

16.2.4 Series Truncations

For practical implementation, the three infinite series in Eqs. (16.5), (16.11), and (16.12) require truncation. To better understand the effects of truncation on these series, let \mathbf{u} represent a $(N+1)^2 \times 1$ vector containing the expansion coefficients U_n^m truncated to degree N :

$$\mathbf{u} = \begin{bmatrix} U_0^0 \\ U_1^{-1} \\ U_1^0 \\ \vdots \\ U_N^{N-1} \\ U_N^N \end{bmatrix}. \quad (16.20)$$

Likewise, let \mathbf{f} and \mathbf{g} be $(P+1)^2 \times 1$ and $(S+1)^2 \times 1$ vectors containing the expansion coefficients of F_n^m and G_n^m truncated to degrees P and S , respectively. The matrix form representation of the

masking operator becomes

$$\mathbf{u} = \mathbf{B}_g \mathbf{f}, \quad (16.21)$$

where the elements of the operator \mathbf{B}_g , represented by a $(N+1)^2 \times (P+1)^2$ matrix, are available from Eq. (16.11). The subscript g indicates that the elements depend on the expansion coefficients G_n^m of the spatial mask. The following sections explore the selection of truncation degrees N , P , and S , which may each take unique values. It is essential to note that Eq. (16.21) requires no matrix inversion. Consequently, even after an initial truncation, one may sequentially add higher-degree terms to improve the accuracy of the U_n^m estimate.

Far-field Propagation Truncation

This section illustrates how far-field propagation effects permit a truncation of the velocity expansion coefficients U_n^m without serious errors in the far-field directivity pattern. In the source's far field, the large-argument relations of the spherical Hankel functions applied to Eq. (16.5) yield the pressure

$$p(r, \theta, \phi) \approx -iz_0 \frac{e^{-ikr}}{kr} \sum_{n=0}^{\infty} \sum_{m=-n}^n \frac{i^{n+1} U_n^m}{h_n^{(2)'}(ka)} Y_n^m(\theta, \phi), \quad ka \gg 1. \quad (16.22)$$

This equation provides the desired radially-independent, unnormalized, far-field directivity function

$$D_{ff}(\theta, \phi) = \sum_{n=0}^{\infty} \sum_{m=-n}^n \frac{i^n U_n^m}{h_n^{(2)'}(ka)} Y_n^m(\theta, \phi), \quad (16.23)$$

from which one may extract a far-field propagator [59]

$$W_n = \frac{i^n}{h_n^{(2)'}(ka)}. \quad (16.24)$$

The propagator modifies U_n^m to obtain the source's far-field directivity spherical harmonic expansion coefficients; its behavior for $n > ka$ will allow truncation of U_n^m with minimal impact on the estimated far-field pattern.

For a sphere of radius a , the large-order relations for the derivative of the spherical Hankel functions [70] suggest that for $n \gg ka$, the magnitude of the far-field propagator decays rapidly [59].

As a result, only the coefficients up to a maximum degree $N \approx ka$ are necessary. To illustrate this effect, Fig. 16.1 plots the magnitude of the far-field propagator W_n over wavenumber k and expansion degree n . Color indicates the relative magnitude of the coefficients for a given degree n on a decibel scale, with white indicating coefficients with large magnitudes and black indicating coefficients with small magnitudes. The dashed-green line indicates $n = ka$. For a given frequency, the most important coefficients are close to this line and are evident as a white band. Above the line, the magnitude of W_n decays rapidly to below -25 dB.

Because W_n acts as a frequency-dependent, low-pass spatial filter, it eliminates U_n^m for $n \gtrsim ka$ when multiplied by U_n^m as in Eq. (16.23). Since W_n effectively eliminates these coefficients, truncating U_n^m to degree $N \approx ka$ does not significantly impact the far-field directivity pattern. For the range $0 \leq ka \leq 20$, an empirically determined, frequency-dependent truncation degree

$$N(k) = \lceil 1.1ka \rceil + 2 \quad (16.25)$$

ensures that the propagator loses no more than 0.1% of the signal energy, where the ceiling function $\lceil \cdot \rceil$ rounds up to the next integer. The solid cyan line in Fig. 16.1 indicates this truncation choice. It essentially follows the trend $n = ka$, but the scale factor of 1.1 and an offset of 2 ensure that the expansion retains some energy from within the filter roll-off region.

A simple illustration of the minimal truncation errors considers the radiation for a radially vibrating cap on a sphere with edge half-angle $\mu = \pi/6$. Figure 16.2(a) plots the surface velocity of this source for $ka = 2$ using only up to degree $N = \lceil 1.1(2) \rceil + 2 = 5$ coefficients in the spherical harmonic expansion. The color on the constant-radius sphere represents the expanded surface velocity magnitude and exhibits a smoothed, gradual velocity transition about the cap's edge. Figure 16.2(b) plots the surface velocity profile for the same source but with $N = 100$ coefficients, which yields a more abrupt velocity transition that agrees better with the boundary conditions. However, Figs. 16.2(c) and (d) demonstrate that the far-field directivity patterns calculated respectively from the $N = 5$ and $N = 100$ degree expansions are virtually identical. For these plots, color and balloon

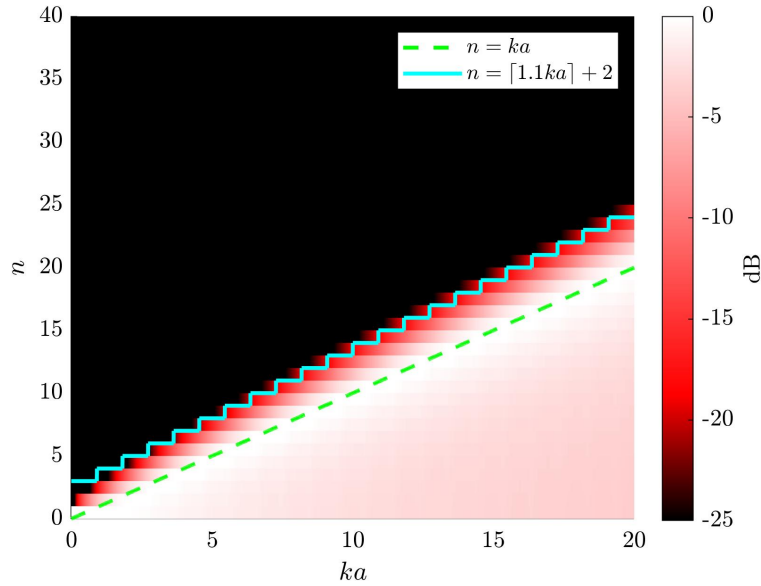


Figure 16.1 Spherical spectrum of the far-field propagator W_n .

radius both indicate the relative levels on a 40 dB scale. An area-weighted directivity factor function deviation level L_Q [81] quantifies a deviation of less than 0.01 dB between the two patterns. Thus, even though the expansion using U_n^m up to $N = 100$ is more accurate on the sphere's surface, the low-pass filtering effect of the far-field propagation renders minimal difference between the high and low-degree expansions for this specific wavenumber.

Thus, truncation according to Eq. (16.25) provides one straightforward approach to minimizing truncation errors of the infinite series appearing in Eq. (16.5). The truncation fixes the operator matrix \mathbf{B}_g to $(N + 1)^2$ rows, since rows corresponding to higher degrees do not significantly contribute to the source's far-field radiation.

Masking Function Truncation

Truncations of Eqs. (16.11) and (16.12) correspond to degree-limited representations of f and g , respectively. Since high-degree spherical harmonics vary rapidly with angle, degree-limited representations tend to smooth these functions' features spatially. With respective truncations to

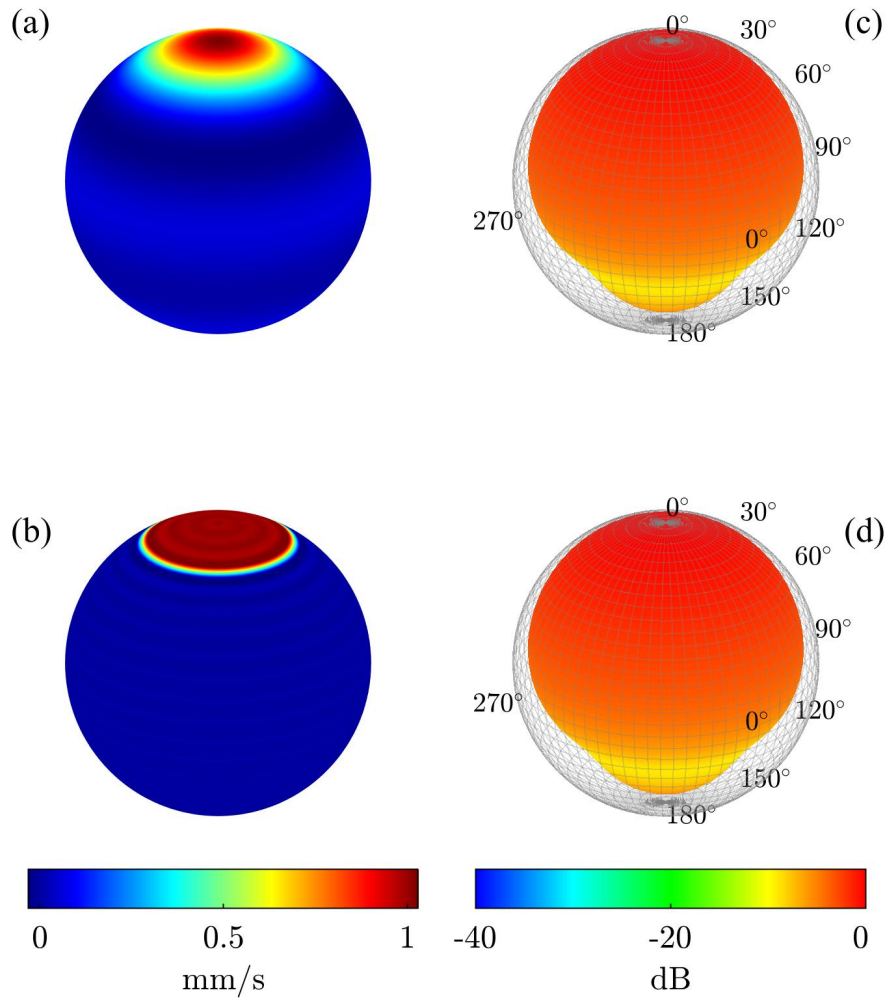


Figure 16.2 Illustration of the low-pass filtering effect of the far-field propagator W_n . Normal velocity distribution on a rigid sphere of radius a with a radially vibrating cap of angle $\mu = \pi/6$ using up to degree (a) $N = 5$ and (b) $N = 100$ spherical harmonic expansions. Far-field directivities for $ka = 2$ using up to degree (c) $N = 5$ and (d) $N = 100$ spherical harmonic expansions.

degrees P and S to create degree-limited functions \tilde{f}_P and \tilde{g}_S , the application of the masking operator [Eq. (16.21)] yields a smoothed, degree-limited version of the desired surface velocity distribution:

$$u_n(\theta, \phi) \approx \tilde{u}_n(\theta, \phi) = \tilde{f}_P(\theta, \phi)\tilde{g}_S(\theta, \phi). \quad (16.26)$$

As $P \rightarrow \infty$ and $S \rightarrow \infty$, \tilde{u}_n converges to u_n . However, as suggested by the preceding section, u_n only requires accurate representation up to degree $N = ka$ for far-field directivity patterns. Any additional accuracy achieved by increasing P and S is then superfluous. Consequently, one may lower P and S in practice without significantly impacting the far-field results. This section considers the selection of P and S in more detail.

Unlike for U_n^m , where far-field radiation defines the truncation degree, one must determine the truncation degrees P and S individually based on convergences of the respective series expansions to f and g . Because this work only considers functions based on products involving a unit-amplitude spherical cap, it is convenient to analyze its convergence properties.

One method to ascertain sufficient expansion convergence is to ensure that the norm in the sequence space converges to that of the original space [78]. For the unit spherical cap, application of Parseval's theorem guarantees that

$$\sum_{n=0}^{\infty} |Q_n^m(\mu, 0, 0)|^2 = \int_0^{2\pi} \int_0^{\pi} |q(\theta, \phi; \mu, 0, 0)|^2 \sin \theta d\theta d\phi \quad (16.27)$$

$$= 2\pi \int_0^{\mu} \sin \theta d\theta \quad (16.28)$$

$$= 2\pi(1 - \cos \mu), \quad (16.29)$$

which is the surface area of the cap. A truncation threshold based on the converging expansion coefficient's norm

$$\varepsilon(N) = \frac{\sum_{n=0}^N |Q_n^m(\mu, 0, 0)|^2}{2\pi(1 - \cos \mu)}, \quad (16.30)$$

quantifies the series convergence with $\varepsilon \rightarrow 1$ as $N \rightarrow \infty$.

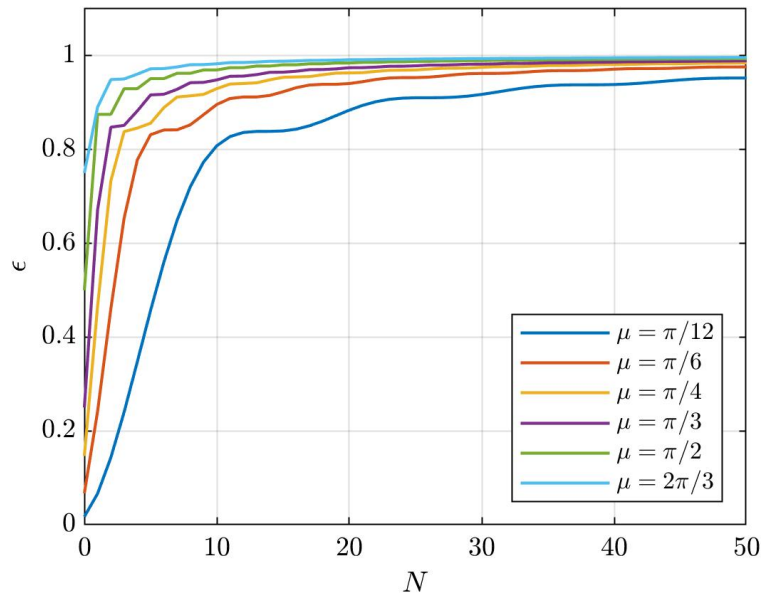


Figure 16.3 Values of the truncation parameter ε for increasing expansion degree N and various cap edge half-angles.

Figure 16.3 plots ε over increasing maximum expansion degree N for selected cap edge half-angles μ . The expansion sequence converges much faster for larger cap angles than smaller cap angles. For example, for $\mu = 2\pi/3$, $\varepsilon = 0.9$ by $N = 2$ whereas for $\mu = \pi/12$, ε does not reach this same value until $N = 22$. Presumably, the differences in convergence rates arises because a smaller cap size requires higher-degree spherical harmonics to represent the rapid change from unity to zero over a smaller interval. For example, in the limiting case $\mu \rightarrow \pi$, the surface velocity is that of a radially oscillating sphere [62] and the expansion requires only Q_0^0 . In the limiting case $\mu \rightarrow 0$, the surface velocity is that of a point source on a sphere [60] and the expansion requires high-degree spherical harmonics to represent the sharp discontinuity.

Figure 16.4 plots the spectrum of $Q_n^m(\mu, 0, 0)$ for varying μ to illustrate this concept further. As in Fig. 16.1, color indicates each coefficient's relative level on a decibel scale. Additionally, the dashed green line indicates the degree of the most significant (largest magnitude) coefficients. The prominent coefficients for large μ fall at low degrees. Consequently, the series will converge

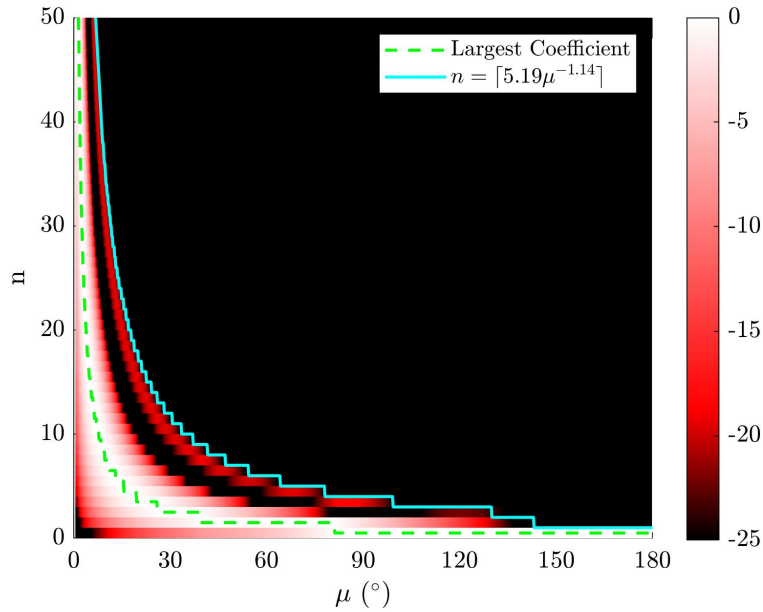


Figure 16.4 Spectrum of a unit-amplitude spherical cap as a function of cap edge half-angle.

quickly for these cap edge half-angles. The most significant expansion coefficients for small-cap angles fall at higher degrees, which requires many terms to ensure convergence.

The solid cyan line in Fig. 16.4 indicates the empirically determined truncation degree

$$N = \lceil 5.19\mu^{-1.14} \rceil, \quad (16.31)$$

which ensures a value of $\varepsilon = 0.9$ for all μ . Most of the coefficients with magnitudes greater than -25 dB relative to the maximum fall below this curve. Consequently, when used with the masking functions f and g , the respective truncation degrees P and S will yield minimal errors if set to the value in Eq. (16.31).

Operator Truncation

Because u_n must be accurate only to truncation degree N for far-field directivity results, the action of \mathbf{B}_g modifies the maximum required values of P and S . The operator elements $B_{n,p}^{m,q}$ arise from the coefficients $\Lambda_{n,p,s}^{m,q,t}$ and G_s^t . Truncating the expansion of the masking function g to degree S likewise

truncates the infinite series in Eq. (16.11) to degree S . Consequently, each $B_{n,p}^{m,q}$ results from adding the $(S+1)^2$ multiplications of $\Lambda_{n,p,s}^{m,q,t}$ and G_s^t for the fixed values of n, p and m, q . However, in practice, the required number of multiplications is far fewer because the Wigner $3j$ symbols are zero for many combinations of n, p, s and m, q, t , such as when [114]

$$p > s + n \quad (16.32)$$

or

$$s > p + n. \quad (16.33)$$

These relations follow because the product of two polynomials of degree N and M can produce a polynomial of degree no greater than $N + M$. This result suggests that for initial truncation degrees N, P and S, P and S should adjust to degree L given by

$$L = \min(N + S, N + P). \quad (16.34)$$

Truncation Synopsis

In summary, the truncation approach used in this work is as follows. For far-field propagation, U_n^m truncates to the degree N given in Eq. (16.25). The spatial masking operator \mathbf{B}_g then requires calculation with only $(N+1)^2$ rows. Studying the convergence characteristics of the f and g expansions provides initial estimates for the truncation degrees P and S . Equation (16.31) serves as the truncation limit for the unit-amplitude spherical cap used in this work. Finally, Eq. (16.34) adjusts P and S to L to ensure that the product of f and g yields a representation of u_n with adequate accuracy. This sets the number of columns of \mathbf{B}_g to $(L+1)^2$, such that \mathbf{B}_g becomes a $(N+1)^2 \times (L+1)^2$ matrix. Because the masking operation described by Eq. (16.12) is linear and does not require an inverse calculation, one can readily add higher-degree terms for further refinement of the solution.

16.3 Results

This section applies the concepts of spatial masking to the radiation solutions of various nonaxisymmetric vibrating caps on spheres. For straightforward implementation, an $N = S = P = 30$ degree expansion ensures adequate convergence for all cases up to the desired maximum frequency of $ka = 15$, based on the bounds suggested by Eqs. (16.25) and (16.31).

16.3.1 Two Opposite-Polarity Semicircular Caps

A radially vibrating cap on a sphere is a simple approximation of a dynamic loudspeaker before its cone breakup. At higher frequencies, different cone regions may vibrate in and out of phase according to its structural modes. A simple model for a mode with a diametric node involves two opposite-polarity radially vibrating semicircular caps. As suggested by Fig. 16.5(a), a spherical mask whose upper and lower hemispheres are out-of-phase provides a means to help generate this source. The expansion coefficient's of the dipole-like mask function g_d are

$$\mathbf{g}_d = \sum_{i=1}^2 u_i \mathbf{q}(\pi/2, \vartheta_i, 0) \quad (16.35)$$

where u_i are the cap amplitudes and \mathbf{q} is the vector form of Q_n^m . Table 16.1 lists the values of u_i , μ_i , ϑ_i , and φ_i for the two caps. Figure 16.5(a) shows the mask expanded to degree $N = 30$.

Figure 16.5(b) shows the velocity distribution for a unit-amplitude cap of edge half-angle $\mu = \pi/5$ oriented toward $(\vartheta, \varphi) = (\pi/2, 0)$. Finally, the product of the cap and dipole-like mask distributions yields the desired source velocity

$$\mathbf{u}_d = \mathbf{B}_{g_d} \mathbf{q}(\pi/5, \pi/2, 0). \quad (16.36)$$

Figure 16.5(c) shows this result expanded to degree $N = 30$.

Figures 16.5(d) through (g) show the far-field directivity patterns of the two opposite-polarity semicircular caps for selected ka values. The volume velocity of the entire vibrating region is zero.

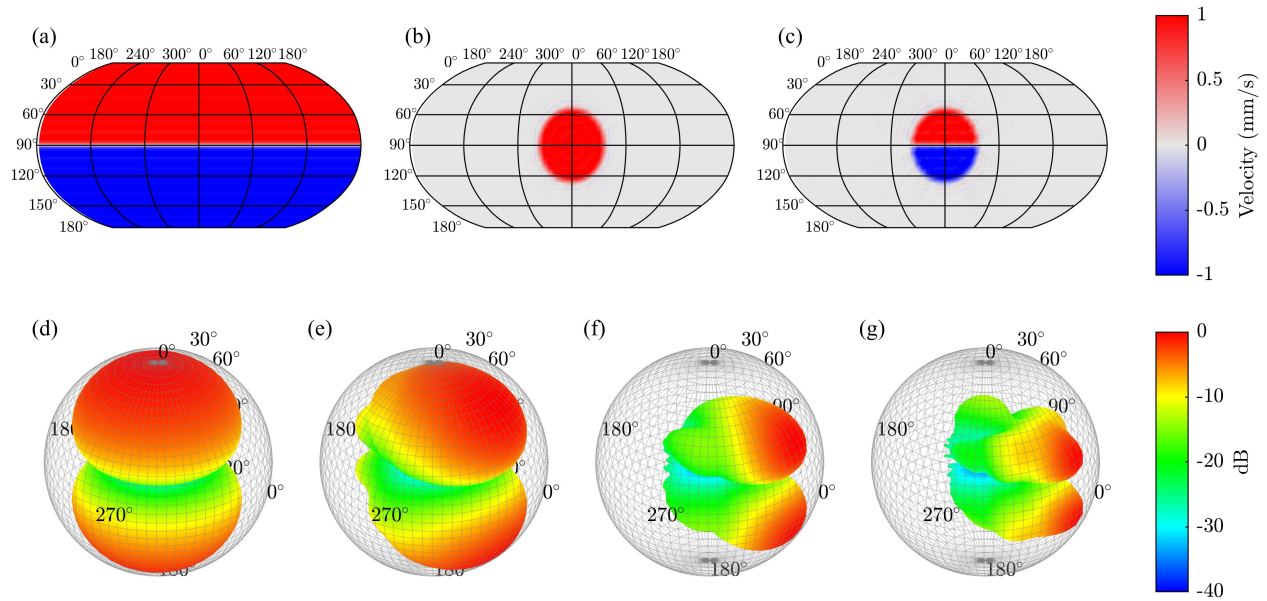


Figure 16.5 Surface velocities for the (a) dipole-like mask function, (b) single radially vibrating cap on a sphere, and (c) product of the mask and cap distributions to create the two opposite-polarity semicircular caps. Normalized far-field directivities for the two opposite-polarity semicircular caps at (d) $ka = 1$, (e) $ka = 5$, (f) $ka = 10$, and (g) $ka = 15$.

Consequently, at low frequencies, one may anticipate a dipole-like directional response. Figure 16.5(d) shows the far-field directivity for $ka = 1$. The directivity is dipolar, with the dipole moment determined by the relative cap locations and the null aligned with the null of the surface velocity distribution. Figures 16.5(e) through (g) show that the primary radiation regions concentrate directly in front of the semicircular caps, as suggested by Morse and Ingard [60], although the nodal line remains. Shadowing behind the rigid sphere becomes more pronounced as the wavelength becomes small relative to the sphere's size.

Table 16.1 Parameters for the dipole-like mask made from two spherical caps.

u_i	μ_i	ϑ_i	φ_i
1	$\pi/2$	0	0
-1	$\pi/2$	π	0

16.3.2 Single Semicircular cap

A single semicircular cap follows from the velocity distribution of two opposite-polarity semicircular caps by adding an additional circular cap whose velocity cancels one of the two semicircular regions. Specifically, the coefficients for the semicircular cap are

$$\begin{aligned}\mathbf{u}_s &= \frac{1}{2}[\mathbf{q}(\mu, \pi/2, 0) + \mathbf{u}_d(\mu, \pi/2, 0)] \\ &= \frac{1}{2}(\mathbf{I} + \mathbf{B}_{g_d}) \mathbf{q}(\mu, \pi/2, 0),\end{aligned}\quad (16.37)$$

where \mathbf{I} is the identity matrix.

Figure 16.6(a) shows the two opposite-polarity semicircular caps from Fig. 16.5(c) but scaled by a factor of 1/2. Figure 16.6(b) shows the additional circular cap with an amplitude of 1/2, and Fig. 16.6(c) shows their sum. The volume velocity is not zero as it was in the preceding example. Consequently, at lower frequencies [Fig. 16.6(d)], the radiation is not dipolar but is similar to that of a radially vibrating circular cap on a sphere. [10] However, for $ka = 5$ [Fig. 16.6(e)], there is less radiation to the sides, and the primary radiation region appears as a distinct lobe. For higher ka values [Figs. 16.6(f) and (g)], the directivity pattern continues to narrow and concentrates in the region directly in front of the semicircular cap.

16.3.3 Four Alternating-Polarity Quarter-Circular Caps

A vibrating cap with two orthogonal diametric nodes follows by taking the mask of Fig. 16.5(c) and multiplying it by a $\pi/2$ rotated version of itself. The rotated dipole-like mask is

$$\mathbf{g}_{dr} = \sum_{i=1}^2 u_i \mathbf{q}(\pi/2, \vartheta_i, 0). \quad (16.38)$$

Table 16.2 lists the parameters for the two caps that generate this result. The product of the two masks, which generates a quadrupole-like mask, becomes

$$\mathbf{g}_q = \mathbf{B}_{g_d} \mathbf{g}_{dr}, \quad (16.39)$$

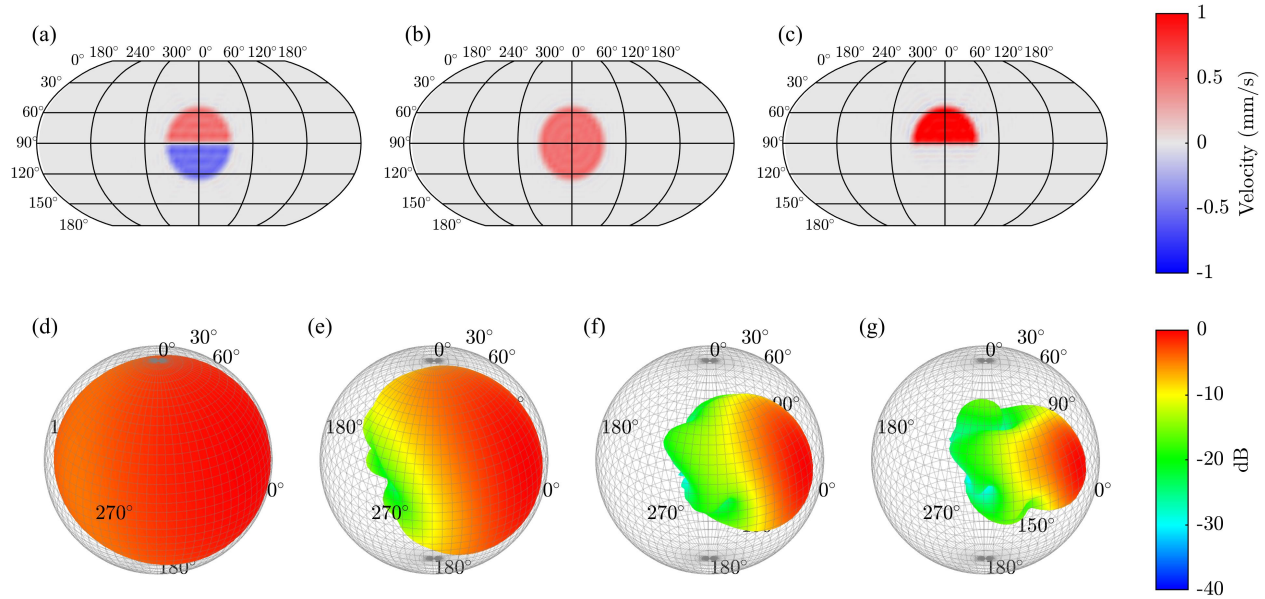


Figure 16.6 Surface velocity for the (a) two opposite-polarity semicircular caps, (b) single cap on a sphere, and (c) summation of the surface velocities in (a) and (b) to cancel the negative polarity region. Normalized far-field directivities for the semicircular cap at (d) $ka = 1$, (e) $ka = 5$, (f) $ka = 10$, and (g) $ka = 15$.

which requires an application of the spatial masking operator. The final velocity distribution requires one more multiplication to reach the desired result:

$$\mathbf{u}_q = \mathbf{B}_{\mathbf{g}_q} \mathbf{q}(\mu, \pi/2, 0) = \mathbf{B}_{\mathbf{g}_d} \mathbf{B}_{\mathbf{g}_{dr}} \mathbf{q}(\mu, \pi/2, 0). \quad (16.40)$$

Figure 16.7(a) shows the quadrupole-like mask, Fig. 16.7(b) shows the spherical cap with $\mu = \pi/5$, and Fig. 16.7(c) shows the velocity distribution for the four alternating-polarity quarter-circular caps. For this configuration, both the monopole and dipole moments must be zero [62]. Thus, one may anticipate quadrupole-like far-field radiation for low frequencies, such as that seen in Fig. 16.7(d) for $ka = 1$. As for the previous two sources, the radiation concentrates in the regions directly in front of the cap segments with increasing frequency [see Figs. 16.7(e) through (f)]. Four primary lobes persist and the nulls between them align with the cap nodal lines.

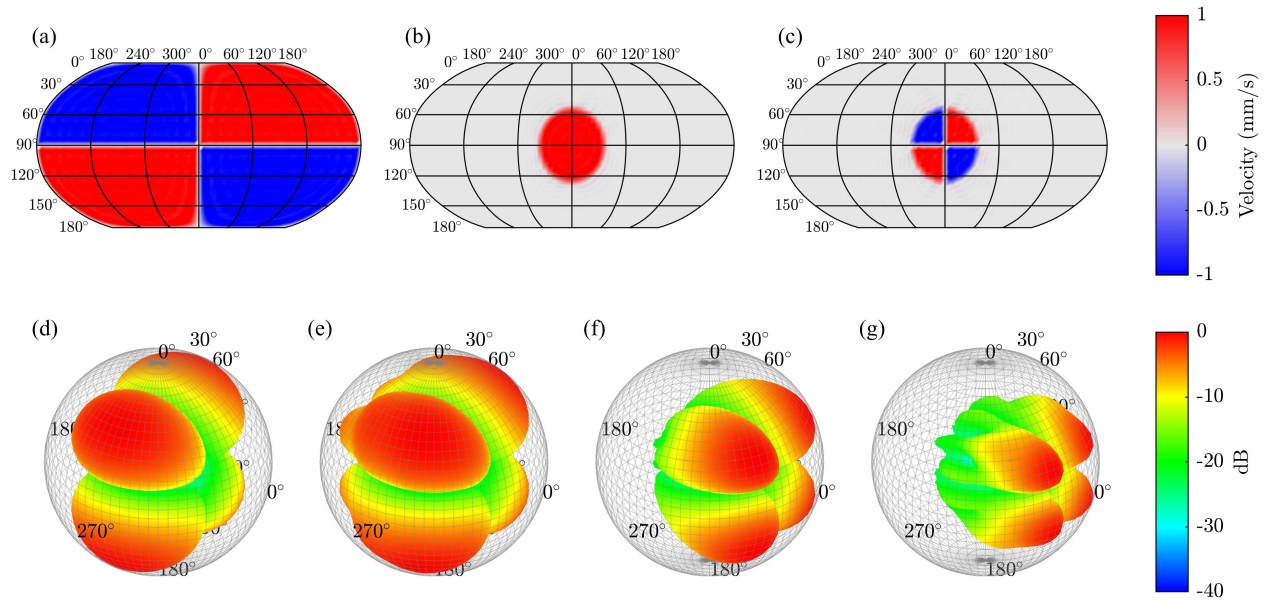


Figure 16.7 Surface velocity for the (a) quadrupole-like mask function, (b) single cap on a sphere, and (c) product of mask and cap distributions to create the four alternating-polarity quarter-circular caps. Normalized far-field directivities for the alternating-polarity cap at (d) $ka = 1$, (e) $ka = 5$, (f) $ka = 10$, and (g) $ka = 15$.

Table 16.2 Parameters for the rotated dipole-like mask made from two caps.

u_i	θ_i	ϑ_i	φ_i
1	$\pi/2$	$\pi/2$	$\pi/2$
-1	$\pi/2$	$\pi/2$	$3\pi/2$

16.3.4 More Complicated Mode Shape

The concept used to generate the quadrupole-like cap generalizes to vibrating caps with other imposed patterns. For example, Fig. 16.8 shows that a mode shape with three diametric and two circular nodes results by combining a mask with six alternating-polarity regions with concentric opposite-polarity caps. The mask shown in Fig. 16.8(a) results by multiplying three dipole-like masks, with the parameters tabulated in Table 16.3. The pattern shown in Fig. 16.8(b) results from adding two circular caps with the parameters also tabulated in Table 16.3. The product of

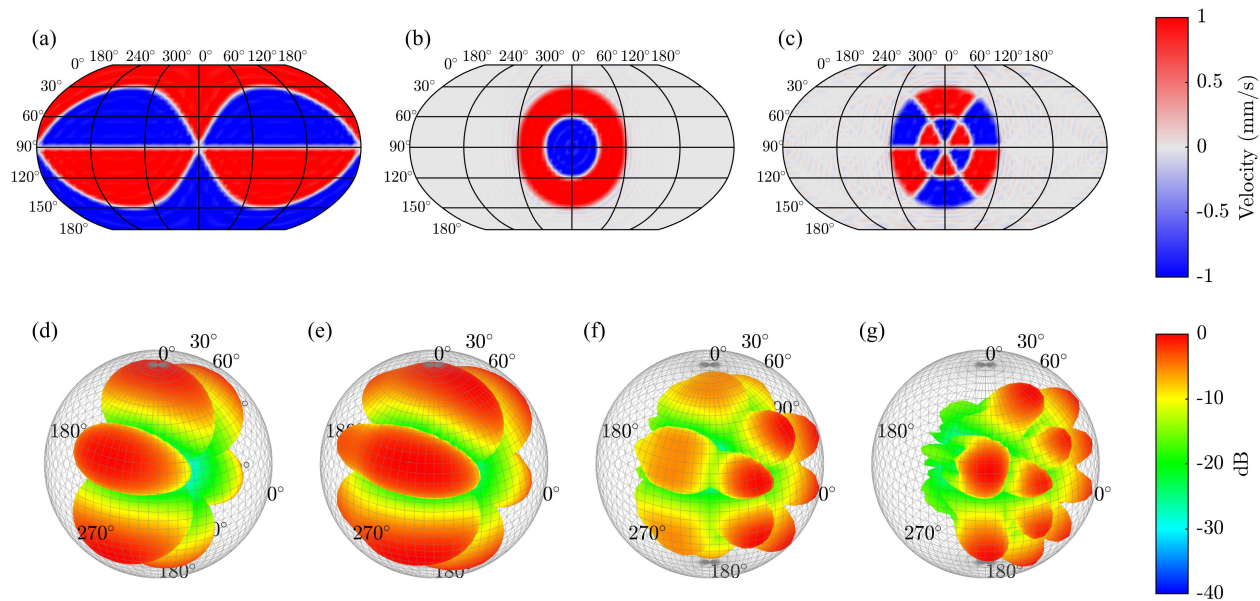


Figure 16.8 Surface velocity for the (a) diametric node masking function, (b) circular node masking function, and (c) product of the two masks. Normalized far-field directivities for the composite cap at (d) $ka = 1$, (e) $ka = 5$, (f) $ka = 10$, and (g) $ka = 15$.

distributions in the to figures yields the final velocity distribution in Fig. 16.8(c), which mimics a vibrating cap with a (3,2)-type mode. Generating this vibrating cap requires four applications of the spatial masking operator.

As shown in Fig. 16.8(d), the far-field directivity pattern for $ka = 1$ has six lobes corresponding to the six angular regions. However, as shown in Figs. 16.8(e) through (f), the six lobes begin to split into sets of two by $ka = 10$ and by $ka = 15$, they comprise twelve visible lobes corresponding to the twelve alternating-polarity regions of the vibrating cap.

16.3.5 Rectangular Cap

A related approach yields a analytic solution for a rectangular vibrating cap on a sphere. Similar to the development of the quadrupole-like circular cap, multiplication of two masks produces the desired rectangular cap. The amplitudes and cap orientations appear in Table 16.4. The first two

Table 16.3 Parameters for the four masking functions used to generate the (3, 2) type mode distribution. The first three masking functions (rows one through six) produce the diametrical nodal mask. The final masking function (rows seven and eight) produce the circular nodes where μ_1 is the total cap edge half-angle and $\mu_2 < \mu_1$ is the angle for the circular node.

u_l	θ_l	ϑ_l	φ_l
1	$\pi/2$	0	0
-1	$\pi/2$	π	0
1	$\pi/2$	$\pi/3$	$\pi/2$
-1	$\pi/2$	$2\pi/3$	$3\pi/2$
1	$\pi/2$	$\pi/3$	$3\pi/2$
-1	$\pi/2$	$2\pi/3$	$\pi/2$
1	$\mu_1 = \pi/3$	$\pi/2$	0
-2	$\mu_2 = \pi/6$	$\pi/2$	0

caps, when added together, generate a rectangular latitudinal strip of width $2\theta_s$, as suggested by Fig. 16.9(a). The second two caps, when multiplied together, create a longitudinal rectangular strip of $2\phi_s$, as suggested by Fig. 16.9(b). The product of the latitudinal and longitudinal strips then yields the rectangular cap in Fig. 16.9(c).

The far-field directivity results in Figs. 16.9(d) through (g) are similar to those of the semicircular cap at the lower frequencies. However, at $ka = 15$, four lobes in 90° spacings form in the frontal plane.

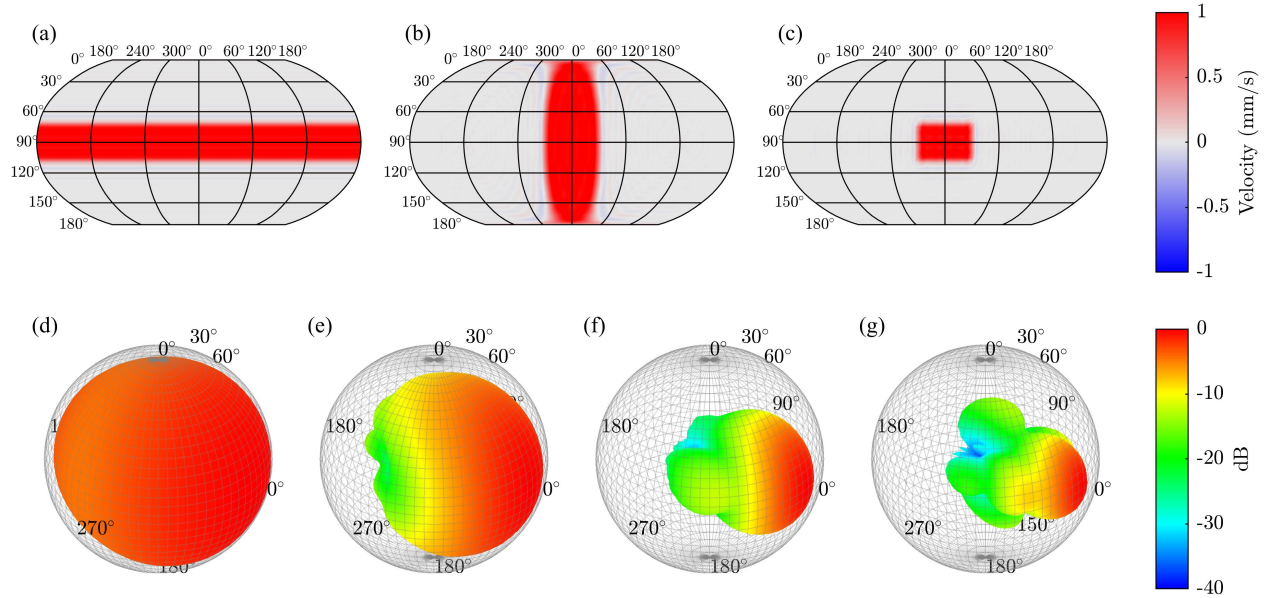


Figure 16.9 Surface velocity for the (a) latitudinal strip of width $2\theta_s$, (b) longitudinal strip of width $2\phi_s$, and (c) rectangular cap. Normalized far-field directivities for the rectangular cap at (d) $ka = 1$, (e) $ka = 5$, (f) $ka = 10$, and (g) $ka = 15$.

Table 16.4 Parameters for the longitudinal and latitudinal strips of width $2\theta_s$ and $2\phi_s$, respectively.

u_l	θ_l	ϑ_l	φ_l
1	$\pi/2 + \theta_s$	0	0
-1	$\pi/2 - \theta_s$	0	0
1	$\pi/2$	$\pi/2$	ϕ_s
1	$\pi/2$	$\pi/2$	$-\phi_s$

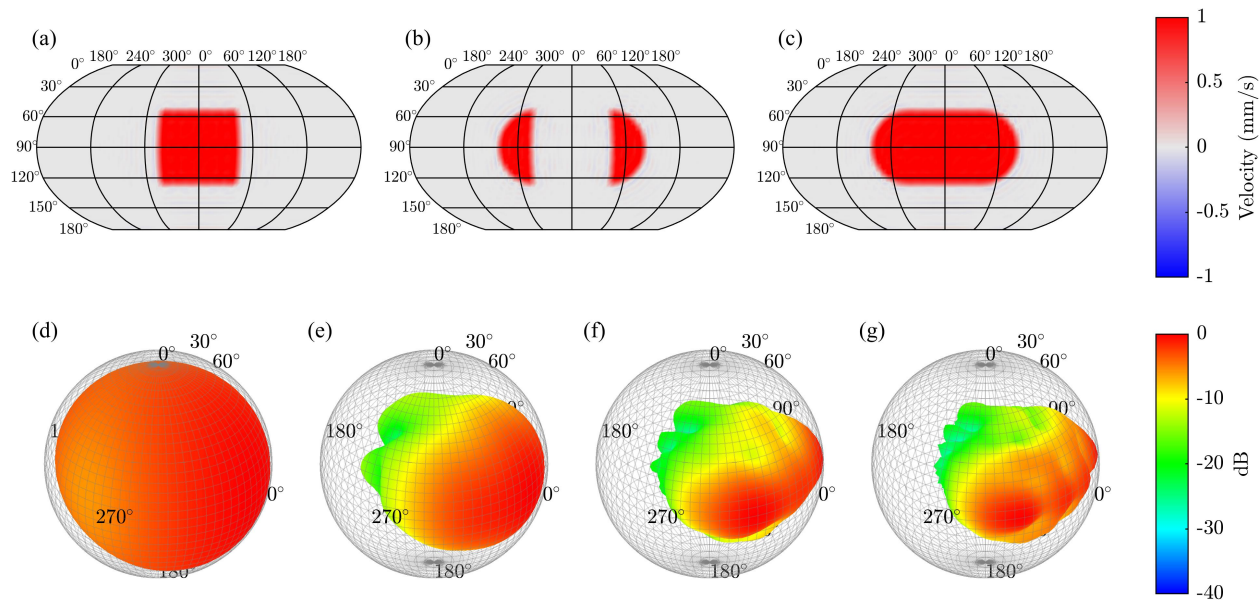


Figure 16.10 Surface velocity for the (a) rectangular cap, (b) two semicircular caps, and (c) sum of the rectangular and two semicircular caps. Far-field directivities for the stadium cap at (d) $ka = 1$, (e) $ka = 5$, (f) $ka = 10$, and (g) $ka = 15$.

16.3.6 Stadium Cap

Another functional cap shape for loudspeaker or human mouth and head modeling is the stadium or obround shape, which comprises two parallel equal-length lines capped with semicircles at their ends. By applying the results of Secs. 16.3.5 and 16.3.2, one can superpose a rectangular cap with two semicircular caps, as shown in Figs. 16.10(a) through (c), to create the desired velocity distribution.

Figures 16.10(d) through (g) show the far-field directivity patterns for this configuration. For $ka = 1$ the directivity is similar to those of the rectangular and semicircular caps seen in Figs. 16.9 and 16.6. However, notable differences arise at higher frequencies, including a significantly wider primary lobe.

16.4 Discussion

A distinct advantage of the proposed method is that it enables the evaluation of radiation from a vast array of spherical cap vibration patterns, including those of the examples presented in this work. Additionally, one may impose different phase distributions on a cap shape using dipole, quadrupole, or more complex mode-shape masks. Significantly, all of the vibrating cap patterns in this work have followed from a single model: a radially vibrating cap on a sphere. Application of other axisymmetric models, such as an axially vibrating cap on a sphere or more advanced velocity profiles, will accommodate even broader classes of cap designs.

Although the approach is highly flexible, it has some limitations. First, the cost of using a spatial masking operator is that the far-field pressure follows from three infinite series instead of only one. The truncation of the triple infinite series leads to truncation errors but still allows feasible implementation. The procedures outlined in Sec. 16.2.4 may minimize these errors, but they may be difficult to mitigate for caps requiring repeated applications of sequential masking operators. For example, when creating a cap with an imposed mode shape, a mode with n diametric and m circular nodes requires $n + 1$ multiplications. Thus, for large n , the truncation errors could cascade and increase significantly. Nonetheless, because the expansion coefficients do not require a matrix inversion, one can overcome truncation errors by adding more terms until achieving a desired level of convergence.

Another limitation of the method is that it requires the calculation of the Wigner $3j$ indices. While many fast and efficient recursive algorithms exist, the number of indices needed for $N = S = P$ is $(N + 1)^6$. Because $N \propto ka$, the required number of indices then goes roughly as $(ka)^6$. Thus, the computational efficiency drastically decreases for $ka \gg 1$. On the other hand, brute-force numerical integration to high accuracy also carries a significant computational burden. The computational complexity of the proposed method is reasonable for the intermediate ranges of ka considered in this work.

16.5 Conclusions

This work has presented a method to determine the spherical harmonic expansion coefficients of several nonaxisymmetric velocity distributions on a sphere. The approach applies a spatial masking operator to calculate the expansion coefficients of a product of two functions. It leads to an analytic solution requiring three infinite series to produce the far-field pressure. Judicious choices of masking functions and their orientations allow the formation of numerous nonaxisymmetric velocity distributions, including caps with imposed phase differences, rectangular, and semicircular caps.

Part V

Microphone Placement Techniques

Chapter 17

Microphone Placement for Sound Power Spectra

This chapter demonstrates how one may employ a single-channel measurement to estimate a source's sound power spectrum. By optimizing the placement through a known frequency-dependent directivity function, one may circumvent radiation filtering effects so that the measured mean-squared pressure is approximately proportional to the source's sound power spectrum. This work appeared previously as:

S. D. Bellows and T. W. Leishman, "Optimal microphone placement for single-channel sound power spectrum estimation and reverberation effects," J. Audio Eng. Soc., 71(1/2), pp. 22-35, (2023).

17.1 Introduction

Audio engineers and acoustical researchers have long sought to establish optimal microphone placements for recording, sound reinforcement, sound design, and other applications. Many professionals place microphones by ear or convention, while others consider basic sound source

directivities to create pleasing or natural-sounding audio. Placement purposes may vary, but one noteworthy aim to complement existing techniques would be to best capture sources' *global* sounds.

Audio engineers have also applied analog and digital reverberation effects to discrete microphone signals for their mixes. Despite the longevity and ubiquity of this practice, the impacts of microphone placements on reverberant effects remain obscure. This paper aims to clarify this topic and explore optimal sound-power-based placements through scientific concepts associated with sound radiation and reverberation.

Researchers have documented rudimentary directional characteristics of selected live sources for decades [3, 4, 7, 30, 64]. Their studies have shown that musical instruments and the human voice, while often quasi-omnidirectional at low frequencies, can become quite directional and develop complex radiation patterns with increasing frequency. In principle, a complete frequency-dependent spherical directivity function is unique to each source and evolves with increasing distance until the distance reaches the geometric and acoustic far field. As a spectrally and spatially dependent feature, the directivity function alters the radiated source spectrum prior to microphone detection. The function consequently affects the timbre heard by listeners, leading some to refer to it as "directional tone color" [36]. Audio engineers consequently exploit source directivities as part of their craft to obtain desired sound qualities [194, 195].

Clark's preferred technique for microphone placement was to position a microphone "at a direction, with respect to the musical instrument, at which the tones sounded the loudest in an attempt to get a quality that might be reasonably representative of that which might be obtained by integration over all directions" [14, 196]. Others have similarly suggested that ideal placements should blend all components of sound generated by the instrument. Bartlett argued that the natural sound of an instrument is that intended for listeners to hear in the far field within a hall, which naturally includes all components of sound generated by the source [15, 16]. Lee likewise encouraged far-field microphone placements, as they provide a sampling of the "plane of diffuse information" at

the listener's position in a hall [197]. Corbett stated that "a close mic does not pick up a complete or natural sonic picture." His rationale likewise pertains to sounds heard by musicians playing acoustic instruments rather than audience members at some distance. Corbett further underscored the concept that microphones placed at sufficient distances should allow "component sounds radiating from all over the instrument . . . to blend together and form the 'whole' and natural acoustic sound we are used to hearing" [194].

Energetically, the sound radiated by a source in all directions is the sound power or total sound energy flux [198]. While capturing this sound is noteworthy in its own right and may have significant audio benefits, its global nature plays a special role in the excitation of a room's acoustic response, which depends upon source emission in myriad directions. Unfortunately, one cannot readily record or reproduce the time-averaged sound power for audio usage; it is a post-processed quadratic acoustic quantity typically derived from special techniques and many microphone signals in anechoic or reverberation chambers [26, 199].

The sounds listeners commonly encounter contain not only direct components from sources but also reflected and reverberant components. Indeed, it is challenging to find listening environments where reflections or reverberation do not affect auditory perception. Because global source radiation drives a natural reverberant field, an ideal microphone position (and response) for reverberant effects should yield an audio signal spectrum very similar to the source sound power spectrum. Consequently, this work explains how one may identify the position whose single-point mean-squared pressure spectrum best mimics this global spectrum. Microphone positions for other objectives may vary.

The sound power spectrum of a source auspiciously follows from its complete spherical directivity function. Past voice and musical instrument studies have provided valuable insights into directivities but have lacked sufficient data to allow investigation of optimal microphone placements. However, the authors and their associates have recently published high-resolution directivities for

speech and musical instruments [17, 18, 19] compatible with the AES standard for loudspeaker directivities [20], making the exploration of optimal sound-power-estimating microphone placements feasible. The general approach also applies to other placements, such as for optimal sharpness, sensory pleasantness, roughness, or loudness [200], but these are beyond the scope of the present work.

The following sections examine the basic theoretical influences of source directivity and reverberation, then present a method to identify optimal microphone placements providing the best source sound power spectral estimates. Subsequent sections apply the method to free-field conditions, then consider placements within reverberant and semi-reverberant environments. The final sections provide recommendations for microphone placements and methodological implementations.

17.2 Theoretical Considerations

17.2.1 Sound Power

The time-averaged sound power spectrum $\langle W(f) \rangle_t$ integrates the frequency-dependent, time-averaged sound-intensity vector $\langle \mathbf{I}(r, \vartheta, \phi, f) \rangle_t$ over a closed surface \mathbf{S} :

$$\langle W(f) \rangle_t = \int \int_S \langle \mathbf{I}(r, \vartheta, \phi, f) \rangle_t \cdot d\mathbf{S}, \quad (17.1)$$

where r is the radius from the source center, ϑ is the elevation angle, ϕ is the azimuthal angle, and f is the frequency. In the free far field, the radial intensity relates to the mean-squared pressure as

$$\langle I_r(r, \vartheta, \phi, f) \rangle_t = \frac{\langle p^2(r, \vartheta, \phi, f) \rangle_t}{\rho_0 c} \quad (17.2)$$

for spherically diverging waves, such that with a spherical enclosing surface, the sound power spectrum becomes

$$\langle W(f) \rangle_t = \frac{r^2}{\rho_0 c} \int_0^{2\pi} \int_{-\pi/2}^{\pi/2} \langle p^2(r, \vartheta, \phi, f) \rangle_t \cos \vartheta d\vartheta d\phi, \quad (17.3)$$

where ρ_0 is the ambient air density and c is the wave speed.

Consequently, a free-field sound power measurement may employ a surrounding spherical array of calibrated microphones and far-field acoustic pressure assessed at several discrete spatial sampling positions. If needed, one may expand the results of closer measurement and propagate them to the far field as an exterior problem [59]. One may also apply a quadrature rule to approximate the integral in Eq. (17.3) [78] or assign effective sampling areas to the mean-squared pressures, as suggested in ISO 3745:2012, a standard describing such an approach for anechoic environments [26]. The ISO 3741:2010 standard presents an entirely different approach employing multiple microphones in a reverberation chamber [199]. Nutter *et al.* explored the similar use of energy density measurements in reverberant environments [201]. In all cases, precision sound power measurements are tedious and time-consuming efforts.

17.2.2 Directivity

The far-field directivity factor function $Q(\vartheta, \phi, f)$ describes the frequency-dependent angular distribution of radiated sound energy from a source. It is the ratio of the far-field radial intensity in a given direction (ϑ, ϕ) to the intensity of an omnidirectional source having the same sound power [10]:

$$Q(\vartheta, \phi, f) = \frac{\langle I_r(r, \vartheta, \phi, f) \rangle_t}{\langle I_{\text{omni}}(r, f) \rangle_t}, \quad (17.4)$$

where

$$\langle I_{\text{omni}}(r, f) \rangle_t = \frac{\langle W(f) \rangle_t}{4\pi r^2}. \quad (17.5)$$

Here, r must satisfy both geometric and acoustic far field requirements such that $r \gg d$, where d is the largest source dimension, $r \gg \lambda/2\pi$, where λ is the acoustic wavelength, and $\langle I_r(r, \vartheta, \phi, f) \rangle_t \propto 1/r^2$. For sound power integration over a sphere, $\langle I_{\text{omni}}(r, f) \rangle_t$ is the spatially averaged intensity.

The directivity index function expresses the directivity factor function on a logarithmic scale:

$$DI(\vartheta, \phi, f) = 10 \log_{10} Q(\vartheta, \phi, f). \quad (17.6)$$

For omnidirectional source radiation, the local intensity equals the spatially averaged intensity, such that $Q(\vartheta, \phi, f) = 1$ and $DI(\vartheta, \phi, f) = 0$ at all angles.

For free-field spherically diverging waves, the far-field mean-squared pressure is the “direct” sound that associates the directivity factor function and sound power as

$$\langle p_d^2(r, \vartheta, \phi, f) \rangle_t = \left[\frac{\rho_0 c Q(\vartheta, \phi, f)}{4\pi r^2} \right] \langle W(f) \rangle_t. \quad (17.7)$$

Consequently, the directivity factor function behaves as a weighted, frequency-dependent magnitude filter that modifies the sound power spectrum to produce the mean-squared pressure spectrum. Audio engineers successfully exploit source directivity to achieve desired timbral effects because the filter changes with angle.

17.2.3 Reverberation

In many practical situations, radiation occurs in a semi-reverberant or reverberant environment rather than a free-field environment. If the reverberant field is diffuse, its mean-squared pressure, locally averaged over a volume V_l with dimensions large compared to wavelength but small compared to room volume V , takes the form [62]

$$\langle p_r^2(f) \rangle_{t, V_l} = \left[\frac{4\rho_0 c}{R(f)} \right] \langle W(f) \rangle_t, \quad (17.8)$$

where $R(f)$ is the frequency-dependent and (ideally) spatially uniform “room constant”

$$R(f) = \frac{S \langle \alpha(f) \rangle_s}{1 - \langle \alpha(f) \rangle_s}. \quad (17.9)$$

Here, S is the room surface area and $\langle \alpha(f) \rangle_s$ is the spatially averaged absorption coefficient, which follows approximately from the Eyring reverberation time $T_{60,E}(f)$ as

$$\langle \alpha(f) \rangle_s = 1 - e^{-0.161V/T_{60,E}(f)S}. \quad (17.10)$$

Equation (17.8) indicates that the source sound power is entirely responsible for exciting the reverberant field, while the inverted room constant acts as a weighted magnitude filter that colors the sound power spectrum to produce the observed reverberant mean-squared pressure spectrum. Therefore, to establish realistic spectral properties for reverberant effects, one should know the sound power spectrum and modify it via this weighted filter while utilizing the frequency-dependent temporal decay associated with the reverberation time.

Of course, this basic theory ignores nondiffuse fields and early room reflections, which some effects aim to simulate before the temporal onset of a diffuse reverberant tail. However, after the first few reflections, numerous additional reflections depend upon the source radiation in many directions plus the exact source and receiver locations within the room. Accordingly, the required radiation directions are unknown without careful measurement or modeling. Consequently, the most acceptable excitation for on-demand reverberant effects involves the ostensibly inaccessible radiation in *all* directions rather than the radiation in only a *single* direction, as commonly employed in current audio practice. Section 3 discusses the exception to this rule that occurs when radiation in one direction represents the spectral properties of the radiation in all directions.

17.2.4 Semi-Reverberant Environments

For semi-reverberant rooms, the Hopkins-Stryker equation (HSE) [202] models the locally averaged total mean-squared pressure as a sum of the direct [Eq. (17.7)] and diffuse reverberant [Eq. (17.8)] field components [62]:

$$\langle p^2(r, \vartheta, \phi, f) \rangle_{t, V_l} = \rho_0 c \langle W(f) \rangle_t \left[\frac{Q(\vartheta, \phi, f)}{4\pi r^2} + \frac{4}{R(f)} \right]. \quad (17.11)$$

The critical distance r_c is the radius at which the direct and reverberant contributions to the locally averaged mean-squared pressure are equal [62]:

$$r_c(\vartheta, \phi, f) = \sqrt{\frac{Q(\vartheta, \phi, f)R(f)}{16\pi}}. \quad (17.12)$$

When $r \ll r_c$, the total field behaves more like a free-field environment and when $r \gg r_c$, it behaves more like a reverberant environment.

While these formulations only approximate the sound field characteristics, they provide a suitable basis for the present investigation. They demonstrate how reverberation effects should rely upon sound radiated in many directions, how use of this global physical characteristic may become practical through a single optimized microphone placement, and how basic room conditions affect that placement. Accordingly, the formulations lead to practical insights that will lay the groundwork for future studies.

17.2.5 Source-Filter Representation

A linear time-invariant system with input $a(t)$, output $b(t)$, and frequency response function $H(f)$ has an averaged input autospectrum $G_{aa}(f)$ and a similar output autospectrum $G_{bb}(f)$ related as [131]

$$G_{bb}(f) = |H(f)|^2 G_{aa}(f). \quad (17.13)$$

From Eq. (17.11), it is evident that the source sound power energizes both the direct and reverberant sound fields. Thus, if one views the sound power spectrum as the input autospectrum and the mean-squared pressure spectrum as the output autospectrum, the HSE energetically characterizes the acoustic system as an LTI system with a time-averaged power response given by the summed direct and reverberant components:

$$|H(r, \vartheta, \phi, f)|^2 = |H_d(r, \vartheta, \phi, f)|^2 + |H_r(f)|^2 = \rho_0 c \left[\frac{Q(\vartheta, \phi, f)}{4\pi r^2} + \frac{4}{R(f)} \right]. \quad (17.14)$$

Accordingly, both the source directivity factor $Q(\vartheta, \phi, f)$ at a given angle and the inverted room constant $1/R(f)$ act as contributing filters that modify the sound power spectrum to produce the resultant total mean-squared pressure spectrum, as suggested by Fig. 17.1.

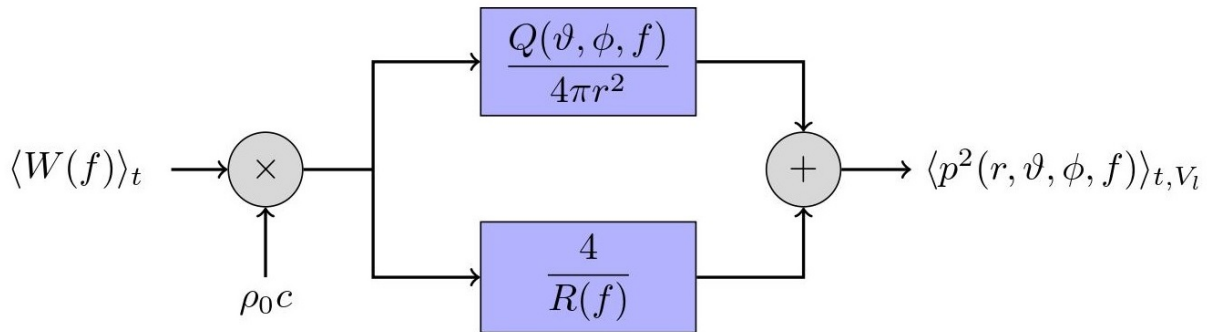


Figure 17.1 An energetic source-filter model representing the Hopkins-Stryker equation. Both the source directivity factor for a given angle and the frequency-dependent room constant color the sound power spectrum to produce the locally averaged total mean-squared pressure spectrum at the observation position.

17.3 Optimal Microphone Placements For Sound Power Estimation and Reverberation Effects

A practical method to estimate the sound power spectrum would help to produce the optimal driving signals for reverberant effects that better simulate diffuse reverberation and early reflections. This spectrum is typically unknown to an audio engineer, but Eq. (17.11), archived source directivities [38], a frequency-dependent room constant, and a single locally averaged sound pressure measurement at an arbitrary position $(r_m, \vartheta_m, \phi_m)$ yield a worthwhile estimate:

$$\langle W(f) \rangle_t = \frac{\langle p^2(r_m, \vartheta_m, \phi_m, f) \rangle_{t, V_l}}{\rho_0 c} \left[\frac{Q(\vartheta_m, \phi_m, f)}{4\pi r_m^2} + \frac{4}{R(f)} \right]^{-1}. \quad (17.15)$$

In the source-filter model context, this energetic calculation generally requires time-domain convolution for real-time processing, where the filter might result from traditional techniques to create a minimum-phase or linear-phase filter whose magnitude-squared response equals Eq. (17.14) [203]. The approach would not cause insurmountable problems, but if one could instead

find the microphone position with the mean-squared pressure spectrum most similar to the sound power spectrum over all frequencies of interest, the summed frequency-dependent parameters of Eq. (17.15) would remain roughly constant. This result would vastly simplify the application and is the essence of the proposed microphone placement scheme. The optimal microphone position $(r_o, \vartheta_o, \phi_o)$ should then produce a mean-squared pressure directly proportional to the sound power as

$$\langle W(f) \rangle_t \approx C \langle p^2(r_o, \vartheta_o, \phi_o, f) \rangle_{t, V_l}, \quad (17.16)$$

where C is a proportionality constant.

The following sections explore the placements of an individual calibrated or flat-response microphone for the best sound power estimates under semi-reverberant, free-field, and reverberant conditions. In each case, two assumptions are that the microphone falls in the geometric and direct acoustic far fields and that any frequency of interest falls above the room's Schroeder frequency f_S [204, 205].

17.3.1 Semi-Reverberant Environments

Optimal microphone placement for sound power estimation in a semi-reverberant environment requires a careful balance between the direct and reverberant fields. The placement radius r_m , angular coordinates (ϑ_m, ϕ_m) , room constant $R(f)$, and far free-field directivity factor function $Q(\vartheta, \phi, f)$ are all relevant. A suitable objective function leading to the optimal position that keeps the bracketed portion of Eq. (17.15) nearly constant over frequency to satisfy Eq. (17.16) has the form

$$J_{sr}(r, \vartheta, \phi) = \text{Var} \left\{ 10 \log_{10} \left[\frac{Q(\vartheta, \phi, f)}{4\pi r^2} + \frac{4}{R(f)} \right] \right\}, \quad (17.17)$$

where

$$\text{Var}[\beta(k)] = \frac{1}{K} \sum_{k=1}^K w(k) [\beta(k) - \langle \beta(k) \rangle_k]^2, \quad (17.18)$$

$\langle \beta(k) \rangle_k$ is the mean of $\beta(k)$, and k is the index for K discrete frequency bands. The frequency-dependent weights $w(k)$ optimize the position for specific frequencies or a selected bandwidth (e.g., one might use heavier weights for bins in the range of 100 Hz to 4 kHz).

The objective function minimum gives the position where the levels of the summed, bracketed parameters in Eq. (17.17) vary least over frequency. While levels tie closely to perceptual acoustic values, one may also adapt the objective function to the bracketed terms alone with similar results. At the optimal position $(r_m, \vartheta_o, \phi_o)$, the total (direct plus reverberant) sound is roughly constant over frequency, such that the sound power in Eq. (17.15) becomes

$$\langle W(f) \rangle_{t,sr} \approx C_{sr} \langle p^2(r_m, \vartheta_o, \phi_o, f) \rangle_{t,V_l}, \quad (17.19)$$

where the semi-reverberant proportionality constant is

$$C_{sr} = \frac{1}{\rho_0 c} \left\langle \left[\frac{Q(\vartheta_o, \phi_o, f)}{4\pi r_m^2} + \frac{4}{R(f)} \right] \right\rangle_f^{-1}. \quad (17.20)$$

17.3.2 Free-field Environments

In an ideal free-field environment, $R(f) \rightarrow \infty$, such that $4/R(f) \rightarrow 0$ in Eq. (17.15). In a dead but not completely anechoic room, the ratio of total propagating sound energy to the time rate at which the boundaries remove sound energy from the room yields a time interval considerably shorter than that required for a wave to travel across the room's characteristic dimension [62]. In addition, $4/R(f)$ tends to be relatively small and r_c relatively large. When $r_m \ll r_c$, which is valid over much of the room, the direct field dominates the mean-squared pressure, so the room acoustics behave much like a free-field environment. In this case, the objective function $J_{sr}(r, \vartheta, \phi)$ in Eq. (17.17) reduces to a weighted DI variance over frequency:

$$J_{sr,d}(\vartheta, \phi) = \frac{1}{K} \sum_{k=1}^K w(k) |DI(\vartheta, \phi, k) - \langle DI(\vartheta, \phi, k) \rangle_k|^2. \quad (17.21)$$

The sound power estimate follows from Eqs. (17.19) and (17.20), where the proportionality constant becomes

$$C_{sr,d} = \frac{4\pi r_m^2}{\rho_0 c} \langle [Q(\vartheta_o, \phi_o, f)] \rangle_f^{-1}. \quad (17.22)$$

An alternative objective function results from a simple observation regarding a source's directivity factor function. At a given frequency, the intermediate and mean-value theorems guarantee the existence of an angular position where the sound intensity equals the average sound intensity over the measurement sphere. In this direction, $Q(\vartheta_m, \phi_m, f) = 1$ and $DI(\vartheta_m, \phi_m, f) = 0$, meaning the source is seemingly *nondirectional*, meaning one cannot distinguish its directivity from that of an omnidirectional source, which, parenthetically, is nondirectional in *all* directions. The benefit of an optimal nondirectional position is that it allows one to apply the simple formulas of Eqs. (17.2) and (17.4) to estimate the sound power. Because the intermediate and mean-value theorems cannot guarantee that a position that is nondirectional at one frequency will be nondirectional at other frequencies, one can choose an approximately optimal angular position for all frequencies of interest by seeking the location that minimizes deviations from $DI = 0$ through the free-field objective function

$$J_{ff}(\vartheta, \phi) = \frac{1}{K} \sum_{k=1}^K w(k) |DI(\vartheta, \phi, k)|^2. \quad (17.23)$$

This form, derived using an approach different than that used to develop $J_{sr,d}(\vartheta, \phi)$, is notably similar to Eq. (17.21). However, unlike $J_{sr,d}(\vartheta, \phi)$, which attempts to produce a flat inverse filter over frequency, $J_{ff}(\vartheta, \phi)$ yields the radiated intensity most similar to the spherically averaged intensity over the weighted bandwidth. In other words, it attempts to find the most nondirectional angular orientation (ϑ_o, ϕ_o, f) , such that $Q(\vartheta_o, \phi_o, f) \rightarrow 1$ and $DI(\vartheta_o, \phi_o) \rightarrow 0$ over all frequencies. From Eqs. (17.15) and (17.16), it is apparent that a measurement in this direction with a calibrated or flat-response microphone leads to the free-field sound power estimate

$$\langle W(f) \rangle_{t,ff} \approx C_{ff} \langle p^2(r_m, \vartheta_o, \phi_o, f) \rangle_{t,V_l}, \quad (17.24)$$

where the proportionality constant is

$$C_{ff} = \frac{4\pi r_m^2}{\rho_0 c}. \quad (17.25)$$

Under free-field conditions, $C_{sr,d}$ collapses to C_{ff} when $Q(\theta_o, \phi_o, f) = 1$.

17.3.3 Reverberant Environments

In a live room, the ratio of total propagating sound energy to the time rate at which the boundaries absorb or transmit sound energy out of the room yields a time markedly longer than that required for a wave to travel across the room's characteristic dimension [62]. In Eqs. (17.11) and (17.17), $4/R(f)$ then becomes considerably larger than for a dead room, and r_c becomes substantially smaller, such that when $r_m \gg r_c$, which is valid over much of the room, the diffuse reverberant field dominates the total mean-squared pressure. If the microphone falls within this region, the objective function in Eq. (17.17) becomes independent of position, so the microphone placement is arbitrary. The ideal room constant has no spatial dependence, and any position will produce a locally averaged mean-squared pressure related to the time-averaged sound power by Eq. (17.8). Point mean-squared pressure measurements are subject to the spatial variance of the diffuse field [206, 207]. A spectrally uniform proportionality between $\langle W(f) \rangle_t$ and $\langle p^2(r_m, \vartheta_m, \phi_m, f) \rangle_{t, V_l}$ requires the room constant $R(f)$ to be constant over frequency. If it is not constant, a compensation filter must correct the coloration.

When the microphone is far from the source in a reverberant field, low-level reverberance may yield poor signal-to-noise ratio, whereas a high-level reverberance may not require added artificial reverberation. Nevertheless, reverberant-field placement is interesting because it shows that one cannot exploit source directivity to achieve a sound power spectral estimate, leaving one to rely only on the room's acoustical properties. Other factors of concern include the initial time delay gap of propagation from the source to the microphone and early reflections that may yield auditory cues differing from those of a desired reverberant effect. After the direct sound arrival at the observation

position, the diffuse field takes approximately $3l/c$ s to build with a sufficient number of substantial reflections, where l is the characteristic room dimension [62].

17.4 Results

Several directivity factor functions and sound power spectra for speech and musical instruments [38] resulted from 5° resolution directivity measurements in an anechoic chamber [1, 6]. The measurements conformed to the AES loudspeaker spherical sampling standard [33]. The speech data resulted from recordings of phonetically balanced speech passages at 2,522 unique measurement positions over a sphere, while the musical instrument data followed similarly from recordings of played chromatic scales over complete instrument working ranges.

Besides the presumably infinite room constant of the anechoic chamber as a free-field environment, other room constant values resulted from experimental measurements in a classroom and a dance studio. Marquez reported the 1/3-octave-band values for the two rooms [208], which appear as $10\log_{10}[4/R(f)]$ in Fig. 17.2. As outlined in Eqs. (11) and (14) and as depicted by the lower branch of the diagram in Fig. 17.1, these curves represent the frequency-dependent weighting that each room applies to the time-averaged sound power of the source to contribute to the mean-squared pressure. Table 17.1 presents the room volumes, surface areas, Schroeder frequencies, frequency-averaged reverberation times, and critical distances (assuming an omnidirectional source). The classroom's room constant is relatively uniform from 600 Hz to 4 kHz, while the dance studio's room constant varies more significantly.

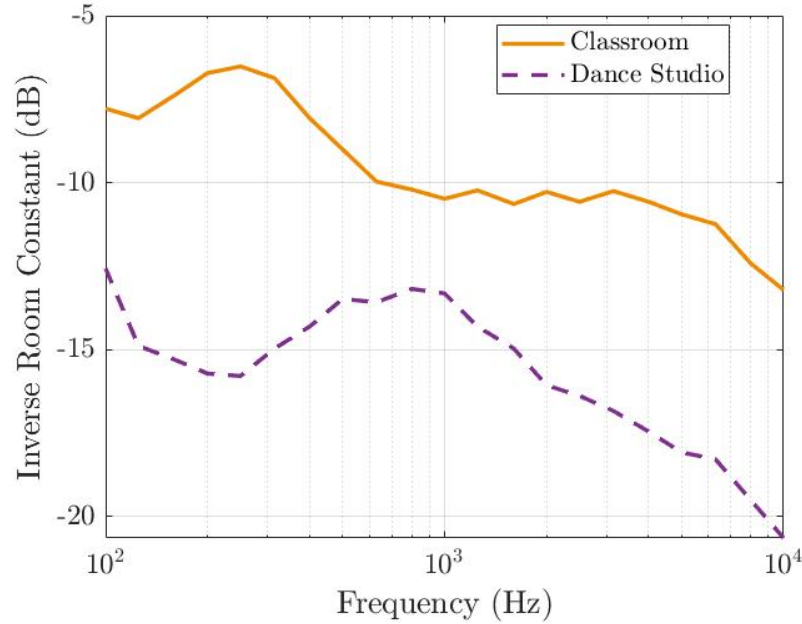


Figure 17.2 Decibel plots $10\log_{10}[4/R(f)]$ of the inverted and scaled room constants, measured in 1/3-octave bands in a classroom and dance studio. The classroom values below $f_S = 154$ Hz (see Table 17.1) are less reliable than the higher-frequency values.

Table 17.1 Geometrical and acoustical properties of the classroom and dance studio used in the semi-reverberant field examples.

	Classroom	Dance Hall
V (m ³)	90.5	532
S (m ²)	128.0	475.7
f_S (Hz)	154	77
$\langle T_{60} \rangle_f$ (s)	0.49	0.73
r_c (m)	0.87	1.77

17.4.1 Source Directivity Characteristics

The frequency-dependent directional characteristics of live sources are sometimes intricate, but many share pattern features, particularly across instrument families, because of related excitation, vibration, and radiation mechanisms. Several sources behave as roughly omnidirectional radiators at low frequencies, but their more distinctive patterns emerge at mid to high frequencies. In fact, significant directivity changes sometimes occur from one frequency band to another. The following sections provide illustrative results for brass, woodwind, and string instruments, plus speech.

Brass Instruments

Brass instruments have characteristically dominant radiation in the direction of the instrument bell, although diffraction effects are also significant. Figure 17.3 illustrates these effects with 1.6 kHz, 1/3-octave-band DI functions plotted on spheres of constant radius for the trumpet, French horn, trombone, and tuba, utilizing a 20 dB color scale. The red color denotes the directional regions where the sound intensity is greater than the average intensity. Blue reveals *anti-directional* regions, meaning the sound intensity is less than the average intensity. White shows regions where the intensity is nearly equal to the average intensity [i.e., $DI(\vartheta, \phi) \approx 0$]. All four plots appear from the same vantage point. The 0° elevation and azimuthal angles indicate the front of the musician and the -90° azimuthal angle indicates the right side of the musician. The solid red line is the positive x -axis in Cartesian coordinates, while the solid blue line is the positive z -axis.

For the trumpet [Fig. 17.3(a)] and trombone [Fig. 17.3(c)], the bright red region falls in front of the musician and slightly downward as expected. For the French horn [Fig. 17.3(b)], it is to the right and behind the musician, and for the tuba [Fig. 17.3(d)], it is almost directly above the musician. Each instrument produces a dark blue region on the opposing side of the bell and musician, demonstrating weaker intensity levels.

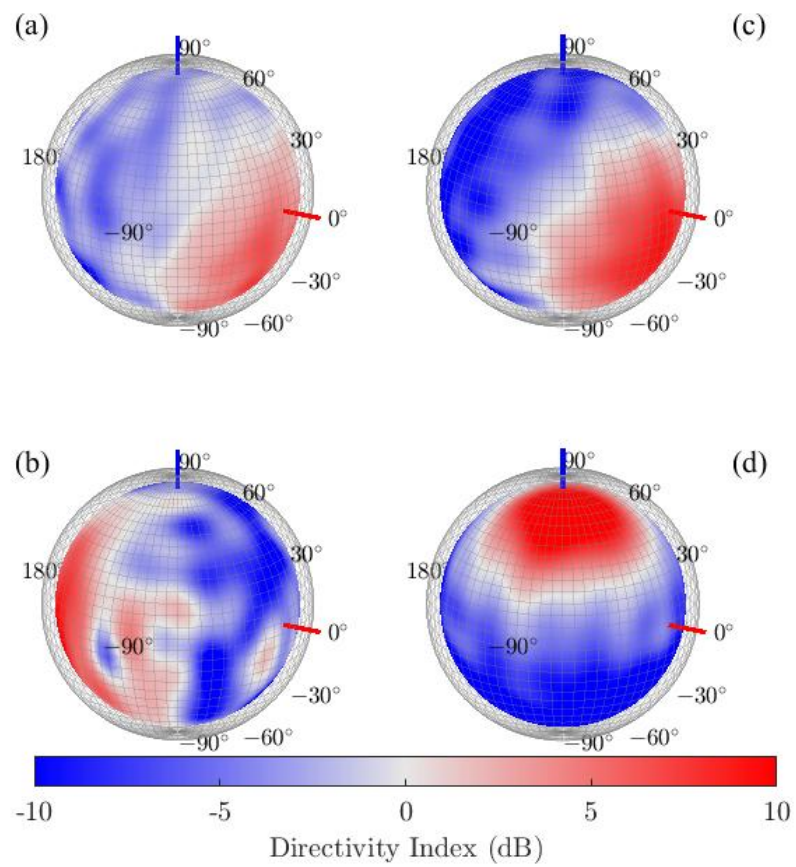


Figure 17.3 Directivity index function color spheres for the 1.6 kHz, 1/3-octave band for (a) trumpet, (b) French horn, (c) trombone, and (d) tuba.

Woodwind Instruments

Woodwind instruments produce directivity lobes or constructive and destructive interference patterns. These features result from the simultaneous radiations of embouchure holes, tone holes, and bells, which act individually as simple sources [40]. Such lobes are apparent in Fig. 17.4, which shows 1 kHz, 1/3-octave-band DI color spheres for the flute, bassoon, tenor saxophone, and baritone saxophone on a 10 dB scale. Areas of constructive and destructive interference appear as alternating regions of red and blue.

The flute DI sphere in Fig. 17.4(a) has four strong lobes that are approximately axisymmetric about the transversely oriented instrument. The other three instruments produce interference lobes about axes oriented in upward directions. Several patches are visible in the bassoon DI plot [Fig. 17.4(b)], two strong lobes are clear in the tenor saxophone plot [Fig. 17.4(c)], and three dominant lobes plus a smaller fourth lobe are apparent to the side of the baritone saxophone [Fig. 17.4(d)]. Unlike brass instruments, woodwind instruments do not produce consistently strong and weak radiation regions toward their front and back sides, respectively. However, a musician's presence produces frequency-dependent diffraction and shadow regions as it does for brass instruments.

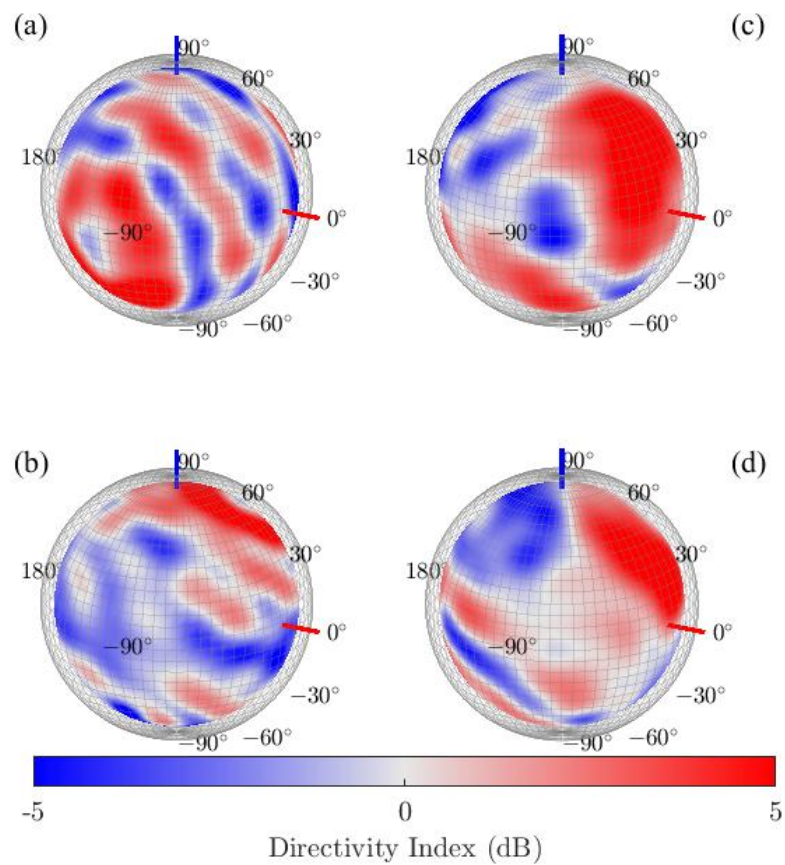


Figure 17.4 Directivity index function color spheres for the 1 kHz, 1/3-octave band for (a) flute, (b) bassoon, (c) tenor saxophone, and (d) baritone saxophone.

String Instruments

String instruments are complex radiators with less predictable directivity patterns. Figure 17.5 presents DI functions for the violin, viola, cello, and double bass in the 400 Hz, 1/3-octave band on a 10 dB scale. Even at this relatively low frequency, the patterns are distinctive. For example, both the violin [Fig. 17.5(a)] and viola [Fig. 17.5(b)] produce strong radiation regions above the instruments and in the directions of the musicians' legs. However, the violin extends substantial radiation to the musician's left side. The cello's [Fig. 17.5(c)] strong directional region curves around the front and side of the instrument, but the instrument also has a significant anti-directional region toward the musician's right leg. The double bass [Fig. 17.5(d)] produces substantial radiation to the instrument's sides and weak intensity behind and directly in front of the musician.

Speech

Speech radiation is similar to brass instrument radiation in that it tends to have a strong region in front of the mouth and a weak region behind the talker. However, speech radiation tends to be less directional because the mouth and nostrils have much smaller openings than brass bells. Figure 17.6 shows speech DI color spheres for various 1/3-octave bands on a 10 dB scale. While the most substantial radiation regions for brass instruments remain close to their bell axes, diffraction shifts the maximum speech radiation axis over frequency [135].

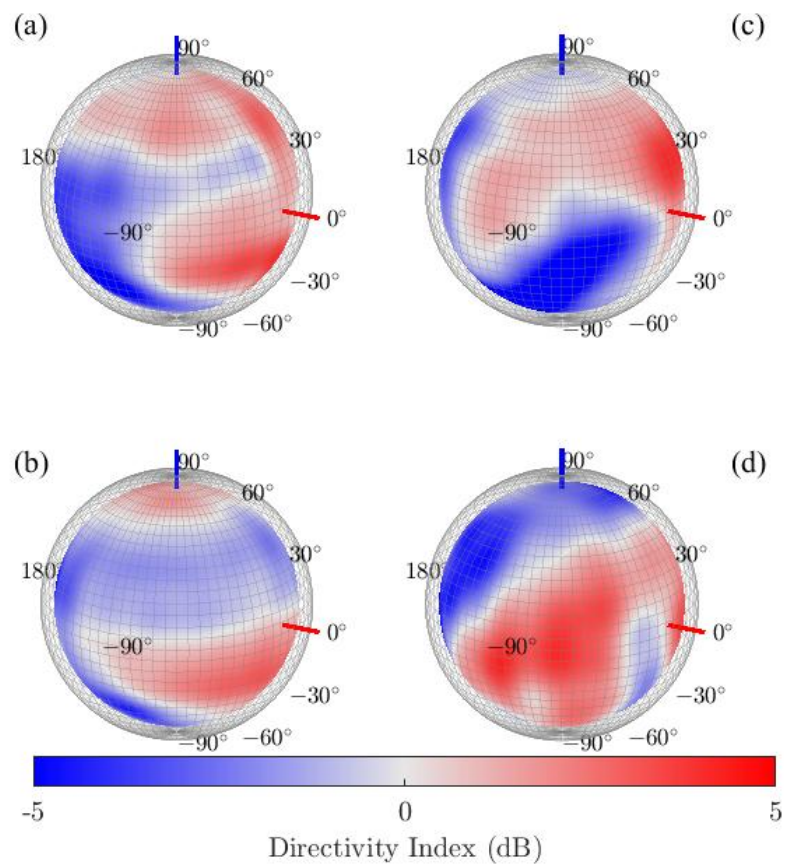


Figure 17.5 Directivity index function color spheres for the 400 Hz, 1/3-octave band for (a) violin, (b) viola, (c) cello, and (d) double bass.

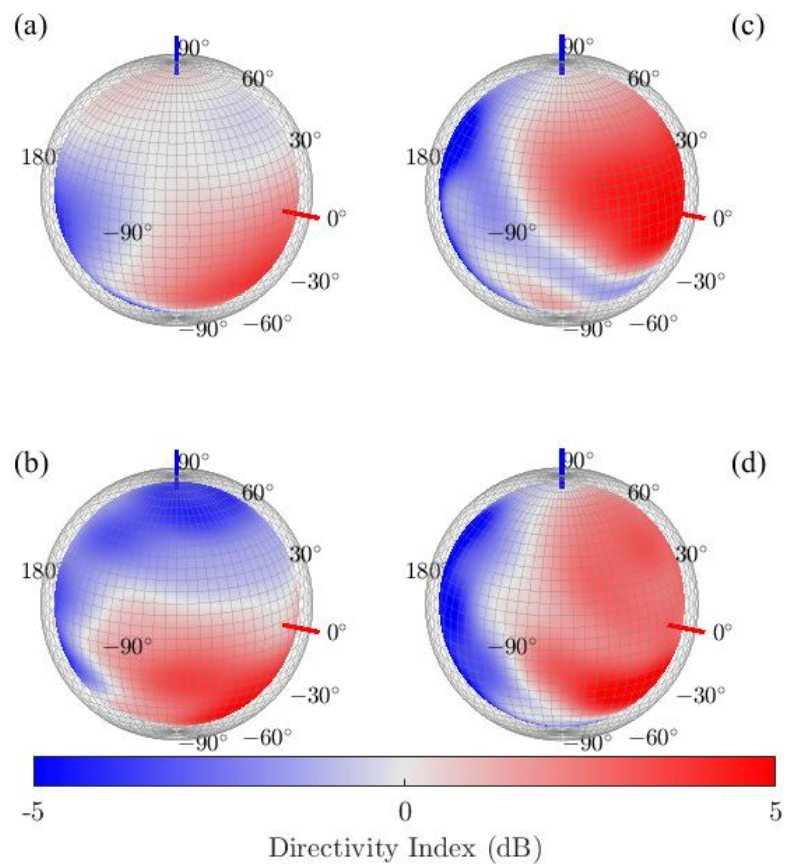


Figure 17.6 Speech directivity index function color spheres for the (a) 400 Hz, (b) 630 Hz, (c) 1.6 kHz, and (d) 2.5 kHz 1/3-octave bands.

17.4.2 Source-Filter Effects

As discussed in Sec. [17.2.5], both source directivity and room effects “color” the sound power spectrum to produce the mean-squared pressure spectrum. Figure 17.7 illustrates these effects for the trombone. The black solid curve shows the scaled 1/3-octave-band sound power spectrum representing the ideal spectral shape that one might use for driving trombone reverberation effects. The green dashed curve shows the mean-squared pressure level at $r_m = 5$ m from the source, assuming omnidirectional radiation over all frequencies. (The assumption simply offsets the curve from the black curve by a constant value.) The red dash-dot curve depicts the simulated mean-squared pressure at the same distance using the on-axis source directivity factor. Because the trombone radiates roughly omnidirectionally at low frequencies, the green and red curves show general agreement up to around 400 Hz. However, as frequency increases and the trombone becomes more directional, the red curve takes on higher values than the green curve. This result suggests that a measured on-axis pressure with its distinct spectral shape will sound too bright compared to the sound power spectrum in free space.

Room effects further affect the spectral shape. As shown in Fig. 17.2, the previously measured dance studio produces a more robust response at low frequencies than at high frequencies. Consequently, the on-axis, mean-squared pressure of the trombone, modeled in the studio using Eq. (17.11), contains a relative low-frequency spectral boost, appearing in the blue dotted curve of Fig. 17.7. The diffuse reverberant field is weak at high frequencies, so the curve closely follows the free-field red curve in that spectral region. Interestingly, while the free-space directivity factor caused the shape of the mean-squared pressure spectrum to diverge from the shape of the sound power spectrum at high frequencies, the room constant counterbalanced those gains with the room’s low-frequency boost. These results illustrate how source directivities and room effects may combine to produce unexpected spectral modifications to acoustic signals.

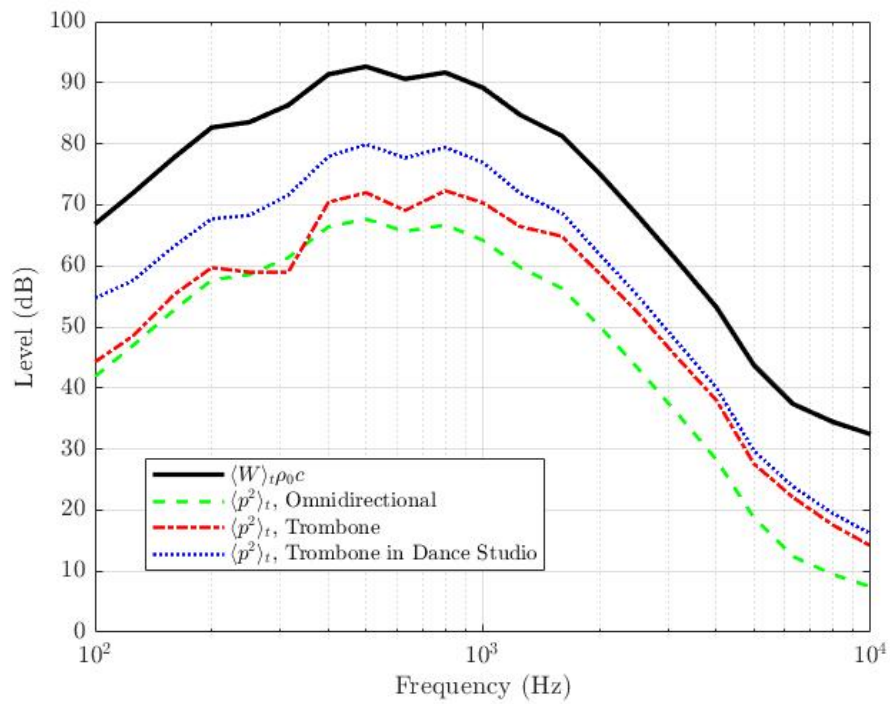


Figure 17.7 The 1/3-octave-band sound power spectrum of a trombone scaled by $\rho_0 c$ and estimated mean-squared pressure spectra under different directional and room conditions at a radius of $r_m = 5.0$ m.

17.4.3 Microphone Placements

Free-field Environments

Figure 17.8 shows a color-mapped projection of the free-field objective function $J_{ff}(\vartheta, \phi)$ for speech, with logarithmic color plotting accentuating the details. The bandwidth considered for this and all other objective functions was 100 Hz to 10 kHz with uniform weighting. Dark purple in the figure corresponds to low objective function values, while bright yellow corresponds to high values. The center of the projection, indicated as $(0^\circ, 0^\circ)$, is front of the talker at mouth level and corresponds to the solid red x -axes in the plots of Fig. 17.6.

As discussed in Ref. [134], the optimal microphone position for free-field speech sound power estimation is toward the *side* of the head and slightly upward in elevation. Because a dominant frontal radiation direction characterizes speech, typical microphone positions in front of the head become more directional with increasing frequency and bias microphone signals with high-frequency content. This result is uncharacteristic of the sound power spectrum energizing a reverberant field. Conversely, after head and body diffraction, speech signals detected in anti-directional regions behind the talker have relatively little high-frequency content, which is also uncharacteristic of the complete radiation driving a reverberant field. Consequently, regions to the talker's side provide a balance between the two extremes for a more natural global spectrum and reverberation-driving signal.

The green dot in Fig. 17.8 pinpoints the location where the mean-squared pressure spectrum most similar to the sound power spectrum. However, a microphone placement anywhere in the lowest (dark purple) objective function region would provide comparable results. Directivity index color spheres, such as those in Fig. 17.8, help validate this optimal position because the regions to the side of the head [near $(\vartheta, \phi) = (0^\circ, -90^\circ)$] for the various 1/3-octave bands are roughly white, meaning the radiation in those directions is approximately equal to the average radiation over the

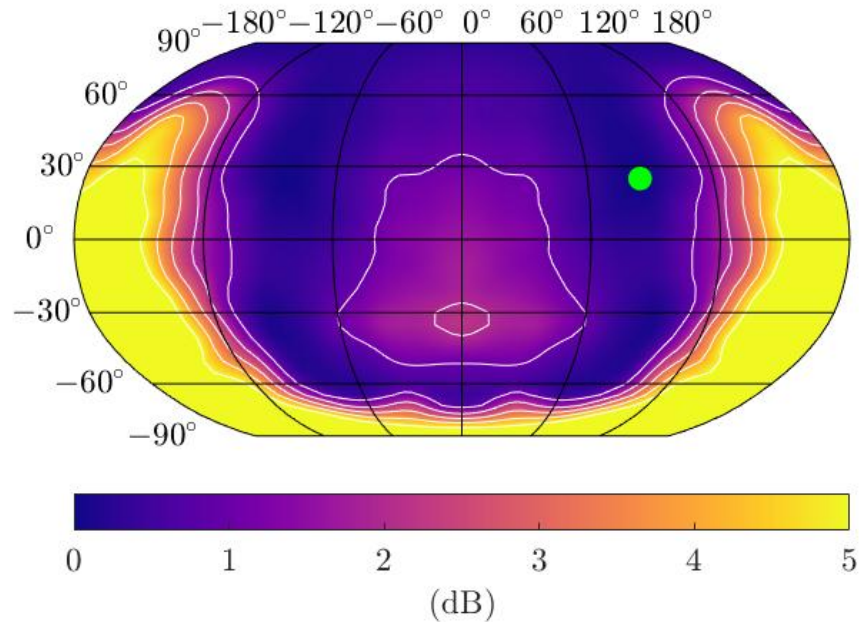


Figure 17.8 A color-mapped projection of the free-field objective function $J_{ff}(\vartheta, \phi)$ for speech. The green dot shows the location for the objective function minimum. Post-processing symmetrized the data set about the median plane.

entire sphere. For this source, $J_{sr}(\vartheta, \phi)$ yielded the same optimal position and had features agreeing well with those of $J_{ff}(\vartheta, \phi)$.

Figure 9 presents further evidence of the optimal position's correct spectral balance. The black solid line represents the 1/3-octave-band sound power spectrum for speech, while the orange dashed line shows the estimated sound power based on Eq. (17.24) at the optimal position $(\vartheta, \phi) = (25^\circ, 85^\circ)$. The red dotted line represents the estimated sound power for the on-axis position $(\vartheta, \phi) = (0^\circ, 0^\circ)$, and the blue dash-dot line shows the estimated sound power directly behind the talker at $(\vartheta, \phi) = (0^\circ, -180^\circ)$. While the optimal estimate agrees well with the sound power spectrum over the entire bandwidth, the on-axis position biases the estimate with excess high-frequency energy and the position directly behind the talker yields deficient high-frequency energy.

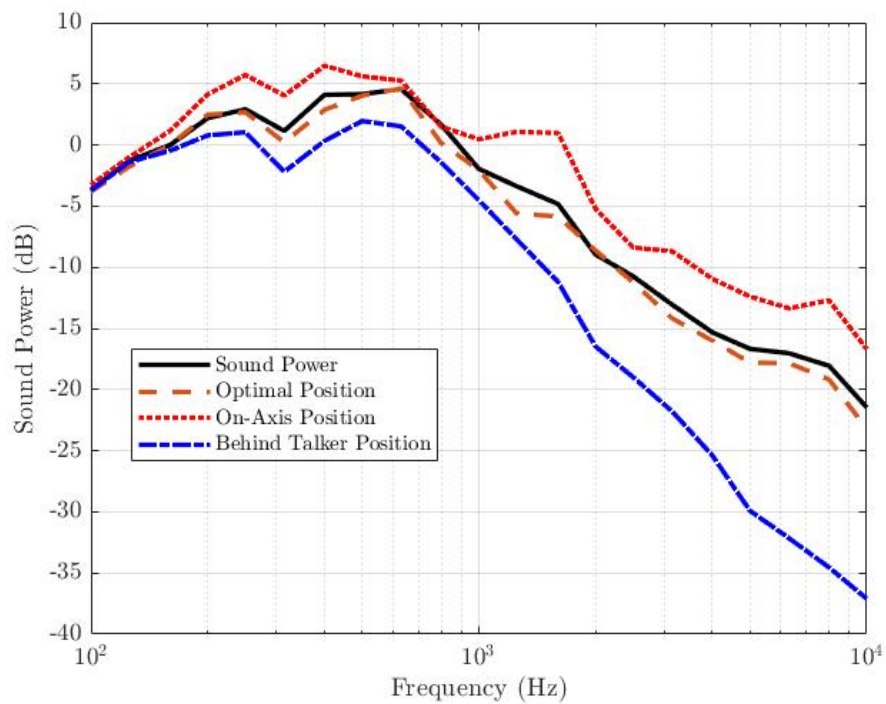


Figure 17.9 Measured sound power spectrum and estimated single-channel sound power spectra for speech at various positions in a free-field environment. The mean-squared pressure of the source has been normalized so that the measured sound power level at 160 Hz is 0 dB. The measurement radius was $r_m = 1.21$ m.

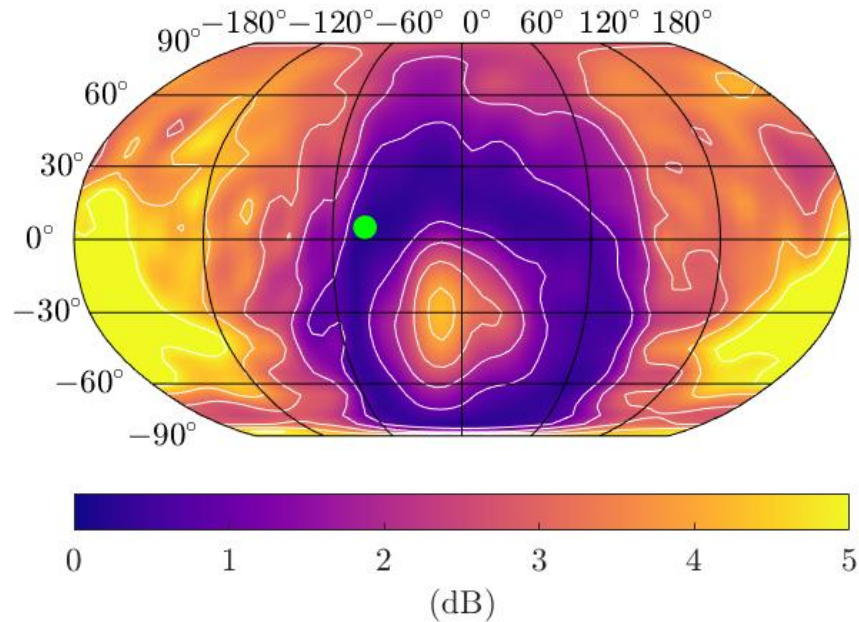


Figure 17.10 Objective function $J_{ff}(\vartheta, \phi)$ for trumpet.

The trumpet free-field objective function appears in Fig. 17.10, where $(0^\circ, 0^\circ)$ is the front of the musician at instrument level and corresponds to the solid red x -axis in Fig. 3(a). The musician angled the trumpet downward by approximately 30° . The ideal microphone placement region forms a dark-purple ring approximately 45° to 60° off the bell axis. As for speech, this region is close enough to the principal axis to have sufficient high-frequency energy but not far enough removed to cause undesirable high-frequency attenuation. However, the trumpet's optimal region is closer to its principal axis because the instrument is more directional than speech. A comparison of the DI plots in Figs. 17.3(a) and 17.6(c) visually supports this assertion for the 1.6 kHz 1/3-octave-band. The white regions, where the intensity nearly equals the average intensity, concentrate more closely around the trumpet bell axis than around the mouth axis.

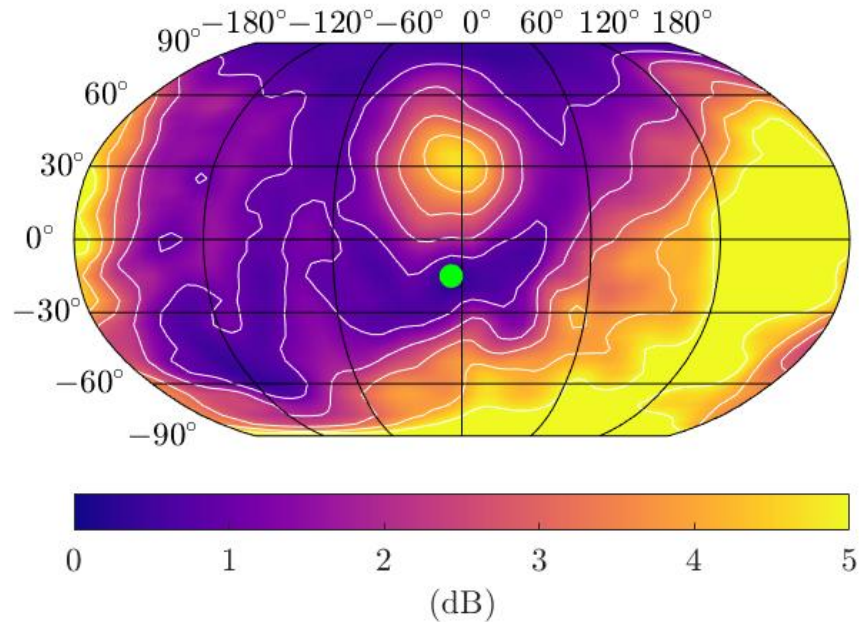


Figure 17.11 Objective function $J_{ff}(\vartheta, \phi)$ for tenor saxophone.

Figure 17.11 shows the free-field objective function projection for the tenor saxophone. As for the trumpet, the best microphone locations for sound power estimation fall in a nearly annular pattern about 45° to 60° off the instrument's bell axis rather than directly in front of it. On the other hand, the error function is not quasi-symmetric about the median plane. An interesting secondary region for optimal placement appears near $(\vartheta, \phi) = (-60^\circ, -150^\circ)$ to the seated musician's right, which includes the saxophone bow. This locale is likely available because of interference lobes in the region such as those visible in Fig. 17.4(c). Microphone positions away from the trumpet bell axis are less optimal than those for the saxophone because they do not capture enough high-frequency content. Interference lobes from woodwind instruments often allow significant high-frequency detection over broader angular regions.

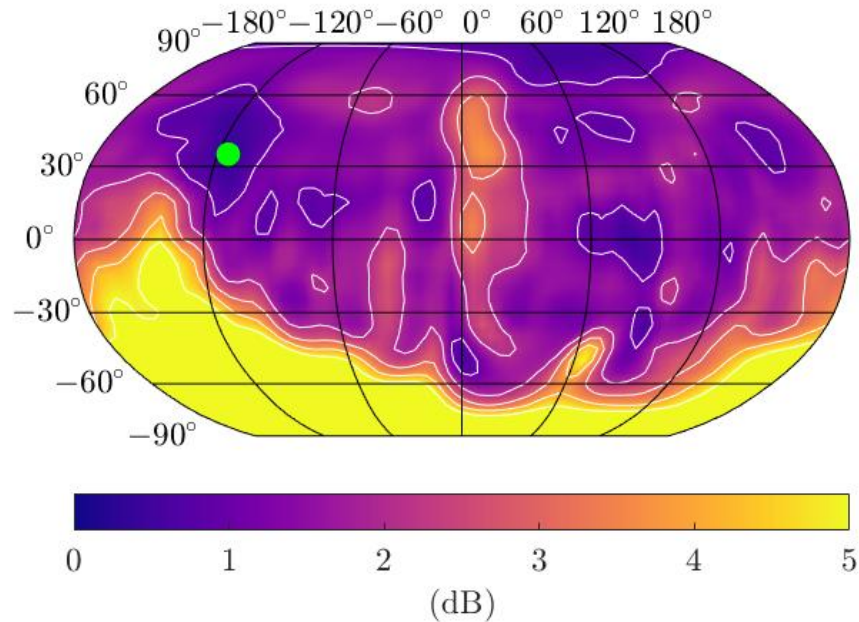


Figure 17.12 Objective function $J_{ff}(\vartheta, \phi)$ for violin.

The violin free-field objective function appears in Fig. 12. Because of the instrument's complex radiation patterns, the function has no single ideal microphone placement region. Instead, it has three areas of dark color: one directly above the instrument, one to the musician's front left $[(\vartheta, \phi) = (0^\circ, 60^\circ)]$, and one to the musician's rear right and slightly upward $[(\vartheta, \phi) = (30^\circ, -120^\circ)]$. A microphone in any of these regions would produce similar results.

Semi-reverberant Environments

In semi-reverberant environments, the microphone placement distance r_m is more crucial because it influences the balance of the direct and reverberant contributions, governed by the source directivity and room acoustics, respectively. The optimal placement should thus consider this distance, along with the angular coordinates ϑ_m and ϕ_m .

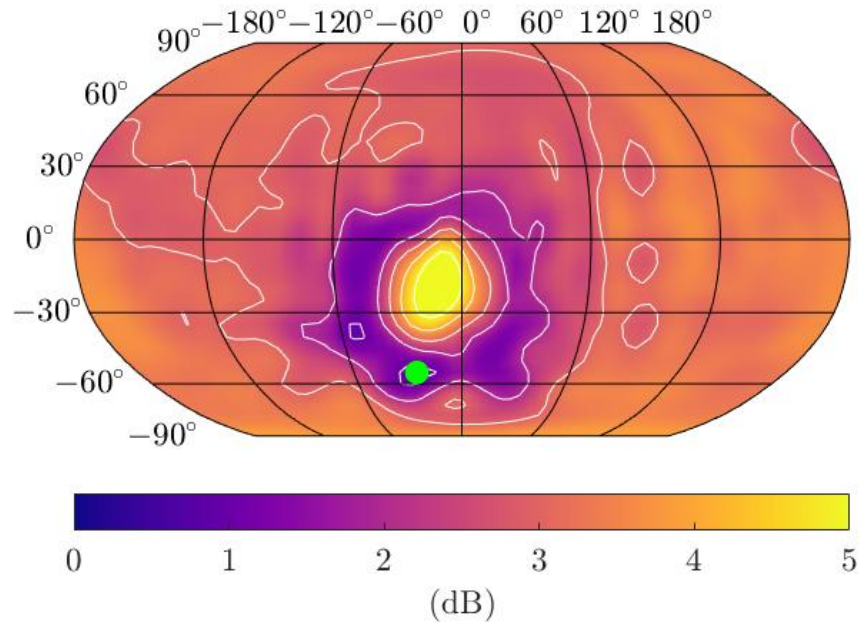


Figure 17.13 Objective function $J_{sr}(\vartheta, \phi)$ for trombone at a microphone placement distance $r_m = 1.83$ m in a dance studio.

The finite room constants for this work involve increasing absorption over frequency, which significantly affects optimal microphone placement. Figures 17.13 and 17.14 illustrate the consequences for a trombone in the dance studio modeled using Eq. (17.11). The figures show the semi-reverberant objective function $J_{sr}(\vartheta, \phi)$ at measurement distances $r_m = 1.83$ m and $r_m = 10.0$ m, respectively. Since the room has a frequency-averaged critical distance of about 1.5 m for the instrument, the microphone placement at 1.83 m, which was also the measurement radius for the anechoic directivity measurements, detects roughly equal contributions from the direct and diffuse reverberant sound fields. The objective function is notably similar to the trumpet free-field objective function in Fig. 17.10, with an optimal annular placement region centered on the bell axis, although the region appears to be more tightly focused.

Figure 17.14 shows that at a distance of 10 m, the optimal annular region collapses to a smaller region directly in front of the trombone bell. The reverberant field dominates the total sound pressure at this distance, but because of the increasing high-frequency room absorption indicated by Fig. 17.2, a sound power estimate based only on the diffuse field does not provide sufficient high-frequency content. Thus, the optimization attempts to compensate for the reduced high-frequency energy by placing the microphone directly in front of the bell where the direct high-frequency energy is most substantial.

As the microphone moves beyond the critical distance into the reverberant field, the objective function becomes more spatially uniform because the locally averaged diffuse field is independent of angular position. Figure 14 shows this effect as the orange level (approximately 3 dB) dominates the entire sphere except in the small area directly in front of the bell, where the direct radiation provides its needed high-frequency contribution.

Figure 17.15 further illustrates the effects of room absorption through plots of the measured and estimated trombone sound powers and estimated diffuse and direct-field contributions at the optimal semi-reverberant field position shown in Fig. 17.14. Because the $r_m = 10$ m placement is well beyond the critical distance, the diffuse field dominates the mean-squared pressure, particularly at lower frequencies. In some cases, the reverberant field levels exceed the direct field levels by 15 dB. Consequently, the diffuse-field contribution at these frequencies almost entirely controls the sound power estimate, as shown by the optimal and diffuse-field curves, which nearly coincide below 1 kHz. However, the relative direct field contribution to the total sound power estimate becomes more substantial at higher frequencies as the source becomes increasingly directional and the diffuse field becomes weaker because of increasing room absorption. Above 1 kHz, the optimal sound power estimate becomes noticeably greater than the diffuse-field estimate alone because of the direct-field contribution. Interestingly, even a microphone directly in front of the bell at $r_m = 10$ m for maximal direct-field contribution does not entirely counter the room absorption at the highest frequencies.

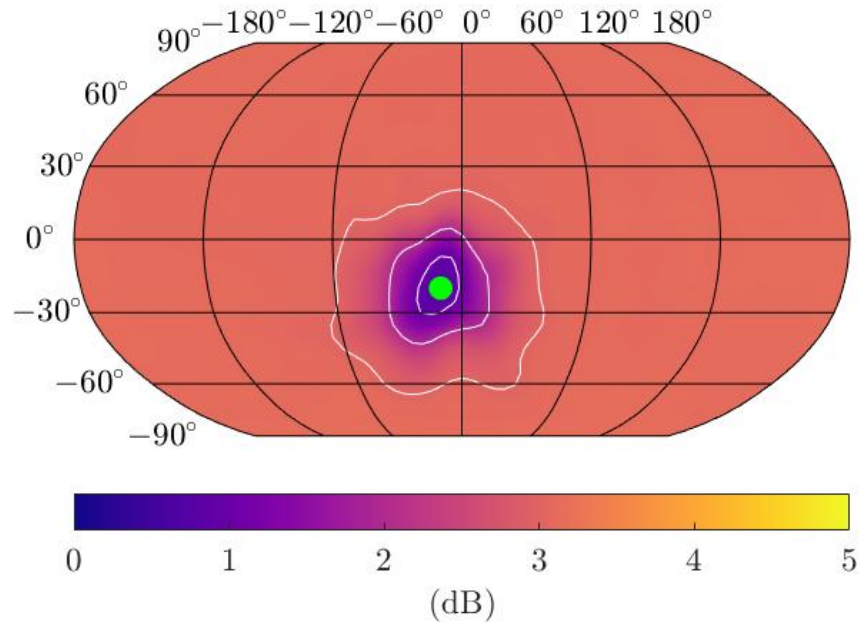


Figure 17.14 Objective function $J_{sr}(\vartheta, \phi)$ for trombone at a microphone placement distance $r_m = 10$ m in a dance studio.

Even at this optimal position, the estimated sound power level drifts several decibels downward from the actual sound power level by 10 kHz.

Room differences can influence optimal angular microphone placement even at the same measurement distance. As an example of this effect, Fig. 17.16 shows the semi-reverberant objective function modeled for speech in the classroom at $r_m = 1.21$ m, while Fig. 17.17 shows the function for the same source and distance in the dance studio. Compared to the best free-field angular regions shown in Fig. 17.8, the best regions for the two rooms shift toward the mouth axis. Figure 17.2 shows that both rooms have progressively increasing high-frequency absorption, which, as observed for the $r_m = 10$ m trombone objective function in Fig. 17.14, moves the optimal placement region closer to the maximum high-frequency radiation axis.

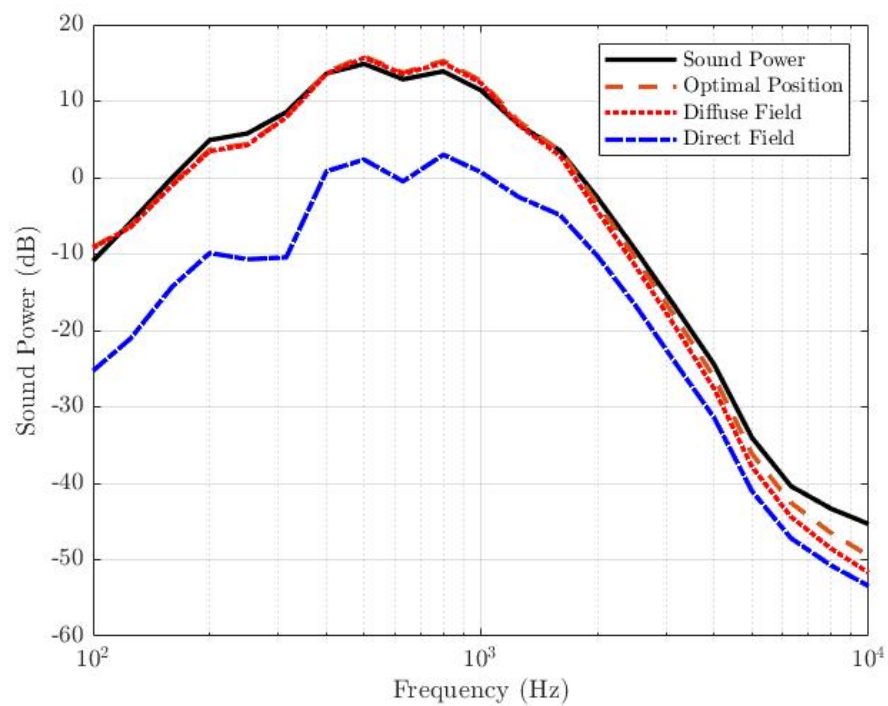


Figure 17.15 Measured and estimated 1/3-octave band sound power spectra for the trombone at $r_m = 10$ m in the dance studio using the optimal angular position shown in Fig. 17.14. Normalization of the mean-squared pressure set the sound power value at 160 Hz to 0 dB.

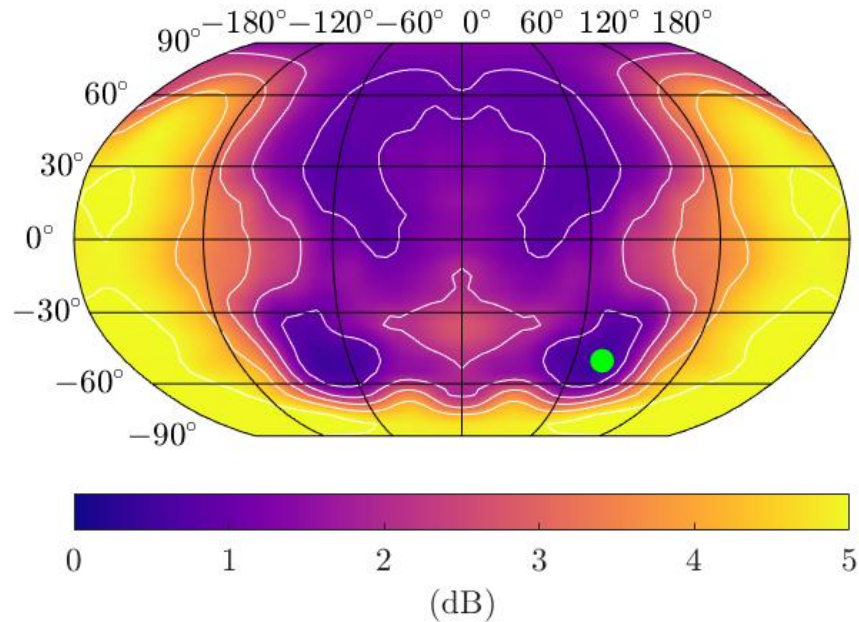


Figure 17.16 Objective function $J_{sr}(\vartheta, \phi)$ for speech at $r_m = 1.21$ m in a classroom. Post-processing symmetrized the data set about the median plane.

The dance studio's room response exhibits slightly stronger high-frequency absorption effects than the classroom's response. The studio room contribution at 10 kHz is down 8 dB from the 100 Hz value, whereas the classroom contribution is down 5 dB. This difference could explain why the optimal region for speech in the dance studio at $r_m = 1.21$ m appears to focus more directly in front of the talker than in the classroom. The outcome relates to the measurement distance relative to the rooms' frequency-dependent critical distances [see Eq. (17.12) and Table 17.1]. In addition, the classroom's diffuse-field contribution is flatter than that of the dance studio over frequency, suggesting that the classroom placement should be closer to the free-field placement since there is less need to compensate for room spectral coloration. Figures 17.8, 17.16, and 17.17 show this effect, in which the free-field objective function appears to be more similar to the classroom function than the dance studio function.

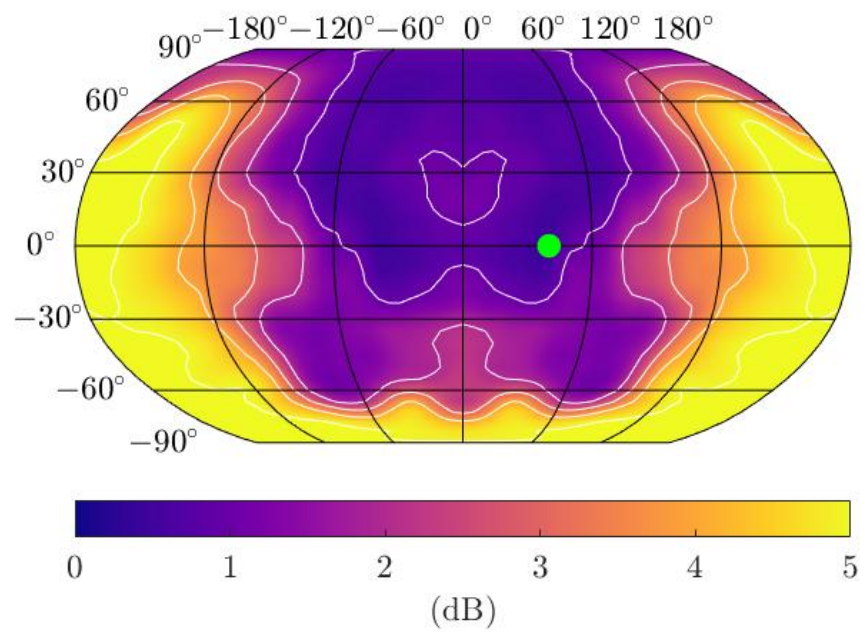


Figure 17.17 Objective function $J_{sr}(\vartheta, \phi)$ for speech at $r_m = 1.21$ m in a dance studio. Post-processing symmetrized the data set about the median plane.

17.5 Discussion

While precise microphone positioning requires the application of the methods outlined in the preceding sections, the developments also suggest three general placement scenarios to estimate a source's approximate sound power spectrum for audio applications, such as reverberation effects.

First, the source's directivity primarily determines the placement when the microphone is much closer to the acoustic source center than the room's critical distance ($r_m \ll r_c$). In this case, the optimal angular position generally lies in regions neither too close to a principal radiation direction nor too distant, especially when the directivity function includes significant acoustic shadowing elsewhere. The microphone location should be off axis for many musical instruments with bells, but it may approach the axis (while still remaining off axis) for highly directional sources.

Second, when the microphone is well beyond the critical distance ($r_m \gg r_c$), the ideal placement is more or less arbitrary. Estimating the sound power without a compensation filter requires a frequency-independent room constant, i.e., constant room absorption and reverberation time.

Finally, when the microphone distance is near the critical distance ($r_m \approx r_c$), two cases arise. If the room constant is approximately uniform over frequency, the optimal microphone placement is similar to that for free-field conditions or when $r_m \ll r_c$. However, the position is usually less stringent because the reverberant-field contribution is directly proportional to the sound power. If the room constant is not uniform over frequency, the error function may change significantly because the source directivity compensates for frequency-dependent room constant variations, e.g., by adding high-frequency energy lost through room absorption.

In all cases, these arguments assume that the microphone is omnidirectional and has a flat or calibrated frequency response. With a different directional response, such as a cardioid pattern, the microphone may reduce the effects of some room reflections so that the optimal angular position more closely approaches the optimal position under free-field conditions. Thus, even when the

placement is near the critical distance, the choice of microphone polar response could allow one to neglect some room effects and rely more heavily on the free-field placement approach.

Optimal sound-power-estimating positions for some instruments are similar to those recommended for aesthetic effects. For example, Corbett suggested a slightly off-axis placement for a “more balanced” trumpet sound and placement above the musician’s shoulder for a “slightly fuller, less edgy [violin] sound” [194]. These two suggestions correspond to favorable placement regions in Figs. 17.10 and 17.12, respectively.

However, for other sources, such as the human voice, the optimal sound-power-estimating position is uncommon in recording or sound reinforcement situations but may serve as a beneficial secondary position to produce a dedicated reverberation effects signal. Such usage would allow audio engineers to continue placing a primary microphone based on desired artistic effect, aesthetic preference, and knowledge of underlying acoustics. A more complicated possibility would be to filter the primary microphone signal to match the desired sound power spectrum before it drives any reverberation effects.

17.6 Conclusions

This paper has explored the influences of source directivities and basic room acoustics on microphone placements for audio. It has proposed and validated techniques using measured directivities and room properties to estimate source sound power spectra with only a single microphone. Because sound power or total sound energy flux comprises radiation in all directions that physically excites room reverberation, the techniques will help audio engineers acquire audio signals closely approximating global source sounds and produce more natural reverberation effects.

The work has focused primarily on selected instruments and speech, but the proposed techniques apply to any sound source with measured directivity of sufficient resolution and a room with known

general acoustical properties. The study's small sample size makes it challenging to prescribe positions applicable to every source type. However, general trends suggest that placements closer than the critical distance should fall angularly between a highly directional region and an anti-directional region to yield an appropriate spectral balance. Placements well beyond the critical distance are more or less arbitrary, but a microphone closer to the dominant source radiation axis often yields compensatory high-frequency content in rooms with progressively increasing high-frequency absorption. Directional source characteristics and room attributes must balance for placements near the critical distance. If the room constant is nearly uniform over frequency, the angular microphone placement is like that much closer to the source center than the critical distance. However, a nonuniform room constant caused by varying average room absorption complicates the positioning and requires more careful analysis. At any distance, the derived formulations yield more exact microphone placements. A directional microphone may reject particular room acoustical contributions and allow audio engineers to place microphones at angular positions like the optimized positions closer to the source.

Future research could apply the proposed techniques to other sound sources, validate ideal placements in various rooms, and optimally locate microphones for different frequency ranges (e.g., 100 Hz to 4 kHz). Other investigations could explore how the techniques apply to near-field directivities for use with close-microphone placements and determine optimal placements for various psychoacoustic metrics. Researchers could consider more advanced acoustical models to understand better how rooms influence microphone placements. Listening tests would establish how discernible optimal and suboptimal sound power estimation positions are for artificial reverberation and other applications. The authors encourage work in these areas to further advance microphone placement techniques.

Chapter 18

Microphone Placement for Maximum Loudness

This chapter considers optimal microphone placements based on the loudest positions around sources and contrasts them with the optimal sound power spectrum placements discussed in Ch. 17.

18.1 Introduction

Microphone placement is a critical aspect of recording, sound reinforcement, and sound design. Typically, audio engineers place microphones by ear or convention, while some consider basic sound source directivities to create pleasing or natural-sounding audio. The basic directional characteristics of selected live sources have been well known and documented for decades [3, 4, 7, 8, 209]. Studies have shown that both musical instruments and the human voice, while often quasi-omnidirectional at low frequencies, can become quite directional as frequency increases. A frequency-dependent spherical directivity function is unique to each radiating source and varies with distance until the distance reaches the geometric and acoustic far field. As a spectrally and spatially dependent function, the directivity function alters the spectrum detected by a microphone. It consequently

affects the timbre heard by listeners, leading some to refer to it as “directional tone color” [36]. Recording and sound reinforcement engineers commonly exploit source directivities as part of their craft to obtain desired timbres [194, 195].

Researchers and practitioners have long sought optimal microphone positions because of their utility in recordings and other audio applications. Clark’s preferred technique was to place a microphone “at a direction, with respect to the musical instrument, at which the tones sounded the loudest in an attempt to get a quality that might be reasonably representative of that which might be obtained by integration over all directions” [14, 196]. Others have similarly suggested that ideal placements should blend all components of sound generated by the instrument. Bartlett argued that the natural sound of an instrument is that intended for the listener to hear in the far field within a hall, which naturally includes all components of sound generated by the instrument [15, 16]. Lee likewise supported far-field placements as they provide a sampling of the “plane of diffuse information” at the listener’s position in a hall [197]. Corbett stated that “a close mic does not pick up a complete or natural sonic picture,” which likewise pertains to the sound heard by a musician playing an acoustic instrument rather than audience members. He emphasized that microphones placed at sufficient distances allow “component sounds radiating from all over the instrument . . . to blend together and form the ‘whole’ and natural acoustic sound we are used to hearing.” [194]. All of these authors have concluded that a desirable or natural instrument corresponds to its global sound radiation.

In a previous report, the authors presented methods to identify an optimal microphone placement that yields the mean-squared pressure spectrum best approximating the source sound power or global spectrum. This is the result Clark sought: the sound radiated in *all* directions [17]. Without immediate means to validate his hypothesis, he assumed the position of maximum loudness about a musical instrument in an anechoic environment provided a tone quality representative of the sound power spectrum. This report explores his proposition using anechoic recordings of various musical instruments at 2,522 positions (5° angular resolution) over an encompassing measurement

sphere. Acoustical researchers and audio engineers interested in informing and expanding their microphone positioning techniques will find analysis of Clark's loudness-placement criterion insightful. Loudness is a human perception correlated with sound pressure that involves both physical waveform amplitudes and sensations produced by the ear-brain system [200].

The sound power placement report found that a microphone in the angular region of most substantial source radiation with increasing directivity over frequency tends to bias spectral content with high-frequency energy compared to the sound power spectrum. However, additional understanding comes from exploring loudness-based source directivities and their influences on microphone placements. The results are especially informative to those who place microphones via sound perception.

The following sections review some basic theory for modeling and estimating loudness and present loudness-based directivities for several musical instruments. Later sections consider the spectral differences between loudness-based and sound-power-based microphone placements and their implications.

18.2 Methods

18.2.1 Overall Sound Pressure and Weighted Levels

The 2,522 recorded channels of emitted sounds from each of several instruments involved a 1.83 m radius microphone array and musicians playing chromatic scales at a mezzo-forte dynamic marking [1]. To determine the direction with the loudest sound, one may begin by formulating the overall sound pressure level (OASPL) at each microphone position of the surrounding spherical array. For a measured mean-squared pressure $\langle p^2(r_m, \vartheta_m, \phi_m, f) \rangle_t$ at radial distance r_m from the acoustic instrument center, elevation angle ϑ_m , azimuthal angle ϕ_m , and frequency f , the OASPL

is [62]

$$OASPL(r_m, \vartheta_m, \phi_m) = 10 \log_{10} \left[\frac{\sum_{k=1}^K w(f_k) \langle p^2(r_m, \vartheta_m, \phi_m, f_k) \rangle_t}{p_{ref}^2} \right], \quad (18.1)$$

where $w(f_k)$ is a weighting function, k is the index for K discrete frequency bins with center frequencies f_k , and $p_{ref} = 20 \times 10^{-6}$ Pa. The OASPL thus provides a weighted or variable-bandwidth level as a function of measurement position that simplifies the directional data's frequency dependence.

An unweighted OASPL simply employs $w(f_k) = 1$, but the weight function provides a convenient means of computing A, B, C, and other weighted sound levels, e.g., such that listeners perceive sounds of different frequencies and the same decibel values as being equally loud [62, 198]. Figure 18.1 shows OASPL balloons of four different spectral weightings for the bassoon. The A-weighted balloon emphasizes higher, more directional frequencies, but the directivity patterns are roughly the same. Consequently, the remainder of this work considers only unweighted levels.

The OASPL formulation likewise applies to $1/n$ -octave bands with limitations placed on the index k , such that f_k falls only within a specified band. Figure 18.2 compares OASPL directivity results for the bassoon with progressively increasing bandwidths about a 500 Hz center frequency. The extended smoothing of wider bandwidths causes a loss of the significant narrowband detail.

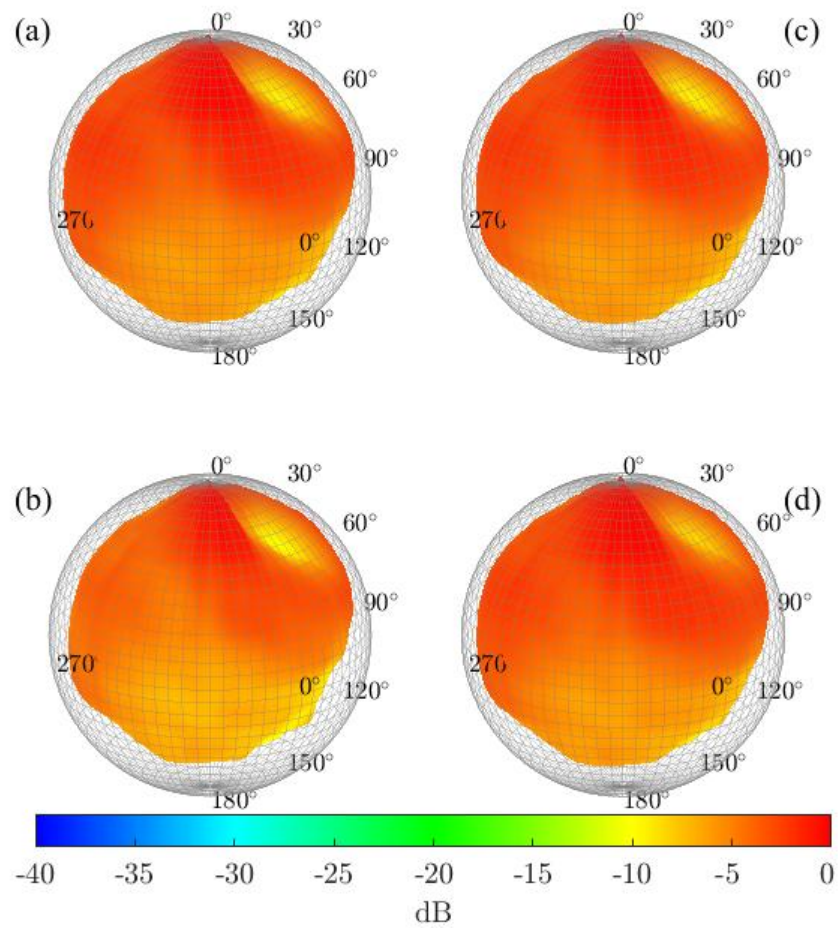


Figure 18.1 Broadband bassoon directivities based on the OASPL formulation. (a) Unweighted. (b) A-weighted. (c) C-weighted. (d) D-weighted.

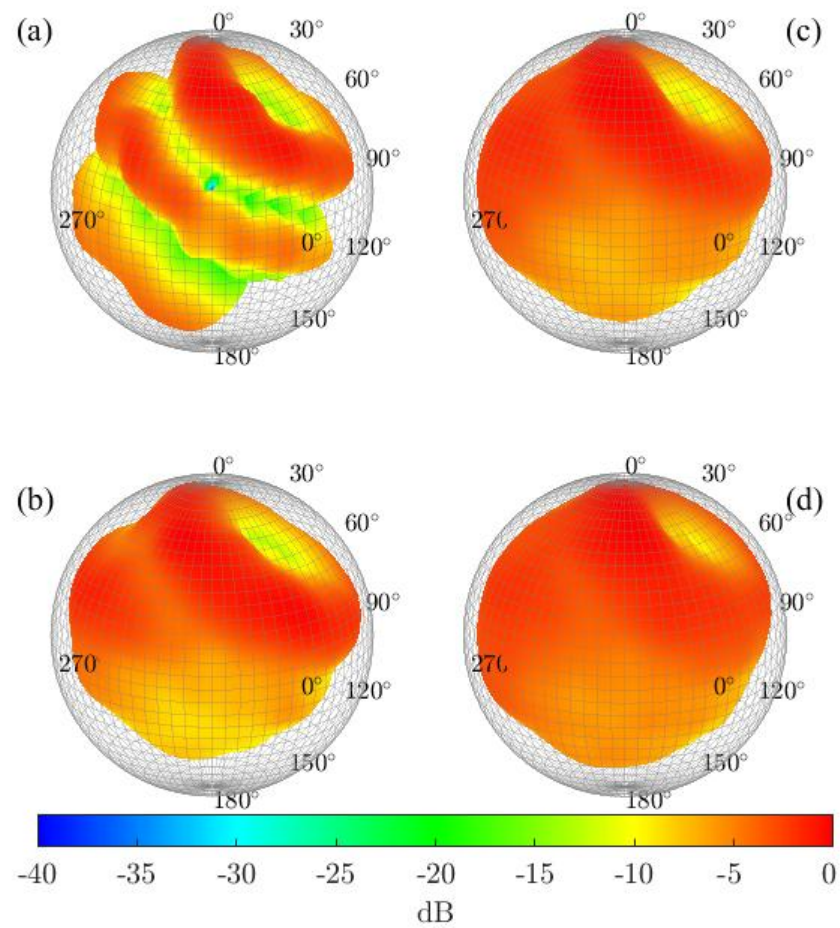


Figure 18.2 Bassoon directivities based on the OASPL formulation for varying bandwidths about a 500 Hz center frequency. (a) 1 Hz narrowband. (b) 1/3-octave band. (c) 1/1-octave band. (d) Full broadband measurement bandwidth.

18.2.2 Zwicker Loudness

While unweighted and weighted OASPL balloons provide straightforward means to assess regions around instruments with the highest overall sound levels, they do not account for the nonlinear effects of human hearing. Fortunately, one may estimate loudness, a perceptual metric, using one of several numerical modeling approaches [210–212]. As discussed in the ISO 532-1 standard, the Zwicker loudness, computed from 1/3-octave bands, is valid for stationary broadband or narrowband sound sources [211]. Its calculation takes the form [200]

$$L = \int_0^{24} L' dz, \quad (18.2)$$

where L is the loudness, L' is the specific loudness, and the integral extends over all 24 critical band rates. The specific loudness follows from third-octave band levels through applied weighting and masking considerations. While more sophisticated loudness models may further account for the complexities of time-varying sounds produced by musical instruments, the Zwicker loudness is a practical tool providing an initial directional loudness metric that incorporates distinct nonlinear perceptual effects.

18.3 Results

18.3.1 Sound Power of Musical Instruments

Absolute levels are irrelevant for *relative* directional OASPLs over a sphere, but they become critical for directional loudness calculations that address hearing nonlinearities. While most musical instruments have dynamic ranges that require consideration of the quietest to loudest dynamic markings for complete loudness-based directivity evaluations, the measurements of this work involved chromatic scales played at only a mezzo-forte dynamic marking. Nevertheless, calculated sound power levels according to the ISO 3745:2012 standard [26] allowed comparisons of the mezzo-forte recordings to pianissimo and fortissimo sound power levels previously published by Weinzierl *et al.* for the same instrument types with lower-resolution directivity measurements [2]. The sound power levels for the various instruments and dynamic markings appear in Table 18.1. This study calculated mezzo-forte sound power levels fell within the previously published ranges for all instruments except the baritone saxophone, whose level exceeded the previously published fortissimo level by only 1 dB. Generally, the level ranges provide solid bases for loudness calculations.

Because the loudness levels produced by the Zwicker calculations depend nonlinearly on absolute sound pressure levels, a change in the sound power produced by a source could alter the loudness-based directivity balloons, even with a fixed amplitude-based directivity. For example, the shape of a loudness-based balloon produced by a pianissimo dynamic could look different than that produced by a fortissimo dynamic, even after normalization to the maximum. Loudness balloons resulted from the initial measurement dynamic and different simulated playing levels by recalibrating the sound pressure levels to produce the same sound power levels suggested by Ref. [2]. For instruments with lower sound pressure levels, such as the violin or viola, the loudness levels in each direction relative to the maximum loudness level changed little. However, for higher-

amplitude instruments, such as those in the brass family, the modeled nonlinear hearing effects significantly altered the relative loudness levels compared to those at lower playing levels. Because the loudest directions remained the same for all cases, the remainder of the work considered only the loudness-based directivities calculated from the measured mezzo-forte sound power levels.

Table 18.1 Measured sound power levels for the mezzo-forte dynamic marking [1] compared to previously published values for the pianissimo and fortissimo dynamic markings [2].

Instrument	L_w pp	L_w mf	L_w ff
Brass			
Tuba	71	108	122
Euphonium		109	
Trombone	82	105	112
French Horn	85	105	112
Trumpet	83	101	107
Woodwind			
Bass Clarinet		100	
Baritone Saxophone	65	103	102
Tenor Saxophone	82	104	113
Bassoon	86	98	101
Flute	89	95	101
String			
Double Bass	70	95	96
Cello	70	91	93
Viola	62	85	93
Violin	56	88	91

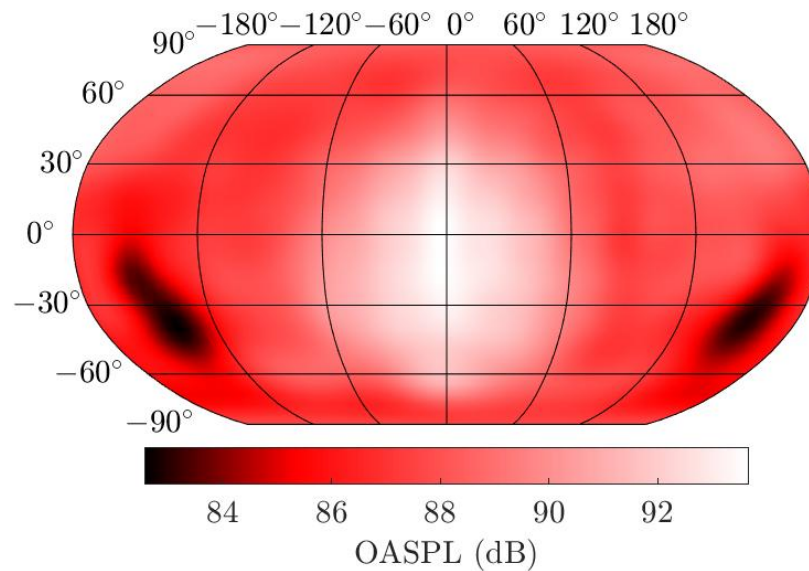


Figure 18.3 OASPL-based directivity of the trombone.

18.3.2 Directivities

Brass Instruments

As one might anticipate, the loudest direction for brass instruments is along the bell axis. Figure 18.3 shows an unweighted broadband OASPL directivity projection for the trombone and Fig. 18.4 shows a comparative Zwicker loudness projection. Even though the latter accounts for some nonlinear hearing effects, both maps show similar features, including substantial level reductions behind the instrument and musician.

The trumpet, French horn, euphonium, and tuba directivities have similar characteristics, with bright regions corresponding to the loudest observation angles near the bell axis and dark regions corresponding to shadow zones on the opposing sides of the musicians. This report does not include their OASPL and loudness-based directivities, but they are available along with those of other instruments in an online archival database [38].

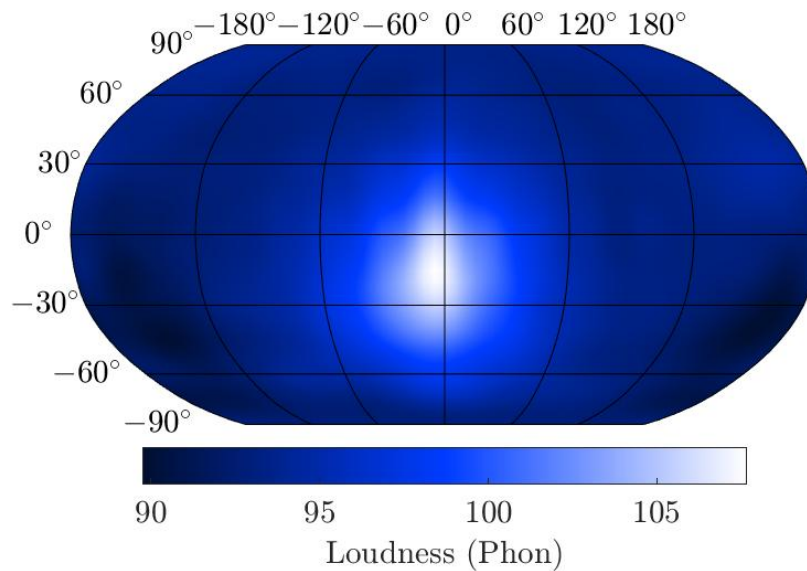


Figure 18.4 Loudness-based directivity of the trombone.

Woodwinds

While the loudness-based directivities of the brass instruments share many similar characteristics, those of the woodwind instruments show more variability. Figure 18.5 presents the loudness-based directivity map for the flute. Anticipated interference lobes, visible as rings encircling the instrument axis, highlight the loudest and quietest directions resulting from the flute's linearly arrayed embouchure and tone holes, whose radiations produce constructive and destructive interference patterns [1, 40].

Other woodwind instruments, including the bassoon, showed similar interference patterns, but the saxophones had loudness-based directivities that also resembled those of the brass instruments, as shown for the tenor saxophone in Fig. 18.6. Interestingly, this composite directivity exhibits a single strong direction, while the narrowband saxophone directivities show interference lobes similar to those of the flute [1]. This effect may follow from the substantial differences in the radiating bell and tone hole areas, causing the saxophones to behave more like brass instruments in

a broadband loudness sense. Shadow regions appear in different areas than those produced by the brass instruments.

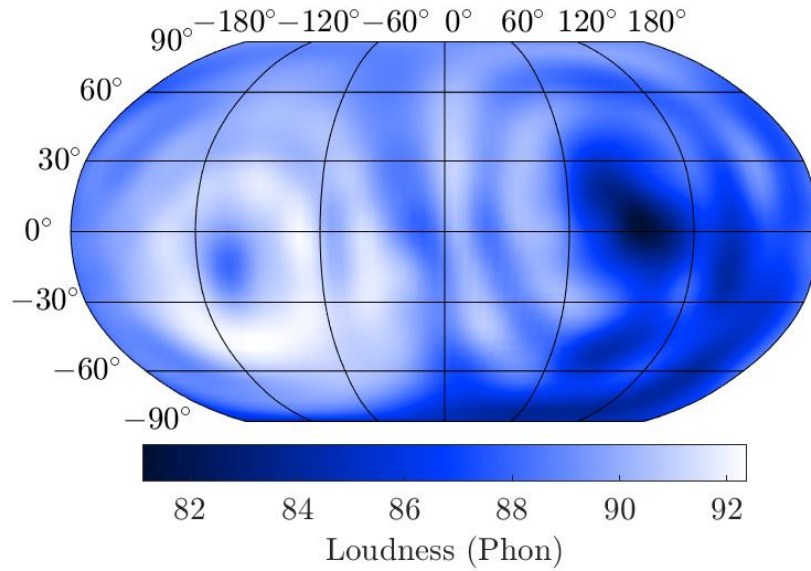


Figure 18.5 Loudness-based directivity for the flute.

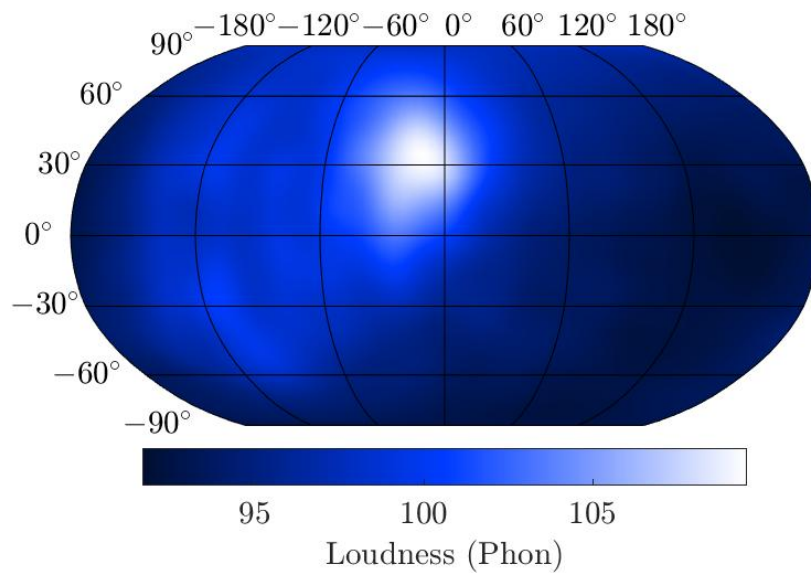


Figure 18.6 Loudness-based directivity for the tenor saxophone.

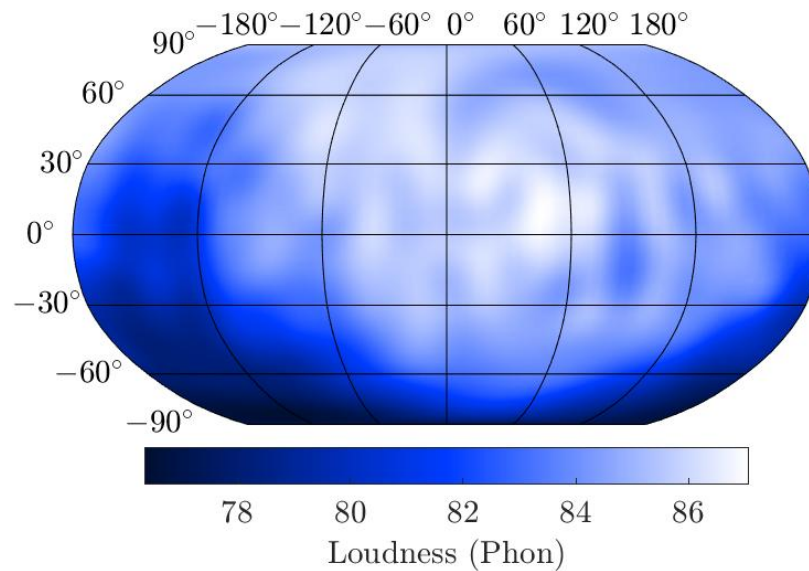


Figure 18.7 Loudness-based directivity for the viola.

Strings

The strings tend to have the most uniform loudness distributions of all the investigated instruments, except in the significant shadow regions behind the instruments and musicians. Figure 18.7 illustrates the effects with the viola's loudness-based directivity projection. Unlike the brass instruments, which have a single strong radiation direction, the viola, violin, and cello all have broad regions over the measurement sphere where loudness remains substantial. The double bass is similar to the other string instruments but exhibits a region of greater loudness directly in front of the instrument. These effects may result from the fact that string instruments are complex radiators whose directivities do not generally follow a single trend, e.g., a dominant single radiation direction or distinctive effects of interference lobes, but have complicated patterns that change significantly over frequency [141, 168]. The loudness directivities tend to divide into two coarse regions: an area of roughly uniform loudness in front of the instrument and musician, and a shadow region behind or below the instrument and musician.

18.4 Analysis

The spectral differences between the measured instrument sound powers and the sound powers estimated from the maximum-loudness-based placements suggested by Clark [14, 196] provide several useful insights. In a free-field environment, a time-averaged sound power estimate from a single microphone position $(r_m, \vartheta_m, \phi_m)$ takes the form [17]

$$\langle W(f) \rangle_t \approx \frac{4\pi r_m^2}{\rho_0 c Q(\vartheta_m, \phi_m, f)} \langle p^2(r_m, \vartheta_m, \phi_m, f) \rangle_t, \quad (18.3)$$

where ρ_0 is the ambient air density, c is the wave speed, and $Q(\vartheta_o, \phi_o, f)$ is the directivity factor function.

Figure 18.8 shows the deviations of the 1/3-octave-band sound power estimates for the brass family derived from microphone placements at the loudest positions. The dashed horizontal red lines indicate ± 3 dB deviations from the actual sound power spectra. For the lowest frequencies, up to about 400 Hz, the loudest positions provide reasonable results. However, by 1 kHz, the estimates are around 5 dB too high and continue to rise with increasing frequency. This indicates a high-frequency estimate bias as anticipated in Ref. [17]. Loudness-based microphone placements for brass instruments will thus sound brighter than those based on optimal sound power placements.

The woodwind family's loudness-based placements yield sound power estimate deviations that are less pronounced than those of the brass family. The estimates are reasonable up to between 500 Hz and 1 kHz. At higher frequencies, the woodwind deviations remain below 10 dB, excluding the tenor and baritone saxophones, whereas the brass deviations exceed 15 dB for some instruments. As mentioned earlier, the saxophones behave more like brass instruments in a broadband sense, with the highest absolute deviations of the considered woodwind instruments. The less severe woodwind deviations likely result from their less directional radiation. In light of the source-filter model discussed in Ref. [17], this suggests that woodwind spatial directivity filtering is less substantial than the brass filtering.

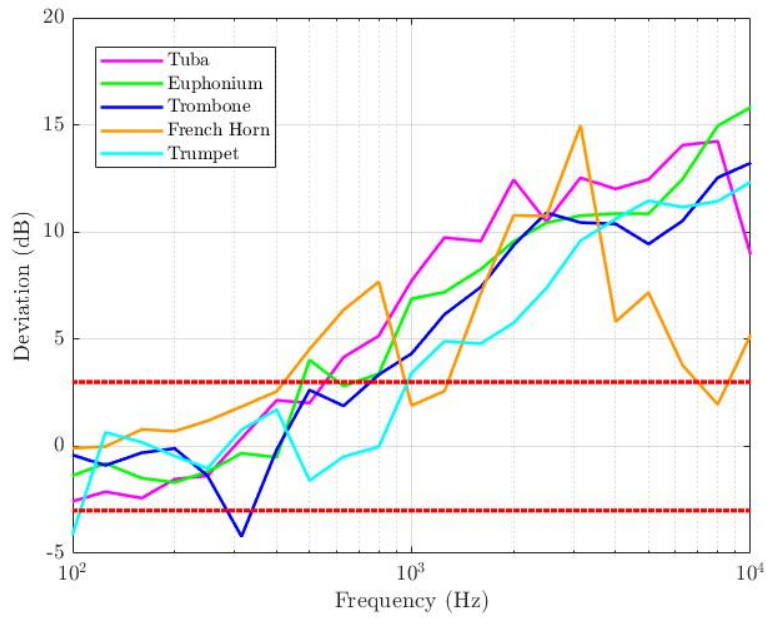


Figure 18.8 Sound power estimate deviations for the brass family.

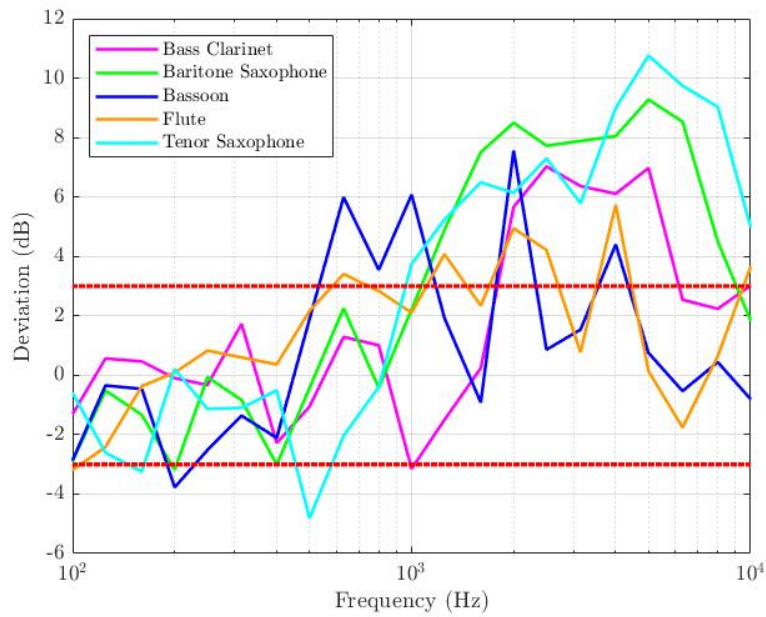


Figure 18.9 Sound power estimate deviations for the woodwind family.

As shown in Fig. 18.10, the loudness-based sound power estimates for the string family are even more reliable. They remain within about 3 dB of the measured sound power spectra for all instruments up to 1 kHz then modestly overestimate values from about 1 kHz to 5 kHz, causing a slight mid-treble excess. However, above 5 kHz, the estimates return to within an acceptable range. This behavior could occur because the loudest spatial regions radiated by string instruments have substantial spatial spreads rather than concentrations in specific directions.

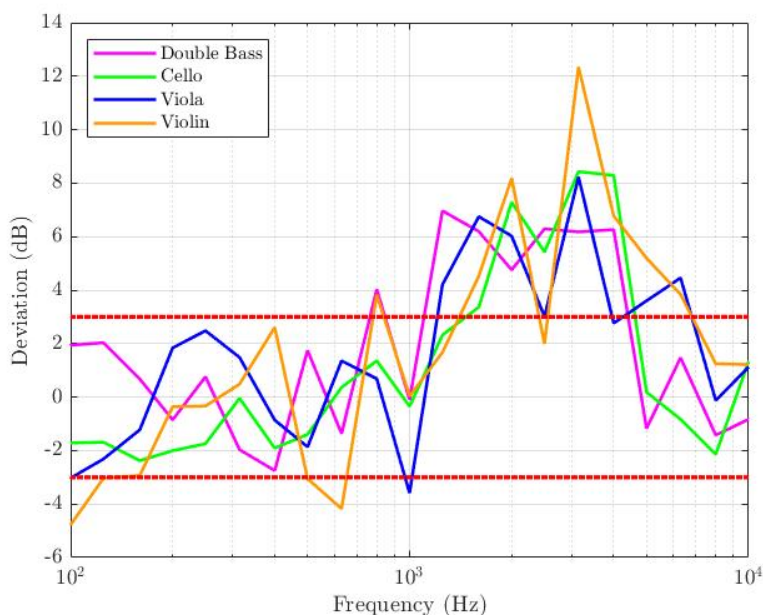


Figure 18.10 Sound power estimate deviations for the string family.

In general, loudness-based placements tend to increase mid-to-high-frequency content in recorded signals compared to sound-power-based placements. This outcome does not imply that loudness-based placements are necessarily inferior—only that they will sound *relatively* bright. Conversely, sound-power-based placements will sound relatively dark compared to loudness-based placements. In some cases, loudness-based placements may be preferable. Corbett noted that on-axis mic placements for brass and some woodwinds could be desirable to produce sufficiently bright sounds [194], which leads some recording engineers to exploit the effect. Listeners typically

experience a combination of direct and reverberant sounds from instruments. The direct sound arrival may fall close to a strong radiation axis, whereas the reverberant sound results from the room-filtered sound power spectrum [17]. In some cases, a loudness-based placement could yield the spectral properties perceived by listeners at selected distances in semi-reverberant environments.

18.5 Conclusions

This work has presented loudness-based directivities of musical instruments as a different means of studying their broadband directional behaviors. The research found that for the purposes of microphone placements, directivities based on both OASPL and Zwicker loudness provided the same directions for the highest-level radiations. Microphone placements in these directions produced increased mid-to-high-frequency energy compared to the sound power spectra, thus yielding brighter overall sounds. Brass instruments had more high-frequency bias than the less-directional woodwinds and strings. The string instruments had the least high-frequency bias. The OASPL and loudness-based directivities for the various instruments are available in an archival database to inform future microphone placements.

While this work numerically changed instrument total sound powers to study the effects on loudness balloons, it only considered directivities based on the mezzo-forte dynamic marking. Because several musical instruments are nonlinear radiators, particularly at high amplitudes, their loudness directivities could change over their complete dynamic ranges. Future studies could explore these effects and incorporate more sophisticated loudness models that include time-varying features or other psycho-acoustic metrics, such as sharpness, sensory pleasantness, or roughness. The authors encourage work in these areas to further optimize microphone placement techniques.

Bibliography

- [1] K. J. Bodon, “Development, Evaluation, and Validation of a High-Resolution Directivity Measurement System for Played Musical Instruments,” Master’s thesis, Brigham Young University (2016).
- [2] S. Weinzierl, S. Lepa, F. Schultz, E. Detzner, H. von Coler, and G. Behler, “Sound power and timbre as cues for the dynamic strength of orchestral instruments,” *J. Acoust. Soc. Am.* **144**, 1347–1355 (2018).
- [3] H. Dunn and D. W. Farnsworth, “Exploration of Pressure Field Around the Human Head During Speech,” *J. Acoust. Soc. Am.* **10**, 184–199 (1939).
- [4] J. L. Flanagan, “Analog Measurements of Sound Radiation from the Mouth,” *J. Acoust. Soc. Am.* **32**, 1613–1620 (1960).
- [5] W. T. Chu and A. C. Warnock, “Detailed Directivity of Sound Fields Around the Human Head During Speech,” National Research Council Canada **IRC-RR-104**, 1–47 (2002).
- [6] T. W. Leishman, S. D. Bellows, C. M. Pincock, and J. K. Whiting, “High-resolution spherical directivity of live speech from a multiple-capture transfer function method,” *J. Acoust. Soc. Am.* **149**, 1507–1523 (2021).

- [7] H. F. Olson, *Musical Engineering: An Engineering Treatment of the Interrelated Subjects of Music, Musical Instruments, Speech, Acoustics, Sound Reproduction and Hearing* (McGraw-Hill, New York, 1952).
- [8] J. Meyer, *Acoustics and the Performance of Music* (Verlag das Musikinstrument, Frankfurt/Main, 1978), Chap. 4.
- [9] G. Weinreich and E. B. Arnold, "Method for measuring acoustic radiation fields," *J. Acoust. Soc. Am.* **62**, 404–411 (1980).
- [10] L. Beranek and T. Mellow, *Acoustics: Sound fields, transducers and vibration*, 2 ed. (Academic Press, 2019).
- [11] T. F. Johansen, "On the Directivity of Horn Loudspeakers," *J. Audio Eng. Soc* **42**, 1008–1019 (1994).
- [12] T. Hélie and X. Rodet, "Radiation of a Pulsating Portion of a Sphere: Application to Horn Radiation," *Acta Acustica united with Acustica* **89**, 565–577 (2003).
- [13] T. W. Leishman, S. Rollins, and H. M. Smith, "An experimental evaluation of regular polyhedron loudspeakers as omnidirectional sources of sound," *J. Acoust. Soc. Am.* **120**, 1411–1422 (2006).
- [14] M. Clark and P. Minter, "Dependence of Timbre on the Tonal Loudness Produced by Musical Instruments," *J. Audio Eng. Soc.* **12**, 28–31 (1964).
- [15] B. A. Bartlett, "Tonal Effects of Close Microphone Placement," *J. Audio Eng. Soc* **29**, 726–738 (1981).
- [16] B. Bartlett, "Tonal Effects of Classical Music Microphone Placement," In *Audio Engineering Society Convention 74*, (1983), paper 1994.

- [17] S. D. Bellows and T. W. Leishman, “Optimal Microphone Placement for Single-Channel Sound-Power Spectrum Estimation and Reverberation Effects,” *J. Audio Eng. Soc.* **71**, 20–33 (2023).
- [18] F. Otondo and J. H. Rindel, “The influence of the directivity of musical instruments in a room,” *Acta Acustica united with Acustica* **90**, 1178–1184 (2004).
- [19] F. Otondo and J. H. Rindel, “A new method for the radiation representation of musical instruments in auralizations,” *Acta Acustica united with Acustica* **91**, 902–906 (2005).
- [20] J. Meyer, “The Sound of the Orchestra,” *The J. Audio Eng. Soc.* **41**, 203–213 (1993).
- [21] C. H. Jeong, J. G. Ih, C. H. Yeon, and C. H. Haan, “Prediction of the Acoustic Performance of a Music Hall Considering the Radiation Characteristics of Korean Traditional Musical Sources,” *J. Acoust. Soc. Kr.* **23**, 146–161 (2004).
- [22] M. Vorländer and H. Bietz, “Novel broad-band reciprocity technique for simultaneous free-field and diffuse-field microphone calibration,” *Acta Acust. Acust.* **80**, 365–367 (1994).
- [23] R. P. Wagner and V. Nedzelnitsky, “Determination of acoustic center correction values for type LS2aP microphones at normal incidence,” *J. Acoust. Soc. Am.* **104**, 192–203 (1998).
- [24] S. Barrera-Figueroa, K. Rasmussen, and F. Jacobsen, “The acoustic center of laboratory standard microphones,” *J. Acoust. Soc. Am.* **120**, 2668–2675 (2006).
- [25] K. A. Cunefare, V. B. Biesel, J. Tran, R. Rye, A. Graf, M. Holdhusen, and A.-M. Albanese, “Anechoic chamber qualification: Traverse method, inverse square law analysis method, and nature of test signal,” *J. Acoust. Soc. Am.* **113**, 881–892 (2003).

- [26] *ISO 3745:2012: Acoustics – Determination of sound power levels and sound energy levels of noise sources using sound pressure – Precision methods for anechoic rooms and hemianechoic rooms* (International Organization for Standardization, Geneva, 2012).
- [27] D. Deboy, “Acoustic centering and rotational tracking in surrounding spherical microphone arrays,” Master’s thesis, Institute of Electronic Music and Acoustics, University of Music and Performing Arts, Graz, Austria (2010).
- [28] I. Ben Hagai, M. Pollow, M. Vorländer, and B. Rafaely, “Acoustic centering of sources measured by surrounding spherical microphone arrays,” *J. Acoust. Soc. Am.* **130**, 2003–2015 (2011).
- [29] N. R. Shabtai and M. Vorländer, “Acoustic Centering of Sources with Higher-Order Radiation Patterns,” *J. Acoust. Soc. Am.* **137**, 1947–1961 (2015).
- [30] J. Meyer, *Acoustics and the Performance of Music: Manual for Acousticians, Audio Engineers, Musicians, Architects, and Musical Instrument Makers*, 5 ed. (Springer Science+Business Media, New York, New York, 2009).
- [31] F. Zotter, “Analysis and Synthesis of Sound-Radiation with Spherical Arrays,” Doctoral Dissertation, Institute of Electronic Music and Acoustics University of Music and Performing Arts (2009).
- [32] N. R. Shabtai, G. Behler, M. Vorländer, and S. Weinzierl, “Generation and analysis of an acoustic radiation pattern database for forty-one musical instruments,” *J. Acoust. Soc. Am.* **141**, 1246–1256 (2017).
- [33] *AES56-2008 (r2019): AES standard on acoustics - Sound source modeling - Loudspeaker polar radiation measurements* (Audio Engineering Society, New York, New York, 2019).

- [34] T. Grothe and M. Kob, “High resolution 3D radiation measurements on the bassoon,” In *Proceedings ISMA*, pp. 139–145 (Detmold, Germany, 2019).
- [35] D. W. Martin, “Directivity and the Acoustic Spectra of Brass Wind Instruments,” *J. Acoust. Soc. Am.* **13**, 309–313 (1942).
- [36] G. Weinreich, “Directional tone color,” *J. Acoust. Soc. Am.* **101**, 2338–2346 (1997).
- [37] L. M. Wang and C. B. Burroughs, “Acoustic radiation from bowed violins,” *J. Acoust. Soc. Am.* **110**, 543–555 (2001).
- [38] S. D. Bellows, C. M. Pincock, J. K. Whiting, and T. W. Leishman, “Directivity,” Brigham Young University ScholarsArchive (2019).
- [39] G. R. Plitnik and W. J. Strong, “Numerical method for calculating input impedances of the oboe,” *J. Acoust. Soc. Am.* **65**, 816–825 (1979).
- [40] A. Chaigne and J. Kergomard, *Acoustics of Musical Instruments* (Springer New York, 2016).
- [41] *ANSI S1.1-1994 (r2004): American National Standard Acoustical Terminology* (American National Standards Institute, Inc., 2004).
- [42] *IEC 61094-3: Electroacoustics-Measurement microphones-Part 3: Primary method for free-field calibration of laboratory standard microphones by the reciprocity technique* (International Electrotechnical Commission (IEC), 2016).
- [43] G. R. Hruska and W. Koidan, “Free-field method for sound-attenuation measurement,” *J. Acoust. Soc. Am.* **58**, 507–509 (1975).
- [44] D. Deboy and F. Zotter, “Tangential intensity algorithm for acoustic centering,” In *Proceedings of the 37th German Annual Conference on Acoustics (DAGA 2011)*, pp. 321–322 (Düsseldorf, Germany, 2011).

- [45] M. S. Ureda, "Apparent apex theory," In *Audio Engineering Society Convention 61*, (1978).
- [46] M. S. Ureda, "Apparent apex revisited," In *Audio Engineering Society Convention 90*, (1991).
- [47] M. S. Ureda, "Apparent apex, Part III: The three-dimensional case," In *Audio Engineering Society Convention 91*, (1991).
- [48] W. J. Trott, "Effective acoustic center redefined," *J. Acoust. Soc. Am.* **62**, 468–469 (1977).
- [49] F. Jacobsen, S. B. Figueroa, and K. Rasmussen, "A note on the concept of acoustic center," *J. Acoust. Soc. Am.* **115**, 1468 – 1473 (2004).
- [50] J. Cox, "Physical limitations on free-field microphone calibration," Doctoral dissertation, Massachusetts Institute of Technology (1954).
- [51] K. Rasmussen, "Acoustic centre of condenser microphones," The Acoustics Laboratory, Technical University of Denmark, Report No. 5 (1973).
- [52] *ANSI S1.10-1966: Method for calibration of microphones* (American National Standards Institute Inc., 1966).
- [53] S. Morita, N. Kyono, S. Sakai, T. Yamabuchi, and Y. Kagawa, "Acoustic radiation of a horn loudspeaker by the finite element method—A consideration of the acoustic characteristic of horns," *J. Audio Eng. Soc.* **28**, 482–489 (1980).
- [54] J. Vanderkooy, "The acoustic center: A new concept for loudspeakers at low frequencies," In *Audio Engineering Society Convention 121*, (2006).
- [55] J. Vanderkooy and D. Henwood, "Polar plots for low frequencies: The acoustic centre," In *Audio Engineering Society Convention 120*, (Paris, France, 2006).

- [56] J. Vanderkooy, "Applications of the acoustic centre," In *Audio Engineering Society Convention 122*, (2007).
- [57] J. Vanderkooy, "The low-frequency acoustic center: Measurement, theory, and application," In *Audio Engineering Society Convention 128*, (2010).
- [58] R. M. Aarts and A. J. E. M. Janssen, "Comparing sound radiation from a loudspeaker with that from a flexible spherical cap on a rigid sphere," *J. Audio Eng. Soc.* **59**, 201 (2011).
- [59] E. G. Williams, *Fourier Acoustics: Sound Radiation and Nearfield Acoustical Holography* (Academic Press, London, 1999).
- [60] P. M. Morse and K. U. Ingard, *Theoretical Acoustics* (Princeton University Press, 1968).
- [61] T. Martin and A. Roure, "Optimization of an active noise control system using spherical harmonics expansion of the primary field," *J. Sound Vib.* **201**, 577–593 (1997).
- [62] A. D. Pierce, *Acoustics* (Springer International Publishing, 2019).
- [63] M. A. Gerzon, "Maximum directivity factor of n th-order transducers," *J. Acoust. Soc. Am.* **60**, 278–280 (1976).
- [64] A. H. Meyer and J. Meyer, "The Directivity and Auditory Impressions of Singers," *Acustica* **58**, 130–140 (1985).
- [65] J. Weinberger, H. F. Olson, and F. Massa, "A Uni-Directional Ribbon Microphone," *J. Acoust. Soc. Am.* **5**, 139–147 (1933).
- [66] W. Williams, N. G. Parke, D. A. Moran, and C. H. Sherman, "Acoustic Radiation from a Finite Cylinder," *J. Acoust. Soc. Am.* **36**, 2316–2322 (1964).

- [67] E. A. G. Shaw, “Transformation of sound pressure level from the free field to the eardrum in the horizontal plane,” *J. Acoust. Soc. Am.* **56**, 1848–1861 (1974).
- [68] H. Møller, M. F. Sørensen, D. Hammershøi, and C. B. Jensen, “Head-related transfer functions of human subjects,” *J. Audio Eng. Soc.* **43**, 300–321 (1995).
- [69] V. P. Sivonen and W. Ellermeier, “Directional loudness in an anechoic sound field, head-related transfer functions, and binaural summation,” *J. Acoust. Soc. Am.* **119**, 2965–2980 (2006).
- [70] T. M. Dunster, in *NIST Handbook of Mathematical Functions*, F. W. J. Olver, D. W. Lozier, R. F. Boisvert, and C. W. Clark, eds., (Cambridge University Press, New York, 2010).
- [71] E. Skudrzyk, *The Foundations of Acoustics* (Springer-Verlag, New York, 1971).
- [72] S. D. Bellows and T. W. Leishman, “Modeling musician diffraction and absorption for artificially excited clarinet directivity measurements,” *Proc. Mtgs. Acoust.* **46**, 035002 (2022).
- [73] M. M. Makoto Otani, Haruki Shigetani and R. Matsuda, “Binaural Ambisonics: Its optimization and applications for auralization,” *Acoustic Science and Technology* (2020).
- [74] N. H. Laurent Bouchet, Thierry Loyau and C. Boisson, “Calculation of acoustic radiation using equivalent-sphere methods,” *J. Acoust. Soc. Am.* **107**, 2387–2397 (2000).
- [75] S. F. Wu, *The Helmholtz Equation Least Squares Method: For Reconstructing and Predicting Acoustic Radiation* (Springer, New York, New York, 2015).
- [76] T. Rother and S. C. Hawkins, “Notes on Rayleigh’s hypothesis and the extended boundary condition method,” *J. Acoust. Soc. Am.* **149**, 2179–2188 (2021).
- [77] B. Rafaely, *Fundamentals of Spherical Array Processing* (Springer-Verlag, Berlin Heidelberg, 2015), Vol. 8.

- [78] S. D. Bellows and T. W. Leishman, “Spherical harmonic expansions of high-resolution musical instrument directivities,” *Proc. Mtgs. Acoust.* 35, 035005 (2018).
- [79] R. D. Gregory, *Classical Mechanics* (Cambridge University Press, Cambridge, England, 2006).
- [80] G. W. Elko, “An acoustic vector-field probe with calculable obstacle bias,” In *NOISE-CON 91 Proceedings*, pp. 525–527 (1991).
- [81] S. Bellows and T. W. Leishman, “Effect of Head Orientation on Speech Directivity,” In *Proc. Interspeech 2022*, pp. 246–250 (2022).
- [82] S. D. Bellows and T. W. Leishman, “Acoustic source centering of musical instrument directivities using acoustical holography,” *Proc. Mtgs. Acoust.* **42**, 055002 (2020).
- [83] G. Weinreich, “Sound hole sum rule and the dipole moment of the violin,” *J. Acoust. Soc. Am.* **77**, 710–718 (1985).
- [84] D. Davis, E. Patronis, and P. Brown, *Sound System Engineering*, 4 ed. (Focal Press, New York, 2013).
- [85] S. Feistel, “Modeling the radiation of modern sound reinforcement systems in high resolution,” Doctoral Dissertation, RWTH Aachen University (2014).
- [86] J. Escolano, J. J. López, and B. Pueo, “Directive sources in acoustic discrete-time domain simulations based on directivity diagrams,” *J. Acoust. Soc. Am.* **121**, EL256–EL262 (2007).
- [87] S. Bilbao, J. Ahrens, and B. Hamilton, “Incorporating source directivity in wave-based virtual acoustics: Time-domain models and fitting to measured data,” *J. Acoust. Soc. Am.* **146**, 2692–2703 (2019).

- [88] S. D. Bellows and T. W. Leishman, “Modeling and measurements of organ pipe sound radiation,” In *Proceedings of the 24th International Congress on Acoustics*, (Gyeongju, South Korea, 2022).
- [89] P. A. Northrop, “Problems in the Analysis of the Tone of an Open Organ Pipe,” *J. Acoust. Soc. Am.* **12**, 90–94 (1940).
- [90] M. Pollow, G. Behler, and M. Vorländer, “Post-processing and center adjustment of measured directivity data of musical instruments,” In *Proceedings Acoustics 2012*, pp. 767–771 (Nantes, France, 2012).
- [91] W. C. Chew, *Waves and Fields in Inhomogeneous Media*, 1 ed. (Wiley-IEEE, New York, 1999), pp. 593–599.
- [92] L. Savioja and U. P. Svensson, “Overview of geometrical room acoustic modeling techniques,” *J. Acoust. Soc. Am.* **138**, 708–730 (2015).
- [93] D. Deboy and F. Zotter, “Comparison of acoustic centering maps for radiation capture of musical instruments with spherical microphone arrays,” In *Proceedings of the 36th German Annual Conference on Acoustics (DAGA 2010)*, pp. 705–706 (Berlin, Germany, 2010).
- [94] T. K. Moon and W. C. Stirling, *Mathematical Methods and Algorithms for Signal Processing* (Prentice Hall, 2000).
- [95] G. Strang, *Linear Algebra and Learning from Data* (Wellesley-Cambridge Press, 2019).
- [96] CLF Group, “CLF: A common loudspeaker format,” *Syn-Aud-Con Newsl.* **32**, 14–17 (2004).
- [97] *GLL Loudspeaker File Format* (Ahnert Feistel Media Group, 2021).
- [98] S. D. Bellows, D. T. Harwood, K. L. Gee, and T. W. Leishman, “Low-frequency directional characteristics of a gamelan gong,” *Proceedings of Meetings on Acoustics* **50**, 035003 (2022).

- [99] M. C. Vigeant, L. M. Wang, and J. H. Rindel, “Investigations of orchestra auralizations using the multi-channel multi-source auralization technique.,” *Acta Acustica united with Acustica* **94**, 866–882 (2008).
- [100] M. Noistering, F. Zotter, R. Desmonet, and W. Ritsch, “Preserving sound source radiation-characteristics in network-based musical performances.,” In *Fortschritte der Akustik, DAGA*, (Düsseldorf, 2011).
- [101] G. Behler, M. Pollow, and M. Vorländer, “Measurements of musical instruments with surrounding spherical arrays,” In *Proceedings Acoustics 2012*, pp. 761–765 (Nantes, France, 2012).
- [102] I. Bork, H. Marshall, and J. Meyer, “Zur Abstrahlung des Anschlaggeräusches beim Flügel,” *Acustica* **81**, 300–308 (1995).
- [103] B. M. Shafer, “Error Sensor Placement for Active Control of an Axial Cooling Fan,” Master’s thesis, Brigham Young University (2007).
- [104] J.-L. Le Carrou, Q. Leclere, and F. Gautier, “Some characteristics of the concert harp’s acoustic radiation,” *J. Acoust. Soc. Am.* **127**, 3203–3211 (2010).
- [105] J. Štěpánek and Z. Otčenášek, “Sound Directivity Spectral Spaces of Violins,” In *Proc. ISMA 2001*, (Perugia, 2001).
- [106] A. Pérez Carrillo, J. Bonada, J. Pätynen, and V. Välimäki, “Method for measuring violin sound radiation based on bowed glissandi and its application to sound synthesis,” *J. Acoust. Soc. Am.* **130**, 1020–1029 (2011).
- [107] D. F. C. na, S. M. Cervera, T. Takeuchi, and K. Holland, “Measuring musical instruments directivity patterns with scanning techniques,” In *Proceedings of the 19th International Congress on Sound and Vibration*, (Vilnius, Lithuania, 2012).

- [108] W. H. Peirce, “Numerical integration over the spherical shell,” *Mathematics of Computation* **11**, 244–249 (1957).
- [109] K. Atkinson and W. Han, *Spherical Harmonics and Approximations on the Unit Sphere: An Introduction* (Springer Berlin Heidelberg, 2012).
- [110] M. J. Evans, J. A. Angus, and A. I. Tew, “Analyzing head-related transfer function measurements using surface spherical harmonics,” *J. Acoust. Soc. Am.* **104**, 2400–2411 (1998).
- [111] B. Bernschütz, “A spherical far field HRIR/HRTF compilation of the Neumann KU100,” *Proceedings of the 40th Italian (AIA) Annual Conference on Acoustics and the 39th German Annual Conference on Acoustics (DAGA)* (2013).
- [112] V. Shukowsky, “A quadrature formula over the sphere with applications to high resolution spherical harmonic analysis,” *Bulletin geodesique* **60**, 1–14 (1986).
- [113] J. R. Driscoll and D. M. Healy, “Computing fourier transforms and convolutions on the 2-sphere,” *Advances in Applied Mathematics* **15**, 202–250 (1994).
- [114] R. Kennedy and P. Sadeghi, *Hilbert Space Methods in Signal Processing* (Cambridge University Press, 2013).
- [115] D. Healy, D. Rockmore, P. Kostelec, and S. Moore, “FFTs for the 2-Sphere-Improvements and Variations,” *Journal of Fourier Analysis and Applications* **9**, 340–385 (2003).
- [116] J. C. Mason and D. C. Handscomb, *Chebyshev Polynomials* (Chapman and Hall/CRC, 2003).
- [117] J. P. Imhof, “On the method for numerical integration of Clenshaw and Curtis,” *Numer. Math.* **5**, 138–141 (1963).
- [118] L. N. Trefethen, “Is Gauss Quadrature Better than Clenshaw–Curtis?,” *SIAM Review* **50**, 67–87 (2008).

- [119] C. W. Clenshaw and C. R. Curtis, “A method for numerical integration on an automatic computer,” *Numer. Math.* **2**, 197–205 (1960).
- [120] I. H. Sloan and W. E. Smith, “Product integration with the Clenshaw–Curtis and related points: Convergence properties,” *Numer. Math.* **30**, 415–428 (1978).
- [121] M. Alkmim, J. Cardenuto, E. Tengan, T. Dietzen, T. Van Waterschoot, J. Cuenca, L. De Ryck, and W. Desmet, “Drone noise directivity and psychoacoustic evaluation using a hemispherical microphone array,” *J. Acoust. Soc. Am.* **152**, 2735–2745 (2022).
- [122] M. R. Bai, “Application of BEM (boundary element method)-based acoustic holography to radiation analysis of sound sources with arbitrarily shaped geometries,” *J. Acoust. Soc. Am.* **92**, 533–549 (1992).
- [123] C. W. Horton and G. S. Innis, “The computation of far-field radiation patterns from measurements made near the source,” *J. Acoust. Soc. Am.* **33**, 877–880 (1961).
- [124] M. Bru, “Cylinder measurement method for directivity balloons,” In *Audio Engineering Society Convention 149*, (2020).
- [125] J. Pätynen and T. Lokki, “Directivities of Symphony Orchestra Instruments,” *Acta acustica united with acustica* **96**, 138–167 (2010).
- [126] S. Weinzierl *et al.*, “A Database of Anechoic Microphone Array Measurements of Musical Instruments,” (2017).
- [127] H. Ghasemi, “Directivity Measurement of Santur Instrument,” In *Proceedings of the 19th International Congress on Sound and Vibration*, pp. 3120–3124 (Vilnius, Lithuania, 2012).
- [128] N. McLachlan, “Finite element analysis and gong acoustics,” *Acoustics Australia* **25**, 103–107 (1997).

- [129] D. W. Krueger, K. L. Gee, and J. Grimshaw, “Acoustical and vibrometry analysis of a large Balinese gamelan gong,” *J. Acoust. Soc. Am.* **128**, EL8–EL13 (2010).
- [130] R. Perrin, D. P. Elford, L. Chalmers, G. M. Swallowe, T. R. Moore, S. Hamdan, and B. J. Halkon, “Normal modes of a small gamelan gong,” *J. Acoust. Soc. Am.* **136**, 1942–1950 (2014).
- [131] J. S. Bendat and A. G. Piersol, *Random Data: Analysis and Measurement Procedures*, 4 ed. (Wiley, Hoboken, NJ, 2010).
- [132] A. J. Berkhout, D. de Vries, and M. M. Boone, “A new method to acquire impulse responses in concert halls,” *J. Acoust. Soc. Am.* **68**, 179–183 (1980).
- [133] J. R. Driscoll and D. M. Healy, “Computing Fourier Transforms and Convolutions on the 2-Sphere,” *Advances in Applied Mathematics* **15**, 202–250 (1994).
- [134] S. Bellows and T. Leishman, “Single-channel sound power estimation for reverberation effects,” In *Audio Engineering Society Convention 149*, (2020).
- [135] S. D. Bellows and T. W. Leishman, “High-Resolution Analysis of the Directivity Factor and Directivity Index Functions of Human Speech,” In *Audio Engineering Society Convention 146*, (2019).
- [136] R. M. Aarts and A. J. E. M. Janssen, “On-axis and far-field sound radiation from resilient flat and dome-shaped radiators,” *J. Acoust. Soc. Am.* **125**, 1444–1455 (2009).
- [137] T. Mellow, “On the sound field of a resilient disk in an infinite baffle,” *J. Acoust. Soc. Am.* **120**, 90–101 (2006).
- [138] R. M. Aarts and A. J. E. M. Janssen, “Sound radiation from a resilient spherical cap on a rigid sphere,” *J. Acoust. Soc. Am.* **127**, 2262–2273 (2010).

- [139] G. Bissinger, E. G. Williams, and N. Valdivia, “Violin f-hole contribution to far-field radiation via patch near-field acoustical holography,” *J. Acoust. Soc. Am.* **121**, 3899–3906 (2007).
- [140] J. Meyer, “Die Richtcharakteristiken von Geigen [The directional characteristics of violins],” *Instrumentenbau-Zeitschrift* **18**, 275–281 (1964).
- [141] L. M. Wang and C. B. Burroughs, “Directivity Patterns of Acoustic Radiation from Bowed Violins,” *CASJ* **3**, 9–17 (1999).
- [142] F. Bozzoli, M. Viktorovitch, and A. Farina, “Balloons of Directivity of Real and Artificial Mouth Used in Determining Speech Transmission Index,” In *Audio Engineering Society 118*, (Barcelona, Spain, 2005).
- [143] J. Meyer, “Die Richtcharakteristiken von Oboen und Fagotten [The directional characteristics of oboes and bassoons],” *Das Musikinstrument* **15**, 958–964 (1966).
- [144] F. S. McKendree, “Directivity Indices of Human Talkers in English Speech,” Paper presented at Inter-Noise 86 Conference: Progress in Noise Control, Cambridge, USA pp. 911–916 (1986).
- [145] A. Moreno and J. Pretzschner, “Human Head Directivity in Speech Emission: A New Approach,” *Acoustics Letters* **1**, 78–84 (1978).
- [146] M. Kob, “Physical Model of the Singing Voice,” (2002).
- [147] B. F. Katz and C. D’Alessandro, “Directivity Measurements of the Singing Voice,” In *Proceedings of the 19th International Congress on Acoustics*, (Madrid, 2007).
- [148] D. Cabrera, P. J. Davis, and A. Connolly, “Long-term horizontal vocal directivity of opera singers: Effects of singing projection and acoustic environment,” *J. Voice* **25**, 291–303 (2011).

- [149] M. Brandner, R. Blandin, M. Frank, and A. Sontacchi, “A pilot study on the influence of mouth configuration and torso on singing voice directivity,” *J. Acoust. Soc. Am.* **148**, 1169–1180 (2020).
- [150] M. Vorländer, *Auralizations: Fundamentals of Acoustics, Modelling, Simulation, Algorithms and Acoustic Virtual Reality* (Springer Berlin, Heidelberg, 2008).
- [151] F. Bozzoli, P. Bilzi, and A. Farina, “Influence of artificialmouth’s directivity in determining Speech Transmission Index,” In *Audio Engineering Society 119*, (New York, New York, 2005).
- [152] T. Halkosaari, M. Vaalgamaa, and M. Karjalainen, “Directivity of Artificial and Human Speech,” *J. Audio Eng. Soc.* **53**, 620–631 (2005).
- [153] M. Kob, “Impact of Excitation and Acoustic Conditions on the Accuracy of Directivity Measurements,” In *Proceedings ISMA*, pp. 639–643 (Le Mans, France, 2014).
- [154] J. Meyer and K. Wogram, “Die Richtcharakteristiken des Hornes [The directional characteristics of the horn],” *Das Musikinstrument* **18**, I–X (1969).
- [155] J. Meyer, “Die Richtcharakteristiken von Klarinetten [The directional characteristics of clarinets],” *Das Musikinstrument* **14**, 21–25 (1965).
- [156] E. Maestre, G. P. Scavone, and J. O. Smith, “State-space modeling of sound source directivity: An experimental study of the violin and the clarinet,” *J. Acoust. Soc. Am.* **149**, 2768–2781 (2021).
- [157] P. R. Cook and D. Trueman, “Spherical Radiation from Stringed Instruments: Measured, Modeled, and Reproduced,” *CASJ* **3**, 8–14 (1999).

- [158] H. Vos, O. Warusfel, N. Misdariis, and D. de Vries, “Analysis and Reproduction of the frequency spectrum and directivity of a violin,” *J. Acoust. Soc. Neth.* pp. 1–11 (2003).
- [159] S. Berge, “Models for Vibration and Radiation of two stringed Instruments,” (1996).
- [160] J. Meyer, “Die Richtcharakteristiken des Flügels,” *Das Musikinstrument* **14**, 1085–1090 (1965).
- [161] B. David, “Vergleich der akustischen Richtwirkung des Konzertflügels Steinway D-274 mit und ohne "Klangspiegel",” Master’s thesis, Institute for Composition and Electroacoustics University of Music and Performing Arts (2010).
- [162] M. Kob and H. Jers, “Directivity measurement of a singer,” In *Collected papers from the joint meeting Berlin 1999: 137th regular meeting of the Acoustical Society of America, 2nd Convention of the European Acoustics Association, Forum Acusticum 1999, integrating the 25th German Acoustics DAGA Conference*,
- [163] P. Welch, “The use of fast Fourier transform for the estimation of power spectra: A method based on time averaging over short, modified periodograms,” *IEEE Trans. Audio Electroacoust.*, AU **15**, 70–73 (1967).
- [164] S. D. Bellows and T. W. Leishman, “A spherical beamforming algorithm for acoustic centering and phase correction of source directivities,” In *Proceedings of the 24th International Congress on Acoustics*, (Gyeongju, South Korea, 2022).
- [165] S. Bellows and T. W. Leishman, “Application of Hilbert space operators on the sphere to directivity measurements,” *J. Acoust. Soc. Am.* **146**, 2803–2803 (2019).
- [166] J. Meyer, “Die Richtcharakteristiken von Violoncelli [The directional characteristics of cellos],” *Instrumentenbau-Zeitschrift* **19**, 281–287 (1965).

- [167] J. Meyer, “Die Richtcharakteristiken von Bratschen und Kontrabässen [The directional characteristics of violas and double basses],” *Instrumentenbau-Zeitschrift* **21**, 3–5 (1967).
- [168] J. Meyer, “Directivity of the Bowed Stringed Instruments and its Effect on the Sound in Concert Halls,” *J. Acoust. Soc. Am.* **51**, 1994–2009 (1972).
- [169] D. F. C. na, S. M. Cervera, T. Takeuchi, and K. Holland, “Measuring under non stationary conditions with scanning techniques,” In *Proc. of Noise and Vibration: Emerging Methods 2*, (Sorrento, Italy, 2012).
- [170] N. J. Eyring, “Development and Validation of an Automated Directivity Acquisition System Used in the Acquisition, Processing, and Presentation of the Acoustic Far-Field Directivity of Musical Instruments in an Anechoic Space,” Master’s thesis, Brigham Young University (2013).
- [171] D. Ackermann, C. Böhm, F. Brinkmann, and S. Weinzierl, “The Acoustical Effect of Musicians’ Movements During Musical Performances,” *Acta Acustica United with Acustica* **105**, 365–367 (2019).
- [172] S. Feistel and W. Ahnert, “The significance of phase data for the acoustic prediction of combinations of sound sources,” In *Audio Engineering Society Convention 119*, (2005).
- [173] N. H. Fletcher and T. D. Rossing, *The Physics of Musical Instruments* (Springer New York, 1998).
- [174] M. Greenspan, “Piston radiator: Some extensions of the theory,” *J. Acoust. Soc. Am.* **65**, 608 (1979).
- [175] P. M. Morse, *Vibration and Sound, International Series in Pure & Applied Physics*, 2 ed. (McGraw-Hill, New York, NY, 1948).

- [176] A. Lindberg and G. Pavić, “Computation of sound radiation by a driver in a cabinet using a substitute source approach,” *J. Acoust. Soc. Am.* **138**, 1132–1142 (2015).
- [177] J. L. Butler, “Solution of Acoustical-Radiation Problems by Boundary Collocation,” *J. Acoust. Soc. Am.* **48**, 325–336 (1970).
- [178] C. C. Gerding and W. Thompson, “Axisymmetric spherical radiator with mixed boundary conditions,” *J. Acoust. Soc. Am.* **61**, 313–317 (1977).
- [179] A. M. Pasqual and V. Martin, “On the acoustic radiation modes of compact regular polyhedral arrays of independent loudspeakers,” *J. Acoust. Soc. Am.* **130**, 1325–1336 (2011).
- [180] J. Mortensen, “Computing the directivities of Platonic-solid loudspeakers,” 2014.
- [181] M. T. Neal and M. C. Vigeant, “A Compact Spherical Loudspeaker Array for Efficiently Recreating Instrument Directivities,” *J. Audio Eng. Soc.* **68**, 796–809 (2020).
- [182] J. W. Miles, “Scattering by a Spherical Cap,” *J. Acoust. Soc. Am.* **50**, 892–903 (1971).
- [183] G. Elias and P. Malbéqui, “Scattering by an open sphere: Exact solution and comparison with a boundary integral method,” *J. Acoust. Soc. Am.* **93**, 609–616 (1993).
- [184] A. Nosich, “The method of analytical regularization in wave-scattering and eigenvalue problems: foundations and review of solutions,” *IEEE Antennas and Propagation Magazine* **41**, 34–49 (1999).
- [185] E. D. Vinogradova, “Axisymmetric acoustic oscillations of a rigid spherical shell with two symmetric circular apertures,” *Journal of Sound and Vibration* **503**, 116115 (2021).
- [186] E. A. G. Shaw, “Cavity resonance in the violin: Network representation and the effect of damped and undamped rib holes,” *J. Acoust. Soc. Am.* **87**, 398–410 (1990).

- [187] *Boundary element acoustics: Fundamentals and computer codes* (WIT Press, Southampton, England, 2000).
- [188] A. J. Burton and G. F. Miller, “The Application of Integral Equation Methods to the Numerical Solution of Some Exterior Boundary-Value Problems,” *Proceedings of the Royal Society of London. Series A, Mathematical and Physical Sciences* **323**, 201–210 (1971).
- [189] P. Filippi, “Layer potentials and acoustic diffraction,” *Journal of Sound and Vibration* **54**, 473–500 (1977).
- [190] T. W. Wu and G. C. Wan, “Numerical modeling of acoustic radiation and scattering from thin bodies using a Cauchy principal integral equation,” *J. Acoust. Soc. Am.* **92**, 2900–2906 (1992).
- [191] C. H. Sherman, “Mutual Radiation Impedance of Sources on a Sphere,” *J. Acoust. Soc. Am.* **31**, 947–952 (1959).
- [192] J. W. Strutt, *The Theory of Sound* (Cambridge University Press, 2011).
- [193] U. Ingard, “On the Theory and Design of Acoustic Resonators,” *J. Acoust. Soc. Am.* **25**, 1037–1061 (1953).
- [194] I. Corbett and D. Scarrett, *Mic It!: Microphones, Microphone Techniques, and Their Impact on the Final Mix* (Taylor and Francis Group, 2014).
- [195] D. M. Huber and R. E. Runstein, *Modern Recording Techniques*, 9 ed. (Routledge, 2018).
- [196] M. Clark, D. Luce, R. Abrams, H. Schlossberg, and J. Rome, “Preliminary Experiments on the Aural Significance of Parts of Tones of Orchestral Instruments and on Choral Tones,” *J. Audio Eng. Soc.* **11**, 45–54 (1963).
- [197] J. B. Lee, “Far-Field Placement of Mono Microphones,” *J. Audio Eng. Soc.* **25**, 38 (1977).

- [198] *EC 60050-801:1994: International Electrotechnical Vocabulary-Part 801: Acoustics and Electroacoustics*, 2 ed. (International Electrotechnical Commission, 2018).
- [199] *ISO 3741:2010: Acoustics – Determination of sound power levels and sound energy levels of noise sources using sound pressure – Precision methods for reverberation test rooms*. (International Organization for Standardization, Geneva, 2010).
- [200] H. Fastl and E. Zwicker, *Psychoacoustics-Facts and Models* (Springer, Berlin, Heidelberg, 2007).
- [201] D. B. Nutter, T. W. Leishman, S. D. Sommerfeldt, and J. D. Blotter, “Measurement of Sound Power and Absorption in Reverberation Chambers Using Energy Density,” *J. Acoust. Soc. Am.* **121**, 2700–2710 .
- [202] H. F. Hopkins and N. R. Stryker, “A proposed loudness-efficiency rating for loudspeakers and the determination of system power,” In *Proc. IRE*, **36**, 315–335 (1948).
- [203] A. V. Oppenheim and R. W. Schaffer, *Discrete-Time Signal Processing* (Prentice Hall, 2010).
- [204] M. R. Schroeder, “Statistical Parameters of the Frequency Response Curves of Large Rooms,” *J. Audio. Eng. Soc.* **35**, 299–306 (1987).
- [205] M. R. Schroeder and K. H. Kuttruff, “On Frequency Response Curves in Rooms. Comparison of Experimental, Theoretical, and Monte Carlo Results for the Average Frequency Spacing Between Maxima,” *J. Acoust. Soc. Am.* **34**, 76–80 (1962).
- [206] M. Kleiner and J. Tichy, *Acoustics of Small Rooms* (CRC Press, 2014).
- [207] B. Xu, S. D. Sommerfeldt, and T. W. Leishman, “Generalized acoustic energy density,” *J. Acoust. Soc. Am.* **130**, 1370–1380 (2011).

-
- [208] D. R. Marquez, “Estimating the Acoustic Power of Sources in Nonideal Enclosures Using Generalized Acoustic Energy Density,” Master’s thesis, Brigham Young University (2014).
- [209] K. D. Marshall, “Modal analysis of a violin,” *J. Acoust. Soc. Am.* **77**, 695–709 (1985).
- [210] *ANSI/ASA S3.4-2007 (R2017): Procedure for the Computation of Loudness of Steady Sounds (Includes Loudness Program)* (American National Standards Institute Inc., Washington, D.C., 2007).
- [211] *ISO 532-1:2017: Acoustics-Methods for calculating loudness-Part 1: Zwicker Method* (International Organization for Standardization, Geneva, Switzerland, 2017).
- [212] *ISO 532-2:2017: Acoustics-Methods for calculating loudness-Part 2: Moore-Glasberg method* (International Organization for Standardization, Geneva, Switzerland, 2017).